

Wrocław University of Science and Technology  
Faculty of Environmental Engineering

**INTERMITTENCY, SCALES, AND EXTREMES  
IN URBAN PRECIPITATION**

*Nieciągłość, skalowanie i ekstrema w opadach miejskich*

A dissertation presented  
by  
**DAGMARA SELENA DŻUGAJ**

Dissertation supervisor:  
**Prof. Paweł Licznar**  
**Wrocław University  
of Science and Technology**

Auxiliary supervisor:  
**Prof. Carlo de Michele**  
**Politecnico di Milano**

Wrocław, Poland

2017

*From where we stand the rain seems random.  
If we could stand somewhere else, we would see the order in it.*

Tony Hillerman

*Autorka składa serdeczne podziękowania i wyrazy wdzięczności dla Promotora dr hab. inż. Pawła Licznara, prof. nadzw. PWr za cierpliwość, wyrozumiałość i wsparcie okazane podczas pisania rozprawy.*

*Szczególne podziękowania kierowane są również dla MPWiK w Warszawie za możliwość wykorzystania danych do celów naukowych z unikalnej w skali Europy sieci 25 deszczomierzy.*

*Acknowledgements:*

This doctoral dissertation was financed with the support from the Polish National Science Centre (NCN) funds allocated on the basis of decision no. 2011/03/B/ST10/06338 as part of the scientific project: *Spatiotemporal analysis and modelling of urban precipitation field*.

Precipitation data was provided by the Municipal Water Supply and Sewerage Company (MPWiK m.st. Warszawa) in Warsaw, Poland.

## Table of contents

Table of contents .....	4
Summary .....	5
1. Introduction.....	10
2. The aim and scope of the thesis .....	15
3. Precipitation process .....	17
3.1 Precipitation measurements.....	17
3.2 Error in precipitation measurements.....	22
4. The rainfall data and the research field .....	24
4.1 Warsaw climatic conditions .....	24
4.2 Warsaw precipitation conditions .....	25
4.3 Guidelines for the location of precipitation stations in urban areas.....	26
4.3.1 Observation scales .....	26
4.3.2 Classes of representativeness .....	29
4.4 Warsaw rain gauge network .....	31
5. Fractal geometry .....	36
5.1 Fractal dimension .....	36
5.2 Box counting method .....	38
6. Multifractals.....	39
6.1 Properties of multifractals .....	39
6.2 Classification of multifractals.....	42
6.3 Box counting method in multifractals .....	44
6.4 Spectral density analysis .....	44
6.5 Functional box-counting method.....	46
6.6 Trace moment method (TM) .....	47
6.7 Probability distribution/multiple scaling (PDMS).....	49
6.8 Double trace moment method (DTM).....	49
6.9 Universal multifractal parameters .....	50
6.10 Hierarchical analysis .....	54
6.11 Universal multifractal generator .....	55
6.12 Evaluation of generated rainfall time series .....	57
7. Results and discussion .....	59
7.1 Functional box-counting method.....	59
7.2 Spectral density analysis .....	65
7.3 Trace moment method (TM) .....	77
7.4 Probability distribution/multiple scaling (PDMS).....	80
7.5 Multifractal exponent functions .....	82
7.6 Double trace moment method (DTM).....	87
7.7 Universal multifractal parameters .....	93
7.8 Universal multifractal generators .....	98
7.8.1. Synthetic precipitation time series .....	99
7.8.2. Evaluation of generated synthetic precipitation time series.....	101
8. Summary and final conclusions .....	118
9. List of appendices .....	121
List of references .....	122
List of web pages.....	130
List of figures and tables .....	131
List of symbols and abbreviations .....	135

## Summary

Precipitation phenomena exhibit highly non-linear properties and strong intensity differentiation across both spatial and temporal scales. The complex space-time distribution of precipitation determines the course of the no less complicated phenomenon of surface runoff. It is particularly visible in urban areas where, due to a large share of watertight surfaces, the response of catchment to rainfall impulse is particularly violent. Rapid drainage of rain water from sealing surfaces and its concentration in drainage systems results in increasingly unfavorable phenomena of urban floods. In recent years, the frequency and extent of urban floods and sewage overflows has been increasing in many cities in Poland and the world. The reason for this is the rapid seal of urban surfaces and climate changes resulting in the intensification of precipitation processes.

Solving the problems of urban floods and sewage overflows requires engineers to use a modern hydrodynamic modeling workshop. According to current European sewage standard EN 752, the application of computer simulation models within urban centers handled by extensive and complex drainage systems is indispensable. However, the development of the hydrodynamic model alone is not sufficient in executing the proper verifications, and access to reliable precipitation data is required. There should be a locally-measured rainfall series in high time resolution with the range of single minutes from a lengthy period of around 30 years of observation. Obviously, access to this class of precipitation data in Poland is very limited. Moreover, in modern engineering practice, it is considered correct to model very large urban drainage systems based on precipitation data from single rain gauges, often located in city suburbs (e.g. airports). This raises questions and doubts. Firstly, how reliable is the use of data from a single rain gauge? Are the frequencies of storm sewer overflows obtained from a series of hydrodynamic simulations statistically correct? In the case of an absence of local observation data, is it possible to generate synthetic precipitation data using random cascades? Finally, in domestic conditions, can we use continuous and easy to set up generators based on the universal multifractal model?

Accordingly, the subject of this dissertation is a comprehensive analysis of fractal and multifractal properties of 1-minute precipitation data recorded on a unique nationwide research field, in the form of a network of 25 electronic rain gauges, property of the Municipal Water Supply and Sewerage Company (MPWiK) in Warsaw. Scaling properties, precipitation intermittencies, and occurrences of extremes in the data series of individual rain gauges for a time scale of 1 minute to over 11 days are investigated using a spectral density

analysis of the time series of rainfall intensity, functional box-counting method, trace moment method, probability distribution/multiple scaling, and double trace moment method.

As a result, the universal multifractal parameters  $\alpha$ ,  $C_1$  and  $H$  (so called Lévy stochastic variables) are estimated for all 25 rain gauges. Subsequently, the universal multifractal parameters are subject to cluster analysis in order to identify groups of similar precipitation gauges. Along these lines, the parameters derived for specific Warsaw rain gauges or clusters of gauges displaying similarities, are used to generate synthetic precipitation series by means of continuous universal random cascade models. The statistical evaluation is carried out of the generated synthetic precipitation time series performed by comparing complementary cumulative distribution function ( $P(R>r)$ ) and the intermittency ( $Ep_0$ ) calculated for synthetic vs. observed time series. As a last step of research, a special filtering algorithm is proposed in order to correct intermittency characteristics of synthetic precipitation time series.

Based on the performed studies, the time structure of the recorded Warsaw precipitation time series is found to be a multifractal set characterized by scale-invariant behaviour over a wide range of scales. Furthermore, it has been observed that the clear majority of Warsaw rain gauges, except for two specific stations (airport and suburbs), have a distinct similarity of multifractal properties of recorded precipitation series, manifested by similar values of universal multifractal parameters  $\alpha$ ,  $C_1$  and  $H$ .

It has also been demonstrated that, for the first time in Poland, the universal continuous cascades could be used in practice for generation of synthetic rainfall series of fine temporal resolution for Warsaw. There is also a possibility of practical parameterization of the cascade generator itself by only two multifractal parameters  $\alpha$  and  $C_1$ . At the same time, the need to use a filter algorithm to improve the structure of generated time series in terms of precipitation intermittency has been noted.

In the summary, there exists a large potential of the developed continuous random cascade models based on universal multifractal models in generating high-resolution precipitation time series for purposes of urban hydrology.

*Key words:*

Rainfall time series, urban hydrology, scale invariance, intermittency, multifractal parameters, universal multifractal model.

## Streszczenie

Opady atmosferyczne charakteryzują się nieciągłością i silnym zróżnicowaniem natężeń zarówno w skalach przestrzennych jak i czasowych. Skomplikowany czasoprzestrzennie rozkład opadów determinuje przebieg nie mniej skomplikowanego zjawiska spływu powierzchniowego. Jest to szczególnie zauważalne na obszarach miejskich, gdzie przy dużym udziale powierzchni nieprzepuszczalnych odpowiedź zlewni na impuls opadowy jest szczególnie gwałtowna. Szybki odpływ wód opadowych z powierzchni utwardzonych i ich koncentracja w systemach odwodnienia skutkuje coraz częściej niekorzystnymi zjawiskami podtopień i powodzi miejskich. W ostatnich latach można mówić o zwiększaniu się częstości podtopień i powodzi miejskich, a także zwiększaniu się ich zasięgu w wielu miastach w Polsce i na świecie. Jako przyczyny tego procesu uznaje się szybki proces uszczelniania powierzchni miast oraz zmiany klimatyczne skutkujące wzmożeniem procesów opadowych.

Rozwiązywanie problemów podtopień i powodzi miejskich wymaga od inżyniera stosowania nowoczesnego warsztatu modelowania hydrodynamicznego. Zgodnie z aktualną europejską normą kanalizacyjną EN 752, w obrębie centrów miast obsługiwanych przez rozległe i skomplikowane systemy odwodnienia, nieodzowne jest stosowanie komputerowych modeli symulacyjnych. Samo jednak opracowanie modelu hydrodynamicznego nie jest wystarczające, jako że dla przeprowadzenia serii symulacji konieczny jest dostęp do wiarygodnych danych opadowych. Winny to być lokalne szeregi opadowe o wysokiej rozdzielczości czasowej rzędu pojedynczych minut, z długiego okresu rzędu około 30 lat obserwacji. W sposób oczywisty dostęp do tej klasy danych opadowych w Polsce jest bardzo ograniczony. Ponadto we współczesnej praktyce inżynierskiej przyjmuje się za prawidłowe modelowanie nawet bardzo dużych, rozległych miejskich systemów odwodnienia w oparciu o dane opadowe pochodzące z pojedynczych deszczomierzy, często zlokalizowanych na przedmieściach miasta (np. na pobliskim lotnisku). Sytuacja ta rodzi pytania i wątpliwości. Po pierwsze na ile wiarygodne jest stosowanie danych z pojedynczego deszczomierza? Czy otrzymywane w wyniku serii symulacji hydrodynamicznych częstości nadpiętnień kanalizacji deszczowych są statystycznie poprawne? Czy przy braku dostępności lokalnych danych obserwacyjnych, możliwe jest generowanie syntetycznych danych opadowych z użyciem kaskad losowych? Na koniec, czy można w warunkach krajowych stosować w praktyce w tym celu ciągłe i łatwe w parametryzacji generatory oparte o uniwersalny model multifraktalny?

W związku z powyższym, przedmiotem niniejszej rozprawy jest w pierwszym rzędzie kompleksowa analiza właściwości fraktalnych i multifraktalnych 1-minutowych szeregów opadowych zarejestrowanych na unikalnym w skali kraju poligonie badawczym, w postaci sieci 25 elektronicznych deszczomierzy, należących do MPWiK w Warszawie. Badania właściwości skalowych, nieciągłości opadów oraz występowania ekstremów w szeregach opadowych z poszczególnych deszczomierzy przeprowadzono dla skal czasowych odpowiadających czasom w przedziale od 1 minuty do 11 dni, z wykorzystaniem warsztatu analizy widmowej szeregów czasowych natężeń deszczów, metody funkcyjnego zliczania pudełek, metody prawdopodobieństwa/wielokrotnego skalowania, metody momentu śladu oraz metody podwójnego momentu śladu.

W wyniku całościowej analizy otrzymanych wyników oszacowano uniwersalne parametry multifraktalne  $\alpha$ ,  $C_1$  i  $H$  (tzw. zmienne stochastyczne Lévy'ego) dla wszystkich 25 deszczomierzy. Zbiór uniwersalnych parametrów multifraktalnych poddano analizie skupień w celu identyfikacji grup deszczomierzy o podobnych własnościach. Uniwersalne parametry multifraktalne charakterystyczne dla specyficznych deszczomierzy lub też grup deszczomierzy wykazujących wzajemne podobieństwo, wykorzystywano do generowania syntetycznych szeregów opadowych przy użyciu uniwersalnych modeli ciągłych kaskad losowych. Jakość generowanych szeregów syntetycznych została zweryfikowana statystycznie poprzez porównanie wyników obliczeń komplementarnej dystrybuanty deszczu ( $P(R>r)$ ) oraz stopnia nieciągłości ( $Ep0$ ) dla syntetycznych i zarejestrowanych szeregów czasowych deszczów. Ostatnim etapem badań była próba stworzenia specjalnego algorytmu filtrującego, w celu poprawy struktury syntetycznych szeregów czasowych z punktu widzenia nieciągłości opadów.

Na podstawie przeprowadzonych badań stwierdzono, że struktura czasowa rejestrowanych w Warszawie szeregów opadowych ma charakter multifraktalny i wykazuje niezmienniczość skalową w szerokim zakresie skal. Zaobserwowano ponadto, że zdecydowana większość deszczomierzy warszawskich za wyjątkiem dwóch specyficznych posterunków (na terenie lotniska i na przedmieściach miasta) wykazuje wyraźne podobieństwo właściwości multifraktalnych zarejestrowanych szeregów opadowych, manifestujące się zbliżonymi wartościami uniwersalnych parametrów multifraktalnych  $\alpha$ ,  $C_1$  i  $H$ .

W pracy zademonstrowano też, po raz pierwszy w Polsce, możliwość stosowania ciągłych kaskad uniwersalnych do generowania syntetycznych szeregów opadowych o wysokiej rozdzielczości czasowej dla Warszawy. Odnotowano przy tym możliwość praktycznego sparametryzowania samego generatora kaskady jedynie przez dwa parametry multifraktalne

$\alpha$  and  $C_1$ . Jednocześnie zauważono konieczność stosowania algorytmu filtrującego w celu poprawy struktury generowanych szeregów czasowych pod kątem nieciągłości opadów. W podsumowaniu pracy stwierdza się wysoki potencjał stosowania modeli ciągłych kaskad losowych opartych o uniwersalne modele multifraktalne do generowania szeregów opadowych o wysokiej rozdzielczości czasowej do wykorzystania w hydrologii miejskiej.

*Słowa kluczowe:*

Szeregi opadowe, hydrologia miejska, niezmienniczość skalowa, nieciągłość, parametry multifraktalne, uniwersalny model multifraktalny.

## 1. Introduction

From all the interrelated components of the hydrological system, precipitation plays the most important role in the global meteorological cycle and has a great impact on everyday life. The worldwide availability of surface and ground water depends on precipitation variability, therefore an accurate estimation of precipitation changes in time and space is crucial in hydrology. The analysis of precipitation for hydrological purposes is focused on providing information in terms of long term average, that is, 30-year normal precipitation, seasonal variability, inter-annual variability, i.e. the deviation of the annual values, and the extreme values particularly useful for the prediction of flooding (e.g. real time monitoring), drainage systems design, or model verification (hydrological modelling of catchments). The latter is particularly subject to spatial variability that can influence the simulation of water behaviours in catchment and sub-catchment responses (He et al., 2011b). The level of accuracy of analysis results is strictly related to knowledge of atmospheric precipitations and forecasting methods, thus the source of data and analysis techniques. Narkhedkar et al. (2010), in their study, pointed that only a combination of different techniques of analysis provides sufficient precipitation estimates, that is: observations from rain gauges and satellites, together with a numerical model prediction lead to satisfactory analysis results, even if with some (if not yet well understood) uncertainty.

Despite the increasingly wider application of hydrological modelling and precipitation estimation using weather radar, these methods are still sources of uncertainties: hydrological modelling is subject to error through model formulation, parameter estimation and model inputs, while radar measurements are performed remotely and indirectly (Refsgaard et al., 2007; He et al., 2011a), thus, rain gauge measurements are still considered the most reliable point scale source of data, according to many authors (Lebel and Amani, 1999; Wang and Wolff, 2010; He et al., 2011a). However, precipitation phenomena exhibit a high non-linear variability in spatial and temporal scale, therefore the variability of both the surface and duration (from minutes to several days) causes strongly irregular fluctuations difficult to capture instrumentally, and even more difficult to describe mathematically (de Lima, 1998; Kiely and Ivanova, 1999). For years, the random character of rainfall phenomena was ignored and the only precipitation model assumed by engineers was of constant intensity.

Very often in hydrological modelling, the complex natural processes are simplified and approximated: for instance, in hydrological modelling the generalization of rainfall phenomena leads to an insufficient analysis of spatial and temporal resolution and an

inadequate usage of rain data. This problem is particularly present in urban hydrology where, due to changes in climate conditions (the increased frequency and intensity of heavy rainfall events), and more rapid urban expansion, the increase of seal surface causes an increase of surface runoff, (the soil absorption capacity is reduced) and specifically, an increase the load of sewerage system (Berggren et al., 2011; Fletcher et al., 2013). Therefore, the implementation of modelling as usual procedure of sewerage system design became necessary. Yet, most of the already build rain water drainage and combined sewage systems in Poland have been designed based on the Błaszczyk IDF (Intensity-Duration-Frequency) rainfall model and the simple surface runoff calculation method (assuming constant intensity rainfall in the catchments), reducing its value with the increasing outflow time, already outdated and no longer recommended (Kotowski et al., 2010; Kaźmierczak and Kotowski, 2012). Only for selected cities in Poland, computer based hydrodynamic drainage systems models were developed and used for assessment of their hydraulic condition.

Practical motivation for the usage of hydrodynamic drainage systems models originates mainly from the European standard EN 752:2008 „Drain and sewer systems outside buildings” (assumed Polish standard PN-EN:752). Computer based drainage system models can be seen as contemporary engineering tools necessary for verification of the recommended frequencies of acceptable drainage systems overtopping, in according to the European standards. Especially for sewage systems covering large areas (over 2 km<sup>2</sup>), a real-time modelling is recommended using software based on equations of slowly varying unsteady flow for both surface runoff and the sewer conduits flow; this implies the application of variable rainfall data in time and in space. Then, the modelled system outpouring has to be verified by different rainfall scenarios at the input to the hydrodynamical modelling. In fact, local rainfall data are required for verification of local results deriving from the model simulations (Narkhedkar et al., 2010).

Commonly used rainfall data for verification are locally-measured intense multidecadal (min 30 years) rainfall series or synthetic hyetograph of Euler type II (Schmitt, 2007; Kaźmierczak and Kotowski, 2012; Kotowski, 2015). The former are very rare or rarely available in Poland, whereas the use of simple and static synthetic hyetographs of Euler type II is in obvious conflict with the variability of rainfall hyetograph shapes and temporal intensities observed in nature. Indeed, the main obstacle for proper hydrological modelling is the lack of free access to relevant rainfall data by Polish designers (Kotowski, 2006; Licznar, 2008). In the past, prior to the exploitation of modern rain gauges (until 2007), the rainfall data series had been registered mainly by pluviographs, whose results needed manual

conversion to the digital format: even the reading of maximum rainfall events was tedious and time-consuming (Licznar, 2005; Licznar et al., 2005; Licznar, 2009). Moreover, the access to “raw” high-resolution rainfall intensity data was (and still is) mainly reserved for authorized persons from the Polish Institute of Meteorology and Water Management. Similarly, local rainfall monitoring systems dedicated to urban hydrology are still rare and usually under development. In case of lack of any (available) multiannual local data, Polish designers tend to build their analysis on rainfall time series from (single) rain gauges located outside the city centres, usually at airports—where the best location conditions recommended by World Meteorological Organization (WMO) are met by modelling even large urban sewage systems without regard to the variability of rainfall on urban precipitation field.

Similar consideration is given to synthetic hyetographs, mainly on Euler type II, commonly used in Germany, and widely used by Polish designers. In a recent study, Licznar and Szeląg (2014) analysed over 400 Warsaw registered rainfall events of a time duration of up to 420 minutes, and stated that the model precipitation of Euler type II significantly deviated from the registered time series in almost every case, and the synthetic hyetograph was strongly inconsistent with the shape of the registered hyetographs. Moreover, it follows that the application of Euler type II rainfall for time series longer than 180 minutes is senseless. Consequently, we need to answer the arising question of whether in the design of urban sewage system only one set of data is suitable for modelling purposes and is able to reflect the spatial and temporal variability of rain. And finally, if no recorded data is available, is it sufficient to use in simulations the defined model precipitations like Euler type II?

A better understanding of the precipitation field, especially improving precipitation modelling tools, is one of the most important tasks of modern hydrology, which so far does not take into consideration the variability of the urban precipitation field, (Licznar, 2009; Dżugaj, 2014). The requirements of rainfall data for purposes of urban hydrology are different from those of natural catchments (Schilling, 1991). Urban hydrology requires high temporal and spatial resolution rainfall time series that are only dedicated to this only purpose gauging networks can provide (Niemczynowicz, 1999; Berne et al., 2004; Bruni et al., 2015). In terms of numbers Emmanuel et al. (2012) defined the adequate spatial resolution of urban field as a maximum distance of 6.5 km between rain gauges for light rain events and 2.5 km for showers, while Berne et al. (2004) developed a mathematical relation between the temporal and the spatial resolution of rainfall for urban applications and, for a catchment of about 100 km<sup>2</sup>, defining the required spatial resolution as 5.2 km and the temporal resolution of 12 minutes. Interestingly, if the temporal resolution is sufficiently high (<5min) for catchments

of areas greater than 1 km<sup>2</sup>, a distance between neighbouring rain gauges of 1 km is satisfactory (for drainage areas up to 8.7 km<sup>2</sup>) (Ochoa-Rodriguez et al., 2015).

The variability of precipitation fields is of particular importance in the implementation of global Real Time Control (RTC) of urban drainage systems (UDS), currently under implementation in many European cities as an effective method for controlling urban wastewater and stormwater systems (e.g. Vezzaro et al., 2014; Viessman et al., 2014). Such systems take advantage of the precipitation field variability, whose description affects the optimization of water retention inside the system itself (Licznar et al., 2005). As for 2010, many European rain gauge networks had already been employed as part of the RTC (e.g. in Barcelona (Spain) a network of 24 rain gauges, in Marseille (France) with 24 rain gauges and Vienna (Austria) with 25 gauges (Thames Tunnel Needs Report Appendix B, 2010)).

In Poland, the lack of appropriate data necessary for modelling sewage systems resulted in the implementation of a local precipitation measuring network in many urban catchments. Gauge networks of Łódź, Gdańsk or Wrocław are worthy of notice, but special attention is given to Warsaw, where from 2008 one of the biggest monitoring systems in Europe is in operation, and for the first time in Poland a local rain gauge network focused on gathering input data for hydrodynamic modelling combined with the monitoring of filling and flows levels within sewers has been created (Licznar, 2009).

The probabilistic evaluation of the urban drainage efficacy and degree of retention of overloaded systems required by the European guidelines, can be performed only on the basis of multidecadal (at least 20-30 years) high temporal resolution time series (up to 10 minutes) (Licznar et al., 2015). The implementation of urban rain gauge networks would allow in the future for a wider access to high resolution time series necessary for hydrodynamic modelling; nevertheless, such data is necessary at present. Currently available computer technologies and development of applied mathematics lead to a conceptual and mathematical modelling of precipitation focused on the improvement of the input data to local simulations such as synthetic rainfall events (Llasat et al, 2007). Effectively, to reflect the actual conditions in modelling, the random nature of rainfall has to be implemented in urban analysis. Such a purpose can be reached by using synthetic data randomly generated, e.g. by the multiplicative random cascade models focused on rainfall disaggregation of coarse daily rainfall to higher resolution by models conserving mass at each branch (microcanonical cascades) or not conserving mass (canonical cascades) (Licznar et al., 2011a; Licznar et al., 2011b; Rupp, 2012; Licznar and Szeląg, 2014). Multiplicative random cascades belong to a general type of fractal and multifractal cascade model which is simpler and characterized by

fewer parameter than the remaining two types: autoregressive and point-process models (Veneziano et al., 2006; Rupp et al., 2012). For the first time in Poland, such an approach has been proposed as a method of analysis of the Wrocław precipitation field by Licznar (2009). As a result, the developed microcanonical random beta-normal cascade enabled the temporal variability and intermittency of rainfall data for time scales from about 24 hours up to 5 minutes. The statistical parameters of the obtained generated synthetic time series are consistent with the parameters of the observed data. Similar results were achieved by Górski (2013) for a rainfall time series from Kielce (Poland) and Licznar et al. for four German cities (2011b).

Notwithstanding, a basic characteristic of microcanonical random cascade models requires a large number of parameters that has to be estimated at each level of cascade. An alternative claimed by many authors (de Lima, 1998; Schertzer and Lovejoy, 1987, 1989) is the approach of the universal multifractal generator limited by only 3 parameters for the whole hierarchy of scales.

The principle of the already mentioned fractal and multifractal theory, subject of the present dissertation, is the invariance of properties across scales that is believed to be the hidden principle of hydrology (de Lima, 1998). Advances in mathematics and computer science also enabled the developing of scaling theories, according to that of which a natural event is *scale-invariant* if its features are independent of scale. The quantification of this scale-invariance is given by the *scaling rules* (power laws) described by *scaling exponents*. In modern math, the generalization of scaling properties of a process is possible using the fractal and multifractal theory as an alternative to the classical Euclidean approach for all the phenomena that do not “fit” into traditional rules. Fractal theory deals with *simple scaling*, while multifractal theory is described by an infinity of scaling exponents. The strongest point of this geometry is the minimum number of parameters needed to describe complex natural phenomena, like turbulence, cloud formation, earthquakes, or finally, rainfall precipitation (de Lima, 1998; Schertzer and Lovejoy, 1993).

The fractal and multifractal analysis of rainfall is not well known in Poland. Yet, first attempts of its application to Polish rainfall time series performed by Licznar in Wrocław, Górski in Kielce and by the author in Warsaw, as is demonstrated, provided promising results to a wider application of such methods in many applications of urban hydrology.

## 2. The aim and scope of the thesis

The aim of the present study is to contribute to a better understanding of the non-linear variability of rainfall by analysing the precipitation time series in terms of the scale-invariant and multifractal behaviour present in precipitation data, originating from the biggest Polish urban precipitation field. The study uses point-rainfall data retrieved from a network of 25 recording rain gauge situated in Warsaw (Poland) providing high resolution data for over 2 years. The registered precipitation time series are subject to multifractal investigation based on spectral analysis and analysis of scaling of probability distributions and statistical moments of rainfall intensity. Based on the multifractal geometry methods, the universal multifractal parameters for all the rain gauge data are determined to characterize the statistical properties of multifractal processes.

Special attention is therefore given to the universal multifractal model, based on Lévy random variables, under which a universal multifractal generator is created, to generate synthetic 1-minute precipitation time series for Warsaw data. The final step is focused on the determination of statistical features of the generated data and their comparison to the statistics of the recorded time series.

The following statements have been hypothesized:

- I. Rainfall (temporal) structure varies within a precipitation field of a large city.
- II. Due to this, the multifractal characteristics of the local rainfall series recorded at different rain gauges, that is: intermittency, scales, and extremes are subjected to significant variation.

The conducted studies are additionally aimed to determine whether:

1. in a large urban field, properties such intermittency and scaling are variable;
2. the Warsaw rainfall time series exhibit multifractal characteristic;
3. it is possible to characterize multifractal behaviour of rainfall series from Warsaw by a simple set of universal multifractal parameters;
4. the universal multifractal model based on universal parameters can be a practical tool for generating synthetic rainfall series;
5. it is possible to somehow impose intermittency observed in natural precipitation into synthetic series generated by continuous universal multifractal model.

## **Outline of the dissertation**

The dissertation is divided in chapters and sections as follows. Chapter 3 is focused on a brief review of type of precipitation measurements and the description of the most common errors encountered in precipitation monitoring. In Chapter 4 the analysed precipitation field of Warsaw (Poland) as well as the Warsaw climatic and precipitation conditions are presented. In addition, guidelines of the proper location of urban precipitation monitoring stations are reported, based on which the analysis of Warsaw gauges recording conditions is discussed. In Chapter 5, the concept of the fractal geometry is introduced and the need of using fractal dimension is clarified, and the basis of simple fractal analysis of sets that is the box-counting method is described. Chapter 6 is dedicated to the assumptions and motivations of multifractal geometry, the description of multifractals is presented, and the multifractal analysis techniques are reviewed to finally obtain the full description of the universal multifractal parameters upon which the universal multifractal generator is constructed. The results and discussion are presented in Chapter 7 and the final conclusions are described in Chapter 8. Furthermore, the references, list of symbols and abbreviation used in the text, as well as all the attachments are found at the end of the dissertation.

### 3. Precipitation process

The interactions occurring between the atmosphere and ground surface are essential for the circulation and distribution of the water in the Earth system. In hydrology, intended as the science studying the global water balance, both in temporal and spatial scale, as in many other earth sciences, the water cycle plays a significant role also as a basis for hydrological investigation. Besides the biological and chemical processes, the water cycle is defined by the physical interactions between the atmosphere and the surface water, among which precipitation and evaporation are the most important.

The formation of precipitation is roughly related to the processes of *evaporation*, when moisture is released into the atmosphere; *condensation*, when moisture is lifted from the atmosphere to the troposphere by convection; *convergence* of air mass; and the *falling down* onto the ground surface by precipitation of rain or snow. Briefly, three basic stages of precipitation formation are defined: 1) occurrence of saturation conditions, 2) phase change from vapour to liquid/solid state, and 3) formation of water/ice crystal droplets to precipitable size (Eagleson, 1970; Chow et al., 1988).

The conditions encouraging the formation of precipitation are related directly to the local patterns of atmospheric circulation and the ground surface. The geographical position such as latitude, altitude, topography, distance from mountains and moisture sources, and local feature like: wind intensity, wind direction with the consequent air masses movements, relative temperature of water and ground, affect the spatial and temporal variability of precipitation (Eagleson, 1970; de Lima, 1998).

#### 3.1 Precipitation measurements

Recent developments in precipitation measurement techniques have led to the replacement of conventional (manual) rain gauges, focused to measure the precipitation intensity (defined as the amount of precipitation, collected per unit time interval, WMO-No. 182) as a secondary parameter deriving from precipitation amounts, to automatic ones, throughout the integration of recorded intensity within a time interval, in order to obtain the rainfall intensity as a primary quantity. In 2001, during the *Expert Meeting on Rainfall Intensity Measurements*, recommendations concerning standardization of rainfall intensity measurements were formulated. Among others, a time resolution of 1 minute for output averaging time and the range 0.02 to 0.2 mm·h<sup>-1</sup> as reporting ‘rain detected’ (Lanza et al., 2005). Snow measurement is possible in rain gauges as well, after the snow melting by providing a melting agent to the

gauge (Viessman and Lewis, 1996). In this dissertation, the term *rain gauge* is used to identify both snow and rain measuring instruments.

A variety of methods have been developed to measure precipitation mainly due to a high variability in time and in space of the phenomena. It is possible to access point type data from rain gauges or network of rain gauges or spatial rainfall data originating from remote sensing by ground radar or by satellites. An example of remote sensing device is presented in Fig. 3.1, where an X-band weather radar is visible.



**Figure 3.1.** Remote sensing X-band weather radar

In ground observations, besides the distrometers and radars, the most common and useful measurement instruments are gauges, also considered in precipitation as a source of reference data (Tapiador et al., 2012). The rain gauges are classified into non-recording, (i.e. standard gauge – Hellmann, or storage gauge Fig. 3.2) and recording types (i.e. tipping-bucket gauge, float gauge or weighing gauge).



**Figure 3.2.** Hellmann rain gauges

The first type of gauge is designed for a daily, weekly, monthly or even seasonal reading. The construction consists of a cylindrical vessel (container) provided with or without a funnel through which the rainfall from the collector above it passes into the container. The rainfall depth is defined usually by a calibrated measuring stick. The results readings have to be

performed manually at regular time-intervals. The recording rain gauges allow continuous recording measurements of precipitation and depending on the type, can provide a high and well defined temporal resolution of the data.

**Tipping-bucket gauges** generate an electrical signal after reaching a certain depth defined by the bucket capacity. Under the funnel, each rain gauge is equipped with a pair of triangular reservoirs (buckets) on a rotation shaft (visible on right in Fig. 3.3). During a rainfall, after one is filled up, the bucket tips and pours out the water into the drain cylinder and releases a signal. The rain then continues to fall into the second bucket. In this manner, the tipping of the buckets provides a measure of rainfall intensity and the results are registered by an electromagnetic recorder.



**Figure 3.3.** Tipping-bucket rain gauge. From the outside (on left) and from the inside (on the right)

These kinds of instruments are the most common, nevertheless they are characterized by a high underestimation of heavy precipitation, i.e. because of the small collection area and the relatively slow recording, and neither they are not suitable for light or solid precipitation due to a high evaporation rate, clock drift, or the necessity of snow melting to log the signal (Vasvári, 2005; Tapiador et al., 2012). In addition, their long-term usage requires systematic maintenance and calibration. An example of tipping-bucket gauge calibration installation is given in Fig. 3.4. (Licznar et al., 2013).



**Figure 3.4.** Measuring set used to rain gauge calibration at IIHR – Hydrosience & Engineering laboratory, Iowa State University (USA) (Licznar et al., 2013)

**Siphon rain gauge** (Fig. 3.5) operates on a pen provided with a floating element that moves upward as the level of water in the storage tank rises, and records the water amount on a chart. When the level equivalent to a fixed amount of water is reached, the rainfall is drained by a siphon into a collecting jar placed below the storage tank. On the graph, the amount from 0 to a fixed maximum is registered. When the rainfall stops, a horizontal line is traced (sample chart visible in Fig. 3.6).



**Figure 3.5.** Siphon rain gauge in field (on left) and (on right) the inside elements. From the top: the funnel, the recording pen, the floating element and the siphon

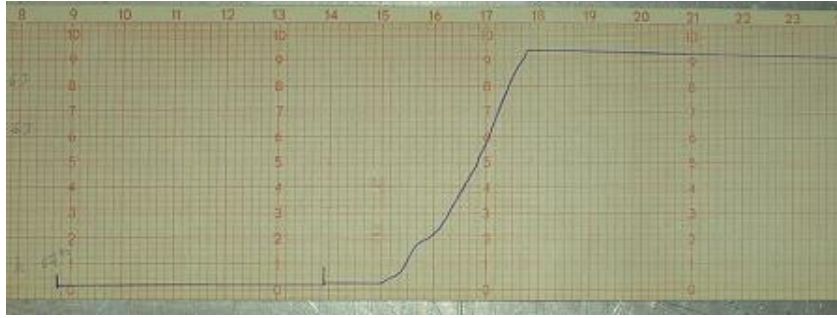


**Figure 3.6.** Sample pluviograph chart obtained by a siphon rain gauge recording

The modern **weighing-type rain gauges** (exemplary weighing rain gauge in Fig. 3.7) are less common and measure the weight of precipitation collected in a vessel. The increase of the deposited weight (measured by a strain-gauge bridge – Fig. 3.8) is converted into a cumulated precipitation recorded in time. The lack of a funnel at the entrance of the gauge orifice, required for previously described tipping-bucket and siphon gauges, allows to record different types of precipitation, e.g. liquid precipitation (rainfall), solid precipitation (snow, graupel) or mixed precipitation (sleet). For all the above-mentioned types of precipitation, weighing type rain gauges are capable of recording the intensity of liquid water content.



**Figure 3.7.** A MPS System weighing-type rain gauge



**Figure 3.8.** The strain-gauge bridge of an electronic weighing-type rain gauge

However, these types of instruments are unable to recognize the rainfall *type* (snow or rain). Nevertheless, the weighing rain gauges were found to be the most accurate instruments for 1-minute rainfall intensity measurements with a good dynamical stability and short step response in comparison to other types of gauges (for further discussion see Vuerich et al., 2009). Additionally, such devices could be easily provided with telemetry systems useful to a real-time monitoring purposes.

The guidelines for the location of precipitation stations in urban areas are described in Section 4.3, and the weighing rain gauges of TRwS type, as well as the phenomenon of step response error, are described in detail in Section 4.4.

### **3.2 Error in precipitation measurements**

The rain gauge measurement errors depend mainly on their source. Usually they can be classified as (i) systematic and (ii) random type of errors. Systematic errors (i) have been relatively well established and are mainly due to instrument imprecisions or the environmental influence on it. Studies about the identification and quantification of systematic errors have been conducted by analysing: wind and turbulence undercatch, evaporation and wetting or splashing losses, calibration effects, the effect of drop size, and wind speed on rainfall measurement as well as the occurrence of relationship between error, intensity and timescale of rainfall, or the existence of mechanical errors affecting the assessment of duration of short and high intensity events (Habib et al., 1999; Nespor et al., 2000; Molini et al., 2001; La Barbera et al., 2002; Ciach, 2003; Testik and Gebremichael, 2010).

The other less known types of discrepancies are defined as ‘local random errors’ (ii) and are caused by unpredictable changes, either in instruments or in environmental data recording conditions. Studies conducted by Habib et al. (2001) and Ciach (2003) on tipping-bucket rain gauge measurements show a significant occurrence of such errors at short-time rainfall scales up to 10-15 minutes and a strong dependence of error from rainfall intensity, timescales, and the way of data collection and processing.

However, the impact of measurement errors on the investigation results have not yet been precisely quantified. Such an error, omitted in practice, may affect significantly the extremes rainfall statistics of high resolution precipitation measurements, required for hydrological purposes (Lanza and Vuerich, 2010). Despite this, it is a very common practice to transfer rainfall data to large areas collected from sparsely distributed point gauges based on a quantitative estimation of the spatial variability of the precipitation field—rain gauges still remain the largest source of acquisition of observational precipitation data, mainly providing data for emergency flood alerts or to the calibration of radar rainfall measurement algorithms (Habib et al., 2001; Ciach, 2003; Tapiador et al., 2012).

A possible solution nowadays to minimize an eventual measurement failure and to improve the quality of measured data is to increase the number of rain gauges at measurement stations to at least two units, in case of relatively cheap tipping-bucket rain gauges, as shown in Fig. 3.9, where a pair of Hellmann rain gauges is presented (Ciach, 2003 and further reference).



**Figure 3.9.** Tipping-bucket rain gauges

Eventually, an even better solution is to supplement the old type siphon or tipping-bucket rain gauge, subjected to numerous limitations and errors, with the modern, more precise and easier in practical use, namely the weighing type gauges. In the following chapters, one of the biggest monitoring systems in Europe—the rain gauge monitoring system in Warsaw (Poland)—is described as a research field for complex multifractal analysis.

## **4. The rainfall data and the research field**

Warsaw city is located in the east-central part of Poland in the heart of the Masovian Plain. The city is divided north to south diagonally by the middle reach of one of the major Polish rivers: the Vistula (Wisła) River. The city is divided in two parts: the left bank, situated almost entirely in a moraine upland (Warsaw Plain), and the right bank, covered by the river valley (Vistula Valley). The boundary of both units is determined by the Warsaw Embankment, one of the most important factor of the natural environment of the city. It extends for almost 31 km along the city and constitutes the main element of the city ventilation system, controlling the direction of the winds discharging pollutants, and supplying clean air to Warsaw. The Vistula River is characterized by a low water level in autumn and early spring water saturation. The average annual vertical water level fluctuations reach 4-5 m, and extremely exceed 7 m (Pawlak and Teisseyre-Sierpińska et al., 2006).

### **4.1 Warsaw climatic conditions**

The Warsaw agglomeration is characterized by a transitional-temperate climate where the clashing continental and Atlantic masses cause frequent weather changes throughout the year. For almost 8 months the polar-marine mass dominates, meaning that for nearly 3 months the climate is formed by the continental mass, and the arctic climate prevails for one month in the year. Even more rarely Warsaw is influenced by the dry hot and tropical mass. The average annual amount of solar radiation in Warsaw is 3538 MJ/m<sup>2</sup>. The average annual air temperature in Warsaw is 8.2°C. The coldest month is January (average temperature of approx. -2.0°C) and the warmest is July (average temperature is 18.0°C) (Płazewski, 2014).

In Warsaw, from the second half of the 20<sup>th</sup> century, a decreasing trend of winter temperature has been noted, especially in the downtown area, where the temperature increase is more pronounced. This behaviour is explained by the phenomenon of ‘urban heat island’ which predominates in compact construction and artificial surfaces. In this area, an increased air temperature compared to the surrounding areas is observed as a result of changes in radiation balance, differences in urban and non-urban thermal conductivity and heat capacity, as well as higher emissions of artificial heat and air pollution in this part of the town (Pawlak and Teisseyre-Sierpińska et al., 2006; Płazewski, 2014; Kicińska and Wawer, 2014). Peng et al. (2012) analysed 419 cities all over the world, including Warsaw, in terms of the diurnal and seasonal variation of the heat island intensity. They found that for 56 analysed cities in Europe the annual daytime heat island effect is higher than during the night. Furthermore, its

intensity is more pronounced in winter than in summer and, interestingly, the greener the city, the smaller the urban heat island effect, which underlines the importance of vegetation in large cities.

#### 4.2 Warsaw precipitation conditions

The average total yearly precipitation for Warsaw, recorded by the meteorological station Warsaw-Okęcie and based on the observation for the 30-years period from 1971 to 2000, amounts to 519 mm. Whereas for the years 2001-2010 this value is slightly increased and amounts to 571 mm. The lowest average monthly precipitation values for the years 1971-2010 are recorded in winter months (Tab.4.1): in January and February (25 mm) and in transitional periods: October (30 mm) and March (31 mm). The highest values are noticed in summer months: July (76 mm) and June (65 mm) (Kozłowska et al., 2013).

**Table 4.1.** Monthly precipitation in Warsaw for years 1971-2012 (Kozłowska et al., 2013)

Years (for Warsaw-Okęcie)	Monthly precipitation in mm											
	I	II	III	IV	V	VI	VII	VIII	IX	X	XI	XII
1971–2000	22	22	28	35	51	71	73	59	49	38	36	34
2001–2010	34	34	39	22	60	48	84	22	33	5	29	81
1971-2010 <sup>a</sup>	25	25	31	32	53	65	76	50	45	30	34	46

*a own elaboration*

During the meteorological winter, defined as a three-month period from the beginning of December to the end of February, in the period range from 1965 to 1995, on average, the coldest month was January (-2.6°C, 12 snow days) followed by February (-1.6°C, 10 snow days) and December (-0.6°C, 10 snow days). The average number of snow days ranged from 19 days in 1990 to 50 days in 1968. Additionally, it is noticeable that the winters grew milder and shorter in the described 1965-1995 period (Płażewski, 2014).

The Warsaw area is dominated by the west winds (W – 25.0%), but there are also present northwest winds (NW – 10.7%) during warm seasons and the southwest winds (SW – 10.5%) during the cold seasons. The North (N – 7.2%) and Northeast winds (5.9%) are the least likely to occur. The urban area hampers the dynamic movement of air masses and it is also a source of condensation nuclei which contributes to increase the total amount of precipitation. The spatial distribution and the amount of precipitation in the city is varied: in central parts the annual rainfall precipitations are lower than in the western districts. Similarly, the wind speed in the city centre is 60% lower than speed of the open suburban spaces.

The Warsaw ventilation system is made of an external system, where the movement of air takes place by city sectors depending on the overall air circulation, and the internal local air circulation resulting from the type and arrangement of the buildings, road network system and

the distribution and size of green areas. The range of the internal ventilation system coincides roughly with the range of occurrence of Warsaw heat island (Pawlak and Teisseyre – Sierpińska et al., 2006). From a comparison between a rural station in Warsaw-Okęcie (situated near the airport, on the suburbs) and an urban one in Warsaw-University station (located on the left bank of Vistula River), a clear change in wind directions and speed is visible. The wind speed in the city centre is not only decreased on an average of 55%, but also deviated to the left by about 22.5°, which is consistent with the Vistula Valley, lying on the SE-NW direction, and the main city streets (WSW direction). It is therefore concluded that the Warsaw wind is significantly impacted by urban buildings (being an area of increased roughness), and by the Vistula River valley (and its proximity to the University measurement station), as an important element of the terrain (Kossowska-Cezak and Bareja, 1998).

### **4.3 Guidelines for the location of precipitation stations in urban areas**

Crucial factors determining the appropriate parameters to adopt in setting an urban station are the spatial-temporal scale and the classes of representativeness of a device. Both these factors are characterized below according to WMO guidelines.

#### **4.3.1 Observation scales**

During the precipitation data recording, the portion of the surroundings only ‘visible’ to the sensor therein placed—called ‘source area’—depends on the sensor height and the recording circumstances. In addition, many disadvantageous events can cause measuring interferences (Oke, 2006). In accordance to the WMO guidelines the attention is drawn, among others, to four different groups of phenomena (Nespor et al., 2000; Oke, 2006; Tapiador et al., 2012; Licznar et al., 2013; Pollock et al., 2016):

1. the ‘rain shadow effect’, meaning the interception of rain out of its trajectory of falling to the ground by the obstructing elements like trees or buildings;
2. the splashing of rain drops, due to the presence of sealed surface in the device surrounding as well as hanging objects above the gauge like tree fruits or leaves, likely to fall inside;
3. the urban canopy layer (UCL) as complex wind layer depending on the mean height of the main roughness city elements like buildings or trees, only wherein the vertical exchange occurs;
4. the air turbulence caused by wind gusts and the presence of the rain gauge itself, that may interfere with the proper amount of the recording rain.

The guidelines (WMO No 8, 2012) determine also three different urban scales defined as follows: the *microscale* (Fig. 4.1c) where it is possible to catch the city microclimate features, usually reflecting the local conditions and having a great impact on the measurement, the *local scale* (Fig. 4.1b)—the climate monitoring meteorological instruments are designed for—and the *mesoscale* (Fig. 4.1a), whose features are not capable of being represented by a single urban station.

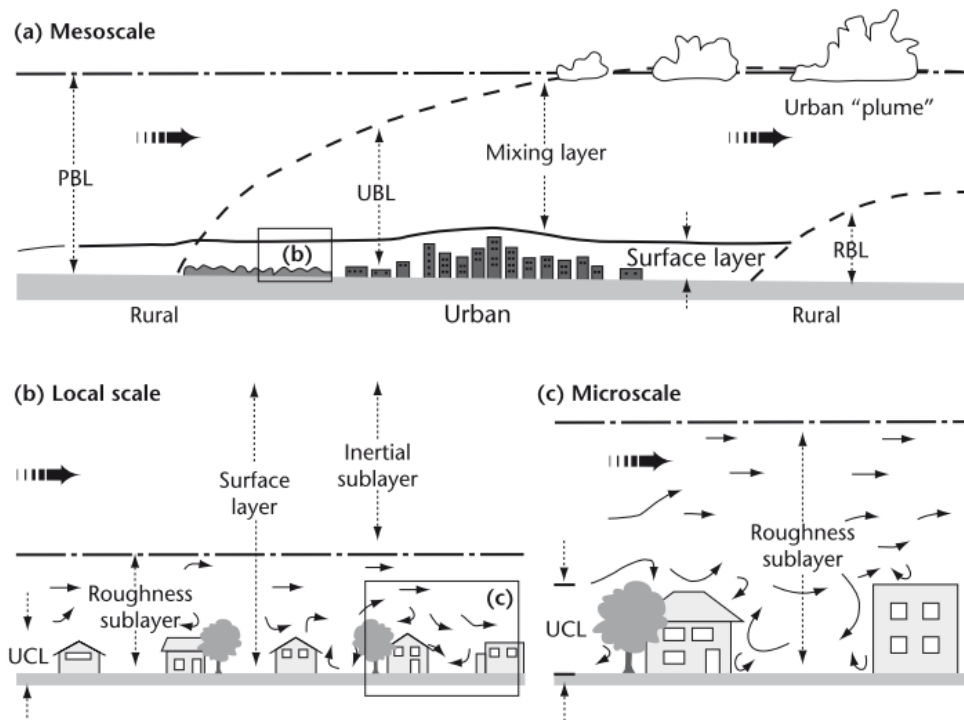


**Figure 4.1.** Scheme of climatic scales and vertical layers found in urban areas: planetary boundary layer (PBL), urban boundary layer (UBL), urban canopy layer (UCL), rural boundary layer (RBL) (from WMO No. 8, 2012)

Meteorological measurements, including the rainfall precipitations, are mainly performed inside the local scale, especially in the urban canopy layer, which is given by the height from the ground to the main roughness elements of the city. Herein, all the isolated microclimatic effects formed in microscale close to the source, are mixed and calmed by the turbulent local winds. In this way, the local climate is influenced by the blending effect, both horizontally, up to a few hundred meters, and vertically, where it persists in the roughness sublayer (RSL), from the ground up to the so-called mixing height. A precipitation recording device, focused on investigating the *intra-urban* patterns, has to be placed below this level to record the local environment of the gauge. Furthermore, in urban areas, due to the heat island effect, large roughness and stability condition, an additional height restriction arises: each local scale surface type is delimited by an internal boundary layer, whose height depends on the distance upwind to the borders of distinctly different surface type (i.e. fetch distance). By analogy, in

rural areas, where the heat island effect and surface roughness is lower, the surface type's boundaries are further apart, the fetch distance is higher and the internal boundary layer is greater. If the source area is not sufficiently uniform, the provided data cannot be local representative (Oke, 2006; Licznar et al., 2014). In practice, for precipitation measurement, the standard is that the obstacles should be no closer to the rain gauge than two times their height.

To reflect the meteorological measurement in the mesoscale the use of many instruments is required. In case of rainfall, the most common solution is to install a rain gauge network. In such a case the locations affected by microscale climate conditions should be excluded. Therefore, the location of the gauges in open spaces or nearby sharp-edged buildings should be avoided. High variable or even turbulent wind activity in UCL or RSL fields can be more dangerous than in case of natural obstacles (Fig. 4.2).

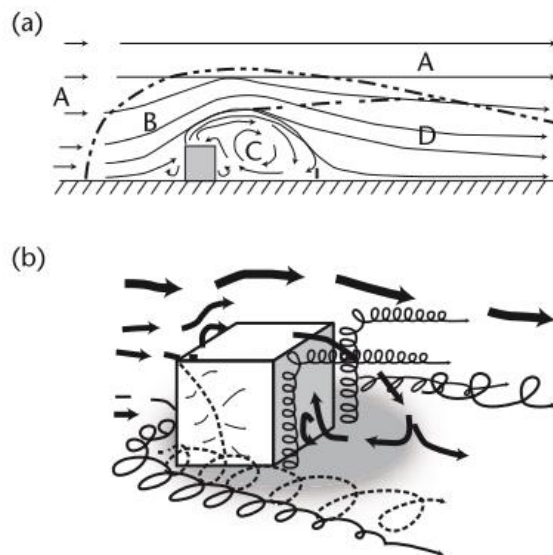


**Figure 4.2.** 2-D flow around a building with flow normal to the upwind face (a) stream lines and flow zones; A -undisturbed, B - displacement, C - cavity, D – wake and (b) flow, and vortex structures (from WMO-No. 8)

Considering all the above, it is recommended in urban areas to collocate the measurement devices like rain gauges in places where the standard exposure conditions on the ground are met, i.e. playgrounds, open parks with low density of trees, urban airports, etc. The best places to install rain gauges are those surrounded by trees, brushwood and bushes or other barriers against the wind. The less preferred option is to collocate the rain gauge on a roof-level. In such locations, greater than normal wind speed and hence a greater error of estimation than on the ground surface occurs, therefore a conjunction with the wind instruments is necessary, to provide rain gauge output corrections (Oke, 2006).

### 4.3.2 Classes of representativeness

The general guidelines for meteorological instruments and observations, WMO No. 8, indicate as preferred observation station for rainfall data a secured fenced area with dimensions of approximately 10×7 m, a device placed at a distance of min. 3 m from the fence and the surrounded area overgrown with regularly moved lawn. The rain gauge orifice should be placed at a certain height of the range between 0.5-1.5 m above the terrain—in Poland it is set 1 m above the ground level.

Furthermore, the usage of automatic recording precipitation gauges is recommended to provide better time resolution and reduction of evaporation and wetting losses in comparison to the manual ones. Particularly, from among three types of automatic rain gauges (the weighing-recording type, the tipping-bucket type, and the float type), only the weighing type is suitable for all kinds of precipitation measurements (both rain and snow). The output of such a device is an electronic signal, recorded continuously, being proportional to the input quantity. Normally, such types of gauges are not designed for emptying themselves automatically, so the capacity of maximum accumulation of a recording gauge given by the size of the internal container, is usually at the range at least comparable with annual precipitation total.

In order to take into account the environmental operating conditions of the devices, which often distort the results and have impact on their representativeness especially in larger spatial scales, for meteorological probes (including the rain gauges) the concept of classes determining the representativeness of the data location is introduced by the above-mentioned guidelines (WMO No 8, 2012). These are defined below:

**Class 1**, meets the following (optional) requirements (Fig. 4.3 and Fig. 4.4):

- Flat, horizontal ground, surrounded by open space, slope less than 1:3 (19°). The rain gauge surrounded by constant height obstacles under elevation angle between 14° and 19° (the obstacles situated at a distance between 2 times and 4 times their height);
- Flat, horizontal area, surrounded by open space, slope less than 1:3 (19°). For rain gauges artificially protected against wind by so called wind-shields, obstacles of constant height are not necessary. In this case, all other barriers should be situated at minimum distance of 4 times their height;

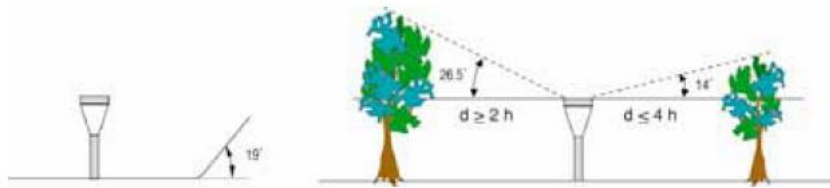


**Figure 4.3.** Site condition for class 1 rain gauge (from WMO No. 8, 2012) – condition 1  
or

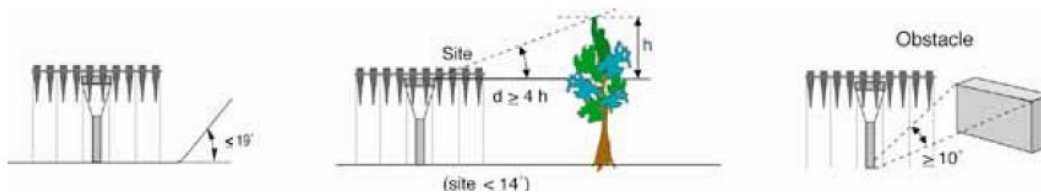


**Figure 4.4.** Site condition for class 1 rain gauge (from WMO No. 8, 2012) – condition 2

**Class 2**, (additional estimated uncertainty of 5% due to site) meets the following requirements (Fig. 4.5):

- Flat, horizontal area, surrounded by open space, slope less than 1:3 ( $19^\circ$ );
- Any possible obstacles should be situated at minimum distance of 2 times their height, (about the orifice height of the rain gauge);

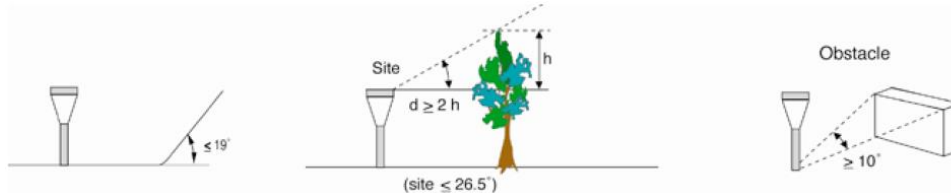


**Figure 4.5.** Site condition for class 2 rain gauge (from WMO No. 8, 2012)

**Class 3**, (additional estimated uncertainty of 10% due to site) meets the following requirements (Fig. 4.6):

- Flat, horizontal area, surrounded by open space, slope less than 1:2 ( $\leq 30^\circ$ );
- Any possible obstacles should be situated at a distance exceeding their height;

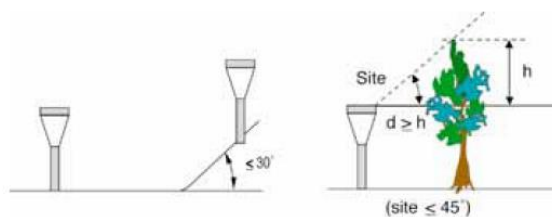


**Figure 4.6.** Site condition for class 3 rain gauge (from WMO No. 8, 2012)

**Class 4**, (additional estimated uncertainty of 25% due to site) meets the following requirements (Fig. 4.7):

- Steeply sloping land ( $>30^\circ$ );
- Any possible obstacles should be situated at a distance exceeding half of their height;

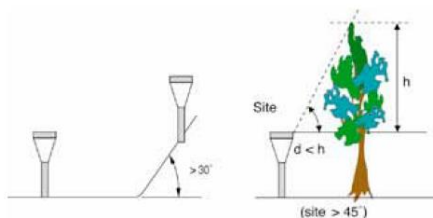


**Figure 4.7.** Site condition for class 4 rain gauge (from WMO No. 8, 2012)

**Class 5**, (additional estimated uncertainty up to 100% due to site) meets the following requirements (Fig. 4.8):

- The obstacles (e.g. trees, roofs, walls) situated at a closer distance of half their height.

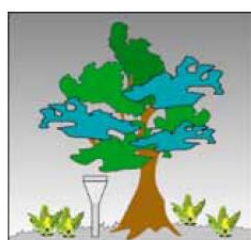


**Figure 4.8.** Site condition for class 5 rain gauge (from WMO No. 8, 2012)

Except gauges classified as mentioned above from 1 to 5, where 1 indicates the best conditions, considered representative, and 5 meaning inappropriate conditions for representative measurements due to the surrounding obstacles in the neighbourhood and which location of the devices should be avoided, the urban gauges are often characterized by high class values, distinguished with an additional letter S (e.g. 4S and 5S).

#### 4.4 Warsaw rain gauge network

The rainfall data series are collected at the precipitation monitoring system of the Municipal Water Supply and Sewerage Company in Warsaw (MPWiK w m.st. Warszawie S.A.). The Warsaw rain gauge network (R01÷R25), installed in 2008, roughly covers the area of 517.2 km<sup>2</sup> and each rain gauge is designed to collect rainfall data from almost 21 m<sup>2</sup> of the city area, obtaining possibly a constant gauge density over the entire surface. Eight rain gauges are located on the right bank of the Vistula River, while 17 are situated on the left

bank, mainly in the city centre, where the areas of sealed surfaces constitute the most to the total rainwater surface outfall (Fig. 4.9).

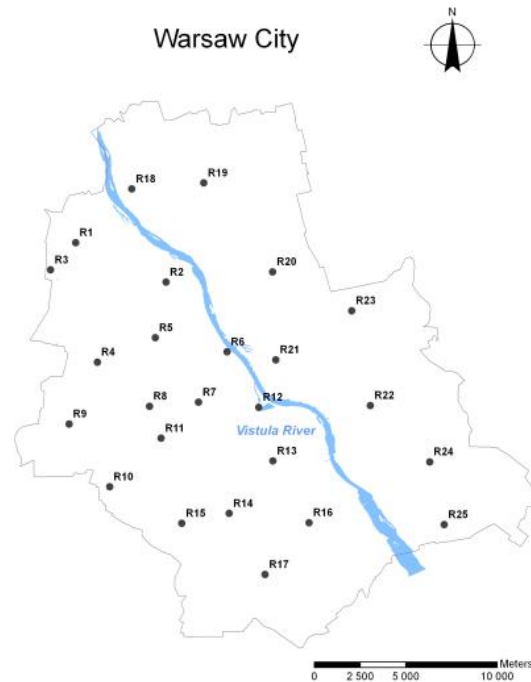


**Figure 4.9.** Locations of rain gauges in Warsaw

The Warsaw rainfall monitoring network is assembled from the weighing type precipitation gauges of TRwS model 200E, manufactured by a Slovakian company MPS Systém Ltd., capable of measuring both rain and snow (Fig. 4.10). According to the manufacturer's technical information, the type TRwS 200E/203E rain gauges are characterized by the following parameters:

1. Orifice area: 200 cm<sup>2</sup>;
2. Range of precipitation: 750 mm;
3. Accuracy: 0.1%;
4. Maximum rain intensity: 60 mm·min<sup>-1</sup>;
5. Resolution: 0.001 mm;
6. Measuring element: strain-gauge bridge;
7. Air temperature measurement: -35°C÷70°C;
8. Weighing range: 0÷12000 g;
9. Operating humidity range: 0÷100%;
10. Dimensions:  $\phi 355 \times 470$  mm (Fig. 10);
11. Weight: 4.5 kg.

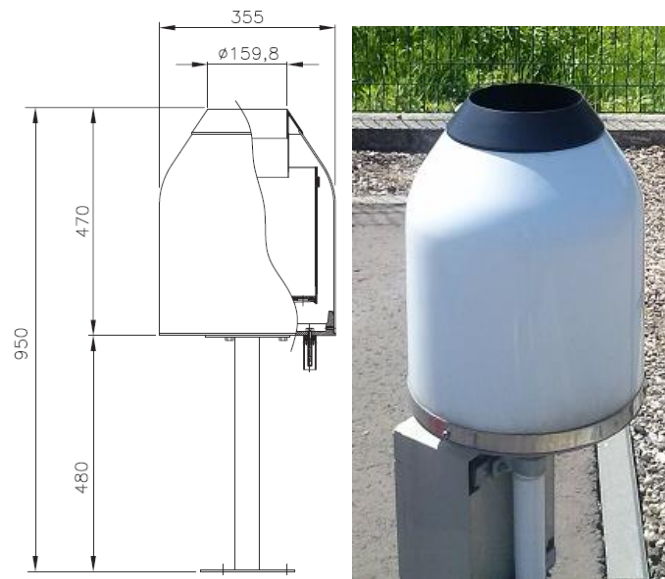


**Figure 4.10.** Scheme with its dimensions (on left) of a rain gauge type TRwS 200E (on right)

The principle of operation of TRwS 200E gauge is based on recording the increase in mass of the precipitation deposited in a rain tank, put on a strain-gauge bridge. The gauge is crowned with a standard intake of  $200 \text{ cm}^2$ , intercepting rainfall to the inner tank. The electronic module calculates the amount of rainfall that occurred within a specified time period. The rain gauges are provided with heating elements on the inlets crown. Since the opening does not freeze in under zero temperatures, and the gauge's openings are not blocked by ice, they can be operative also in winter.

A qualitative gauge performance field tests with the implementation of a precise peristaltic pump revealed a dampening of the first 3 min of the initial phase and a longer 5 min broadening of the final phase of simulated rainfall hyetograph (Licznar et al., 2015). The phenomenon of a dampening or broadening of the registration data over the range of few minutes by rain gauges is known as *step response error*. Detailed laboratory test of different gauges confirmed the presence of a 3-minutes step error for rain gauge of type TRwS and revealed that the error magnitude as quite small in comparison to other analysed gauges (Lanza et al., 2005).

Furthermore, during construction of the rain gauge network, the most important parameter is the optimal gauge location. It is significant to obtain a slightly higher density network measurement in the central part of the city where the degree of sealing surfaces is the highest and the sewage system is the richest, and the buildings are the tallest. The major part of the

network gauges (21 of 25) is located on the Warsaw MPWiK properties. All the gauges are installed 1 m above ground level, as requested by Polish meteorological standards.

On the basis of the characteristics of each class of representativeness of the instruments location (described in Section 4.3.2) a classification of each rain gauge location is made. The results of this classification are summarized in Tab.4.2.

All the gauges are connected to a GSM/GPRS modules and all the recorded data is stored as total mass (WABS) and 1-minute precipitation layer (PR1M) with a resolution of 0.001 g and 0.001 mm respectively. The so called Absolute Weight (WABS) in this case, is not only the weight of the precipitation inside the container, but the sum of both the weight of rain and the precipitation tank.

**Table 4.2.** List of locations of Warsaw rain gauges and the assessment of the local measurement condition.

Rain gauge	Address	Location on MPWiK ground	Representativeness class according to WMO no 8
R01	Wóycickiego St.	No	4
R02	Rudzka St.	Yes	5
R03	Arkuszowa St.	Yes	4
R04	Górczewska St.	Yes	5
R05	Ostroroga St.	No	3
R06	Dobra/Karowa St.	Yes	5
R07	Koszykowa/Krzywickiego St.	Yes	2
R08	Jerozolimskie Blvd/P. Tysiąclecia St.	No	2
R09	Chroscickiego/Obywatelska St.	Yes	3
R10	Dzwonkowa St.	Yes	2
R11	Grójecka/Kotoryńskiego St.	Yes	5
R12	Zaruskiego/Czerniakowska St.	Yes	5
R13	Powsinska/Limanowskiego St.	Yes	4
R14	Ken/Dolina Służewiecka St.	Yes	3
R15	Wyrazowa St.	No	2
R16	Przyczółkowa/Vouglą St.	Yes	5
R17	Strwieńskich St.	Yes	1
R18	Mehoffera/Strumykowa St.	Yes	2
R19	Borecka St. (Białoleka)	Yes	2
R20	Rolanda/Rajmunda St.	Yes	5
R21	Waszyngtona St.	Yes	4
R22	Dzielnicowa St.	Yes	5
R23	Chelmyńska/Gwarków St.	Yes	4
R24	Patriotów/Pajęcza St.	Yes	4
R25	Bysławska St.	Yes	4

The database of a 1-minute rainfall time series for the period from 15<sup>th</sup> September 2008 to 19<sup>th</sup> November 2010 recorded on the network of all 25 gauges is used as a material of this dissertation. All the recorded data are presented below in Fig. 4.11. The locations of all the 25 gauges of Warsaw rain gauge network is presented in Appendix I.

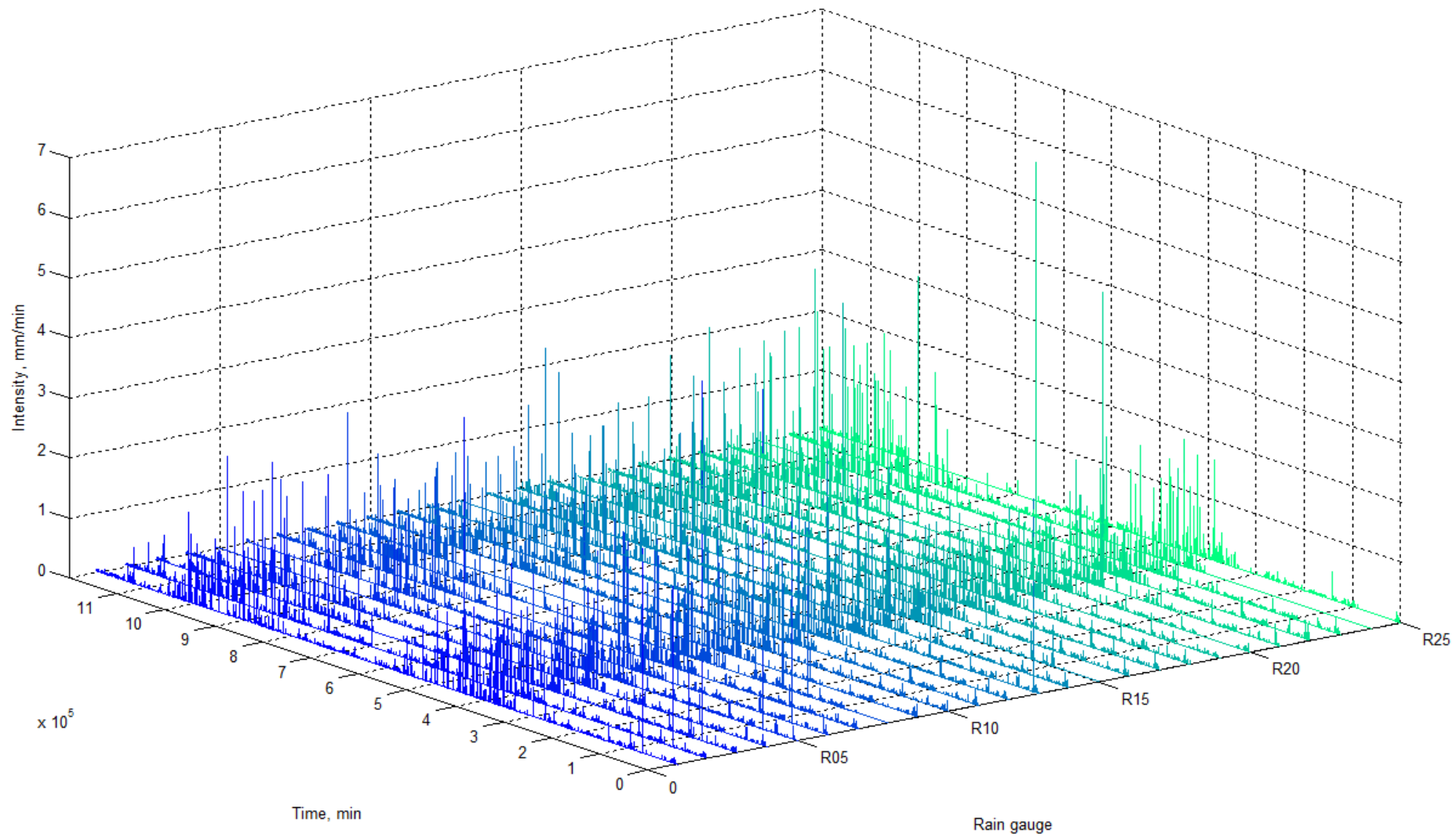


**Figure 4.11.** Hyetographs of Warsaw 1-minute rainfall data recorded in 2008-2010 by 25 rain gauges

## 5. Fractal geometry

First reports about the idea of fractal geometry, non-properly named at that time, can be found in 1872, when a mathematician Karl Weierstrass proved the existence of a function that produced a non-differentiable curve, previously introduced but not demonstrated by Riemann. During the decades, many attempts to handle the non-linear geometry has been done; the self-similar sets were developed by G. Cantor (1883) and H. von Koch (1904), the definition of dimension was expanded by F. Hausdorff (1918), the *attractors* and *repellers* were studied at the same time by G. Julia and P. Fatou in 1918, and the generalization of self-similarity properties was done by P. Lévy. All these contributed to the development of the later fractal geometry by Mandelbrot (History of fractals).

The term *fractal*—from Latin: *fractus* meaning broken—was coined and introduced for the first time by Benoit B. Mandelbrot in 1975 (Encyclopedia Britannica; Mandelbrot, 1975, 1977) to describe jagged and broken objects that do not fit the patterns of traditional Euclidean geometry. Mandelbrot, more willing to visual representations of mathematical problems using high performance computing power to which he had access, developed Julia's equation by mapping the equation values and created, now famous, the Mandelbrot set. By doing so, he defined a new geometry enabling the study of simple structures of nature not yet described by mathematic formulas. Instead of measuring the length of an object, he discovered to be able to measure its roughness. To do so, he had to rethink the basic concept of dimension.

### 5.1 Fractal dimension

The dimension of a standard Euclidean or topological object can be defined unequivocally as an integer value (0-dimensional for a point, 1-dimensional for a line, 2-dimension for a plane) providing us geometric information of the set, therefore its 'qualitative' properties, that is *how* an object fills the space. In fractal geometry, the notion of fractal dimension is used to measure the complexity of an object, here intended as a 'quantitative' definition of it, or rather how fast our measurement will change while varying the scale of observation. The fractal dimension determines an overall structure of the set, the degree to which it covers the space in which is embedded, in other words, the measure of its sparseness (e.g. Seuront, 2009).

The mathematical expression of objects dimension is generally expressed by the Hausdorff-Besicovitch dimension, which assumes integer values in case of Euclidean objects

and (in general) non-integer values for fractals. We talk about fractals if the so called ‘capacity dimension’ of a physical object is different (always larger) than its topological (Lebesgue covering) dimension, but in any case, remains less than the space dimension in which it is settled (Shivamoggi, 2014). Fractals have a property of ‘self-similarity’, meaning that each section of the set constitutes a completed reduced-scale copy of the whole (Mandelbrot, 1967). The dimension of a self-similar figure follows a power law relation:

$$N_s \approx \lambda^D \quad (1)$$

where  $N_s$  is the number of self-similar objects created by dividing the original image by the scale factor  $\lambda$ , defined as the quotient between the largest scale of observation and the homogeneity scale (see section 6.1). It means that there is a proportionality between  $N_s$  and  $\lambda^D$  in the limit  $\lambda \rightarrow \infty$  (e.g de Lima, 1998). In this way, the fractal dimension  $D$  is a non-integer number and it is determined by the equation:

$$D = \frac{\log(N_s)}{\log(\lambda)} \quad (2)$$

where  $D$  is the Hausdorff - Besicovitch dimension, which coincides with the similarity dimension and the capacity dimension for self-similar objects (Mandelbrot, 1967). As specific case of fractals, the Equation (2) is also suitable for the definition of Euclidean dimensions.

A fractal measurement, in a probabilistic framework considered even more fundamental than the fractal dimension, is the *codimension*. Given the fractal dimension  $D_A$  of a fractal set  $A$ , the codimension  $c_A$  is the dimension of its complementary space expressed as follows:

$$c_A = D - D_A \quad (3)$$

where  $D$  is the dimension of the topographic (Euclidean) space wherein the fractal set is embedded. Frequent events are characterized by high values of dimension of a set and thus by low values of codimension.

However, a certain limitation occurs for  $c_A > D$  which implies  $D_A < 0$ , not admissible for a negative definition of Hausdorff-Besicovitch dimension (Seuront, 2009; Lovejoy and Schertzer, 2013). More versatile than the geometric definition of codimension is the probability of a  $D$ -dimensional object of size  $1/\lambda$  to intersect the set  $A$  defined as the ratio between the number of non-overlapping objects  $N_A$  necessary to cover the set and total number of  $D$ -dimensional objects  $N_D$  necessary to cover the entire space containing the set  $A$  (de Lima, 1998; Seuront, 2009; Lovejoy and Schertzer, 2013):

$$\frac{N_A}{N_D} \approx \frac{\lambda^{D_A}}{\lambda^D} = \lambda^{D_A - D} = \lambda^{-c} \quad (4)$$

While the dimension stands for the measure of *relative sparseness*, the codimension is the measure of *absolute sparseness*, (Seuront, 2009; Lovejoy and Schertzer, 2013).

## 5.2 Box counting method

To calculate the dimension of complicated fractal (or even not self-similar) objects the *box counting method* is preferred. It consists on covering the image with defined, gradually decreasing mesh size non-overlapping grids (called boxes) of size  $1/\lambda$  and determining the number of boxes (box-counting) containing at least a part of the object. The resulting number of boxes  $N_\lambda$  will be proportional to the box size  $L \approx (1/\lambda)$  according to Equation (1):

$$N_\lambda \approx L^{-D} \quad (5)$$

where  $D$  is the fractal dimension given by the Equation (2) as the ratio of the number of boxes containing the object to the magnification or the inverse of grid/box size, usually identified as the fractal dimension (Lovejoy and Schertzer, 2013). Graphically, by plotting the values of  $\log(N)$  against the value of box size  $\log(\lambda)$  (from the Equation (2)) a scale-invariant set will exhibit a linear relation defined by the power law (defined by Equation (1)) and the fractal dimension will be determined by the slope of the line fitted to the data. Nevertheless, the dimension of measured object cannot exceed the dimension of the unit used to carry out the measurement, which can be seen as a limitation of the method as well as problem that may arise in case of low data resolution or size of unit boxes tending to zero while rescaling.

## 6. Multifractals

The theoretical and observational approach to the statistical properties of rainfall phenomena was developed at the beginning of 1960s (Marani, 2003). The high nonlinear dynamics of rainfall precipitation changes in spatial and in temporal scale have led, during last decades, to the development of applied mathematics and to an expansion of scaling theories, based on the invariance of properties across scales, as well as the diffusion of multifractal geometry (de Lima, 1998; de Lima and Grasman, 1999; Lovejoy and Schertzer, 2006), mainly for the study of atmospheric purposes, especially for meteorology, thus rainfall phenomena.

A multifractal approach in theory deals with the description of self-affine objects in place of simpler self-similar mono fractals. It is mainly focused on the analysis of intensity changes (rainfall intensity) of a non-linear process across the entire hierarchy of scales (time framework).

### 6.1 Properties of multifractals

In context of the *turbulence* formalism, a multifractal behaviour exhibits a hyperbolic *intermittency* over an intensity scale (Fraedrich and Larnder, 1993). In a time domain of rainfall processes, the intermittency is referred to two aspects of variability: (i) the alternation of wet and dry periods, that is the variability of the support of the measure (Mascaro et al., 2013) or the percentage of no-rain periods within a rainfall event and at high rainfall frequencies (which strongly influence the rain measurements) it can be considered as a random variable, and (ii) as a sudden variation of rainfall intensity, i.e. the intensity fluctuations of a given support (Molini et al., 2001; Molnar and Burlando, 2005; Mascaro et al., 2013).

A multifractal set is a set of non-uniformly interlaced fractals exhibiting multiscaling, scale-invariance and variability of features. In nature, one usually must deal with multifractal phenomena revealing more complex scaling relation than monofractals. In short, it can be said that multifractal objects are somehow ‘supported’ by a combination of simple self-similar fractals of low dimensions (Mandelbrot, 1989; de Lima, 1998), each of them characterized by a fractal dimension and single scaling exponent.

The multifractal theory deals with multiple scaling, that is the generalization of scaling properties of natural phenomena. A single fractal interpretation of a rain event provides only the information about the rainfall occurrences, while the multifractal approach allows to study

the variability over time and space of a such high non-linear process like rain, for different levels of intensity. To obtain a significant description of the *multiple scaling* of a process, a multifractal object can be described by nothing but an infinite number of fractal dimensions (dimension function) and infinite scaling exponents (scaling exponent function) (de Lima, 1998; Mandelbrot, 1989; Pathirana et al., 2003).

Because of scaling, the *scale-invariance* of a phenomenon is given by a power-law behaviour of its energy spectra (e.g. Tessier, 1993; de Lima, 1998; Burlando and Rosso, 1996), and can be tested by standard spectral analysis (described in section 6.4). However, some deviations from power law behaviour are possible (Fraedrich and Larnder, 1993; Olsson, 1995; de Lima and Grasman, 1999; Olsson and Burlando, 2002; Pathirana et al., 2003): whether a multiple scaling regions are present in a graphical representation of the data, some breaks in the scaling regime at few hours may occur. It has not yet been explained if the nature of scaling breaks is related directly to the rainfall structure fluctuations or to the limitations of the measuring device (Olsson, 1995; Harris et al., 1997; Marani, 2003; Licznar, 2009), nevertheless, deviations described above are reflected in several multifractal analyses conducted on rainfall time-series from different climatic locations. To determine the scaling behaviour providing information about the existence of scaling breaks, among the most frequently used, two methods (described further in detail) have been chosen: (i) the *spectral analysis*, which has shown a pronounced spectral break for various resolution data sets in the range of few minutes to few hours (e.g. Olsson and Burlando, 2002) and (ii) the empirical *probability distribution function* (PDF). These together with the multifractal parameters analysing techniques, lead to a divergence of results somehow related to the rainfall process nature (Olsson, 1995).

Multifractal processes are also characterized by high *variability*, concerning a large range of scales, from high scales down to the small ones. Particularly, the latter corresponds to the ‘inner’ scale of a phenomenon where the very small scales causes that the processes are homogeneous, the intensity is constant and the variability vanishes. It is practically impossible to register the innermost scale of a process experimentally; the limitations of the available devices allow only an average (or even accumulated) discrete registration of the densities of a continuous process, and that depends on the device resolution.

As shown in Fig. 6.1, there is a strong dependence of the range of intensity values on the scale of observation for a continuous process. The rainfall intensity decreases with the increasing of observation resolution.

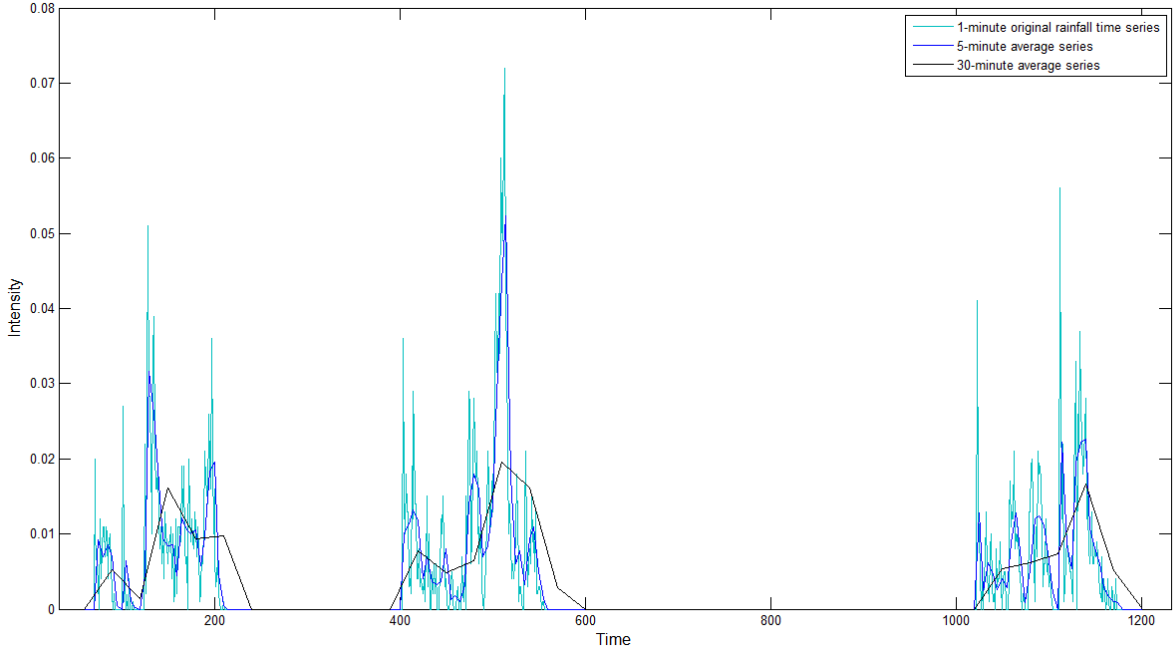


**Figure 6.1.** Illustration of the relation between the intensity of rainfall process and the temporal resolution of recorded data. Original series recorded by gauge R05 in Warsaw, at 29<sup>th</sup> September 2009

Furthermore, the method of data recording significantly affects the obtained measured values. In recording geophysical processes, the ‘observable’ scale gains importance in the context of ‘missing’ the smallest scale of observation, and thus the true scale of homogeneity during experiments. As noted by Schertzer and Lovejoy (1989), de Lima (1998) and Licznar (2009) there is a noticeable loss in context of singular statistics of small scale behaviour.

According to the traditional mathematical approach, it is desirable to describe all measurements of natural processes by function, assuming that the obtained function will reflect the continuous process at the scale of discrete observation tending to zero. This practice puts aside the strong variable behaviour occurring on a smaller scale than on that observable. Is therefore necessary to use measures instead of using functions to describe natural continuous processes (de Lima, 1998; Licznar, 2009). Since the Lebesgue measures are not applicable here because of the non-integer values of fractal dimensions, the  $D$ -dimensional Hausdorff measure should be used (as already described in section 5.1). Consequently, the intensity of a multifractal process is defined as follows:

$$\varepsilon_\lambda \approx \lambda^\gamma \quad (6)$$

where  $\varepsilon$  is the intensity (or density) of a multifractal process at the scale ratio  $\lambda$ , and  $\gamma$  the *singularity* or *order of singularity*. These singularities correspond to all the range of intensities of a process, from the very high to the very low. The parameter  $\gamma$ , is scale-independent and characterizes ‘qualitatively’ the strength of the process intensity on a given

scale resolution. Usually, as the scale  $\lambda \rightarrow \infty$  for all singularities  $\gamma > 0$  and  $\varepsilon_\lambda \rightarrow \infty$  (Schertzer and Lovejoy, 1989; de Lima, 1998).

Hereby, the multitude of intensity levels leads to obtain an infinite number of fractal dimensions, dependent on the order of singularity  $\gamma$ . In this way, the so-called *fractal dimension function*,  $D(\gamma)$ , and, consequently, the *codimension function*  $c(\gamma)$  is defined as follows:

$$c(\gamma) = D - D(\gamma) \quad (7)$$

where  $D$  is the dimension of the embedding space and  $D(\gamma)$  is the fractal dimension (also non-integer, i.e. fractal) of the ‘support’ of singularities of order greater than  $\gamma$ . In terms of probabilities, according to the equation (Tessier et al., 1993):

$$\Pr(\varepsilon_\lambda \geq \lambda^\gamma) \approx \lambda^{-c(\gamma)} \quad (8)$$

the codimension of the singularities shows the changes of histograms depending on resolution and provides an exponent for each intensity level of the process.

## 6.2 Classification of multifractals

To characterize multifractal processes, a classification of *bare* and *dressed* processes is used most frequently. These terms, used in theoretical physics, were introduced in multifractal geometry by Schertzer and Lovejoy (1987) in order to identify two types of nature of cascade processes (Licznar, 2009; Lovejoy and Schertzer, 2013).

*Bare* processes are theoretical and all their moments are finite ( $\lambda$  is finite), whereas *dressed* processes are derived from observation, usually on a larger scale than the ‘inner scale’ of a process. For *dressed* processes, there is a divergence for all moments greater than a critical value depending also on the space dimension (Lovejoy and Schertzer, 2013). This divergence comes from the more ‘violent’ variability of *dressed* processes characterized by larger singularities than the ones resulting from *bare* processes, for the same probability.

The *bare* multifractals arise because of fine-grained process (Tessier et al., 1993), shown on the left-hand side in Fig. 6.2, where descending process from larger to smaller scales occurs (Lovejoy and Schertzer, 2013). The opposite process is the coarse-grained process, (right-hand side in Fig. 6.2), where the *dressed* data obtained experimentally are averaged in time or in space on ascending scales. The small-scale interactions are considered in *dressed* processes despite of smoothing of data, hence the origin of the term indicating that they are ‘dressed’ with the small-scale interactions (Licznar, 2009; Schertzer and Lovejoy, 1989; Lovejoy and Schertzer, 2013).

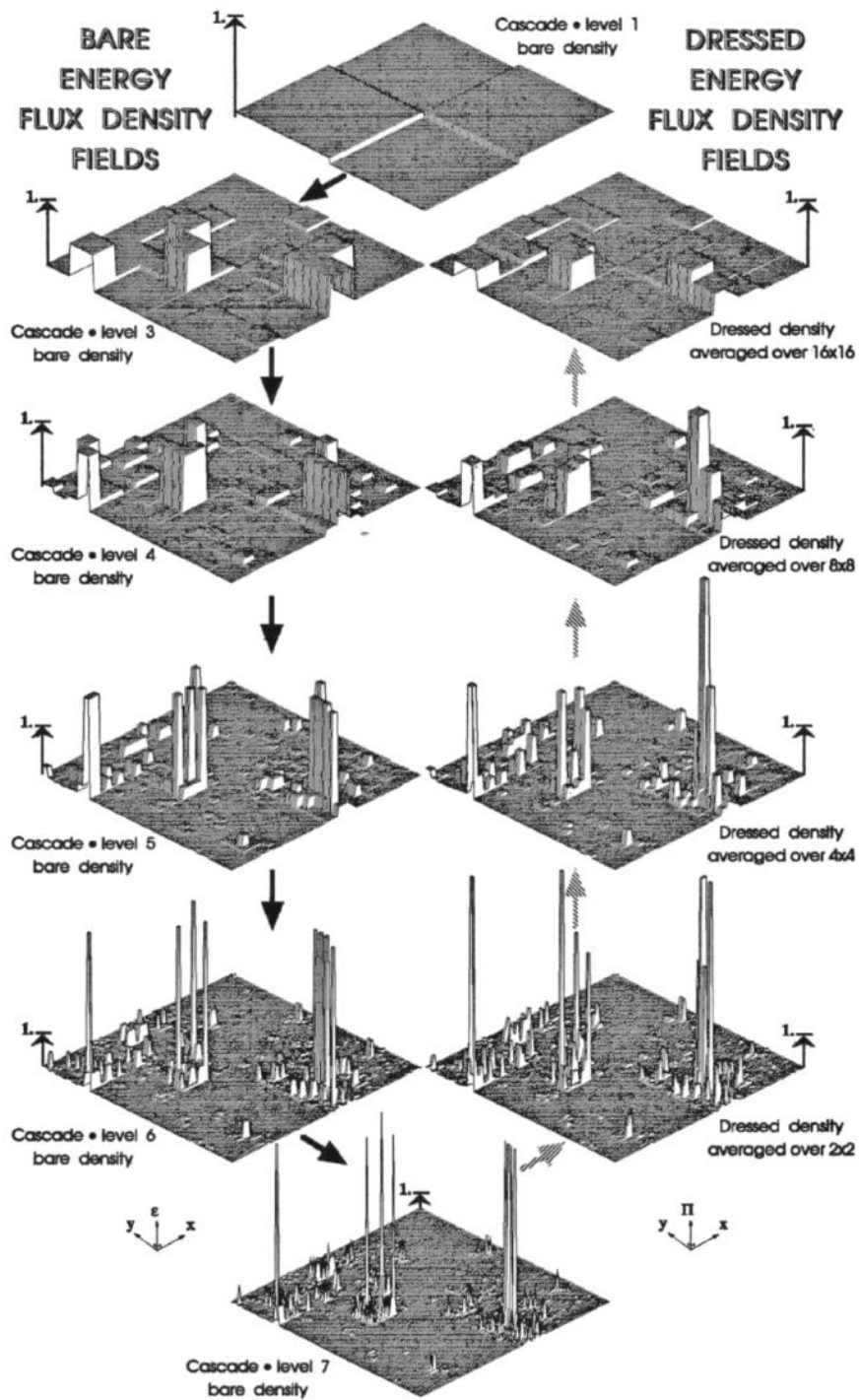


**Figure 6.2.** Illustration of construction of ‘bare’ (on left-hand side) and ‘dressed’ (on right-hand side) multifractal process. On the bottom centre the scale factor equals to  $\lambda = 2^7$ . Reproduced from Lovejoy and Schertzer (2013)

### 6.3 Box counting method in multifractals

To describe a multifractal, a sequence of generalized fractal dimensions is used. To provide a statistical description of self-similarity properties of fractals, the multifractal formalism is applied (Lynch, 2004; Saa et al. 2007). In practice, by applying the box counting method (described in section 5.2) to a multifractal object, the sought value is the sum of measure of interest  $p_{N_\lambda}$  within a given box  $N_\lambda$ . For multifractals, the dimension expressed by Equation (1) takes the following form:

$$p_{N_\lambda} \approx L^D \quad (9)$$

where  $L$  is the box size and  $D$  the fractal dimension, considered here as local variable. To determine the multifractal properties of a set, the moments of order  $q$  of the measure  $p_{N_\lambda}$  are calculated according to the function:

$$m_q(L) = \sum_{n=1}^{n(L)} p_{N_\lambda}^q \quad (10)$$

where  $n(L)$  is the total number of non-empty boxes. Therefore the generalized dimension of the set (e.g.  $D_0$  for capacity dimension) is dependent on the moment  $q$  and is defined by (Lynch, 2004):

$$m_q(L) \sim L^{(q-1)D_q} \quad (11)$$

Rainfall process, as an example of natural multifractal phenomena, are characterized by scale invariance as well as by intermittency which, given a sampling time, provides additional information about the variability of the intensity of the time series. All the mentioned properties are subject to verification in this dissertation, by using the multifractal methods described in following sections.

### 6.4 Spectral density analysis

An efficient computational tool for time series analysis as well as time series modelling are *spectral methods*, also known as the *Fourier transform methods* (Pathirana et al., 2003; Licznar et al., 2011). These methods involve converting (by the Fourier transform equations) the data series in time domain, where the data is described as a function of time, into a frequency domain where the amplitude of the data is a function of frequency.

Indeed, in a scaling field, a power-law dependency between the power spectrum and the corresponding frequency is observed holding the equation:

$$P(f) \approx f^{-\beta} \quad (12)$$

where  $f$  is the frequency,  $P(f)$  is the power energy of the spectrum and  $\beta$  is the spectral exponent and it act as an indicator of the of the range of scales of the analysed field. The Equation (12) indicates that in a log-log plot there is a linear relationship between the frequency and the spectrum energy of the process (Pandey et al., 1998; Licznar, 2009).

In data series modelling, a spectrum analysis is based on the *power spectral density function* (PSD function), focused mainly in detention of the seasonal (cyclic) components of the process, shown as spectrum peaks on the signal graphs, and their separation from that randomly present i.e. noise (STATSOFT Electronic Statistic Textbook). In environmental engineering this approach is widely used i.e. in forecasting water consumption, wherein the occurring daily and weekly periodicity must be considered while creating a model.

Given a discrete time series of precipitation  $x(n)$ , recorded in strictly defined and constant time intervals, by using the discrete Fourier transform (DFT) can be converted in a discrete series of harmonic frequency-domain values  $X(m)$ , in accordance to the equation:

$$X(m) = \sum_{n=0}^{N-1} x(n)e^{-j2\pi nm/N} \quad (13)$$

where  $j$  equals to  $\sqrt{-1}$ ,  $N$  is the total integer sample number,  $n$  is the sample number and  $m$  is the harmonic number.

Numerical calculations necessary to carry out the DTF transformation requires substantial memory and processing time resources, due to the rapidly increasing amount of data undergoing calculations. Here, it is of use the faster equivalent to DFT, namely the *fast Fourier transform* (FFT), also called the base-2 algorithm. The function involves the Danielson - Lanczos lemma that assumes the idea to break up the series, and rewrite it as the sum of two discrete Fourier transforms, each of length  $N/2$ ; one is formed from the even-numbered samples and the other from the odd-numbered samples. For that reason, an even dimension of the data series  $N$  is recommended (Lyons, 2006; Wolfram Mathworld).

The Warsaw data series are subjected to FFT algorithm and the resulting sequence of harmonic values  $X(m)$  is ultimately used to compute the power spectrum  $P(f)$  for  $N/2 + 1$  of the frequency  $f$  according to the methods described in detail by Licznar (2009). To execute the calculations, two scripts – SPECTRUM\_Warsaw and EvaluateSpectrum2b - are used. A

limiting factor for the considered upper frequency range is critical Nyquist frequency  $f_c$  determined by the temporal resolution of Warsaw precipitation, described by:

$$f_c = \frac{1}{2\Delta} \quad (14)$$

where  $\Delta$  is equal to 1 minute which is the recording time resolution of the data. Subsequently a smoothing of the output calculation spectrum for the high frequency using MAIN script is carried out, considered as a standard practice by other researches (i.e. de Lima, 1998; Licznar, 2009). Thus, a PSD function following the  $P(f)$  dependence a double logarithmic scale is obtained.

### 6.5 Functional box-counting method

The functional box-counting method was developed at the end of the 20th century by Lovejoy (et al., 1987), as a method to obtain a functional description of the dimension  $D$ . It is based on the classical box-counting method, since the test sets are repeatedly covered entirely with non-overlapping boxes of fixed and increasing each time dimension  $1/\lambda$ . Whenever the number of boxes containing at least one element of the set (non-empty boxes) is counted, the amount of non-empty boxes is presented in logarithmic scale as a function of the box dimension. A fractal set exhibits a linear relationship between the number of the boxes and the corresponding boxes size, and the slope of the curve determines the fractal dimension. In terms of 1-dimension time series, the box size becomes a time interval, and a non-empty box is the one containing at least a non-zero rain element.

The innovation proposed by Lovejoy is to introduce, beside the box size, a boundary precipitation intensity rate, then to count the number of boxes containing rain, the amount of which is below the given threshold limit (intensity threshold  $T_{hr}$ ), and to repeat the counting process of each time for the increasing boundary intensity rate. By this means, it is possible to perform an analysis of the fractal dimension variability depending on the variation of boundary conditions. Finally, by relating the obtained fractal dimension  $D(T_{hr})$  to the order of singularity  $\gamma$ , it is possible to indirectly obtain the codimension function  $c(\gamma)$ , conforming to the approximation  $T_{hr} \approx \lambda^\gamma$ . The main advantage of this method is that there is no need to use statistical moments; nevertheless, a significant limitation of the method stands in the “saturation” effect which occurs for certain intensity threshold values, above which, all the boxes are filled with rainfall. Such a situation may cause artificial breaks on the resulting graphs.

For the Warsaw precipitation time series, time intervals from 1 minute to 1048576 minutes (~2years) and for boundary precipitation intensity rates of 0, 0.04, 0.08 and 0.16 mm/min are analysed. To perform the functional box-counting analysis for Warsaw time series a special application BOX\_Warsaw in Pascal and an additional MATLAB script called BoxPlot for visualization of the results are developed.

## 6.6 Trace moment method (TM)

A technique allowing to perform a multifractal analysis with no need of using the Legendre transformation is the *trace moment* method (TM) focused on determining the moments scaling exponent function,  $K(q)$  and the codimension function,  $c(q)$ .

The method is based on the analysis of the moments of order  $q$  of the density  $\varepsilon_\lambda$  within the timescales  $\lambda$  and in part uses the principle of the functional box counting method already described in section 6.5. Statistical moments  $q$  are expressed as central moments, whose low values are commonly used in statistics, and are preferred over the ordinary moments.

A multifractal process exhibits a defined relation between the moments of its intensity  $\varepsilon_{\lambda,i}$  (for  $i = 1, \dots, \lambda^D$ ) and the resolution scale  $\lambda$ . The scaling moment function  $K(q)$  is the linking function of the average  $q^{\text{th}}$  moments  $\langle \varepsilon_\lambda^q \rangle$  of the intensities of a multifractal process at different resolutions with the scales of this process resolution levels  $\lambda$ , as defined by the equation (Lovejoy et al., 1987; Lovejoy and Schertzer, 1990):

$$\langle \varepsilon_\lambda^q \rangle \approx \lambda^{K(q)} \quad (15)$$

where  $q$  is the order of statistical moments and  $K(q)$  the moments scaling exponent function. Because of the singular behaviour for the small-scale limit  $\lambda \rightarrow \infty$ , the Equation (15) tends to infinity for all moments  $q > 1$ , since  $K(q)$  is an increasing function, so  $K(q) > 0$  for  $q > 0$  (de Lima, 1998); furthermore, the moments are calculated only for integers values, which leads to an inaccurate estimation of the  $K(q)$  curve.

A possible solution is to study the scaling moments using the fluxes (integrals) of the densities of a process defined as the trace moment of the flux over the set  $A$  as its ensemble average, expressed as follows:

$$\text{Tr}_\lambda [\varepsilon_\lambda^q] = \left\langle \int_A (\varepsilon_\lambda)^q d^{qD} x \right\rangle \quad (16)$$

where the flux is called the  $q^{\text{th}}$  – order trace moment, at resolution  $\lambda$ . It is therefore possible to obtain the fluxes of the statistical moment values also for not integer  $q$  values ( $q < 1$ ), overcoming the limitations imposed by applying the usual statistical moments.

By using the functional box counting method, the set  $A$  is covered with non-overlapping boxes of side  $1/\lambda$ , it means that a set  $A$  is divided in  $\lambda^D$  sub-sets  $A_{\lambda,i}$ , (for  $i = 1, \dots, \lambda^D$ ), given that for rainfall time series the boxes are defined as 1-dimensional time segments of length  $1/\lambda$ . Then, the flux of a single sub-set is defined as:

$$\prod_{\lambda'} A_{\lambda,i} = \int_{A_{\lambda,i}} \varepsilon_{\lambda'} d^D x \quad (17)$$

where  $\lambda < \lambda'$  intended as the ratio of scale of interest to the smallest scale of homogeneity and  $\varepsilon_{\lambda'}$  is the intensity of ‘inner’ scales, components of  $\varepsilon_{\lambda}$  of the sub-sets  $A_{\lambda,i}$ . For each one of the sub-sets the intensity  $\varepsilon_{\lambda,i}$  is determined by summing the flux over all the sub-sets needed to cover the set  $A$ . Therefore, at resolution  $\lambda$ , the Equation (16) defines the  $q^{\text{th}}$ -order trace moment becomes:

$$\text{Tr}_{\lambda} [\varepsilon_{\lambda}^q] \approx \left\langle \sum_{i=1}^{\lambda^D} (\varepsilon_{\lambda,i})^q \lambda^{-qD} \right\rangle \quad (18)$$

Finally, the above described average intensities  $\varepsilon_{\lambda}$  are raised to powers  $q$ , and due to an existence of a relationship between Equation (18) and the scale  $\lambda$  and moment scaling function  $K(q)$  defined in Equation (15), according to de Lima (1998) could be expressed as follows:

$$\text{Tr}_{\lambda} [\varepsilon_{\lambda}^q] \approx \lambda^D \lambda^{K(q)} \lambda^{-qD} = \lambda^{K(q)-(q-1)D} = \lambda^{(q-1)(C(q)-D)} \quad (19)$$

The final value of the  $K(q)$  function for order moments  $q$  is the slope of the linear relationship between the log values of the flux moments  $\log(\text{Tr}_{\lambda}[\varepsilon_{\lambda}^q])$  and the log values of scales  $\log(\lambda)$ . A more detailed trace moment description could be found in papers of Lovejoy and Schertzer (1990) and Lovejoy et al. (1987).

Additionally, the TM method determines the codimension function  $c(q)$ , here defined as:

$$c(q) = \frac{K(q)}{q-1} \quad (20)$$

where  $K(q)$  is the moments scaling exponent function and  $q$  is the order of the statistical moments. It relates to the dimension function  $D(q)$  by:

$$D(q) = D - c(q) \quad (21)$$

which is defined as the distance between the value of  $K(q=0) = -c$  and the origin of the axis (de Lima, 1998; Licznar, 2009).

The TM analysis of the Warsaw precipitation time series is carried out by a calculation program written in Pascal called TRACE\_Warsaw, and a MATLAB script called TracePlot, for scales from 1 minute up to 11.4 days ( $\lambda=16384$  to  $\lambda=1$ ).

## 6.7 Probability distribution/multiple scaling (PDMS)

The statistical analysis of multifractal sets can be achieved either by scaling the statistical moments of the process intensity, i.e. by applying the *trace moment* method (TM) as described above, or alternatively by applying the PDMS method, focused on determining the scale invariant probability distribution, that is the codimension  $c(\gamma)$  of a rainfall process, whose intensity exceeds certain sequentially increasing algebraic thresholds, dependent on scale ratio proportional to  $\lambda^\gamma$  (Schertzer and Lovejoy, 1988).

The analysis is undertaken over a large range of scales, by covering the entire set of elements, in case of Warsaw the rainfall time series, with disjoint boxes (time intervals) as in the case of box-counting method, of size (length)  $\lambda$  and counting the number of non-empty intervals  $N_\lambda(\gamma)$  with the intensity  $\varepsilon_\lambda$  verifying the inequality:

$$\frac{\log(\varepsilon_\lambda)}{\log(\lambda)} \geq \gamma \quad (22)$$

By modifying the Equation (8), the probability distribution for decreasing scale ratio  $\lambda$  and for many different values of  $\gamma$  is given by:

$$\Pr(\varepsilon_\lambda \geq \lambda^\gamma) \propto \frac{N_\lambda(\gamma)}{N_\lambda} = F \lambda^{-c(\gamma)} \quad (23)$$

where  $F$  is the proportionality pre-factor slowly varying with  $\lambda$  and weakly depending on  $\gamma$  (de Lima, 1998). In practice, it is possible to estimate the values of  $c(\gamma)$  as the slopes of the probability distributions curves  $N_\lambda(\gamma)/N_\lambda$  functions versus  $\lambda$  scale ratios for the given  $\gamma$  levels, in a log-log graphs (Schertzer and Lovejoy, 1988; Lovejoy and Schertzer, 1991).

The PDMS analysis of the Warsaw precipitation time series is supported by a Pascal program called PDMS\_Warsaw and a MATLAB script called PDMSPlot. The analysis is carried out for 24 values of singularity orders  $\gamma$  of the range  $\gamma \in [0.04; 0.96]$ .

## 6.8 Double trace moment method (DTM)

*Double trace moment method* (DTM) is a generalization of the classical trace moment method and it is widely used to estimate the universal multifractal parameters  $\alpha$ ,  $C_1$  and  $H$  (Schertzer and Lovejoy, 1987; de Lima, 1998) especially from conservative multifractal fields, for which the flux of the process is conserved while going from scale to scale (Pandey et al., 1998). For further description of the universal multifractal parameters refer to Section 6.9.

The generalization of TM method is here achieved through the introduction of a *second* (double) *moment*  $\eta$  to the analysis of data. The intensity  $\varepsilon_\lambda$ , related directly to the finest

(known) resolution  $\lambda'$  of the process, is hereby raised to power  $\eta$  (being a real positive number) and then normalized with the ensemble average  $\langle \varepsilon_{\lambda'}^{\eta} \rangle$  of the entire set:

$$\varepsilon_{\lambda'}^{(\eta)} = \frac{\varepsilon_{\lambda'}^{\eta}}{\langle \varepsilon_{\lambda'}^{\eta} \rangle} \quad (24)$$

where  $\varepsilon_{\lambda'}^{(\eta)}$  is the  $\eta$ -normalized intensity  $\varepsilon_{\lambda'}$ , widening the dynamic range of the process which can be subjected to analysis.

Based on the  $\eta$  - power normalization defined in Equation (24), the flux  $\Pi$  described by Equation (17) is transformed in a ' $\eta$  - flux'  $\Pi^{(\eta)}$  in according to the relation:

$$\prod_{\lambda'}^{(\eta)} (A_{\lambda,i}) = \int_{A_{\lambda,i}} \varepsilon_{\lambda'}^{(\eta)} d^D x \quad (25)$$

where  $\lambda < \lambda'$  and  $\varepsilon_{\lambda'}^{(\eta)}$  is the  $\eta$ -normalized intensity  $\varepsilon_{\lambda'}$  at scale resolution  $\lambda$  intended as a component of the intensity  $\varepsilon_{\lambda,i}$  associated with sub-sets  $A_{\lambda,i}$ . Similarly, at resolution  $\lambda$ , the  $q^{th}$  - order double trace moment is defined as:

$$\text{Tr}_{\lambda} [\varepsilon_{\lambda}^{(\eta)q}] \approx \lambda^{K(q,\eta)-(q-1)D} \quad (26)$$

where  $K(q,\eta)$  is a double moments scaling exponent function and for  $\eta = 1$ ,  $K(q,\eta)$  is consistent with  $K(q)$ , defined by the trace moment method. Practically, as for TM method, the DTM function  $K(q,\eta)$  is obtained as the slope of plots of  $\log(\text{Tr}_{\lambda} [\varepsilon_{\lambda}^{(\eta)q}])$  against  $\log(\lambda)$  for different moments  $q$  and, in this case, also for different values of  $\eta$ .

In addition, the re-normalized version of multifractal process is applicable as the initial step for the probability distributions/multiple scaling function and for the determination of co-dimension function as well, here defined equal to  $c(\gamma,\eta)$ , being a dual function in relation to  $K(q,\eta)$  (for details see de Lima, 1998 and Licznar, 2009).

The DTM analysis of the Warsaw precipitation time series is performed using the DTM\_Warsaw Pascal program and a MATLAB script called DTMPLOT. The analysis is carried out for 12 values of moment order  $q \in [0.9; 2.1]$  and 20 specific  $\eta$  values,  $\eta \in [0.13; 10.00]$ .

## 6.9 Universal multifractal parameters

The statistics of multifractals can be described by scaling exponent function  $K(q)$ , however as there is only a conservation  $K(1) = 0$  and convexity constraint on this function, it implies an infinity of parameters to describe the scaling behaviour of an ideal multifractal process (Pathirana et al., 2003; Lovejoy and Schertzer, 2013). Therefore, the concept of *universality* is introduced, which assumes an existence of a few relevant parameters among the infinity of

them, especially taking into consideration a realistic system, liable to perturbations, rejecting some theoretical features. Such a system is expected to ‘converge’ to some *universal attractor* in the same way as a class of models based on the same domain attractor leads to the same processes defined by few parameters (Tessier et al., 1993; Licznar, 2009; Lovejoy and Schertzer, 2013). In this way, the definition of  $K(q)$  by an infinity of parameters is reduced only to three universal parameters:  $\alpha$ ,  $C_1$  and  $H$ . For further discussion, see Tessier et al. (1993) and Lovejoy and Schertzer (2013).

To obtain a *bare* multifractal process (see Section 6.2), discrete cascades are used. These kinds of generators apply fixed scale ratios at each cascade step leading to not realistic physical processes. For satisfactory results, instead of using an infinite number of cascade steps, over a wide range of scales it is possible to introduce many intermediate steps (Fig. 6.3) to ‘densify’ the steps. This way of processing is a valid alternative to obtain a process exhibiting ‘universal’ behaviour (de Lima, 1998; Lovejoy and Schertzer, 2013). It is therefore possible to obtain a multifractal process in according to the relation:

$$\varepsilon_\lambda \approx e^{\Gamma_\lambda} \quad (27)$$

where  $\Gamma_\lambda$  is the generator of the process. Thus, the modelling of multifractal processes is given by multiplying densities with densities, what in practice means adding generators to generators of the type  $\Gamma_\lambda \approx \ln(\varepsilon_\lambda)$  (in Equation (27)) (De Lima, 1998). Consequently, the average  $q^{th}$  moment  $\langle \varepsilon_\lambda^q \rangle$  in Equation (15) takes the form as follows:

$$\langle e^{q\Gamma_\lambda} \rangle \approx e^{K_\lambda(q)} \approx e^{K(q)\ln(\lambda)} \quad (28)$$

Then,  $K_\lambda(q) \approx K(q)\ln(\lambda)$ , resulting from Equation (28) is called the second characteristic function of generator  $\Gamma_\lambda$ .

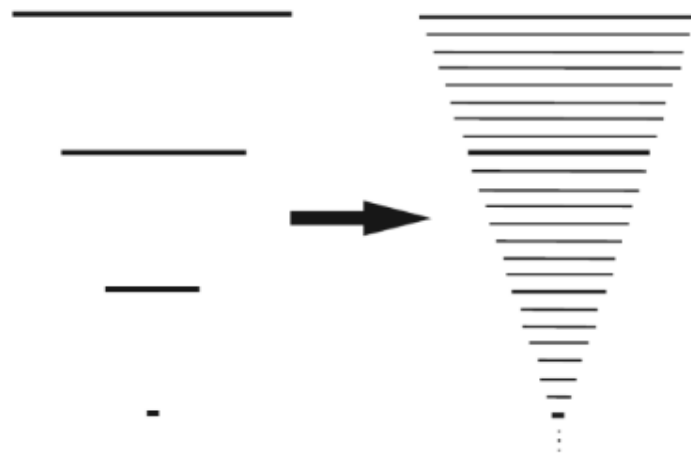


**Figure 6.3.** Scheme of densification of scales. Reproduced from Lovejoy and Schertzer (2013)

The *bare* generator  $\Gamma_\lambda$  of a scale-invariant multiplicative cascade process must follow the basic properties (de Lima, 1998):

1. the (finite resolution) generator is a random noise process restricted to the range  $[1, \lambda]$ ; this ensures that the process will be smooth on scales smaller than  $\lambda^{-1}$ ;
2. the second characteristic function  $K_\lambda(q)$  of the generator  $\Gamma_\lambda$  has a logarithmic behaviour with scale ( $\lambda \rightarrow \infty$ ) to assure multiple scaling;
3. the probability distribution of positive fluctuations of the generator  $\Gamma_\lambda$  must fall-off more quickly than exponentially, to have some finite moments  $q \geq 0$ ;
4. the generator must be normalized so that  $K_\lambda(1) = 0$  (i.e.  $\langle \varepsilon_\lambda \rangle = 1$ ) to assure (canonical – energy) conservation of the flux.

Properties 1. and 2. define the presence of so called *pink noises*, also called  $1/f$  noise, that is the proportionality of the spectrum of generator and the inverse of the wave-number:  $E_\Gamma(\omega) \approx \omega^{-1}$ .

A generator that satisfies all the above-mentioned properties and is also an example of *pink noise* is the ‘universal’ class of multifractals, based on Lévy stochastic variables (de Lima and Grasman, 1999), characterized by a *Lévy index*  $\alpha$ , determining the order of divergence of the statistical moments of the generator:

$$\Pr(-\Gamma \geq s) \approx s^{-\alpha}, \text{ for } s \gg 1 \Rightarrow \langle (-\Gamma)^q \rangle \geq \infty, \text{ for } q > \alpha \quad (29)$$

where  $0 < \alpha < 2$  and  $s$  in an intensity threshold.

Generators based on Equation (29) are ‘universal’ and characterized by two fundamental equations, describing the scale probability distribution  $c(\gamma)$  and the moments scaling exponent function  $K(q)$  as follows (Tessier et al., 1993):

$$c(\gamma - H) = \begin{cases} C_1 \left( \frac{\gamma}{C_1 \alpha'} + \frac{1}{\alpha} \right)^{\alpha'} & \text{for } \alpha \neq 1 \\ C_1 \exp\left(\frac{\gamma}{C_1} - 1\right) & \text{for } \alpha = 1, \end{cases} \quad (30)$$

$$K(q) - qH = \begin{cases} \frac{C_1}{\alpha - 1} (q^\alpha - q) & \text{for } \alpha \neq 1 \\ C_1 q \ln(q) & \text{for } \alpha = 1, \end{cases} \quad (31)$$

where in Equation (31)  $q = \frac{dc}{d\gamma} \geq 0$ ,  $\alpha$  is valid for the interval  $[0, 2]$  and  $\alpha'$  fulfils the relation:

$$\frac{1}{\alpha} + \frac{1}{\alpha'} = 1 \quad \text{for } \alpha \neq 1 \quad (32)$$

The parameters described by Equations (30) and (31) that is  $\alpha$ ,  $C_1$  and  $H$  are the ‘universal’ multifractal parameters, described in detail below (de Lima, 1998; Bernardara, 2007):

$H$  – characterizes the *deviation from conservation* (that is:  $\langle \varepsilon_\lambda \rangle = \lambda^{-H}$ ), it is also called *index of nonstationarity* (smoothness of data). Usually is determined experimentally. As is demonstrated by Pandey et al. (1998), for conserved processes  $H = 0$ , and the thus functions in Equations (30) and (31) become two-parameter  $\alpha$  and  $C_1$  function. For the analysis of the Warsaw field, the precipitation series are generated as for a conserved process (the generation process of synthetic rainfall series made as for conserved process is described in Section 6.11).

$C_1$  – is the *index of intermittency*; it describes the sparseness or inhomogeneity (i.e. the distance from homogeneity) of the mean of the process. It stands for the codimension of the singularity of the mean: for non-conserved processes  $C_1 = c(C_1 - H)$ . For conserved processes is at the same time the order of singularity and the codimension of the mean of the process. A process with  $C_1 = 0$  is homogeneous.

$\alpha$  – is the *degree of multifractality*, or the deviation from monofractality. Is fundamental to the classification of multifractal process. It is also the *Lévy index* already described. The influence of  $\alpha$  parameter on the magnitude of codimension function and moment scaling function curvature is shown in Fig. 6.4:

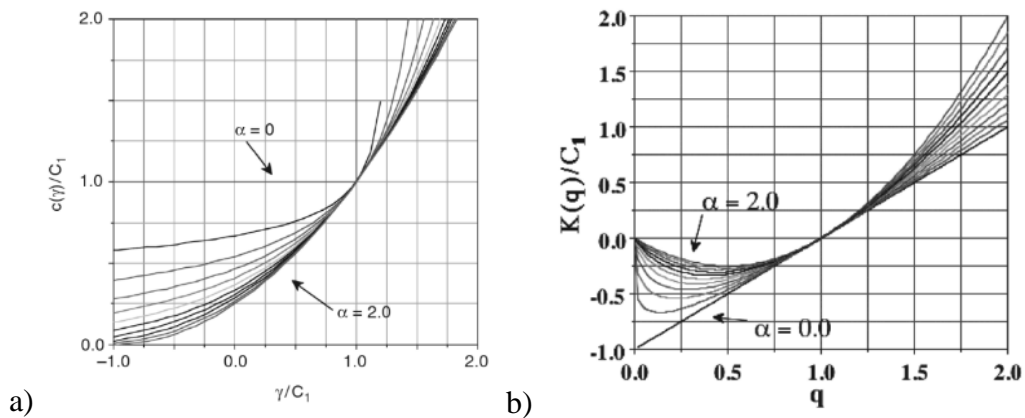


**Figure 6.4.** Universal scaling exponent functions for  $\alpha$  from 0 to 2. a) Codimension functions,  $c(\gamma)/C_1$ ; b) Moment scaling functions,  $K(q)/C_1$ . From Lovejoy and Schertzer (2013)

The degree of multifractality is also suitable to determine the universality classes, defined as the magnitude of the parameter  $\alpha$  (de Lima, 1998):

- *Unconditionally hard* multifractals are given for the interval  $1 \leq \alpha \leq 2$ . In particular
  - $\alpha = 2$ , are the log-normal (Gaussian) sets,
  - $1 < \alpha < 2$ , are the (log) Lévy processes with unbounded singularities,
  - $\alpha = 1$ , corresponds to log-Cauchy multifractals;
- *Conditionally hard* multifractals are defined in the interval  $0 \leq \alpha \leq 1$ , corresponding to the (log) Lévy processes with bounded singularities. They arise as an integration of such multifractals over an observational set with large dimension  $D$ , leading to a *soft* behaviour;
- *Monofractals* corresponding to the case  $\alpha = 0$ , whose singularities all have the same fractal dimension.

### 6.10 Hierarchical analysis

The previous sections described the path to the determination of the universal multifractal parameters, whose results are presented and discussed in Chapter 7. Once the parameters are obtained, at each rain gauge a group of universal parameters is assigned and their variability among the stations of the Warsaw rain gauge network is analysed by using the cluster analysis. The method is a data-mining tool, used both for meaningful or useful definition of groups based only on the information provided by the data (Tan et al., 2005). The analysis implies at first the aggregation of data into groups (or clusters) on the basis of their similarity, and then the determination of similarities (or differences) between the groups.

There are many types of clustering methods (Tan et al., 2005), but the most common are the (*agglomerative*) *hierarchical* techniques, where is permitted to the cluster to have subclusters, i.e. nesting of subclusters until one overall cluster containing all the elements remains. The final result is given by a tree-like diagram called a *dendrogram* on which the cluster-subclusters relationships are displayed as well as the order of merging data.

In the analysis of rainfall data, the groups of parameters for each rain gauge is considered as a single cluster of equal distance to the other. To determine the similarity between clusters specific measures of distance are used starting from the basic single link (minimum of distance between any two points in any two clusters) and ending with complex formulas depending on the analysis purposes. A detailed description of the measures is available in Tan et al. (2005).

For the Warsaw analysis, the data are subject to cluster investigation by using all the methods available in MATLAB software that is the combination of metric distance functions with the linkage methods according to the Tab.6.1 (Mathworks documentation):

**Table 6.1.** Summary of the distances functions and linkage methods used in hierarchical analysis of Warsaw data

Metric distance function	Description	Linkage method
euclidean	Euclidean distance	Average
squaredeuclidean	Squared Euclidean distance	Centroid
seuclidean	Standardized Euclidean distance	Complete
cityblock	City block metric	Median
minkowski	Minkowski distance	Single
chebychev	Chebychev distance	Ward
mahalanobis	Mahalanobis distance	Weighted
cosine	One minus the cosine of the included angle between points	
correlation	One minus the sample correlation between points	
spearman	One minus the sample Spearman's rank correlation	
hamming	Hamming distance	
jaccard	One minus the Jaccard coefficient	

The suitability of the methods employed in cluster analysis is performed by determining the *cophenetic correlation*, which is a measure of how faithfully the dendrograph represents the dissimilarities among observations. All the obtained results are presented and discussed in Chapter 7.

### 6.11 Universal multifractal generator

To generate synthetic rainfall data, a generator GENERATOR\_R, satisfying all the requirements described in Section 6.9, is adopted. It is based on the Multifractal Fields Simulation Software *EpsID* created by S. Lovejoy in 2014 (McGill University). The original *EpsID* code was developed to generate 1-dimensional multifractal fields. All the simulations are performed in MATLAB software.

The input data are: the resolution  $\lambda$  of the field, the multifractality index  $\alpha$ , the codimension index  $C_l$  and a switch to make the process causal (switch  $\cong 0$ ) or not (switch = 0). The generation process is set up for the universal parameters characterizing 3 single rain gauges (R06, R15 and R25 - Fig. 6.5) and two groups of gauges (RM23 and RM22 - Fig. 6.6) whose parameters are averaged for 23 rain gauges (excluding R15 and R25 gauges) and 22 rain gauges (excluding R06, R15 and R25 gauges) respectively.

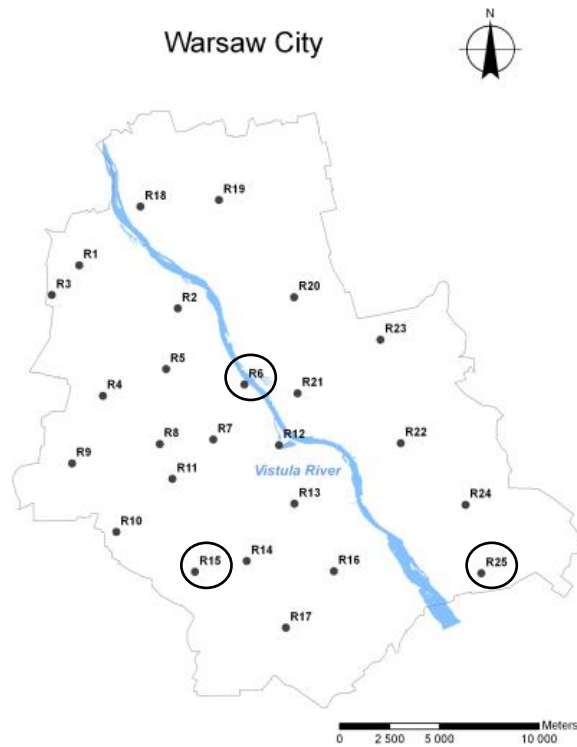


**Figure 6.5.** Locations of gauges R06, R15 and R25 for which synthetic series are generated from universal cascades for gauge – specific  $\alpha$  and  $C_1$  parameters, at the frame of so called single simulations

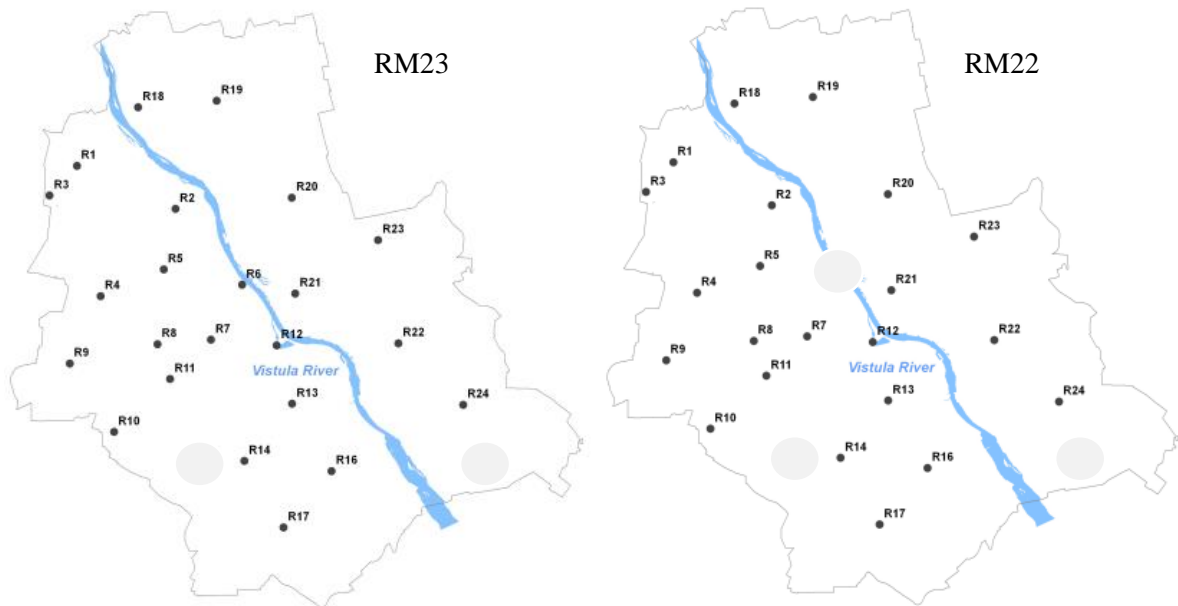


**Figure 6.6.** Locations of gauge groups RM23 and RM22 containing 23 and 22 gauges respectively for which synthetic series were performed from universal cascades for gauge – group averaged  $\alpha$  and  $C_1$  parameters, at the frame of so called average simulations

All the simulations are performed for 1-minute resolution data. The length of the time series is  $\lambda = 2^{20}$  minutes ( $\lambda \approx 2$  years). However, the quality analysis of the obtained data (in detail described in Section 6.12 and Chapter 7) revealed that the casual feature of the generator lead to obtain also very small values of precipitation intensities, far below the resolution of the rain gauges claimed by the manufacturer as 0.001 mm (compare to rain gauges technical data presented in Section 4.4), which implies the need for elimination of all the generated values smaller than 0.001 mm. For this purpose, a script called FILTR has been created in order to accumulate very small values below the recording resolution of the device. A detailed description of the obtained results is provided in Chapter 7.

After the generating process, the synthetic rainfall data are subjected to quality analysis, by the comparison of their certain statistical parameters to the ones derived for observation series. The analysis is carried out through the determination of the statistics of both types of the data series using the probability of occurrence of rain  $P(R>r)$  and the intermittency  $E(p_0)$ . Both the measures are described in the following Section.

## 6.12 Evaluation of generated rainfall time series

The qualitative assessment of the obtained data series in GENERATOR\_R is performed by comparing the statistical parameters of the generated data to the statistics of recorded rainfall time series. The parameters taken into consideration during assessment were already selected by other researches in selected evaluation of synthetic rainfall data quality originating from multifractal generation (Molnar and Burlando, 2005; Licznar, 2009; Licznar et al., 2011a; Rupp et al., 2012). The first parameter is the probability of rain  $P(R>r)$ , computed by the complementary cumulative distribution function (cCDF). The basic CDF function is the fraction of density that falls below some particular value  $x$   $CDF = Pr(X<x)$ , where  $x$  is a random variable, whose distribution is defined as  $Pr(x)$ , and here is used to evaluate the ability of the model to reproduce cumulative distribution frequency (Rupp et al., 2012). The complementary CDF is defined as  $1 - CDF = 1 - Pr(X<x) = Pr(X \geq x)$ —that is the probability that the signal power will be above the average power level (Clauset A.). While the second parameter is the intermittency  $E(p_0)$ , defined as the expected value (or the probability) of the no-rain occurrence, given by percentage of zero-rain values for 11 time scales  $\lambda = 1, 5, 10, 20, 40, 80, 160, 320, 740, 1580, 2560$  minutes ( $\sim 43$ hours). The comparison of both the parameters between generated data and the recorded series allows the assessment of the performance of the generator. To perform the statistical analysis of data two MATLAB

scripts are written: CCDF and EP0 and the computation are conducted for the data obtained directly from the generator as well as for the data after filtering process (after synthetic series postprocessing by FILTR procedure).

## 7. Results and discussion

In this Chapter, the results of analysis of the 1-minute rainfall data collected by the Warsaw rain gauge network from September 2008 to November 2010 are presented. The analysis is carried out using fractal and multifractal methods already described in Chapter 5, i.e. spectral density analysis (Section 6.4), functional box-counting method (Section 6.5) trace moment method (Section 6.6), probability distribution/multiple scaling (Section 6.7) and double trace moment method (Section 6.8), in order to determine the universal multifractal parameters. Thereafter, results of fractal and multifractal studies are used for taxonomic division of analysed rain gauges into groups of gauges displaying similarities. Synthetic precipitation series are generated from universal cascade generators parametrized by derived multifractal parameters  $\alpha$ ,  $C_1$  and  $H$ . Finally, these synthetic precipitation series are analysed and statistically compared versus recorded series based on the complementary cumulative distribution function and the intermittency studies (Section 6.12).

Hereafter, having in mind sample set of results for a 25-gauge group, all the obtained results are presented and discussed in detail only for selected rain gauges. These are distinctive gauges: R06, R15 and R25. The gauge R06 is chosen as the city centre location; the R15 due to its location at the Warsaw airport, and the R25 as the city limits location (for further discussion see Section 7.7). For the remaining rain gauges, the results are assembled in Appendices II – VI.

### 7.1 Functional box-counting method

Results of the functional box-counting method for rain gauges R06, R15 and R25 are presented in Figs 7.1÷7.3. The similar results of functional box-counting method for remaining Warsaw's rain gauges are accessible in Appendix II, Section A. The relationships between the log values of non-empty boxes and the log values of the size of the analysed boxes are plotted in all figures. The analysis is performed for four different intensity thresholds: 0, 0.04, 0.08 and 0.16 mm/min. For the first intensity threshold of 0 mm/min, the ranges of linear relationships are delineated and outlined by the dotted lines in plots.

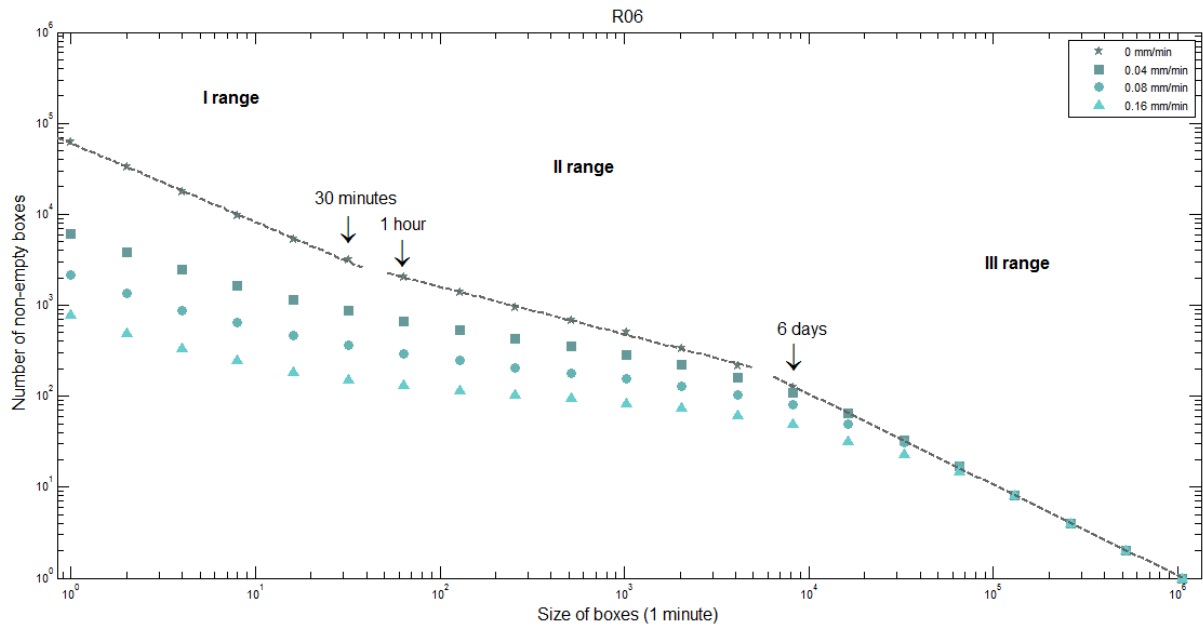


**Figure 7.1** Results of functional box-counting method for 1-minute rainfall time-series from Warsaw, for rain gauge R06

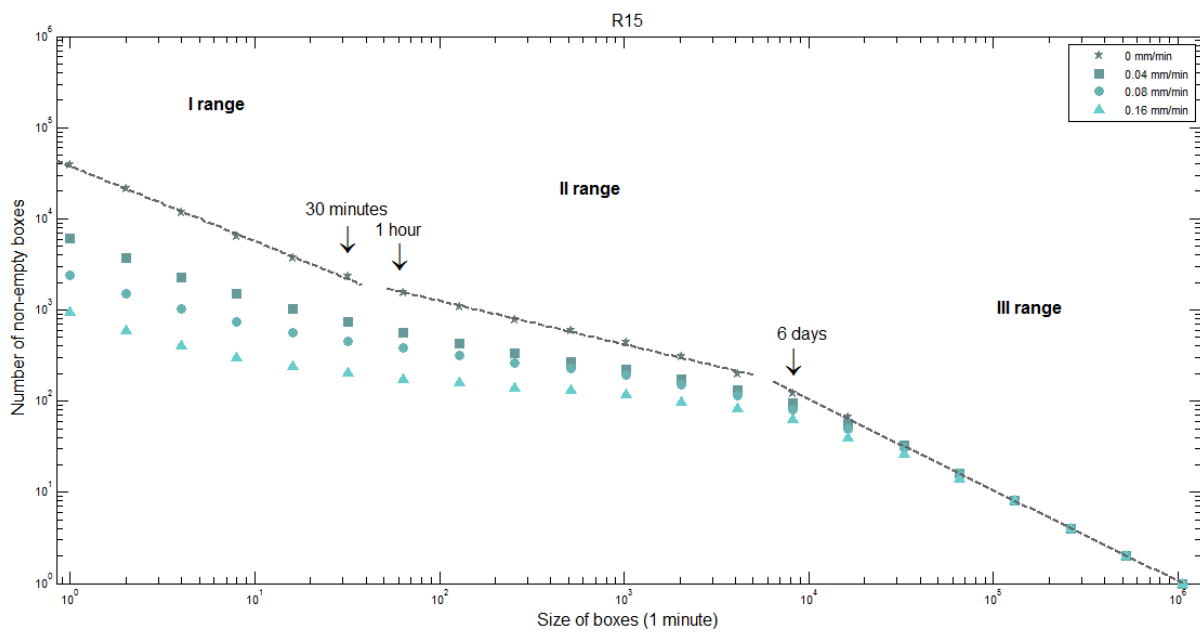


**Figure 7.2** Results of functional box-counting method for 1-minute rainfall time-series from Warsaw, for rain gauge R15

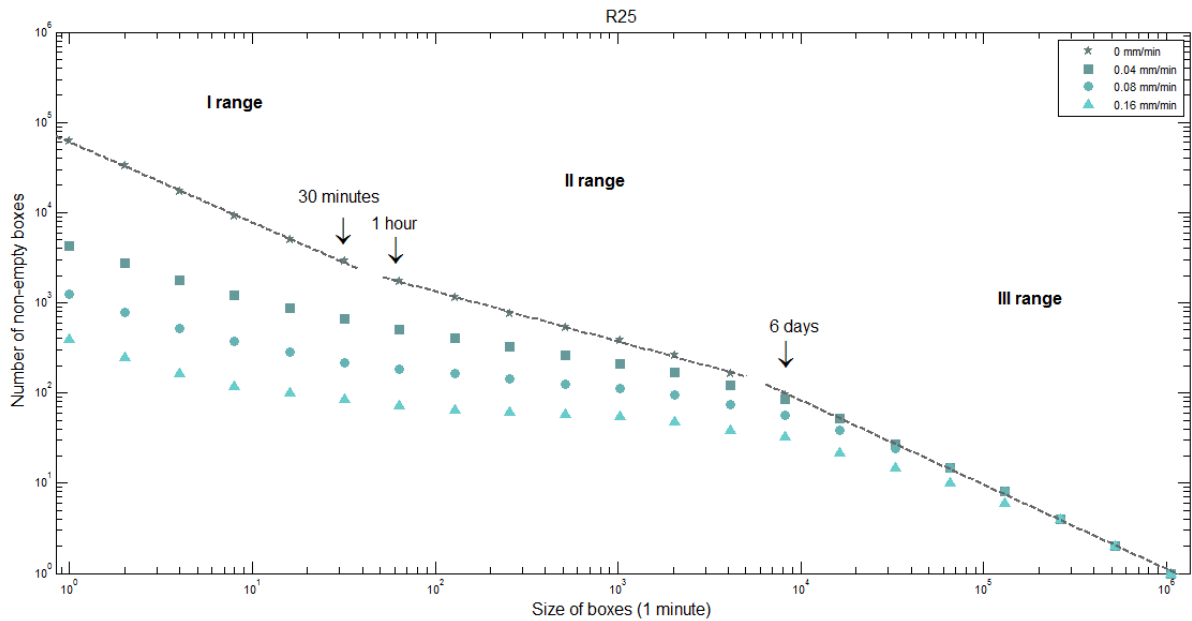


**Figure 7.3** Results of functional box-counting method for 1-minute rainfall time-series from Warsaw, for rain gauge R25

Ranges of linear relationships between the number of non-empty boxes and their size are evident on log-log plots for all 25 rain gauges. Three different ranges of scaling relationship are clearly visible on the graphs. Range I occurs between 1 and 30 minutes, range II between 60 and 300 minutes (i.e. between 1 and 5 hours), and range III – between 8640 and 1048576 minutes (i.e. 6 days and almost 2 years). For all the observed ranges of intensity threshold, the calculated slopes of linear relationship are presented in Tab.7.1. The results for all other gauges and chosen intensity thresholds are provided in Appendix II, Section B.

**Table 7.1.** Slope values of the relationships between the number of non-empty boxes and their sizes for the identified time ranges, for 1-minute time series of rainfall intensities in Warsaw from September 2008 to November 2010

Rain gauge	Intensity threshold		Range of times/box sizes		
			1-30 min	60-300 min	8640-1178710 min
R01	0	mm/min	-0.86	-0.51	-1.02
	0.04		-0.57	-0.32	-1.00
	0.08		-0.52	-0.22	-0.93
	0.016		-0.47	-0.12	-0.86
R02	0	mm/min	-0.84	-0.53	-1.01
	0.04		-0.53	-0.32	-0.99
	0.08		-0.49	-0.22	-0.94
	0.016		-0.44	-0.15	-0.85
R03	0	mm/min	-0.87	-0.54	-1.01
	0.04		-0.56	-0.34	-0.99
	0.08		-0.50	-0.23	-0.94
	0.016		-0.48	-0.15	-0.84
R04	0	mm/min	-0.88	-0.52	-1.02
	0.04		-0.57	-0.32	-0.99
	0.08		-0.54	-0.23	-0.92
	0.016		-0.50	-0.14	-0.83
R05	0	mm/min	-0.84	-0.51	-0.95
	0.04		-0.53	-0.33	-0.92
	0.08		-0.49	-0.23	-0.85
	0.016		-0.43	-0.13	-0.78
R06	0	mm/min	-0.87	-0.52	-1.00
	0.04		-0.57	-0.33	-0.98
	0.08		-0.51	-0.24	-0.92
	0.016		-0.48	-0.17	-0.81
R07	0	mm/min	-0.86	-0.53	-0.99
	0.04		-0.55	-0.35	-0.98
	0.08		-0.51	-0.24	-0.92
	0.016		-0.50	-0.14	-0.81
R08	0	mm/min	-0.86	-0.54	-0.99
	0.04		-0.55	-0.36	-0.97
	0.08		-0.53	-0.25	-0.93
	0.016		-0.47	-0.15	-0.87
R09	0	mm/min	-0.88	-0.52	-0.93
	0.04		-0.58	-0.34	-0.90
	0.08		-0.56	-0.23	-0.83
	0.016		-0.52	-0.16	-0.73
R10	0	mm/min	-0.87	-0.52	-1.02
	0.04		-0.59	-0.32	-0.99
	0.08		-0.54	-0.24	-0.92
	0.016		-0.51	-0.15	-0.82
R11	0	mm/min	-0.86	-0.55	-1.00
	0.04		-0.59	-0.34	-0.97
	0.08		-0.52	-0.24	-0.93
	0.016		-0.48	-0.15	-0.84
R12	0	mm/min	-0.87	-0.55	-1.02
	0.04		-0.60	-0.34	-0.98
	0.08		-0.52	-0.25	-0.91
	0.016		-0.47	-0.17	-0.82
R13	0	mm/min	-0.87	-0.51	-0.99
	0.04		-0.59	-0.33	-0.96
	0.08		-0.54	-0.23	-0.92
	0.016		-0.51	-0.16	-0.85
R14	0	mm/min	-0.84	-0.57	-1.03
	0.04		-0.58	-0.33	-0.99
	0.08		-0.53	-0.25	-0.92
	0.016		-0.53	-0.16	-0.82

Rain gauge	Intensity threshold		Range of times/box sizes		
			1-30 min	60-300 min	8640-1178710 min
R15	0	mm/min	-0.82	-0.48	-1.00
	0.04		-0.61	-0.34	-0.95
	0.08		-0.48	-0.28	-0.92
	0.016		-0.44	-0.18	-0.86
R16	0	mm/min	-0.88	-0.53	-1.02
	0.04		-0.58	-0.34	-0.99
	0.08		-0.52	-0.24	-0.91
	0.016		-0.50	-0.15	-0.83
R17	0	mm/min	-0.86	-0.52	-1.02
	0.04		-0.58	-0.35	-0.98
	0.08		-0.53	-0.26	-0.91
	0.016		-0.50	-0.19	-0.81
R18	0	mm/min	-0.84	-0.50	-1.03
	0.04		-0.55	-0.32	-1.01
	0.08		-0.51	-0.21	-0.93
	0.016		-0.43	-0.13	-0.84
R19	0	mm/min	-0.86	-0.50	-1.02
	0.04		-0.60	-0.31	-0.99
	0.08		-0.52	-0.23	-0.91
	0.016		-0.43	-0.16	-0.83
R20	0	mm/min	-0.88	-0.52	-1.00
	0.04		-0.59	-0.33	-0.98
	0.08		-0.53	-0.25	-0.91
	0.016		-0.47	-0.14	-0.83
R21	0	mm/min	-0.87	-0.53	-1.00
	0.04		-0.57	-0.36	-0.98
	0.08		-0.52	-0.25	-0.92
	0.016		-0.47	-0.16	-0.83
R22	0	mm/min	-0.88	-0.52	-1.00
	0.04		-0.58	-0.33	-0.97
	0.08		-0.51	-0.24	-0.91
	0.016		-0.46	-0.16	-0.83
R23	0	mm/min	-0.85	-0.52	-1.01
	0.04		-0.59	-0.31	-0.98
	0.08		-0.52	-0.23	-0.91
	0.016		-0.48	-0.16	-0.79
R24	0	mm/min	-0.89	-0.53	-0.93
	0.04		-0.61	-0.34	-0.92
	0.08		-0.54	-0.24	-0.88
	0.016		-0.49	-0.17	-0.77
R25	0	mm/min	-0.89	-0.55	-0.94
	0.04		-0.54	-0.34	-0.92
	0.08		-0.50	-0.21	-0.84
	0.016		-0.44	-0.13	-0.70

A mutual comparison and statistical analysis of the obtained slopes for all 25 Warsaw rain gauges (Tab.7.2) indicates statistical similarities between the rain gauge data within the same intensity threshold. For all four thresholds, the slopes are very close to the mean value as evidenced by a low standard deviation, even though the variability of the slopes slightly increases with the increasing of intensity. The external ranges of linear relationships (I and III) for the intensity threshold equal to 0 mm/min are very close to each other, and amount on average to -0.86 and -1.00 (Tab.7.2). Similar results are found by Licznar (2009) for 5-minute precipitation data series from gauges located in Wrocław, about 350 km south-west of Warsaw: -0.91 and -1,00 respectively.

**Table 7.2.** Basic statistics of the slope values obtained from box-counting method for three distinctive time ranges and for the analysed intensity thresholds for Warsaw rain gauge network

Intensity threshold	0 mm/min			0.04 mm/min		
Range	I	II	III	I	II	III
Average	-0.86	-0.53	-1.00	-0.57	-0.33	-0.97
Median	-0.87	-0.52	-1.00	-0.58	-0.33	-0.98
Standard deviation	0.02	0.02	0.03	0.02	0.01	0.03
Minimum	-0.89	-0.57	-1.03	-0.61	-0.36	-1.01
Maximum	-0.82	-0.48	-0.93	-0.53	-0.31	-0.90
First quartile (25th %)	-0.88	-0.53	-1.02	-0.59	-0.34	-0.99
Third quartile (75th %)	-0.86	-0.52	-0.99	-0.56	-0.32	-0.97
Intensity threshold	0.08 mm/min			0.16 mm/min		
Range	I	II	III	I	II	III
Average	-0.52	-0.24	-0.91	-0.48	-0.15	-0.82
Median	-0.52	-0.24	-0.92	-0.48	-0.15	-0.83
Standard deviation	0.02	0.02	0.03	0.03	0.02	0.04
Minimum	-0.56	-0.28	-0.94	-0.53	-0.19	-0.87
Maximum	-0.48	-0.21	-0.83	-0.43	-0.12	-0.70
First quartile (25th %)	-0.53	-0.25	-0.92	-0.50	-0.16	-0.84
Third quartile (75th %)	-0.51	-0.23	-0.91	-0.46	-0.14	-0.81

The slope values of the middle plots' sections for all the 25 rain gauges differ from the two external ranges; for instance, for the rain gauges R06, R15 and R25 these range slopes are equal to -0.52, -0.48 and -0.55 respectively (Tab.7.1), whereas the overall value of 25 rain gauges is -0.53. The middle range of linear relationship (range II) between 60 and 300 minutes is considered the multifractal dimension of the geometrical "support" of rainfall occurrence (de Lima, 1998; Licznar, 2009). Hereby, the multifractal dimension of the geometrical "support" of rainfall occurrence for the Warsaw rain gauge network is  $D \approx 0.53$ . For comparison, for a 5-minute data series from Wrocław, Licznar (2008) reported the multifractal dimension of support  $D \approx 0.58$  (Licznar, 2009), while for 1-minute rainfall data series from Vale Formoso (Portugal) de Lima (1998) obtained  $D \approx 0.50$ .

The above-mentioned authors point out a limitation to the functional box-counting method to the proper investigation of multifractal dimensions in the two external ranges due to the "saturation" effect, visible here for scales smaller than 30 minutes and larger than 6 days. The saturation of the III range is easily explained: for scales larger than 6 days, all boxes are filled with data, so the number of non-empty (full) boxes is always equal to the number of boxes. Therefore, the decreasing slope of the graph is given by the decreasing overall number of boxes of higher dimension, thus the slope of range III will be always 1.

The case of I range is more complex: for time scales smaller than 30 minutes (range I), the slope of the graph indicates the occurrence of almost non-zero rainfall periods, i.e., the set of observed data almost entirely covers the available space of time. The presence of such a critical scale in box-counting method can be explained by the poor ability of the measuring device to capture the intermittency and variability of rain (no rain periods). It could result

from superposition of gauge resolution and *step response error*, i.e. the already discussed phenomenon of dampening/broadening (averaging) of the registration data by rain gauges over the range of few minutes.

From the analysis of the middle section of the plots (I range), a dependency emerges between the absolute values of the slope and the magnitude of the threshold: the values of the slope, for all the analysed rain gauges, decreases with the increasing of the intensity threshold. To the intensity thresholds: 0, 0.04, 0.08 and 0.16 correspond the average slope values for 25 Warsaw rain gauges equal to: -0.53, -0.33, -0.24 and -0.15, i.e. the fractal dimension  $D$  is respectively: 0.53, 0.33, 0.24 and 0.15. It follows that for infinite magnitude values an infinite number of fractal dimension would be found, so it implies an infinite hierarchy of dimension. This is the first proof that the precipitation process has a multifractal structure, thus the further application of multifractal analysis techniques is justified.

## 7.2 Spectral density analysis

The resulting power spectra plots obtained for the Warsaw gauges by the spectral density analysis are presented in a log-log scale. The plots are smoothed for high frequencies. The sample energy spectra obtained for 1-minute of the Warsaw gauges time series for rain gauges R06, R15 and R25 are presented in Figs 7.4-7.6. They evidently display scale-invariant behaviour over a range of scales. The power-law described by Equation (12) holds for two distinctive ranges of highest frequencies. The first range of frequencies plot in Fig. 7.4 starts from 29 1/h and ends at 0.7 1/h, while the second is in the range from 2 to 0.042 1/h. The spectrum plot shown in Fig. 7.5 presents the first range from 30 1/h up to 0.7 1/h, while the second range is delimited is set between 2.5-0.042 1/h. Finally, in case of the spectrum in Fig. 7.6, the first range includes frequencies from 1.7 to 30 1/h, whereas the second range starts at a frequency of 2.2 1/h and reaches up to 0.042 1/h. For both the ranges the linear regressions of  $\log(P(f))$  and  $\log(f)$  are marked on the graphs with a dotted line and their slopes are stated. Similar behaviour is found in almost all the remaining Warsaw rain gauges (Appendix III, Section A). To determine the power spectral densities of the Warsaw precipitation 1-minute time series, recorded from September 2008 to November 2010, a Pascal program SPECTRUM\_Warsaw and a MATLAB script EvaluateSpectrum2b are used.

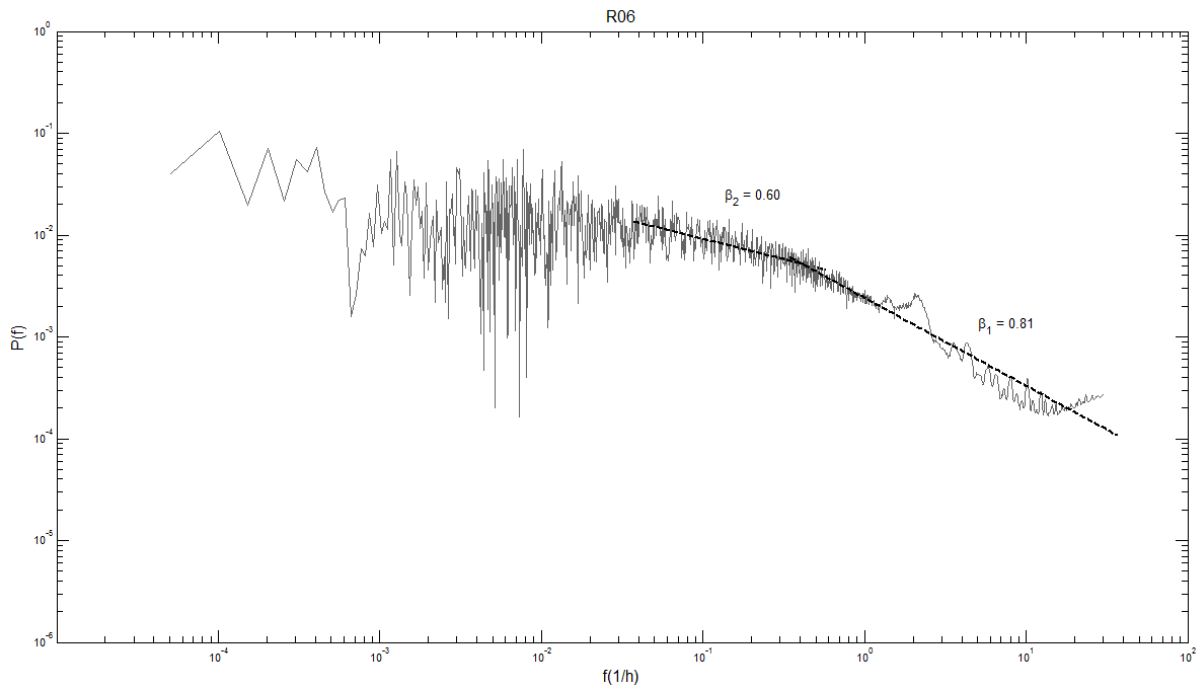


**Figure 7.4.** Energy spectrum for 1-minute rainfall time-series from Warsaw, from September 2008 to November 2010, for rain gauge R06

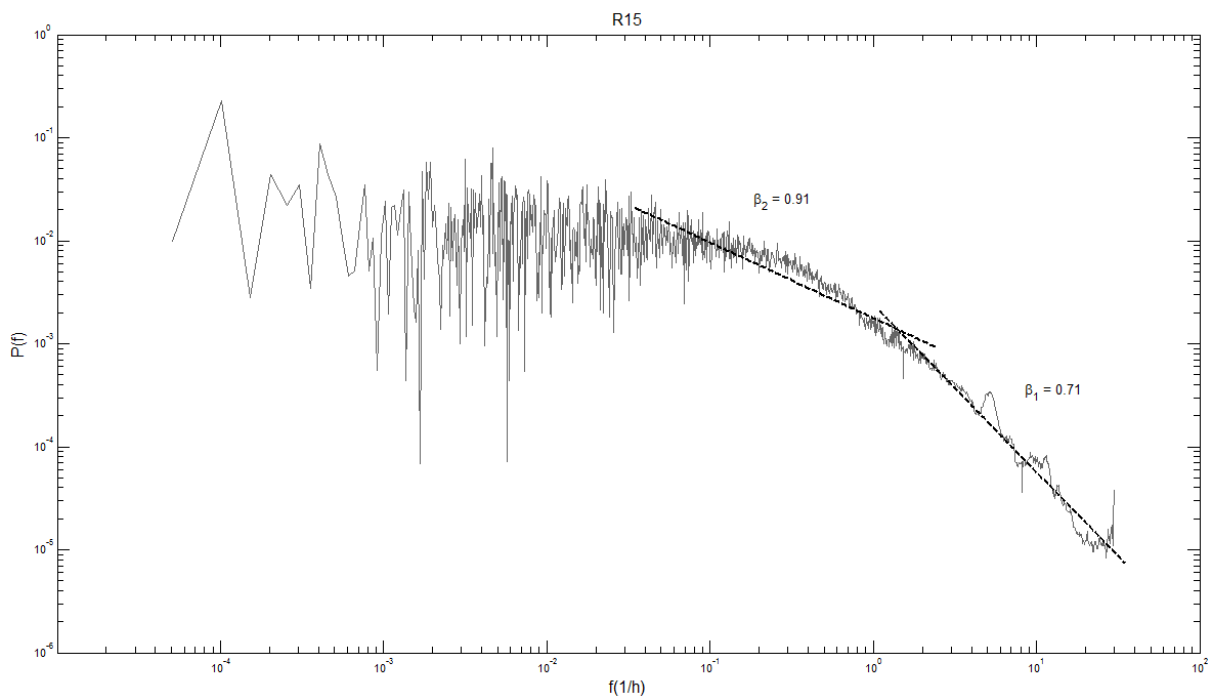


**Figure 7.5.** Energy spectrum for 1-minute rainfall time-series from Warsaw, from September 2008 to November 2010, for rain gauge R15

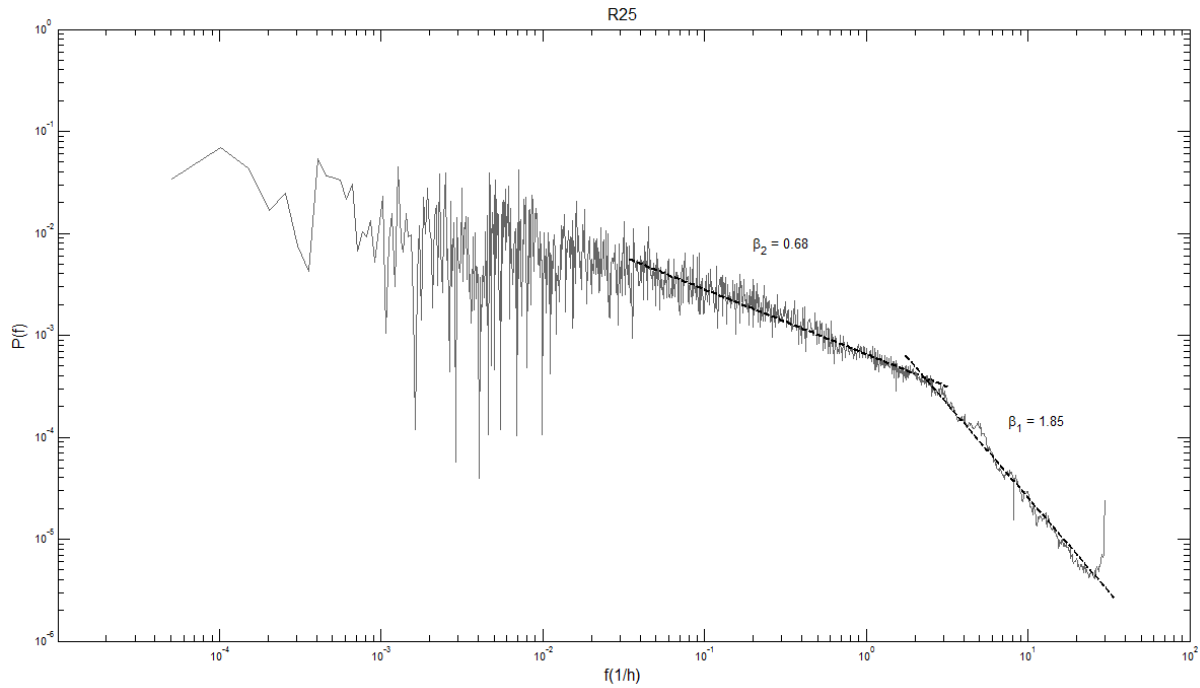


**Figure 7.6.** Energy spectrum for 1-minute rainfall time-series from Warsaw, from September 2008 to November 2010, for rain gauge R25

Most of the energy spectra exhibit no distinct spectral peaks, indicating the presence of periodicity in the time series; only in case of R09 and R23 a slight peak can be seen for the frequency corresponding to about 2 months (Figs III.8 and III.21 Appendix III, Section A).

As shown in Tab.7.3, in almost every case for high frequencies the spectrum slope, i.e. the exponent  $\beta_1$ , is greater than 1 (excluding R03 and R06), and is equal on average to 1.68. Moving down in frequency, excluding the significantly outlying R06, a spectral “brake” is observable in correspondence of the frequencies ranging from 0.42 to 0.91 1/h (i.e. 25-55 minutes). This spectral brake agrees with the critical scale obtained during functional box-counting analysis (Figs 7.4÷7.6, range of break: 30-60 minutes). By that means, on a time scale corresponding to a frequency of about  $f = 1.8$  1/h ( $\approx 33$  minutes) a transition region from one scaling behaviour (for higher frequencies) to another (for lower frequencies) is recognizable. For the latter, the fluctuation of energy spectra is significant but, at least up to a frequency of about 0.042 1/h (that is 24 hours) a power law relation is still observable. The spectral exponent  $\beta_2$  for this range of frequencies is smaller than 1 in almost all the cases (excluding R17) and on average is 0.68. All the mentioned above parameters had been read directly from the graphs.

**Table 7.3.** Spectral exponents of two scaling regimes for 1-minute time series energy spectra, from 25 rain gauges with basic statistics

Rain gauge	$\beta_1$	$\beta_2$	Break point (minutes)
R01	1.53	0.63	35
R02	1.60	0.57	40
R03	1.00	0.72	32
R04	1.85	0.74	25
R05	1.20	0.57	55
R06	0.81	0.60	150*
R07	1.74	0.77	43
R08	1.34	0.85	40
R09	1.75	0.77	35
R10	1.92	0.72	30
R11	1.72	0.80	27
R12	1.79	0.67	33
R13	1.53	0.61	40
R14	2.01	0.73	30
R15	1.71	0.91	29
R16	1.91	0.80	25
R17	1.86	1.00	32
R18	1.56	0.59	46
R19	1.91	0.59	33
R20	2.06	0.51	32
R21	2.12	0.51	27
R22	1.32	0.48	50
R23	1.72	0.59	38
R24	2.18	0.63	26
R25	1.85	0.68	25
Average	1.68	0.68	34
Median	1.74	0.67	32
Standard deviation	0.34	0.13	8
Minimum	0.81	0.48	25
Maximum	2.18	1.00	55
First quartile (25th)	1.53	0.59	28
Third quartile (75th)	1.91	0.77	40

\*value omitted as extremely outlying at calculation of set statistics

The basic statistics demonstrate variability of the analysed values within the set of the time series from 25 Warsaw rain gauge network. The values of the spectral exponents change between 0.81 and 2.18 for  $\beta_1$  and between 0.48 and 1.00 for  $\beta_2$ . Despite the clear variation of extreme values, it should be noted that the analysed sets of parameters are relatively tightly clustered around the mean values, as evidenced, especially for  $\beta$  exponents, by a low value of standard deviation and the proximity of the first and third quartiles to the mean values.

The above described results concerning the rain gauge network in Warsaw are in good agreement with the results obtained by the study conducted by Licznar et al. (2011) in 4 locations in Germany revealing a spectral break at 60 minutes. The values of spectral exponents for rainfall data collected by 4 rain gauges are:  $\beta_1$  greater than 1, and  $\beta_2$  around 0.5 (Licznar et al., 2011). The same study conducted by Licznar (2009) in Wrocław (Poland) for rainfall data series recorded in 1964 and 1997 provides similar results: the spectral break

occurs for 110 and 85 minutes and the values of spectral exponents amount to 0.27 and 0.28 for  $\beta_1$ , and 1.40 and 1.11 for  $\beta_2$  (Licznar, 2009; Licznar et al., 2011). Analogously, de Lima (1998) obtained  $\beta_1$  equal to 0.73 and 0.96, and  $\beta_2$  equal to 0.15 and 0.21 for rainfall data series collected in Vale Formoso (Portugal) and Nancy (France). Furthermore, spectral breaks are observed respectively for frequencies corresponding to around 100 minutes for Vale Formoso and from 17 to 80 minutes for Nancy (de Lima, 1998).

In all the above-mentioned studies, a scale invariant behaviour is detected over a range of scales as well as the spectrum break, which, however occurs for different time scales; this fact is strictly related to the difficulty of calculating the exact point where the spectral break arises, and therefore, the determination of the precise value of the spectral exponent  $\beta$  is problematic. A detailed study conducted by de Lima (1998) on over 20-years rainfall time series demonstrates that there is no fundamental character of the observed energy spectral break; indeed, on analysed power spectra of different  $\eta$ -power renormalized rainfall process, the spectral break does not occur at a fixed scale, and by that means, it does not depend on the intensity of the process. Therefore, the presence of a break is directly related to the scale-dependent difficulties of measuring and/or the technique adopted to processing data.

It is reasonable to say, that the quantization of the rainfall process by the currently available measuring devices, like those forming the Warsaw rain gauge network, affects significantly the proper reflection of natural rainfall process for time series resolution smaller than 5 minutes. Thus, it raises the question whether such a level of resolution in recording data it is achievable by generally accessible devices. Studies conducted by Menabde et al. (1997) on 17 hours of 15-seconds rainfall rime series, recorded by a high-time-resolution rain gauge in Norfolk Island and Matawai (New Zealand) confirm the scale invariant behaviour and moreover, the presence of a single spectral exponent ( $\beta = 1,52$  – Norfolk Island and  $\beta = 1,37$  – Matawai) for the time scales form 4 minutes up to 17 hours. Despite the high resolution of the data, the analysis is not performed by Menabde et al. (1997) for time scales smaller than 4 minutes, clearly avoiding quantization of data for higher frequencies.

It is important to note that the discussed energy spectra are obtained for a precipitation time series (containing both liquid and solid precipitation records) whereas the mentioned studies of de Lima (1998) and Licznar (1998) were limited to only rainfall time series analysis. In Warsaw, most rainfall precipitation falls between May and August (Fig. 7.7) and the summer precipitation, in many cases (R06 and R15), is twice (or triple) that of winter precipitation when low intensity events dominate. In addition, winter precipitation is dominated by stratiform-type, long-lasting and small or moderate intensity events. Whereas in

summer, except long-lasting and small intensity stratiform events, one can expect also convective rainfalls of shorter durations but much higher and more variable intensities. In order to have a better insight into this phenomenon, sample energy spectra are calculated for separate periods of summer and winter half-years.

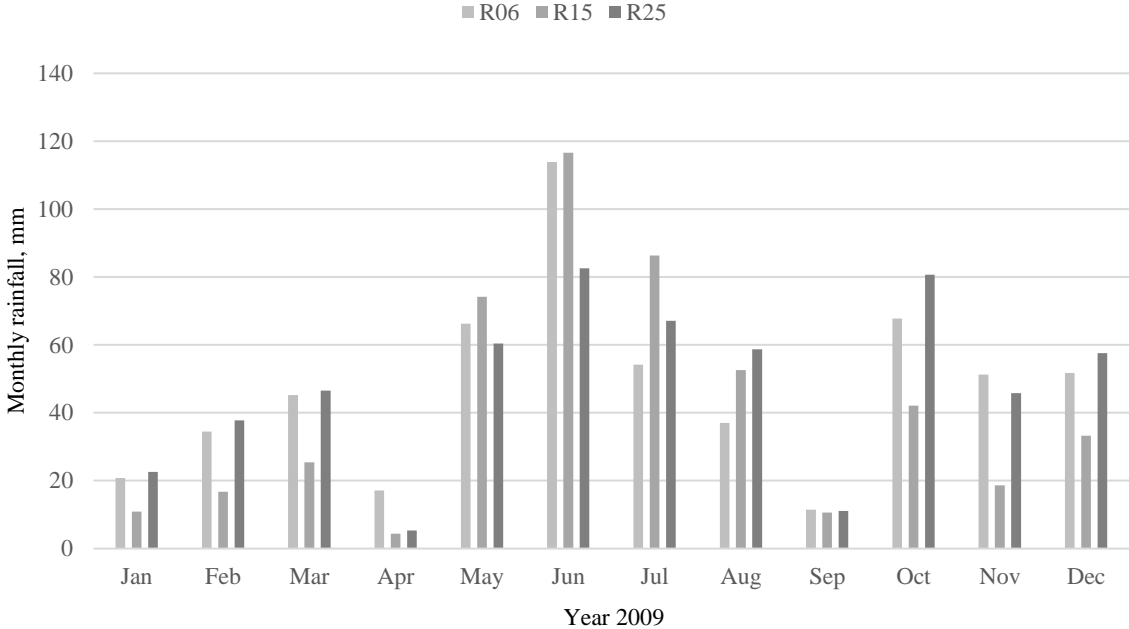


**Figure 7.7.** Monthly rainfall in Warsaw (2009) for gauges R06, R15 and R25

Sample energy spectra for summer and winter season, for rain gauges R06, R15 and R25 are presented in Figs 7.8÷7.10 (all the remaining result are listed in Appendix III, Section B). As for the already discussed all year long spectra, the seasonal graphs present a scale-invariant (power-law) behaviour over a range of scales, occurring in almost all the cases, although winter spectra are generally characterized by a smoother behaviour. The analysis of seasonal energy spectra reveals the presence of spectral breaks, but at shifted frequencies locations are compared to a year-long series. As shown in Tab.7.4, the spectral break in summer is formed for frequency corresponding on average to times of 61 minutes, while the winter spectral break is observed form small frequencies, corresponding on average to time of 13 hours and 24 minutes.

The above discussed observations confirm the hypothesis that the precipitation forming mechanisms have influence on energy spectra shape. The vivid shift of a spectral break occurrence for separate summer and winter half-years could be explained by the seasonality of precipitation: summer precipitation generally occurs as short-duration and high intensity storms; during summertime, there is a high frequency of convective storms, forming along a fast-moving cold front, whereas winter stratiform precipitation occurs usually as low-intensity

rain or snow, generated by a slow-moving cold fronts. A stratiform precipitation can be distinguished from a convective event if its vertical air velocity is less than the terminal fall velocity of ice crystals and snow (Houze, 1993). Most probably, the estimated times of spectral breaks of 61 minutes, and 13 hours and 24 minutes could be associated with the duration times of respectively shorter convective storms and much longer stratiform precipitations in Warsaw.

**Table 7.4.** Spectral energy breaks for 1-minute summer and winter time series, from 25 rain gauges with their basic statistics.

Rain gauge	Summer season	Winter season
	Break point	
	min	-
R01	67	16h 24 min
R02	56	28h 11 min
R03	67	34h 28 min
R04	59	14h 17 min
R05	59	10h 55 min
R06	56	14h 17 min
R07	74	13h 9 min
R08	85	18h 46 min
R09	77	7h 16 min
R10	60	9h 48 min
R11	61	12h 20 min
R12	52	14h 19 min
R13	61	6h 32 min
R14	61	12h 30 min
R15	85	4h 30 min
R16	61	10h 12 min
R17	222*	5h 24 min
R18	51	34h 31 min
R19	231*	4h 30 min
R20	55	17h 33 min
R21	43	4h 12 min
R22	51	153h 50 min*
R23	61	16h 40 min
R24	55	11h 41 min
R25	55	9h 32 min
Average	61	13h 24 min
Median	60	12h 25 min
Standard deviation	11	8h 26 min
Minimum	43	4h 27 min
Maximum	85	34h 28 min
First quartile (25th %)	55	8h 29 min
Third quartile (75th %)	64	16h 30 min

\*value omitted as extremely outlying at calculation of set statistics

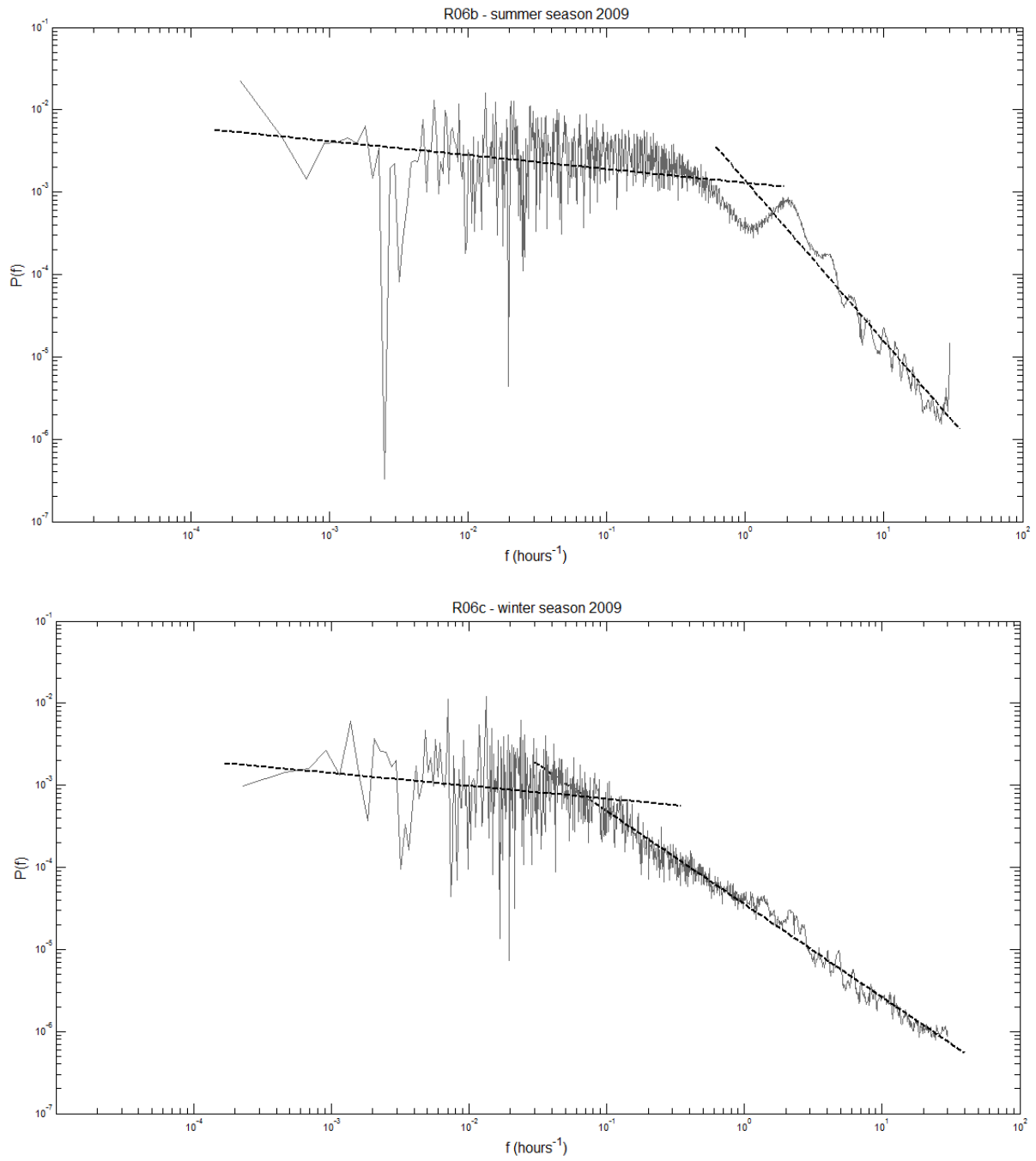


**Figure 7.8.** Energy spectra for 1-minute rainfall time-series from Warsaw, for rain gauge R06 in 2009. Summer season (upper graph) and winter season (lower graph)

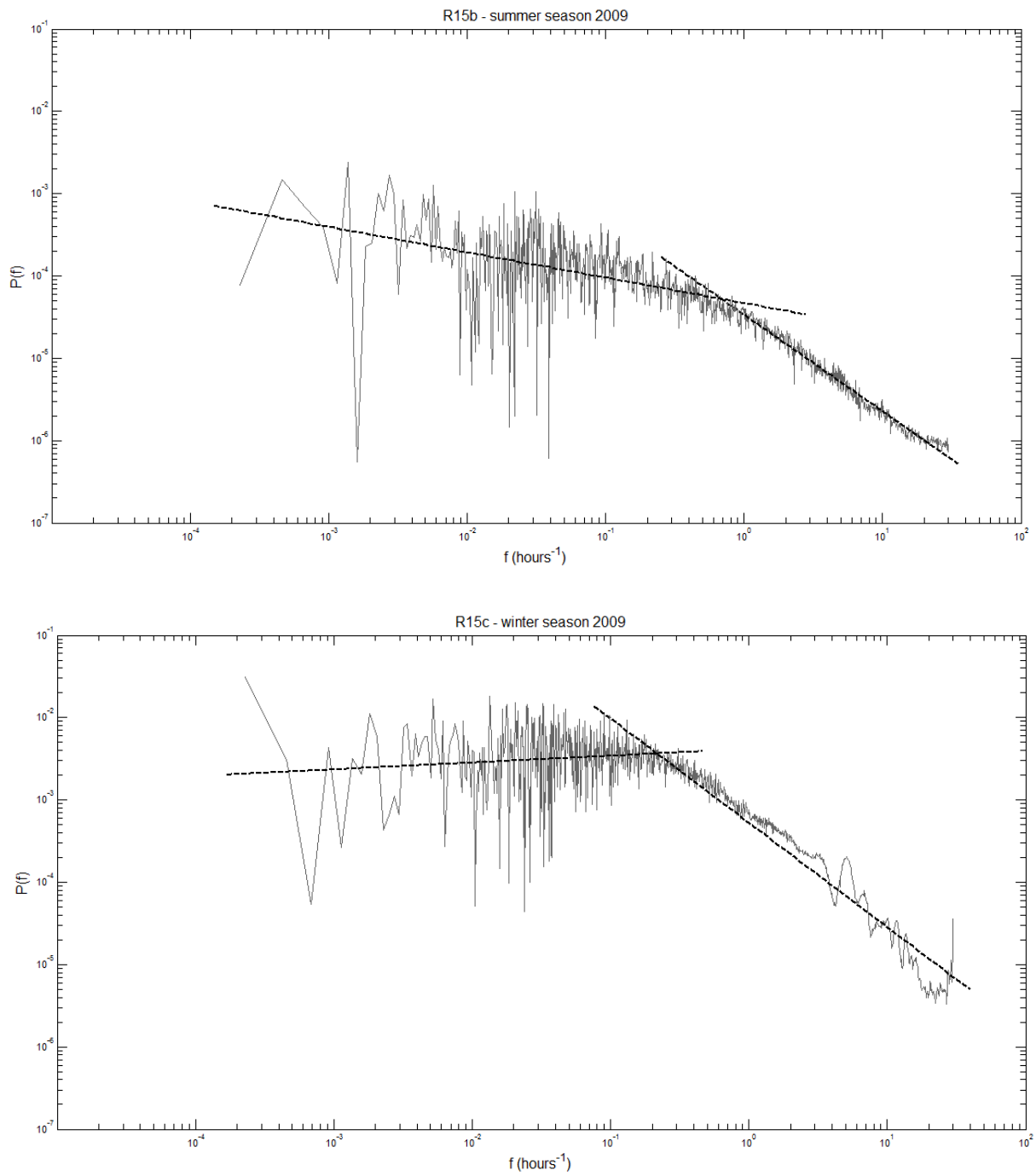


**Figure 7.9.** Energy spectrum for 1-minute rainfall time-series from Warsaw, for rain gauge R15 in 2009. Summer season (upper graph) and winter season (lower graph)

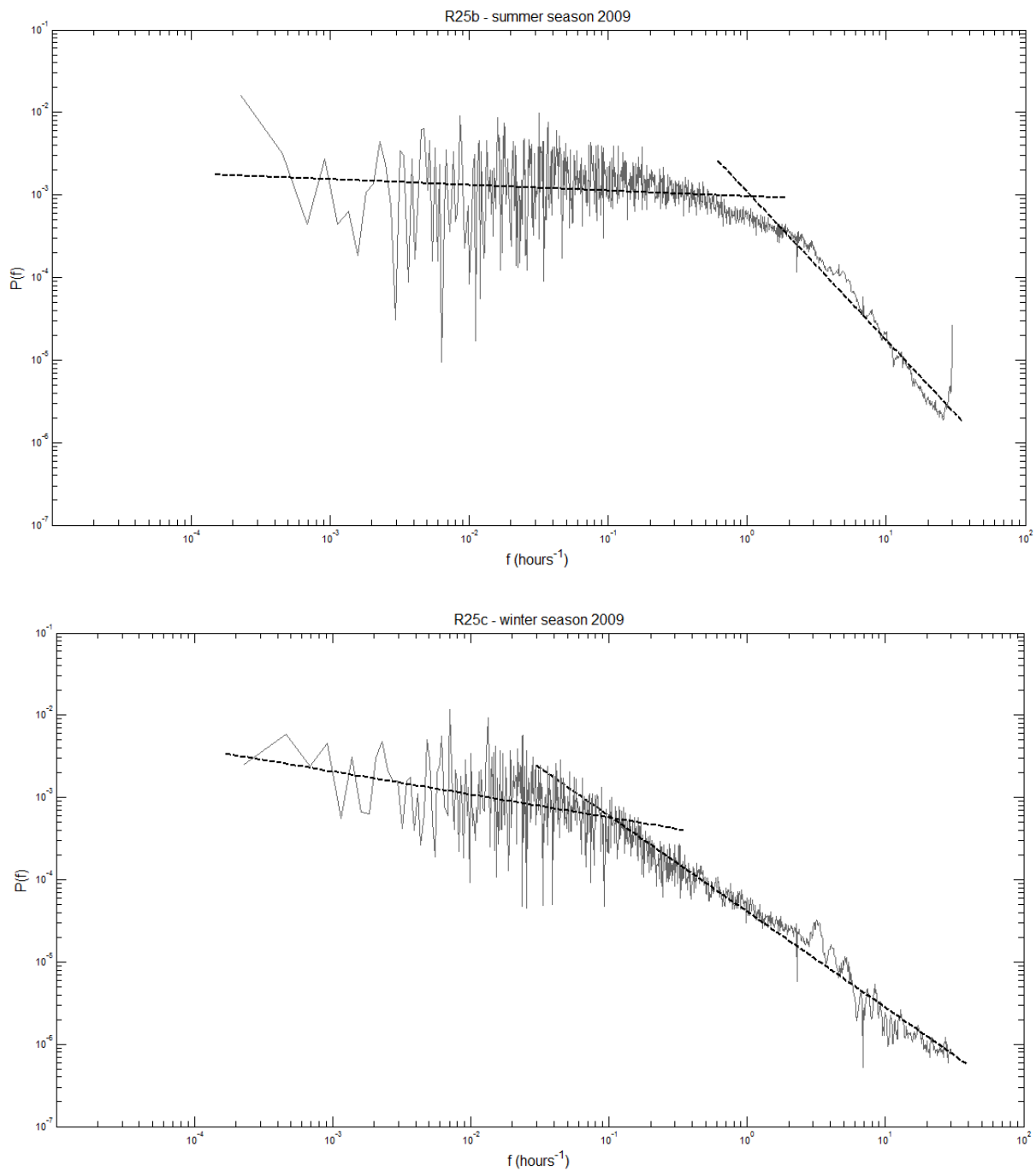


**Figure 7.10.** Energy spectrum for 1-minute rainfall time-series from Warsaw, for rain gauge R25 in 2009. Summer season (upper graph) and winter season (lower graph)

In multifractal studies, the  $\beta$  exponent plays an important role in the determination of the universal *nonstationarity index*  $H$ , which is obtained by the comparison of the spectral exponent of the examined non-stationary process to the spectral exponent of a stationary process (the calculation steps are discussed in detail in Section 7.7). To this end, the last step of spectral density analysis is the estimation of the  $\beta$  exponent for the overall time series i.e. for the total average of analysed frequencies. In Figs 7.11÷7.13 the overall slopes of the sample rain gauges R06, R15 and R25 are presented. The graphical results for the remaining 22 of the Warsaw rain gauges are set up in Appendix III, Section C.

The calculated spectral exponents of the Warsaw time series are listed in Tab.7.5. These values are the ones considered for the estimation of the multifractal parameter  $H$ .

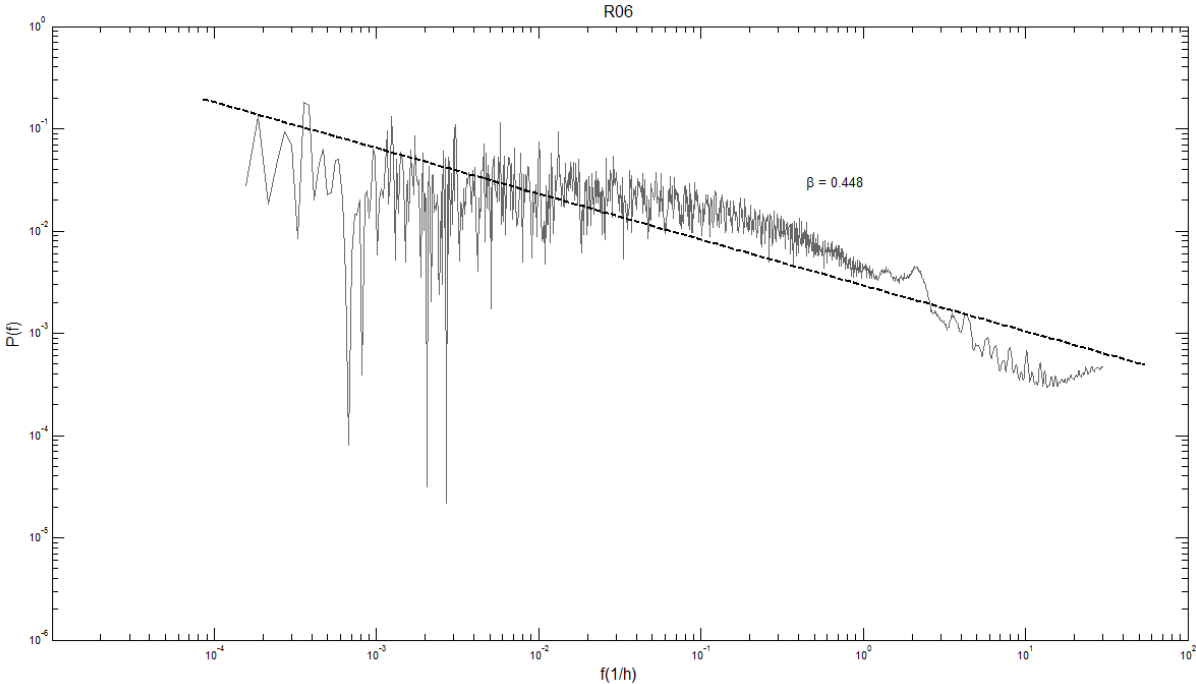


**Figure 7.11.** Energy spectrum for 1-minute rainfall time-series from Warsaw, for rain gauge R06 with the overall slope

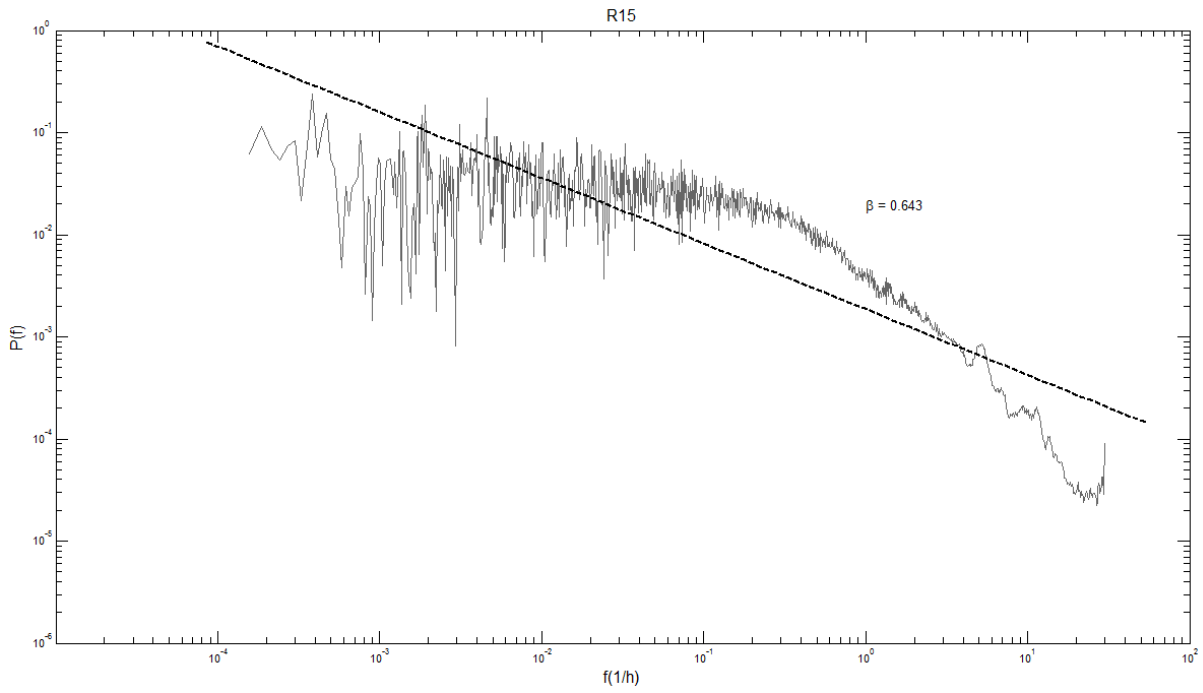


**Figure 7.12.** Energy spectrum for 1-minute rainfall time-series from Warsaw, for rain gauge R15 with the overall slope

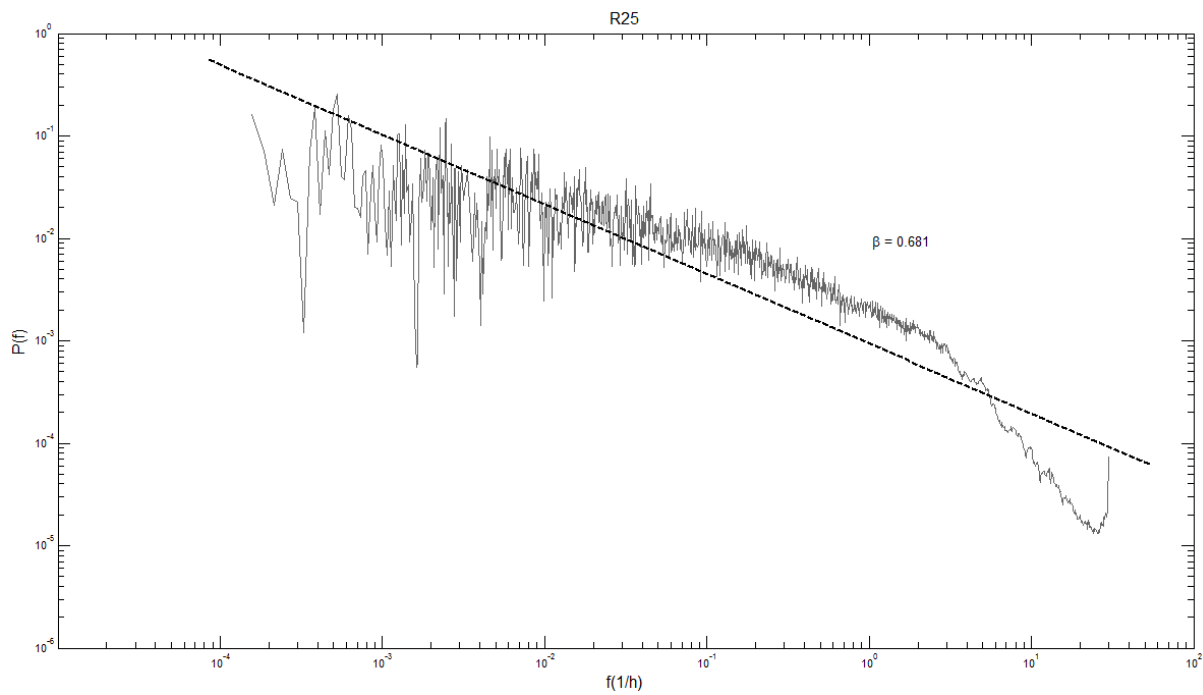


**Figure 7.13.** Energy spectrum for 1-minute rainfall time-series from Warsaw, for rain gauge R25 with the overall slope

**Table 7.5.** Spectral exponents of energy spectra for 1-minute time series from 25 rain gauges with basic statistics calculated for the whole frequency range

Rain gauge	$\beta$
R01	0.577
R02	0.569
R03	0.522
R04	0.662
R05	0.504
R06	0.448
R07	0.660
R08	0.613
R09	0.645
R10	0.647
R11	0.641
R12	0.644
R13	0.558
R14	0.670
R15	0.643
R16	0.676
R17	0.709
R18	0.573
R19	0.621
R20	0.603
R21	0.604
R22	0.532
R23	0.601
R24	0.677
R25	0.681
Average	0.611
Median	0.621
Standard deviation	0.063
Minimum	0.448
Maximum	0.709
First quartile (25th %)	0.573
Third quartile (75th %)	0.660

To sum up the spectral analysis, it can be said that the obtained results for the Warsaw rainfall time series indicate a scale-invariance of the local rainfall process, occurring particularly for time scales from 1 minute up to at least 24 hours. This peculiarity is even more pronounced in a seasonal analysis, where a scale-invariant behaviour reflects the features of summer/winter precipitation, defined by convective/stratiform nature of the process. Furthermore, the spectral breaks, separating two different scaling domains, demonstrate the existence of more than one scaling behaviour (typical of monofractals) and involves the application of more complex methods of Warsaw precipitation series studies, such as multifractal methods.

### 7.3 Trace moment method (TM)

The sample results for rain gauges R06, R15 and R25 obtained by applying the trace moment method to the 1-minute Warsaw precipitation time series are presented in Figs

7.14÷7.16 in double logarithmic scale. The results of the remaining 22 rain gauges are set up in Appendix IV, Section A. The graphs display the relationships between the log values of the average  $q$  moment of the rainfall intensity  $\varepsilon_\lambda$  and the logarithms of the scale coefficients  $\lambda$ .

The analysis is performed using TRACE\_Warsaw program and the results are plotted by means of TracePlot script for time scales from 1 minute ( $\lambda = 16384$ ) to over 16384 minutes (11 days,  $\lambda = 1$ ). The calculations are carried out for 27 values of the moments  $q \in [0.01; 7.00]$ , depending on the intensity of the event rain: 14 values smaller than 1 for low-intensity rains (to be found on the left side of the pictures) and 13 greater than or equal to 1 for high-intensity events (on the right side of the pictures). For simplicity, the pictures present only selected values of the moments  $q$  (to be read in the legend).

All the results obtained for the 25 rain gauges have a similar nature. It is possible to notice the linear relationship between the log mean values of the moments and the log scaling values  $\lambda$ , indicating the scaling nature of the analysed rainfall time series. However, for the highest and lowest values of time scales, a deviation of the expected power law (linear) behaviour is visible: a power-law line slope is decreasing at a time scale around 32 minutes to 1 hour (i.e.  $\log(\lambda) \approx 3.01 \div 2.41$ , so  $t \approx 16 \div 64$  min) for all the  $q$  moments. It is consistent with the results obtained so far by spectral density analysis and functional box counting where similar magnitude time scales were identified as “break” in scaling.

The lowering of the slope values is particularly evident for low-intensity precipitation (i.e.  $q < 1$ ) in all the 25 plots, especially for the lowest values of  $q$  (0.05, 0.3) at a time scale around 34 hours to 11 days (i.e.  $\log(\lambda) \approx 0.9 \div 0.0$ , thus  $t \approx 2048 \div 16384$  min). Whereas in the same range of scales, this kind of the slope lowering behaviour is slightly visible for the high-intensity precipitation (i.e.  $q > 1$ ). Actually, the higher the  $q$  moment, the more magnified the highest rainfall intensities and averaged  $q$ -moments values are, determined by their magnitude.

It follows that the precipitation series during recording are subjected to a clear overestimation of lower intensities and a slight underestimation of higher intensities. The obtained results are comparable with those achieved by de Lima (1998) for data from Vale Formoso, where a power law deviation at a time scale of around 30 minutes to 1 hour is observed as well as the same under/overestimation of the smallest and highest rainfall intensities.

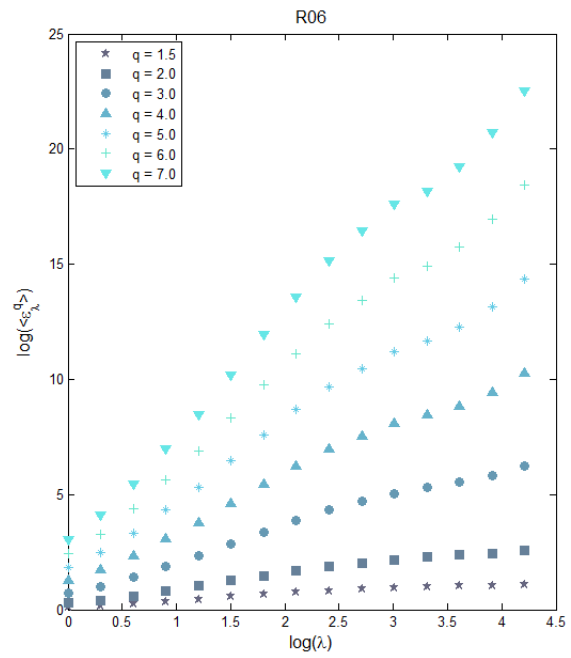
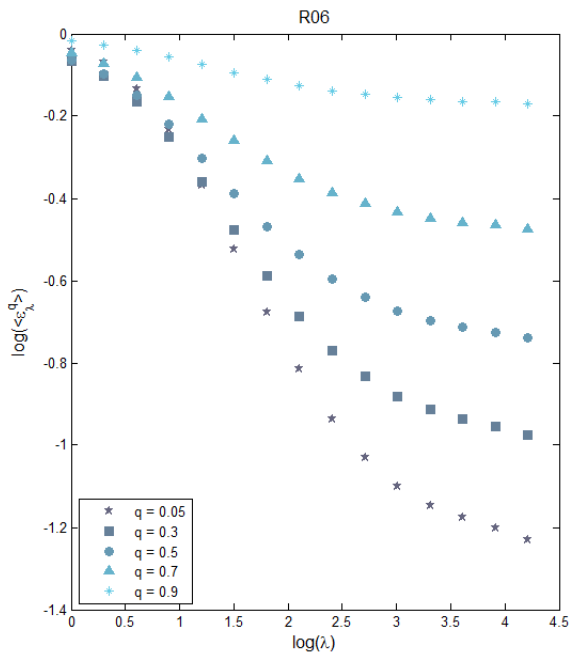


**Figure 7.14.** Log-log plot of the mean  $q$  moments of the rainfall intensity  $\varepsilon_\lambda$  against the scale coefficient  $\lambda$  for 1-minute precipitation data series from Warsaw rain gauge R06, for  $q < 1$  (on left) and for  $q > 1$  (on right). The time scales range from  $\lambda = 16384$  (1 minute) to  $\lambda = 1$  (11.4 days)

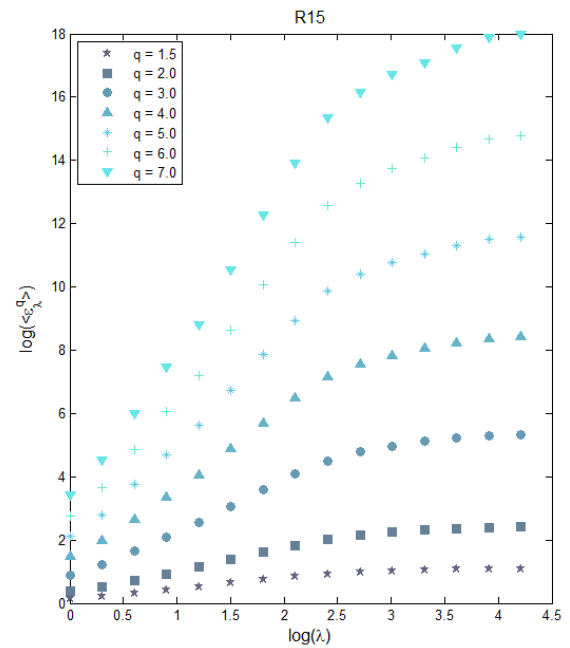
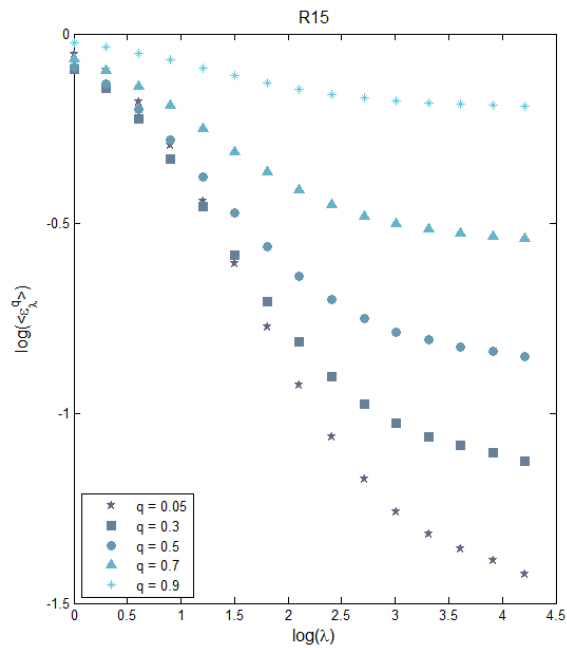


**Figure 7.15.** Log-log plot of the mean  $q$  moments of the rainfall intensity  $\varepsilon_\lambda$  against the scale coefficient  $\lambda$  for 1-minute precipitation data series from Warsaw rain gauge R15, for  $q < 1$  (on left) and for  $q > 1$  (on right). The time scales range from  $\lambda = 16384$  (1 minute) to  $\lambda = 1$  (11.4 days)

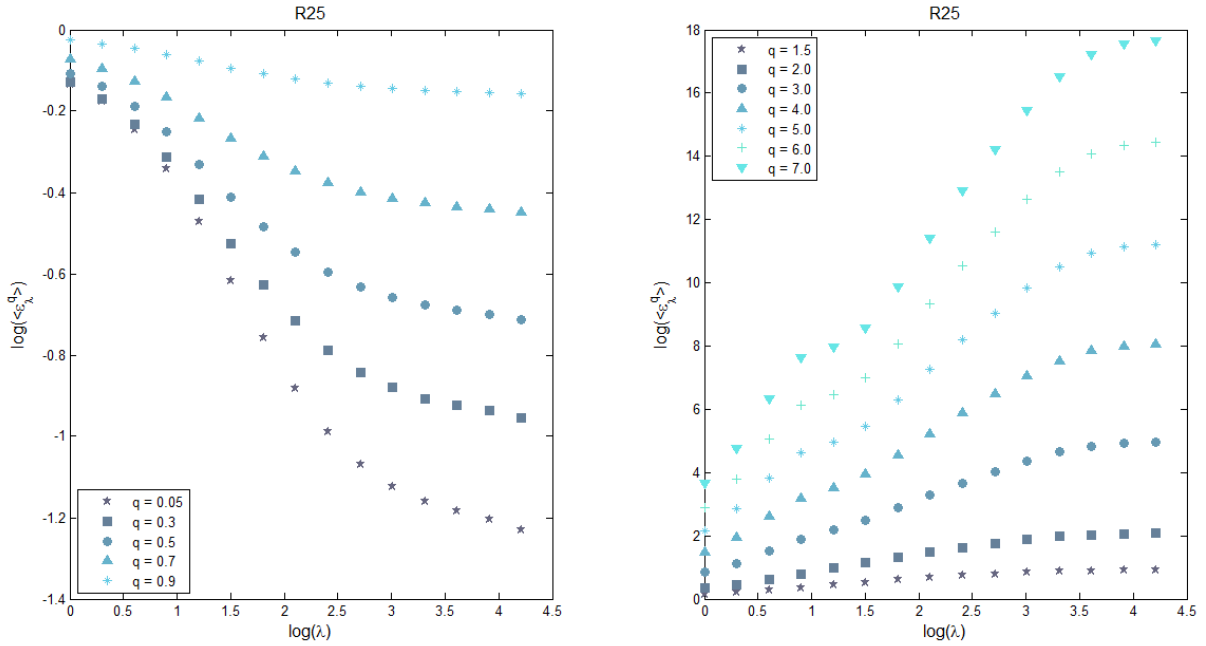


**Figure 7.16.** Log-log plot of the mean  $q$  moments of the rainfall intensity  $\varepsilon_\lambda$  against the scale coefficient  $\lambda$  for 1-minute precipitation data series from Warsaw rain gauge R25, for  $q < 1$  (on left) and for  $q > 1$  (on right). The time scales range from  $\lambda = 16384$  (1 minute) to  $\lambda = 1$  (11.4 days)

The second part of the trace moment analysis is focused on the determination of the moment scaling function  $K(q)$  which, in turn, is strictly related to the codimension function  $c(\gamma)$  obtained by the probability distribution/multiple scaling method, described in the following Section. Hereby, the results of  $K(q)$  function are discussed together with the results of  $c(\gamma)$  function in Section 7.5.

#### 7.4 Probability distribution/multiple scaling (PDMS)

PDMS method is mainly focused on determining the codimension function  $c(\gamma)$ , i.e. the scaling of the probability distributions of the given process (described in detail in the following Section). To reach this goal, it must first be appointed the relationship of the probability of exceeding rainfall-intensity levels of singularity  $\gamma$ , observed on scales of resolution  $\lambda$ , against the scale ratio  $\lambda$ . Such relationships sample log-log plots for selected Warsaw rain gauges R06, R15 and R25 as shown in Figs 7.17÷7.19. The analysis is performed for 24 values of singularity  $\gamma \in [0.04; 0.96]$ , using PDMS\_Warsaw program and PDMSplot script. For simplicity, the graphs refer only to selected singularity orders  $\gamma$  (to be read in the legend). The remaining plots for other 22 gauges are provided in Appendix V, Section A.

In all the analysed cases a scale relation of the probability  $\Pr(\varepsilon_\lambda \geq \lambda^\gamma)$  is well preserved, as evidenced by a linear shape of the log-log values, particularly for the singularity levels  $\gamma$  close

to 0.4. For the specific case of  $\gamma = 0.4$ , the linear fitting is almost exact (what is visible by the dotted line in the plots). The resulting slopes of linear relationships for  $\gamma = 0.4$ , for the sample rain gauges are -0.480, -0.441 and -0.475 respectively, and the average slope for all the Warsaw rain gauges is equal to -0.475. The absolute value of the slope corresponds to the codimension value of  $c(\gamma)$  for  $\gamma = 0.4$  (see Fig. 7.24 in the following Section).

The overestimation of low intensity precipitation and underestimation of highest intensity precipitation in recorded series as reported by several authors (e.g. de Lima, 1998; Licznar, 2009) and confirmed by the already discussed results could also be observed for the Warsaw gauges log-log plots for probability exceeding rainfall. The observed course of the plots suggests the presence of two different scaling regimes (reported by e.g. Tessier and al., 1996), one for time scales from 1 minute to 1 hour and another from 1 hour up to 11 days. Interestingly, the scale time around 1 hour ( $\log(\lambda) = 2.4$ ,  $\lambda = 251$ ,  $t = 63$  min) constitutes a kind of boundary value between two different scaling regimes: the linear behaviour of the probability plots deviates upwards from the straight line for small singularities (related to low-intensity events) and downwards for high-intensity events, remaining however in a power-law relation. The discussed results are very similar to those observed by Licznar (2009) for rainfall time series for Wrocław.

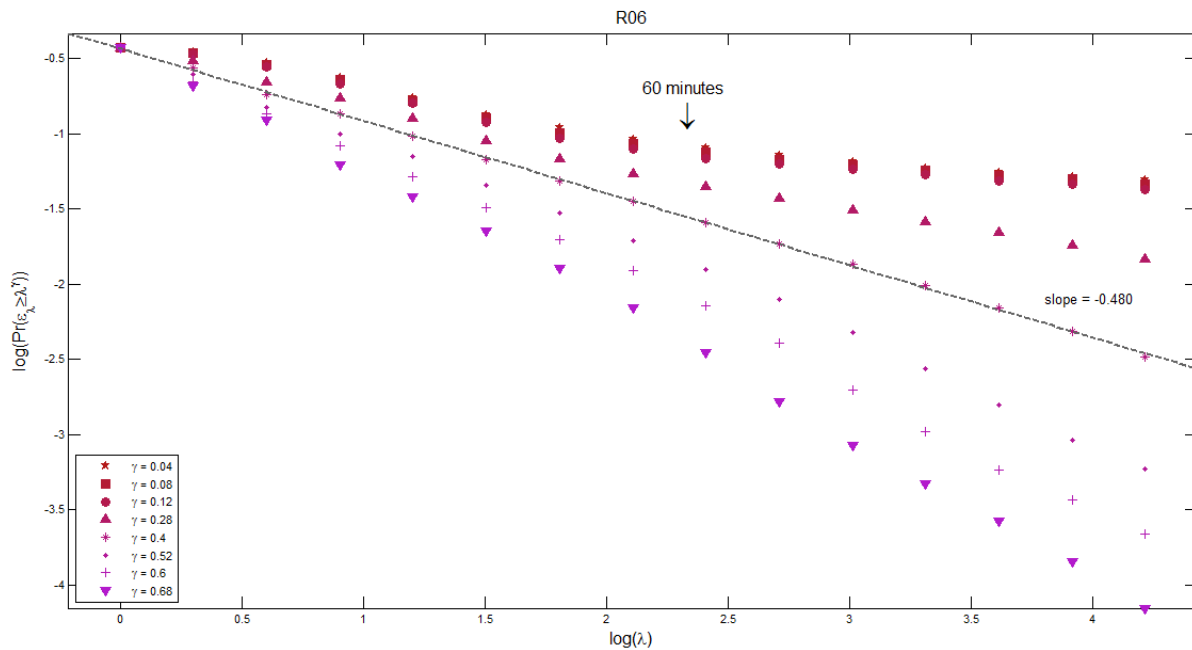


**Figure 7.17.** Log-log plot of the probability of exceeding rainfall-intensity levels for selected values of singularity  $\gamma$  relation against scale parameter  $\lambda$ , obtained for 1-minute precipitation data series from Warsaw rain gauge R06. The time scales range from  $\lambda = 16384$  (1 minute) to  $\lambda = 1$  (11.4 days)

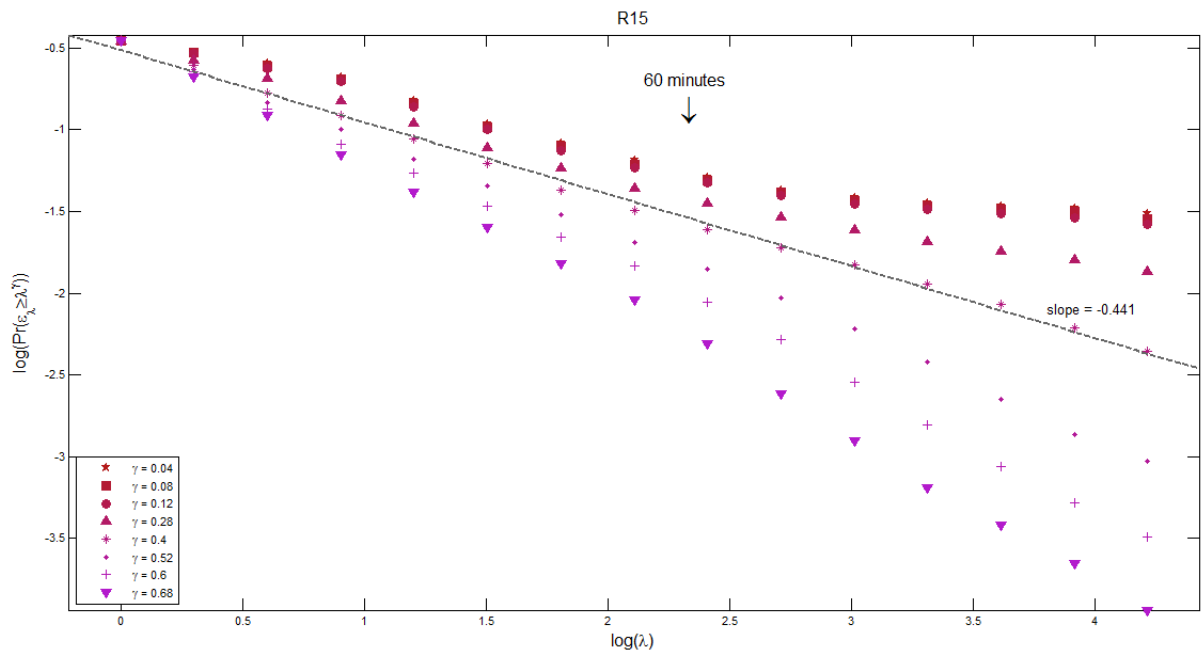


**Figure 7.18.** Log-log plot of the probability of exceeding rainfall-intensity levels for selected values of singularity  $\gamma$  relation against scale parameter  $\lambda$ , obtained for 1-minute precipitation data series from Warsaw rain gauge R15. The time scales range from  $\lambda = 16384$  (1 minute) to  $\lambda = 1$  (11.4 days)

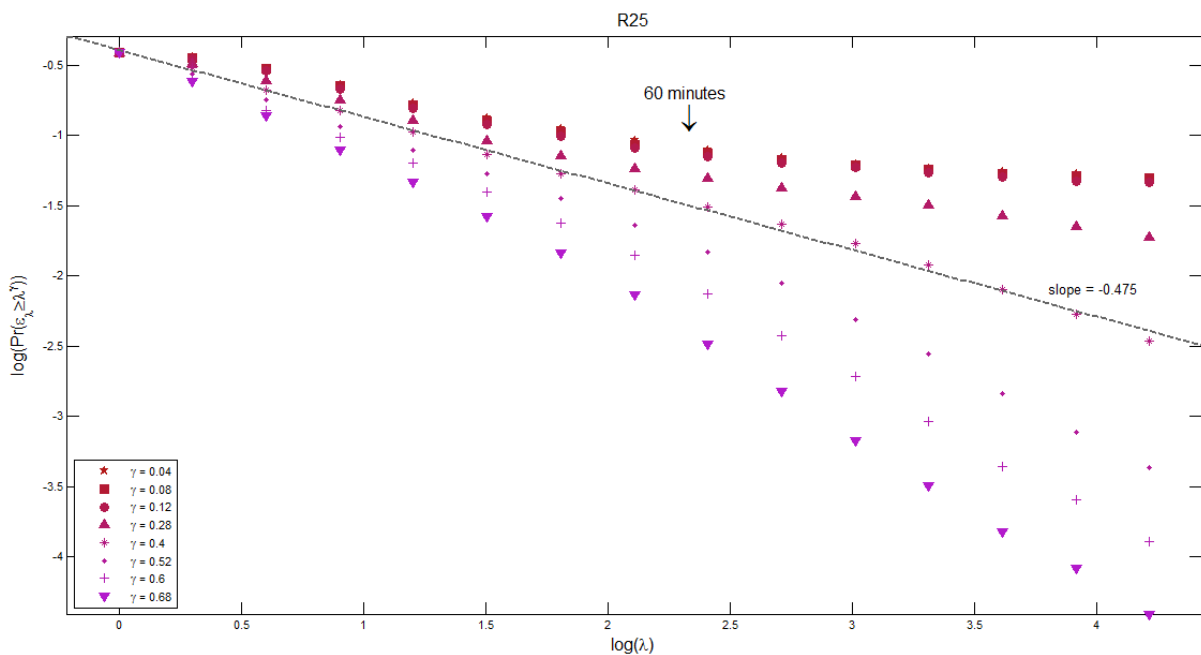


**Figure 7.19.** Log-log plot of the probability of exceeding rainfall-intensity levels for selected values of singularity  $\gamma$  relation against scale parameter  $\lambda$ , obtained for 1-minute precipitation data series from Warsaw rain gauge R25. The time scales range from  $\lambda = 16384$  (1 minute) to  $\lambda = 1$  (11.4 days)

## 7.5 Multifractal exponent functions

The statistical description of a multifractal process, as for all other random variables, leads to the analysis of the probability distribution or its statistical moments. In multifractal processes a duality exists between probabilities and moments, both related to each other by a

type of Legendre transform (Frish and Parisi, 1985; Schertzer and Lovejoy, 1993). Thus, the scaling behavior, verified by the trace moment analysis (Figs 7.14÷7.16) and probability distribution/multiple scaling analysis (Figs 7.17÷7.19), may be also described by multifractal exponent functions: the moment scaling function  $K(q)$  and the codimension function  $c(\gamma)$  (see Sections 6.1 and 6.6).

The sample empirical moments scaling function  $K(q)$ , determined by the trace moment method, are plotted in Figs 7.21÷7.23 for Warsaw rain gauge R06, R15 and R25. Their shapes are almost identical and similar to shapes obtained for other 22 gauges (the remaining plot are presented in Appendix IV, Section B). Regions of linear and non-linear relationship, below and above one single point, of coordinates  $(2.48; 0.73)$  are visible on the graphs. The abscissa of this point is identified as the critical order moments  $q_D$  and the ordinate as  $K(q_D)$  of a process.

All the 25 plots of empirical  $K(q)$  function for Warsaw gauges exhibit linear relationship for moment larger than 2.48. They differ from the theoretical moment scaling function  $K(q)$ , defined by Schertzer and Lovejoy (1987, 1993). The theoretical  $K(q)$  function has a fully curvilinear shape presenting two intersections with the x axis,  $K(q) = 0$ , namely at  $q = 1$  and  $q = 0$  (Fig. 7.20 left), wherein the latter condition is fulfilled only for multifractals filling the available space in simple manner (Lovejoy and Schertzer, 2013).

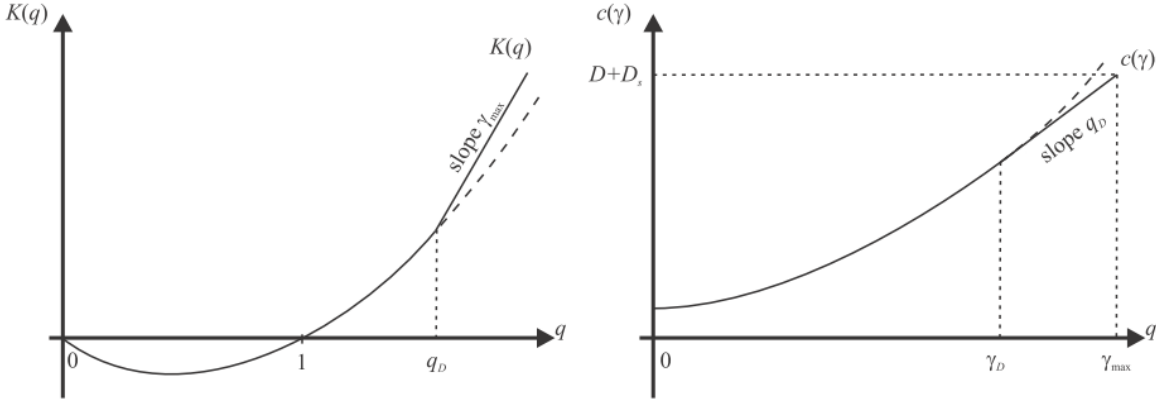


**Figure 7.20.** Shape of the theoretical scaling exponent functions  $K(q)$  and  $c(\gamma)$  for multifractal first-order phase transformations (from Lovejoy and Schertzer, 2013)

As shown on the sample graphs of empirical  $K(q)$  function, the curvilinear shape is perceivable only for the lowest values of the moments. Moreover, the empirical  $K(q)$  function equals to 0 only in case of  $q = 1$ . Both the straightness and the presence of only one zero point is typical for real rainfall time series. It is an expected behavior due to the deviations detected in TM plots (Figs 7.14÷7.16), and it corresponds to the results obtained by other researchers (e.g. de Lima, 1998; Licznar, 2009).

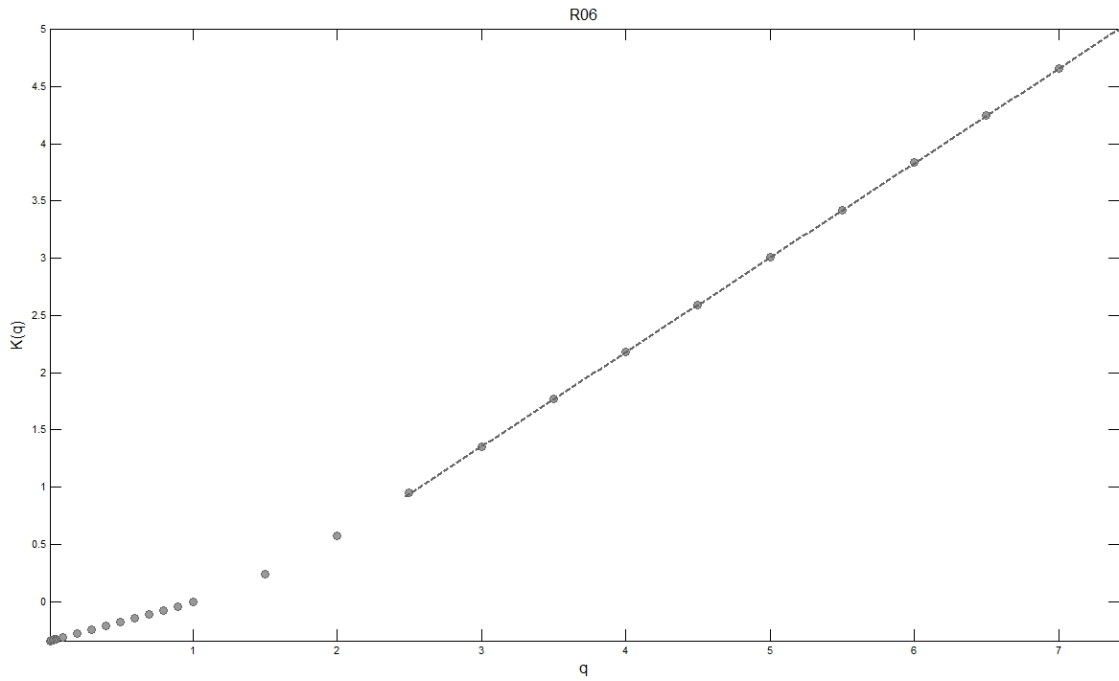


**Figure 7.21.** The empirical scaling moment function log-log plot obtained for 1-minute precipitation data series from Warsaw rain gauge R06 for time scales from  $\lambda = 16384$  (1 minute) to  $\lambda = 1$  (11.4 days)

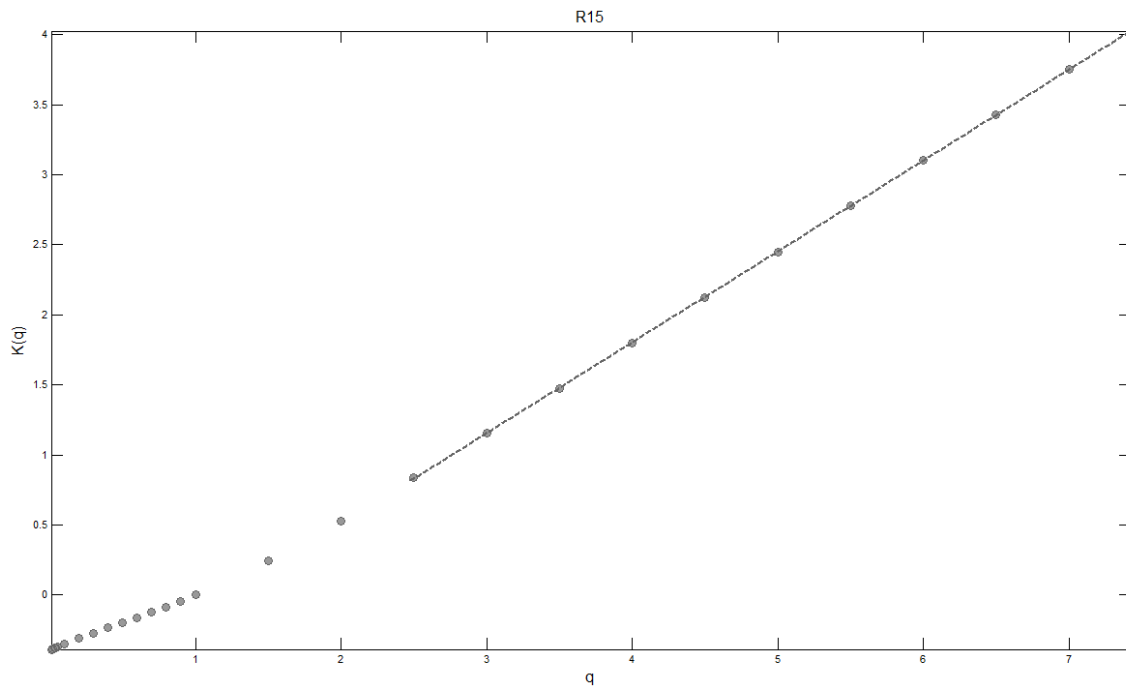


**Figure 7.22.** The empirical scaling moment function log-log plot obtained for 1-minute precipitation data series from Warsaw rain gauge R15 for time scales from  $\lambda = 16384$  (1 minute) to  $\lambda = 1$  (11.4 days)

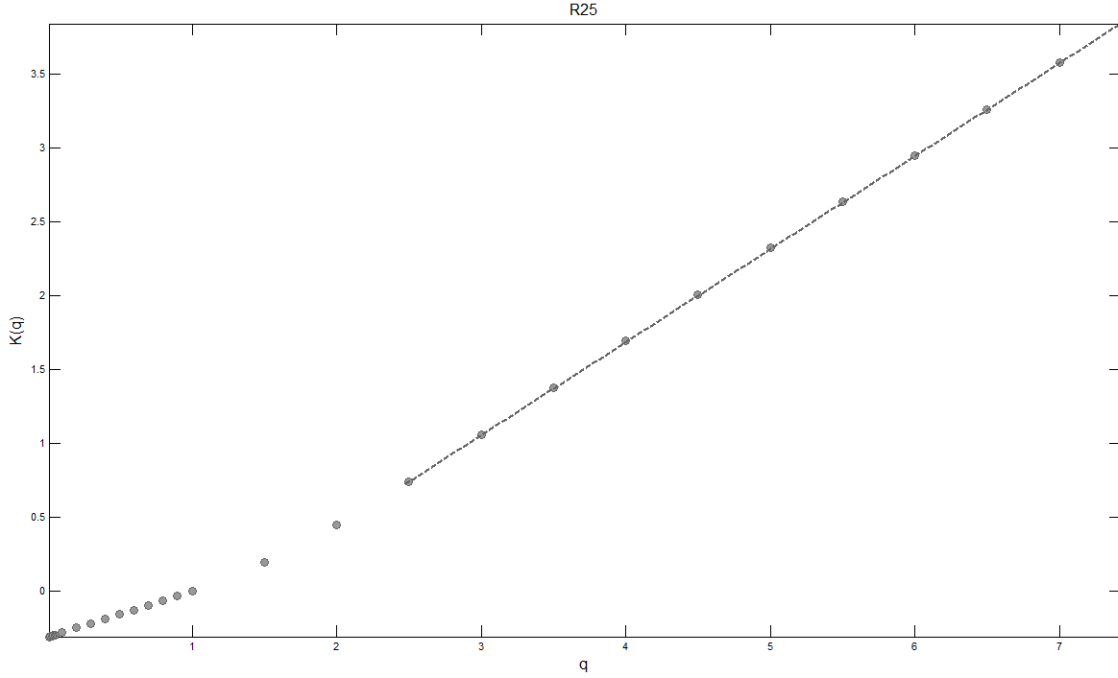


**Figure 7.23.** The empirical scaling moment function log-log plot obtained for 1-minute precipitation data series from Warsaw rain gauge R25 for time scales from  $\lambda = 16384$  (1 minute) to  $\lambda = 1$  (11.4 days)

Additionally, if the processes covers the available 1-dimensional space in a more complex manner, the empirical moment scaling function  $K(q)$  provides the value of codimension, defined as the intercept of the function for  $K(q = 0) = -c$ . In this way,  $c$  is the codimension of the “support” of the process and it is strictly related to the dimension as follows:

$$c = 1 - D \quad (33)$$

Based on the plots, the Warsaw time series codimension value amounts to 0.35, and the average dimension  $D$  is equal to  $D = 1 - c = 0.65$ .

The empirical codimension functions  $c(\gamma)$ , determined by the probability distribution/multiple scaling method, for selected rain gauges are plotted in Fig. 7.24 (the remaining plots are presented in Appendix V, Section B). The shape of the curve is consistent with the theoretical codimension function (Fig. 7.20 right) namely, includes both linear and non-linear sections. The non-linear behavior concerns the middle section of the plots, for orders of singularity from 0.08 to  $0.65 \pm 0.06$ . For orders  $\gamma > 0.65$  the curves become linear, and  $\gamma \approx 0.65$  is identified as the critical singularity  $\gamma_D$ .

First order multifractal transformation, resulting from the observation (recording) carried out in a scale larger than the scale of the internal homogeneity of the actual process, are often due to the limitations of measuring instruments, is characterized by a linear behavior of the  $c(\gamma)$  function, for  $\gamma > \gamma_D$ . The equation of such a line, allows to determine the value of  $q_D$  as the slope, and  $K(q)$  as the negative value of the intercept.

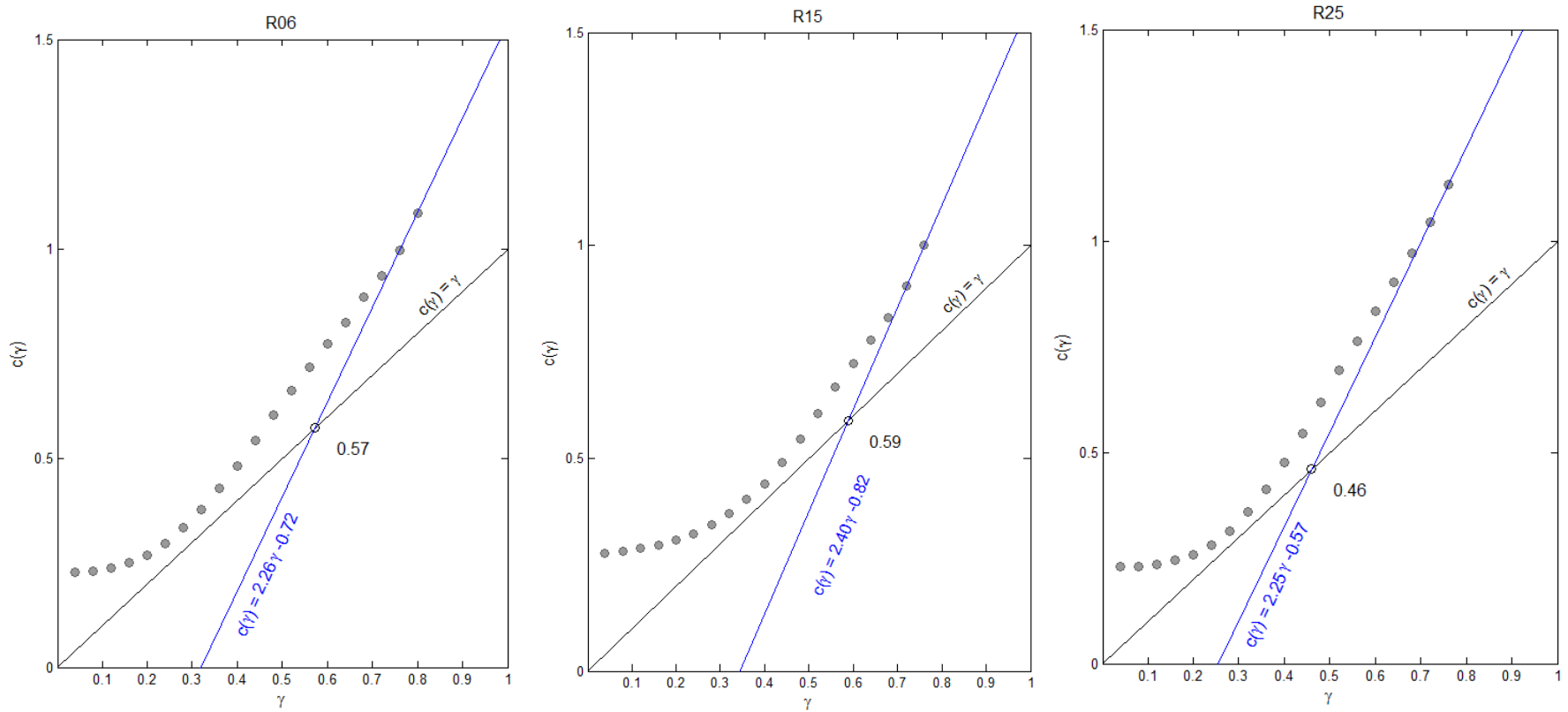


**Figure 7.24.** Empirical codimension function (dotted line) obtained for 1-minute precipitation data series from Warsaw rain gauge R06, R15 and R25, for time scales from 1 minute 11.4 days

For singularity orders,  $\gamma > \gamma_D$ , the fitting lines (blue lines in figures) and their equations are visible on the graphs. The estimated slopes for the selected rain gauges R06, R15 and R25 are equal to 2.26, 2.40 and 2.25 respectively (Fig. 7.24). The overall slope value for the entire network is on average  $2.44 \pm 0.26$ . As it could be noticed, the empirical  $c(\gamma)$  codimension function for all the 25 Warsaw gauges are characterized by strong variability of the slopes for the linear sections marking the first-order multifractal phase transformation.

Regarding the intercepts of the fitted lines, they are equal to -0.72, -0.82 and -0.57 respectively for gauges R06, R15 and R25, and for all the network the intercept is on average  $-0.74 \pm 0.36$ . In accordance to the duality between the codimension and the moment scaling functions, the slope and its negative intercept of the fitting line defined by  $c(\gamma)$ , should satisfy the critical scaling moment  $q_D$  and its corresponding function value, defined by  $K(q)$ . It is easily seen that the overall value of the slope ( $2.44 \pm 0.26$ ), i.e.  $q_D = 2.44$ , as well as the negative intercept  $-0.74 \pm 0.36$ , i.e.  $K(q_D) = 0.74$ , are both defined by  $c(\gamma)$ , and coincide with values of the coordinates of the beginning point of the linear section of  $K(q)$  that is (2.48; 0.73). Hence, the duality of those two parameters confirms the correctness of the independently performed the PDMS and the TM analysis of Warsaw time series.

The PDMS method additionally defines the fractal dimension of the geometrical “support” of the process, already determined by functional box counting method. It is determined by the intersection of the obtained fitting lines for values  $\gamma > \gamma_D$  with the line of equation  $c(\gamma) = \gamma$  (as visible in Fig. 7.24). The resulting point of coordinates ( $D; D$ ) is defined by Schertzer and Lovejoy (1993) as the mentioned fractal dimension. For the selected rain gauges R06, R15 and R25,  $D$  is equal to 0.57, 0.59 and 0.46 respectively. The overall value for the entire network is  $D = 0.55 \pm 0.05$ . These results coincide with the values already obtained by the functional box counting method namely  $D = 0.52, 0.48$  and  $0.55$  for rain gauges R06, R15 and R25 and the average value for 25 rain gauges set  $D \approx 0.53$ . The results are also close to  $D \approx 0.65$  obtained by the TM method as an average value for 25 gauges’ group.

## 7.6 Double trace moment method (DTM)

The DTM analysis, focused on the determination of order moments  $q$  for  $\eta$ -normalized intensities of events, is performed using the modified version of the DTM\_Warsaw program and by a MATLAB script DTMPLOT. The calculations, set for several values of parameters, thus oriented to the estimation of basic universal multifractal parameters, cover ranges of moment order  $q \in [0.9; 2.1]$  and  $\eta \in [0.13; 10.00]$ . As a result, sample plots of  $\log|K(q, \eta)|$  against  $\log(\eta)$  for selected order moments  $q$  (indicated in the legend), are provided in Figs

7.25÷7.27. These figures concern Warsaw rain gauges R06, R15 and R25; the remaining plots for other 22 gauges are set up in Appendix VI, Section A).

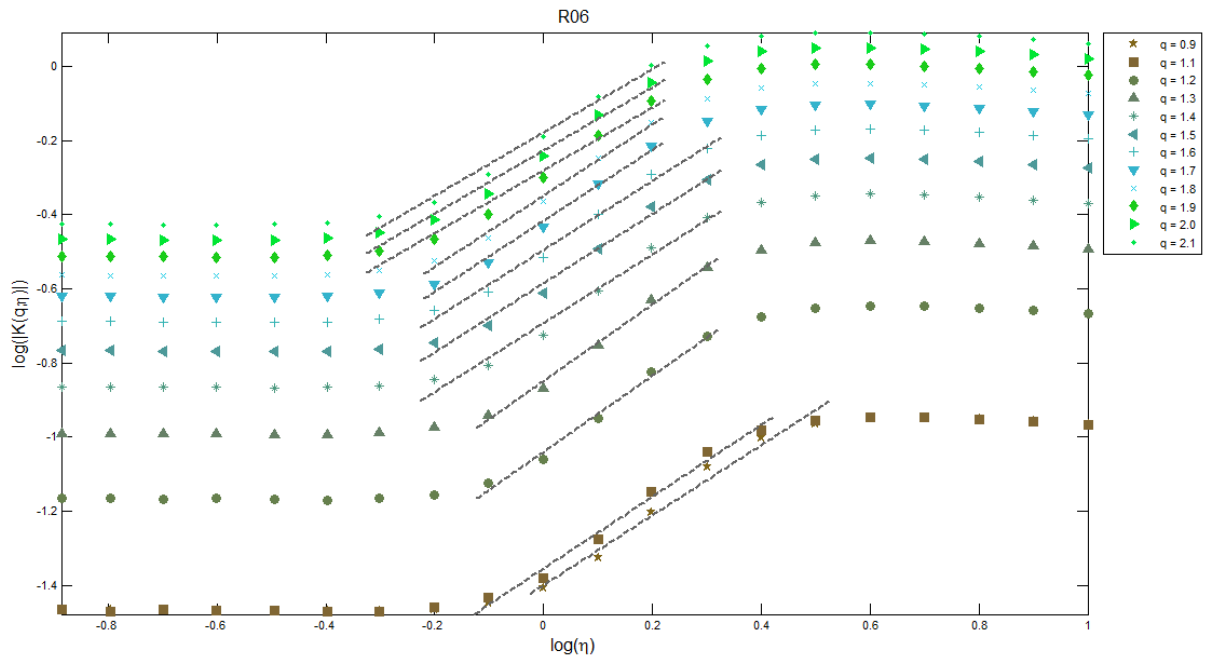


**Figure 7.25.** DTM plots of  $\log|K(q, \eta)|$  against  $\log(\eta)$  for selected order moments  $q$  obtained for 1-minute precipitation data series from Warsaw rain gauge R06

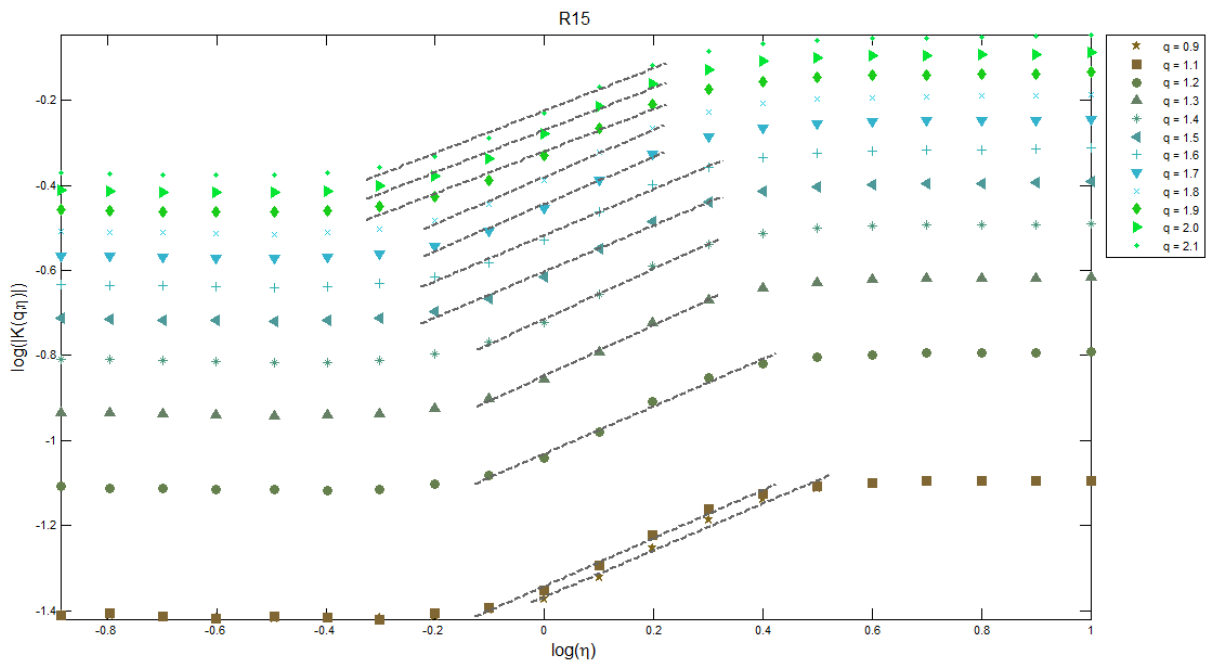


**Figure 7.26.** DTM plots of  $\log|K(q, \eta)|$  against  $\log(\eta)$  for selected order moments  $q$  obtained for 1-minute precipitation data series from Warsaw rain gauge R15

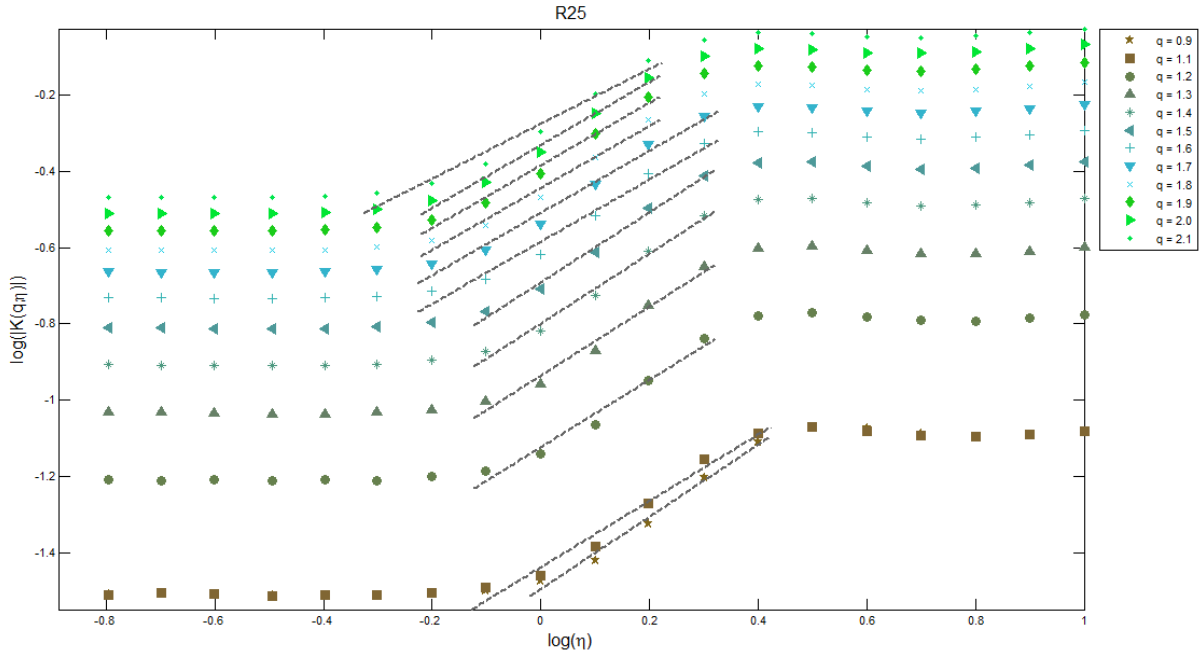


**Figure 7.27.** DTM plots of  $\log|K(q, \eta)|$  against  $\log(\eta)$  for selected order moments  $q$  obtained for 1-minute precipitation data series from Warsaw rain gauge R25

The confirmation of the “universality” of the process is granted by the parallel shapes of the obtained graphs, observed for the entire period of analysis. Two scaling “breaks” causes the characteristic “S”-shaped bend of the curves and the linear relation of the middle section of the graph (dotted lines) is therefore delimited by two critical orders of moments  $q_{min}$  and  $q_{max}$ . The section between these two values is the one suitable for the estimation of universal parameter  $\alpha$ , as the slope of the graph of the linear relationship, according to the relation for conservative processes ( $H = 0$ ):

$$K(q, \eta) = \eta^\alpha K(q) \quad (34)$$

Based on Equation (34), it is possible to rewrite the Equation (31) as follows:

$$K(q, \eta) = \begin{cases} \frac{C_1}{\alpha - 1} \eta^\alpha (q^\alpha - q) & \text{for } \alpha \neq 1 \\ C_1 \eta q \ln(q) & \text{for } \alpha = 1, \end{cases} \quad (35)$$

where  $\alpha$  assumes values at the range  $[0; 2]$ , and  $q > 0$  for  $\alpha \neq 2$ .

From the log-log plots the values of  $\log(\eta)$  limiting the linear relationships (namely  $\log(\eta)_{min}$  and  $\log(\eta)_{max}$ ) are read for each order moment  $q$ . Then, the values of  $\eta$  are calculated, and the critical moments are determined by the product of the moments  $q$  and  $\eta$  (for further discussion please refer to Tessier et al. 1993). All the estimated values for the sample rain gauges R06, R15 and R25 are listed in Tab.7.6 (the values obtained for all the remaining gauges are given in Tables VI.a in Appendix VI, Section B). The critical moments

for selected rain gauges R05, R15 and R25 are equal to: 0.98, 1.00 and 1.07 for  $q_{min}$  and 2.89, 2.94 and 2.90 for  $q_{max}$  respectively. The overall averaged results obtained for the entire Warsaw network are  $q_{min} = 1.04 \pm 0.06$  and  $q_{max} = 2.91 \pm 0.23$ . Nevertheless, it has to be underlined that the estimate of critical moments is liable to subjective error while reading data from graphs. Indeed, it should be noticed that estimated values of  $q_{max}$  for Warsaw gauges ( $q_{max} = 2.91 \pm 0.23$ ) is higher than the already discussed values of  $q_D$  from the TM ( $q_D = 2.48$ ) and the PDMS studies ( $q_D = 2.44 \pm 0.26$ ).

**Table 7.6.** Critical moments  $q_{min}$  and  $q_{max}$  estimated based on Figs 7.25÷7.27 for selected values of order moment  $q$ , obtained for 1-minute precipitation series from Warsaw rain gauges R06, R15 and R25

R06						
Curve for $q$	Minimal critical moment $q_{min}$			Maximal critical moment $q_{max}$		
	$\log(\eta)$	$\eta$	$q_{min} = q\eta$	$\log(\eta)$	$\eta$	$q_{max} = q\eta$
0.90	0.0	1.00	0.90	0.5	3.16	2.85
1.10	-0.1	0.79	0.87	0.4	2.51	2.76
1.20	-0.1	0.79	0.95	0.3	2.00	2.39
1.30	-0.1	0.79	1.03	0.3	2.00	2.59
1.40	-0.2	0.63	0.88	0.3	2.00	2.79
1.50	-0.2	0.63	0.95	0.3	2.00	2.99
1.60	-0.2	0.63	1.01	0.3	2.00	3.19
1.70	-0.2	0.63	1.07	0.2	1.58	2.69
1.80	-0.2	0.63	1.14	0.2	1.58	2.85
1.90	-0.3	0.50	0.95	0.2	1.58	3.01
2.00	-0.3	0.50	1.00	0.2	1.58	3.17
2.10	-0.3	0.50	1.05	0.2	1.58	3.33
Average			0.98	Average		2.89
Standard deviation			0.08	Standard deviation		0.27

R15						
Curve for $q$	Minimal critical moment $q_{min}$			Maximal critical moment $q_{max}$		
	$\log(\eta)$	$\eta$	$q_{min} = q\eta$	$\log(\eta)$	$\eta$	$q_{max} = q\eta$
0.90	0.0	1.00	0.90	0.5	3.16	2.85
1.10	-0.1	0.79	0.87	0.4	2.51	2.76
1.20	-0.1	0.79	0.95	0.4	2.51	3.01
1.30	-0.1	0.79	1.03	0.3	2.00	2.59
1.40	-0.1	0.79	1.11	0.3	2.00	2.79
1.50	-0.2	0.63	0.95	0.3	2.00	2.99
1.60	-0.2	0.63	1.01	0.3	2.00	3.19
1.70	-0.2	0.63	1.07	0.2	1.58	2.69
1.80	-0.2	0.63	1.14	0.2	1.58	2.85
1.90	-0.3	0.50	0.95	0.2	1.58	3.01
2.00	-0.3	0.50	1.00	0.2	1.58	3.17
2.10	-0.3	0.50	1.05	0.2	1.58	3.33
Average			1.00	Average		2.94
Standard deviation			0.08	Standard deviation		0.22

R25						
0.90	0.00	1.00	0.90	0.4	2.51	2.26
1.10	-0.10	0.79	0.87	0.4	2.51	2.76
1.20	-0.10	0.79	0.95	0.3	2.00	2.39
1.30	-0.10	0.79	1.03	0.3	2.00	2.59
1.40	-0.10	0.79	1.11	0.3	2.00	2.79
1.50	-0.10	0.79	1.19	0.3	2.00	2.99
1.60	-0.20	0.63	1.01	0.3	2.00	3.19
1.70	-0.20	0.63	1.07	0.3	2.00	3.39
1.80	-0.20	0.63	1.14	0.2	1.58	2.85
1.90	-0.20	0.63	1.20	0.2	1.58	3.01
2.00	-0.20	0.63	1.26	0.2	1.58	3.17
2.10	-0.30	0.50	1.05	0.2	1.58	3.33
Average			1.07	Average		2.90
Standard deviation			0.12	Standard deviation		0.36

Estimations of the universal parameter  $\alpha$ , as the slope of  $\log|K(q,\eta)|$  against  $\log(\eta)$  for the range of data delimited by  $q_{min}$  and  $q_{max}$ , and consequently, the parameter  $C_1$  are the final step of the DTM analysis. All the obtained results for selected gauges R06, R15 and R25 are listed in Tab.7.7 (and in Tables VI.b in Appendix VI, Section B for all the remaining 22 gauges of the set). For the sample rain gauges R06, R15 and R25 the parameter  $\alpha$  amounts to 0.938, 0.546 and 0.848. The value of  $\alpha$  parameter for 25 gauges set is  $\alpha = 0.77 \pm 0.09$ .

Because of  $\alpha \neq 1$ , the Equation (35) becomes suitable to the estimation of  $C_1$  as follows (the identity  $K(q) \equiv K(q,1)$  is visible in Fig. 7.28):

$$K(q) \equiv K(q, 1) = \frac{C_1}{\alpha - 1} (q^\alpha - q) \quad (36)$$

For the selected rain gauges R06, R15 and R25 the universal parameters  $C_1$  are 0.413, 0.439 and 0.337 respectively. The overall value of  $C_1$  for the whole analysed group of 25 gauges in Warsaw is equal to  $C_1 = 0.40 \pm 0.02$ .

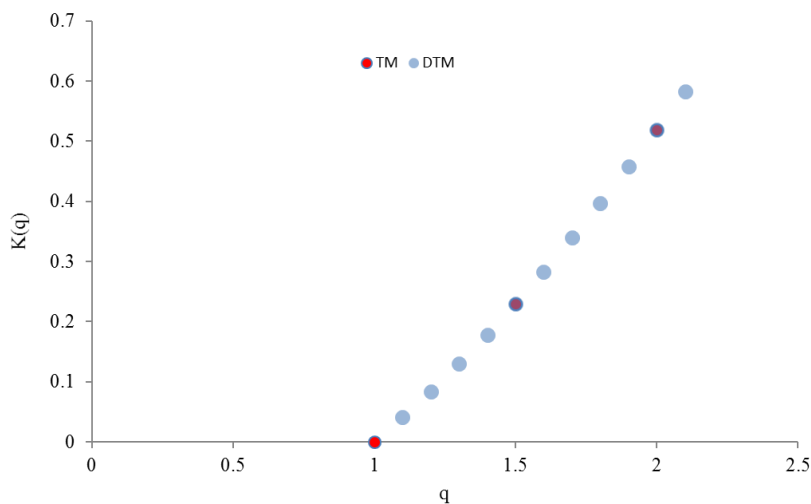


**Figure 7.28.** Empirical moment scaling function  $K(q)$  obtained by TM method on the background of  $K(q,1)$  obtained by DTM method (based on the results for gauge R06)

The degree of multifractality  $\alpha$  determines the universality class of an event. According to the classification of the multifractals for  $0 \leq \alpha \leq 1$  in case of Warsaw gauges, it is a (log) Lévy process with bounded singularities, presenting soft behaviour, what means, is a dressed process (see Section 6.2). The universal multifractal parameters  $\alpha$  and  $C_1$  are also used to determine the critical moment  $q_D$  associated with multifractal first-order phase transition, according to the equation:

$$\frac{C_1}{\alpha - 1} \frac{q_D^\alpha - q_D}{q_D - 1} = D \quad (37)$$

By that means, for  $\alpha = 0.77$ ,  $C_1 = 0.40$  and  $D = 0.55$  i.e. averaged values for a set of 25 Warsaw gauges, the critical moment  $q_D$  is equal to 2.50. This value is at least comparable to  $q_D = 2.48$  and  $q_D = 2.44 \pm 0.26$  originating from the TM and the PDMS studies respectively.

**Table 7.7.** Calculation of  $\alpha$  and  $C_1$  parameters for 1-minute precipitation series from Warsaw rain gauges R06, R15 and R25

Gauge R06			
Curve for $q$	$K(q,1)$	$\alpha$	$C_1$
1.10	-1.378	0.971	0.400
1.20	-1.060	1.034	0.396
1.30	-0.868	1.038	0.396
1.40	-0.726	0.931	0.404
1.50	-0.612	0.935	0.407
1.60	-0.517	0.935	0.410
1.70	-0.435	0.958	0.412
1.80	-0.363	0.961	0.414
1.90	-0.299	0.848	0.433
2.00	-0.241	0.853	0.436
2.10	-0.189	0.856	0.438
Average		0.938	0.413
Standard deviation		0.066	0.015

Gauge R15			
Curve for $q$	$K(q,1)$	$\alpha$	$C_1$
1.10	-1.352	0.563	0.433
1.20	-1.042	0.559	0.432
1.30	-0.856	0.596	0.430
1.40	-0.722	0.593	0.431
1.50	-0.616	0.544	0.436
1.60	-0.529	0.543	0.437
1.70	-0.454	0.553	0.438
1.80	-0.388	0.555	0.439
1.90	-0.330	0.496	0.449
2.00	-0.278	0.498	0.450
2.10	-0.231	0.500	0.451
Average		0.546	0.439
Standard deviation		0.035	0.008

Gauge R25			
1.10	-1.454	0.865	0.337
1.20	-1.142	0.888	0.333
1.30	-0.955	0.910	0.329
1.40	-0.818	0.921	0.327
1.50	-0.709	0.923	0.326
1.60	-0.618	0.816	0.335
1.70	-0.538	0.819	0.337
1.80	-0.468	0.814	0.339
1.90	-0.406	0.822	0.341
2.00	-0.349	0.826	0.343
2.10	-0.297	0.719	0.359
Average		0.848	0.337
Standard deviation		0.061	0.009

### 7.7 Universal multifractal parameters

In this section, the final results of the multifractal studies are presented. In Tab.7.8 the universal multifractal parameters  $\alpha$ ,  $C_1$  and  $H$ , together with the global scaling exponent  $\beta$  are listed. The parameters in Tab.7.8 concern 1-minute precipitation time series from all the 25 rain gauges of the Warsaw rain gauge network, and cover the period from September 2008 to November 2010. The universal parameters  $\alpha$  and  $C_1$  are determined by the double trace moment method (DTM) already described in Section 7.6, whereas the global scaling exponent  $\beta$  is estimated by the spectral density analysis, discussed in Section 7.2.

Knowing the parameters  $\alpha$  and  $C_1$ , the universal parameter  $H$  is calculated according to the following equation

$$H = \frac{\beta - 1}{2} + \frac{C_1(2^\alpha - 2)}{2(\alpha - 1)} \quad (38)$$

The overall multifractal parameter  $H = 0.06 \pm 0.02$  for all the Warsaw gauging network together with the already determined parameters  $\alpha = 0.77 \pm 0.09$  and  $C_1 = 0.40 \pm 0.02$  forms a parameter set very similar to the results obtained by Tessier et al. (1996) for 30 locations in France, for rainfall data from 1 day to 30 years ( $\alpha = 0.7 \pm 0.2$ ,  $C_1 = 0.4 \pm 0.1$  and  $H = -0.1 \pm 0.1$ ). Moreover, comparable results are reported by de Lima (1998) for Vale Formoso, Portugal ( $\alpha = 0.49$ ,  $C_1 = 0.51$  and  $H = -0.13$ ) and Licznar (2009) for Wrocław, Poland ( $\alpha = 0.69$ ,  $C_1 = 0.34$  and  $H = -0.01$ ).

However, to quantify the level of variability of universal multifractal parameter among the network, the taxonomic investigation is performed using the hierarchical analysis. The calculations are performed for two groups of multifractal parameters: first group covers a set of all the 3 parameters  $\alpha$ ,  $C_1$  and  $H$ , the second only  $\alpha$  and  $C_1$ , assuming  $H = 0$  (as for conserved process). The universal multifractal parameters for specific gauges of Warsaw

network are in majority of cases very similar. The results are summarized in dendrograms, where the distance between rain gauges is measured by metric distance and linkage methods listed in Tab.6.1.

**Table 7.8.** Universal multifractal parameters  $\alpha$ ,  $C_1$  and  $H$ , and the global scaling exponent  $\beta$  for Warsaw rain gauges, for 1-minute time series, recorded from September 2008 to November 2010

Rain gauge		Parameter			
		$\alpha$	$C_1$	$H$	$\beta$
R01	Average	0.80	0.40	0.05	0.58
	St. dev.	0.03	0.01	-	-
R02	Average	0.79	0.40	0.04	0.57
	St. dev.	0.04	0.01		
R03	Average	0.81	0.39	0.01	0.52
	St. dev.	0.04	0.01		
R04	Average	0.65	0.38	0.04	0.66
	St. dev.	0.04	0.01		
R05	Average	0.76	0.42	0.02	0.50
	St. dev.	0.04	0.01	-	
R06	Average	0.94	0.41	0.00	0.45
	St. dev.	0.07	0.02	-	
R07	Average	0.75	0.40	0.08	0.66
	St. dev.	0.05	0.01	-	
R08	Average	0.70	0.39	0.05	0.61
	St. dev.	0.04	0.01	-	
R09	Average	0.73	0.39	0.07	0.65
	St. dev.	0.06	0.01	-	
R10	Average	0.72	0.40	0.07	0.65
	St. dev.	0.04	0.01	-	
R11	Average	0.72	0.40	0.07	0.64
	St. dev.	0.05	0.01	-	
R12	Average	0.82	0.38	0.07	0.64
	St. dev.	0.04	0.01	-	
R13	Average	0.71	0.43	0.05	0.56
	St. dev.	0.03	0.01	-	
R14	Average	0.82	0.38	0.08	0.67
	St. dev.	0.05	0.01	-	
R15	Average	0.55	0.44	0.08	0.64
	St. dev.	0.04	0.01	-	
R16	Average	0.74	0.38	0.08	0.68
	St. dev.	0.05	0.01	-	
R17	Average	0.71	0.40	0.10	0.71
	St. dev.	0.04	0.01	-	
R18	Average	0.83	0.40	0.05	0.57
	St. dev.	0.05	0.01	-	
R19	Average	0.87	0.39	0.07	0.62
	St. dev.	0.04	0.01	-	
R20	Average	0.87	0.40	0.07	0.60
	St. dev.	0.05	0.01	-	
R21	Average	0.93	0.39	0.07	0.60
	St. dev.	0.06	0.01	-	
R22	Average	0.78	0.40	0.03	0.53
	St. dev.	0.05	0.01	-	
R23	Average	0.74	0.40	0.05	0.60
	St. dev.	0.03	0.01	-	
R24	Average	0.74	0.40	0.09	0.68
	St. dev.	0.03	0.01	-	
R25	Average	0.85	0.34	0.06	0.68
	St. dev.	0.06	0.01	-	
Average		0.77	0.40	0.06	0.61
Standard deviation		0.09	0.02	0.02	0.06

In Figure 7.29 the results of clustering for all three universal parameters:  $\alpha$ ,  $C_1$  and  $H$  using average linkage and Euclidean distance are plotted. The vertical scale shows the binding distance, whereas the names of the rain gauges are presented on horizontal scale. The majority of gauges is in a single group. The gauges of similar bending distance smaller than 0.051 are marked in red. The biggest binding distance is observed only for three outlying gauges R21, R06 and R15. In case of gauges R21 and R06 the binding distances are comparable and are equal to 0.058 and 0.067 respectively, whereas for gauge R15 the binding distance is equal to 0.124. It has to be underlined, that this last value is at least twice bigger than the binding distances obtained among other 22 closely located on dendrogram gauges.

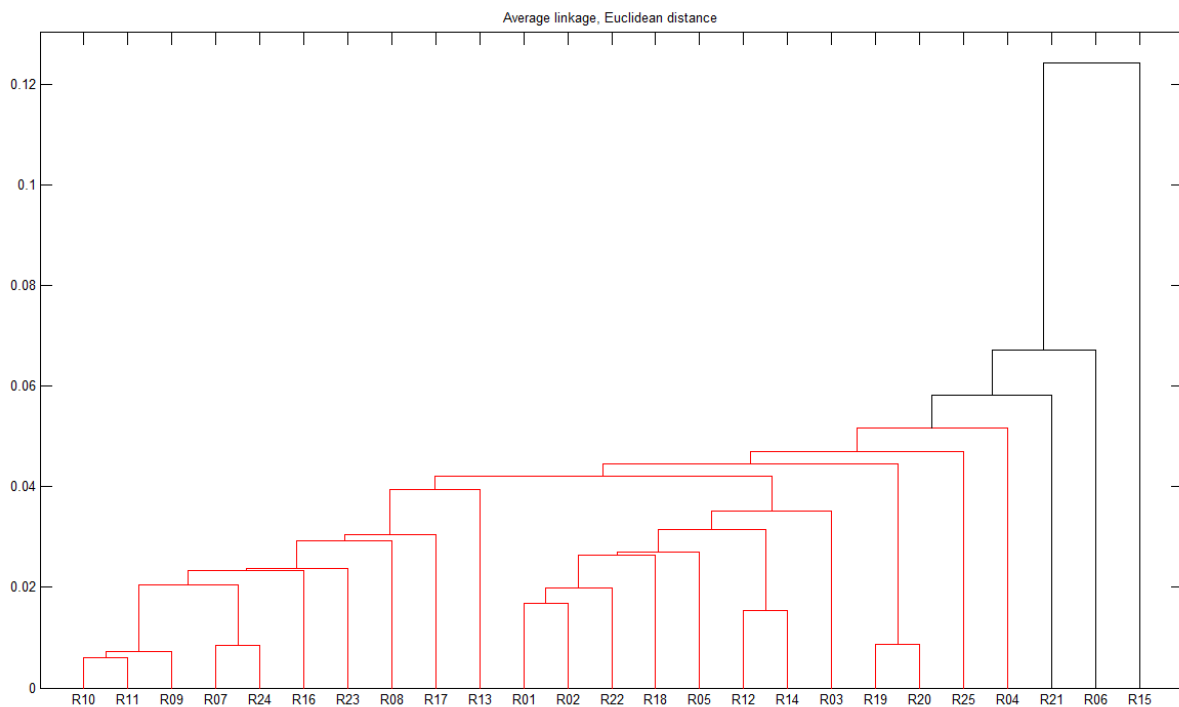


**Figure 7.29.** Dendrogram resulting from cluster analysis of universal multifractal parameters  $\alpha$ ,  $C_1$  and  $H$  for Warsaw rain gauge network, using average linkage and Euclidean distance

Due to a conserved nature of rainfall processes (confirmed by the obtained values of  $H$  oscillating around 0), the similarity of gauges based only on 2 remaining  $\alpha$  and  $C_1$  parameters is investigated. The results of these studies in the form of dendrograms are plotted in Fig. 7.30 and Fig. 7.31. The largest distance from the nearest neighbour defined both by Euclidean and Minkowski distance is equal to 0.240 for gauge R15 and 0.166 for both the gauges R21 and R06. The behaviour of the remaining gauges is very similar as in case previous analysis shown in Fig. 7.29. They are grouped practically in one big cluster with binding distances (defined by Euclidean and Minkowski distance) not exceeding the boundary value of 0.104. This value could not be directly compared to the distances presented in Fig. 7.29. However, it should be noticed, that also in case of Fig. 7.30 and Fig. 7.31 the binding distance for the

outermost outlying gauge R15 exceeds by double the binding values of the other gauges forming the main cluster.

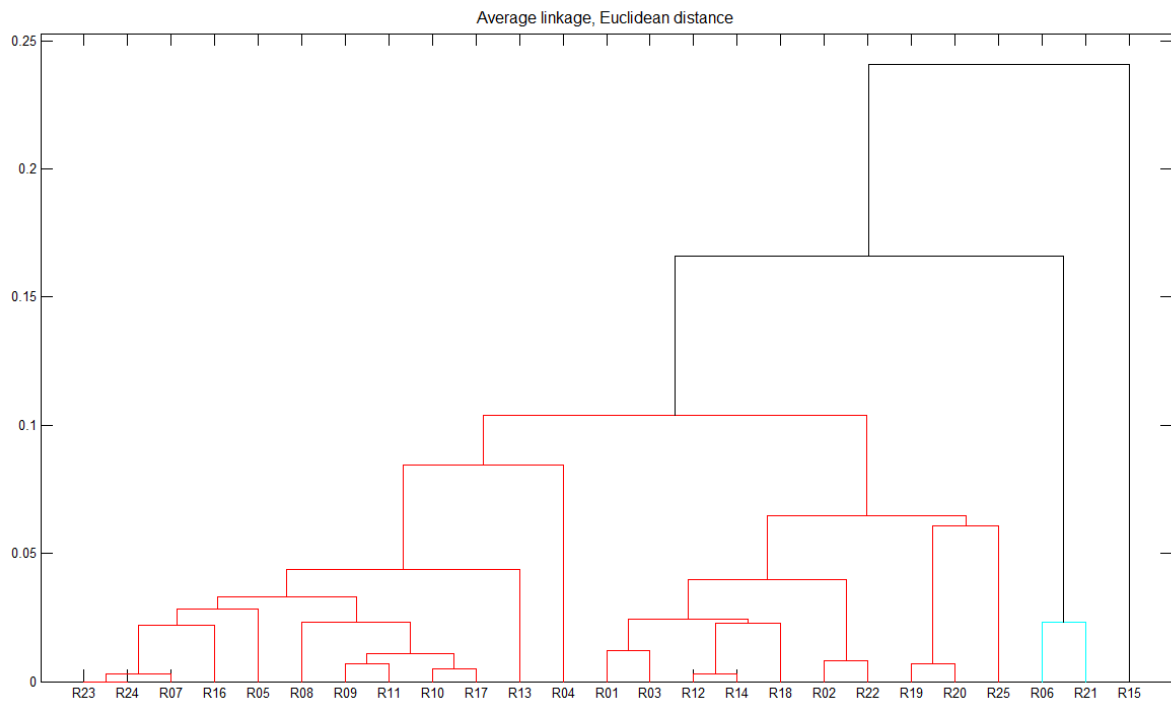


**Figure 7.30.** Dendrogram resulting from cluster analysis of universal multifractal parameters  $\alpha$  and  $C_1$  for Warsaw rain gauge network, using average linkage and Euclidean distance

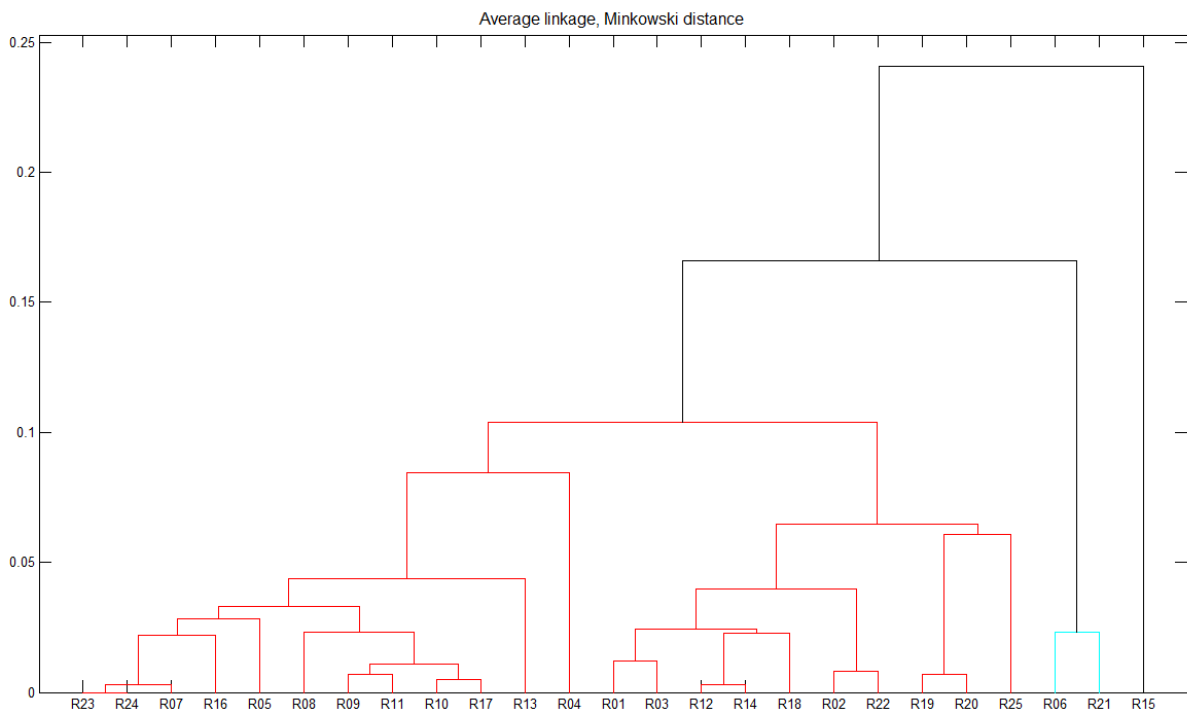


**Figure 7.31.** Dendrogram resulting from cluster analysis of universal multifractal parameters  $\alpha$  and  $C_1$  for Warsaw rain gauge network, using average linkage and Minkowski distance

A quality measure of all the combination of methods used during hierarchical analysis is the *cophenetic correlation*, showing the goodness of fit of the clustering: the closest to 1 is the

value of this correlation, the better is the result. Among all the obtained dendrograms, the above-presented in Fig. 7.29÷7.31 are the ones with the highest value of cophenetic correlation, equal to 0.831 and 0.834 respectively for the analysis of all 3 and only 2 universal parameters. For other combinations of linkage methods and distance definition smaller values of cophenetic correlation are reached as it could be seen from the Tab.7.9.

**Table 7.9.** Cophenetic correlation values obtained for different combination of linkage method and distance definition

Cophenetic correlation		Linkage method			
		Average	Centroid	Average	Centroid
		For $\alpha$ , C1 and H		For $\alpha$ and C1	
Metric distance	Euclidean	<b>0.831</b>	0.830	<b>0.834</b>	<b>0.834</b>
	Seuclidean	0.643	0.673	0.660	0.652
	Cityblock	0.812	0.808	0.799	0.798
	Minkowski	<b>0.831</b>	0.830	<b>0.834</b>	<b>0.834</b>
	Chebyshev	0.830	0.829	<b>0.834</b>	<b>0.834</b>
	Mahalanobis	0.633	0.628	0.652	0.630
	Cosine	0.658	0.661	0.643	0.684
	Correlation	0.623	0.631	-0.249	-0.258
	Spearman	NaN	-0.087	*	*
	Hamming	0.062	-0.008	*	*
Jaccard	0.062	-0.008	*	*	

\*values too small

The similarity of the majority of the Warsaw gauges with respect to their multifractal parameters is in good agreement with former results of Licznar et al. (2015) analysis performed on the same dataset but with alternative methodology, based on studies of BDCs (breakdown coefficients distributions) for hierarchy of sub-daily timescales. In the mentioned study of Licznar et al. (2015) the clearly outlying gauges were the gauges R15 and R25. Their outlying position on dendrograms was explained by the location of gauges in untypical for urban precipitation field conditions. Gauge R15 is an airport gauge and in its neighbourhood there are no buildings, trees or other obstacles typical for city centre. Gauge R25 is located in city limits and is surrounded by green areas of forests and grasslands. Most probably this type of neighbourhood eliminates or drastically reduces the effects of urban heat island which has to have influence on recorded precipitation. This in mind, in subsequent part of the research, both gauge R15 and R25 are selected for generation of synthetic precipitation series from continuous universal cascade generators. Finally, to the group of outliers, gauges R06 and R21 should be added. They are closely located geographically in the centre of Warsaw. This is the section of the city with the highest density of high buildings. In addition, gauge R06 is located very close to the Vistula River. Most probably this specific and close location of gauge R06 and R21 explain both small binding distance among both gauges and bigger binding distances to other Warsaw gauges. Consequently, this gauge R06 is also selected for

generation of synthetic precipitation series from continuous universal cascade generator. The location of the above-mentioned gauges R06, R15 and R25 representing the variability of universal cascade parameters among Warsaw precipitation field is shown in Fig. 7.32.

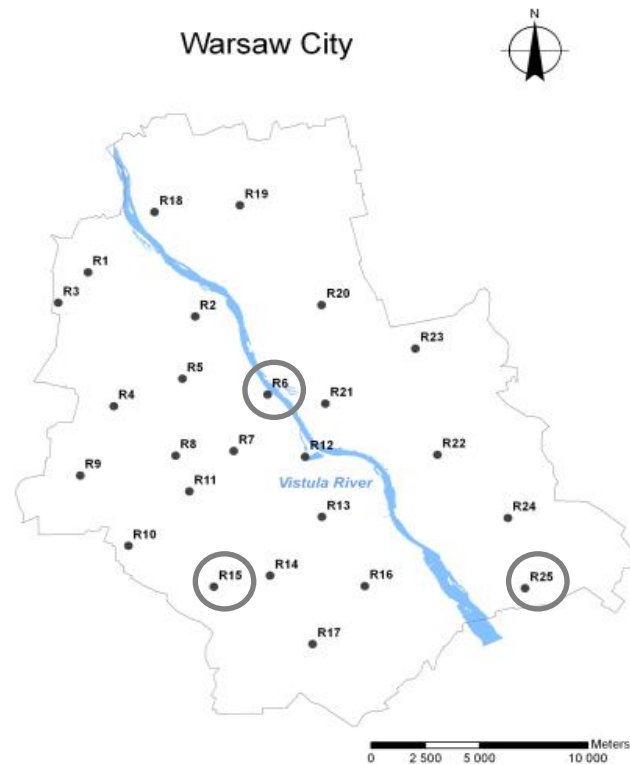


**Figure 7.32.** The locations of the rain gauges chosen as the most representative of the variability of Warsaw rain gauge network: R06, R15 and R25

## 7.8 Universal multifractal generators

In this section, results of synthetic precipitation time series generation by means of continuous universal cascades generators are presented. Generators are parametrized by universal parameters derived for selected specific gauges R06, R15 and R25, as well as, for average parameters for other remaining 22 gauges (excluding R06, R15 and R25) or 23 gauges (excluding R15 and R25) of the Warsaw precipitation field. Samples of generated 1-minute precipitation series are presented and their quality with respect of precipitation variability and intermittency is assessed determining the probability of rain by the complementary cumulative distribution function (cCDF) and investigating the probability of zero rainfall occurrence  $E(p_0)$  for a hierarchy of sub-daily timescales. A comparison of cCDF and  $E(p_0)$  parameters between synthetic and recorded precipitation time series is carried out. Finally, attempts of correction of the intermittency structure of generated precipitation time series by means of specially developed post processing filter algorithm FILTR are reported.

### 7.8.1. Synthetic precipitation time series

In order to generate a synthetic precipitation time series for the Warsaw gauging network, the universal multifractal generator, a MATLAB script GENERATOR\_R, is oriented to the simulation of 1-minute resolution data of length  $\lambda = 2^{20}$  minutes ( $\lambda \approx$  over 2 years). The synthetic data are generated on basis of the universal multifractal parameters  $\alpha$ ,  $C_1$  and  $H$ , assuming a conservative nature of the data, thus  $H = 0$ . The simulations are carried out five times: three times for single rain gauges R06s, R15s and R25s (“s” stands for synthetic) and two times for groups of gauges RM23s and RM22s, whose parameters are averaged for 23 rain gauges (excluding of R15 and R25) and 22 rain gauges (excluding R06, R15 and R25) respectively.

In Figure 7.34 sample synthetic results obtained for R06s are presented. The overall view of time series suggests the proper structure of rainfall time series. Precipitation is distributed irregularly in time in the form of rainfall clusters of variable temporal intensity with alternating (almost) no-rain periods. However, some peaks of very high rainfall intensity reaching up to 6-8 mm/min are visible. Simultaneously, in more detail (the enlarged section of the obtained time series is presented in Fig. 7.34), very small rainfall intensity values, far below the resolution of rain gauges (0.001 mm) are very frequent. These features of generated time series are discussed further in more detail. Despite that, positive observations about the quality of generated time series could also be derived from the evaluation of the total annual precipitations - TAP. The TAPs of the synthetic time series are very close to the observed values, i.e. the TAP of R06s is 612 mm/year, whereas the TAP of R06 is equal to 659 mm/year; for R15s the TAP is 544 mm/year (for R15 is 502 mm/year), and for R25s the TAP is 480 mm/year (for R25 is 424 mm/year). To some extent the differences in TAP values for observed and synthetic time series could be explained by the fact, that the synthetic series do not cover entirely two years of observation ( $2^{10}$  minutes are  $\approx 1.995$  years), since the length of the simulated data should be a multiple of 2, and  $2^{10}$  is the closest value to two years of observation.

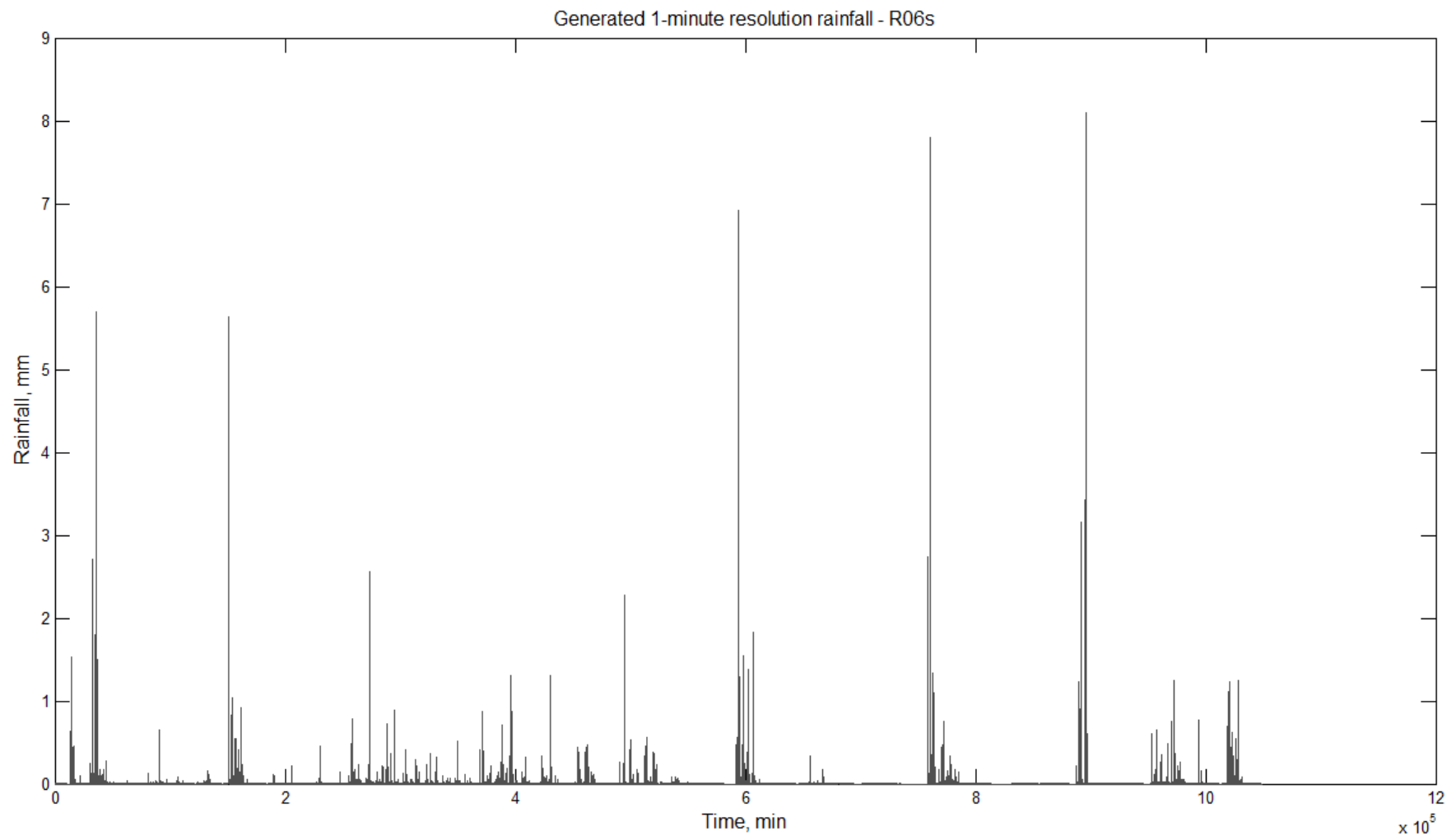


**Figure 7.33.** Sample result of the universal multifractal generator. The plot of an almost 2-year time series for R06s

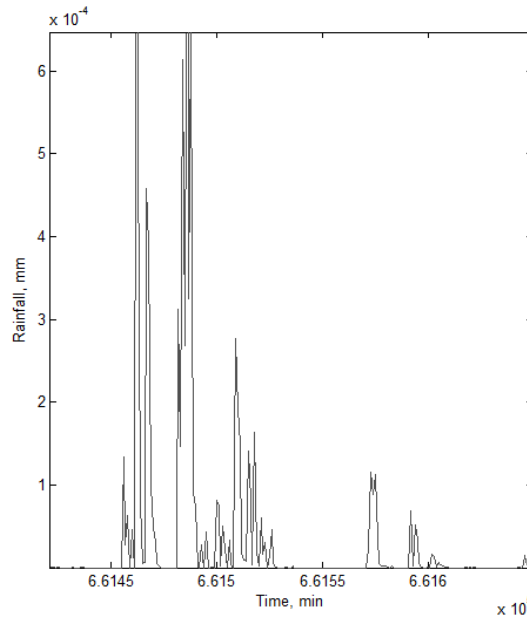


**Figure 7.34.** Sample result of the universal multifractal generator. An enlarged section of the time series, with very small values of rainfall intensities (one magnitude below weighing gauges' resolution)

### 7.8.2. Evaluation of generated synthetic precipitation time series

From the perspective of future engineering use of a synthetic time series, the generation of synthetic data from continuous universal cascades is focused on obtaining the most probable rainfall events as possible. The generated time series should represent probable realizations of local rainfall process. Thus, the statistical features of the synthetic rainfall series should be similar to the observed ones.

The first step of the evaluation of the generated synthetic rainfall time series R06s, R15s and R25s and RM22s and RM23s originating from the single gauge or set of gauges' models, is based on the studies of probabilities of non-zero rainfall values occurrence  $P(R>r)$  in synthetic and real datasets. For this purpose, a MATLAB script CCDF calculating the complementary cumulative distribution function is implemented and the ability of the universal continuous cascades to reproduce cumulative distribution frequency of rainfall is assessed.

The probability distributions of the synthetic time series R06s, R15s and R25s are compared with the distributions of the respective observed time series in Figs 7.35÷7.37. The same non-zero rainfall distributions for time series R06s, R15s and R25s are drawn on the background of similar distributions found for recorded series from all 25 rain gauges of the Warsaw network in Figs 7.38÷7.40. All distributions in Figs 7.35÷7.40 are plotted in logarithmic scales to highlight the tails of the distributions, most interesting from the point of view of extreme values analysis.

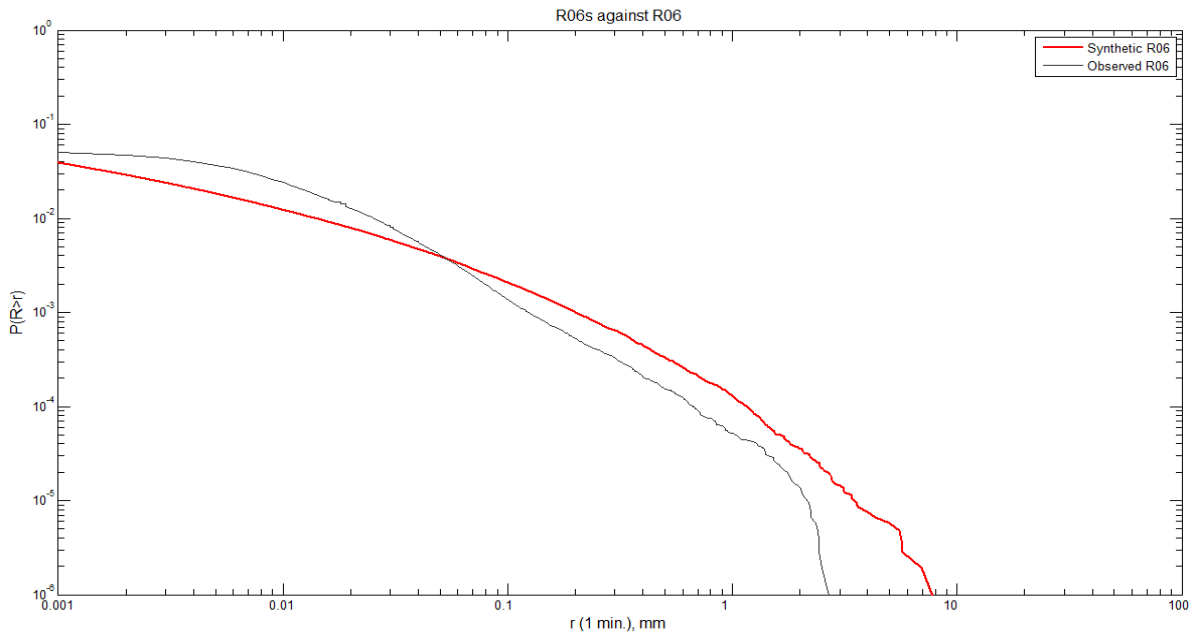


**Figure 7.35.** The complementary cumulative distribution function (cCDF) calculated for the synthetic precipitation time series R06s against the cCDF for observed precipitation time series for Warsaw rain gauge R06

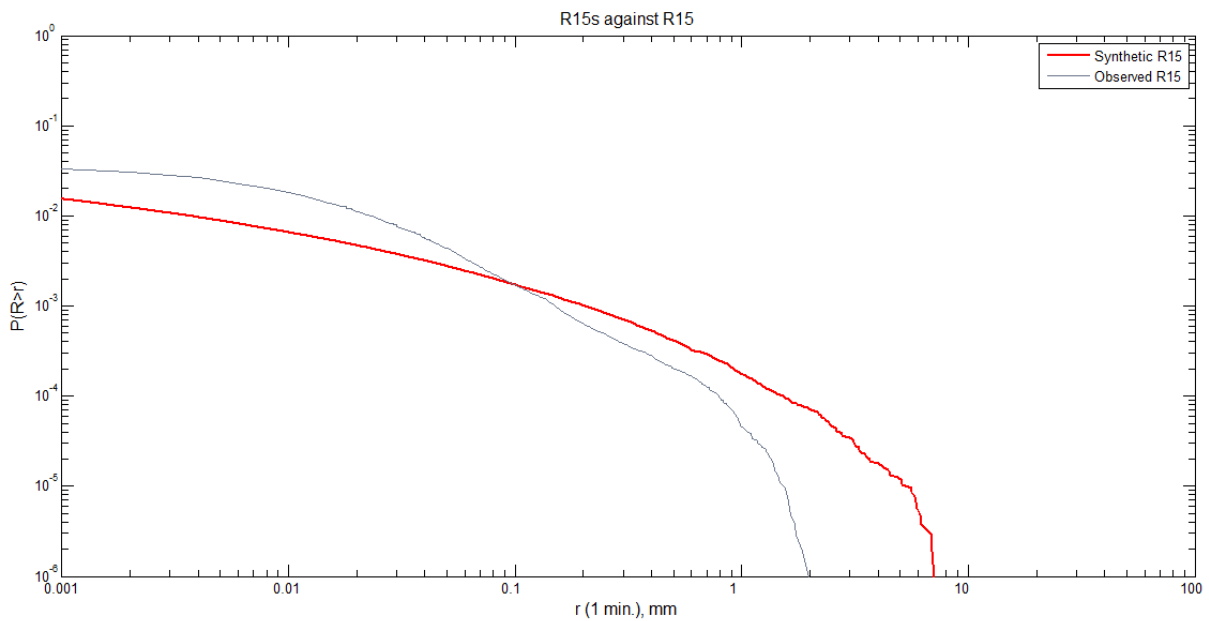


**Figure 7.36.** The complementary cumulative distribution function (cCDF) calculated for the synthetic precipitation time series R15s against the cCDF for observed precipitation time series for Warsaw rain gauge R15

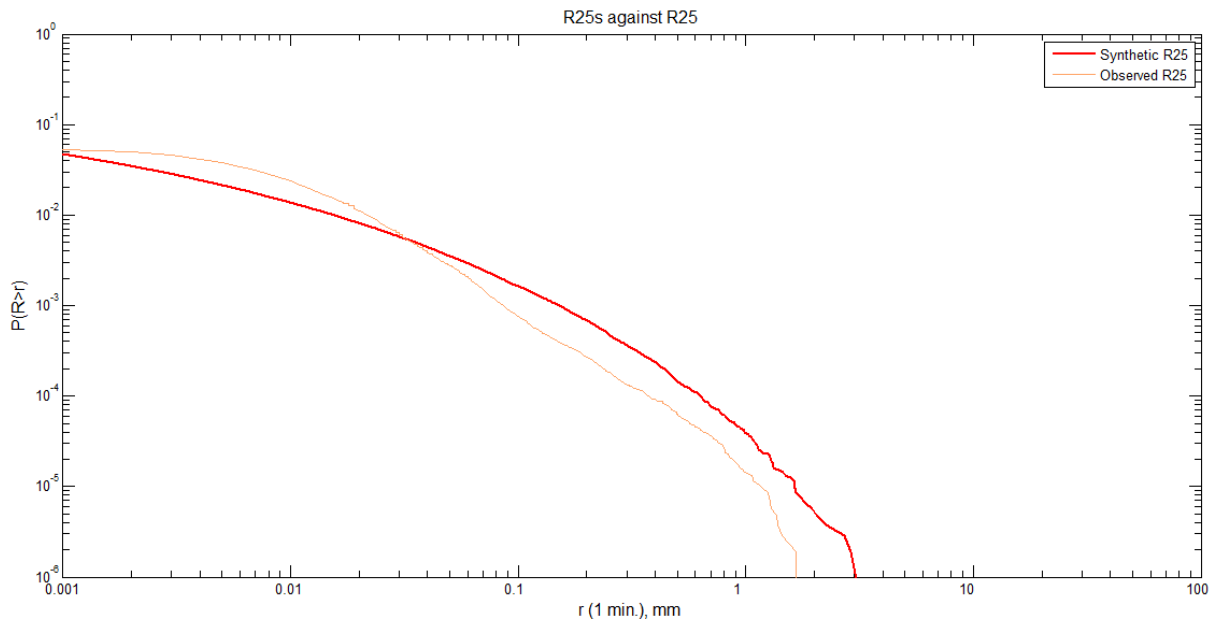


**Figure 7.37.** The complementary cumulative distribution function (cCDF) calculated for the synthetic precipitation time series R25s against the cCDF for observed precipitation time series for Warsaw rain gauge R25

The best agreement between cCDFs for synthetic and observed time series is maintained for gauge R25 (Fig. 7.37). Both cCDF curves have quite similar shapes. However, a noticeable departure of synthetic vs. observed curve is observed for rainfall intensities exceeding 0.04 mm/min. The universal cascade model seems to produce a rainfall series with higher temporal rainfall intensities occurring more frequently than in observed time series. Whereas, for rainfall intensities less than 0.04 mm/min. an opposite phenomenon is found. Frequencies of occurrence of small temporal rainfall intensities in synthetic series (exceeding however the minimum boundary level of 0.001 mm, i.e. weighing gauge resolution) are obviously lower than for observed time series. Quite similar observations could also be made for other two gauges R06 (Fig. 7.35) and R15 (Fig. 7.36). But for these gauges the departure of the cCDF for synthetic and observed time series is more visible (especially for gauge R15). In addition, the point of both curves intersection is shifted from 0.04 mm/min. to about 0.055 mm/min. and 0.1 mm/min. in case of gauges R06 and R15 respectively.

Owning in mind the rather limited size of accessible observational sets and to understand better the magnitude of diagnosed differences between cCDFs for synthetic and observed time series, distributions of  $P(R>r)$  for synthetic series R06s, R15s and R25s are additionally compared to distributions produced for all 25 Warsaw rain gauges in Figs 7.38÷7.40.

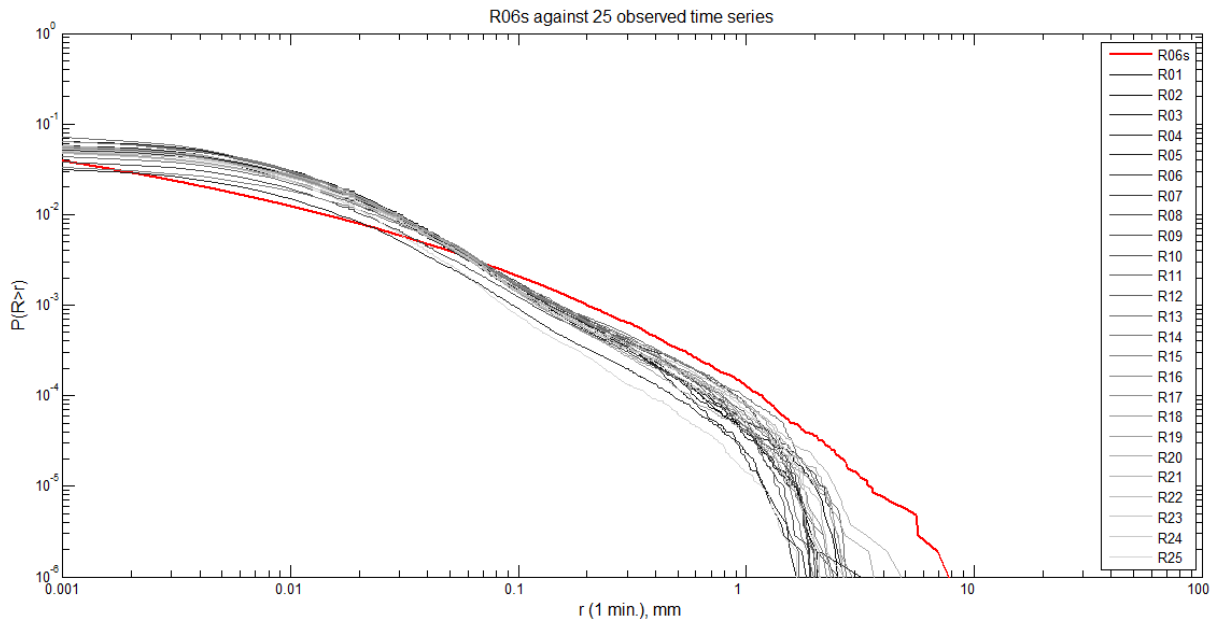


**Figure 7.38.** The complementary cumulative distribution function (cCDF) calculated for the synthetic precipitation time series R06s against the cCDFs for observed precipitation time series for all 25 Warsaw rain gauges

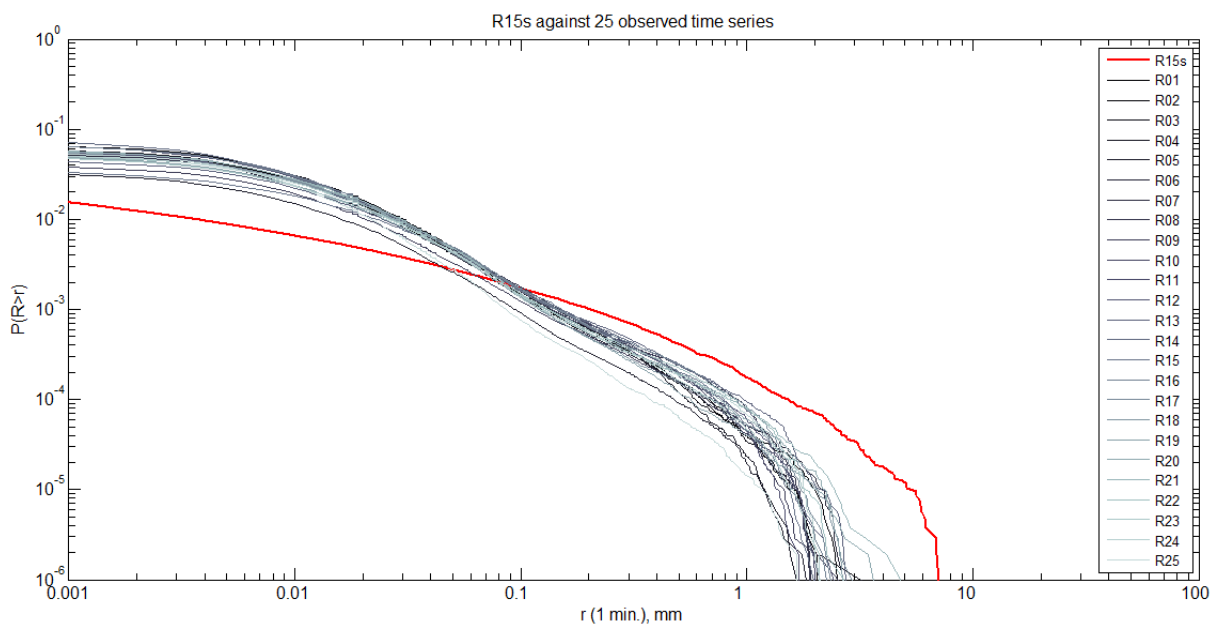


**Figure 7.39.** The complementary cumulative distribution function (cCDF) calculated for the synthetic precipitation time series R15s against the cCDFs for observed precipitation time series for all 25 Warsaw rain gauges

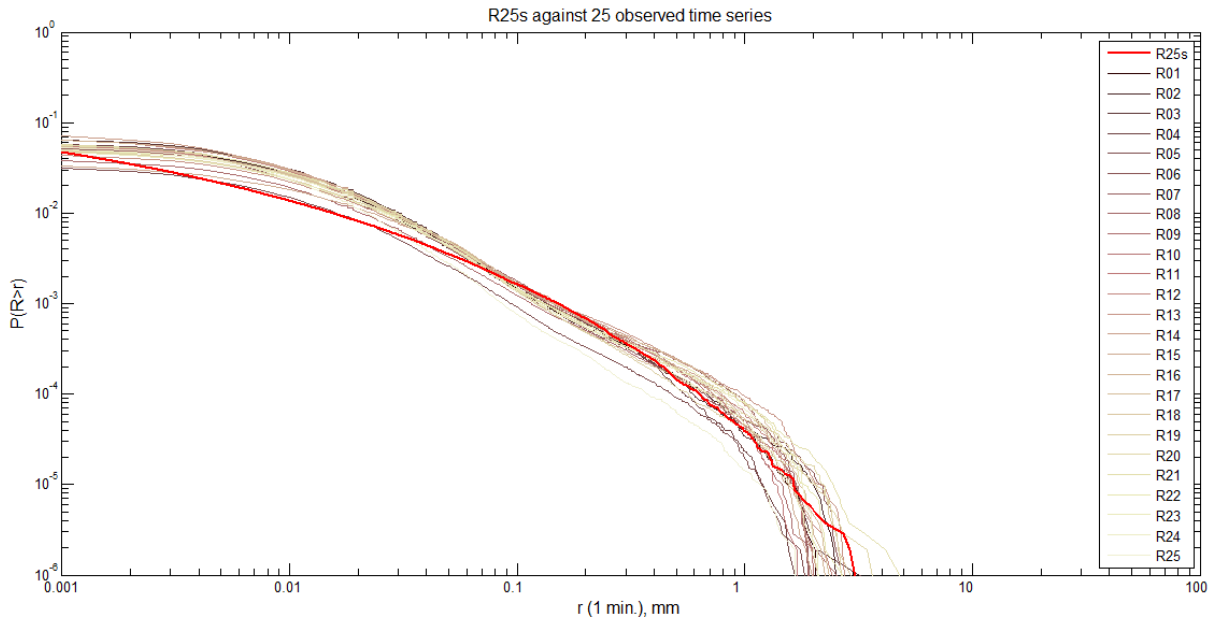


**Figure 7.40.** The complementary cumulative distribution function (cCDF) calculated for the synthetic precipitation time series R25s against the cCDFs for observed precipitation time series for all 25 Warsaw rain gauges

It is clear that the noticeable variability of cCDFs is natural inside the gauges distributed over the whole area of Warsaw city. In practice, distribution of  $P(R>r)$  for synthetic series R25s is completely positioned inside the group of Warsaw gauges distributions. The cCDF for synthetic series R06s is also very close to the bunch of distributions originating from real precipitation observations. Only for very specific gauge R15 located at the airport, discrepancies in distributions of  $P(R>r)$  for synthetic and real Warsaw gauges distributions are more pronounced. It is clear that the universal cascade generator for this gauge does not capture well the heavy-tail observed in Warsaw rainfall data.

Nonetheless, obtained results for all three gauges should be evaluated at least as promising, with respect to already published by Molnar and Burlando (2005), Licznar et al. (2011a, 2011b) distributions of  $P(R>r)$  for synthetic series generated by means of canonical and microcanonical discrete cascade models. Above mentioned authors reported also the lack of an ideal imitation of cCDFs for synthetic vs. observed precipitation series for a majority of tested models, despite working in coarser time resolution of only with 5 or 10-minute time series and implementing simple cascades, parametrized by numerous factors and capable only to disaggregate quasi-daily precipitation totals.

The evaluation of performance of the universal continuous cascade models for two groups of gauges RM23 and RM22, whose parameters are averaged for 23 rain gauges (excluding of R15 and R25) and 22 rain gauges (excluding R06, R15 and R25) respectively, is conducted in the same way, as for single rain gauges. The creation of these two models for two groups of

gauges is guided by the assumption, that exclusion of outlying rain gauges would allow to develop models parametrized by average universal parameters, capable of generating synthetic series preserving better statistical properties of precipitations throughout Warsaw. The distributions of  $P(R>r)$  for synthetic series RM23s are compared to distributions derived for all 25 Warsaw rain gauges in Fig. 7.41. As it might have been expected, the elimination of specific gauges like R15 and R25 allows to create model for averaged parameters reproducing quite well the distributions of non-zero rainfall intensities in synthetic series.

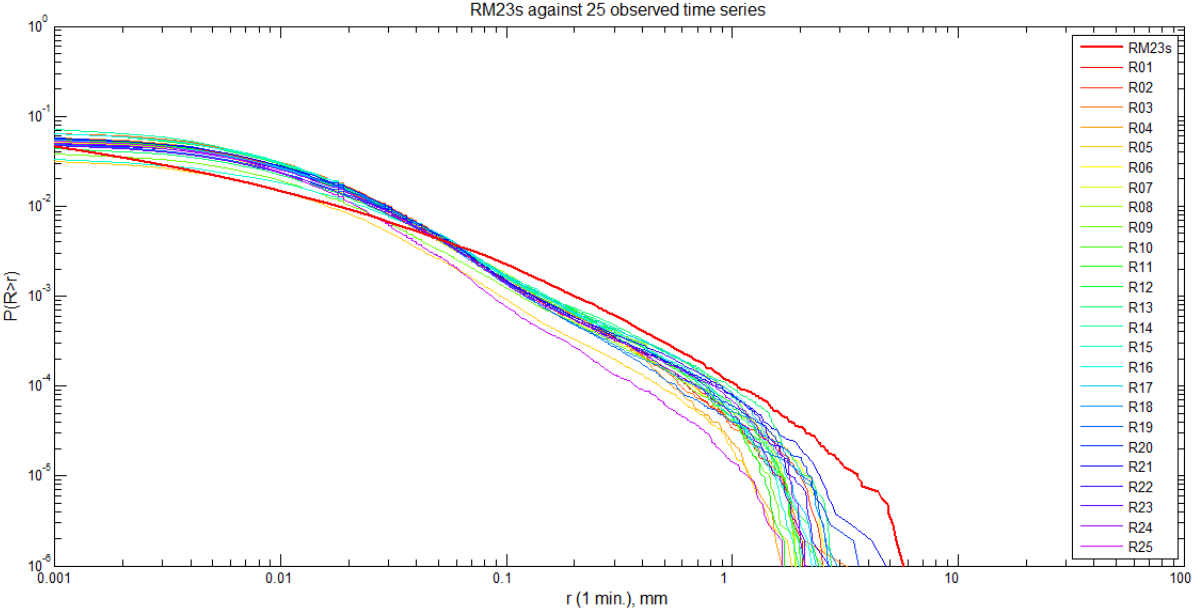


**Figure 7.41.** The complementary cumulative distribution function (cCDF) calculated for the synthetic precipitation time series RM23s against the cCDFs for observed precipitation time series for all 25 Warsaw rain gauges

Results presented for synthetic series RM22s in Fig. 7.42 are not only comparable but even slightly better than already discussed results for synthetic series R06s. Distributions of  $P(R>r)$  of synthetic time series RM22s are also very close to the bunch of distributions originating from real precipitation series. Overestimation of occurrence frequency for the highest rainfall intensities is only apparent. These findings are in logical consequence of the fact that the gauge R06 is located in the Warsaw city centre. But it has to be remembered that gauge R06 displayed simultaneously some outlying tendency diagnosed by clustering analysis. Thus, performance of continuous cascade model parametrized for universal parameters average for 22 gauges (with additional exclusion of gauge R06) is even better. This model is capable of generating synthetic series with distributions of  $P(R>r)$  close to the bunch of observed precipitation distributions, also for a distribution tail, i.e. for highest rainfall intensities values.

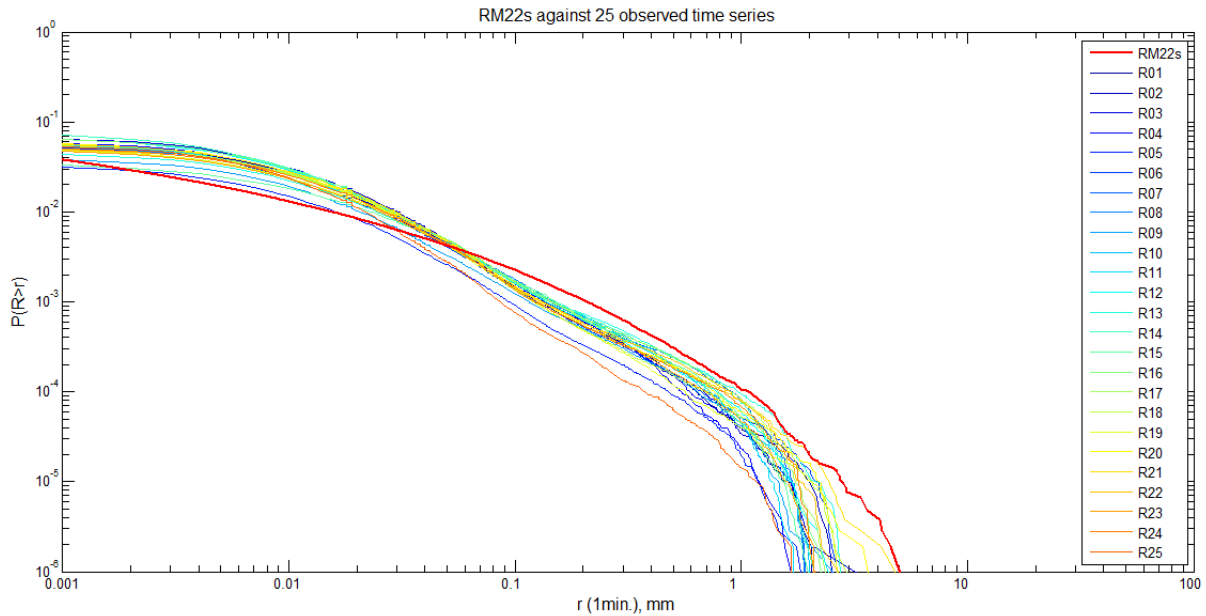


**Figure 7.42.** The complementary cumulative distribution function (cCDF) calculated for the synthetic precipitation time series RM22s against the cCDFs for observed precipitation time series for all 25 Warsaw rain gauges

Results found for models for groups of gauges RM23 and RM22 with respect to analysis of cCDFs for synthetic and observed time series should be evaluated as acceptable and satisfying the needs of urban hydrology. As suggested by Licznar (2010), some overprediction of high intensity rainfall values in synthetic time series is acceptable if the major field of synthetic series application is the hydrodynamic simulation of urban drainage systems, for the purpose of their design and hydraulic performance evaluation.

The second step of the evaluation of synthetic precipitation time series quality is the assessment of the rainfall intermittency. It is made using MATLAB script EP0, calculating the probability of no-rain occurrence  $E(p_0)$  for precipitation time series (synthetic and observed) across timescales  $t = 1 \div 2560$  min ( $\approx 43$  hours).

The results of  $E(p_0)$  calculations for synthetic series for single gauges R06s, R15s, R25s and for groups of gauges RMS23s and RM22s are shown in Figs 7.43÷7.45, and Fig. 7.46 and Fig. 7.47 respectively.

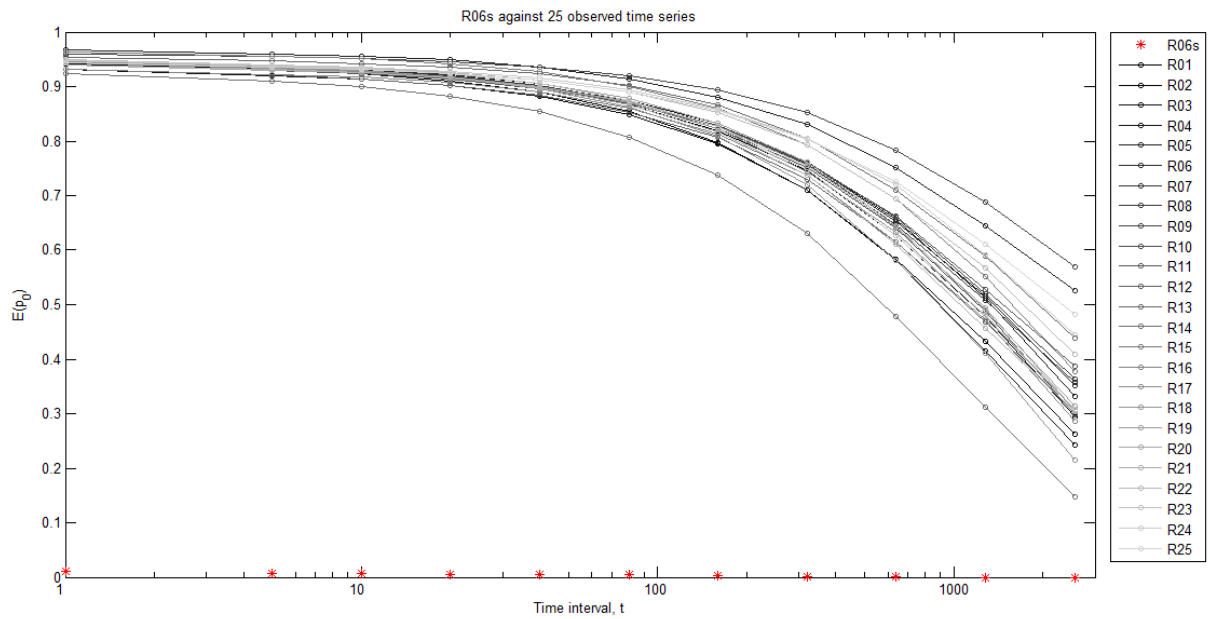


**Figure 7.43.** Comparison of intermittency found for the synthetic time series R06s and for observed precipitation time series for all 25 Warsaw rain gauges

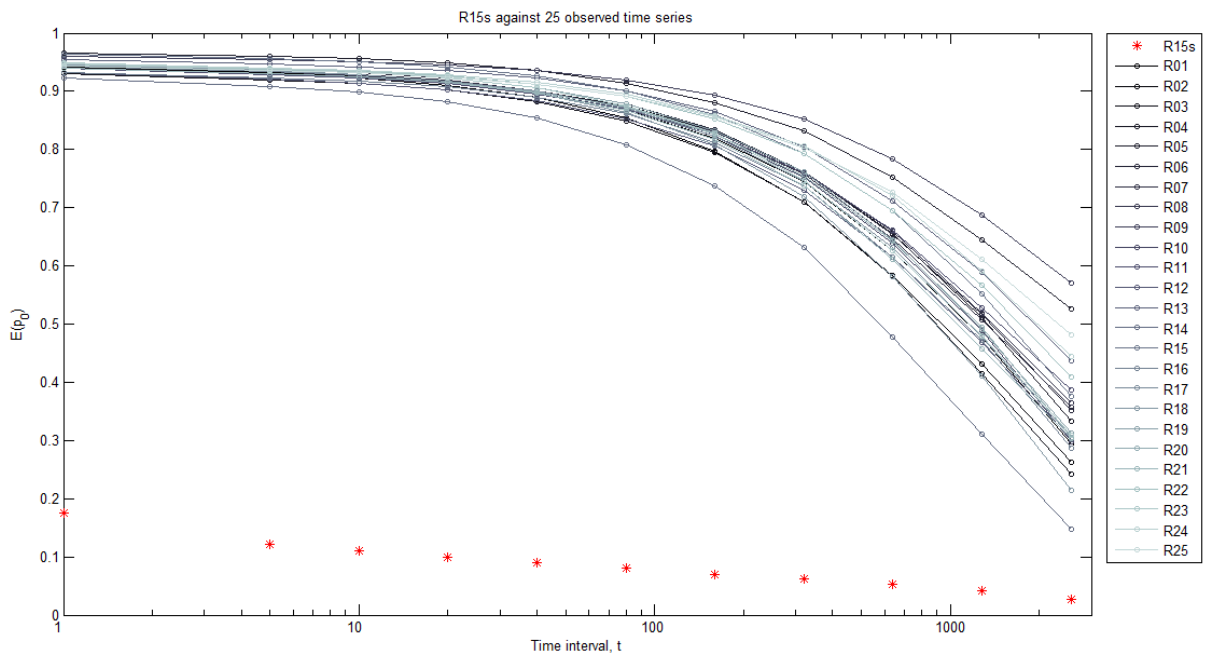


**Figure 7.44.** Rainfall intermittency calculated for the synthetic time series R15s against the all the observed Warsaw rain gauges

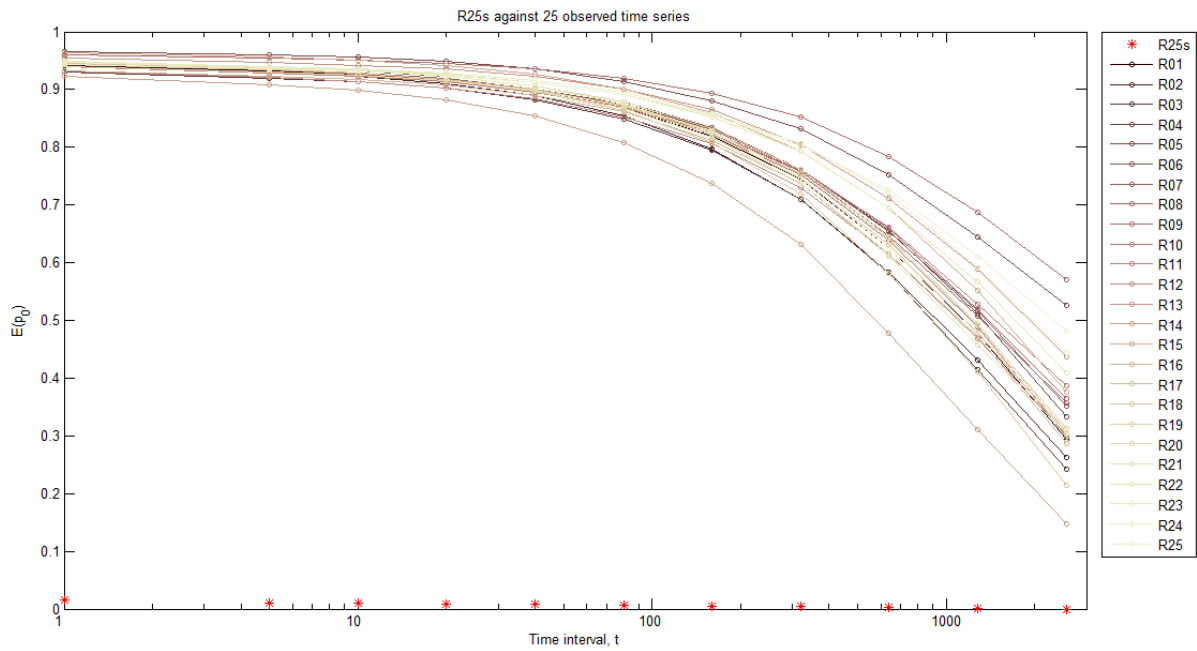


**Figure 7.45.** Rainfall intermittency calculated for the synthetic time series R25s against the all the observed Warsaw rain gauges

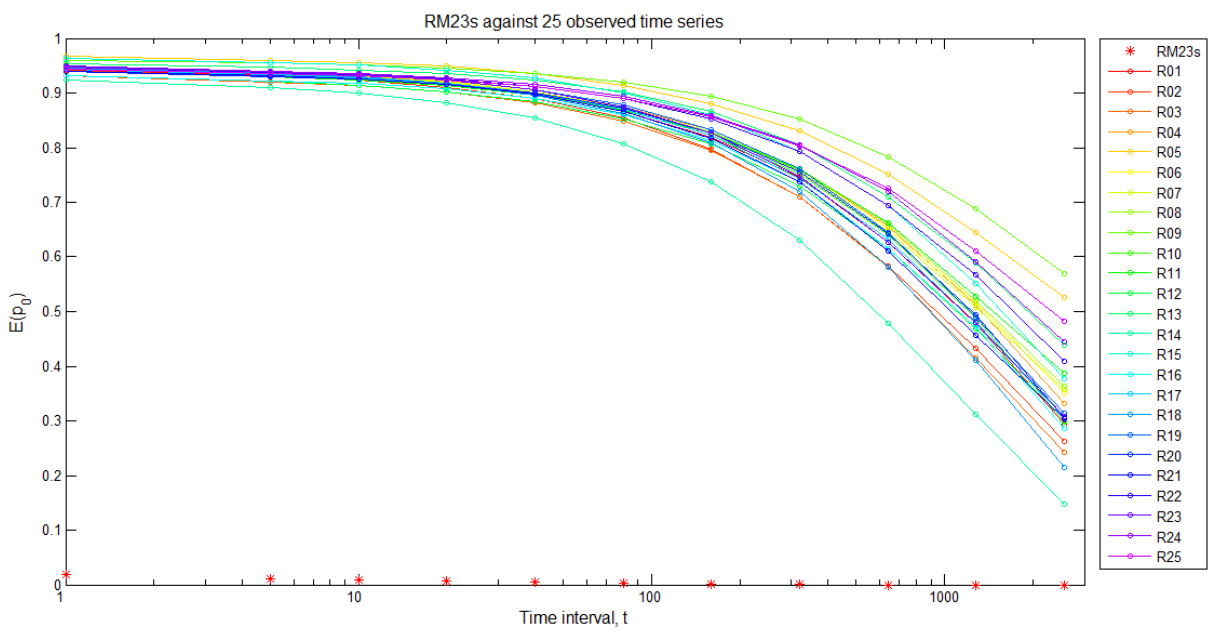


**Figure 7.46.** Rainfall intermittency calculated for the synthetic time series RM23s against the all the observed Warsaw rain gauges

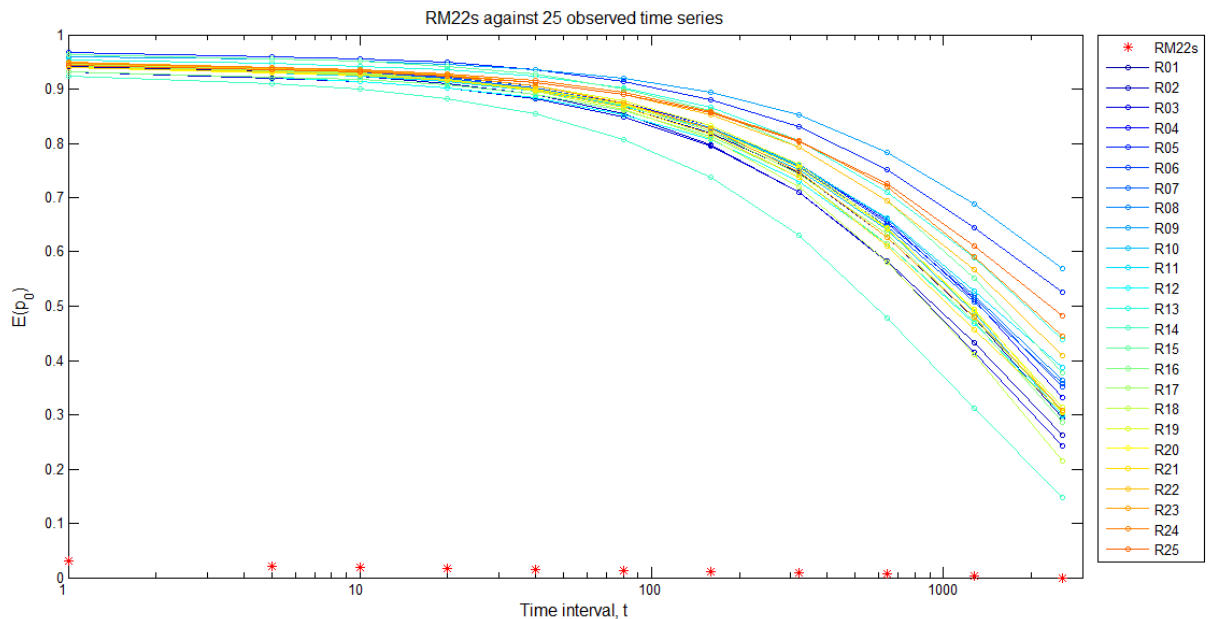


**Figure 7.47.** Rainfall intermittency calculated for the synthetic time series RM22s against the all the observed Warsaw rain gauges

The results plotted for all gauges and groups of gauges in Figs 7.43÷ 7.45, and Fig. 7.46 and Fig. 7.47 reveal a total lack of compatibility between synthetic and observed precipitation time series with respect of rainfall intermittency. The intermittency of rainfall, measured as the probability of a zero-rainfall occurrence for synthetic rainfall, is almost reduced to zero on all plots with exception of gauge R15. But also in the case of gauge R15 and synthetic time series R15s, the probability of a zero rainfall occurrence, even for the shortest time interval of 1-minute, does not exceed 0.2 and is still almost 5 times smaller than for the observed time series. An explanation of these observations is found in Fig. 7.34, presenting the zoomed section of synthetic time series dominated by small but still non-zero rainfall intensities. A generation of such small precipitation intensity values could be considered as a peculiar feature of continuous cascades. Theoretically, a simple ad hoc solution of this error might be imposing some boundary rainfall intensity value below which all time series elements should be zeroed. This solution has a clear disadvantage of reducing the total precipitation in a series. Moreover, it should be not implemented since we are not able to answer the fundamental question: to which extent arrival of very small precipitation intensity values in a series could be a natural feature for precipitation process, and which are not able to be recorded due to gauge resolution limits?

For these reasons, to correct a synthetic series, a special filtering algorithm FILTR in MATLAB has been prepared. The functioning of this filter, at least to some level of generality, reflects the functioning of electronic weighing type gauges. The following

1-minute precipitation depths in series are accumulated by filter as precipitation in inner container of the gauge. At the same time the following 1-minute precipitation depths in a series are supplemented by zeros until the accumulated precipitation depth does not exceed the resolution of gauge equal to 0.001 mm. In such cases the accumulated precipitation is written in the resulting series as 1-minute precipitation depth adjusted to resolution of 0.001 mm. The remaining depth value less than 0.001 mm is accumulated with next precipitation depths in original synthetic series. Obviously, the filtering algorithm FILTR does not change the total precipitation depth in a series, and produces precipitation series with non-zero rainfall intensities with resolution of 0.001 mm/min. as in the case of the Warsaw gauge records. Synthetic precipitation time series postprocessed by the filtering algorithm FILTR are afterwards named as R06sf, R15sf, R25sf, RM23sf and RM22sf respectively for analysed single gauges and gauges groups.

One can expect to observe some influence of filtering algorithm FILTR application for already discussed probabilities of non-zero rainfall values occurrence  $P(R>r)$  in synthetic series. In order to assess the magnitude of this influence, the cCDFs are calculated for postprocessed synthetic series R06sf, R15sf, R25sf, RM23sf and RM22sf and compared with the cCDFs for original synthetic precipitation series as well as recorded precipitation series (see Figs 7.48÷7.52). The results obtained for all synthetic series are consistent. They prove that proposed filtering algorithm FILTR does not affect the distributions of  $P(R>r)$  for synthetic series. The only observed modification is manifested by the minimal shift downward of cCDFs sections for the smallest boundary values of  $r$  below 0.005 mm.

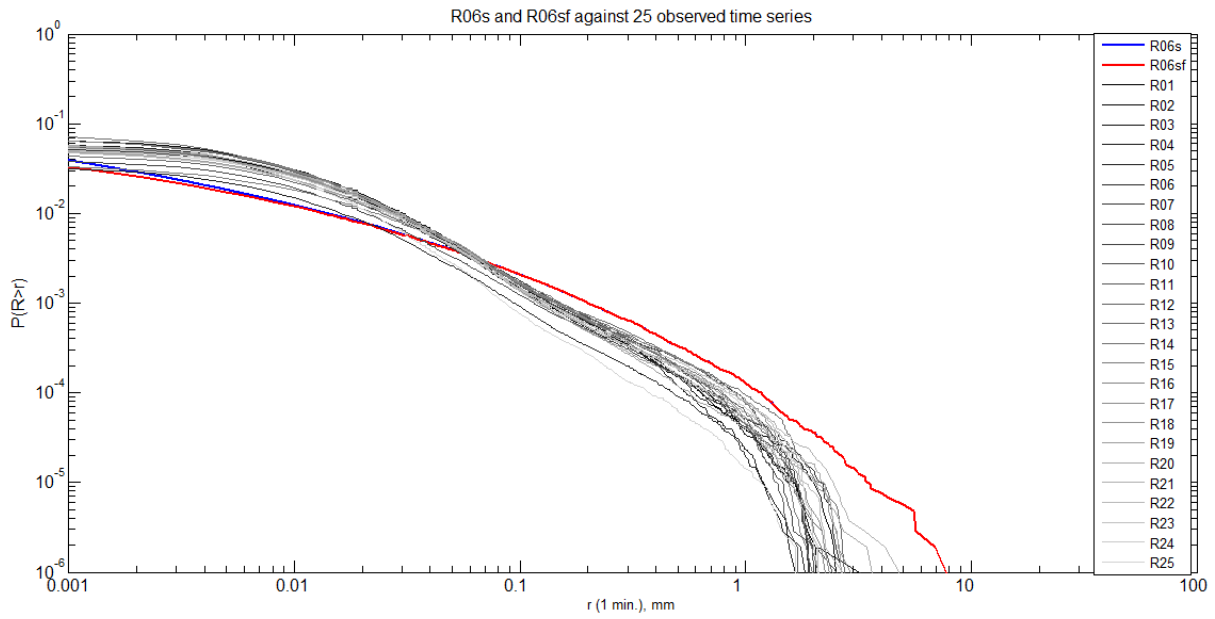


**Figure 7.48.** The complementary cumulative distribution function (cCDF) calculated for the synthetic precipitation time series R06s and R06sf against the cCDFs for observed precipitation time series for all 25 Warsaw rain gauges

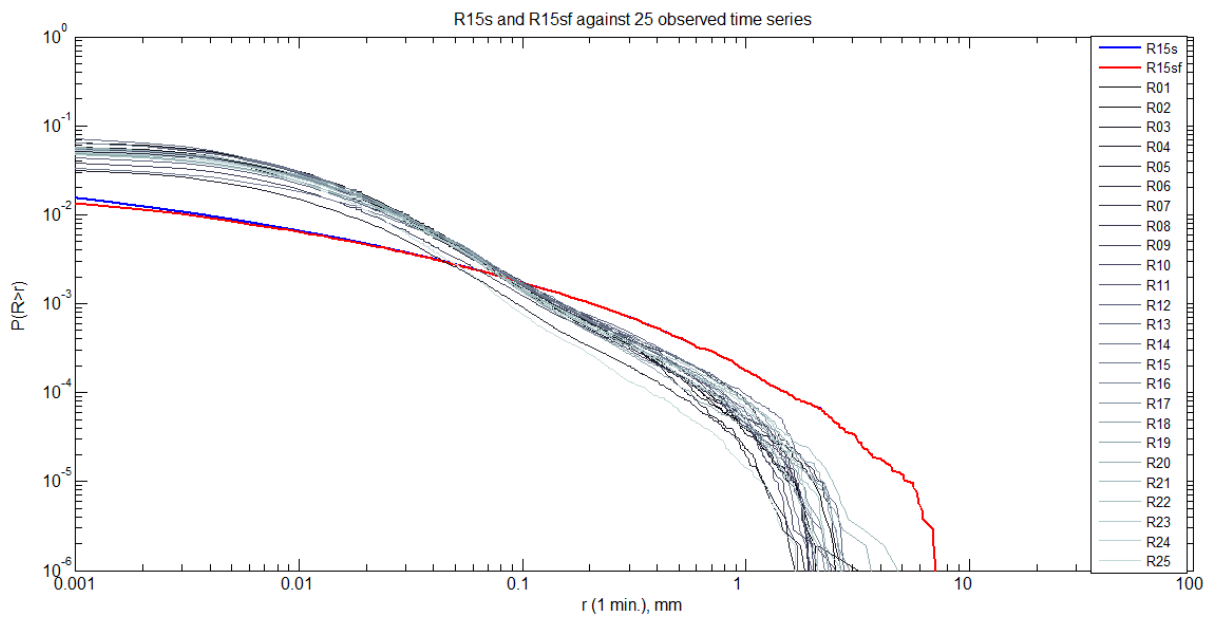


**Figure 7.49.** The complementary cumulative distribution function (cCDF) calculated for the synthetic precipitation time series R15s and R15sf against the cCDFs for observed precipitation time series for all 25 Warsaw rain gauges

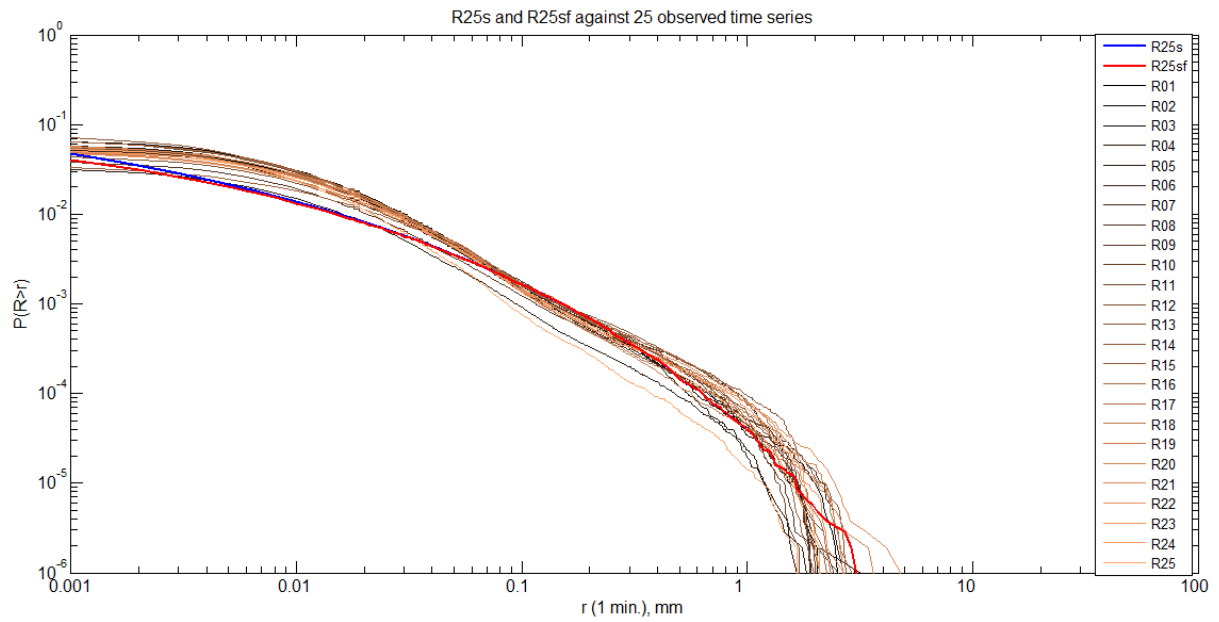


**Figure 7.50.** The complementary cumulative distribution function (cCDF) calculated for the synthetic precipitation time series R25s and R25sf against the cCDFs for observed precipitation time series for all 25 Warsaw rain gauges

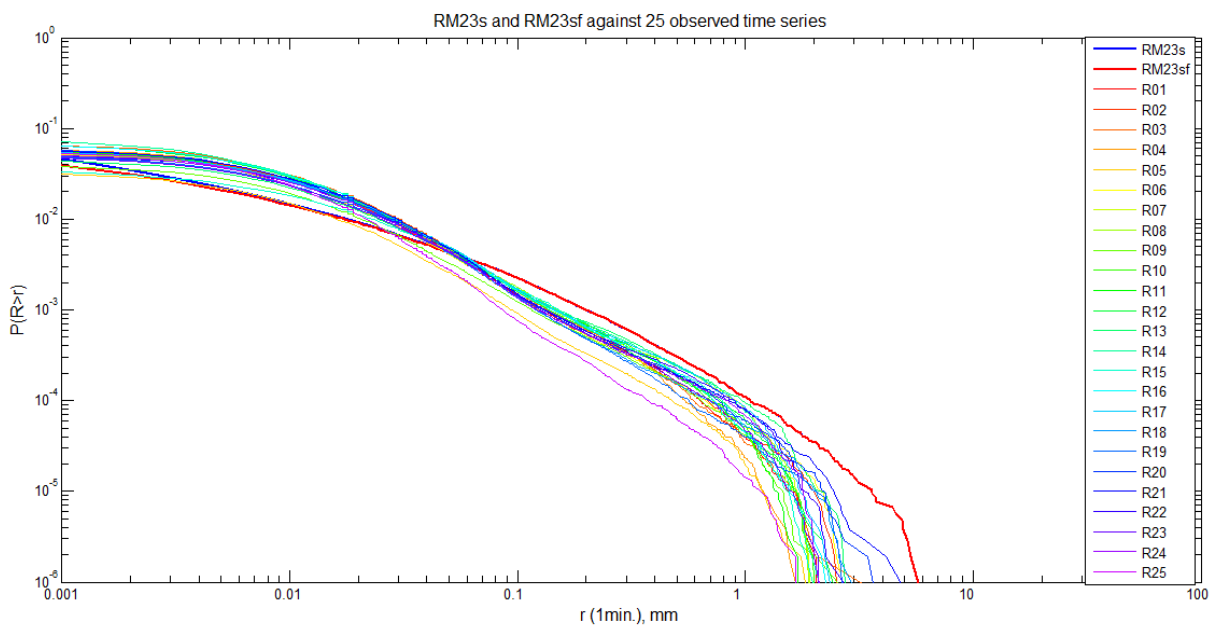


**Figure 7.51.** The cumulative distribution functions calculated for the synthetic time series RM23s and RM23sf after filtering against the cCDF all the observed Warsaw rain gauges. The graphs for data before (in blue) and after filtering (in red) almost entirely coincide

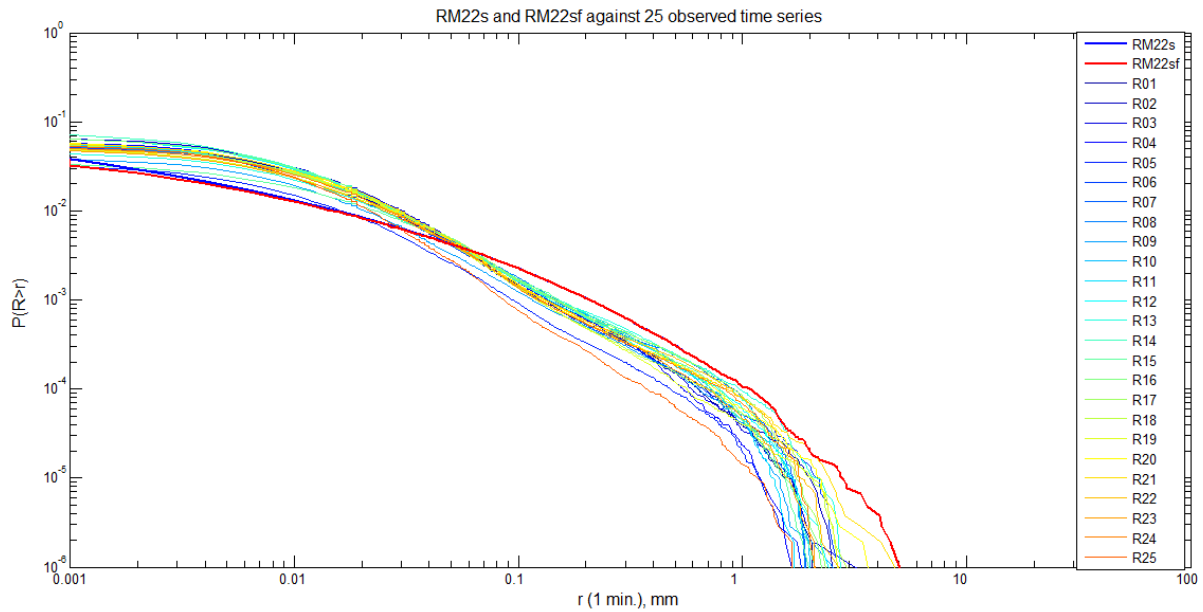


**Figure 7.52.** The cumulative distribution functions calculated for the synthetic time series RM22s and RM22sf after filtering against the cCDF all the observed Warsaw rain gauges. The graphs for data before (in blue) and after filtering (in red) almost entirely coincide

The effects of developed filtering algorithm FILTR on the preservation of the rainfall intermittency in postprocessed synthetic time series could be seen in Figs 7.53–7.57. It is clear that the application of filtering algorithm effectively increases probabilities of no-rain occurrence  $E(p_0)$  in synthetic series across all timescales. Moreover, in postprocessed series a natural phenomenon of  $E(p_0)$  values reduction with increasing time intervals is observed. However, for most plots,  $E(p_0)$  values coincide with probabilities derived for the set of precipitation time series recorded by 25 Warsaw gauges only for the shortest and longest time interval. The only exception could be noticed for gauge R15 where almost all  $E(p_0)$  values for different time intervals are located among  $E(p_0)$  values characterizing observed time series by the Warsaw gauges. Still, the perfect fit between  $E(p_0)$  values calculated for synthetic time series R15sf and observed time series originating from gauge R15 is not reached. In addition,  $E(p_0)$  calculated for synthetic time series R15sf exceeds respective  $E(p_0)$  values for observed time series. Concluding the discussion of intermittency in postprocessed synthetic time series, it should be underlined that the noticeable underestimation of probabilities of no-rain occurrence for time intervals at the range of 10 minutes to 640 minutes was also reported by Licznar et al. (2011a) for a synthetic time series generated by means of discrete canonical cascades models. It seems that only in case of discrete microcanonical cascade models one can expect perfect projection of intermittency pattern of observed rainfall series. But it is achieved in rather primitive manner, by forcing some certain frequencies of 0/1 or 1/0 breaks (empirically estimated for observational series) at following cascade levels.

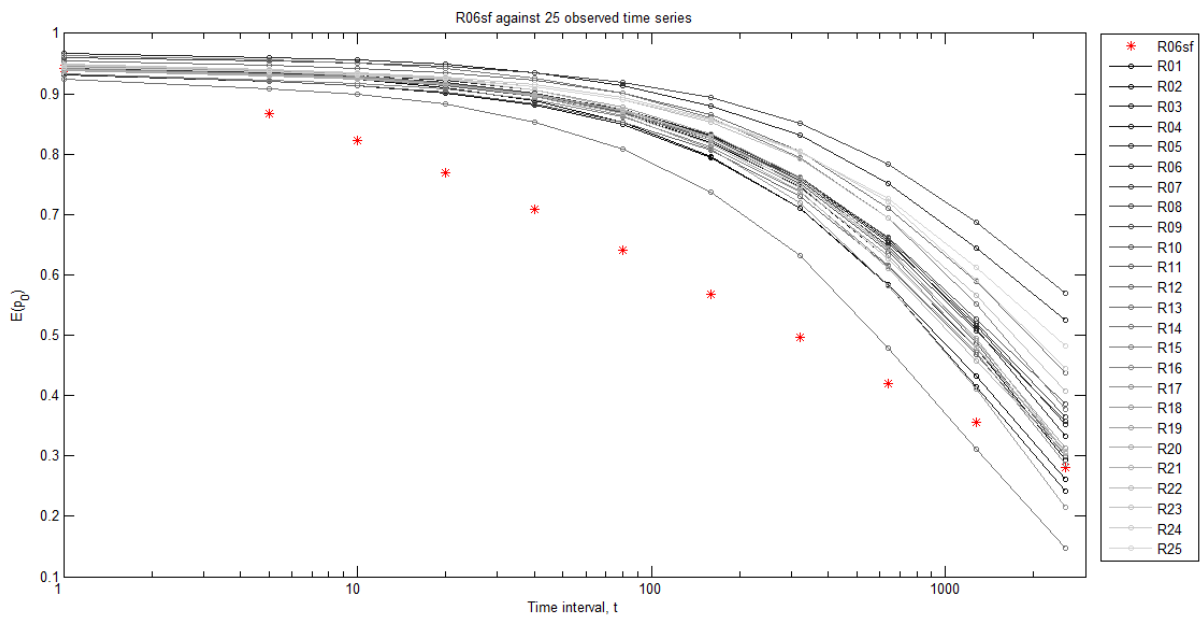


**Figure 7.53.** Comparison of intermittency found for the synthetic time series R06sf (after filtering) and for observed precipitation time series for all 25 Warsaw rain gauges

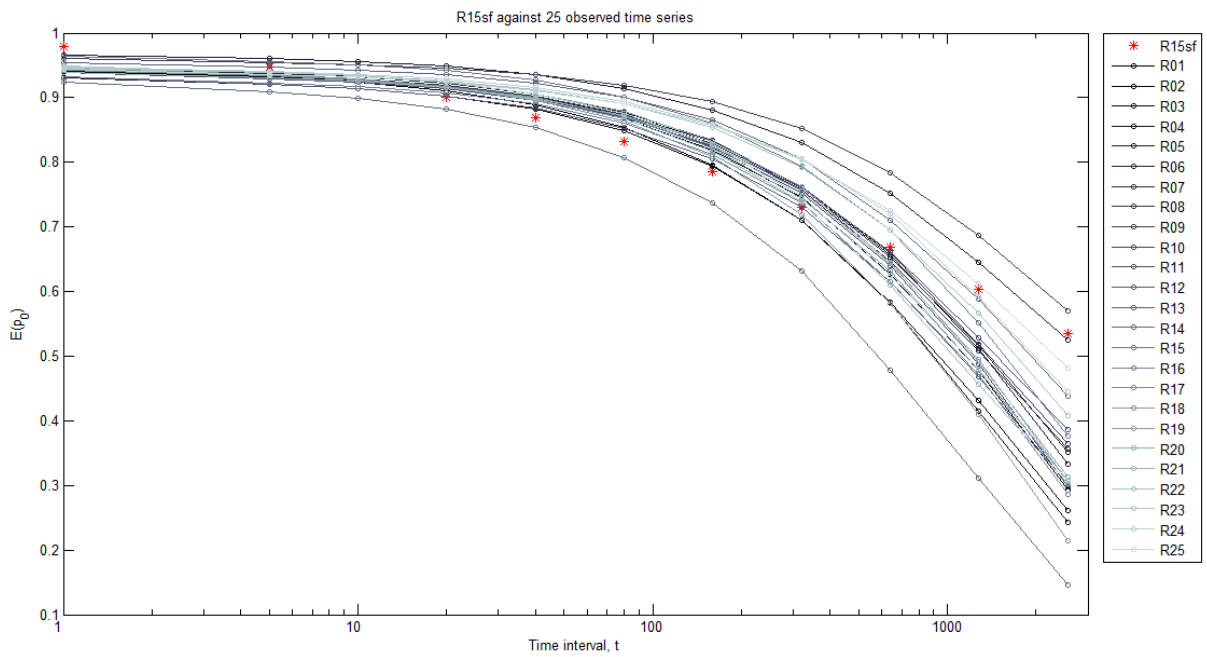


**Figure 7.54.** Comparison of intermittency found for the synthetic time series R15sf (after filtering) and for observed precipitation time series for all 25 Warsaw rain gauges

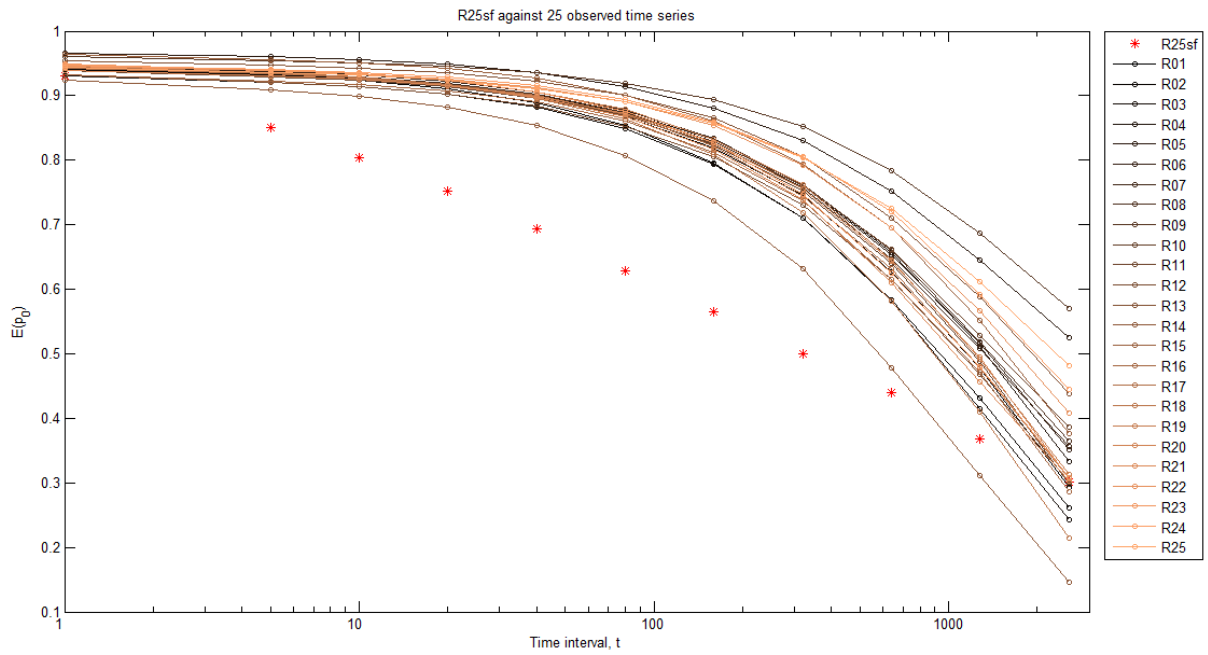


**Figure 7.55.** Comparison of intermittency found for the synthetic time series R25sf (after filtering) and for observed precipitation time series for all 25 Warsaw rain gauges

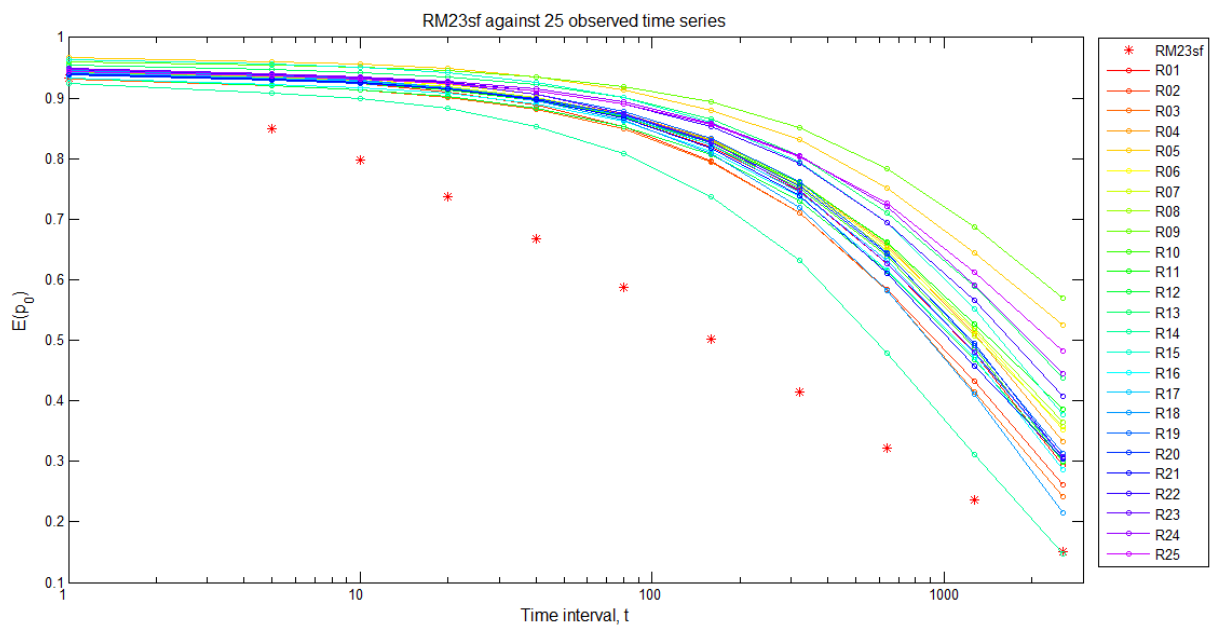


**Figure 7.56.** Rainfall intermittency calculated for the synthetic time series RM23sf after filtering against all the observed Warsaw rain gauges

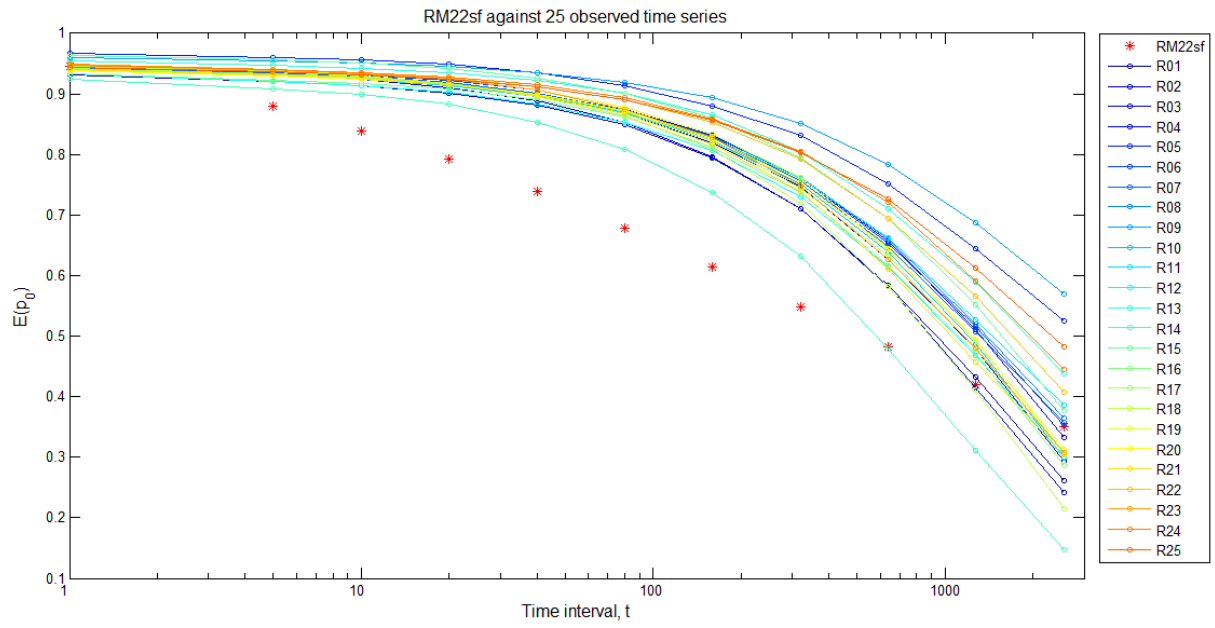


**Figure 7.57.** Rainfall intermittency calculated for the synthetic time series RM22sf after filtering against the all the observed Warsaw rain gauges

## 8. Summary and final conclusions

In this dissertation, an attempt to assess the scaling and the intermittency parameters variability over urban precipitation field of capital city of Poland, Warsaw, is made based on precipitation records on the network of 25 electronic weighing gauges. The assessment is based on the fractal and multifractal analysis techniques, not implemented never before for such a large rainfall data collection in Poland. For this purpose, 1-minute precipitation year-round time series recorded from September 2008 to November 2010 were analysed by using the following fractal and multifractal methods: spectral density analysis, functional box-counting method, trace moment method, probability distribution/multiple scaling and double trace moment method. The multifractal analysis is conducted for a hierarchy of time scales from 1 minute ( $\lambda = 16384$ ) to over 11 days ( $\lambda = 1$ ) and their results are confronted together and interpreted from perspective of electronic weighing gauges functioning.

Concluding the fractal and multifractal studies, the universal multifractal parameters  $\alpha$ ,  $C_1$  and  $H$  are estimated for the first time for a network of urban gauges in Poland. Subsequently, derived universal multifractal parameters are used for taxonomy studies performed with application of clustering methods focused on identification of rain gauges displaying similarities as well as the outlying ones. A discussion and interpretation of obtained results are conducted on the base of previously published studies concerning variability of the Warsaw precipitation field as well as based on an analysis of information about local conditions of specific gauges' exposure.

In the final part of the research, synthetic precipitation series are generated by means of continuous universal random cascade models for the first time in Poland. Cascades generators are parameterized by universal parameters derived for specific Warsaw rain gauges or rain gauge clusters displaying similarity of multifractal parameters. The generated synthetic precipitation time series are subject to statistical evaluation, performed by comparing complementary cumulative distribution function (cCDF) and the intermittency ( $E(p_0)$ ) calculated for synthetic vs. observed time series. Finally, a special filtering algorithm is proposed in order to correct intermittency characteristics of synthetic precipitation time series.

Based on literature studies and performed complex studies of the Warsaw precipitation time series, the following conclusions are formulated:

1. The 1-minute precipitation time series recorded on the network of 25 rain gauges in Warsaw are a 1-dimensional multifractal set. Their proper analysis requires application of fractal and multifractal techniques.

2. The time structure of the recorded precipitation time series is characterized by a scale-invariant behaviour, over a wide range of scales, corresponding to time scales from 1 minute to at least 11 days. Simultaneously simple scaling structure of analysed time series is noticeable complicated by the scaling break, detected for scales corresponding to times at the range from 30 minutes to 1 hour.
3. In the analysed precipitation sets, a multifractal first-order phase transformation is detected. This statistical feature is characteristic for multifractal processes observed in scales higher than the inner homogeneity scale of a process. This observation reveals the presence of relevant metrological limitations in recording properly intermittency and small scale variability of precipitation intensities by the electronic weighing rain gauges installed on the Warsaw network. In addition, evident distortions of the codimension functions  $c(\gamma)$  and the moment scaling functions  $K(q)$  are originating from the rain gauges limited precision at recording the smallest and the highest rainfall intensities, as well as from imperfect recording of rapid variations of rainfall intensities. To some extent, all these limitations could be explained by the diagnosed step response error, typical for electronic weighing type gauges.
4. The degrees of multifractality  $\alpha$  determined for precipitation series recorded by all 25 Warsaw rain gauges are at the range  $0 \leq \alpha \leq 1$ . Thus, point precipitation in Warsaw could be considered as a (log) Lévy process with bounded singularities, presenting soft behaviour (a dressed multifractal process).
5. As revealed by cluster analysis of universal multifractal parameters:  $\alpha$ ,  $H$  and  $C_1$  set, the majority of Warsaw gauges display similarity of multifractal properties for recorded rainfall time series. The same analysis showed outlying behavior for gauges R06 and R15. Most probably the outlying behavior of these gauges, manifested by miscellaneous universal multifractal parameters could be at least partly explained by untypical locations of measuring devices exposure.
6. Universal continuous cascades could be used in practice for generating synthetic rainfall series of fine temporal resolution of 1-minute in Warsaw. Keeping in mind the very close to zero values of parameter  $H$ , the generation of synthetic precipitation could be realized as for a conservative process and for model parameterization on knowledge of only:  $\alpha$  and  $C_1$  values.
7. Based on the analysis of synthetic precipitation series analysis, by means of the complementary cumulative distribution function (cCDF) of non-zero rainfall values, the performance of continuous universal cascade models in preserving variability of

temporal rainfall intensities for Warsaw gauges could be rated as at least good for all analysed groups of gauges and specific gauges, with the only exception of the outlying gauge R15.

8. Continuous universal cascade models developed for Warsaw gauges are not capable of generating synthetic series with intermittency characteristics comparable to observed precipitation time series, recorded with limited resolution of 1 mm/min. Developed accumulation filtering algorithm FILTR allows for synthetic series postprocessing and significantly corrects intermittency of rainfall at synthetic series. Still however the probability of zero rain occurrence in postprocessed precipitation time series does not fit exactly the same probability values derived for observational time series for all time scales. There is a vivid need for future research concerning improvement of intermittency preservation at synthetic precipitation series generated by continuous universal cascade models
9. The general results of universal multifractal parameters variability analysis among the Warsaw precipitation field, and results of the overall performance evaluation of developed universal cascade models at the generation of synthetic precipitation series suggest a large potential for the use of these models in urban hydrology. A practical possibility of a generation of synthetic rainfall series, representative of almost the entire city through a single continuous universal cascade model parametrized by only two values and their further use for hydrodynamic drainage systems modelling, should be explored more deeply in the future.

## **9. List of appendices**

- I. Location of the Warsaw rain gauge network
- II. Functional box-counting plots
- III. Energy spectra computed by FFT method
- IV. Trace moment method plots
- V. Probability distribution/multiple scaling method plots
- VI. Double trace moment method results

## List of references

- Bernardara P., Lang M., Sauquet E., Schertzer D., Tchiriguyskaia I., 2007. Multifractal Analysis in Hydrology: Application to Time Series. Collection Update sciences & technologies. Editions Quae.
- Berggren K., Olofsson M., Viklander M., Svensson G., Gustafsson A.-M., 2011. Hydraulic impacts on urban drainage systems due to changes in rainfall caused by climatic change. *Journal of Hydrological Engineering*: 17(1), 92–98.
- Berne A., Delrieu G., Creutin J.-D., Obled C., 2004. Temporal and spatial resolution of rainfall measurements required for urban hydrology. *Journal of Hydrology*: 299, 166-179.
- Bruni G., Reinoso R., van de Giesen N. C., Clemens F. H. L. R., ten Veldhuis J. A. E., 2015. On the sensitivity of urban hydrodynamic modelling to rainfall spatial and temporal resolution, *Hydrology and Earth System Sciences*: 19, 691-709.
- Burlando P., Rosso R., 1996. Scaling and multiscaling models of depth-duration-frequency curves for storm precipitation. *Journal of Hydrology*: 187, 45-64.
- Chow V.T., Maidment D.R., Mays L.W., 1988. Applied Hydrology, McGraw-Hill, New York.
- Ciach G.J., 2003. Local random errors in tipping-bucket rain gauge measurements. *Journal of Atmospheric and Oceanic Technology*: 20, 752–759.
- de Lima M.I.P., 1998. Multifractals and the temporal structure of rainfall. Doctoral dissertation, Wageningen Agricultural University, Wageningen.
- de Lima M.I.P., Grasman J., 1999. Multifractal analysis of 15-min and daily rainfall from a semi-arid region in Portugal. *Journal of Hydrology*: 220, 1-11.
- Dżugaj D., 2014. Trace moment analysis of urban precipitation field. 12th Students' Science Conference: Boguszów-Gorce, 18-21 September 2014, Oficyna Wydawnicza Politechniki Wrocławskiej, Wrocław, 43-148.
- Eagleson P.S., 1970. Dynamic hydrology. McGraw-Hill, New York. ISBN 9780070185968
- EN 752:2008: Drain and sewer systems outside buildings, PKN.
- Emmanuel I., Andrieu H., Leblois E., Flahaut B., 2012. Temporal and spatial variability of rainfall at the urban hydrological scale. *Journal of Hydrology*: 430-431, 162–172.
- Fletcher T., Andrieu H., Hamel P., 2013. Understanding, management and modelling of urban hydrology and its consequences for receiving waters: a state of the art. *Advances in Water Resources*: 51, 261–279.

- Fraedrich K., Larnder C., 1993. Scaling regimes of composite rainfall time series. *Tellus*, 45A (4): 289–298.
- Frish U., Parisi G., 1985. Fully developed turbulence and intermittency. In: Ghil M., Benzi R. and Parisi G. *Turbulence and predictability in geophysical fluid dynamics and climate dynamics*. Proceedings of the International School of Physics “Enrico Fermi”, Course LXXXVIII, Italian Physical Society, North-Holland, Amsterdam.
- Górski J., 2013. Analiza szeregów opadowych dla potrzeb hydrologii miejskiej na przykładzie Kielc. Doctoral dissertation. Politechnika Świętokrzyska w Kielcach, Kielce.
- Guide to Meteorological Instruments and Methods of Observation. World Meteorological Organization - WMO, 2012. (WMO-No. 8).
- Habib E., Krajewski W.F., Nespor V., Kruger A., 1999. Numerical simulation studies of rain gage data correction due to wind effect, *Journal of Geophysical Research*: 104 (D16), 19723-19733.
- Habib E., Krajewski W.F., Nespor V., Kruger A., 2001. Sampling errors of tipping-bucket rain gauge measurements, *Journal of Hydrologic Engineering*: 6, 159–166.
- Harris D., Seed A., Menabde M., Austin G., 1997. Factors affecting multiscaling analysis of rainfall time-series. *Nonlinear Processes in Geophysics*: 4, 137-155.
- He X., Refsgaard J. C., Sonnenborg T. O., Vejen F., Jensen K. H., 2011a. Statistical analysis of the impact of radar rainfall uncertainties on water resources modeling, *Water Resources Research*: 47, W09526.
- He X., Vejen F., Stisen S., Sonnenborg T. O., Jensen K. H., 2011b. An operational weather radar based QPE and its application in catchment water resources modelling, *Vadose Zone Journal*:10, 1–17.
- Houze Jr., R.A., 1993. *Cloud Dynamics*. Academic Press.
- International meteorological vocabulary. WMO, No. 182. 1966. TP. 91. Geneva
- Kaźmierczak B., Kotowski A. 2012. Weryfikacja przepustowości kanalizacji deszczowej w modelowaniu hydrodynamicznym. Oficyna Wydawnicza Politechniki Wrocławskiej, Wrocław.
- Kicińska B., Wawer J., 2014. Wpływ urbanizacji na warunki klimatyczne w Warszawie, The climate of Warsaw and its suburbs, Atlas of interdependence of meteorological and geographical parameters in Poland, Warszawa.
- Kiely G., Ivanova K. 1999. Multifractal analysis of hourly precipitation, *Physics and Chemistry of the Earth*: 24(7), 781-786.

- Kossowska-Cezak U., Bareja P., 1998. Influence of Warsaw built area on wind direction and Speed, *Acta Universitatis Lodzianis Folia Geographica Physica*: 3, 463-465.
- Kotowski A., 2006. O potrzebie dostosowania zasad wymiarowania kanalizacji w Polsce do wymagań normy PN-EN 752 i zaleceń Europejskiego Komitetu Normalizacji. *Gaz, Woda i Technika Sanitarna*: 6, 20–26.
- Kotowski A., 2015. Podstawy bezpiecznego wymiarowania odwodnienia terenów. Seidel-Przywecki, Warszawa.
- Kotowski A., Kaźmierczak B., Danczewicz A. 2010. Modelowanie opadów do wymiarowania kanalizacji. Wyd. Komitetu Inżynierii Lądowej i Wodnej PAN. Studia z zakresu Inżynierii nr 68, Warszawa.
- Kozłowska Z. et al., 2013. Statistical Yearbook of Warsaw, Statistical Office in Warsaw.
- La Barbera P., Lanza L.G. and Stagi L., 2002. Influence of systematic mechanical errors of tipping-bucket rain gauges on the statistics of rainfall extremes. *Water Science and Technology*: 45(2), 1-9.
- Lanza L., Leroy M., Alexandropoulos C., Stagi L., Wauben W., 2005. WMO Laboratory Intercomparison of Rainfall Intensity Gauges. Final Report.
- Lanza L.G. and Vuerich E., 2010. The accuracy of rain intensity measurements and its influence on extreme events statistics. European Commission – Wfd Common Implementation Strategy, Wg F Thematic Workshop On Implementation of the Floods Directive 2007/60/Ec ‘Flash Floods and Pluvial Flooding’ 26th – 28th May 2010, Cagliari, Italy.
- Lebel T., Amani A., 1999. Rainfall Estimation in the Sahel: What Is the Ground Truth? *Journal of Applied Meteorology and Climatology*: 38(5), 555-568.
- Licznar P., 2005: Propozycja metody przetwarzania danych pluwiograficznych na potrzeby projektowania i eksploatacji miejskich systemów odwodnienia. *Woda Środ. Obsz. Wiej.*: 5 (14), 197–207.
- Licznar P., 2008: Obliczenia częstotliwości nadpiętrzenia sieci kanalizacji deszczowej. *Gaz, Woda i Technika Sanitarna*: 7-8, 16-21.
- Licznar P., 2009. Generatory syntetycznych szeregów opadowych do modelowania sieci kanalizacji deszczowych i ogólnospławnych, Wrocław: Wydawnictwo Uniwersytetu Przyrodniczego we Wrocławiu.
- Licznar P., De Michele C., Adamowski W., 2015. Precipitation variability within an urban monitoring network via microcanonical cascade generators, *Hydrology, and Earth System Science*: 19, 485-506.

- Licznar P., Dżugaj D., Niesobska M., 2013. Ekspertyza techniczna polegająca na weryfikacji poprawności działania deszczomierzy wchodzących w skład sieci monitoringu opadów atmosferycznych należącego do MPWiK S.A. we Wrocławiu, Wrocław.
- Licznar P., Łomotowski J., Rojek M. 2005. Sposoby pomiaru natężenia deszczu na potrzeby projektowania i eksploatacji systemów odwodnienia terenów zurbanizowanych, *Water-Environment-Rural areas*: 5(14), 209-219.
- Licznar P., Łomotowski J., Rupp D. E., 2011a. Random cascade driven rainfall disaggregation for urban hydrology: An evaluation of six models and a new generator, *Atmospheric Research*: 99 (3-4), 563–578.
- Licznar P., Schmitt T.G., Rupp D.E, 2011b. Distribution of Microcanonical Cascade Weights of Rainfall at Small Timescales, *Acta Geophysica*: 5, 1013-1043.
- Licznar P., Szelağ B., 2014. Analiza zmienności czasowej opadów atmosferycznych w Warszawie. *Ochrona środowiska*, 36(3), 23-28.
- Lovejoy S., Schertzer D., 1990. Multifractals, universality classes and satellite and radar measurements of clouds and rain. *Journal of Geophysical Research*: 95, 2021-2034.
- Lovejoy S., Schertzer D., 1991. Multifractal analysis techniques and the rain and clouds fields from  $10^{-3}$  to  $10^6$ m. *Nonlinear Variability in Geophysics: Scaling and Fractals*, Luwer Academic Publishers, the Netherlands, 112-144.
- Lovejoy S., Schertzer D., 2006. Multifractals, cloud radiances and rain. *Journal of hydrology*: 322, 59–88.
- Lovejoy S., Schertzer D., 2013. *The Weather and Climate: Emergent Laws and Multifractal Cascades*, Cambridge University Press.
- Lovejoy S., Schertzer D., Tsonis A.A., 1987. Functional box-counting and multiple elliptical dimensions in rain. *Science*: 235, 1036-1038.
- Lynch S., 2004. *Dynamical Systems with Applications using MATLAB*. Birkhäuser Basel.
- Lyons G.R., 2006. *Wprowadzenie do cyfrowego przetwarzania sygnałów*, Warszawa: Wydawnictwa Komunikacji i Łączności.
- Mandelbrot B., 1967. How long is the coast of Britain? Statistical self-similarity and fractional dimension, *Science*: 156, 636-638.
- Mandelbrot B., 1977. *Fractals: Form, Chance and Dimension*. W. H. Freeman & Company.
- Mandelbrot B.B., 1989. Multifractal Measures, Especially for the Geophysicist, *Pure and Applied Geophysics*: 131(1/2), 5-42.
- Marani M., 2003. On the correlation structure of continuous and discrete point rainfall. *Water Resources Research*: 39(5), 1128-1135.

- Mascaro G., Deidda R., Hellies M., 2013. On the nature of rainfall intermittency as revealed by different metrics and sampling approaches. *Hydrology and Earth System Science*: 17, 355-369.
- Menabde M., Harris D., Seed A., Austin G., Stow D., 1997. Multiscaling properties of rainfall and bounded random cascades. *Water Resources Research*: 33(12), 2823-2830.
- Molini A., La Barbera P., Lanza L.G., Stagi L., 2001. Rainfall intermittency and the sampling error of tipping-bucket rain gauges. *Physics and Chemistry of the Earth (C)*: 26(10-12), 737-742
- Molnar P., Burlando P., 2005. Preservation of rainfall properties in stochastic disaggregation by a simple random cascade model. *Atmospheric Research*: 77, 137-151.
- Narkhedkar S. G., Sinha S. K., Mukhopadhyay P., 2010. Rainfall analysis using conventional and non-conventional rainfall information on monthly scale. *Atmósfera*: 23(2), 141-164.
- Nespor V., Krajewski W.F., Kruger A., 2000. Wind-induced error of raindrop size distribution measurement using a two-dimensional video disdrometer. *Journal of Atmospheric and Oceanic Technology*: 17(11), 1483-1492.
- Niemczynowicz J., 1999. Urban hydrology and water management—present and future challenges. *Urban Water*: 1(1), 1-14.
- Ochoa-Rodriguez S., Wang L.-P., Gires A., Pina R.D., Reinoso-Rondinel R., Bruni G., Ichiba A., Gaitan S., Cristiano E., Assel J.v., Kroll S., Murlà-Tuyls D., Tisserand B., Schertzer D., Tchiguirinskaia I., Onof C., Willems P., ten Veldhuis M.-C., 2015. Impact of spatial and temporal resolution of rainfall inputs on urban hydrodynamic modelling outputs: a multi-catchment investigation. *Journal of Hydrology*: 531(2), 389–407.
- Oke T. R., 2006. Initial Guidance to Obtain Representative Meteorological Observations at Urban Sites. World Meteorological Organization - WMO Instruments and Observing Methods Report No. 81 (WMO/TD-No. 1250).
- Olsson J., 1995. Limits and characteristics of the multifractal behaviour of a high-resolution rainfall time series. *Nonlinear Processes in Geophysics*: 2(1), 23–29.
- Olsson J., Burlando P., 2002. Reproduction of temporal scaling by a rectangular pulses rainfall model. *Hydrological Processes*: 16, 611-630.
- Pandey G., Lovejoy S., Schertzer D., 1998. Multifractal analysis of daily river flows including extremes for basins of five to two million square kilometres, one day to 75 years. *Journal of Hydrology*: 208, 62-81.

- Pathirana A., Herath S., Yamada T., 2003. Estimating rainfall distributions at high temporal resolution using a multifractal model. *Hydrology and Earth System Science: 7(5)*, 668-679.
- Pawlak J., Teisseyre – Sierpińska M., Badałow G., Pawlak J., Pietrusiewicz W., Cieszewska A., Kaliszuk E., Salwicka J., Szablowska K., Szulczewska B., Wolski P., Zantonowicz K., 2006. Opracowanie ekofizjograficzne do studium uwarunkowań i kierunków zagospodarowania przestrzennego m. St. Warszawy, Urząd Miasta Stołecznego Warszawy, Warszawa.
- Płażewski R., 2014. Ostrość i śnieżność zim w Warszawie w latach 1965-95, The climate of Warsaw and its suburbs, Atlas of interdependence of meteorological and geographical parameters in Poland, Warszawa.
- PN-EN 752:2008: Drain and sewer systems outside buildings (Zewnętrzne systemy kanalizacyjne). PKN, Warszawa 2008.
- Pollock M., Colli M., O'Donnell G., Stagnaro M., Lanza L.G., Quinn P., Dutton M., Wilkinson M., Black A., Kilsby C., and O'Connell P.E., 2016. A novel experimental design to investigate the wind-induced undercatch. Conference materials: Technical Conference on Meteorological and Environmental Instruments and Methods of Observation (CIMO TECO 2016), Spain.
- Refsgaard J. C., van der Sluijs J. P., Hojberg A. L., Vanrolleghem P. A., 2007. Uncertainty in the environmental modelling process – a framework and guidance, *Environmental Modelling & Software*, 22, 1543-1556.
- Rupp D.E., Licznar P., Adamowski W., Leśniewski M., 2012. Multiplicative cascade models for fine spatial downscaling of rainfall: parameterization with rain gauge data. *Hydrology and Earth System Science: 16*, 671-684.
- Saa A., Gasco' G., Grau J.B., Anton' J.M., Tarquis A.M., 2007. Comparison of gliding box and box-counting methods in river network analysis, *Nonlinear Processes in Geophysics: 14*, 603–613.
- Schertzer D., Lovejoy S., 1987: Physical modeling and analysis of rain and clouds by anisotropic scaling multiplicative processes. *Journal of Geophysical Research: 92*, 9692–9714.
- Schertzer D., Lovejoy S., 1988. Nonlinear variability in geophysics: multifractal simulation and analysis. In: *Fractals' Physical Origin and Properties*, Ed. L. Pietronero, New York, Plenum, 49-82.

- Schertzer D., Lovejoy S., 1989. Nonlinear variability in Geophysics: multifractal simulations and analysis. Pietronero, L., Fractals' physical origin and properties. Plenum Press, New York, 49-79.
- Schertzer D., Lovejoy S., 1993. Nonlinear variability in Geophysics 3: scaling and multifractal processes. Lecture notes, AGU/EGS Conference, September 10-17, 1993. Cargèse, France.
- Schilling W., 1991. Rainfall data for urban hydrology: what do we need? *Atmospheric Research*: 2(1-3), 5-21.
- Schmitt T.G., 2007. Kommentar zum Arbeitsblatt A 118 "Hydraulische Bemessung und Nachweis von Entwässerungssystemen". DWA, Hennef 2000. Seidel-Przywecki, Warszawa.
- Seuront L., 2009. Fractals and Multifractals in Ecology and Aquatic Science, CRC Press.
- Shivamoggi B.K., 2014. Nonlinear Dynamics and Chaotic Phenomena: An Introduction, Springer.
- Tan P., Steinbach M., Kumar V., 2005. Introduction to Data Mining, Addison-Wesley Longman Publishing Co., Inc. Boston, MA, USA.
- Tapiador F.J., Turk F.J., Petersen W., Hou A.Y., García-Ortega E., Machado L.A.T, Angelis C.F., Salio P., Kidd C., Huffman G.J., de Castro M., 2012. Global precipitation measurement: Methods, datasets and applications. *Atmospheric Research*: 104-105, 70-97.
- Tessier Y., Lovejoy S., Hubert P., Schertzer D., Pecknold S., 1996. Multifractal analysis and modelling of rainfall and river flows and scaling, casual transfer functions, *Journal of Geophysical Research*: 101(D21), 26427-26440.
- Tessier Y., Lovejoy S., Schertzer D., 1993. Universal Multifractals: theory and observations for rain and clouds. *Journal of Applied Meteorology*: 2, 223-250.
- Testik F. Y. and Gebremichael M., 2010. Rainfall: State of the Science, American Geophysical Union, Washington, D. C.
- Thames Tunnel needs report. Appendix B, 2010.
- Vasvári V., 2005. Calibration of tipping bucket rain gauges in the Graz urban research area. *Atmospheric Research*: 77, 18-28.
- Veneziano D., Furcolo P., Iacobellis V. 2006. Imperfect scaling of time and space-time rainfall. *Journal of Hydrology*: 322, 105-119.

- Vezzaro L., Christensen M. L., Thirsing C., Grum M., Mikkelsen P. S. 2014. Water quality-based real time control of integrated urban drainage systems: a preliminary study from Copenhagen, Denmark. *Procedia Engineering*: 70, 1707-1716.
- Viessman W. Jr., Lewis G. L., 1996. Introduction to hydrology. Harpercollins College Publishers, New York, USA.
- Vuerich E., Monesi C., Lanza L.G., Stagi L., Lanzinger E., 2009. WMO Field Intercomparison of Rainfall Intensity Gauges, Instruments and Observing Methods Report No.99, WMO/TD-No. 1504.
- Wang J., Wolff D. B., 2010. Evaluation of TRMM Ground-Validation Radar-Rain Errors Using Rain Gauge Measurements, *Journal of Applied Meteorology and Climatology*: 49(2), 310-324.
- Weierstrass K., 1872. Über continuirliche Functionen eines reellen Arguments, die für keinen Werth des Letzteren einen bestimmten Differentialquotienten besitzen. *Classics on Fractals*. Ed. A. E. Gerald (Addison -Wesley, 1993).

## List of web pages

Encyclopedia Britannica, Mandelbrot, B. B., Fractals and the Geometry of Nature, [online access: January 11<sup>th</sup>, 2016], available at:

<https://www.britannica.com/topic/The-Fractal-Geometry-of-Nature>

Clauset A., Inference, Models and Simulation for Complex Systems, Santa Fe Institute, [online access: June 29<sup>th</sup>, 2016], available at:

[http://tuvalu.santafe.edu/~aaronc/courses/7000/csci7000-001\\_2011\\_L0](http://tuvalu.santafe.edu/~aaronc/courses/7000/csci7000-001_2011_L0)

History of fractals, [online access: January 25<sup>th</sup>, 2016], available at:

<http://www-groups.dcs.st-and.ac.uk/history/HistTopics/fractals.html>

McGill University, [online access: June 29<sup>th</sup>, 2016], available at:

<http://www.physics.mcgill.ca/~gang/software/>

Mathworks documentation, [online access: June 30<sup>th</sup>, 2016], available at:

<http://www.mathworks.com/>

STATSOFT Electronic Statistic Textbook, [online access: October 31<sup>st</sup>, 2015], available at:

<http://www.statsoft.pl/textbook/stathome>

WOLFRAM MATHWORLD, [online access: October 31<sup>st</sup>, 2015], available at:

<http://mathworld.wolfram.com/>

## List of figures and tables

### Figures

<b>Figure 3.1.</b> Remote sensing X-band weather radar .....	18
<b>Figure 3.2.</b> Hellmann rain gauges .....	18
<b>Figure 3.3.</b> Tipping-bucket rain gauge. From the outside (on left) and from the inside (on the right).....	19
<b>Figure 3.4.</b> Measuring set used to rain gauge calibration at IIHR – Hydrosience & Engineering laboratory, Iowa State University (USA) (Licznar et al., 2013) .....	20
<b>Figure 3.5.</b> Siphon rain gauge in field (on left) and (on right) the inside elements. From the top: the funnel, the recording pen, the floating element and the siphon .....	20
<b>Figure 3.6.</b> Sample pluviograph chart obtained by a siphon rain gauge recording .....	21
<b>Figure 3.7.</b> A MPS Systém weighing-type rain gauge .....	21
<b>Figure 3.8.</b> The strain-gauge bridge of an electronic weighing-type rain gauge .....	22
<b>Figure 3.9.</b> Tipping-bucket rain gauges.....	23
<b>Figure 4.1.</b> Scheme of climatic scales and vertical layers found in urban areas: planetary boundary layer (PBL), urban boundary layer (UBL), urban canopy layer (UCL), rural boundary layer (RBL) (from WMO No. 8, 2012).....	27
<b>Figure 4.2.</b> 2-D flow around a building with flow normal to the upwind face (a) stream lines and flow zones; A - undisturbed, B - displacement, C - cavity, D – wake and (b) flow, and vortex structures (from WMO-No. 8) .....	28
<b>Figure 4.3.</b> Site condition for class 1 rain gauge (from WMO No. 8, 2012) – condition 1 .....	30
<b>Figure 4.4.</b> Site condition for class 1 rain gauge (from WMO No. 8, 2012) – condition 2 .....	30
<b>Figure 4.5.</b> Site condition for class 2 rain gauge (from WMO No. 8, 2012) .....	30
<b>Figure 4.6.</b> Site condition for class 3 rain gauge (from WMO No. 8, 2012) .....	30
<b>Figure 4.7.</b> Site condition for class 4 rain gauge (from WMO No. 8, 2012) .....	31
<b>Figure 4.8.</b> Site condition for class 5 rain gauge (from WMO No. 8, 2012) .....	31
<b>Figure 4.9.</b> Locations of rain gauges in Warsaw .....	32
<b>Figure 4.10.</b> Scheme with its dimensions (on left) of a rain gauge type TRwS 200E (on right) .....	33
<b>Figure 4.11.</b> Hyetographs of Warsaw 1-minute rainfall data recorded in 2008-2010 by 25 rain gauges .....	35
<b>Figure 6.1.</b> Illustration of the relation between the intensity of rainfall process and the temporal resolution of recorded data. Original series recoded by gauge R05 in Warsaw, at 29 <sup>th</sup> September 2009.....	41
<b>Figure 6.2.</b> Illustration of construction of ‘bare’ (on left-hand side) and ‘dressed’ (on right-hand side) multifractal process. On the bottom centre the scale factor equals to $\lambda = 2^7$ . Reproduced from Lovejoy and Schertzer (2013) .....	43
<b>Figure 6.3.</b> Scheme of densification of scales. Reproduced from Lovejoy and Schertzer (2013).....	51
<b>Figure 6.4.</b> Universal scaling exponent functions for $\alpha$ from 0 to 2. a) Codimension functions, $c(\gamma)/C_1$ ; b) Moment scaling functions, $K(q)/C_1$ . From Lovejoy and Schertzer (2013).....	53
<b>Figure 6.5.</b> Locations of gauges R06, R15 and R25 for which synthetic series are generated from universal cascades for gauge – specific $\alpha$ and $C_1$ parameters, at the frame of so called single simulations .....	56
<b>Figure 6.6.</b> Locations of gauge groups RM23 and RM22 containing 23 and 22 gauges respectively for which synthetic series were performed from universal cascades for gauge – group averaged $\alpha$ and $C_1$ parameters, at the frame of so called average simulations .....	56
<b>Figure 7.1</b> Results of functional box-counting method for 1-minute rainfall time-series from Warsaw, for rain gauge R06.....	60
<b>Figure 7.2</b> Results of functional box-counting method for 1-minute rainfall time-series from Warsaw, for rain gauge R15.....	60
<b>Figure 7.3</b> Results of functional box-counting method for 1-minute rainfall time-series from Warsaw, for rain gauge R25.....	61
<b>Figure 7.4.</b> Energy spectrum for 1-minute rainfall time-series from Warsaw, from September 2008 to November 2010, for rain gauge R06 .....	66
<b>Figure 7.5.</b> Energy spectrum for 1-minute rainfall time-series from Warsaw, from September 2008 to November 2010, for rain gauge R15 .....	66
<b>Figure 7.6.</b> Energy spectrum for 1-minute rainfall time-series from Warsaw, from September 2008 to November 2010, for rain gauge R25 .....	67
<b>Figure 7.7.</b> Monthly rainfall in Warsaw (2009) for gauges R06, R15 and R25 .....	70
<b>Figure 7.8.</b> Energy spectra for 1-minute rainfall time-series from Warsaw, for rain gauge R06 in 2009. Summer season (upper graph) and winter season (lower graph) .....	72

<b>Figure 7.9.</b> Energy spectrum for 1-minute rainfall time-series from Warsaw, for rain gauge R15 in 2009. Summer season (upper graph) and winter season (lower graph) .....	73
<b>Figure 7.10.</b> Energy spectrum for 1-minute rainfall time-series from Warsaw, for rain gauge R25 in 2009. Summer season (upper graph) and winter season (lower graph) .....	74
<b>Figure 7.11.</b> Energy spectrum for 1-minute rainfall time-series from Warsaw, for rain gauge R06 with the overall slope .....	75
<b>Figure 7.12.</b> Energy spectrum for 1-minute rainfall time-series from Warsaw, for rain gauge R15 with the overall slope .....	76
<b>Figure 7.13.</b> Energy spectrum for 1-minute rainfall time-series from Warsaw, for rain gauge R25 with the overall slope .....	76
<b>Figure 7.14.</b> Log-log plot of the mean $q$ moments of the rainfall intensity $\varepsilon_\lambda$ against the scale coefficient $\lambda$ for 1-minute precipitation data series from Warsaw rain gauge R06, for $q < 1$ (on left) and for $q > 1$ (on right). The time scales range from $\lambda = 16384$ (1 minute) to $\lambda = 1$ (11.4 days) .....	79
<b>Figure 7.15.</b> Log-log plot of the mean $q$ moments of the rainfall intensity $\varepsilon_\lambda$ against the scale coefficient $\lambda$ for 1-minute precipitation data series from Warsaw rain gauge R15, for $q < 1$ (on left) and for $q > 1$ (on right). The time scales range from $\lambda = 16384$ (1 minute) to $\lambda = 1$ (11.4 days) .....	79
<b>Figure 7.16.</b> Log-log plot of the mean $q$ moments of the rainfall intensity $\varepsilon_\lambda$ against the scale coefficient $\lambda$ for 1-minute precipitation data series from Warsaw rain gauge R25, for $q < 1$ (on left) and for $q > 1$ (on right). The time scales range from $\lambda = 16384$ (1 minute) to $\lambda = 1$ (11.4 days) .....	80
<b>Figure 7.17.</b> Log-log plot of the probability of exceeding rainfall-intensity levels for selected values of singularity $\gamma$ relation against scale parameter $\lambda$ , obtained for 1-minute precipitation data series from Warsaw rain gauge R06. The time scales range from $\lambda = 16384$ (1 minute) to $\lambda = 1$ (11.4 days) .....	81
<b>Figure 7.18.</b> Log-log plot of the probability of exceeding rainfall-intensity levels for selected values of singularity $\gamma$ relation against scale parameter $\lambda$ , obtained for 1-minute precipitation data series from Warsaw rain gauge R15. The time scales range from $\lambda = 16384$ (1 minute) to $\lambda = 1$ (11.4 days) .....	82
<b>Figure 7.19.</b> Log-log plot of the probability of exceeding rainfall-intensity levels for selected values of singularity $\gamma$ relation against scale parameter $\lambda$ , obtained for 1-minute precipitation data series from Warsaw rain gauge R25. The time scales range from $\lambda = 16384$ (1 minute) to $\lambda = 1$ (11.4 days) .....	82
<b>Figure 7.20.</b> Shape of the theoretical scaling exponent functions $K(q)$ and $c(\gamma)$ for multifractal first-order phase transformations (from Lovejoy and Schertzer, 2013) .....	83
<b>Figure 7.21.</b> The empirical scaling moment function log-log plot obtained for 1-minute precipitation data series from Warsaw rain gauge R06 for time scales from $\lambda = 16384$ (1 minute) to $\lambda = 1$ (11.4 days) .....	84
<b>Figure 7.22.</b> The empirical scaling moment function log-log plot obtained for 1-minute precipitation data series from Warsaw rain gauge R15 for time scales from $\lambda = 16384$ (1 minute) to $\lambda = 1$ (11.4 days) .....	84
<b>Figure 7.23.</b> The empirical scaling moment function log-log plot obtained for 1-minute precipitation data series from Warsaw rain gauge R25 for time scales from $\lambda = 16384$ (1 minute) to $\lambda = 1$ (11.4 days) .....	85
<b>Figure 7.24.</b> Empirical codimension function (dotted line) obtained for 1-minute precipitation data series from Warsaw rain gauge R06, R15 and R25, for time scales from 1 minute 11.4 days .....	86
<b>Figure 7.25.</b> DTM plots of $\log K(q,\eta) $ against $\log(\eta)$ for selected order moments $q$ obtained for 1-minute precipitation data series from Warsaw rain gauge R06 .....	88
<b>Figure 7.26.</b> DTM plots of $\log K(q,\eta) $ against $\log(\eta)$ for selected order moments $q$ obtained for 1-minute precipitation data series from Warsaw rain gauge R15 .....	88
<b>Figure 7.27.</b> DTM plots of $\log K(q,\eta) $ against $\log(\eta)$ for selected order moments $q$ obtained for 1-minute precipitation data series from Warsaw rain gauge R25 .....	89
<b>Figure 7.28.</b> Empirical moment scaling function $K(q)$ obtained by TM method on the background of $K(q,1)$ obtained by DTM method (based on the results for gauge R06) .....	91
<b>Figure 7.29.</b> Dendrogram resulting from cluster analysis of universal multifractal parameters $\alpha$ , $C_1$ and $H$ for Warsaw rain gauge network, using average linkage and Euclidean distance .....	95
<b>Figure 7.30.</b> Dendrogram resulting from cluster analysis of universal multifractal parameters $\alpha$ and $C_1$ for Warsaw rain gauge network, using average linkage and Euclidean distance .....	96
<b>Figure 7.31.</b> Dendrogram resulting from cluster analysis of universal multifractal parameters $\alpha$ and $C_1$ for Warsaw rain gauge network, using average linkage and Minkowski distance .....	96
<b>Figure 7.32.</b> The locations of the rain gauges chosen as the most representative of the variability of Warsaw rain gauge network: R06, R15 and R25 .....	98
<b>Figure 7.33.</b> Sample result of the universal multifractal generator. The plot of an almost 2-year time series for R06s .....	100
<b>Figure 7.34.</b> Sample result of the universal multifractal generator. An enlarged section of the time series, with very small values of rainfall intensities (one magnitude below weighing gauges' resolution) .....	101

<b>Figure 7.35.</b> The complementary cumulative distribution function (cCDF) calculated for the synthetic precipitation time series R06s against the cCDF for observed precipitation time series for Warsaw rain gauge R06 .....	102
<b>Figure 7.36.</b> The complementary cumulative distribution function (cCDF) calculated for the synthetic precipitation time series R15s against the cCDF for observed precipitation time series for Warsaw rain gauge R15 .....	102
<b>Figure 7.37.</b> The complementary cumulative distribution function (cCDF) calculated for the synthetic precipitation time series R25s against the cCDF for observed precipitation time series for Warsaw rain gauge R25 .....	103
<b>Figure 7.38.</b> The complementary cumulative distribution function (cCDF) calculated for the synthetic precipitation time series R06s against the cCDFs for observed precipitation time series for all 25 Warsaw rain gauges.....	104
<b>Figure 7.39.</b> The complementary cumulative distribution function (cCDF) calculated for the synthetic precipitation time series R15s against the cCDFs for observed precipitation time series for all 25 Warsaw rain gauges.....	104
<b>Figure 7.40.</b> The complementary cumulative distribution function (cCDF) calculated for the synthetic precipitation time series R25s against the cCDFs for observed precipitation time series for all 25 Warsaw rain gauges.....	105
<b>Figure 7.41.</b> The complementary cumulative distribution function (cCDF) calculated for the synthetic precipitation time series RM23s against the cCDFs for observed precipitation time series for all 25 Warsaw rain gauges.....	106
<b>Figure 7.42.</b> The complementary cumulative distribution function (cCDF) calculated for the synthetic precipitation time series RM22s against the cCDFs for observed precipitation time series for all 25 Warsaw rain gauges.....	107
<b>Figure 7.43.</b> Comparison of intermittency found for the synthetic time series R06s and for observed precipitation time series for all 25 Warsaw rain gauges .....	108
<b>Figure 7.44.</b> Rainfall intermittency calculated for the synthetic time series R15s against the all the observed Warsaw rain gauges.....	108
<b>Figure 7.45.</b> Rainfall intermittency calculated for the synthetic time series R25s against the all the observed Warsaw rain gauges.....	109
<b>Figure 7.46.</b> Rainfall intermittency calculated for the synthetic time series RM23s against the all the observed Warsaw rain gauges.....	109
<b>Figure 7.47.</b> Rainfall intermittency calculated for the synthetic time series RM22s against the all the observed Warsaw rain gauges.....	110
<b>Figure 7.48.</b> The complementary cumulative distribution function (cCDF) calculated for the synthetic precipitation time series R06s and R06sf against the cCDFs for observed precipitation time series for all 25 Warsaw rain gauges.....	112
<b>Figure 7.49.</b> The complementary cumulative distribution function (cCDF) calculated for the synthetic precipitation time series R15s and R15sf against the cCDFs for observed precipitation time series for all 25 Warsaw rain gauges.....	112
<b>Figure 7.50.</b> The complementary cumulative distribution function (cCDF) calculated for the synthetic precipitation time series R25s and R25sf against the cCDFs for observed precipitation time series for all 25 Warsaw rain gauges.....	113
<b>Figure 7.51.</b> The cumulative distribution functions calculated for the synthetic time series RM23s and RM23sf after filtering against the cCDF all the observed Warsaw rain gauges. The graphs for data before (in blue) and after filtering (in red) almost entirely coincide .....	113
<b>Figure 7.52.</b> The cumulative distribution functions calculated for the synthetic time series RM22s and RM22sf after filtering against the cCDF all the observed Warsaw rain gauges. The graphs for data before (in blue) and after filtering (in red) almost entirely coincide .....	114
<b>Figure 7.53.</b> Comparison of intermittency found for the synthetic time series R06sf (after filtering) and for observed precipitation time series for all 25 Warsaw rain gauges.....	115
<b>Figure 7.54.</b> Comparison of intermittency found for the synthetic time series R15sf (after filtering) and for observed precipitation time series for all 25 Warsaw rain gauges.....	115
<b>Figure 7.55.</b> Comparison of intermittency found for the synthetic time series R25sf (after filtering) and for observed precipitation time series for all 25 Warsaw rain gauges.....	116
<b>Figure 7.56.</b> Rainfall intermittency calculated for the synthetic time series RM23sf after filtering against the all the observed Warsaw rain gauges .....	116
<b>Figure 7.57.</b> Rainfall intermittency calculated for the synthetic time series RM22sf after filtering against the all the observed Warsaw rain gauges .....	117

## Tables

<b>Table 4.1.</b> Monthly precipitation in Warsaw for years 1971-2012 (Kozłowska et al., 2013).....	25
<b>Table 4.2.</b> List of locations of Warsaw rain gauges and the assessment of the local measurement condition. ....	34
<b>Table 6.1.</b> Summary of the distances functions and linkage methods used in hierarchical analysis of Warsaw data .....	55
<b>Table 7.1.</b> Slope values of the relationships between the number of non-empty boxes and their sizes for the identified time ranges, for 1-minute time series of rainfall intensities in Warsaw from September 2008 to November 2010 .....	62
<b>Table 7.2.</b> Basic statistics of the slope values obtained from box-counting method for three distinctive time ranges and for the analysed intensity thresholds for Warsaw rain gauge network .....	64
<b>Table 7.3.</b> Spectral exponents of two scaling regimes for 1-minute time series energy spectra, from 25 rain gauges with basic statistics .....	68
<b>Table 7.4.</b> Spectral energy breaks for 1-minute summer and winter time series, from 25 rain gauges with their basic statistics. ....	71
<b>Table 7.5.</b> Spectral exponents of energy spectra for 1-minute time series from 25 rain gauges with basic statistics calculated for the whole frequency range .....	77
<b>Table 7.6.</b> Critical moments $q_{min}$ and $q_{max}$ estimated based on Figs 7.25÷7.27 for selected values of order moment $q$ , obtained for 1-minute precipitation series from Warsaw rain gauges R06, R15 and R25 .....	90
<b>Table 7.7.</b> Calculation of $\alpha$ and $C_1$ parameters for 1-minute precipitation series from Warsaw rain gauges R06, R15 and R25 .....	92
<b>Table 7.8.</b> Universal multifractal parameters $\alpha$ , $C_1$ and $H$ , and the global scaling exponent $\beta$ for Warsaw rain gauges, for 1-minute time series, recorded from September 2008 to November 2010.....	94
<b>Table 7.9.</b> Cophenetic correlation values obtained for different combination of linkage method and distance definition .....	97

## List of symbols and abbreviations

### Symbols

$E_{\Gamma}(\omega)$	– energy spectrum of the multifractal generator $\Gamma$ ( $1/f$ noise)
$A$	– fractal set of dimension $D$
$A_{\lambda}$	– sub-set of a given set $A$ observed on a $D$ -dimensional space, at a scale resolution $\lambda$
$c(q)$	– codimension function
$c(\gamma, \eta)$	– codimension function of a $\eta$ -power renormalized process
$C_1$	– multifractal parameter - degree of non-homogeneity of a process; singularity of the mean of a process
$c_A$	– (fractal) codimension of a given set $A$
$D$	– fractal dimension
$D(q)$	– dimension function for moments $q$ of the density of a process
$D(\gamma)$	– fractal dimension function defined for the singularities $\gamma$
$D_A$	– fractal dimension of a given set $A$
$E(p_0)$	– intermittency of rainfall
$f$	– frequency; for temporal processes $f = 1/t$
$f_c$	– critical Nyquist frequency
$H$	– multifractal parameter - degree of non-conservation of a process
$K(q)$	– moments scaling exponent function
$K(q, \eta)$	– double-moment scaling exponent function proper to a $\eta$ -power renormalized process (for $\eta \neq 1$ ).
$K_{\lambda}(q)$	– second characteristic function of generator $\Gamma_{\lambda}$
$L$	– size of non-overlapping box; $L \approx (1/\lambda)$
$m$	– harmonic number in DTF
$N$	– Total integer sample number in DTF
$n$	– sample number in DTF
$N_A$	– number of non-overlapping objects necessary to cover a given set $A$
$N_D$	– number of $D$ -dimensional objects necessary to cover the entire space containing the given set $A$
$N_s$	– number of self-similar objects created by dividing the original image by the scale factor $\lambda$
$N_{\lambda}$	– number of non-overlapping boxes of size $L$
$N_{\lambda}(\gamma)$	– number of $n$ -dimensional boxes of size $L$ satisfying $\varepsilon_{\lambda} \geq \lambda^{\gamma}$
$P(f)$	– power energy of the energy spectrum
$P(r)$	– probability of occurrence of rain
$q$	– order of statistical moment
$q_D$	– critical order moment for divergence of statistical moments
$q_{max}$	– critical moment defined as $q_{max} = \min(q_s, q_D)$
$q_{min}$	– critical moment of the exponent function $K(q)$ , with $0 < q_{min} < 1$
$q_s$	– critical order of the statistical moment caused by undersampling
$R$	– Number of rain gauge, for $R = 01, \dots, 25$
$RM_s$	– synthetic time series for group of rain gauges' parameters, for $R = 22$ and $23$
$RS_f$	– synthetic time series after filtering, for $R = 01, \dots, 25$
$T_{hr}$	– Intensity threshold
$X(m)$	– discrete harmonic time series continuous in frequency domain
$x(n)$	– discrete time series continuous in time domain
$\langle \dots \rangle$	– ensemble average

$\prod_{\lambda'}(A_\lambda)$	– flux density over the sub-set $A_\lambda$ for $\lambda' > \lambda$
$\alpha$	– multifractal parameter - degree of multifractality; the Lévy index
$\alpha'$	– parameter related to the Lévy index by relation $1/\alpha + 1/\alpha' = 1$
$\beta$	– spectral exponent
$\Gamma$	– generator of a multifractal process
$\Delta$	– time resolution of the registered data
$\eta$	– second moment used to renormalize a process
$\lambda$	– scale ratio; the quotient between the largest scale of observation and the homogeneity scale
$\lambda'$	– the finest known scale resolution of a process
$\gamma$	– order of singularity of the intensity of a process
$\varepsilon_\lambda$	– intensity (or density) of a multifractal process at the scale ratio $\lambda$
$\varepsilon_\lambda$	– (non-dimensional) intensity of a process on a scale of resolution $\lambda$
$\varepsilon_{\lambda,i}$	– all (non-dimensional) intensity of a process observed on a $D$ -dimensional space, at a scale resolution $\lambda$ , for $i = 1, \dots, \lambda^D$
$\varepsilon_{\lambda'}$	– intensity of ‘inner’ scales, component of $\varepsilon_\lambda$ of the sub-set $A_\lambda$
$\varepsilon_{\lambda'}^{(\eta)}$	– $\eta$ -power renormalized intensity of a process on fines scale of resolution $\lambda'$
$\Gamma_\lambda$	– multifractal generator of the density $\varepsilon_\lambda$ of a process; $\Gamma_\lambda = \ln(\varepsilon_\lambda)$

## Abbreviations

cCDF	– complementary cumulative distribution function
CDF	– cumulative distribution function
DFT	– discrete Fourier transform
DTM	– double trace moment method
FFT	– fast Fourier transform
PDMS	– probability distribution/multiple scaling method
PSD	– power spectral density analysis
RSL	– roughness sublayer
TM	– trace moment method
UCL	– urban canopy layer

## APPENDIX I.

### LOCATION OF THE WARSAW RAIN GAUGE NETWORK

The rain gauge network consists in 25 rain gauges (here called R01, R02, ..., R25). The black arrows indicate the distance from the closest surrounding objects (possible obstacles due to which height precipitation shadow effect may occur). The numbers in rectangles show the height of the obstacles above terrain level.



**Figure I.1.** Location site of rain gauge R01 of the Warsaw rain gauge network (in Wóycickiego St.)



**Figure I.2.** Location site of rain gauge R02 of the Warsaw rain gauge network (in Rudzka St.)



**Figure I.3.** Location site of rain gauge R03 of the Warsaw rain gauge network (in Arkuszowa St.)



**Figure I.4.** Location site of rain gauge R04 of the Warsaw rain gauge network (in Górczewska St.)



**Figure I.5.** Location site of rain gauge R05 of the Warsaw rain gauge network (in Ostroroga St.)

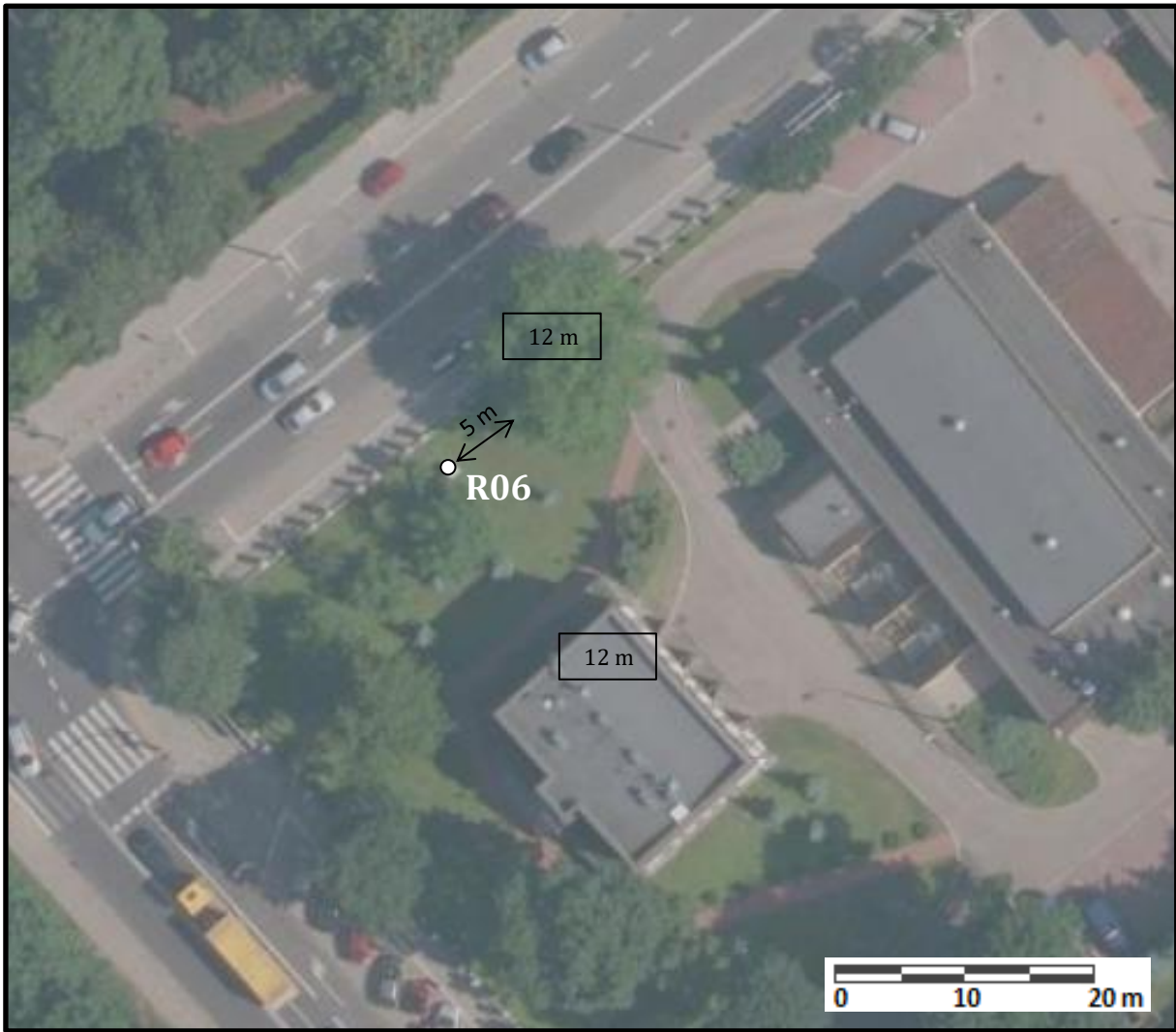


**Figure I.6.** Location site of rain gauge R06 of the Warsaw rain gauge network (in Dobra/Karowa St.)



**Figure I.7.** Location site of rain gauge R07 of the Warsaw rain gauge network (in Koszykowa/Krzywickiego St.)



**Figure I.8.** Location site of rain gauge R08 of the Warsaw rain gauge network (in Jerozolimskie Blvd/P. Tysiąclecia)



**Figure I.9.** Location site of rain gauge R09 of the Warsaw rain gauge network (in Chroscickiego/Obywatelska St)



**Figure I.10.** Location site of rain gauge R10 of the Warsaw rain gauge network (in Dzwonkowa St.)



**Figure I.11.** Location site of rain gauge R11 of the Warsaw rain gauge network (in Grójecka/Kotoryńskiego St.)



**Figure I.12.** Location site of rain gauge R12 of the Warsaw rain gauge network (in Zaruskiego/Czerniakowska St.)



**Figure I.13.** Location site of rain gauge R13 of the Warsaw rain gauge network (in Powsinska/Limanowskiego St.)



**Figure I.14.** Location site of rain gauge R14 of the Warsaw rain gauge network (in Ken/Dolina Służewiecka St.)



**Figure I.15.** Location site of rain gauge R15 of the Warsaw rain gauge network (in Wyrazowa St.)

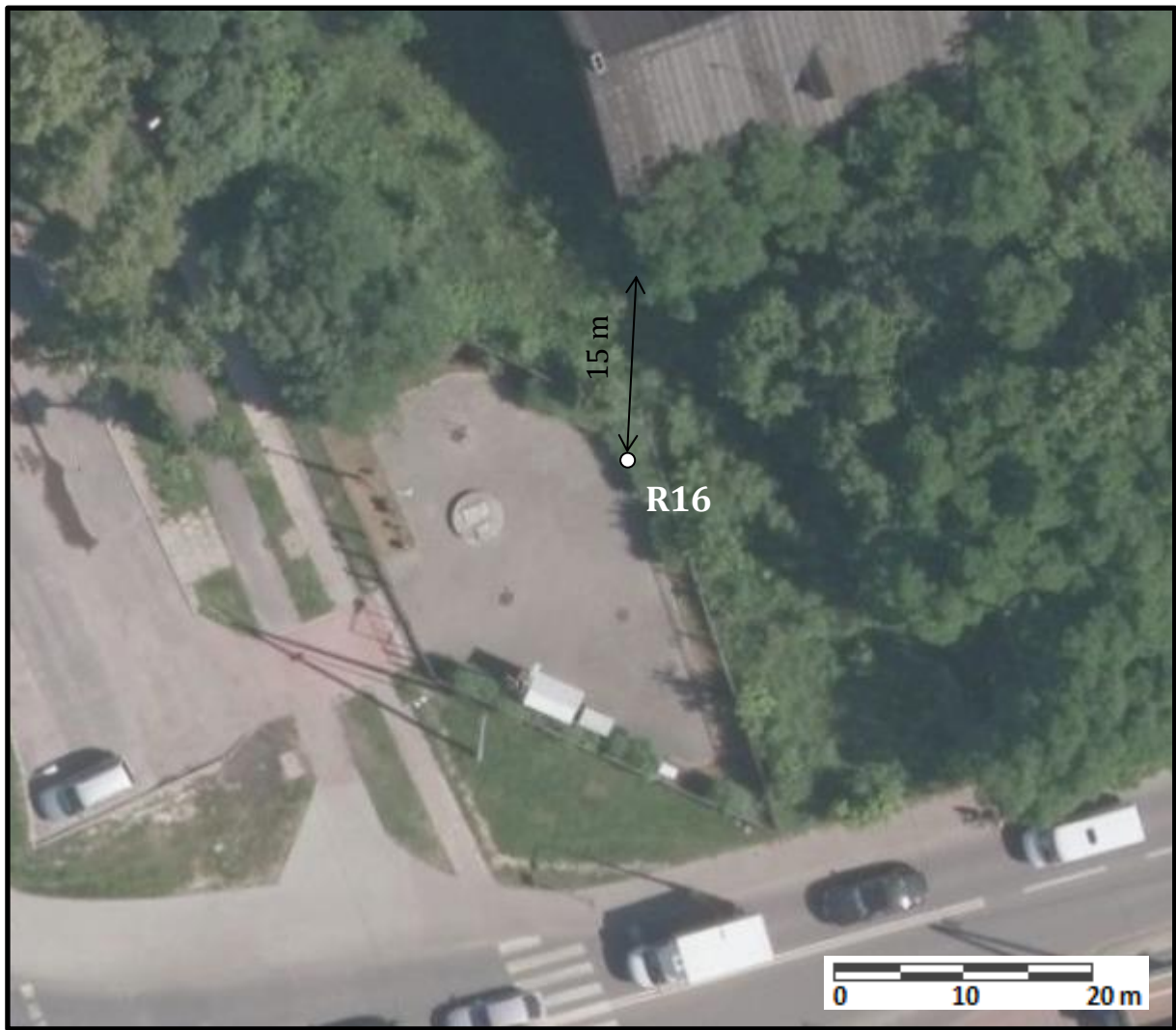


**Figure I.16.** Location site of rain gauge R16 of the Warsaw rain gauge network (in Przychódzka/Vouglą St.)



**Figure I.17.** Location site of rain gauge R17 of the Warsaw rain gauge network (in Stryjeńskich St.)



**Figure I.18.** Location site of rain gauge R18 of the Warsaw rain gauge network (in Mehoffera/Strumykowa St.)

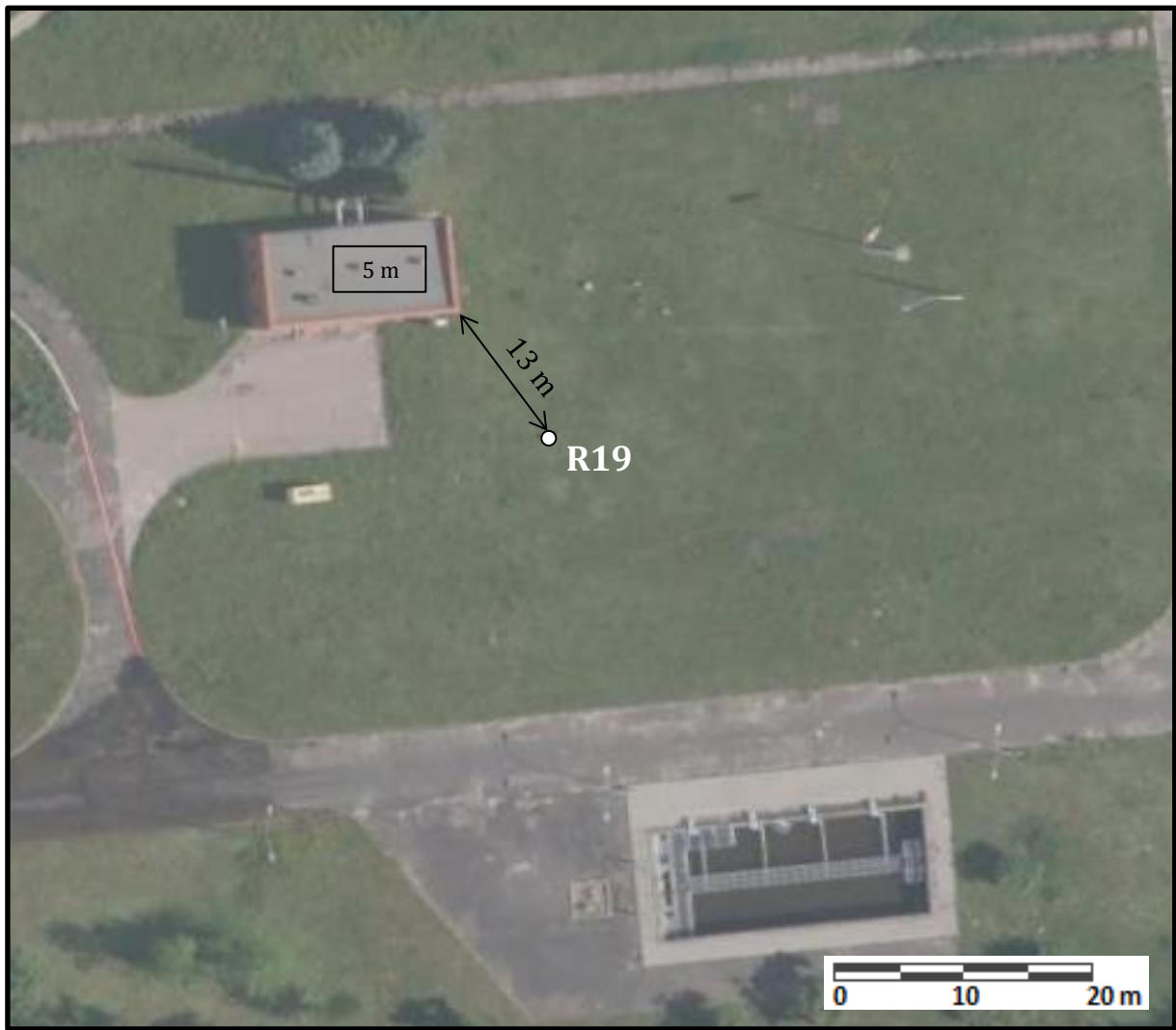


**Figure I.19.** Location site of rain gauge R19 of the Warsaw rain gauge network (in Borecka St. (Białoleka))



**Figure I.20.** Location site of rain gauge R20 of the Warsaw rain gauge network (in Rolanda/Rajmunda St.)

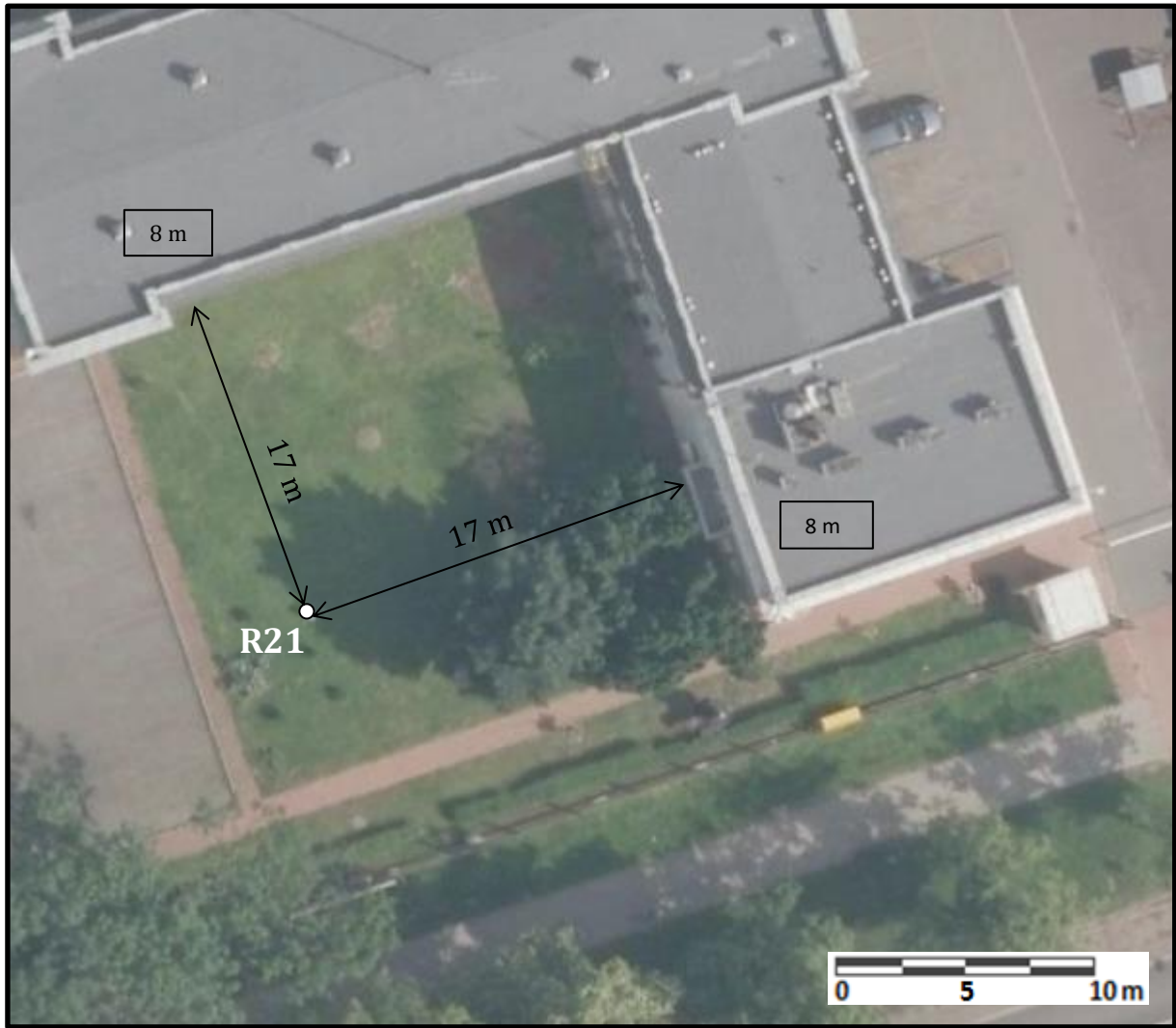


**Figure I.21.** Location site of rain gauge R21 of the Warsaw rain gauge network (in Waszyngtona St.)



**Figure I.22.** Location site of rain gauge R22 of the Warsaw rain gauge network (in Dzielnicowa St.)



**Figure I.23.** Location site of rain gauge R23 of the Warsaw rain gauge network (in Chełmżyńska/Gwarków St.)



**Figure I.24.** Location site of rain gauge R24 of the Warsaw rain gauge network (in Patriotów/Pajęcza St.)



**Figure I.25.** Location site of rain gauge R25 of the Warsaw rain gauge network (in Bysławska St.)

## APPENDIX II.

### FUNCTIONAL BOX-COUNTING PLOTS

#### Section A

Functional box-counting log-log plots obtained with 1-minute rainfall from Warsaw, from 2008 to 2010. A box of unit-size corresponds to 1 minutes. The plots display time scales from 1 minute up to over 2 years for four different intensity thresholds, that is: 0, 0.04, 0.08 and 0.16 mm/min. The dotted line underlines the linear relationship between the analyzed parameters.

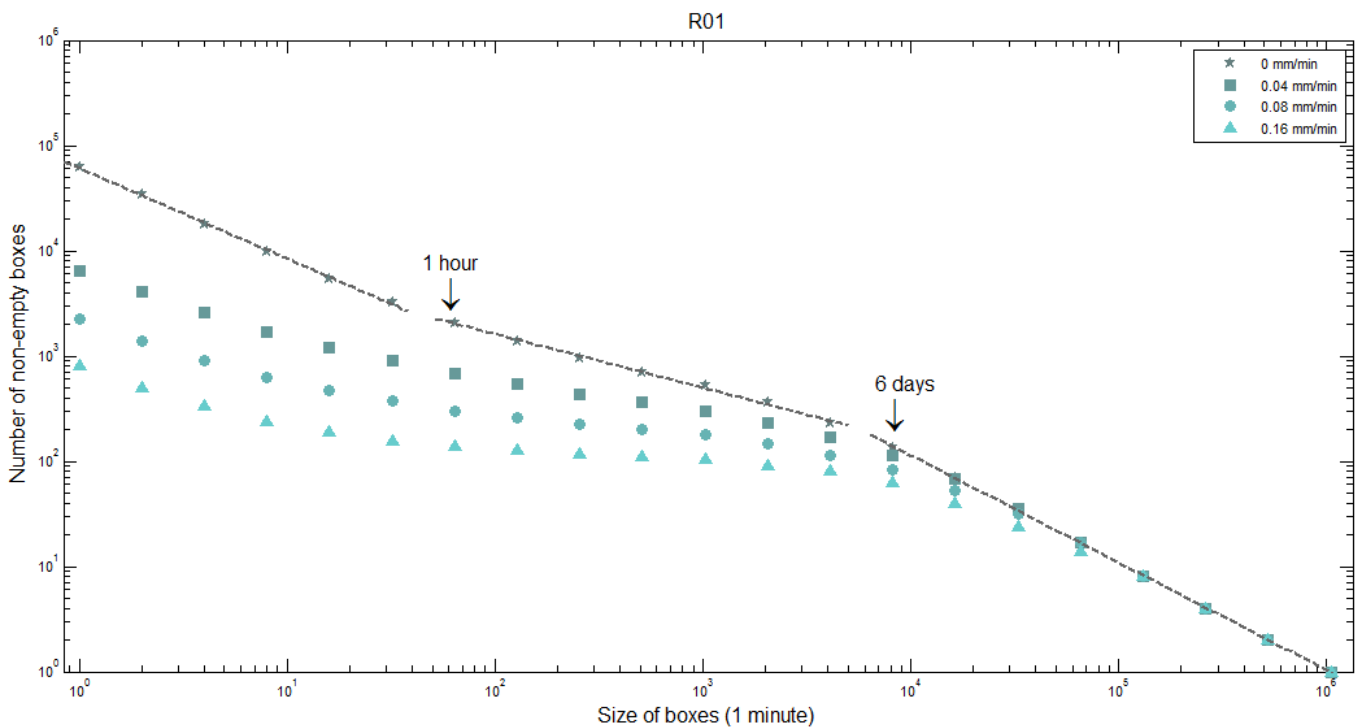


**Figure II.1.** Results of functional box-counting method for 1-minute rainfall time-series from Warsaw, for rain gauge R01

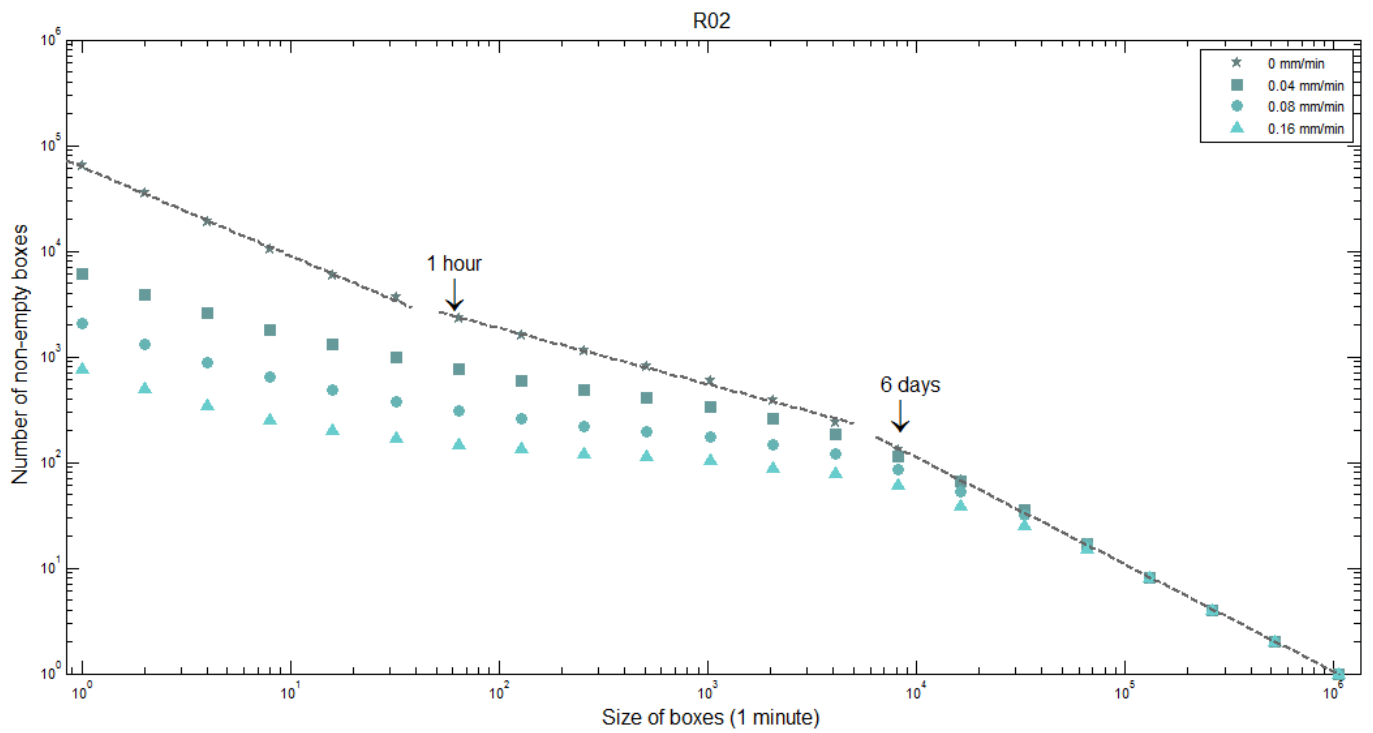


**Figure II.2.** Results of functional box-counting method for 1-minute rainfall time-series from Warsaw, for rain gauge R02

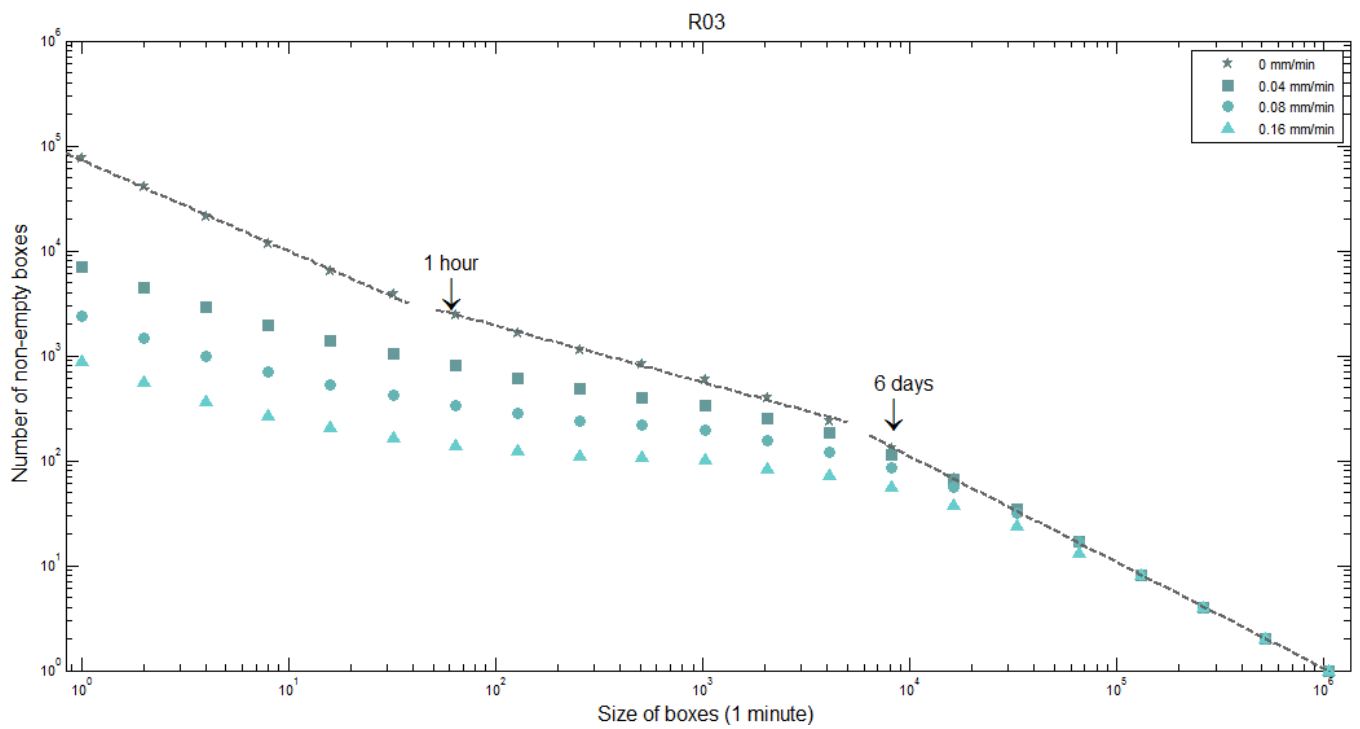


**Figure II.3.** Results of functional box-counting method for 1-minute rainfall time-series from Warsaw, for rain gauge R03

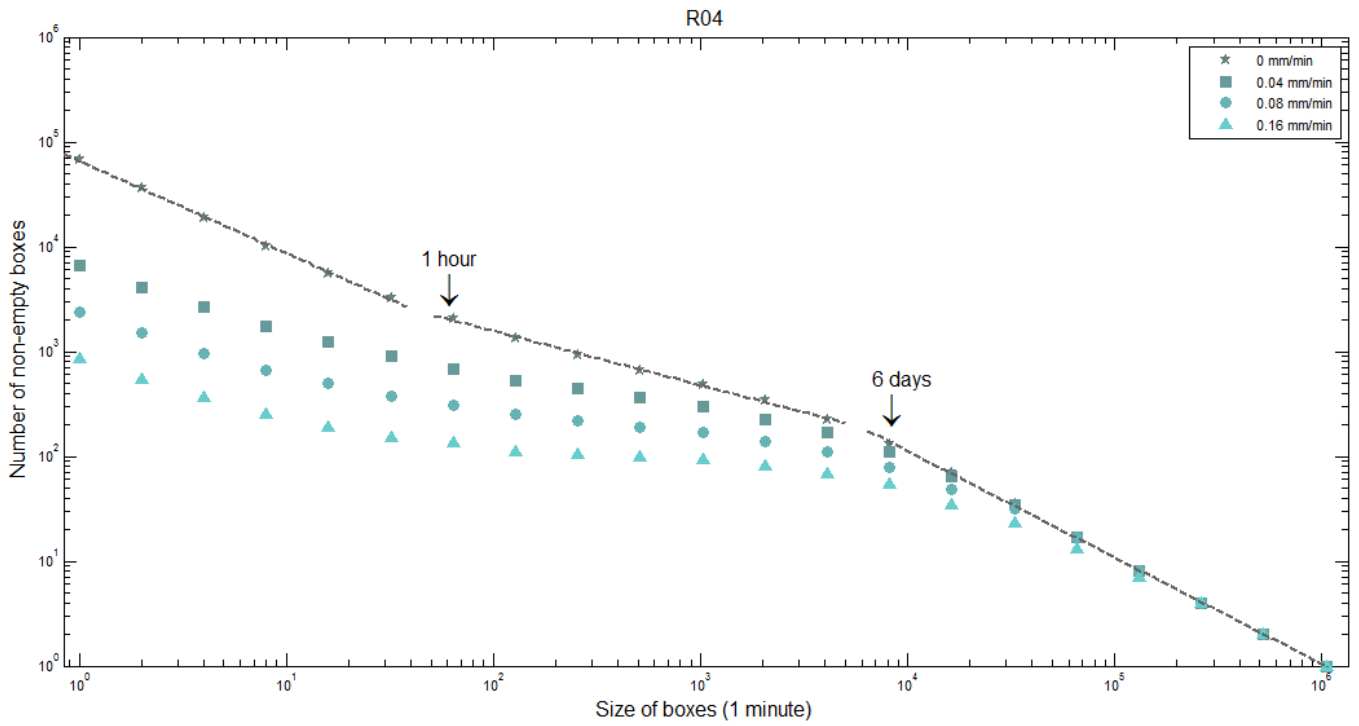


Figure II.4. Results of functional box-counting method for 1-minute rainfall time-series from Warsaw, for rain gauge R04

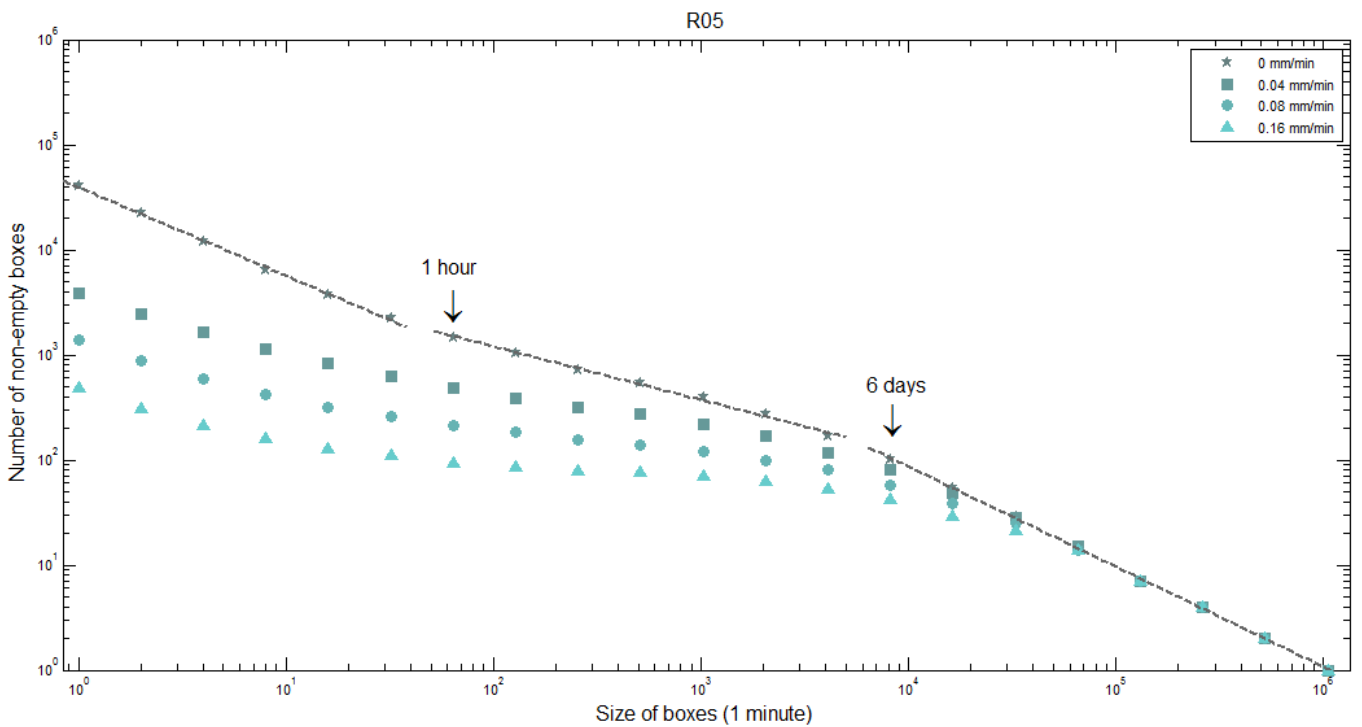


Figure II.5. Results of functional box-counting method for 1-minute rainfall time-series from Warsaw, for rain gauge R05

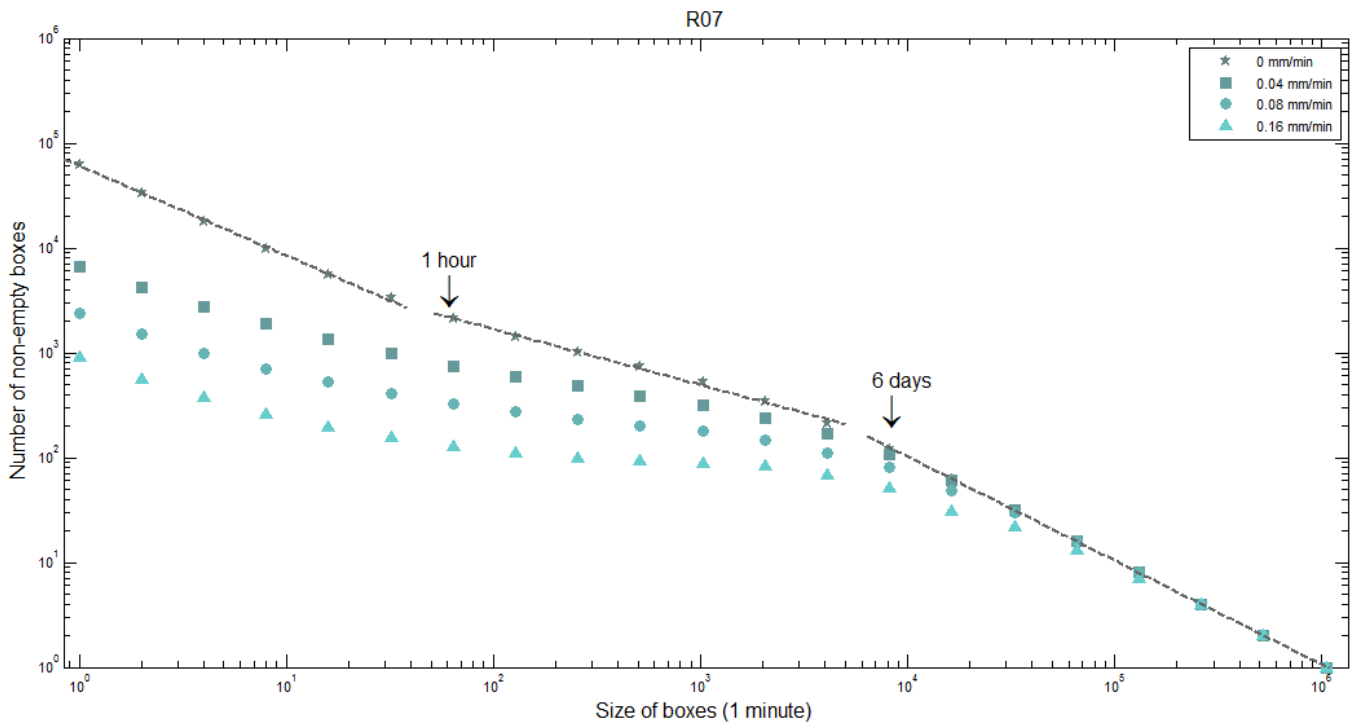


Figure II.6. Results of functional box-counting method for 1-minute rainfall time-series from Warsaw, for rain gauge R07

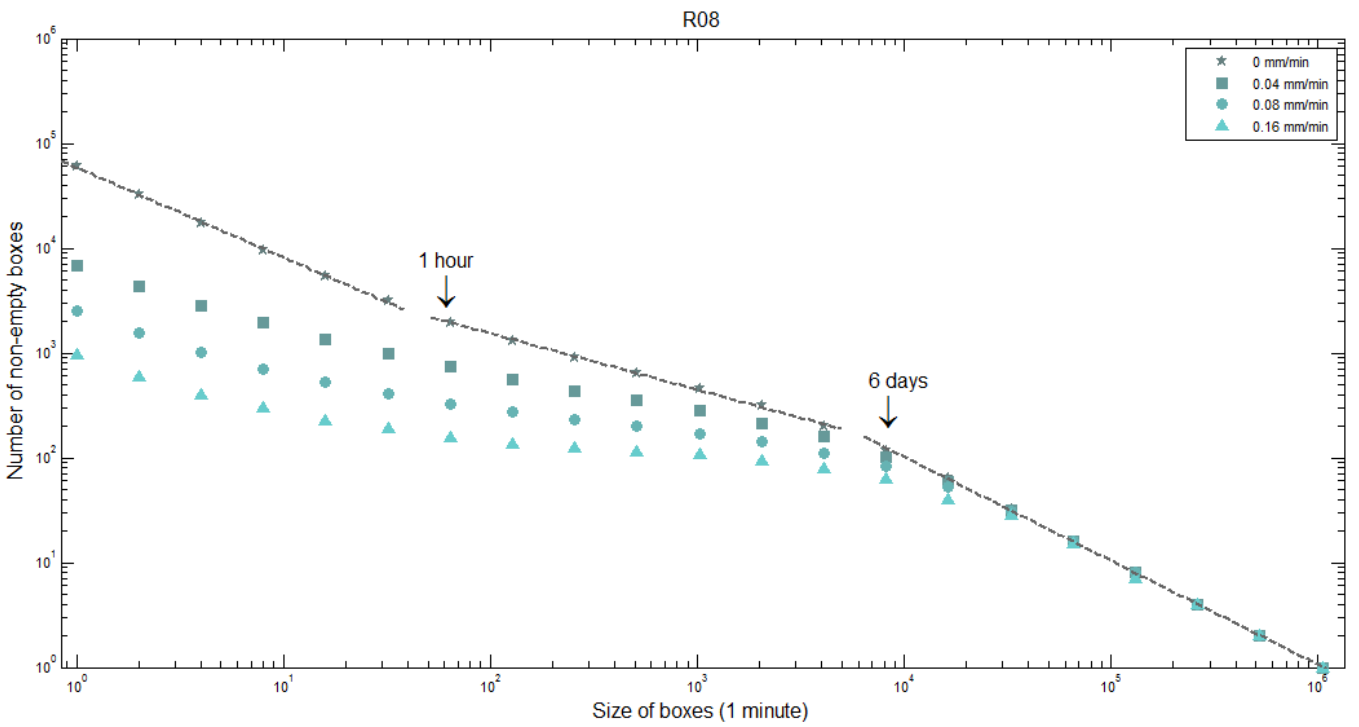
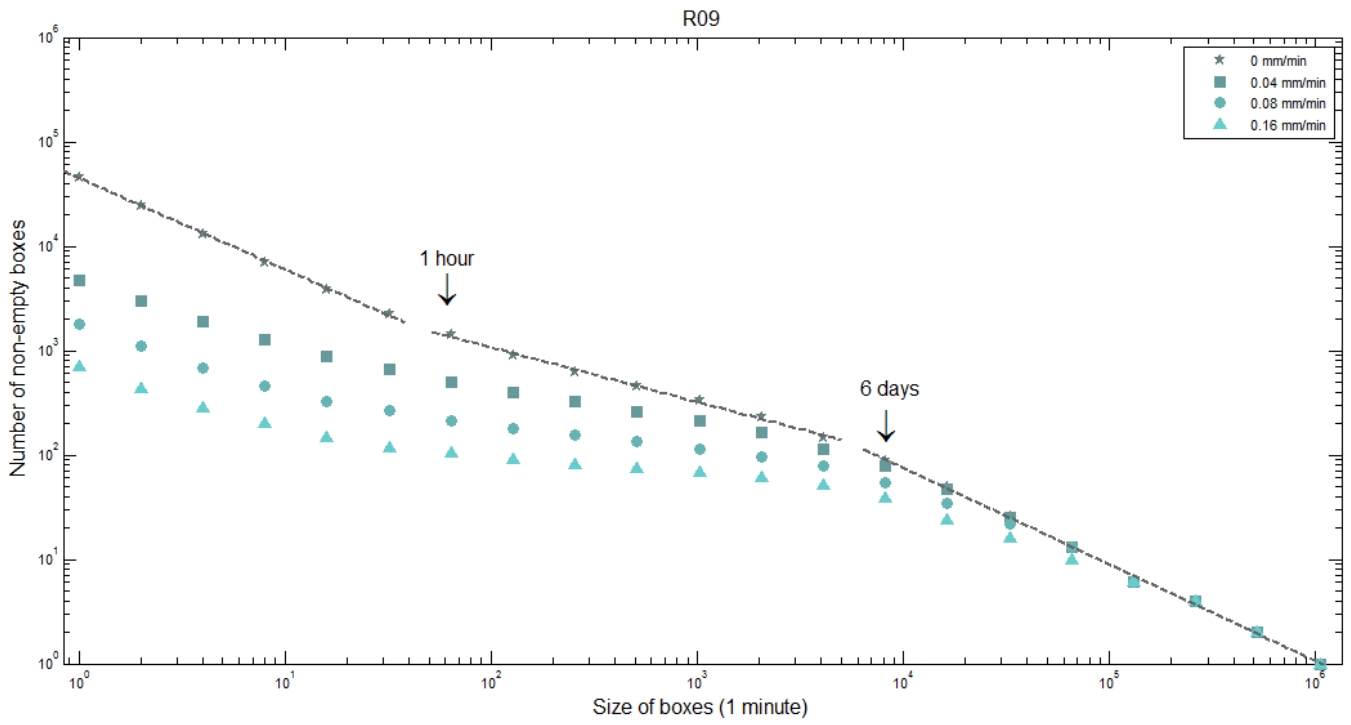
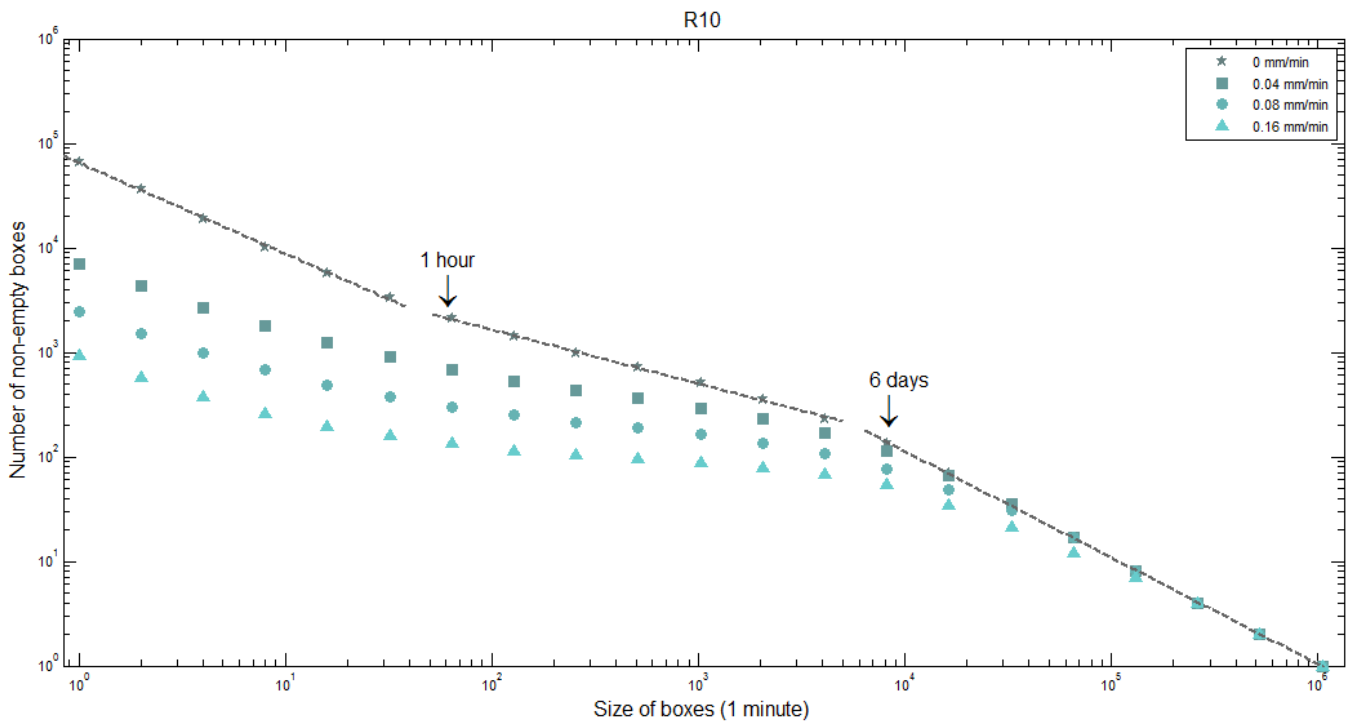


Figure II.7. Results of functional box-counting method for 1-minute rainfall time-series from Warsaw, for rain gauge R08



**Figure II.8.** Results of functional box-counting method for 1-minute rainfall time-series from Warsaw, for rain gauge R09



**Figure II.9.** Results of functional box-counting method for 1-minute rainfall time-series from Warsaw, for rain gauge R10

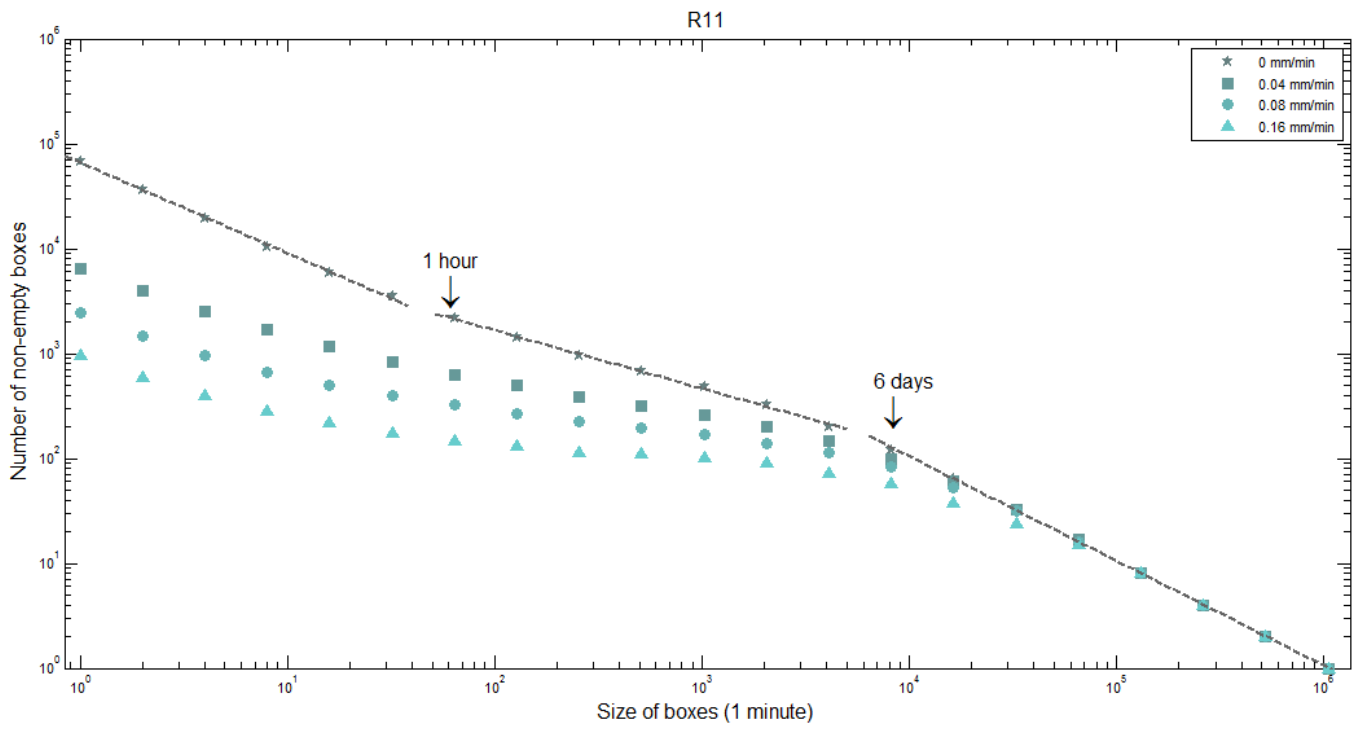


**Figure II.10.** Results of functional box-counting method for 1-minute rainfall time-series from Warsaw, for rain gauge R11

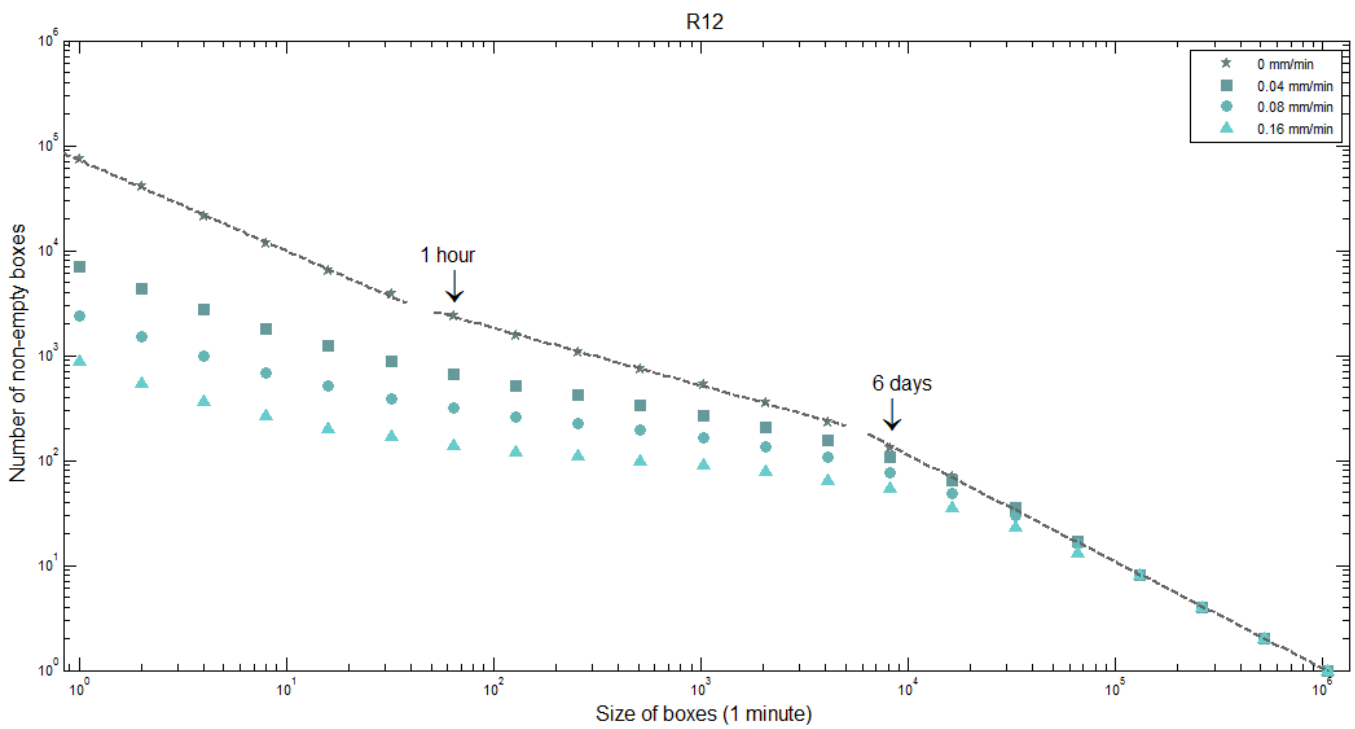


**Figure II.11.** Results of functional box-counting method for 1-minute rainfall time-series from Warsaw, for rain gauge R12

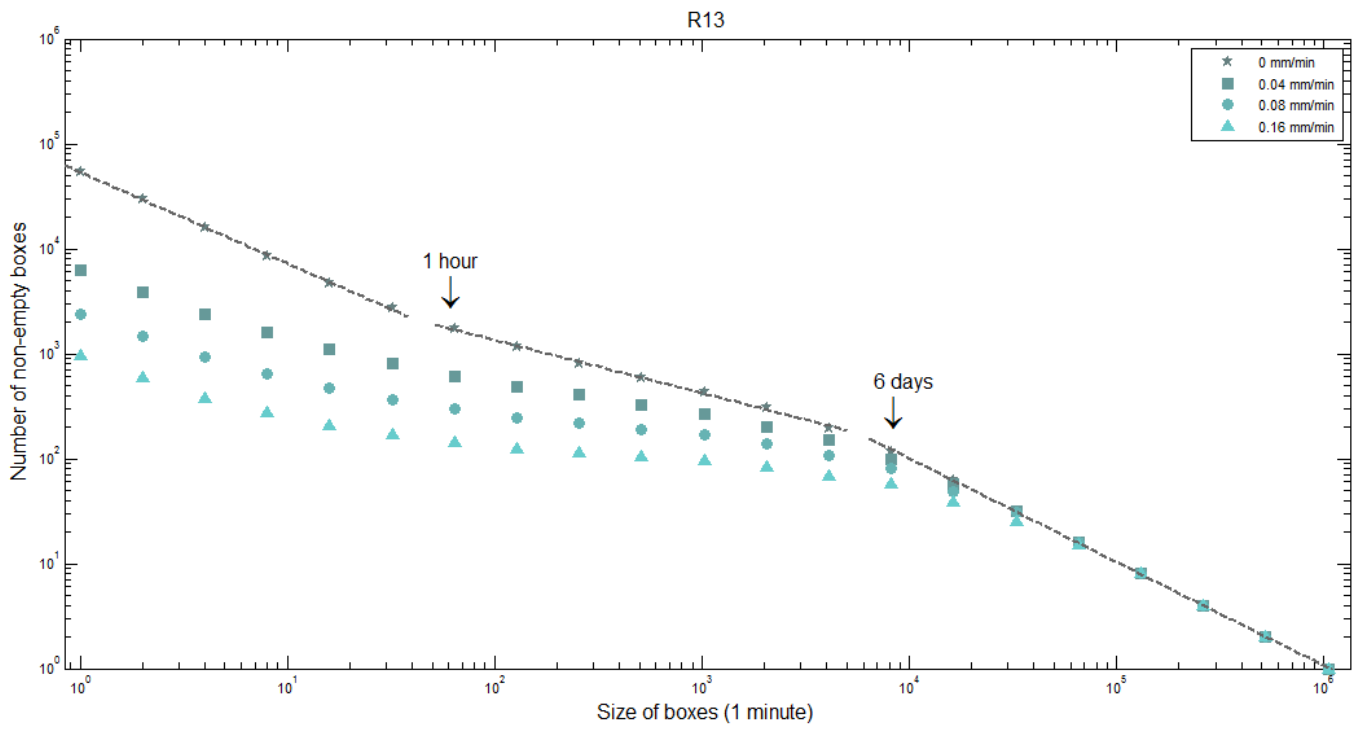


**Figure II.12.** Results of functional box-counting method for 1-minute rainfall time-series from Warsaw, for rain gauge R13

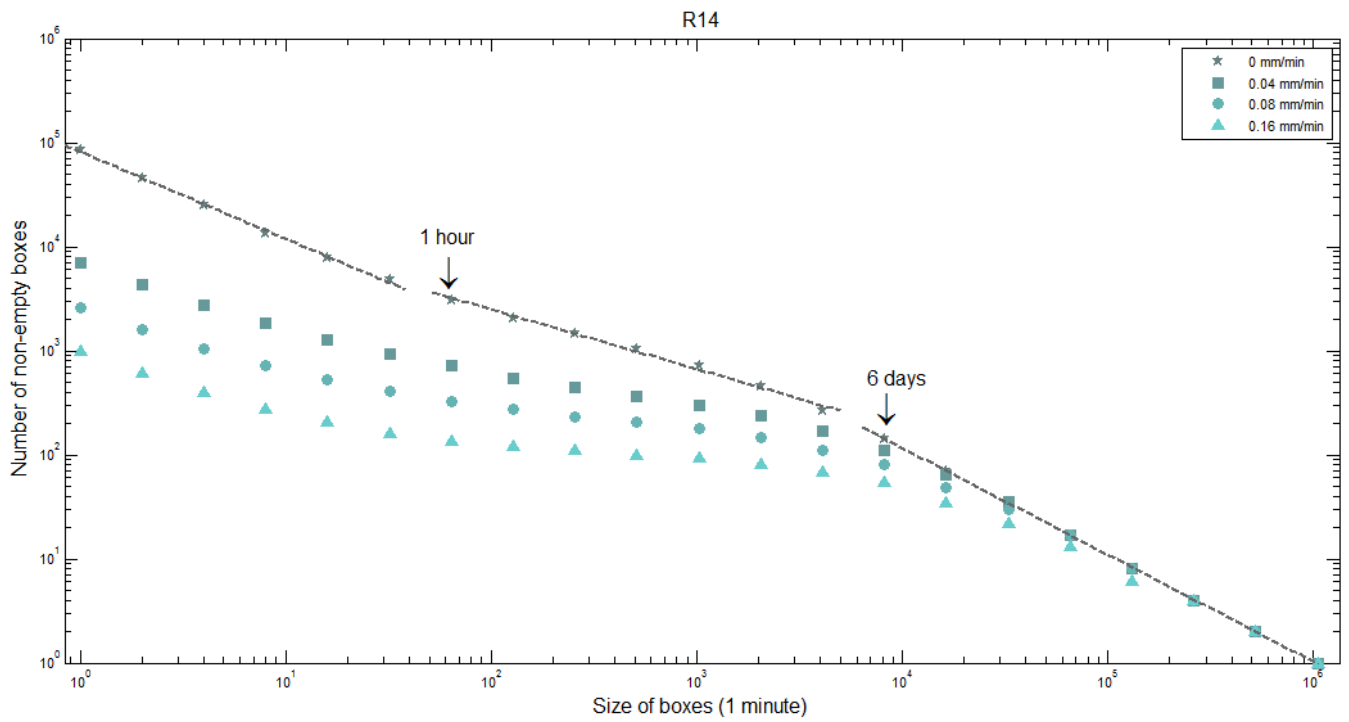


**Figure II.13.** Results of functional box-counting method for 1-minute rainfall time-series from Warsaw, for rain gauge R14

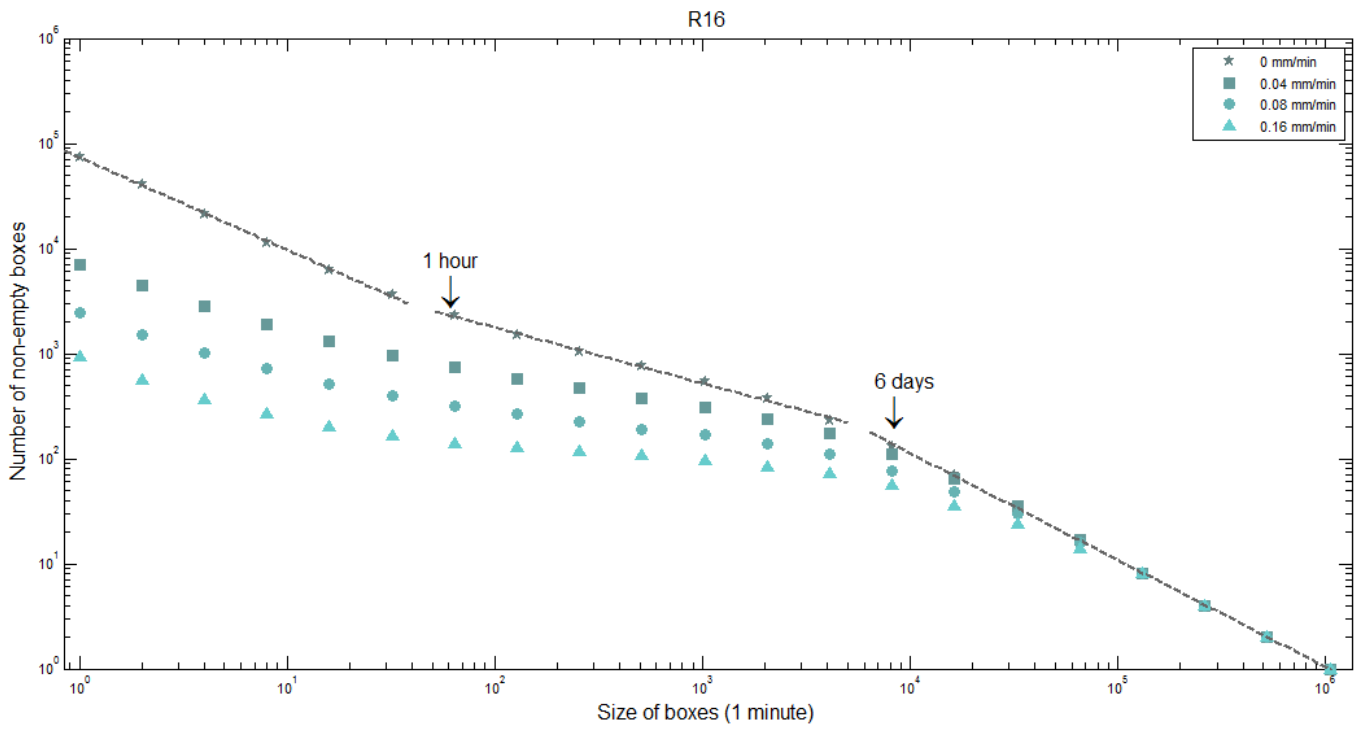


**Figure II.14.** Results of functional box-counting method for 1-minute rainfall time-series from Warsaw, for rain gauge R16

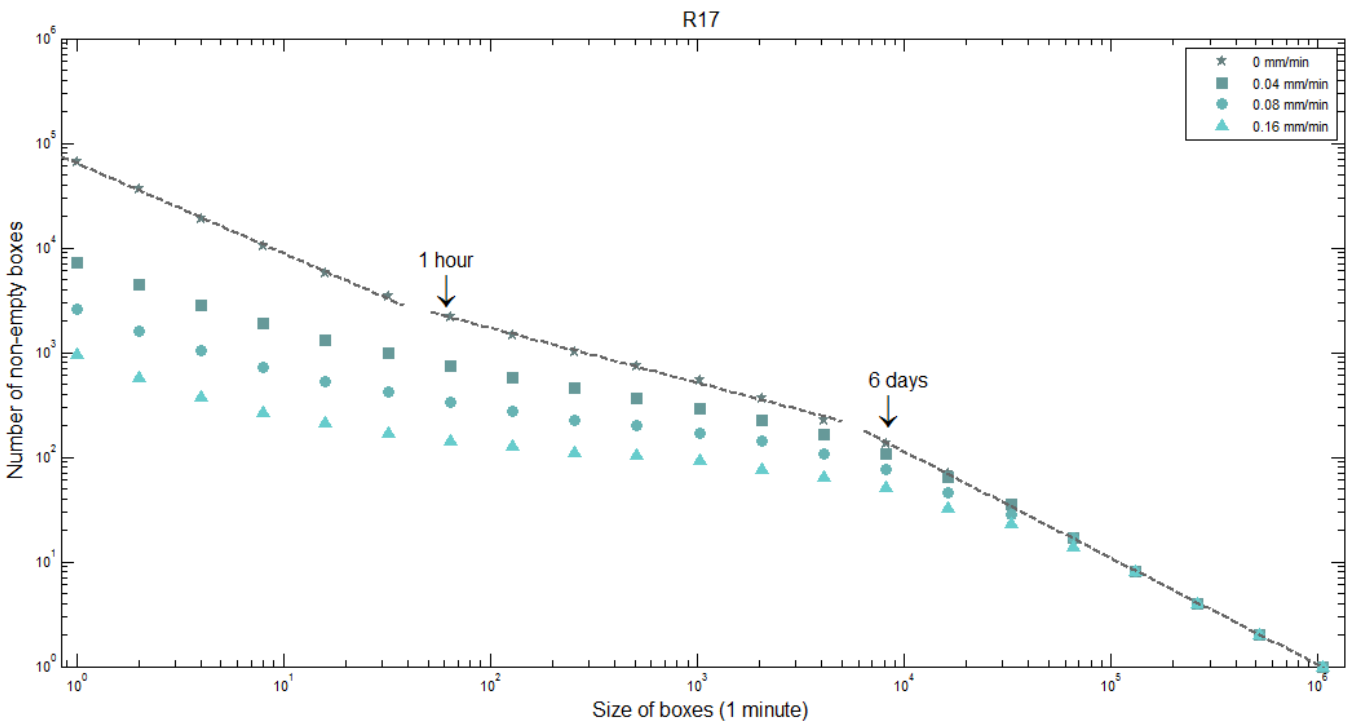


**Figure II.15.** Results of functional box-counting method for 1-minute rainfall time-series from Warsaw, for rain gauge R17

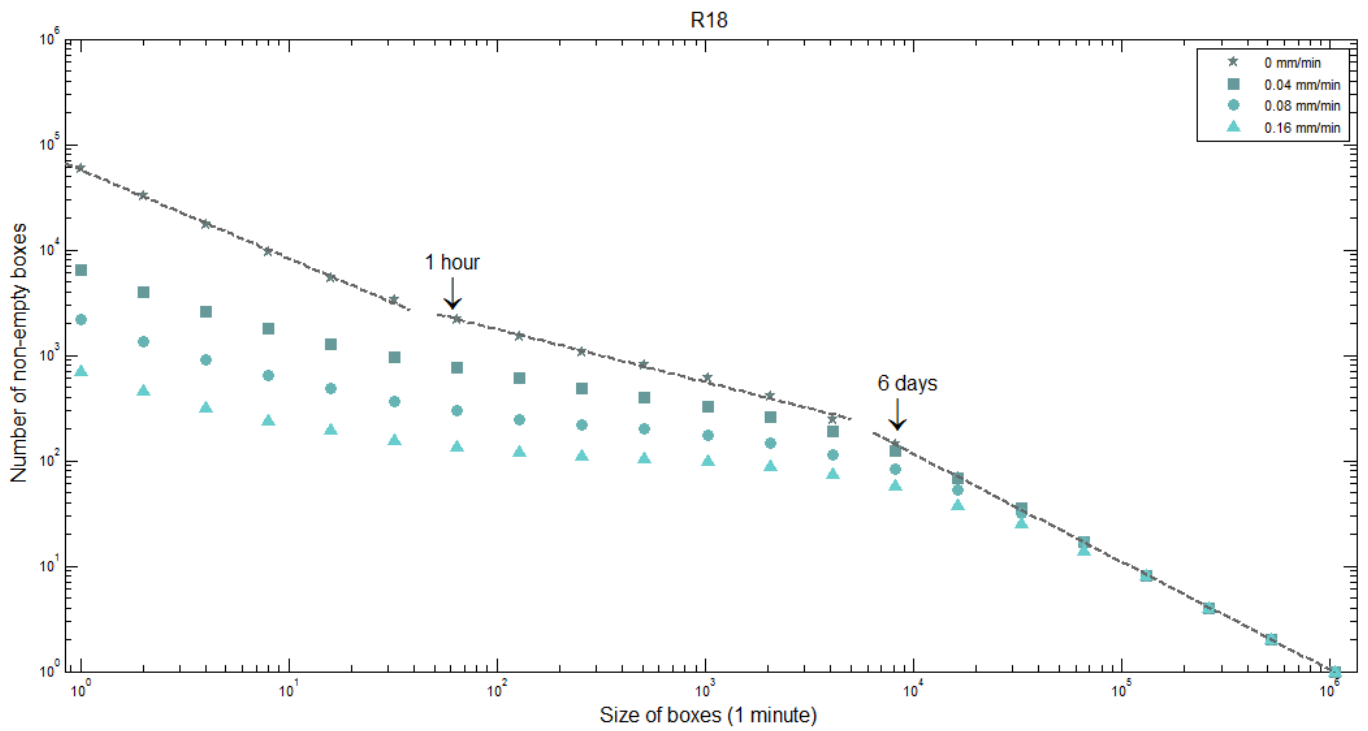


**Figure II.16.** Results of functional box-counting method for 1-minute rainfall time-series from Warsaw, for rain gauge R18

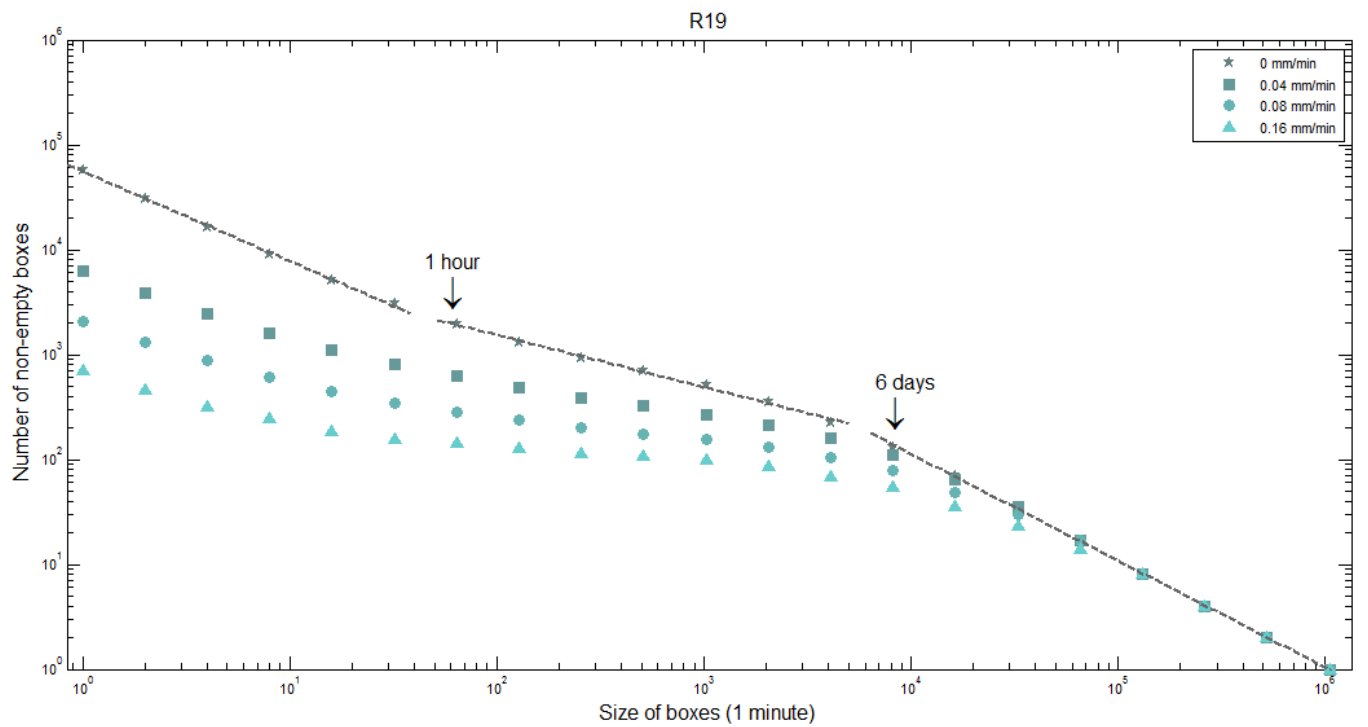


**Figure II.17.** Results of functional box-counting method for 1-minute rainfall time-series from Warsaw, for rain gauge R19

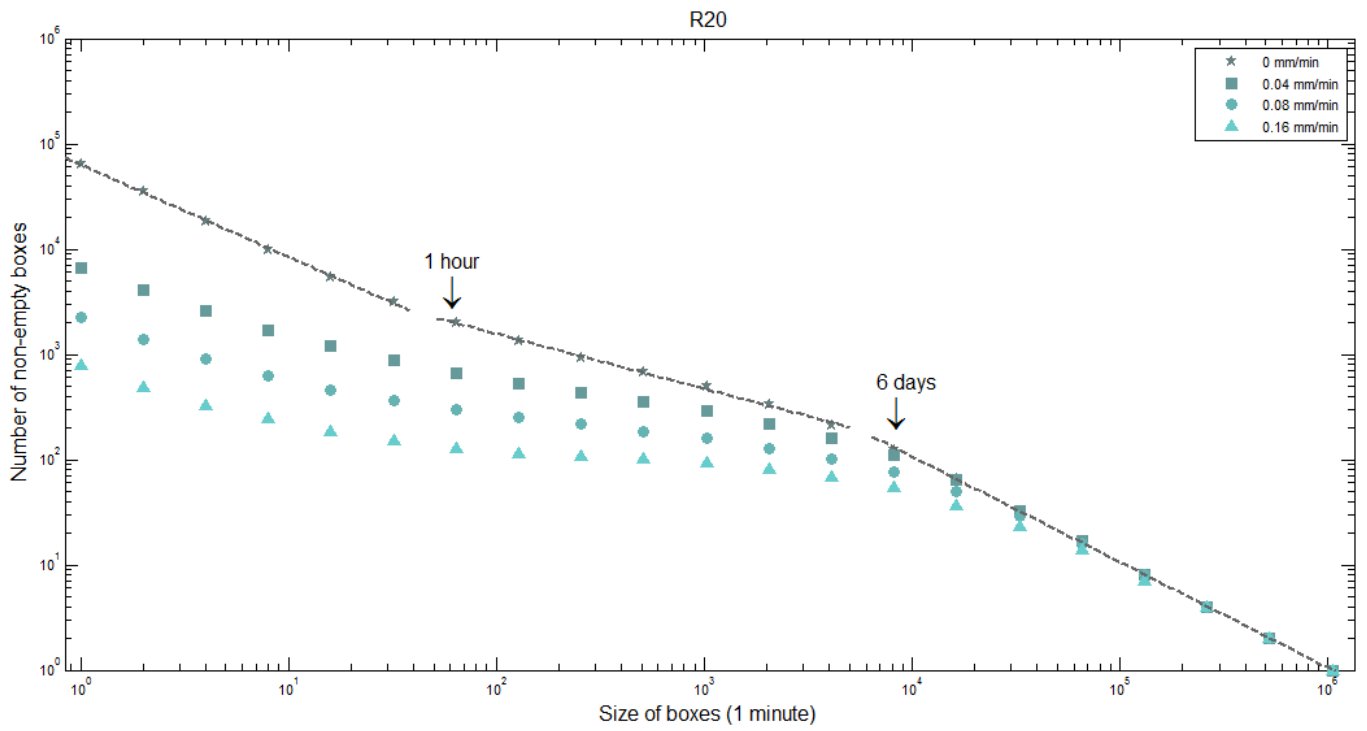


**Figure II.18.** Results of functional box-counting method for 1-minute rainfall time-series from Warsaw, for rain gauge R20

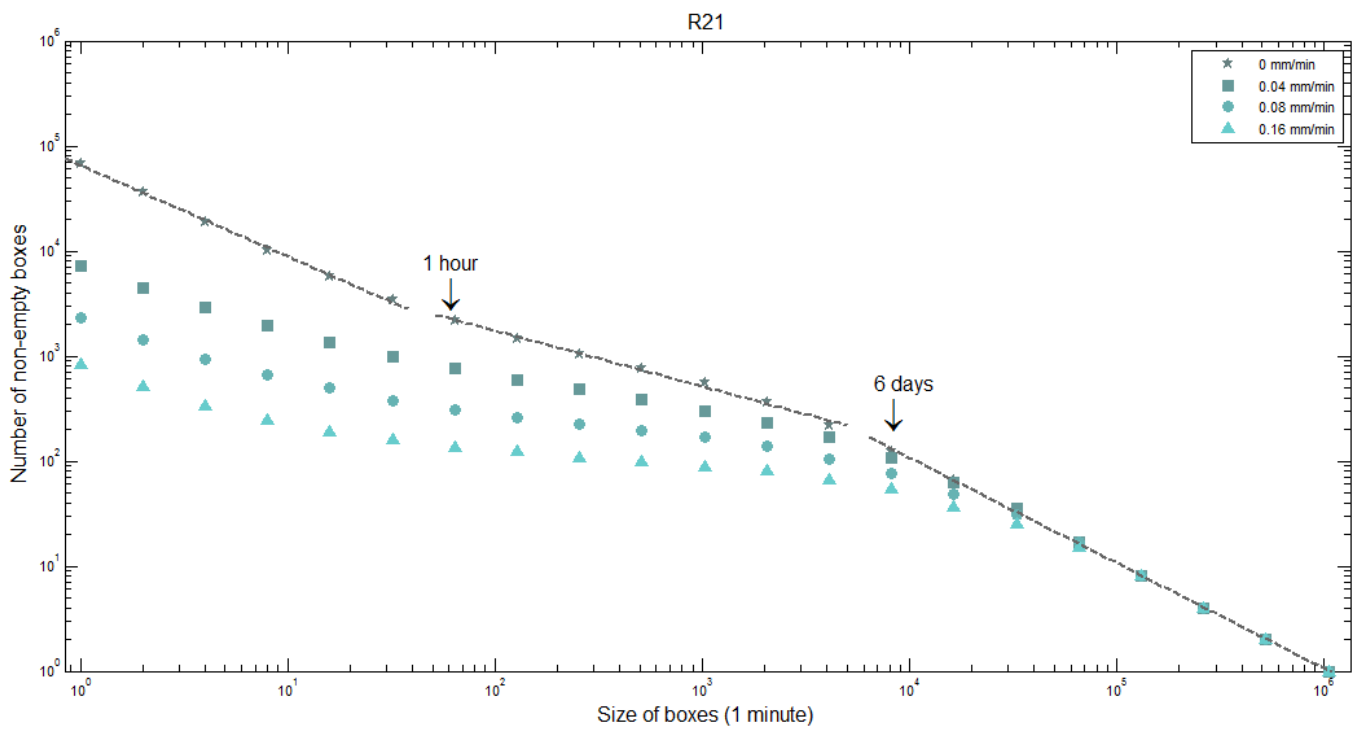


**Figure II.19.** Results of functional box-counting method for 1-minute rainfall time-series from Warsaw, for rain gauge R21

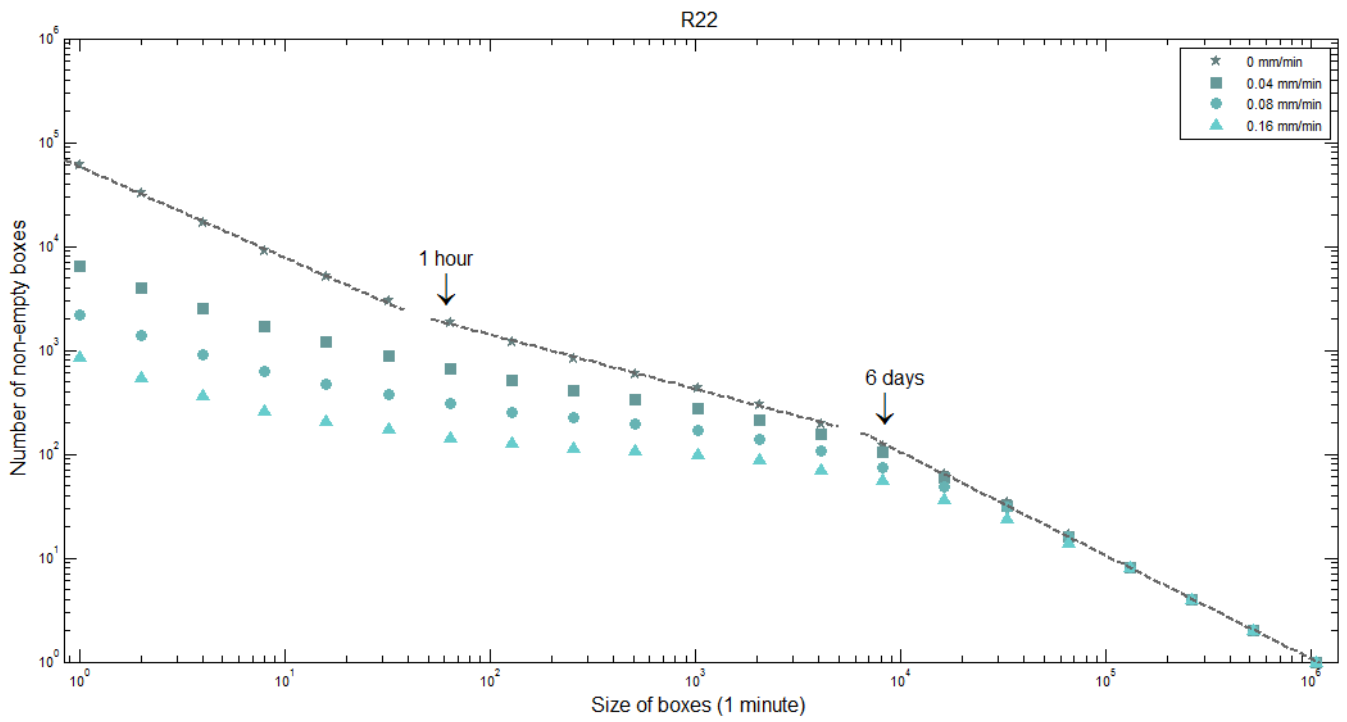


Figure II.20. Results of functional box-counting method for 1-minute rainfall time-series from Warsaw, for rain gauge R22

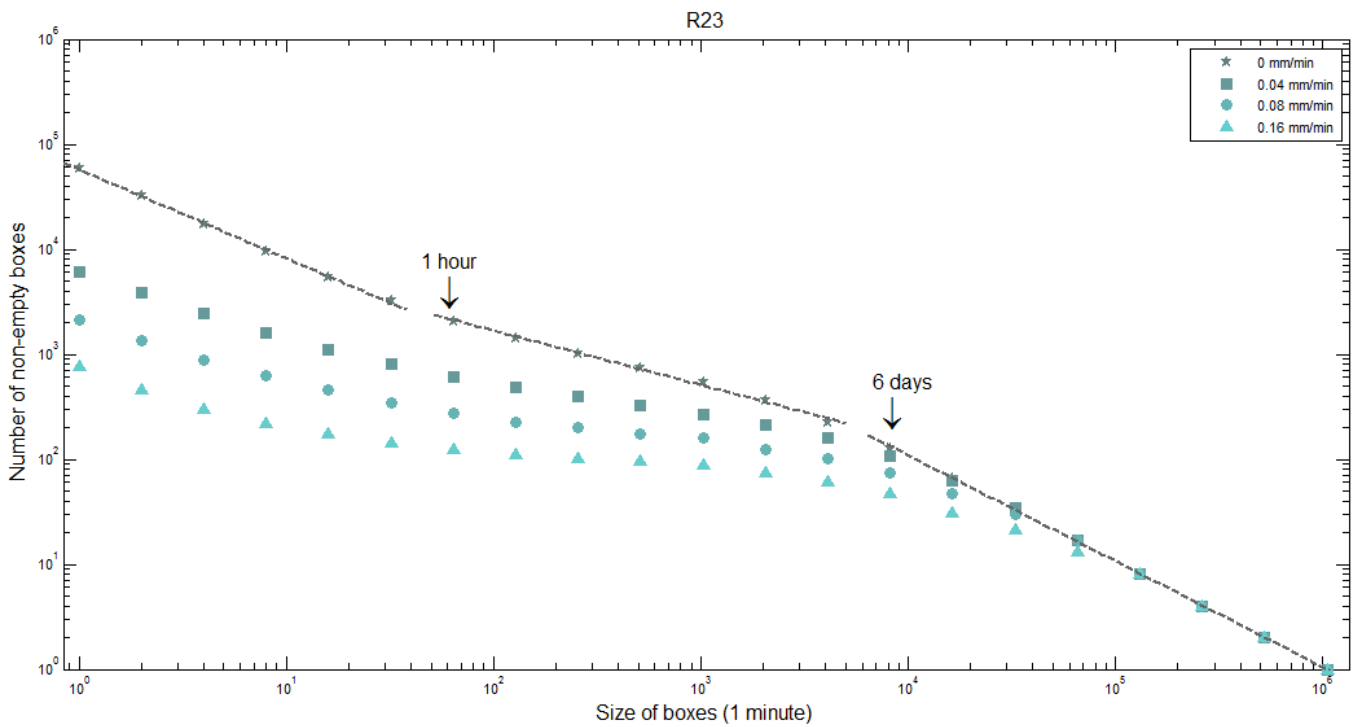
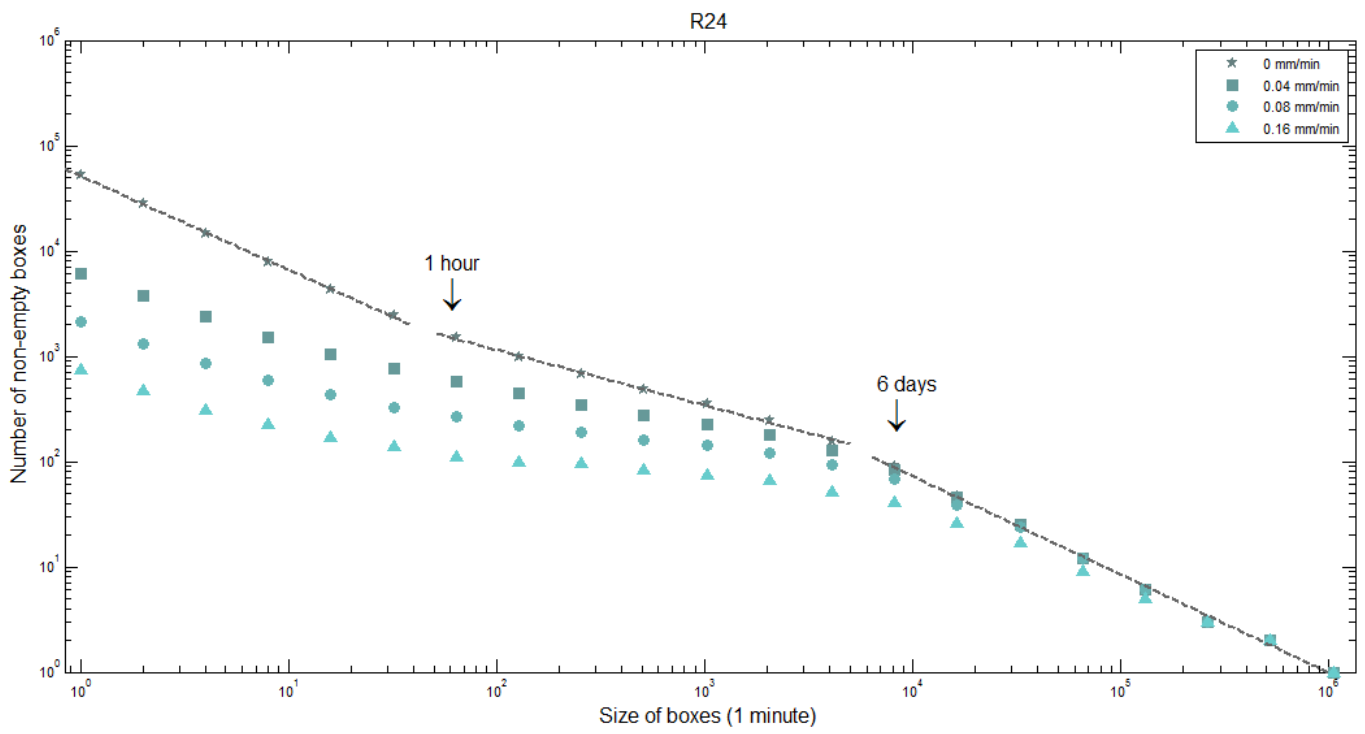


Figure II.21. Results of functional box-counting method for 1-minute rainfall time-series from Warsaw, for rain gauge R23



**Figure II.22.** Results of functional box-counting method for 1-minute rainfall time-series from Warsaw, for rain gauge R24

## Section B

Results of functional box-counting method obtained with 1-minute rainfall for 25 rain gauges in Warsaw, from 2008 to 2010. A box of unit-size corresponds to 1 minutes. The log-log plots display time scales from 1 minute up to over 2 years for intensity threshold equal to 0 mm/min.

**Table II.1.** Results of functional box-counting method obtained with 1-minute rainfall for 25 rain gauges in Warsaw, from 2008 to 2010 and intensity threshold 0 mm/min

n	R01	R02	R03	R04	R05	R06	R07	R08	R09	R10	R11	R12	R13	R14	R15	R16	R17	R18	R19	R20	R21	R22	R23	R24	R25
1	62982	65056	75278	67622	40764	62207	63054	60302	46306	66844	68021	74929	54722	84808	39440	75133	66358	59848	57568	65007	67620	60116	59272	52723	61888
2	33987	35369	40626	36174	22191	33536	33934	32689	24812	35972	36914	40336	29759	46396	21564	40484	36032	32402	31126	34942	36214	32345	32333	28094	33039
4	18065	18966	21522	19020	11901	17786	18075	17493	13093	19045	19603	21429	15783	24885	11658	21334	19104	17384	16607	18462	19116	17093	17361	14705	17299
8	9792	10353	11559	10138	6478	9556	9776	9509	7000	10219	10517	11558	8478	13637	6428	11391	10306	9524	8987	9856	10279	9137	9449	7797	9180
16	5494	5934	6462	5612	3708	5332	5530	5367	3904	5708	5902	6468	4713	7830	3754	6300	5786	5455	5085	5474	5783	5068	5395	4266	5019
32	3270	3596	3854	3283	2279	3162	3308	3167	2273	3356	3504	3811	2758	4790	2340	3662	3441	3325	3046	3204	3423	2950	3235	2465	2881
64	2077	2312	2444	2040	1487	2019	2111	1977	1413	2110	2169	2375	1717	3093	1552	2281	2175	2169	1944	2013	2184	1843	2080	1499	1747
128	1385	1584	1638	1350	1029	1376	1423	1315	913	1407	1420	1559	1158	2093	1097	1504	1459	1501	1310	1331	1475	1216	1433	980	1142
256	971	1131	1145	928	728	954	1007	899	623	978	952	1065	815	1470	792	1052	1026	1084	932	931	1043	835	1021	672	767
512	706	811	829	671	546	690	735	649	456	713	682	752	592	1046	587	757	747	812	695	672	758	598	746	479	539
1024	523	591	596	491	395	503	527	463	331	518	483	532	434	719	438	543	541	601	518	495	552	433	547	351	386
2048	361	385	395	341	271	338	344	314	234	359	324	358	307	456	305	370	368	406	359	338	366	303	360	243	261
4096	229	239	237	222	167	216	215	198	147	231	202	230	196	266	201	232	228	247	226	212	220	196	226	157	163
8192	136	131	130	131	101	125	122	117	89	133	121	132	117	142	121	132	134	141	132	125	123	119	128	90	95
16384	70	68	68	70	54	65	63	64	50	70	65	70	63	71	66	70	70	71	70	66	66	64	67	47	52
32768	35	35	34	35	29	33	32	33	26	35	33	35	32	35	33	35	35	35	35	33	35	34	34	25	27
65536	17	17	17	17	15	17	16	16	13	17	17	17	16	17	16	17	17	17	17	17	17	17	17	12	15
131072	8	8	8	8	7	8	8	8	6	8	8	8	8	8	8	8	8	8	8	8	8	8	8	6	8
262144	4	4	4	4	4	4	4	4	4	4	4	4	4	4	4	4	4	4	4	4	4	4	4	3	4
524288	2	2	2	2	2	2	2	2	2	2	2	2	2	2	2	2	2	2	2	2	2	2	2	2	2
1048576	1	1	1	1	1	1	1	1	1	1	1	1	1	1	1	1	1	1	1	1	1	1	1	1	1

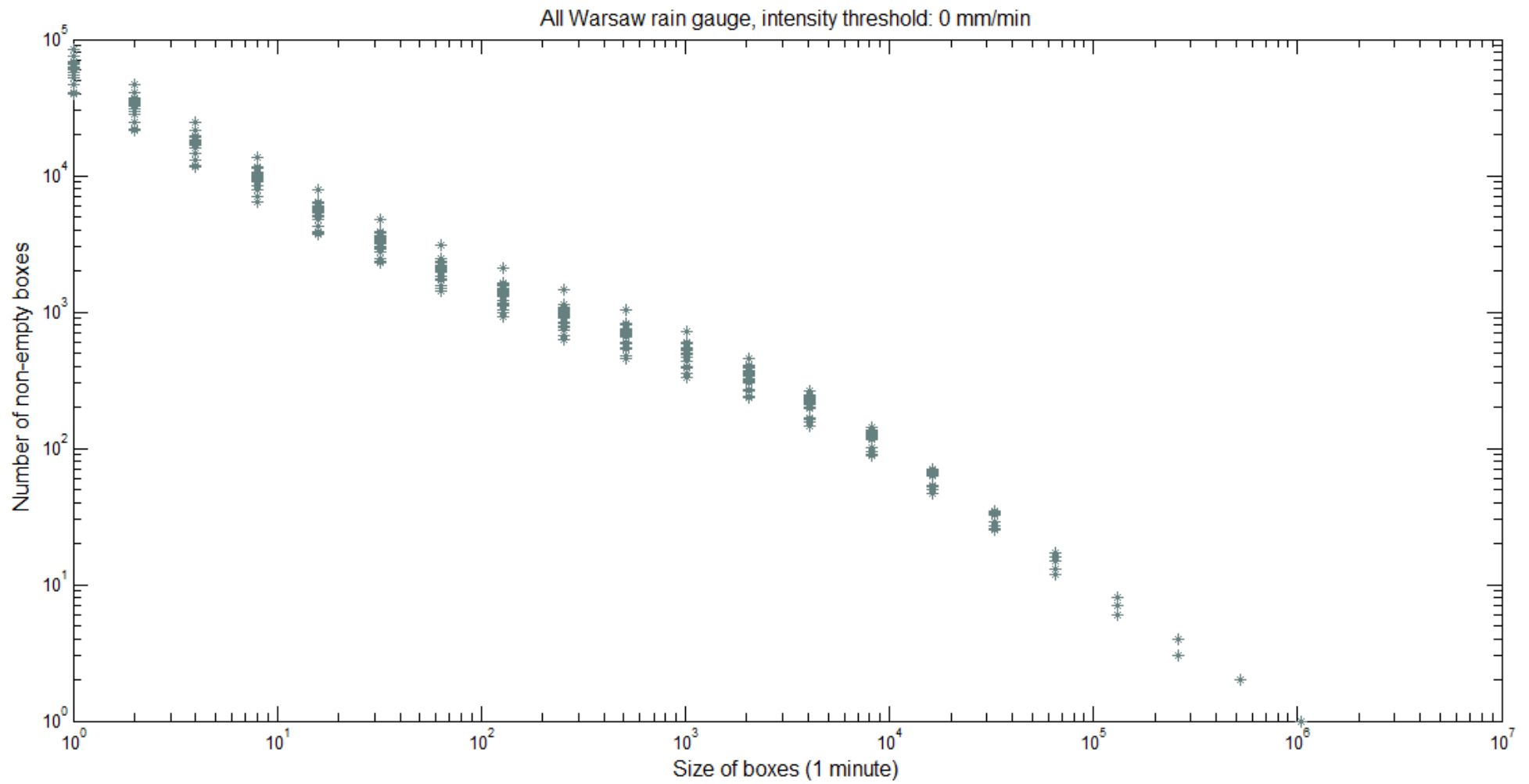


**Figure II.23.** Log-log plot of functional box-counting method for 1-minute rainfall time-series from Warsaw, for all the 25 rain gauges, and intensity threshold 0 mm/min

Results of functional box-counting method obtained with 1-minute rainfall for 25 rain gauges in Warsaw, from 2008 to 2010. A box of unit-size corresponds to 1 minutes. The log-log plots display time scales from 1 minute up to over 2 years for intensity threshold equal to 0.04 mm/min.

**Table II.2.** Results of functional box-counting method obtained with 1-minute rainfall for 25 rain gauges in Warsaw, from 2008 to 2010 and intensity threshold 0.04 mm/min

n	R01	R02	R03	R04	R05	R06	R07	R08	R09	R10	R11	R12	R13	R14	R15	R16	R17	R18	R19	R20	R21	R22	R23	R24	R25
1	6483	6088	7095	6614	3895	6116	6670	6827	4768	6952	6378	6998	6192	7006	6073	7027	7226	6417	6287	6627	7156	6433	6149	6142	4225
2	4027	3883	4457	4113	2477	3840	4245	4308	2950	4281	3989	4325	3835	4358	3687	4409	4486	3989	3890	4128	4466	4021	3817	3795	2720
4	2567	2570	2874	2645	1630	2459	2774	2834	1889	2690	2536	2715	2412	2756	2303	2815	2852	2599	2443	2603	2882	2542	2424	2356	1768
8	1703	1795	1938	1761	1134	1639	1881	1935	1258	1771	1680	1787	1591	1835	1498	1871	1893	1774	1606	1712	1940	1698	1601	1530	1210
16	1205	1299	1386	1234	823	1158	1333	1364	879	1239	1167	1230	1111	1269	1034	1309	1322	1279	1114	1192	1359	1195	1115	1054	877
32	898	973	1048	911	630	865	981	997	654	903	842	888	810	936	745	960	976	964	805	877	988	873	818	764	661
64	677	755	797	688	489	665	746	741	504	678	628	662	614	712	565	744	740	753	618	667	758	659	616	571	510
128	541	599	607	532	391	528	597	557	395	530	492	512	485	550	432	581	567	601	488	523	597	511	480	439	408
256	435	491	487	439	318	425	480	436	323	427	391	416	404	442	334	465	452	481	388	427	483	410	393	344	328
512	364	408	399	360	274	356	390	357	261	360	320	338	328	367	272	373	364	402	323	356	388	336	327	277	262
1024	301	339	331	300	219	281	316	284	210	291	260	270	264	303	222	304	290	330	267	291	299	272	270	228	209
2048	230	259	249	228	168	223	239	213	166	232	202	209	202	238	174	238	222	261	215	216	231	214	210	178	167
4096	170	184	182	169	117	161	168	158	115	171	146	154	149	167	132	174	163	191	160	162	167	157	160	129	121
8192	113	113	113	109	80	109	108	102	79	114	99	107	99	110	95	112	107	123	110	109	107	103	107	84	85
16384	68	66	66	64	49	64	61	59	47	66	60	64	57	65	56	65	64	69	64	64	63	59	62	46	52
32768	35	35	34	34	28	33	32	32	25	35	33	35	32	35	33	35	35	35	35	33	35	32	34	25	27
65536	17	17	17	17	15	17	16	16	13	17	17	17	16	17	16	17	17	17	17	17	17	16	17	12	15
131072	8	8	8	8	7	8	8	8	6	8	8	8	8	8	8	8	8	8	8	8	8	8	8	6	8
262144	4	4	4	4	4	4	4	4	4	4	4	4	4	4	4	4	4	4	4	4	4	4	4	3	4
524288	2	2	2	2	2	2	2	2	2	2	2	2	2	2	2	2	2	2	2	2	2	2	2	2	2
1048576	1	1	1	1	1	1	1	1	1	1	1	1	1	1	1	1	1	1	1	1	1	1	1	1	1

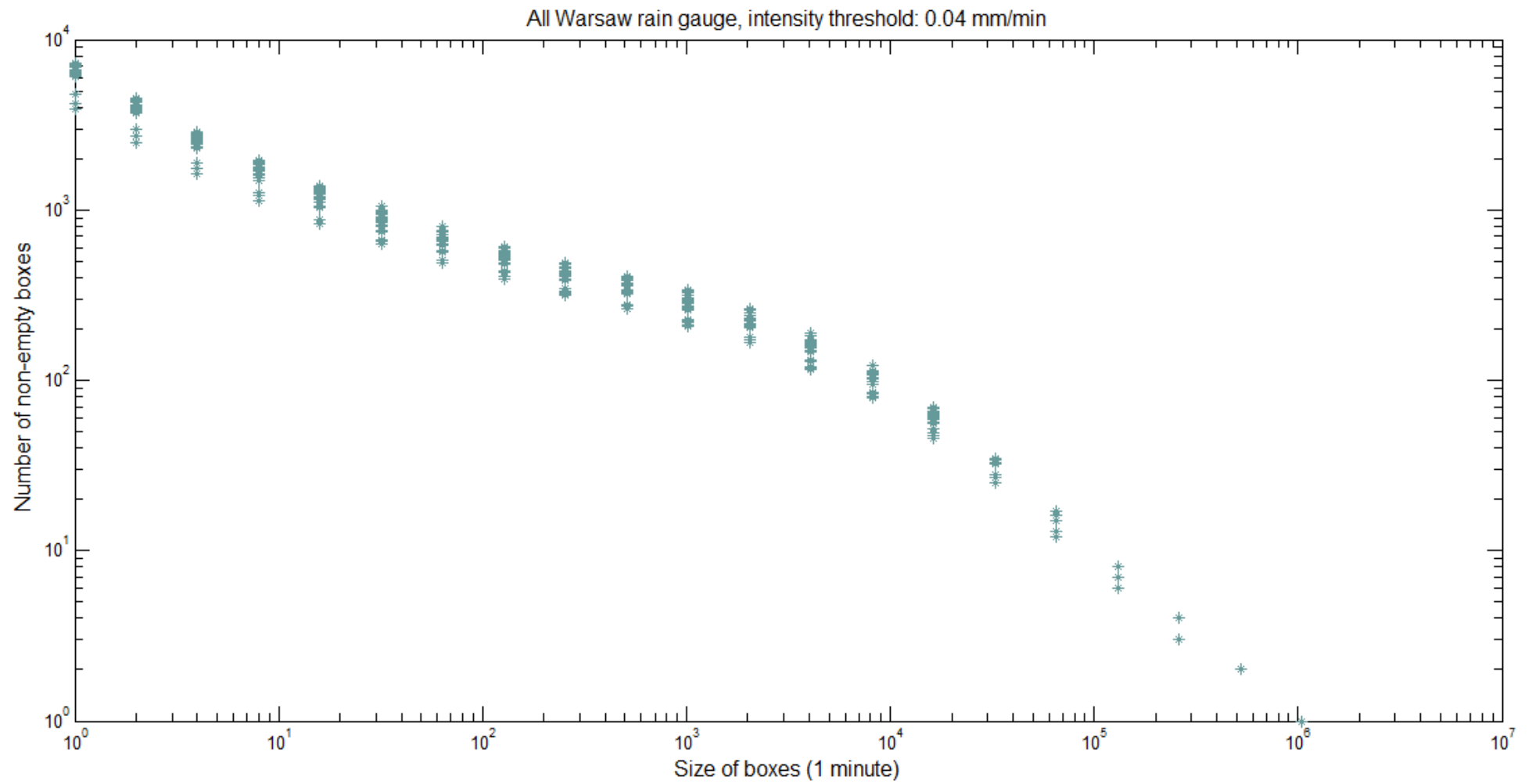


**Figure II.24.** Log-log plot of functional box-counting method for 1-minute rainfall time-series from Warsaw, for all the 25 rain gauges, and intensity threshold 0.04 mm/min

Results of functional box-counting method obtained with 1-minute rainfall for 25 rain gauges in Warsaw, from 2008 to 2010. A box of unit-size corresponds to 1 minutes. The log-log plots display time scales from 1 minute up to over 2 years for intensity threshold equal to 0.08 mm/min.

**Table II.3.** Results of functional box-counting method obtained with 1-minute rainfall for 25 rain gauges in Warsaw, from 2008 to 2010 and intensity threshold 0.08 mm/min

n	R01	R02	R03	R04	R05	R06	R07	R08	R09	R10	R11	R12	R13	R14	R15	R16	R17	R18	R19	R20	R21	R22	R23	R24	R25
1	2268	2088	2412	2396	1397	2136	2394	2536	1800	2454	2431	2402	2404	2567	2414	2453	2571	2188	2085	2253	2307	2195	2142	2111	1238
2	1400	1322	1488	1493	888	1335	1501	1549	1097	1496	1486	1493	1461	1582	1524	1529	1599	1366	1312	1396	1417	1372	1341	1321	792
4	918	886	975	964	590	883	992	1007	680	979	966	990	942	1035	1027	1023	1035	899	869	905	941	896	884	867	520
8	621	636	699	668	420	637	703	708	459	674	669	691	642	727	737	714	716	639	613	624	663	622	620	593	369
16	467	480	530	494	319	470	533	522	328	490	500	509	475	534	567	520	530	478	447	456	500	475	464	431	284
32	372	378	416	371	256	364	412	403	263	379	395	389	365	409	458	398	416	369	347	360	378	371	346	323	218
64	301	309	334	308	214	289	324	328	213	303	321	312	297	330	380	316	334	297	283	299	305	304	276	263	184
128	259	258	282	250	182	249	272	271	178	249	265	262	248	276	318	265	276	247	236	249	260	255	224	219	164
256	226	220	240	218	157	207	233	232	156	213	224	224	220	234	265	223	226	217	200	217	226	222	201	190	145
512	203	196	220	191	138	180	200	200	135	188	195	193	190	204	228	191	202	198	175	186	195	193	176	162	125
1024	180	175	194	171	122	156	179	171	114	166	170	163	167	181	192	167	171	176	155	160	168	170	158	141	113
2048	148	145	155	139	99	128	147	141	97	136	139	134	138	148	152	140	141	147	131	128	139	140	125	120	95
4096	114	119	120	110	80	102	110	112	78	108	113	106	106	111	115	110	106	115	105	102	104	106	101	94	75
8192	83	85	85	79	58	81	81	82	55	77	82	77	80	80	81	77	77	84	78	76	77	75	74	68	57
16384	53	53	56	49	39	49	48	53	34	49	53	48	49	48	49	49	46	53	48	50	49	48	47	39	39
32768	32	32	32	32	25	31	30	31	22	31	32	30	31	30	31	30	28	32	30	29	31	31	30	24	24
65536	17	17	17	17	14	17	16	16	13	17	16	16	16	17	16	16	17	17	17	16	17	16	17	12	15
131072	8	8	8	8	7	8	8	8	6	8	8	8	8	8	8	8	8	8	8	8	8	8	8	6	8
262144	4	4	4	4	4	4	4	4	4	4	4	4	4	4	4	4	4	4	4	4	4	4	4	3	4
524288	2	2	2	2	2	2	2	2	2	2	2	2	2	2	2	2	2	2	2	2	2	2	2	2	2
1048576	1	1	1	1	1	1	1	1	1	1	1	1	1	1	1	1	1	1	1	1	1	1	1	1	1

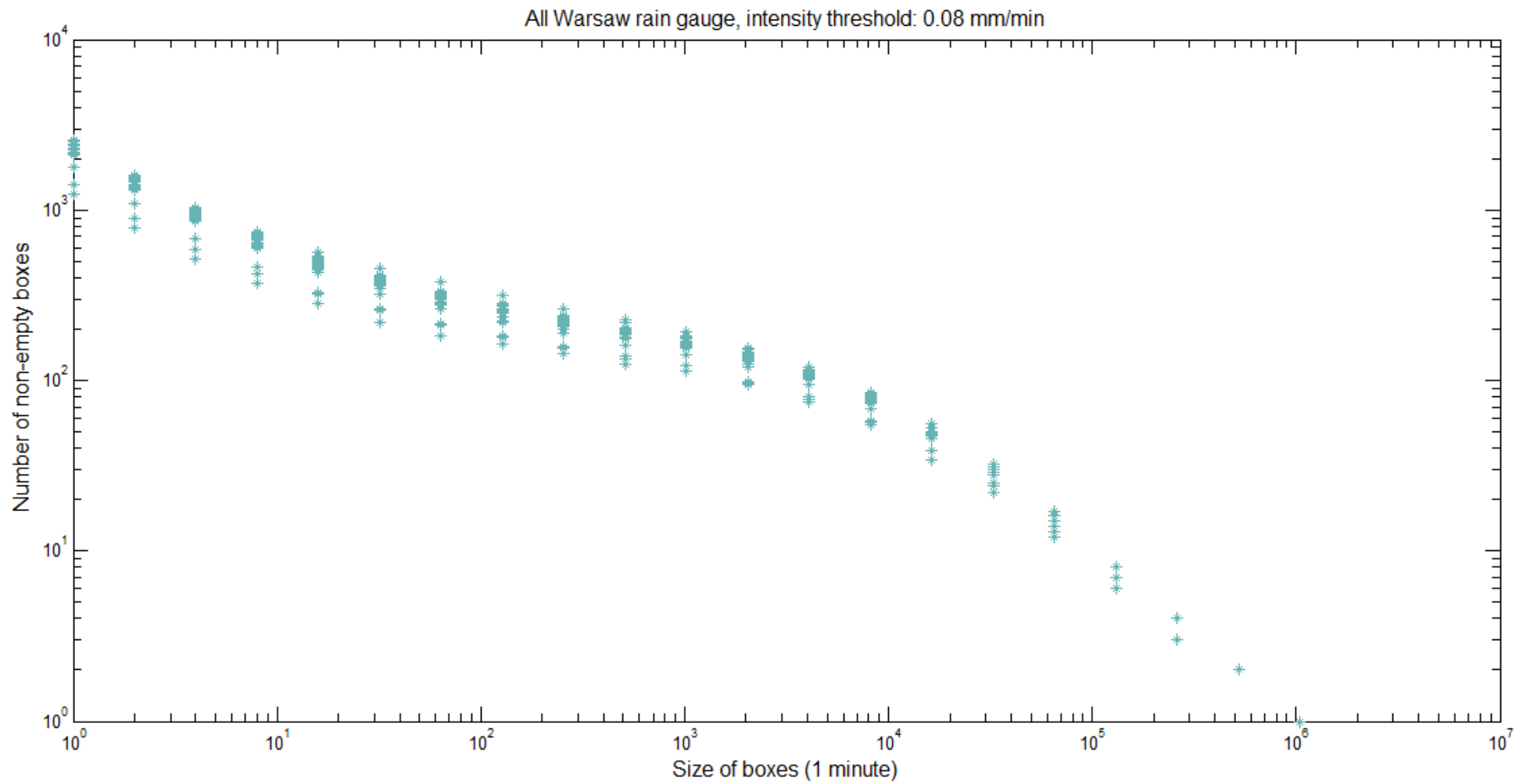


**Figure II.25.** Log-log plot of functional box-counting method for 1-minute rainfall time-series from Warsaw, for all the 25 rain gauges, and intensity threshold 0.08 mm/min

Results of functional box-counting method obtained with 1-minute rainfall for 25 rain gauges in Warsaw, from 2008 to 2010. A box of unit-size corresponds to 1 minutes. The log-log plots display time scales from 1 minute up to over 2 years for intensity threshold equal to 0.16 mm/min.

**Table II.4.** Results of functional box-counting method obtained with 1-minute rainfall for 25 rain gauges in Warsaw, from 2008 to 2010 and intensity threshold 0.16 mm/min

n	R01	R02	R03	R04	R05	R06	R07	R08	R09	R10	R11	R12	R13	R14	R15	R16	R17	R18	R19	R20	R21	R22	R23	R24	R25
1	798	774	882	861	479	781	894	950	695	936	946	870	970	991	944	919	955	709	698	777	824	848	756	751	394
2	497	501	554	537	305	495	554	597	434	572	589	548	589	607	598	566	582	455	454	489	512	536	461	466	249
4	336	341	364	360	212	331	372	398	286	376	394	368	378	398	409	364	380	314	319	324	337	366	303	308	164
8	241	249	266	250	159	245	261	297	198	260	281	264	272	275	302	264	267	238	242	243	244	262	219	222	120
16	188	200	208	189	126	184	196	226	145	197	220	203	206	205	240	198	210	196	186	183	190	207	175	171	100
32	157	169	164	150	109	150	157	189	118	160	175	169	168	160	203	164	171	155	155	149	160	172	141	139	85
64	138	147	139	133	94	131	128	156	103	136	145	138	142	136	173	140	144	133	141	127	136	143	124	112	72
128	126	135	124	112	86	116	112	135	90	114	130	122	124	120	160	126	127	120	126	114	123	128	110	99	65
256	116	122	112	103	79	102	100	123	81	103	115	112	113	109	141	116	112	111	115	107	108	115	102	95	62
512	111	114	107	98	77	94	93	113	74	95	109	100	104	98	132	106	104	104	106	101	99	107	95	83	58
1024	103	105	102	92	71	84	89	106	69	89	101	91	95	92	119	95	93	98	99	94	88	99	88	74	55
2048	91	89	84	81	63	74	82	94	61	79	90	78	83	80	98	83	77	87	85	81	81	88	75	66	48
4096	80	79	73	68	53	62	68	79	51	68	73	65	68	68	82	73	64	74	69	69	67	71	60	52	39
8192	62	60	56	55	42	49	52	63	39	54	57	54	58	54	63	56	51	57	54	55	54	56	47	41	33
16384	40	39	37	34	29	32	31	40	24	34	38	35	39	34	40	35	33	37	35	36	36	36	31	26	22
32768	24	25	24	23	21	23	22	28	16	21	24	23	25	22	26	24	23	25	23	23	25	24	21	17	15
65536	14	15	13	13	14	15	13	15	10	12	15	13	15	13	14	14	14	14	14	14	15	14	13	9	10
131072	8	8	8	7	7	8	7	7	6	7	8	8	8	6	8	8	8	8	8	7	8	8	8	5	6
262144	4	4	4	4	4	4	4	4	4	4	4	4	4	4	4	4	4	4	4	4	4	4	4	3	4
524288	2	2	2	2	2	2	2	2	2	2	2	2	2	2	2	2	2	2	2	2	2	2	2	2	2
1048576	1	1	1	1	1	1	1	1	1	1	1	1	1	1	1	1	1	1	1	1	1	1	1	1	1

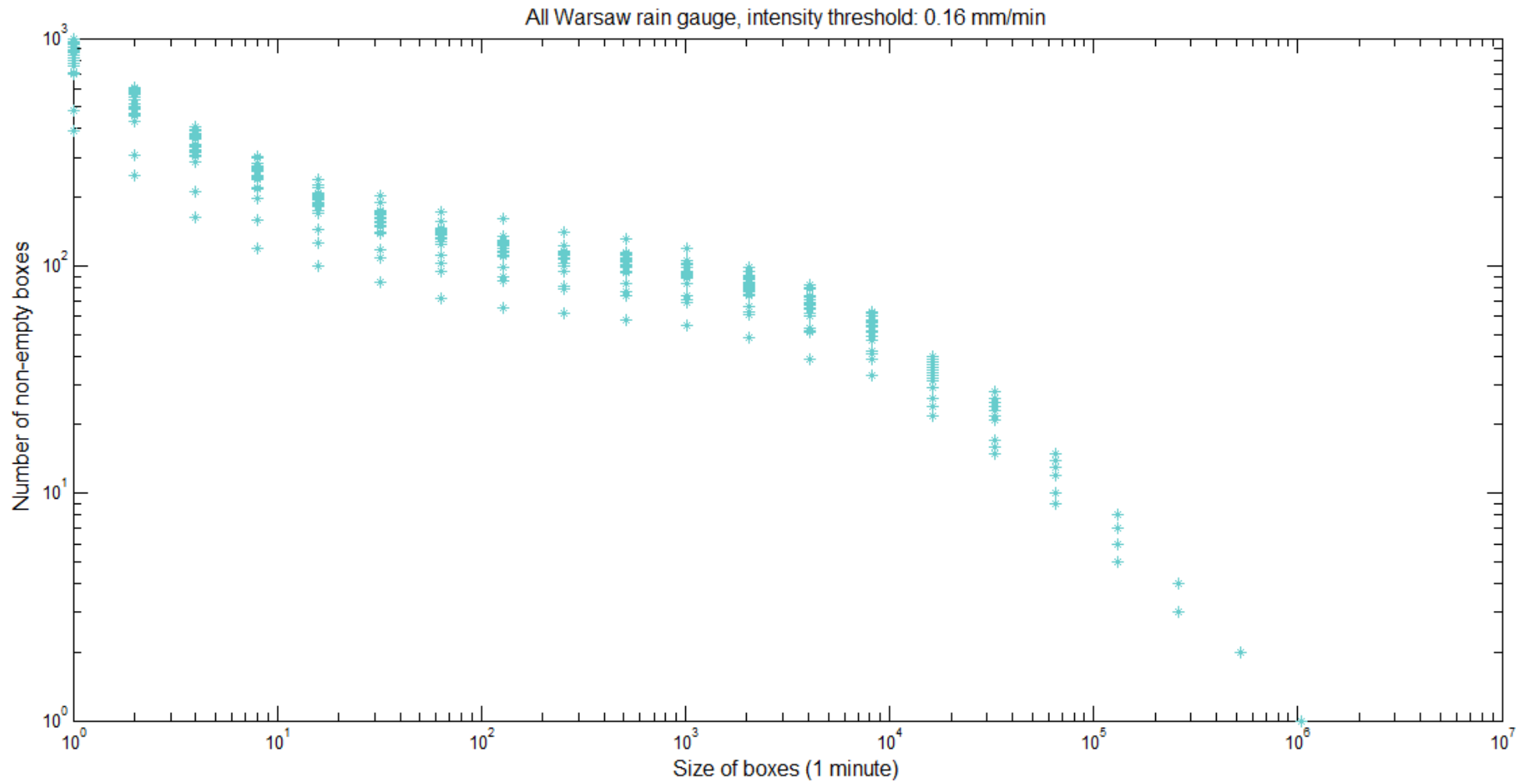


**Figure II.26.** Log-log plot of functional box-counting method for 1-minute rainfall time-series from Warsaw, for all the 25 rain gauges, and intensity threshold 0.16 mm/min

## APPENDIX III.

### ENERGY SPECTRA COMPUTED BY FFT METHOD

#### Section A

Energy spectra obtained for 1-minute rainfall time-series from Warsaw, recorded from September 2008 to November 2010. The scaling exponent is calculated for two different scaling regimes.

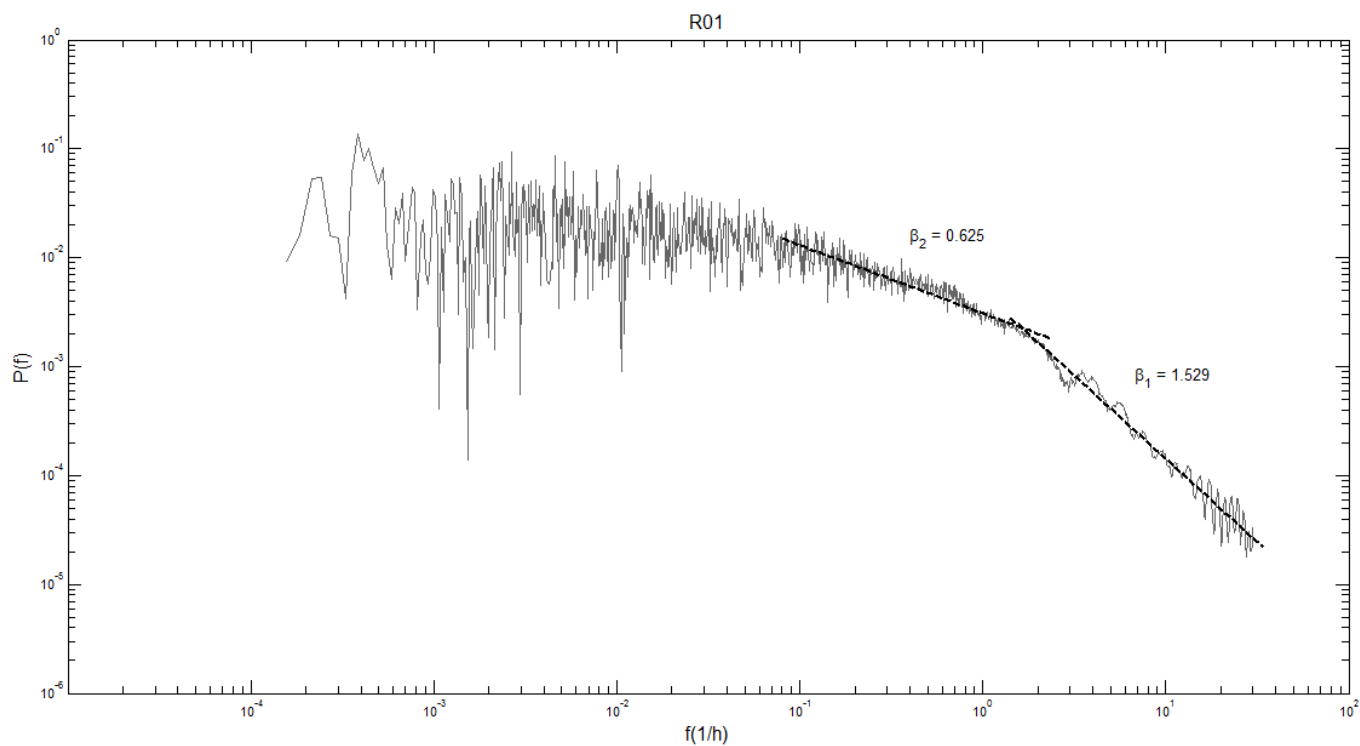


**Figure III.1.** Energy spectrum for 1-minute rainfall time-series from Warsaw, from September 2008 to November 2010, for rain gauge R01

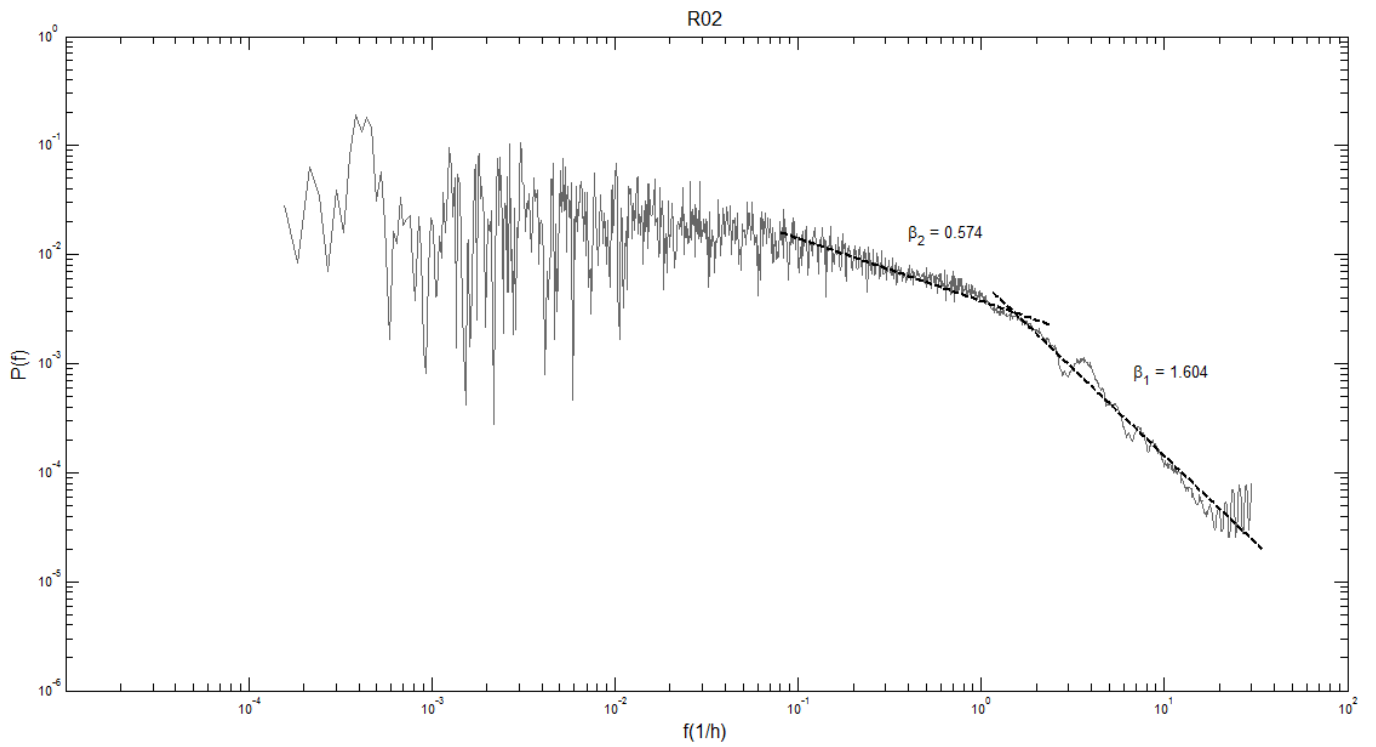


**Figure III.2.** Energy spectrum for 1-minute rainfall time-series from Warsaw, from September 2008 to November 2010, for rain gauge R02

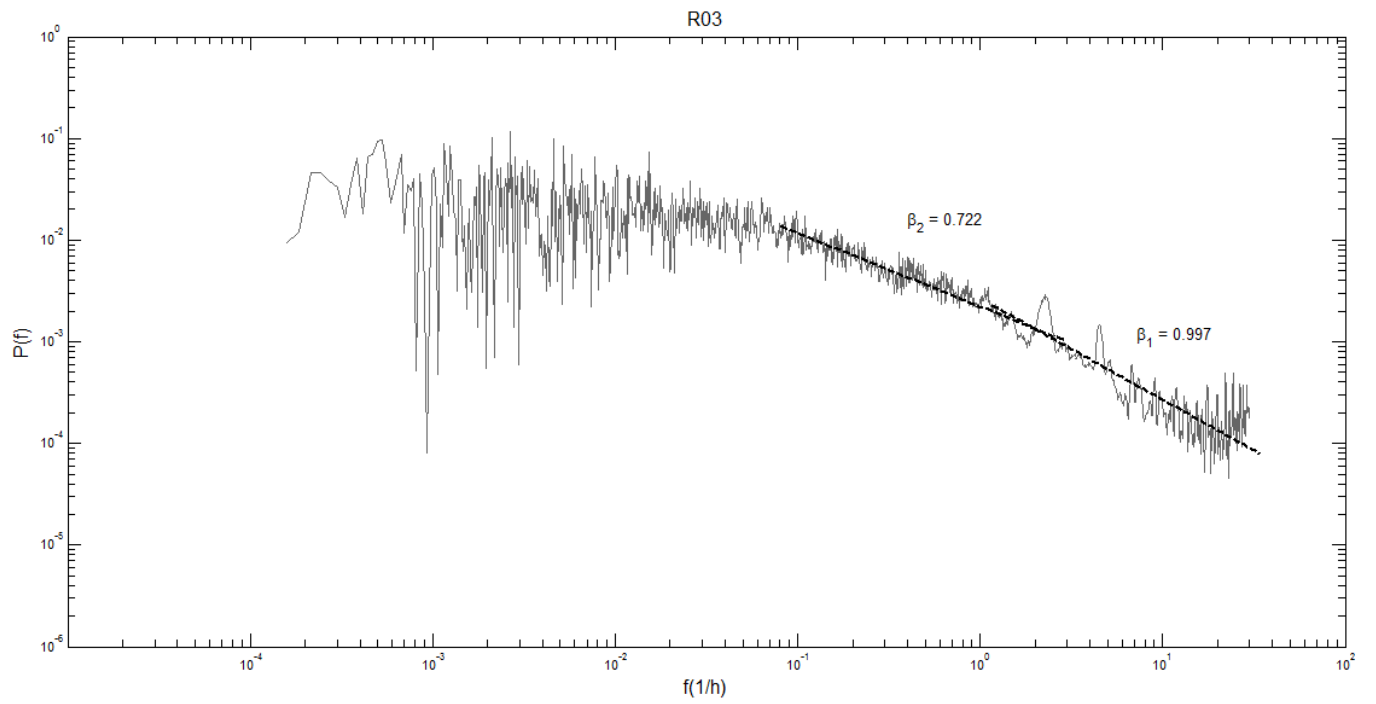


**Figure III.3.** Energy spectrum for 1-minute rainfall time-series from Warsaw, from September 2008 to November 2010, for rain gauge R03

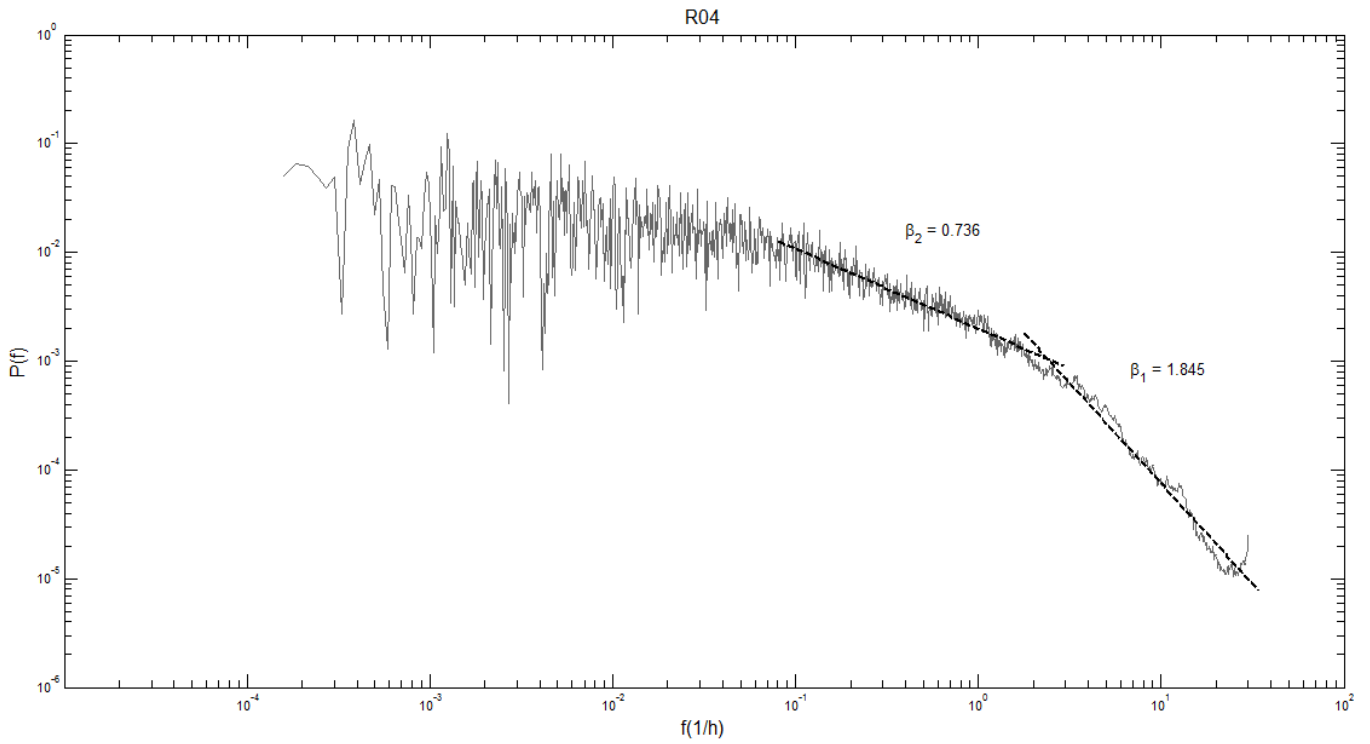


**Figure III.4.** Energy spectrum for 1-minute rainfall time-series from Warsaw, from September 2008 to November 2010, for rain gauge R04

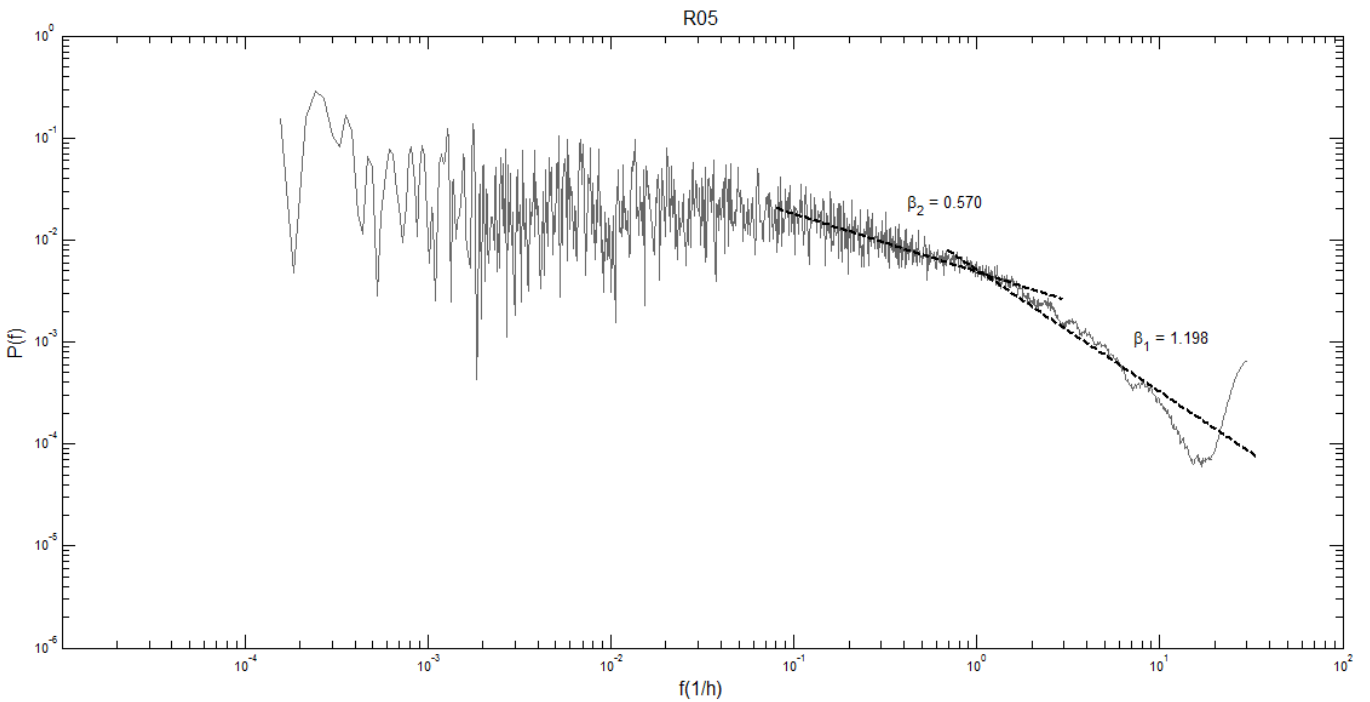


**Figure III.5.** Energy spectrum for 1-minute rainfall time-series from Warsaw, from September 2008 to November 2010, for rain gauge R05

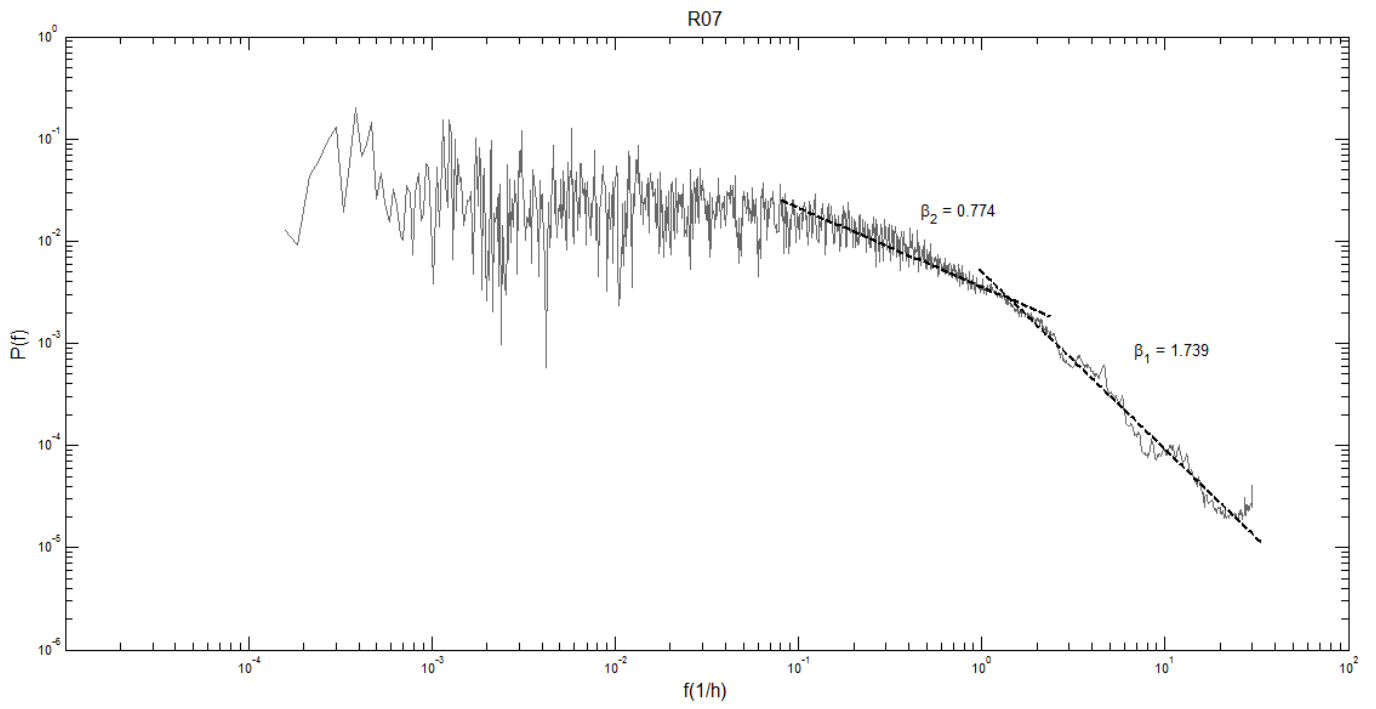


**Figure III.6.** Energy spectrum for 1-minute rainfall time-series from Warsaw, from September 2008 to November 2010, for rain gauge R07

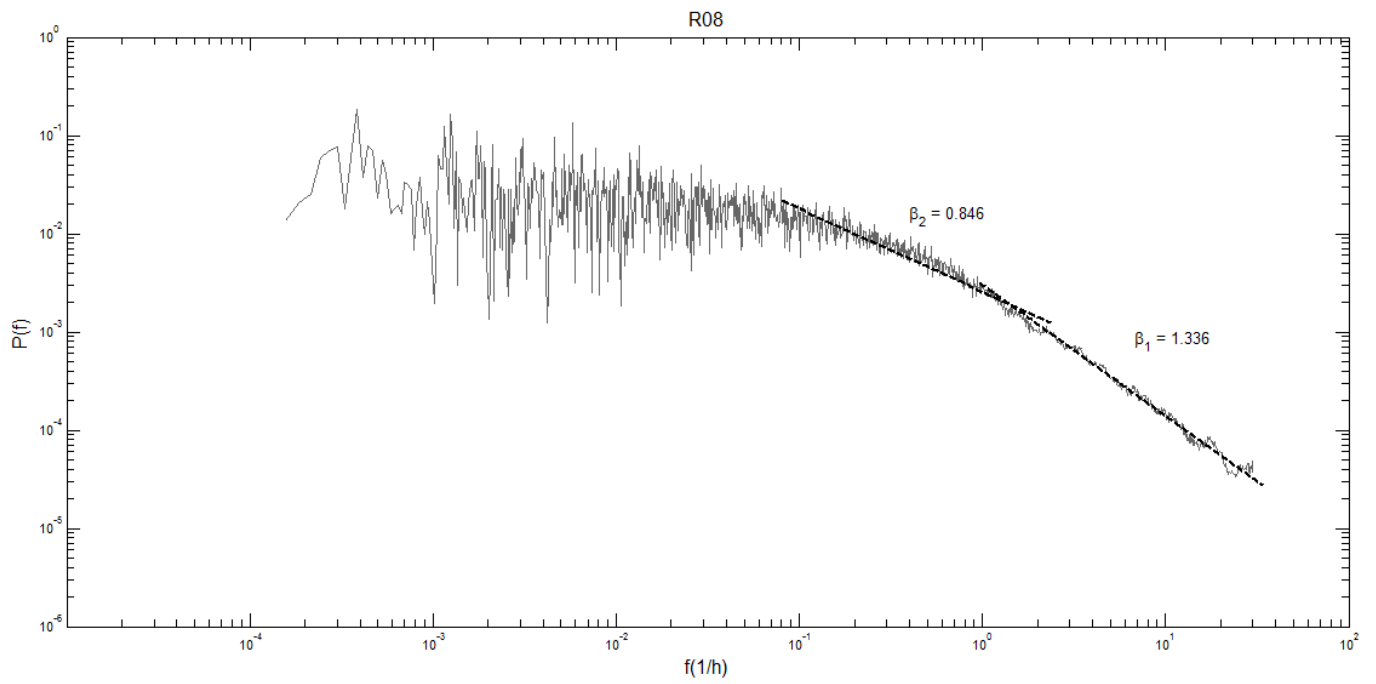


**Figure III.7.** Energy spectrum for 1-minute rainfall time-series from Warsaw, from September 2008 to November 2010, for rain gauge R08

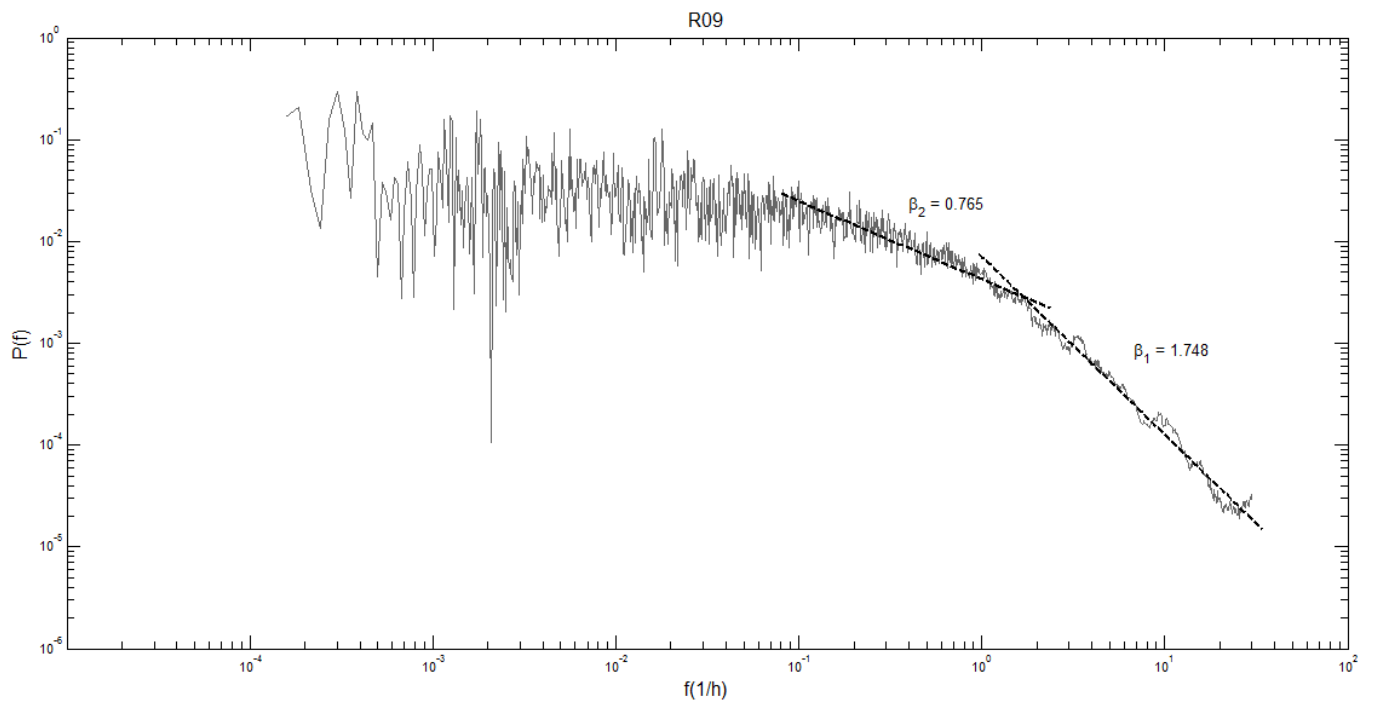


**Figure III.8.** Energy spectrum for 1-minute rainfall time-series from Warsaw, from September 2008 to November 2010, for rain gauge R09

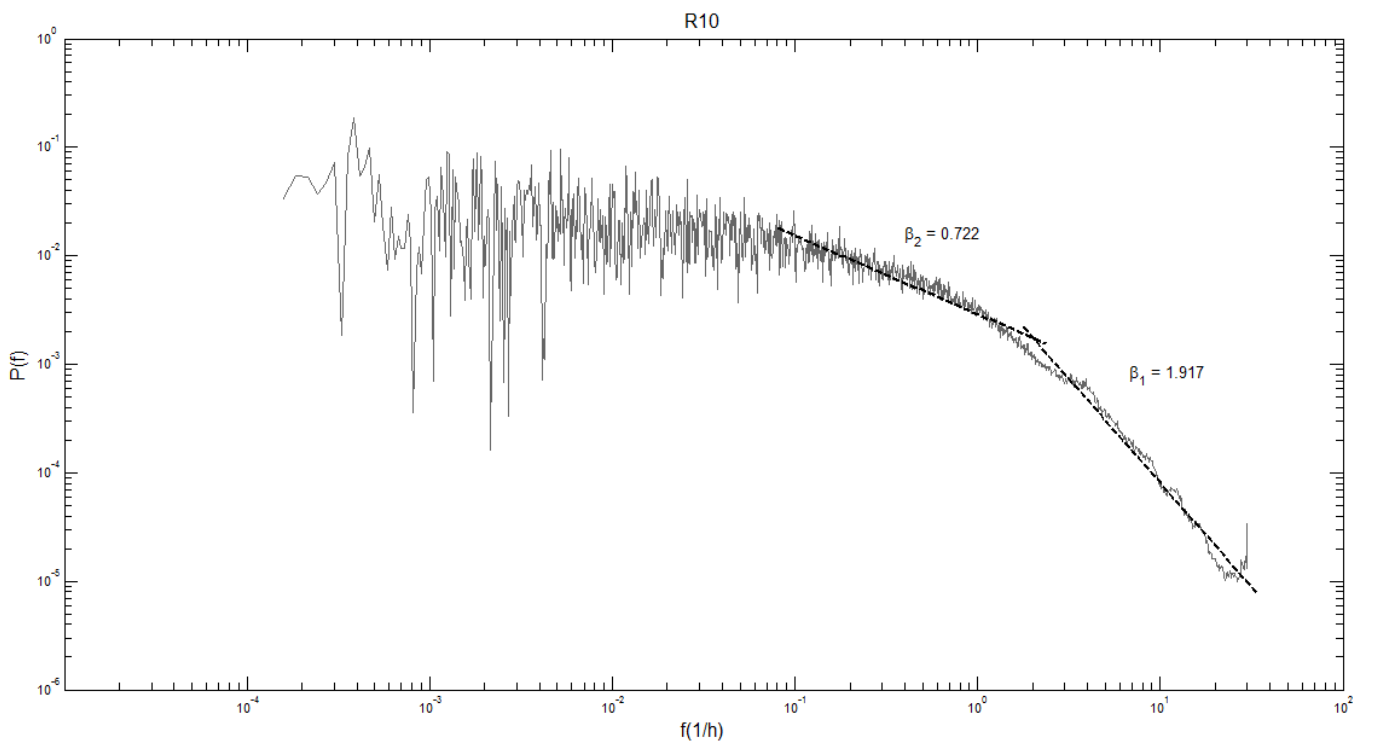


**Figure III.9.** Energy spectrum for 1-minute rainfall time-series from Warsaw, from September 2008 to November 2010, for rain gauge R10

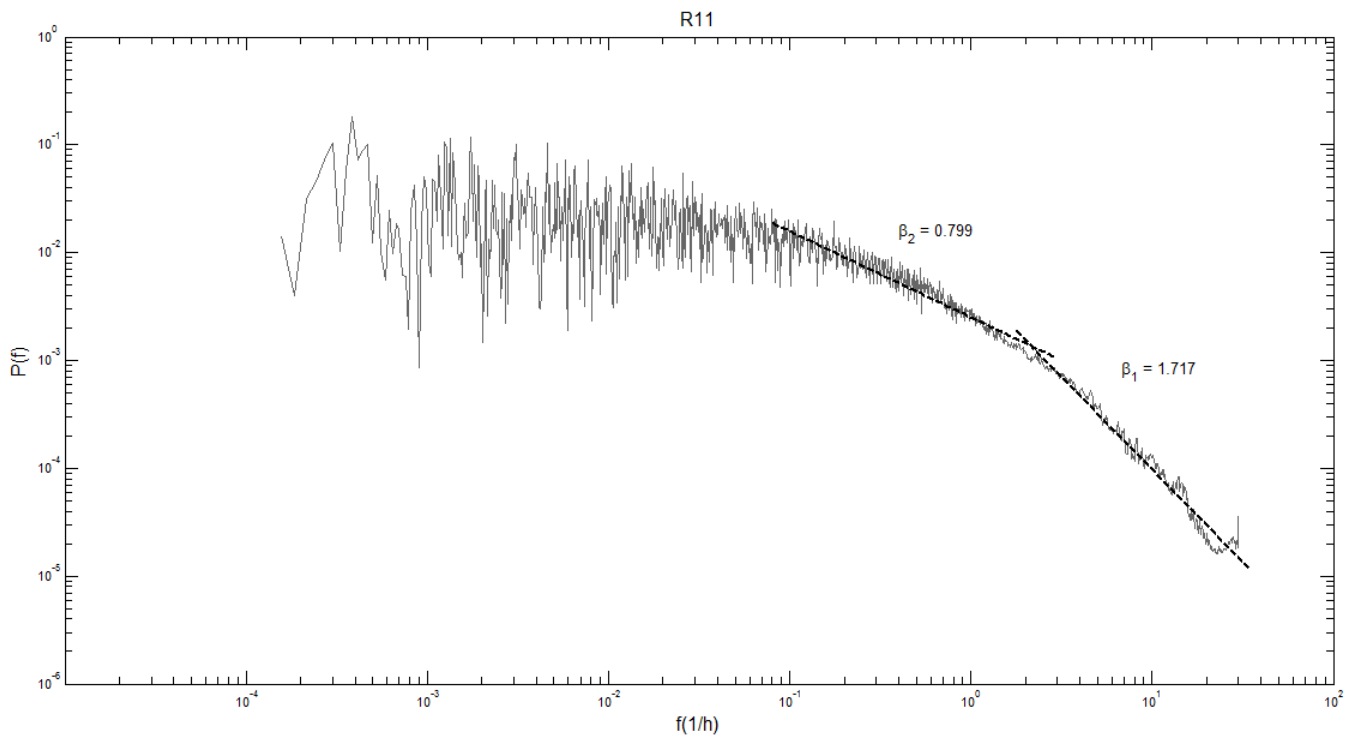


**Figure III.10.** Energy spectrum for 1-minute rainfall time-series from Warsaw, from September 2008 to November 2010, for rain gauge R11

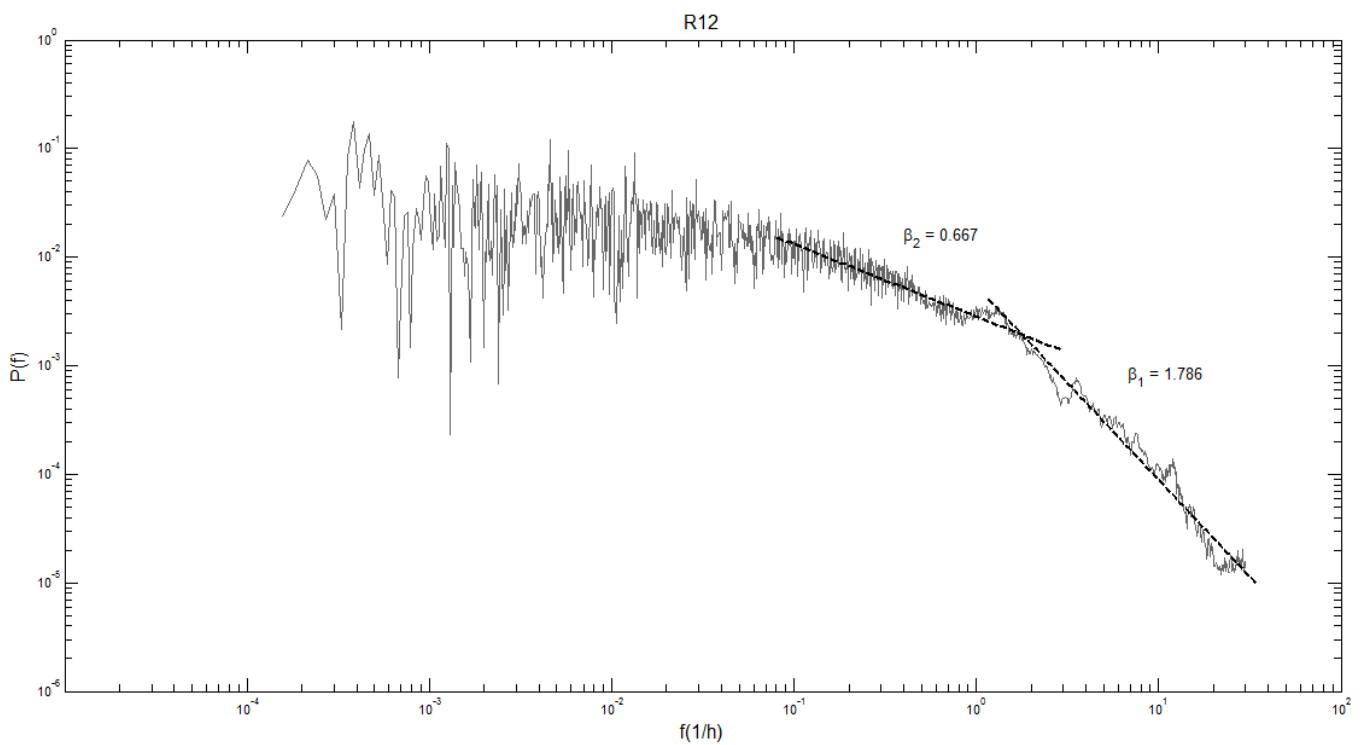


**Figure III.11.** Energy spectrum for 1-minute rainfall time-series from Warsaw, from September 2008 to November 2010, for rain gauge R12

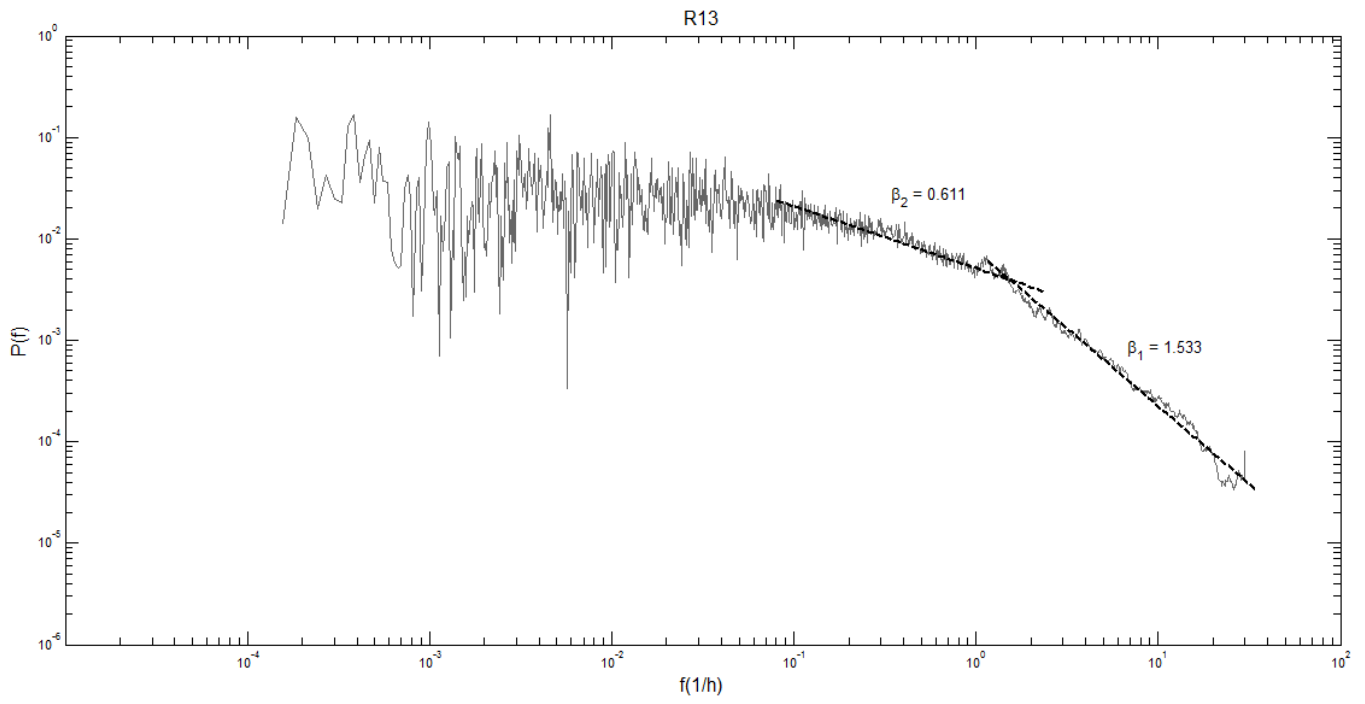


**Figure III.12.** Energy spectrum for 1-minute rainfall time-series from Warsaw, from September 2008 to November 2010, for rain gauge R13

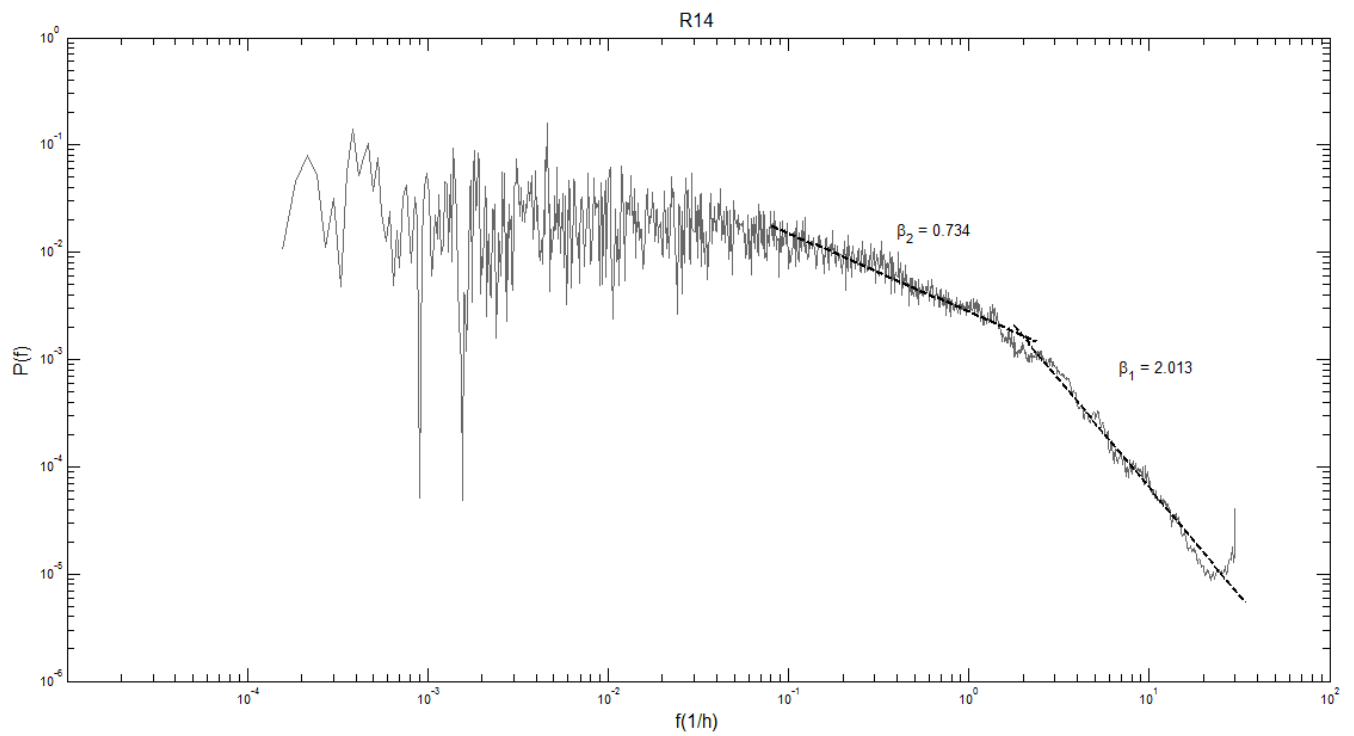


**Figure III.13.** Energy spectrum for 1-minute rainfall time-series from Warsaw, from September 2008 to November 2010, for rain gauge R14

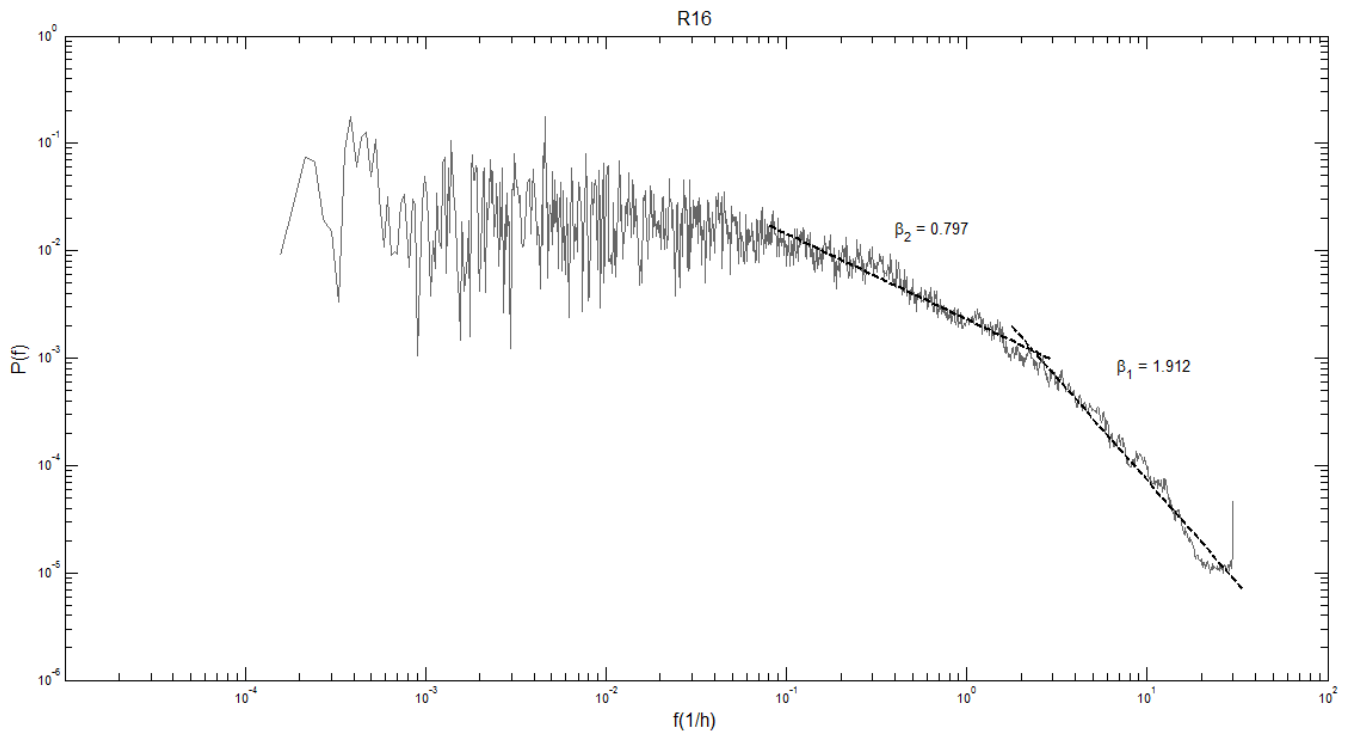


**Figure III.14.** Energy spectrum for 1-minute rainfall time-series from Warsaw, from September 2008 to November 2010, for rain gauge R16

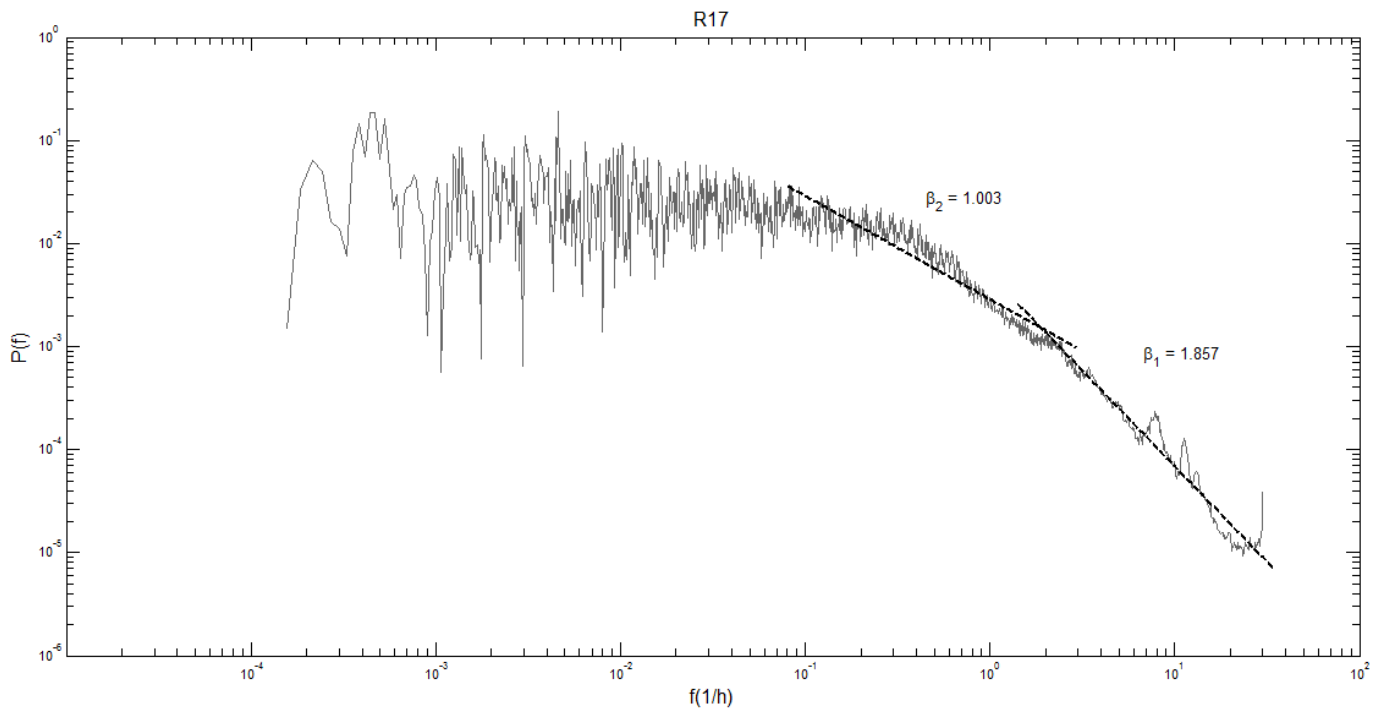


**Figure III.15.** Energy spectrum for 1-minute rainfall time-series from Warsaw, from September 2008 to November 2010, for rain gauge R17

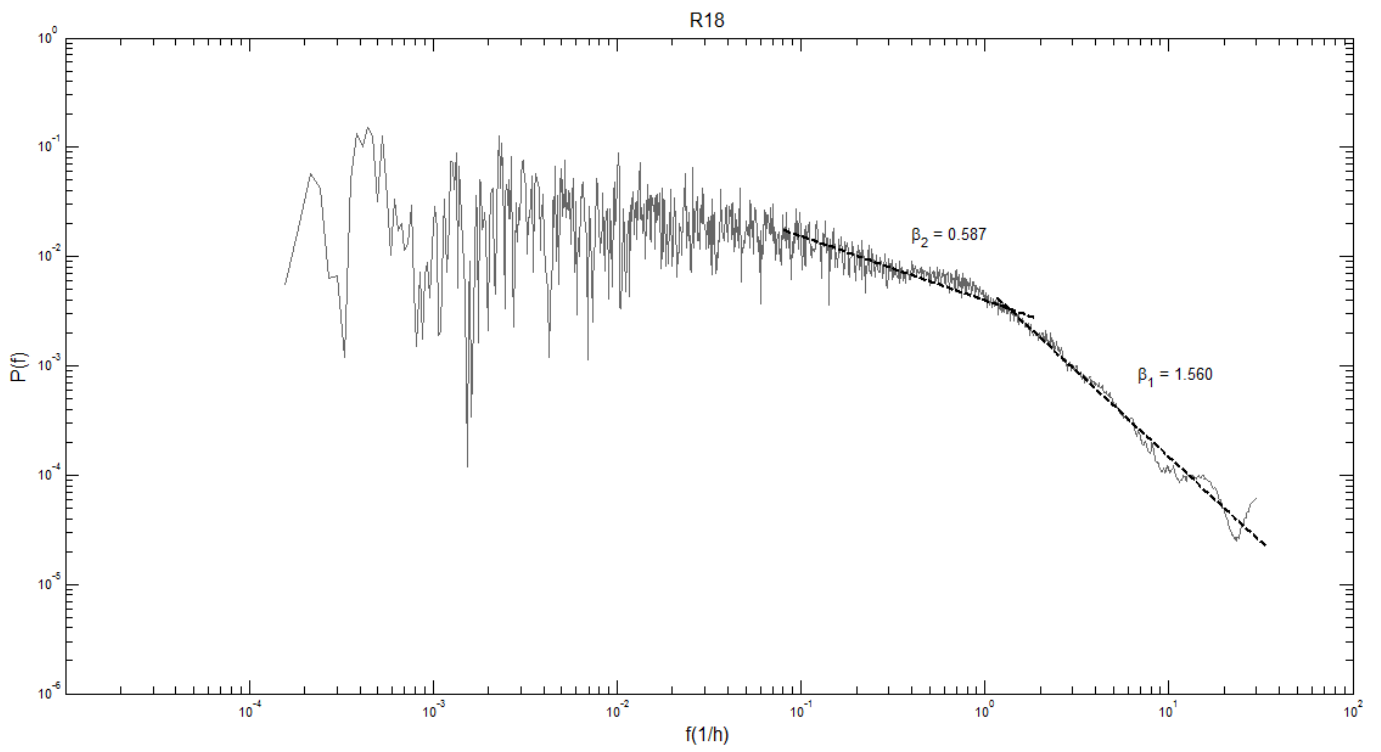


**Figure III.16.** Energy spectrum for 1-minute rainfall time-series from Warsaw, from September 2008 to November 2010, for rain gauge R18

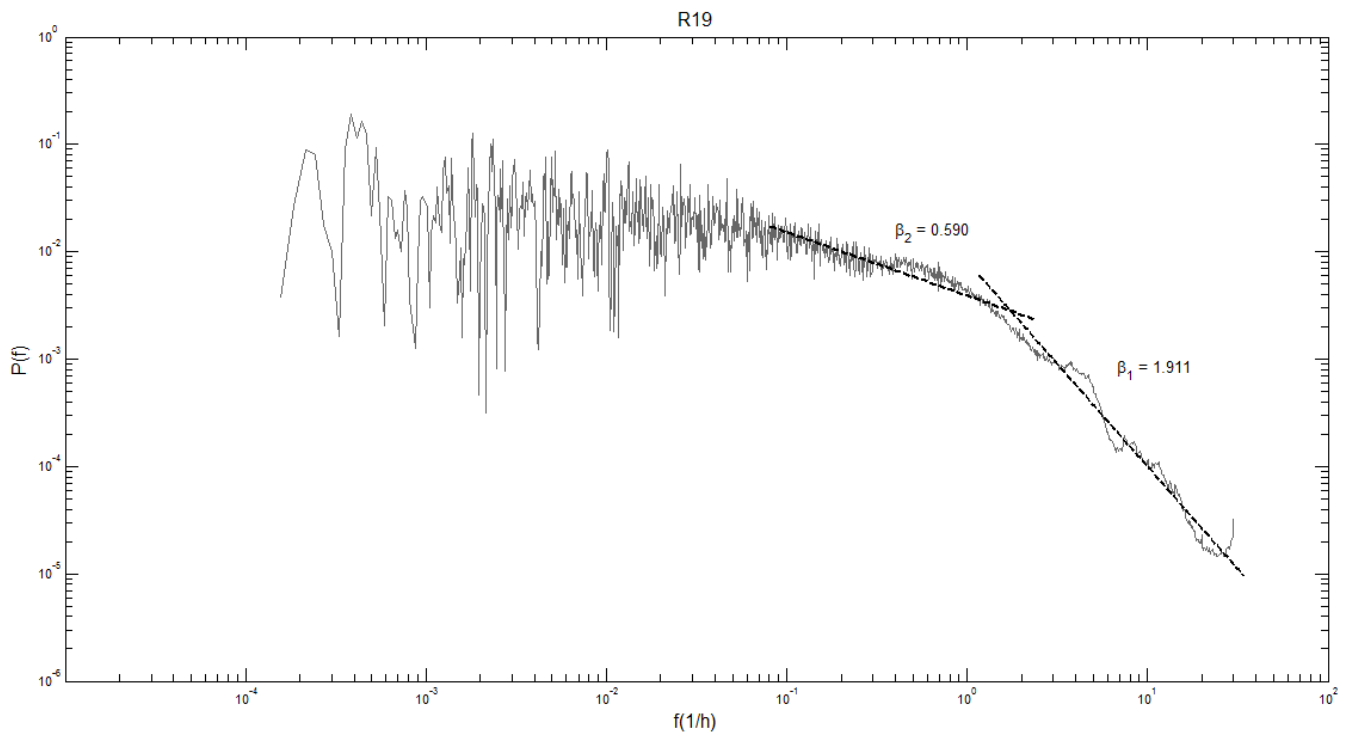


**Figure III.17.** Energy spectrum for 1-minute rainfall time-series from Warsaw, from September 2008 to November 2010, for rain gauge R19

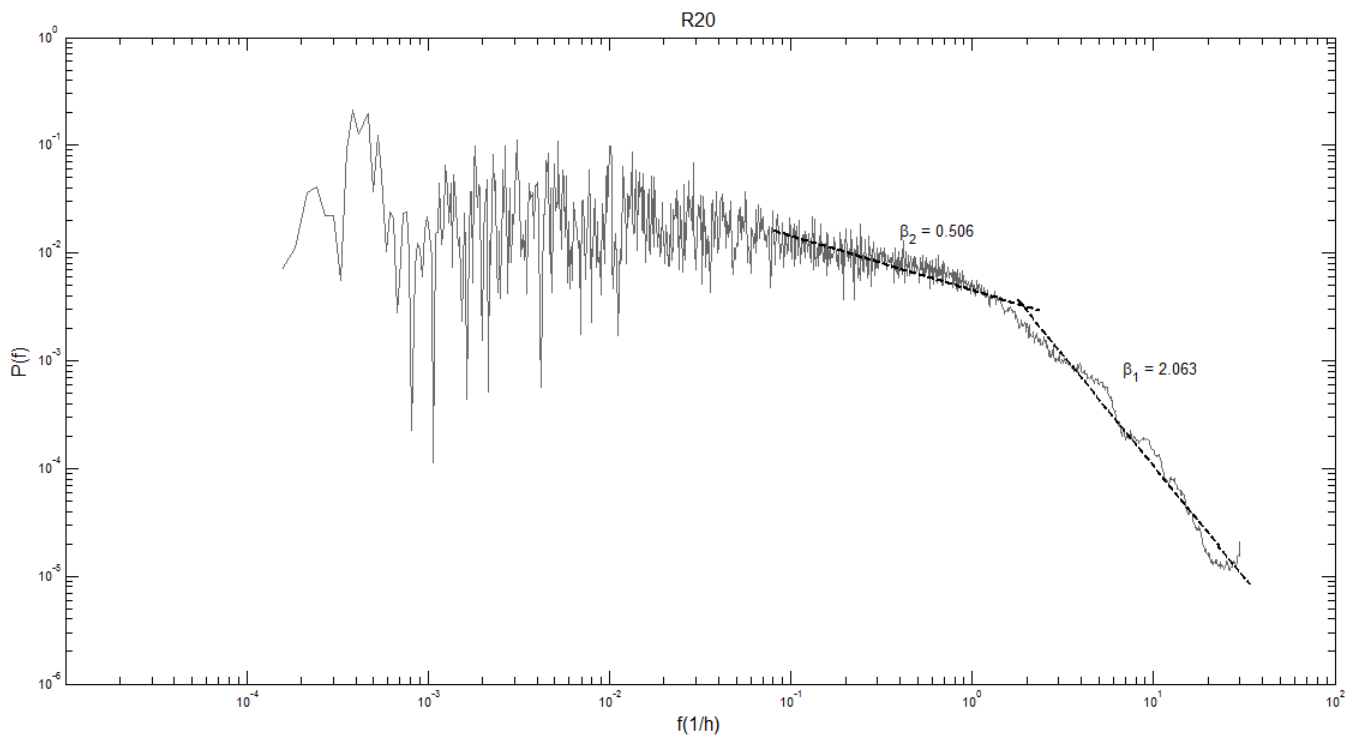


**Figure III.18.** Energy spectrum for 1-minute rainfall time-series from Warsaw, from September 2008 to November 2010, for rain gauge R20

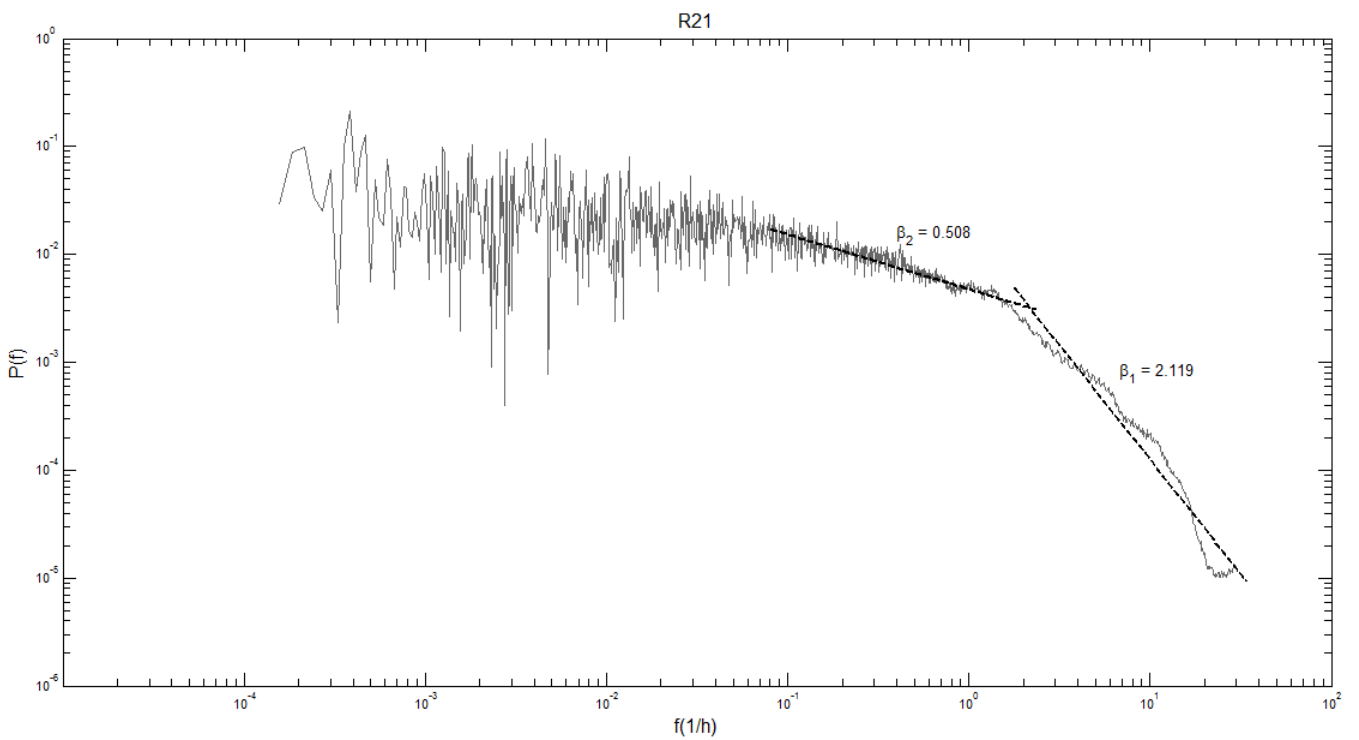


**Figure III.19.** Energy spectrum for 1-minute rainfall time-series from Warsaw, from September 2008 to November 2010, for rain gauge R21

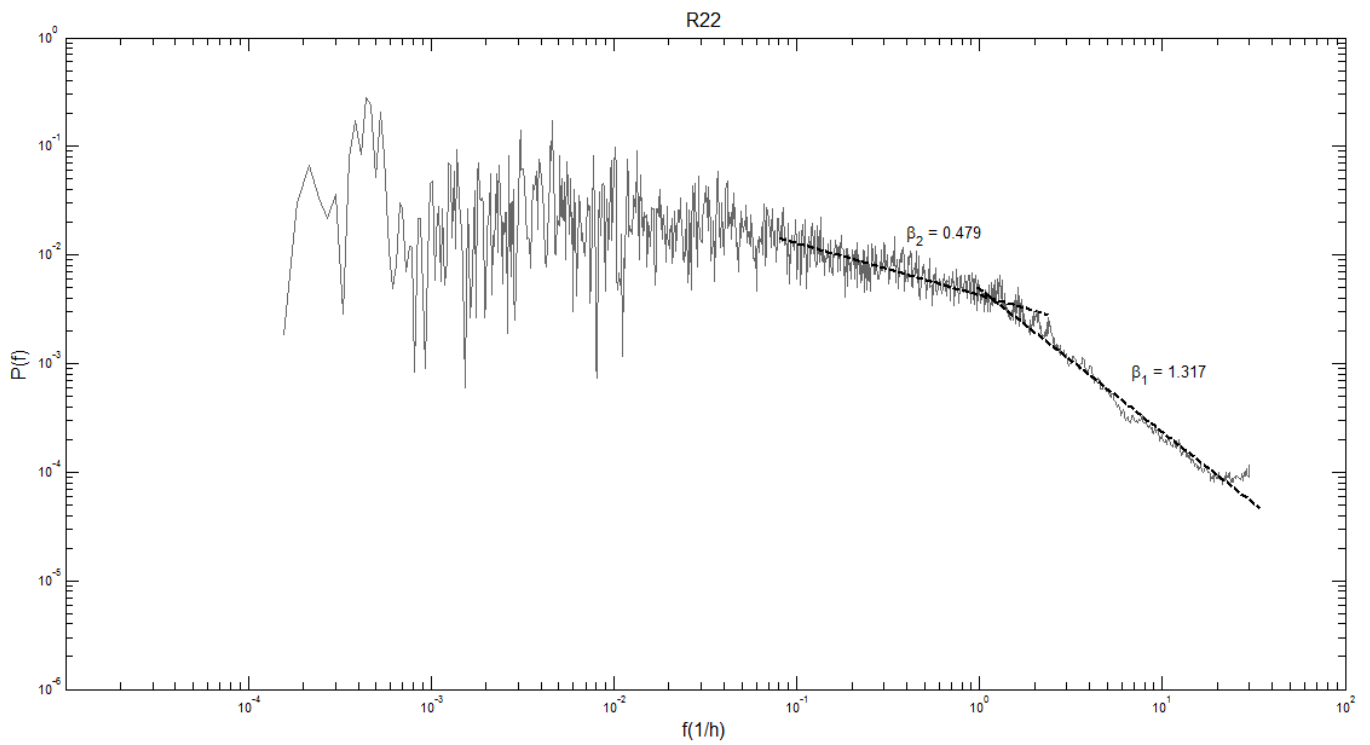


**Figure III.20.** Energy spectrum for 1-minute rainfall time-series from Warsaw, from September 2008 to November 2010, for rain gauge R22

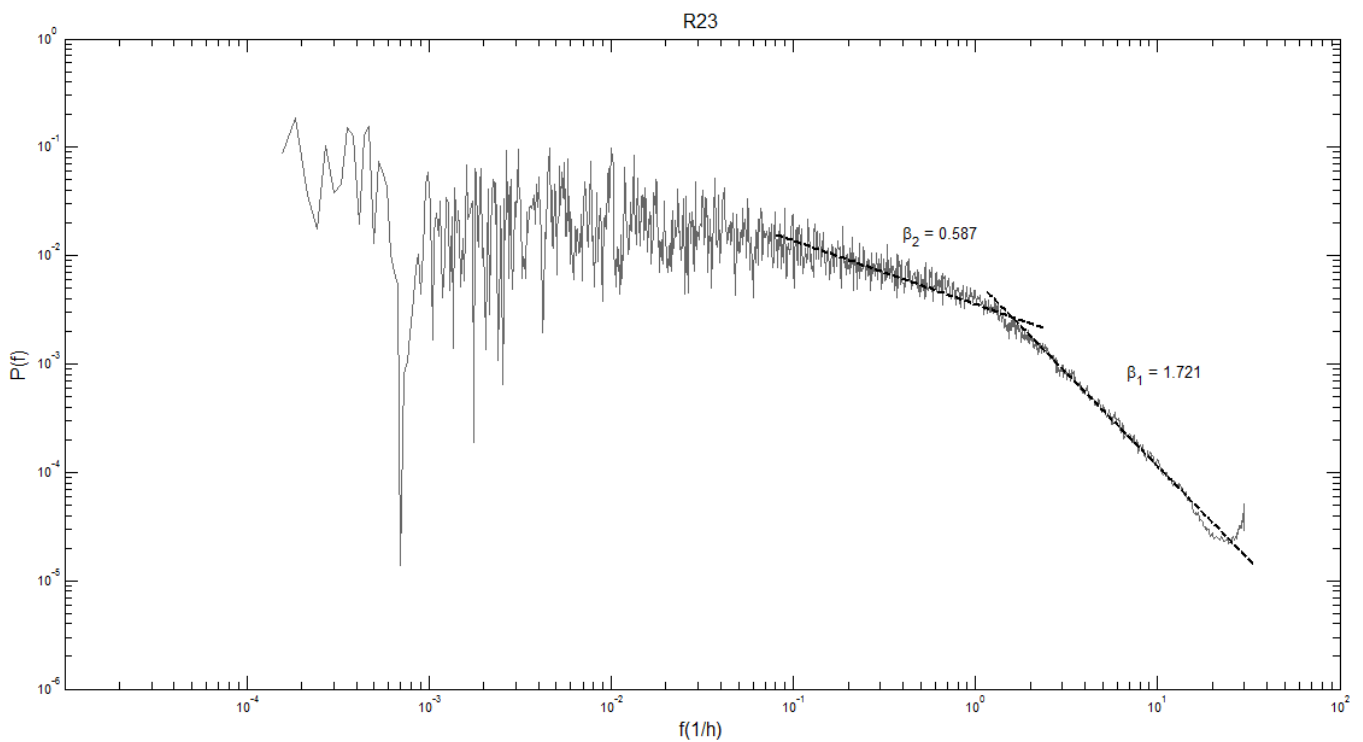


**Figure III.21.** Energy spectrum for 1-minute rainfall time-series from Warsaw, from September 2008 to November 2010, for rain gauge R23

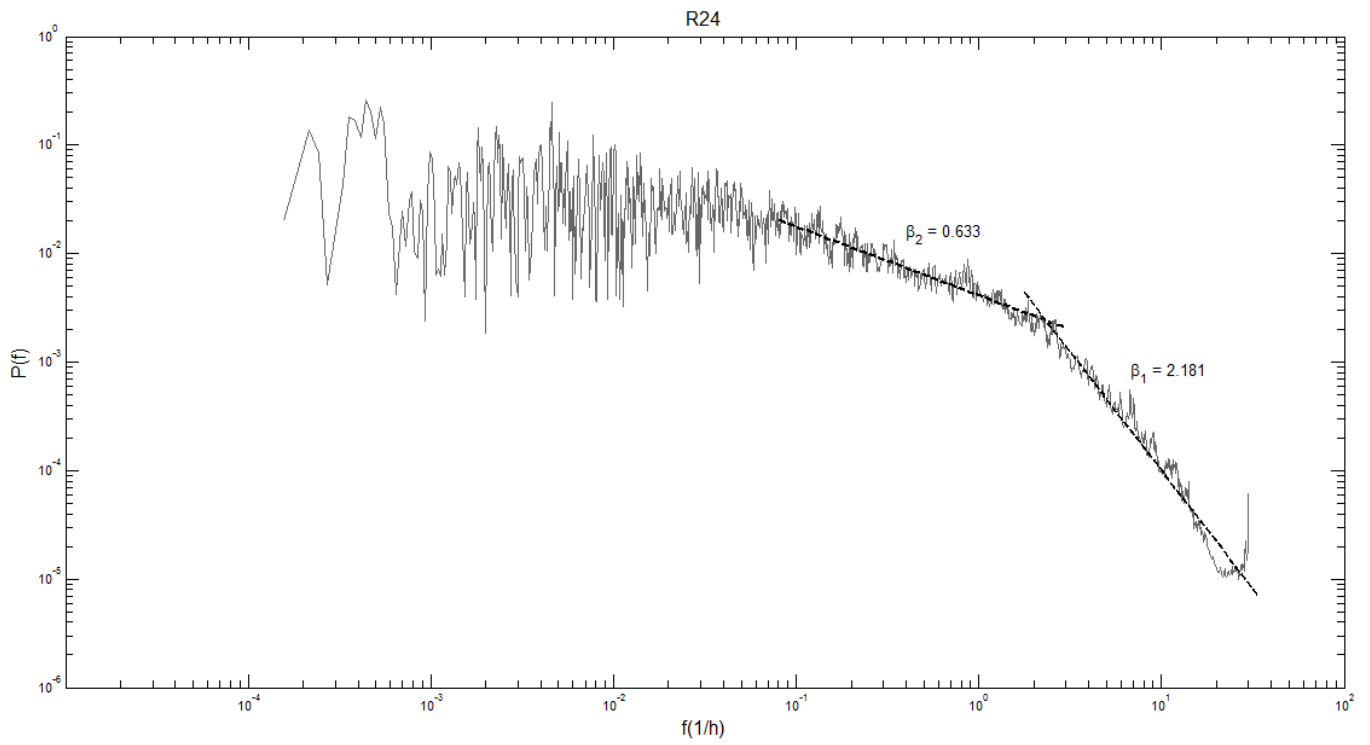


**Figure III.22.** Energy spectrum for 1-minute rainfall time-series from Warsaw, from September 2008 to November 2010, for rain gauge R24

## Section B

Energy spectra obtained for 1-minute rainfall time-series from Warsaw, recorded in 2009. The spectra are computed for data divided into summer (b) and winter (c) season. The intersection of trend lines of two scaling regimes gives the break point.

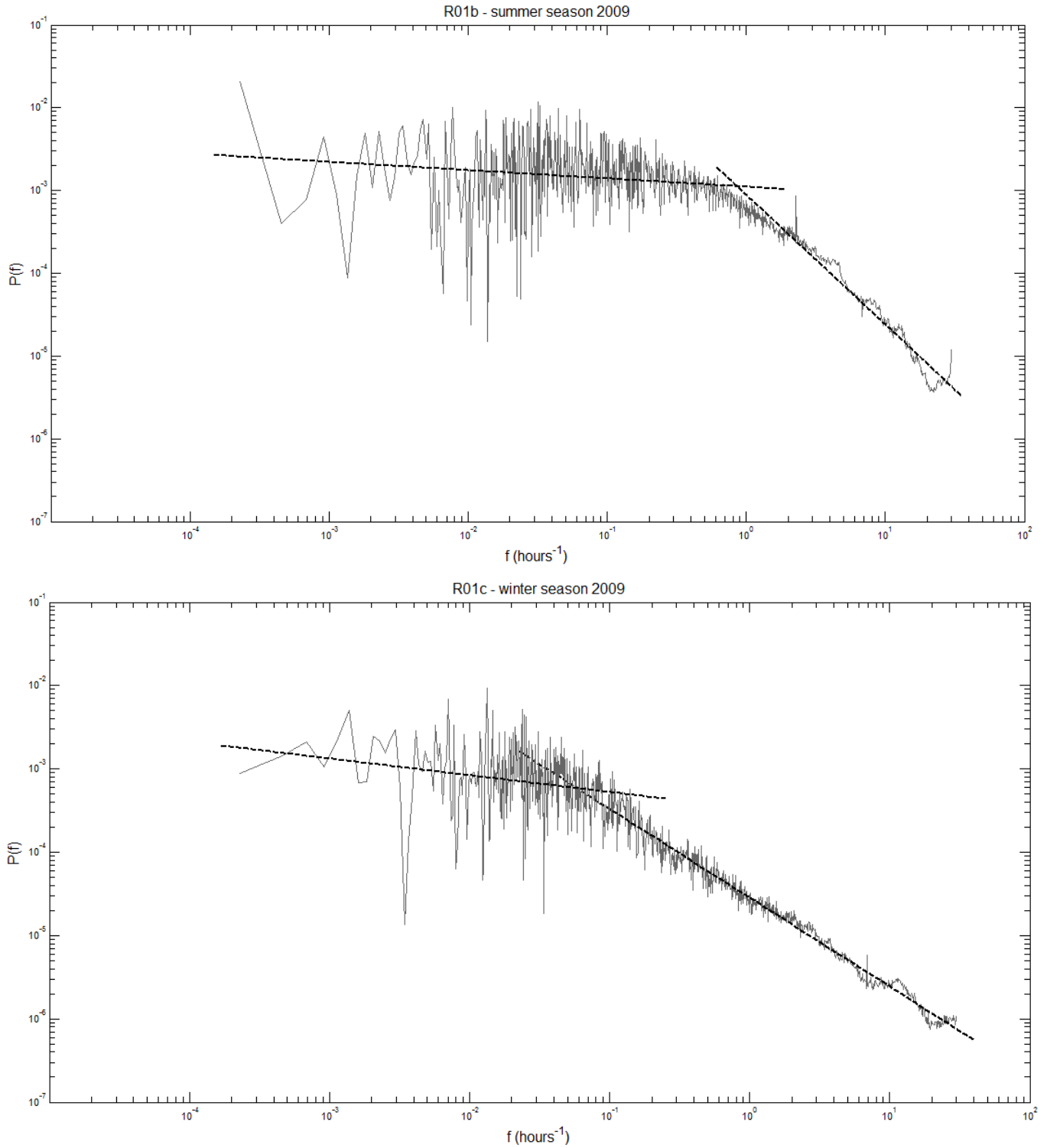


**Figure III.23.** Energy spectra for 1-minute rainfall time-series from Warsaw, for rain gauge R01 in 2009. Summer season (upper graph) and winter season (lower graph)

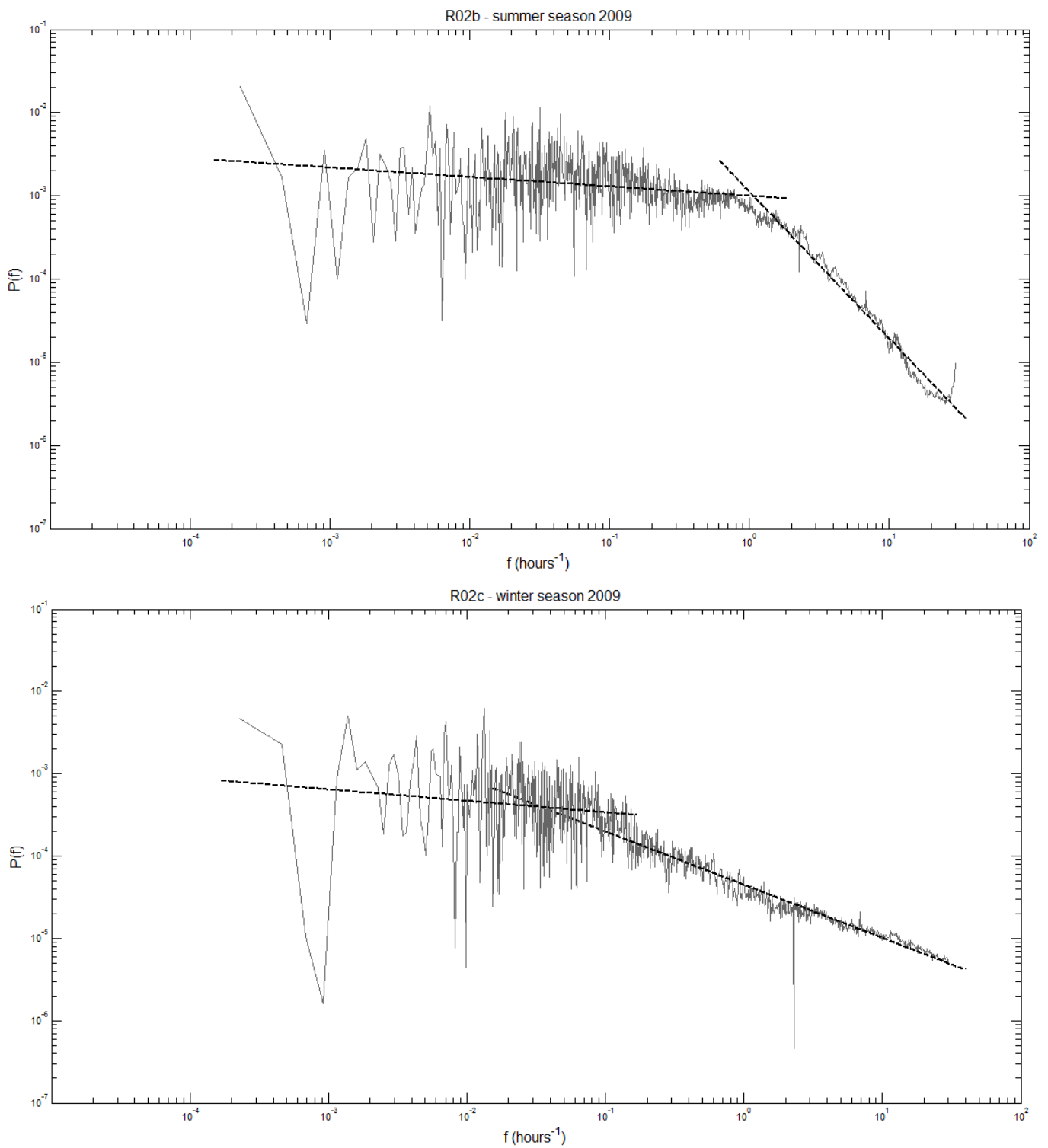


**Figure III.24.** Energy spectra for 1-minute rainfall time-series from Warsaw, for rain gauge R02 in 2009. Summer season (upper graph) and winter season (lower graph)

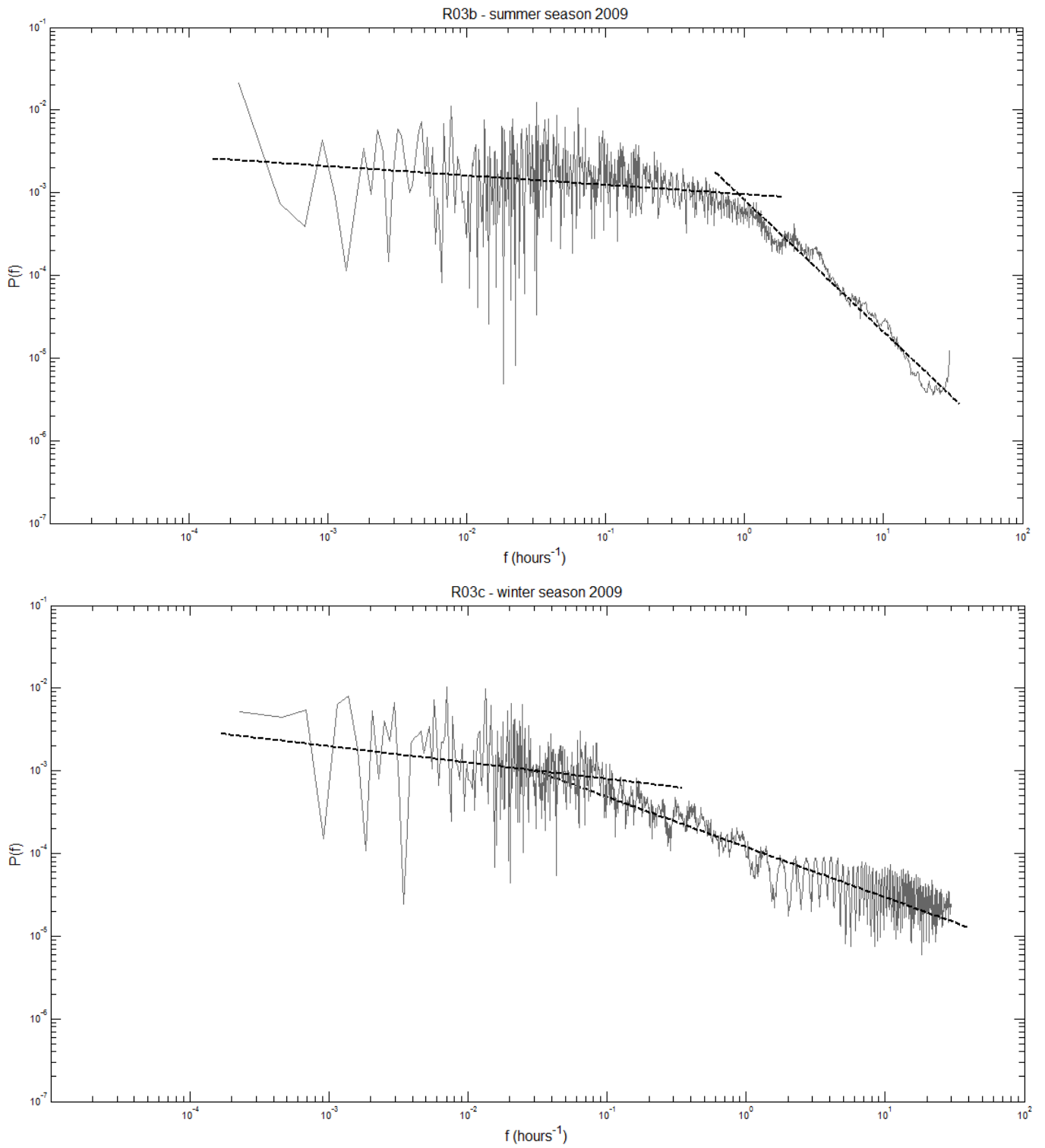


**Figure III.25.** Energy spectra for 1-minute rainfall time-series from Warsaw, for rain gauge R03 in 2009. Summer season (upper graph) and winter season (lower graph)

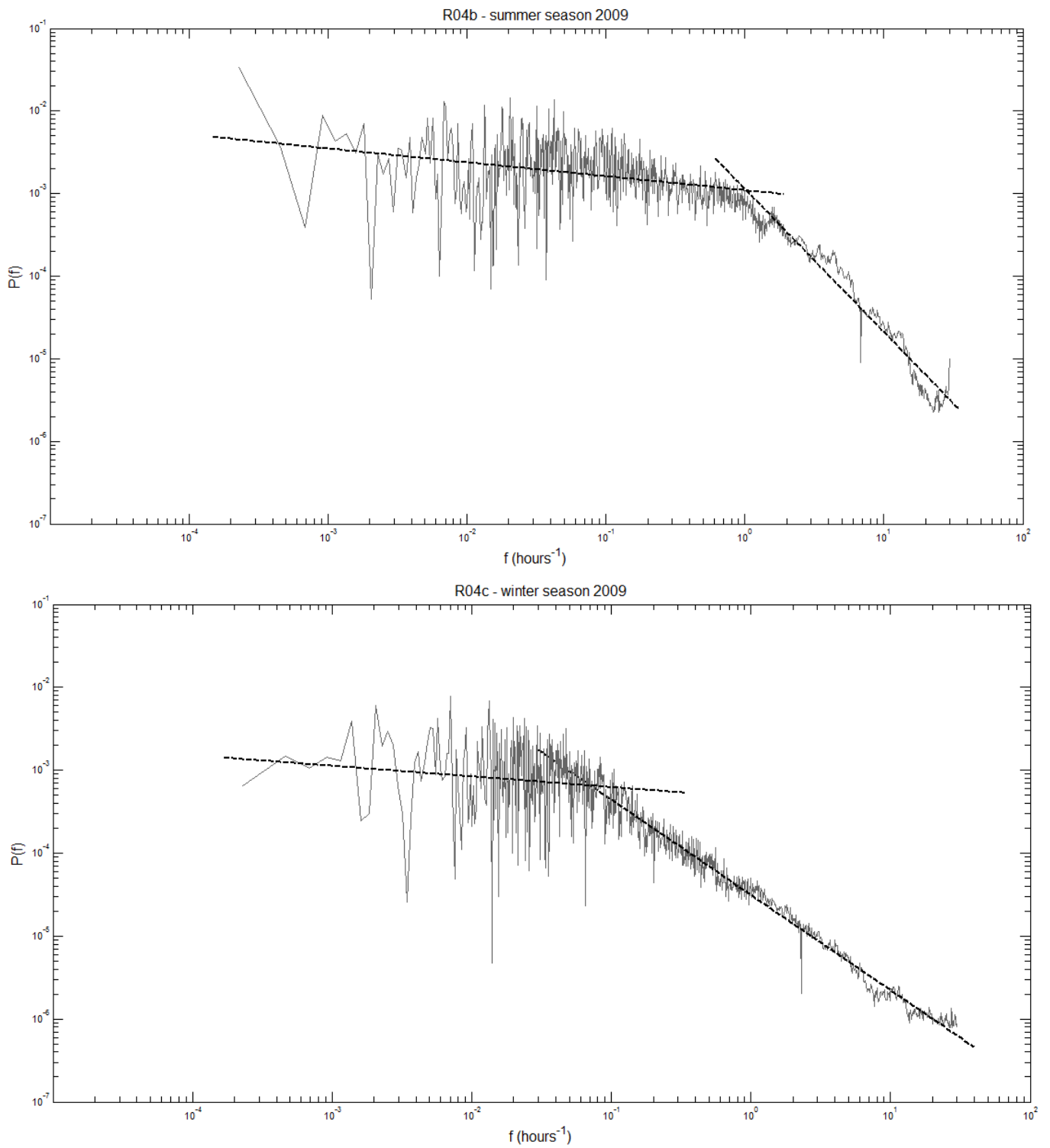


**Figure III.26.** Energy spectra for 1-minute rainfall time-series from Warsaw, for rain gauge R04 in 2009. Summer season (upper graph) and winter season (lower graph)

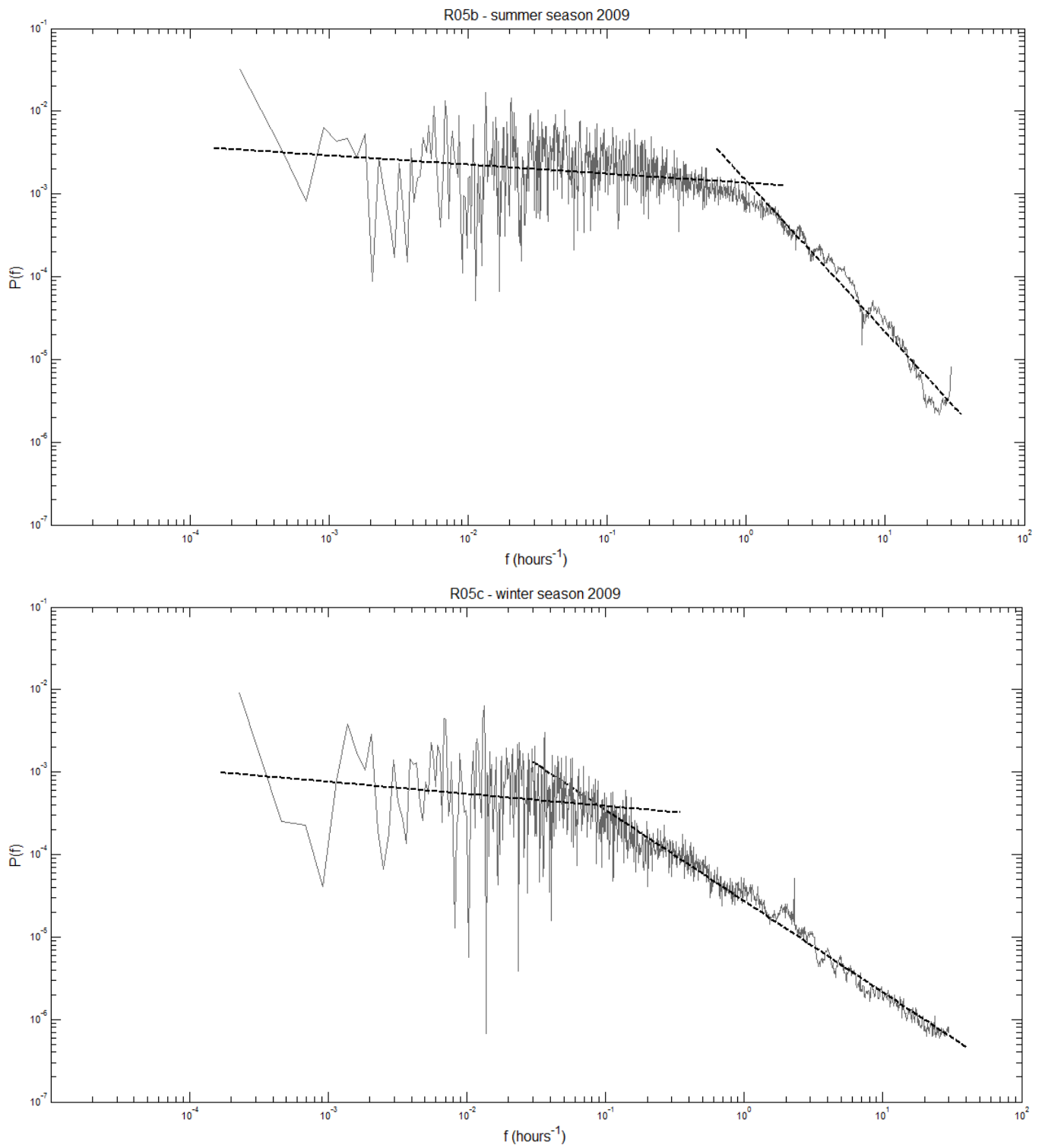


**Figure III.27.** Energy spectra for 1-minute rainfall time-series from Warsaw, for rain gauge R05 in 2009. Summer season (upper graph) and winter season (lower graph)

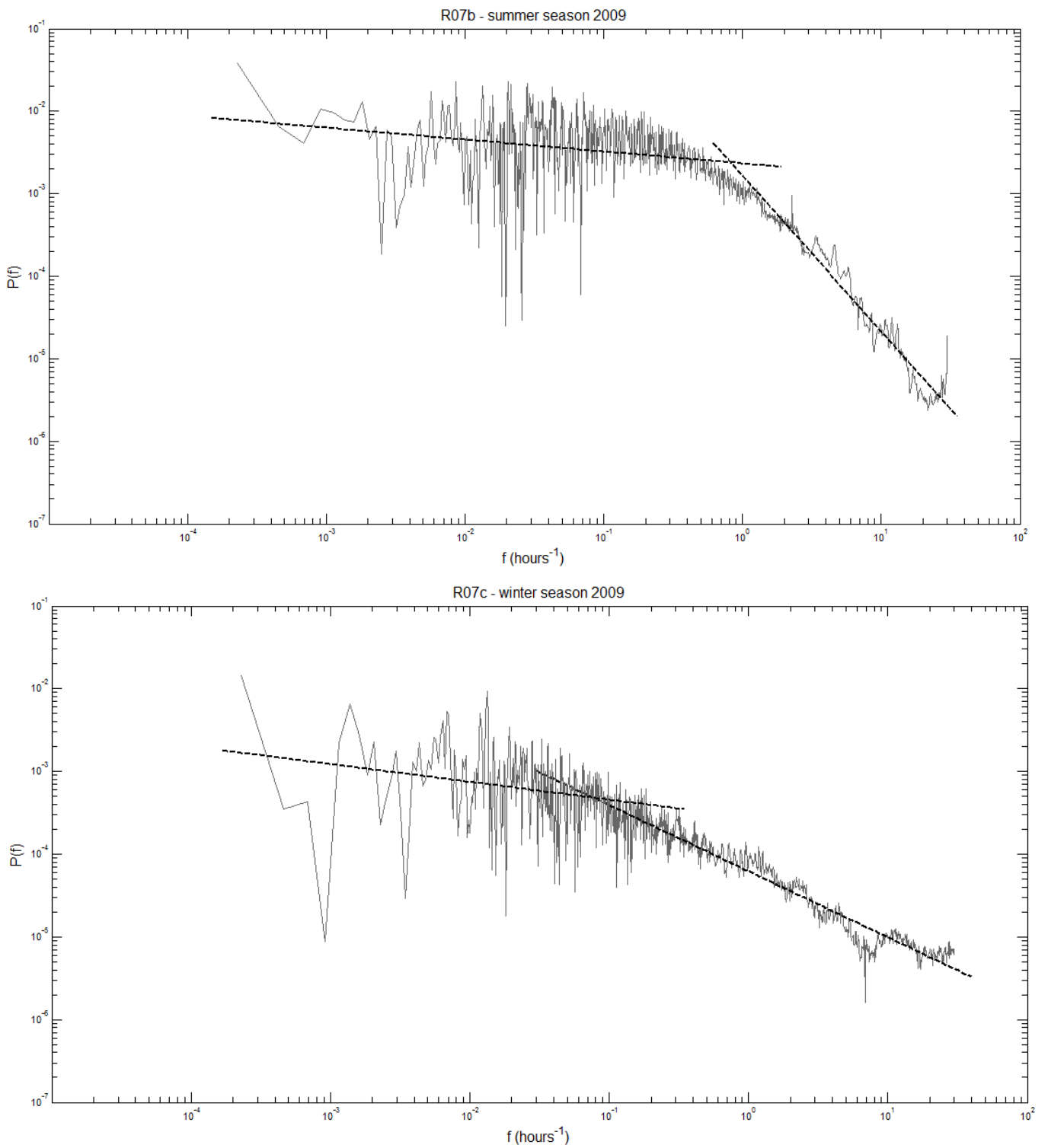


**Figure III.28.** Energy spectra for 1-minute rainfall time-series from Warsaw, for rain gauge R07 in 2009. Summer season (upper graph) and winter season (lower graph)

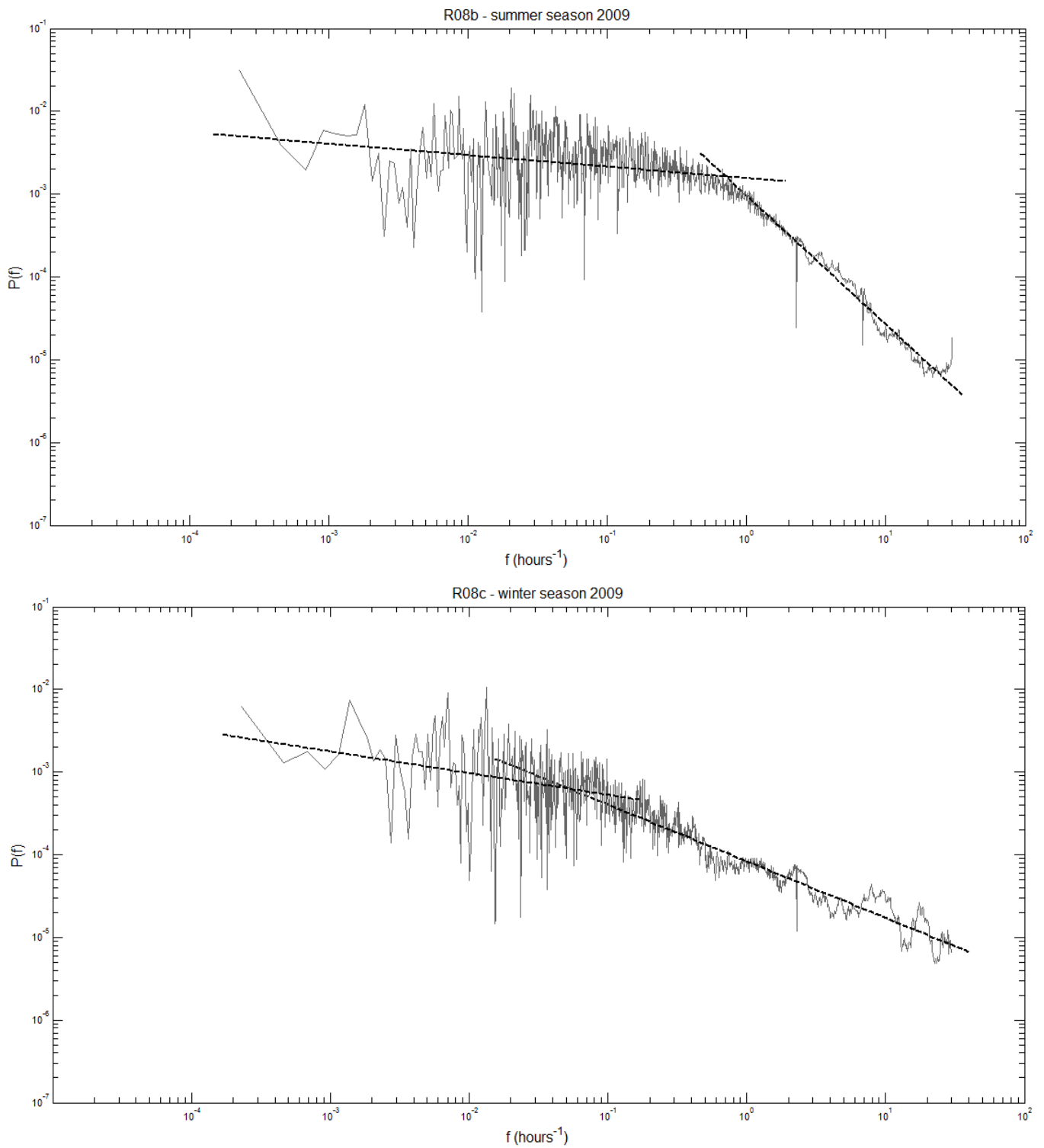


**Figure III.29.** Energy spectra for 1-minute rainfall time-series from Warsaw, for rain gauge R08 in 2009. Summer season (upper graph) and winter season (lower graph)

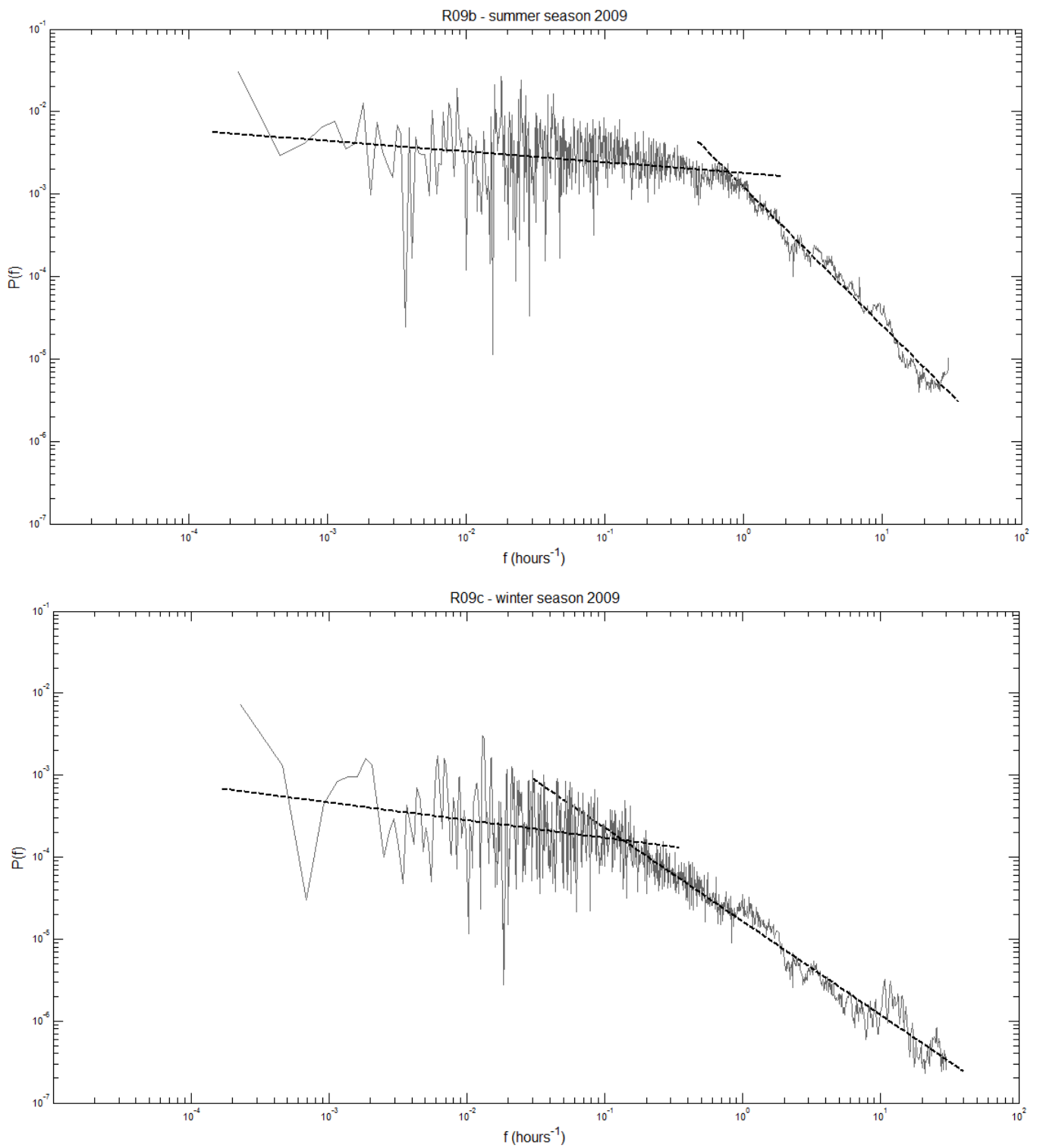


**Figure III.30.** Energy spectra for 1-minute rainfall time-series from Warsaw, for rain gauge R09 in 2009. Summer season (upper graph) and winter season (lower graph)

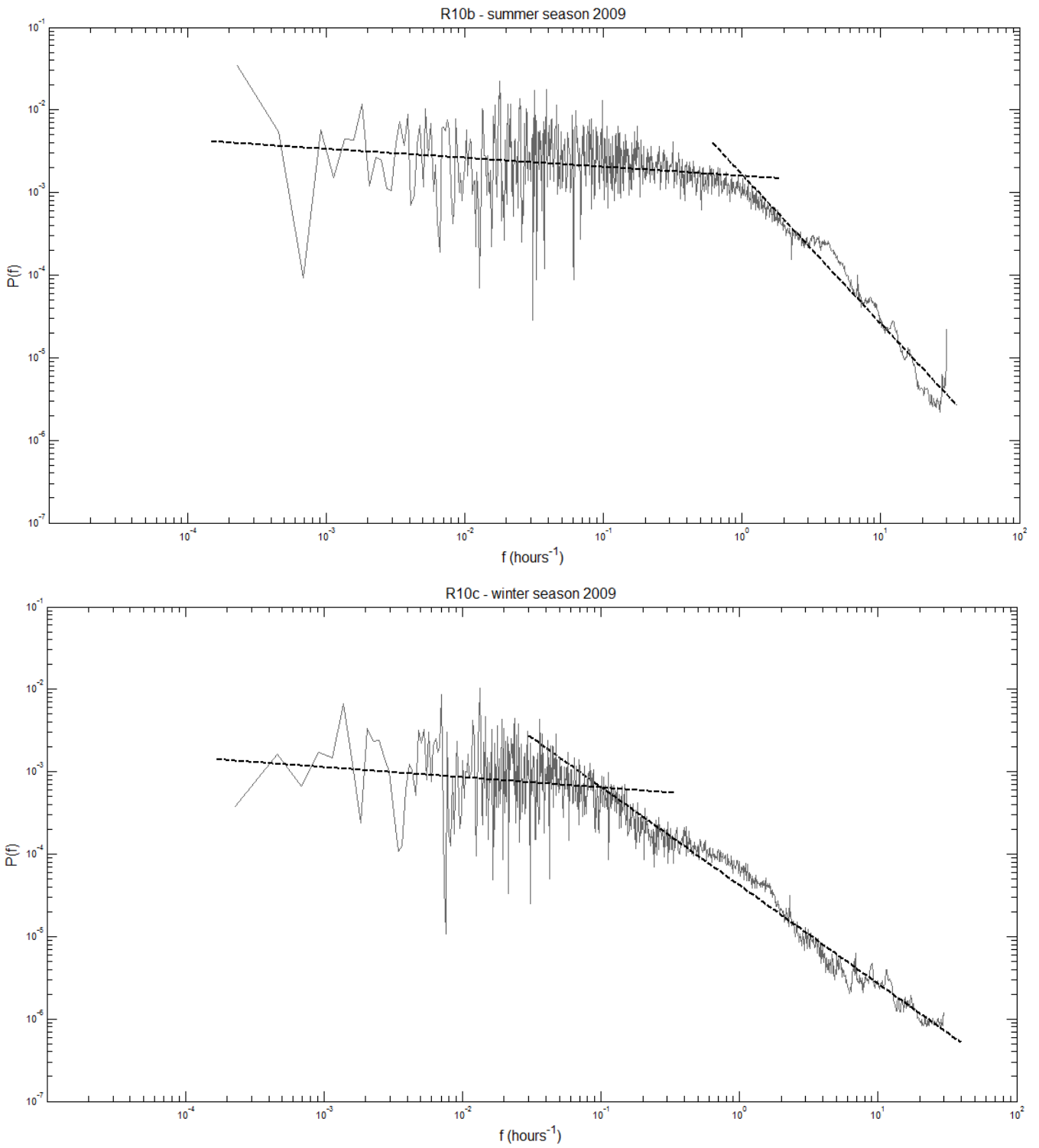


**Figure III.31.** Energy spectra for 1-minute rainfall time-series from Warsaw, for rain gauge R10 in 2009. Summer season (upper graph) and winter season (lower graph)

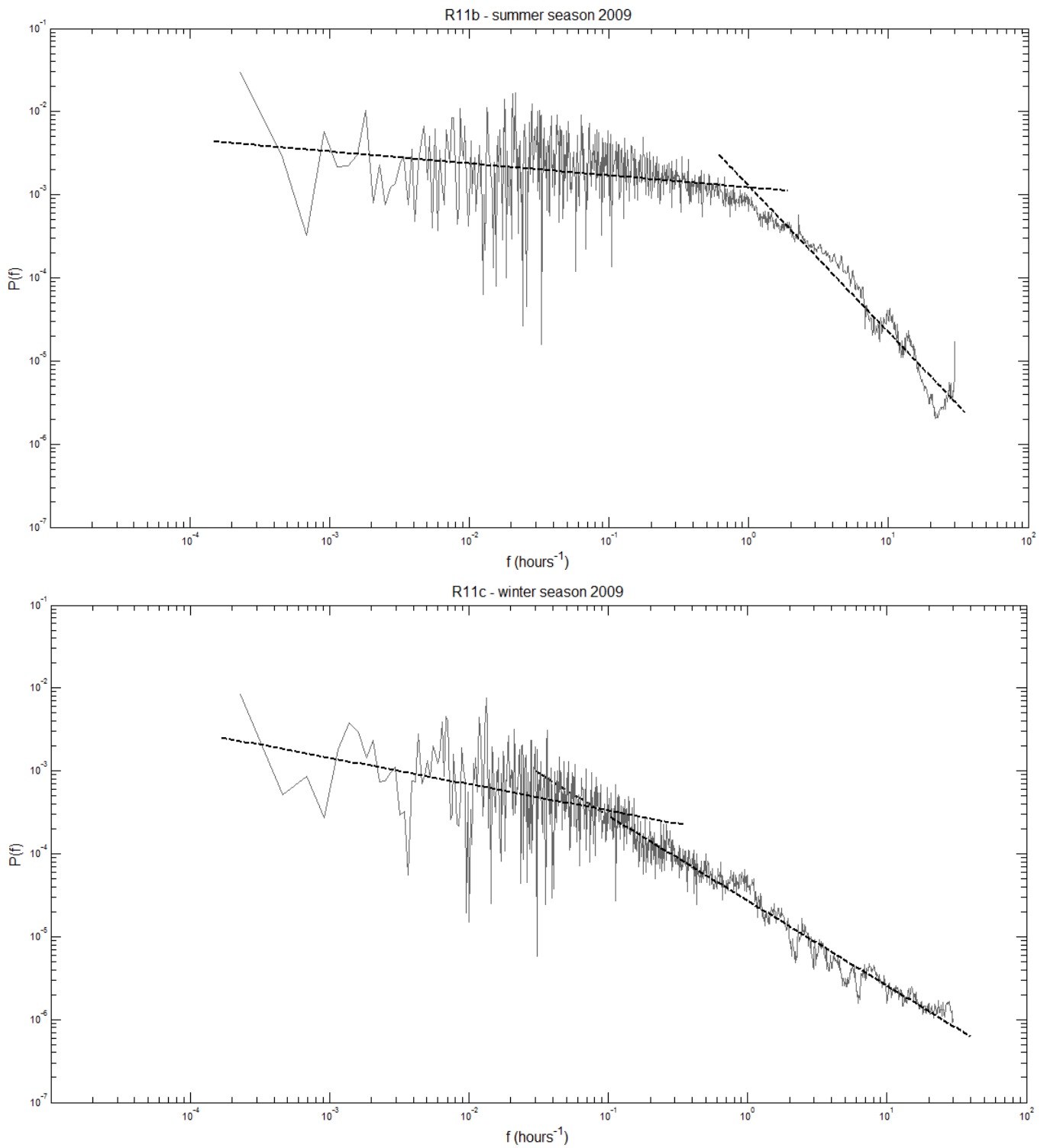


**Figure III.32.** Energy spectra for 1-minute rainfall time-series from Warsaw, for rain gauge R11 in 2009. Summer season (upper graph) and winter season (lower graph)

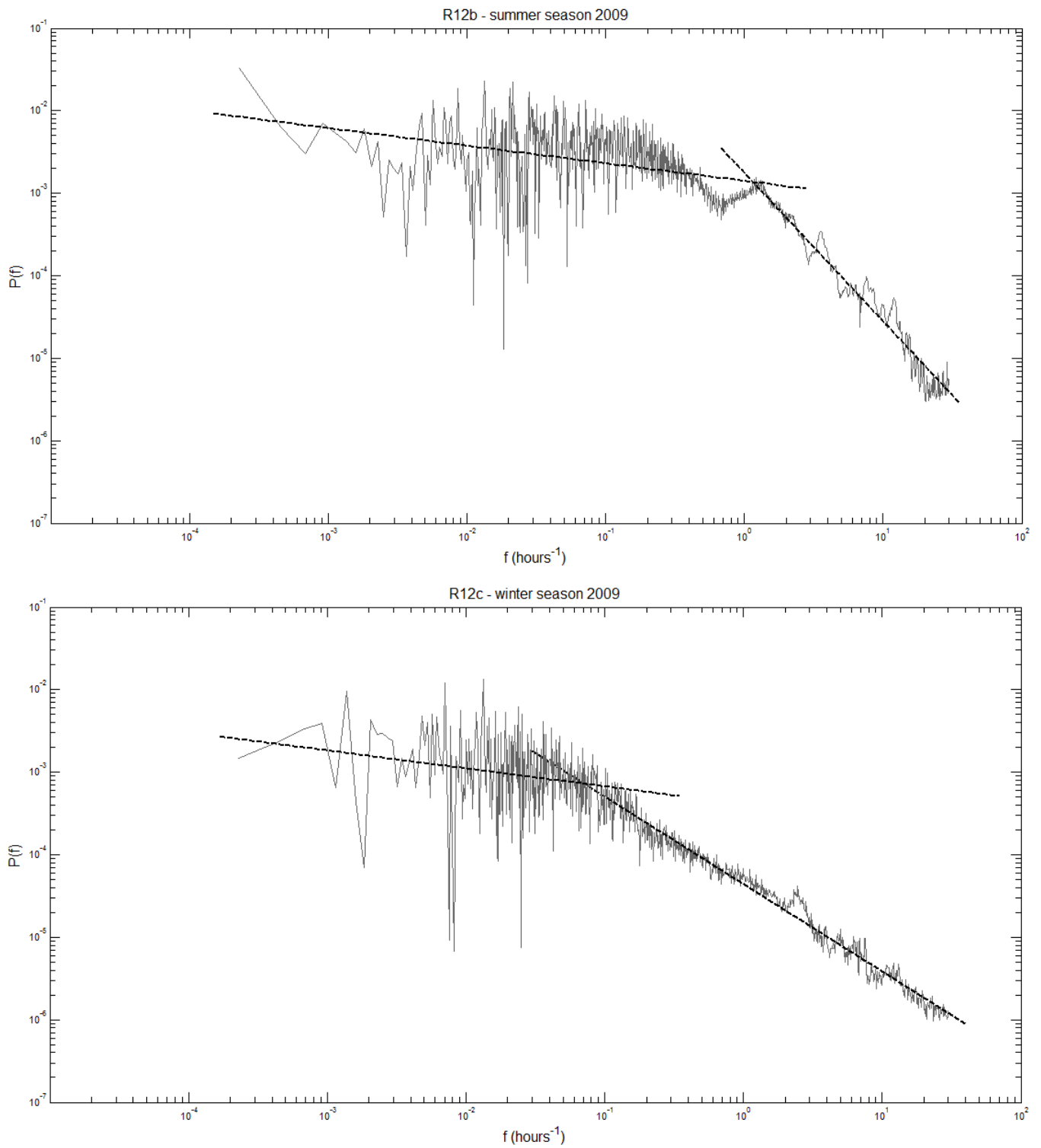


**Figure III.33.** Energy spectra for 1-minute rainfall time-series from Warsaw, for rain gauge R12 in 2009. Summer season (upper graph) and winter season (lower graph)

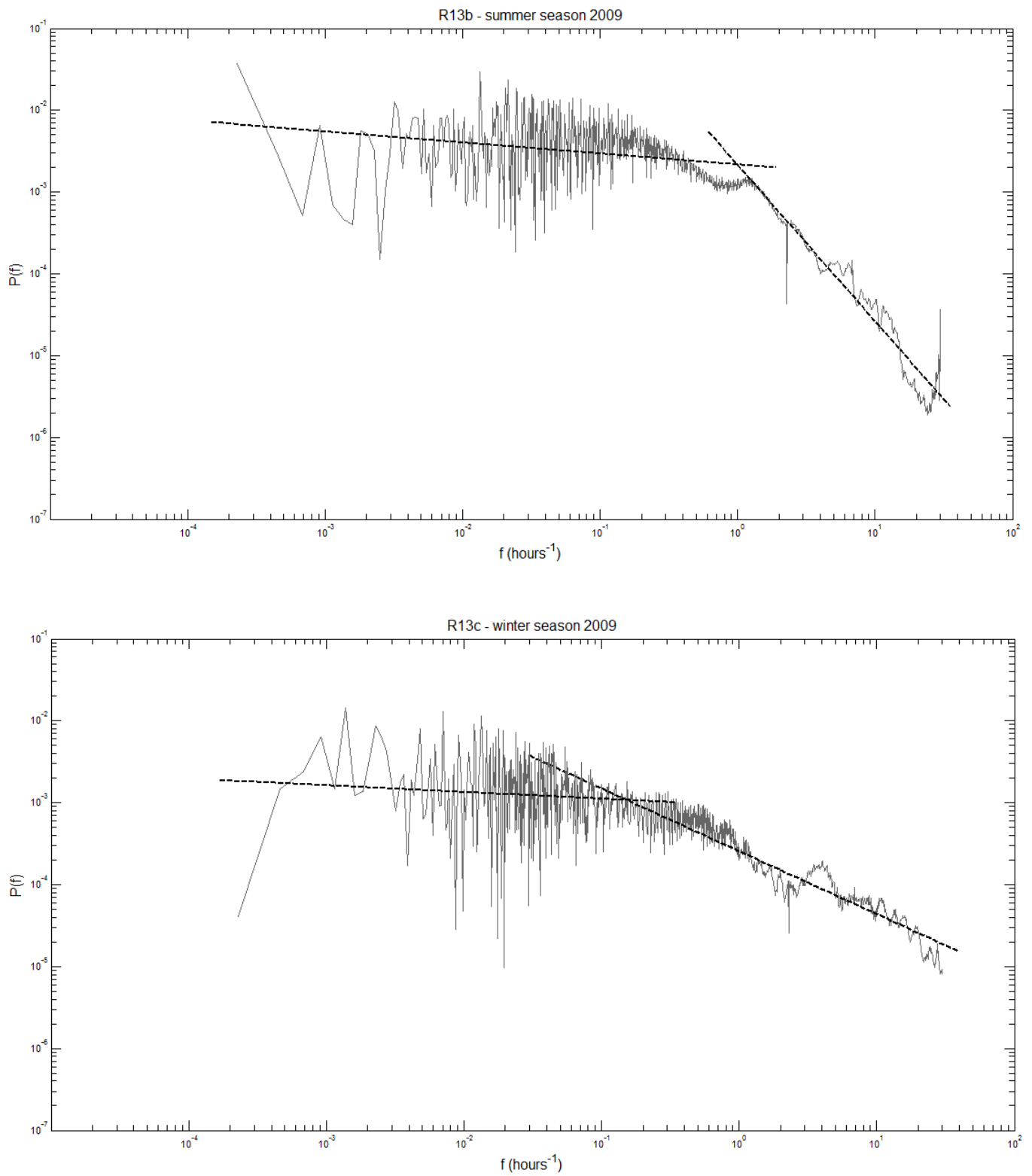


**Figure III.34.** Energy spectra for 1-minute rainfall time-series from Warsaw, for rain gauge R13 in 2009. Summer season (upper graph) and winter season (lower graph)

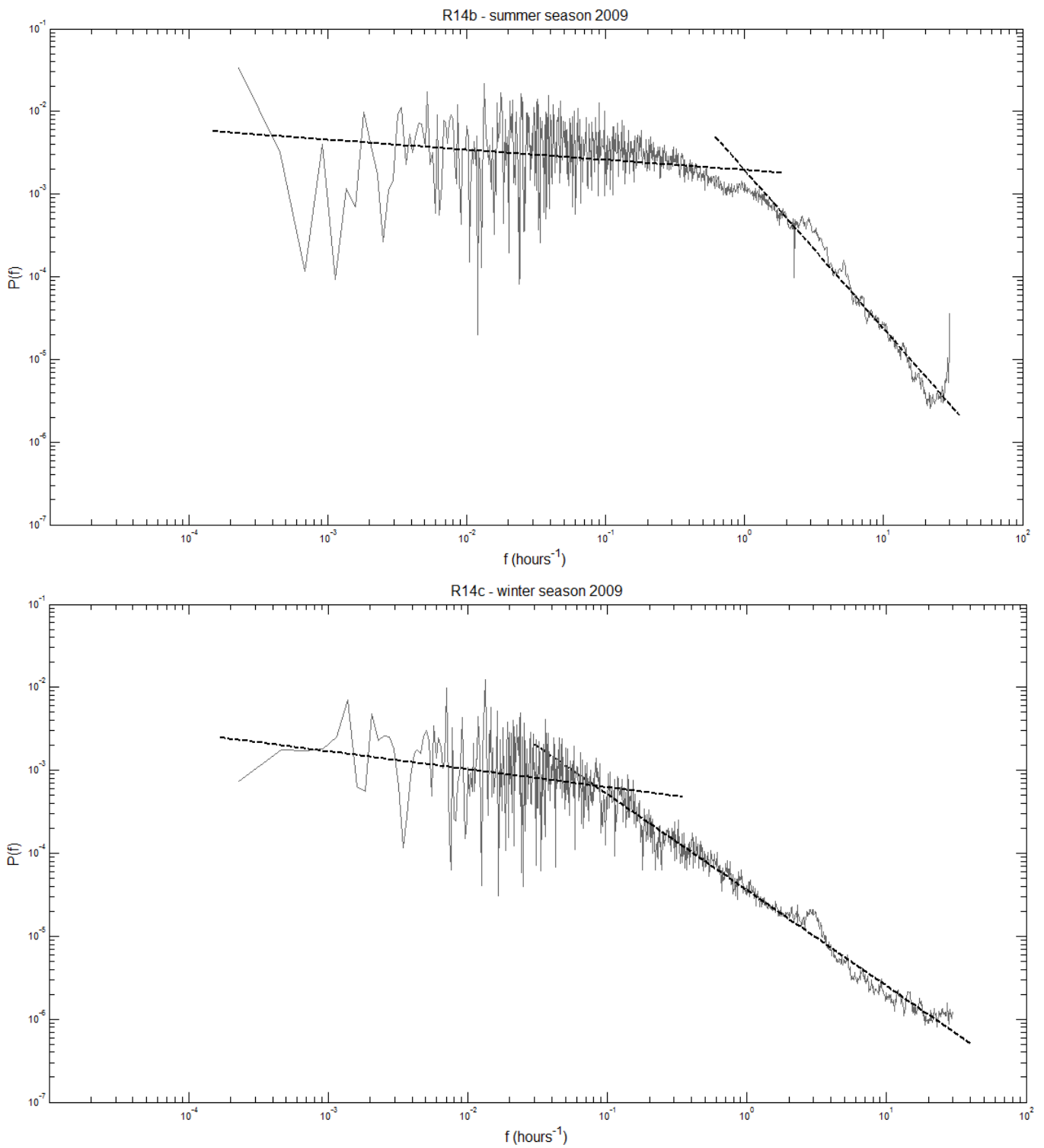


**Figure III.35.** Energy spectra for 1-minute rainfall time-series from Warsaw, for rain gauge R14 in 2009. Summer season (upper graph) and winter season (lower graph)

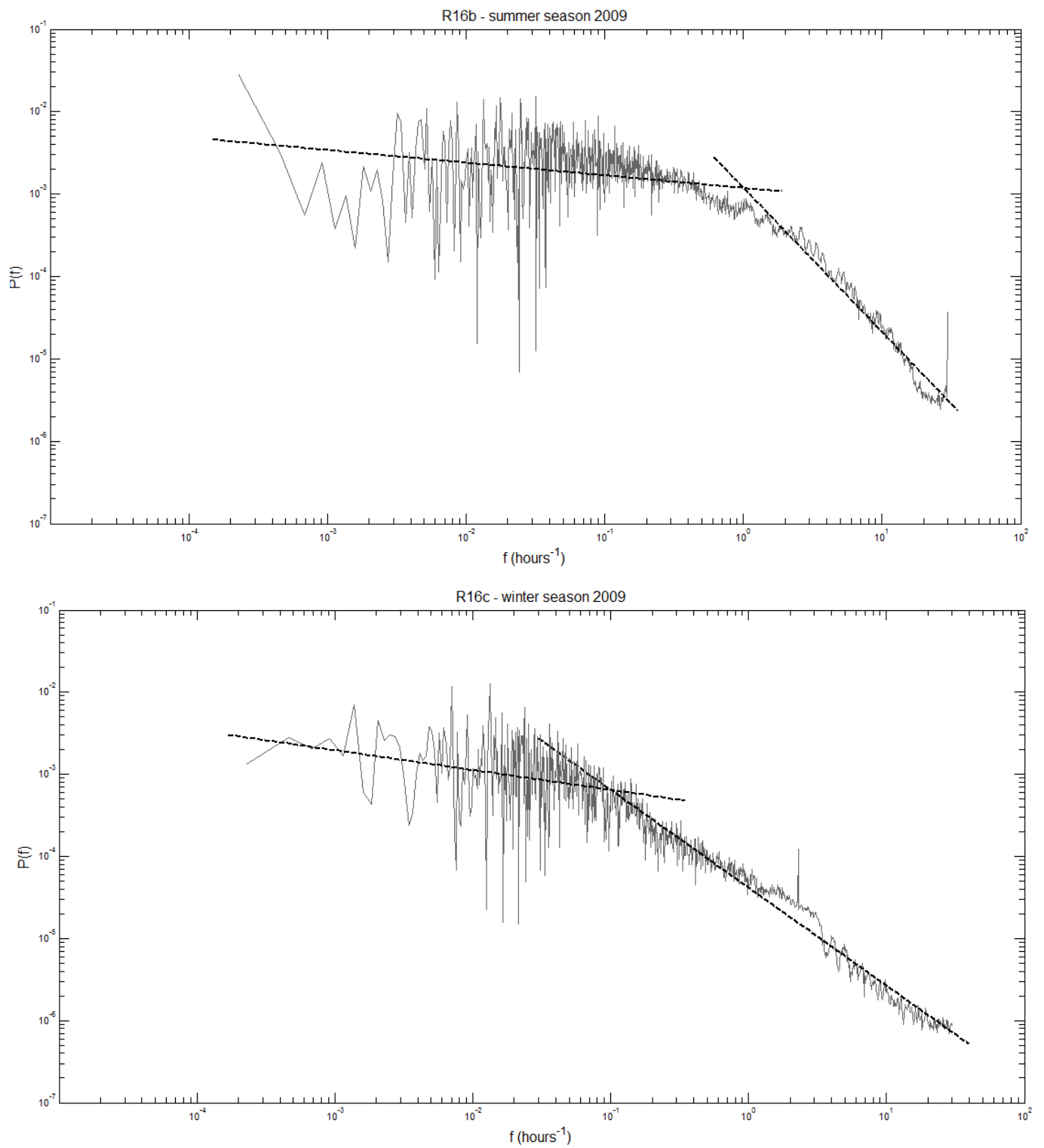


**Figure III.36.** Energy spectra for 1-minute rainfall time-series from Warsaw, for rain gauge R16 in 2009. Summer season (upper graph) and winter season (lower graph)

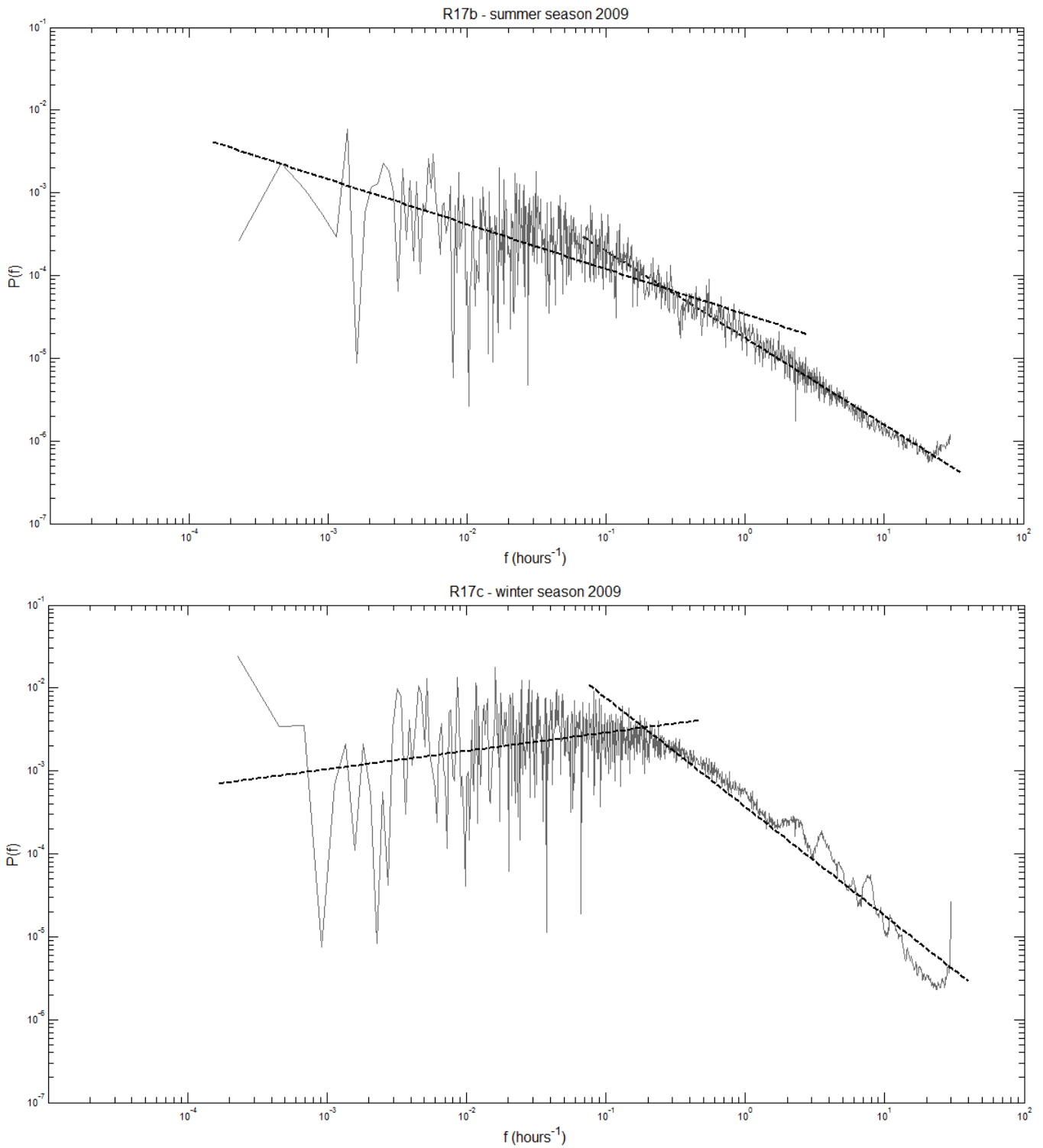


**Figure III.37.** Energy spectra for 1-minute rainfall time-series from Warsaw, for rain gauge R17 in 2009. Summer season (upper graph) and winter season (lower graph)

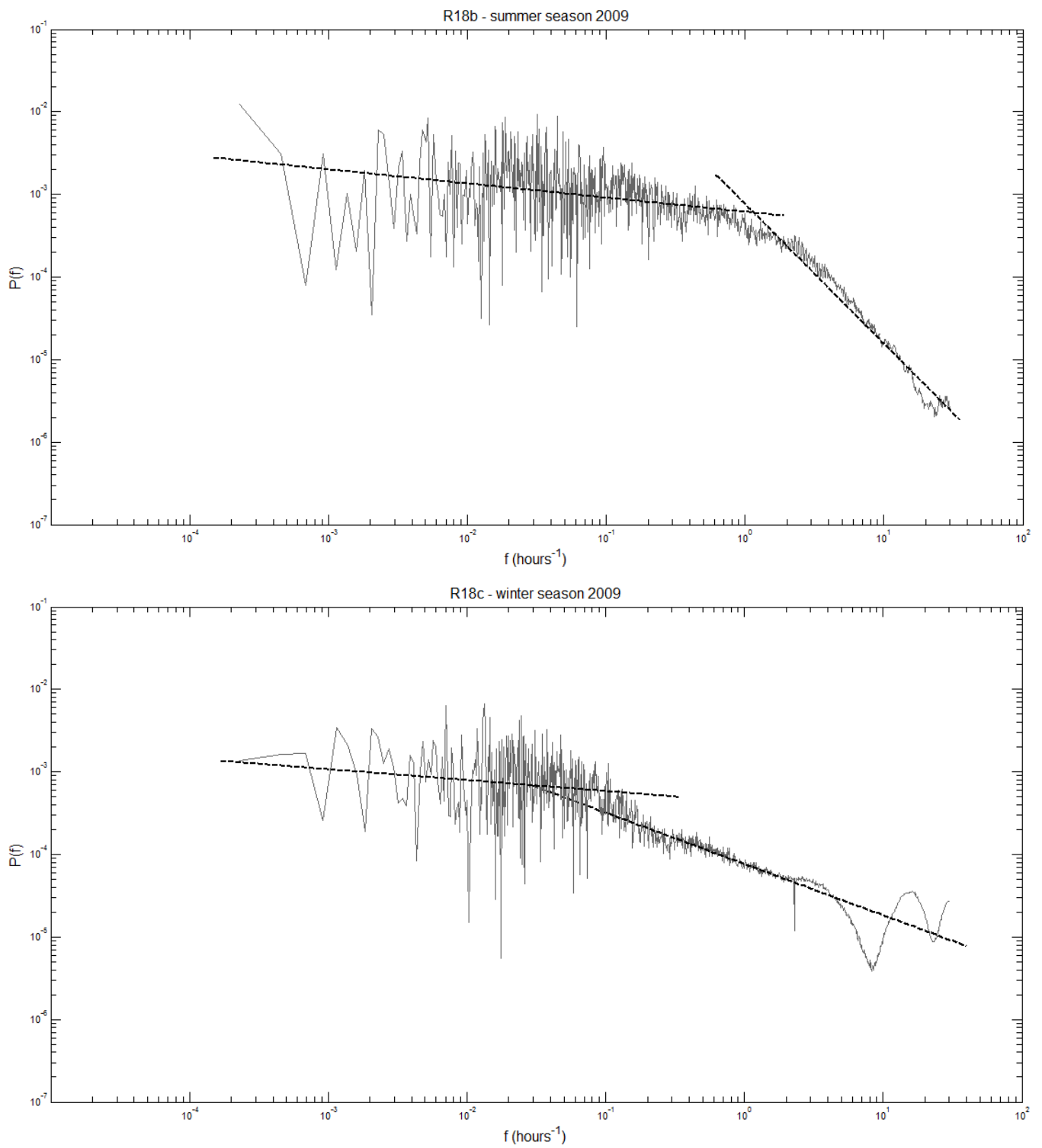


**Figure III.38.** Energy spectra for 1-minute rainfall time-series from Warsaw, for rain gauge R18 in 2009. Summer season (upper graph) and winter season (lower graph)

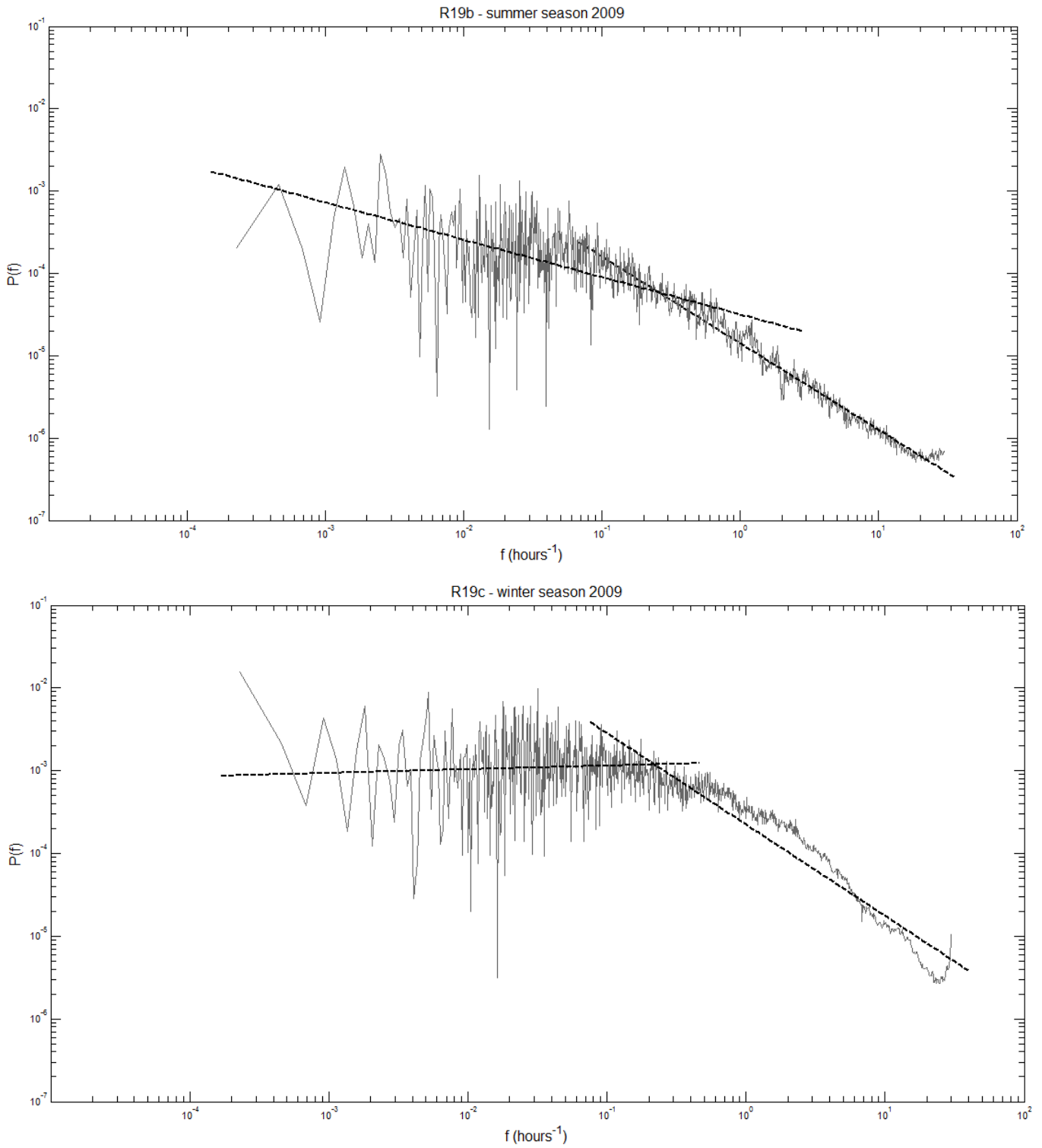


**Figure III.39.** Energy spectra for 1-minute rainfall time-series from Warsaw, for rain gauge R19 in 2009. Summer season (upper graph) and winter season (lower graph)

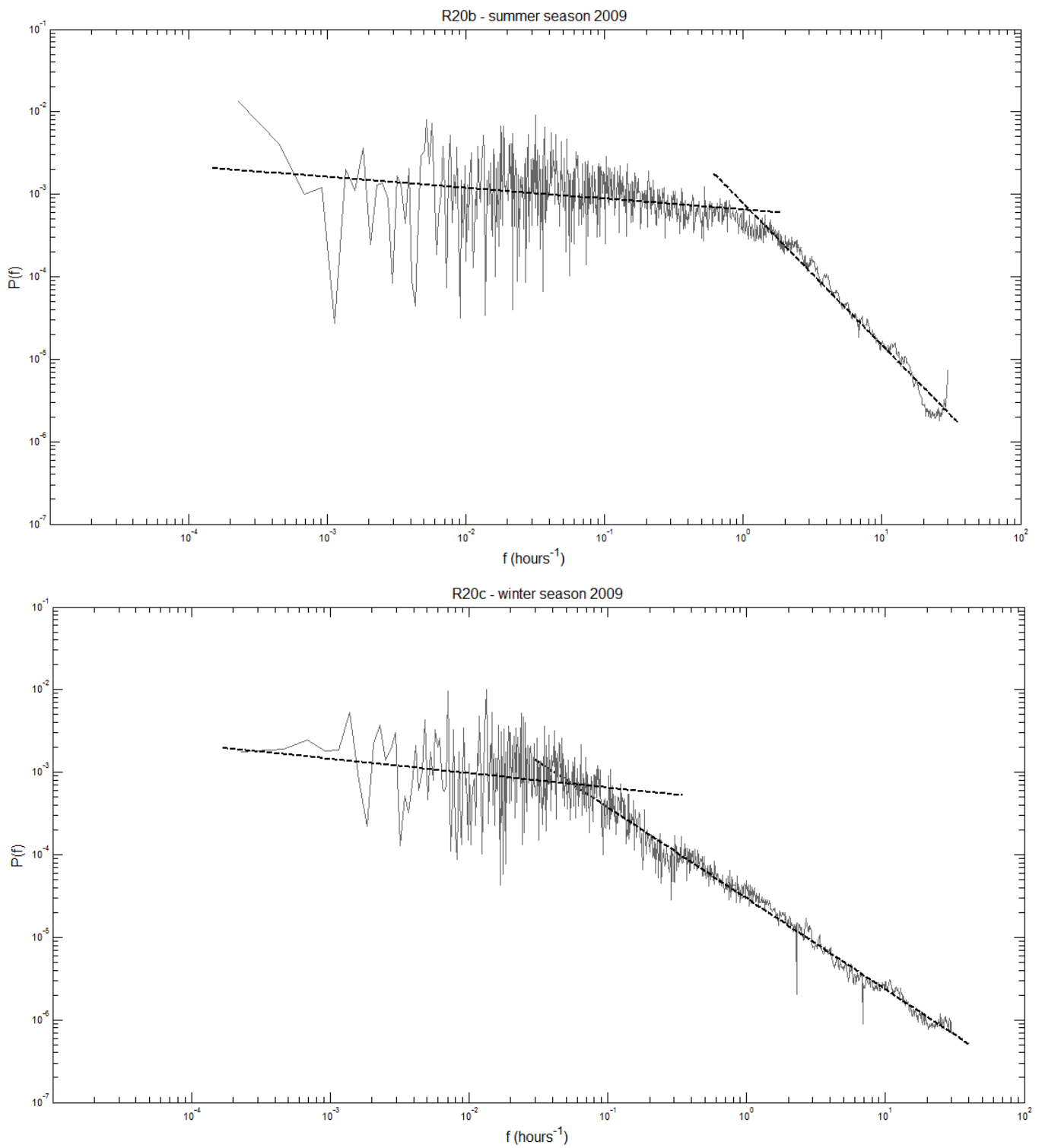


**Figure III.40.** Energy spectra for 1-minute rainfall time-series from Warsaw, for rain gauge R20 in 2009. Summer season (upper graph) and winter season (lower graph)

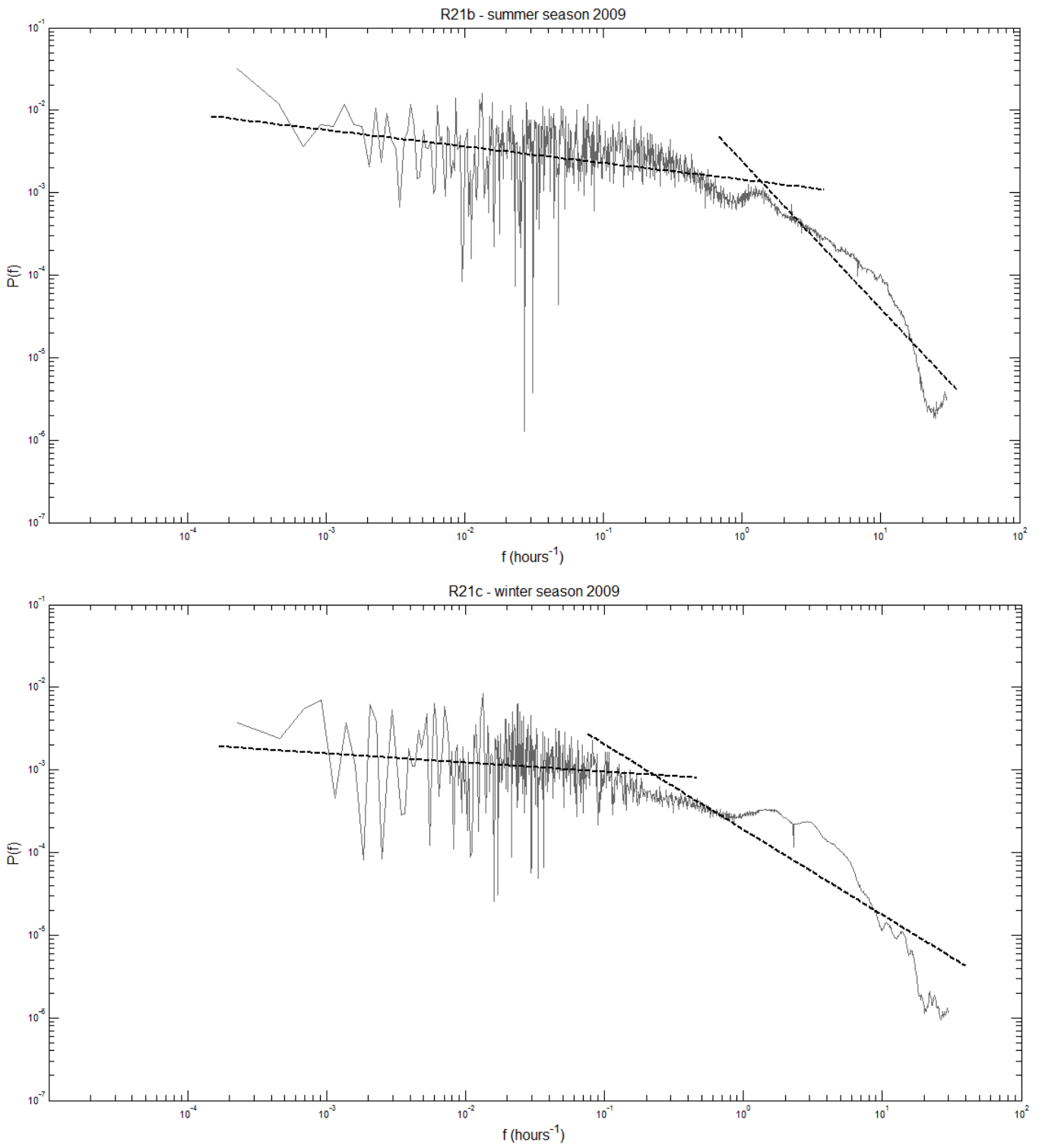


**Figure III.41.** Energy spectra for 1-minute rainfall time-series from Warsaw, for rain gauge R21 in 2009. Summer season (upper graph) and winter season (lower graph)

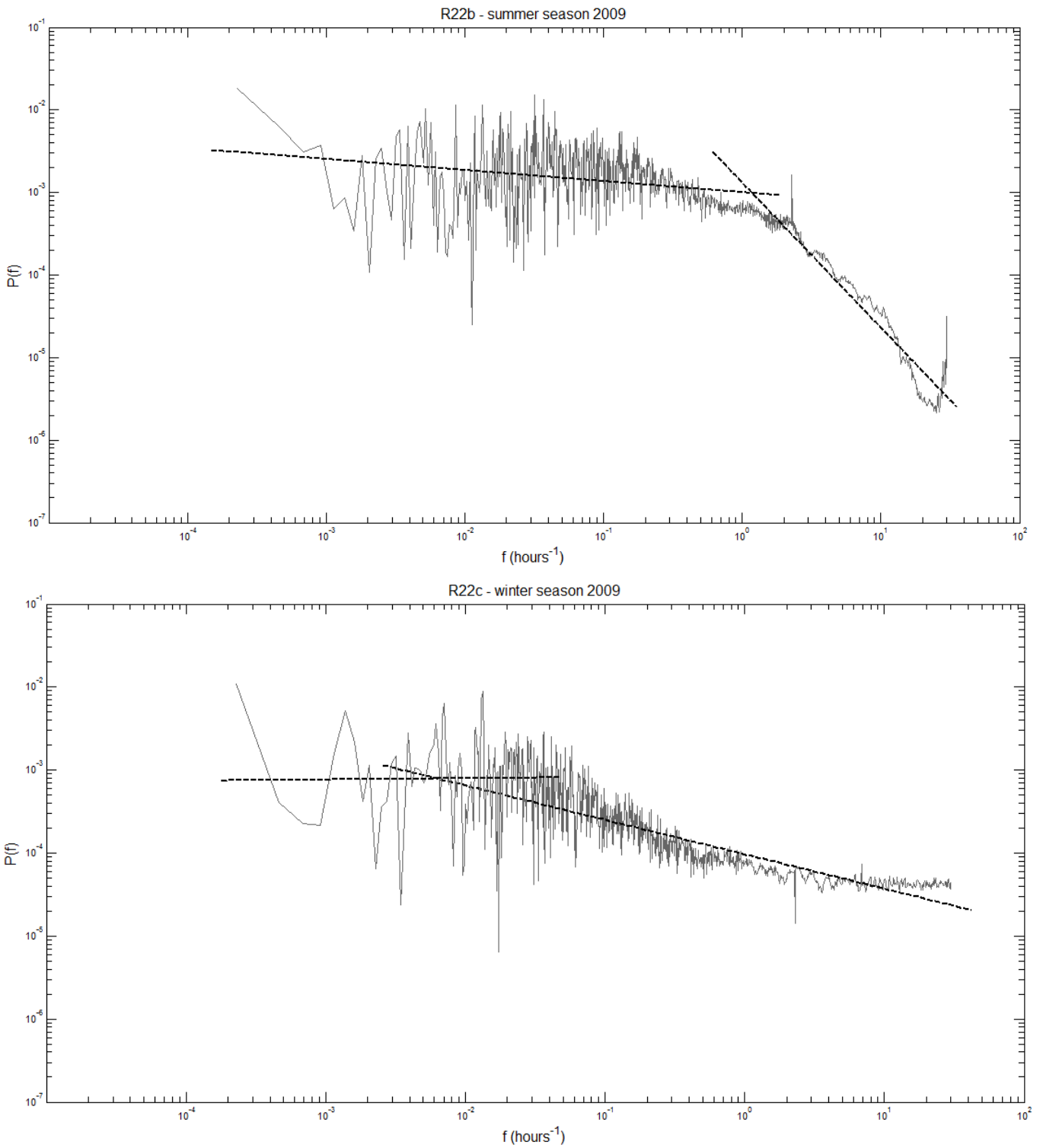


**Figure III.42.** Energy spectra for 1-minute rainfall time-series from Warsaw, for rain gauge R22 in 2009. Summer season (upper graph) and winter season (lower graph)

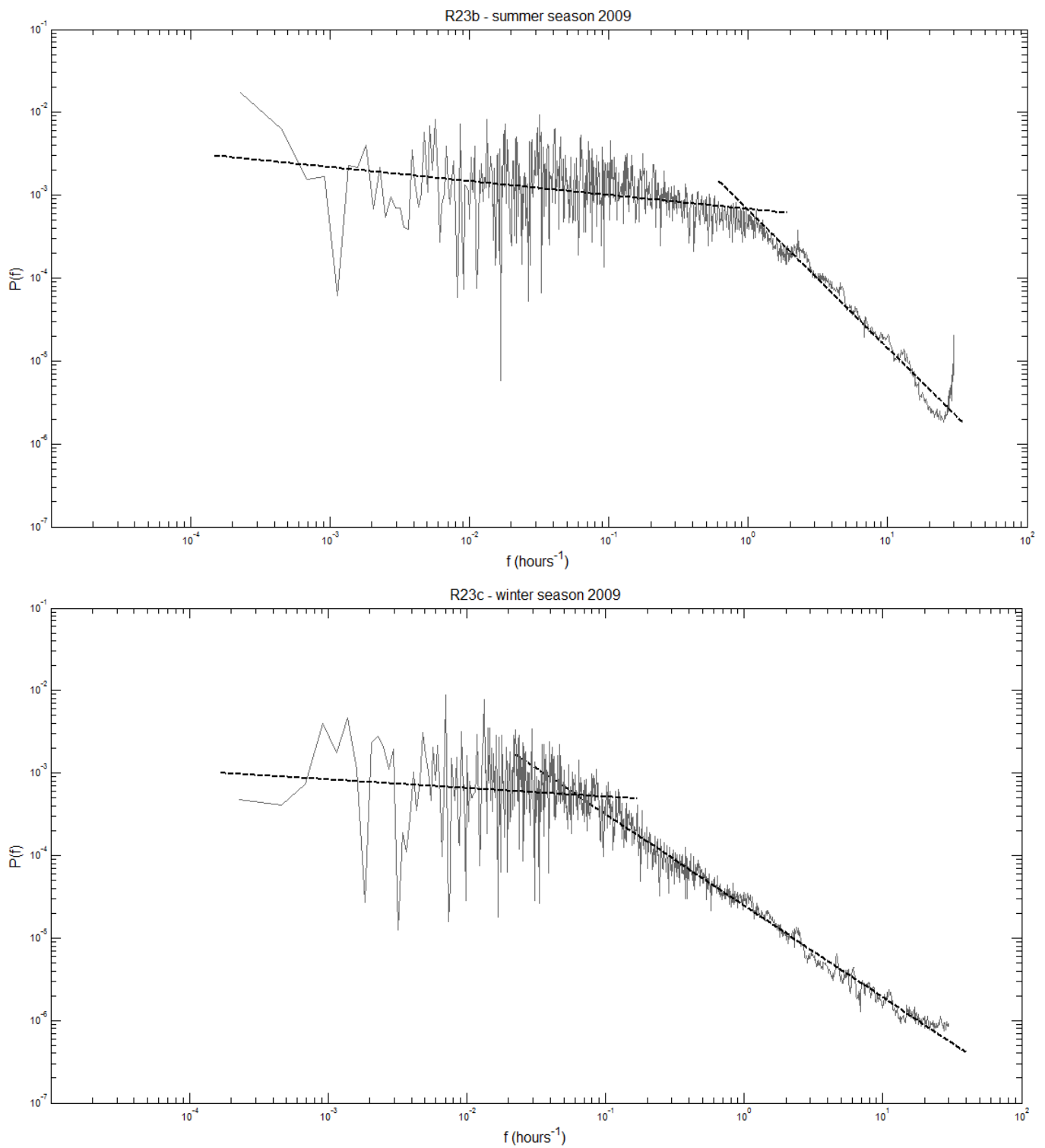


**Figure III.43.** Energy spectra for 1-minute rainfall time-series from Warsaw, for rain gauge R23 in 2009. Summer season (upper graph) and winter season (lower graph)

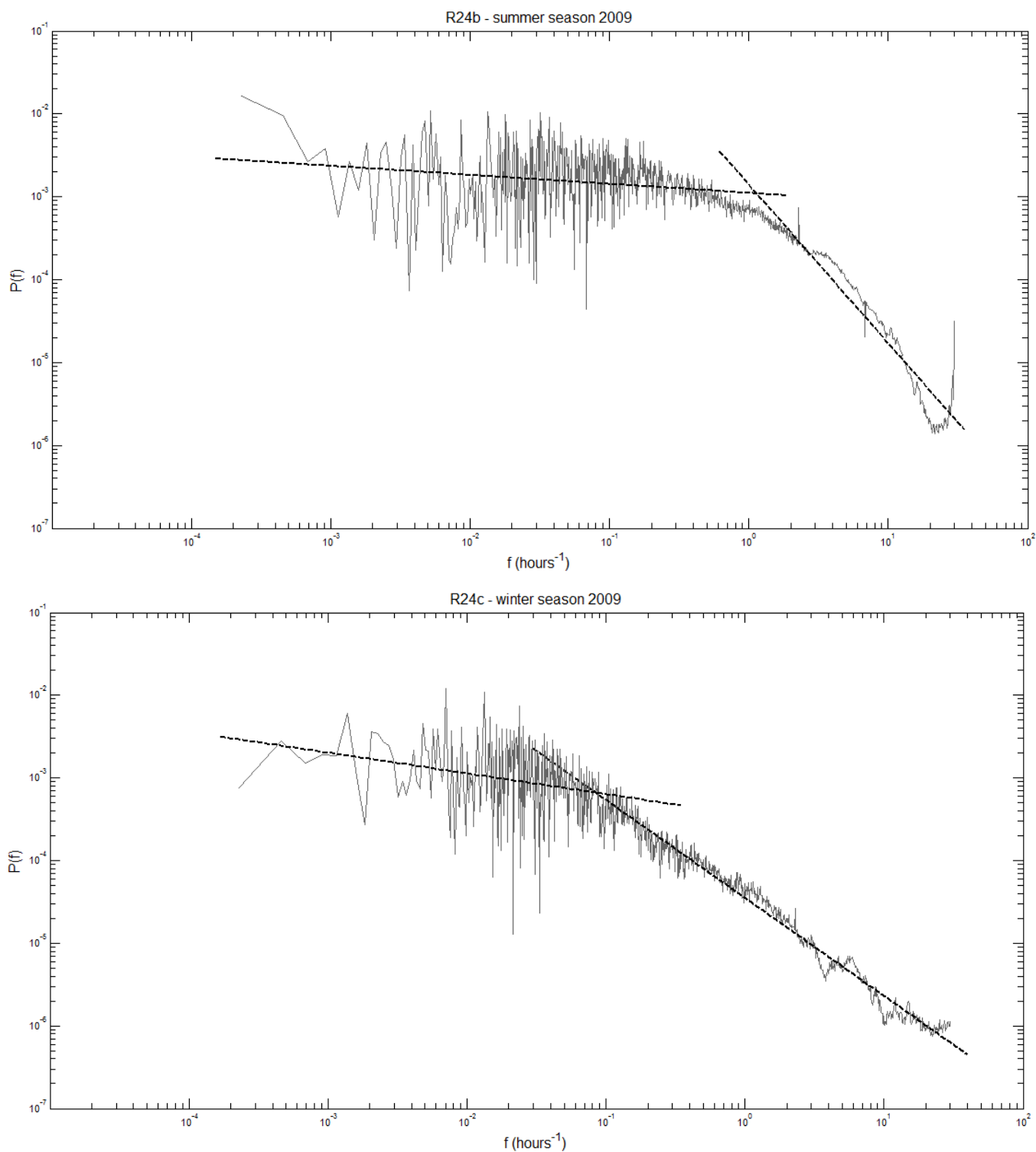


**Figure III.44.** Energy spectra for 1-minute rainfall time-series from Warsaw, for rain gauge R24 in 2009. Summer season (upper graph) and winter season (lower graph)

## Section C

Energy spectra obtained for 1-minute rainfall time-series from Warsaw, recorded from September 2008 to November 2010. The scaling exponent is calculated for all the recorded period.

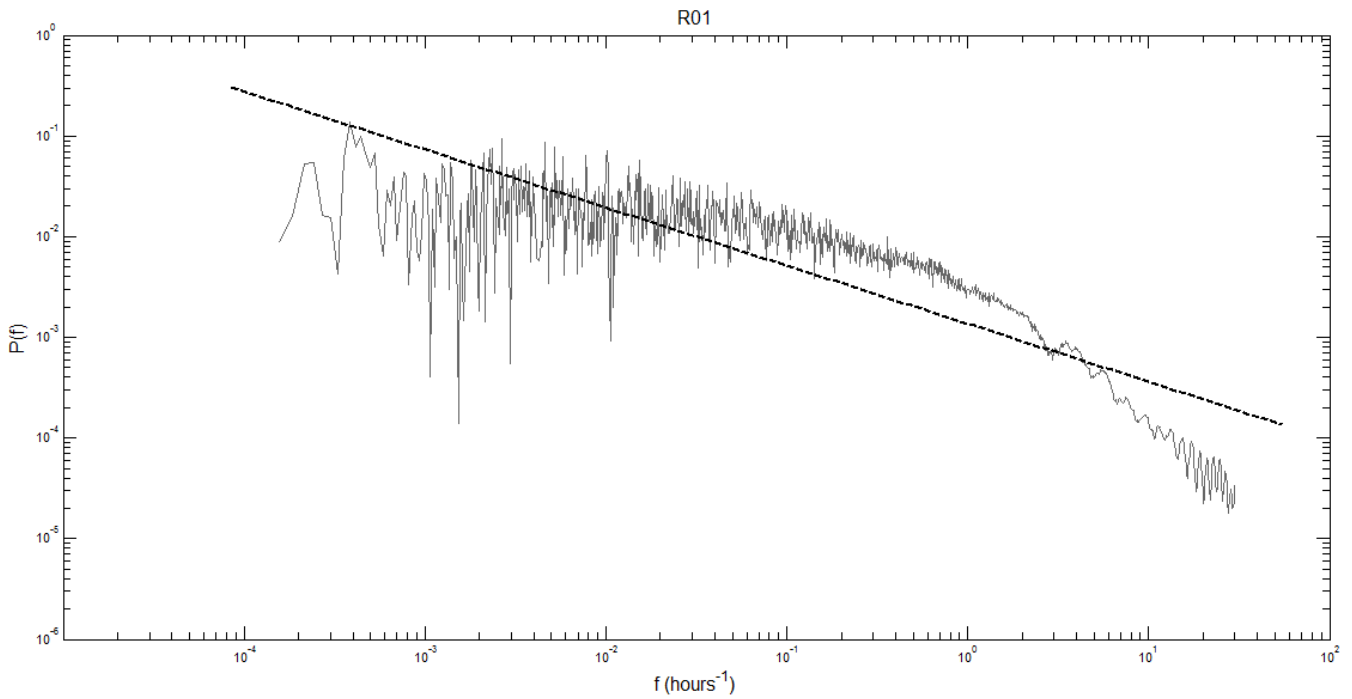


**Figure III.45.** Energy spectrum for 1-minute rainfall time-series from Warsaw, for rain gauge R01 with the overall slope

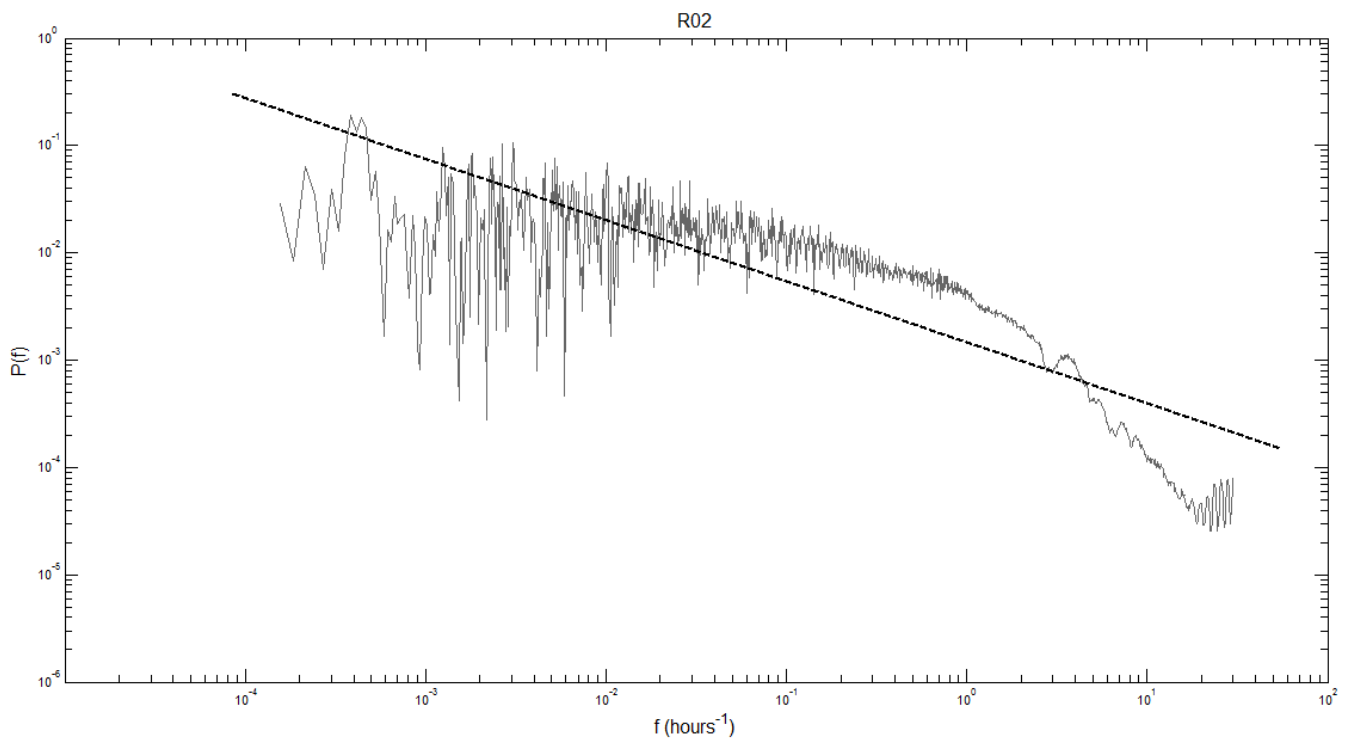


**Figure III.46.** Energy spectrum for 1-minute rainfall time-series from Warsaw, for rain gauge R02 with the overall slope

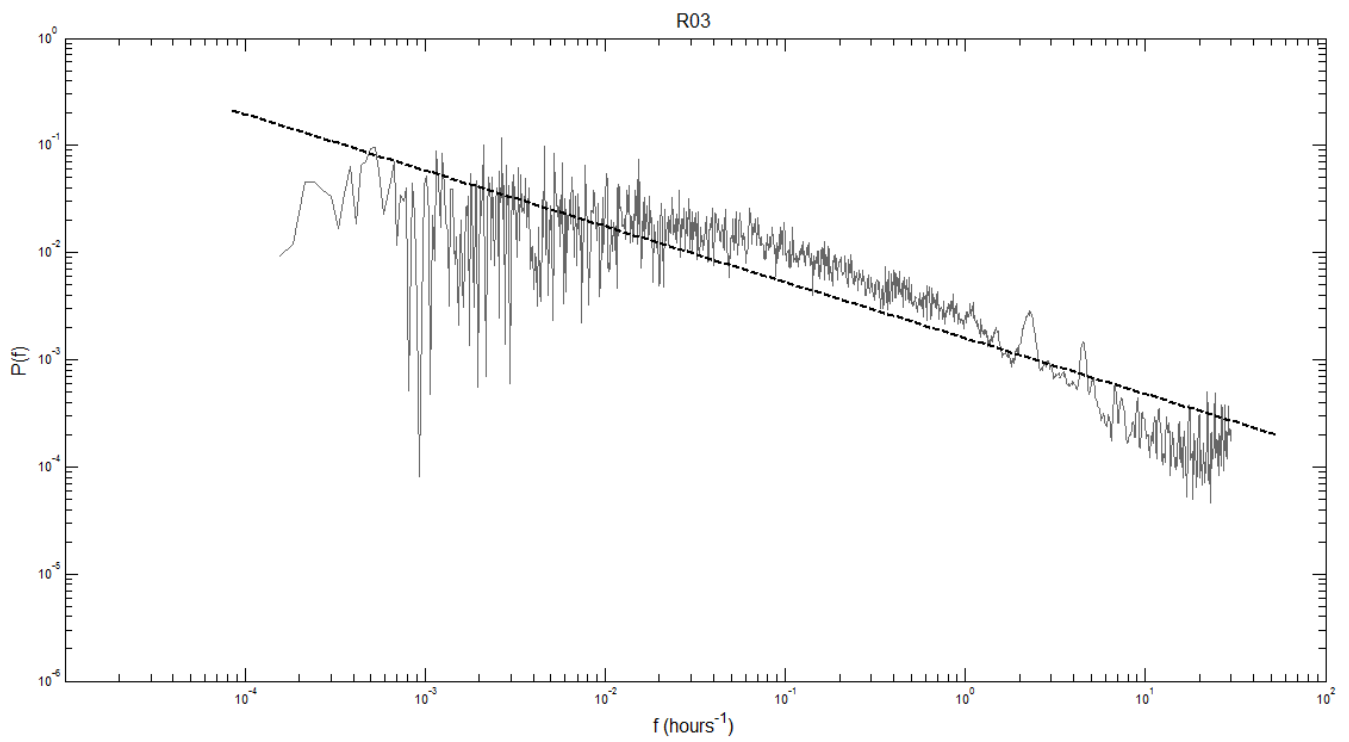


**Figure III.47.** Energy spectrum for 1-minute rainfall time-series from Warsaw, for rain gauge R03 with the overall slope

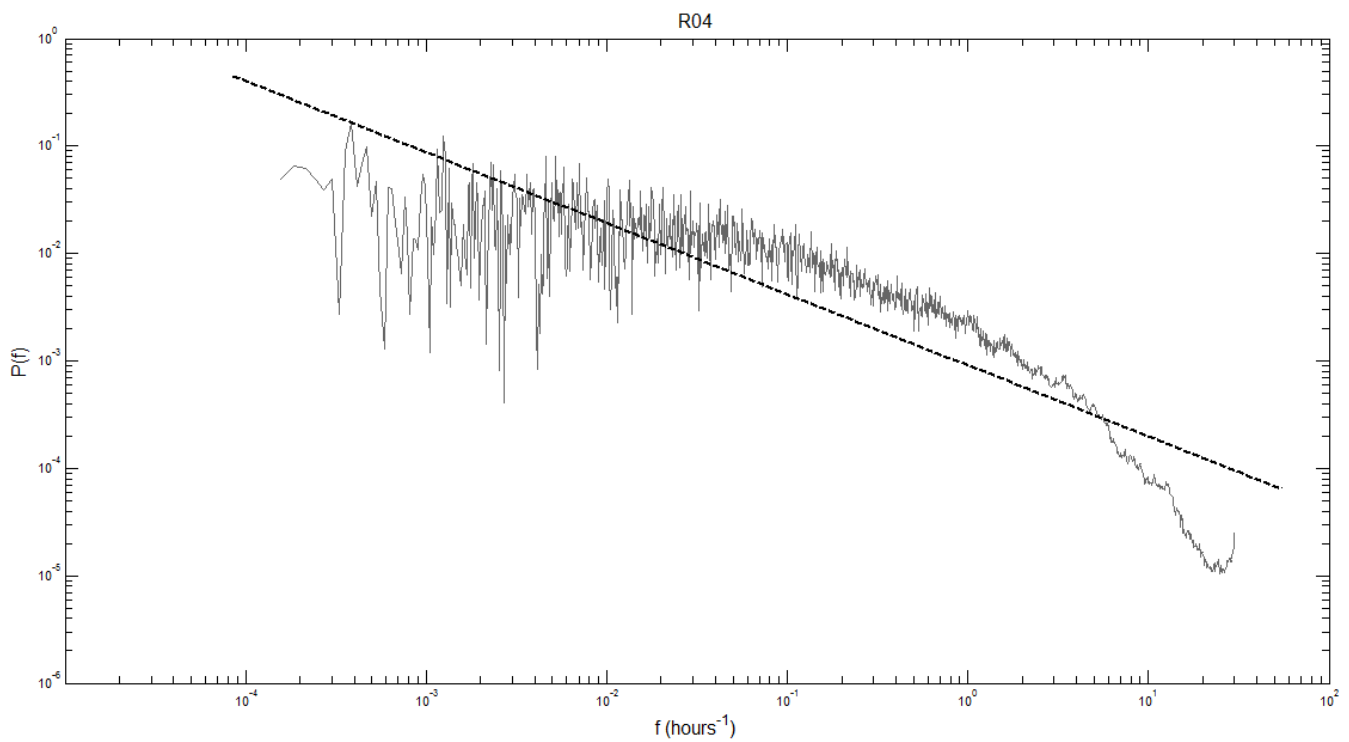


**Figure III.48.** Energy spectrum for 1-minute rainfall time-series from Warsaw, for rain gauge R04 with the overall slope

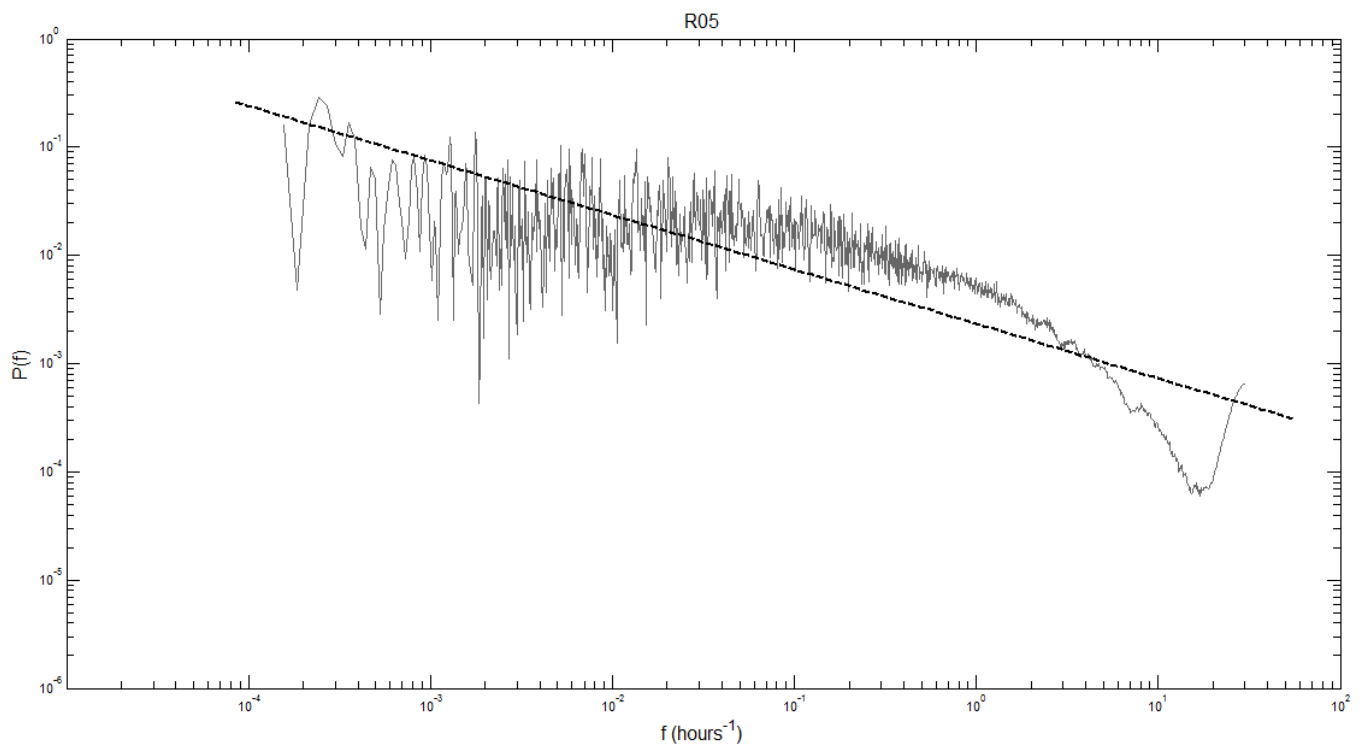


**Figure III.49.** Energy spectrum for 1-minute rainfall time-series from Warsaw, for rain gauge R05 with the overall slope

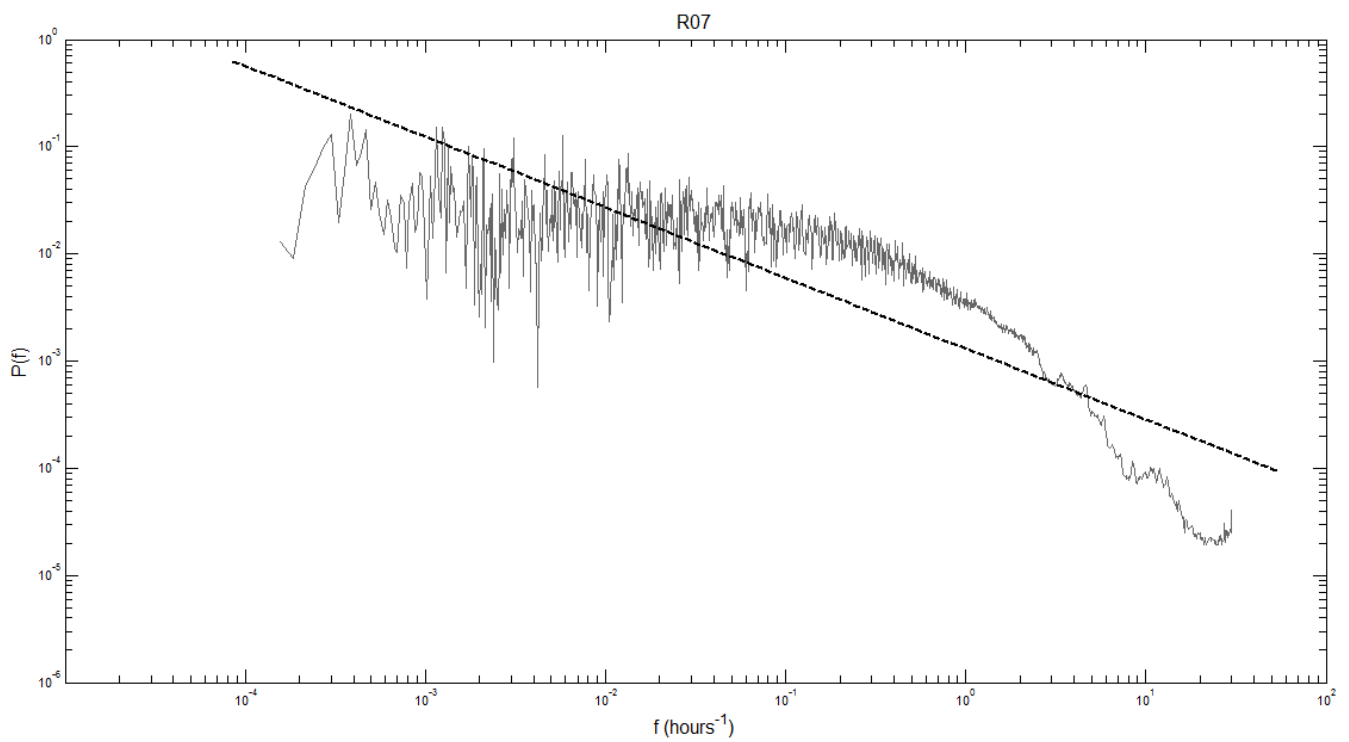


**Figure III.50.** Energy spectrum for 1-minute rainfall time-series from Warsaw, for rain gauge R07 with the overall slope

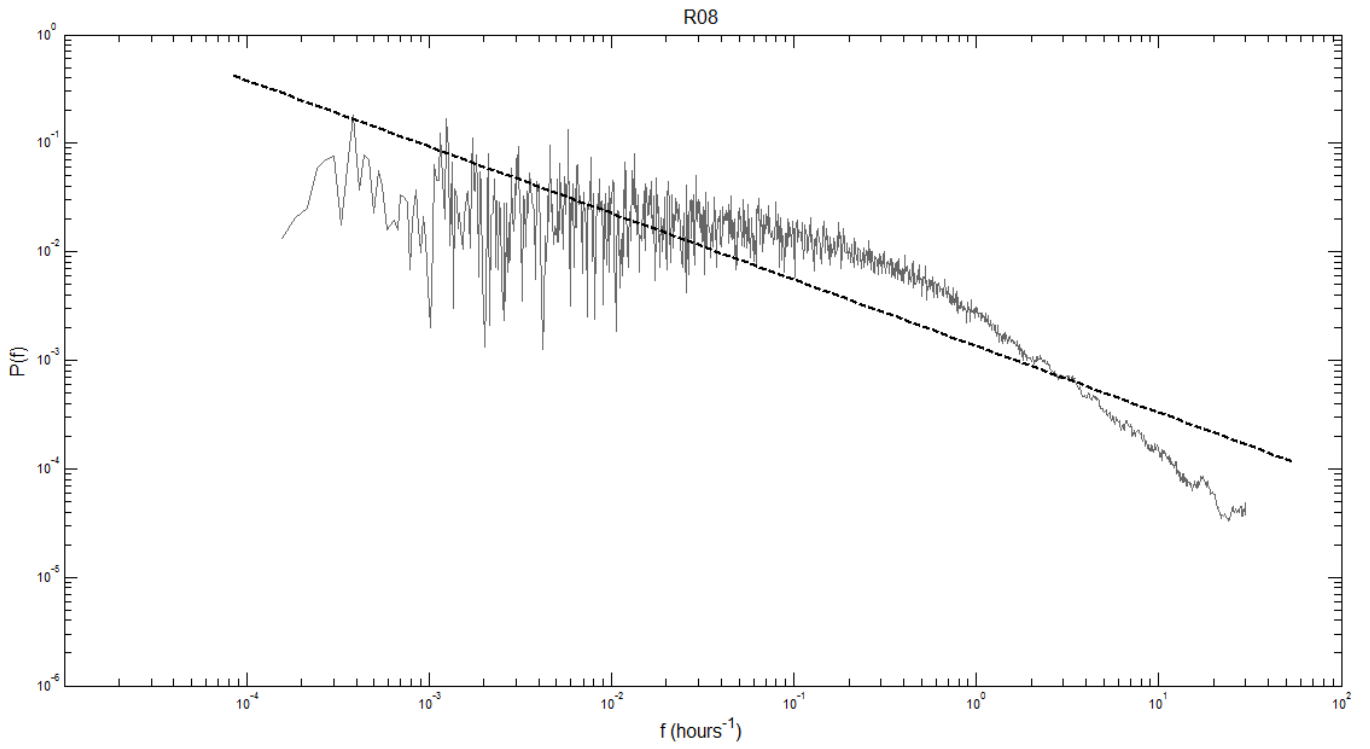


**Figure III.51.** Energy spectrum for 1-minute rainfall time-series from Warsaw, for rain gauge R08 with the overall slope

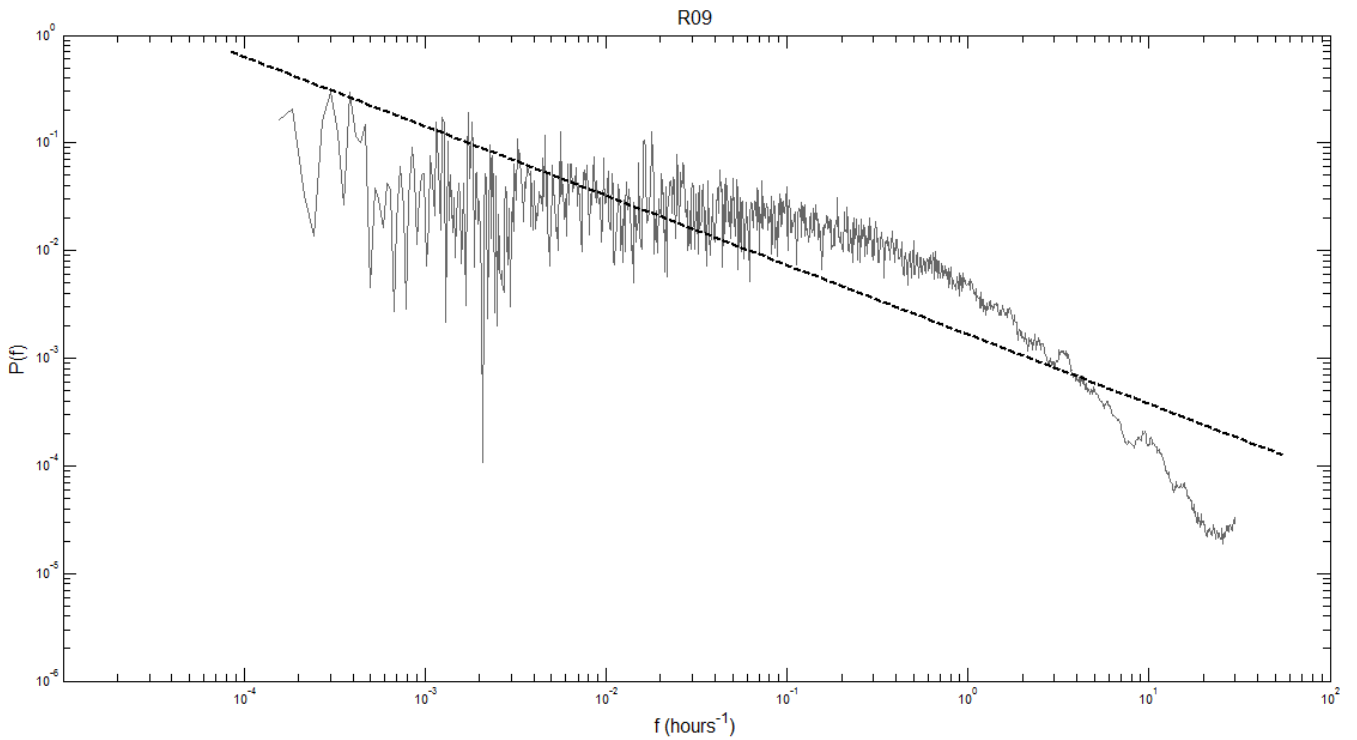


**Figure III.52.** Energy spectrum for 1-minute rainfall time-series from Warsaw, for rain gauge R09 with the overall slope

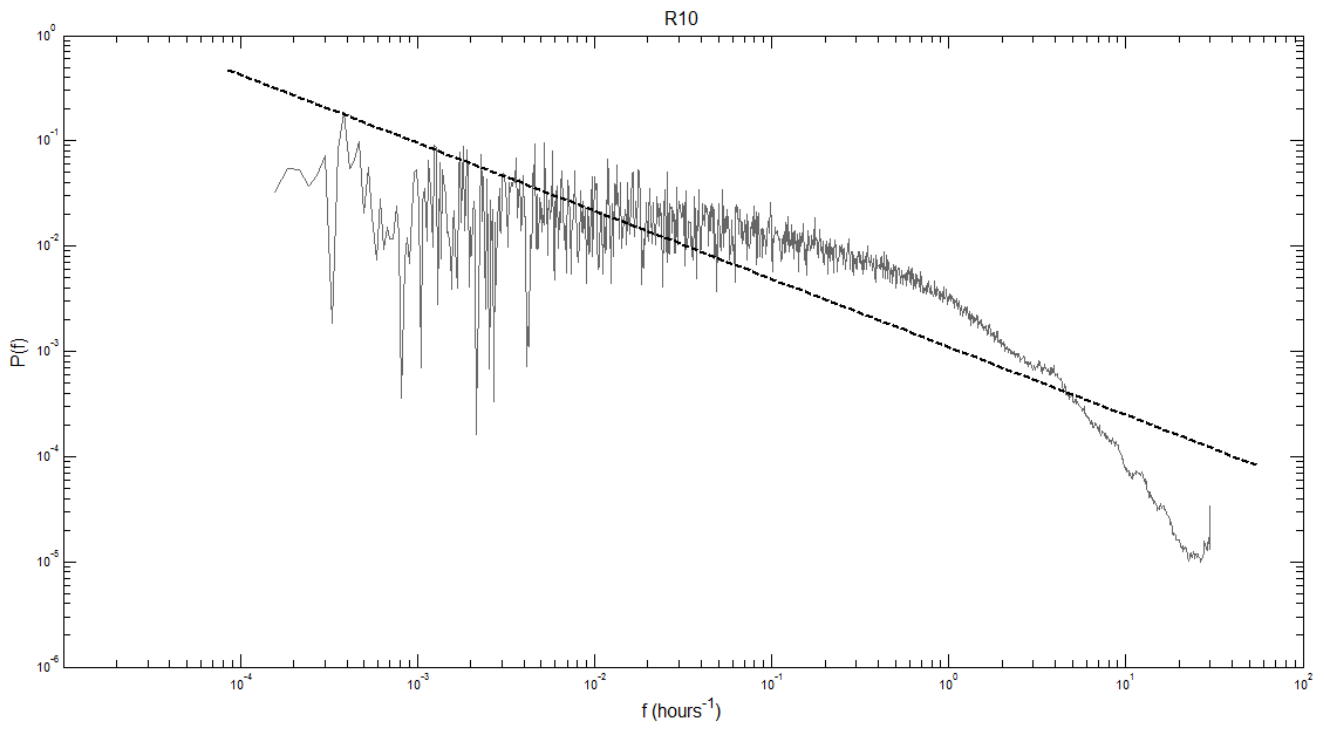


**Figure III.53.** Energy spectrum for 1-minute rainfall time-series from Warsaw, for rain gauge R10 with the overall slope

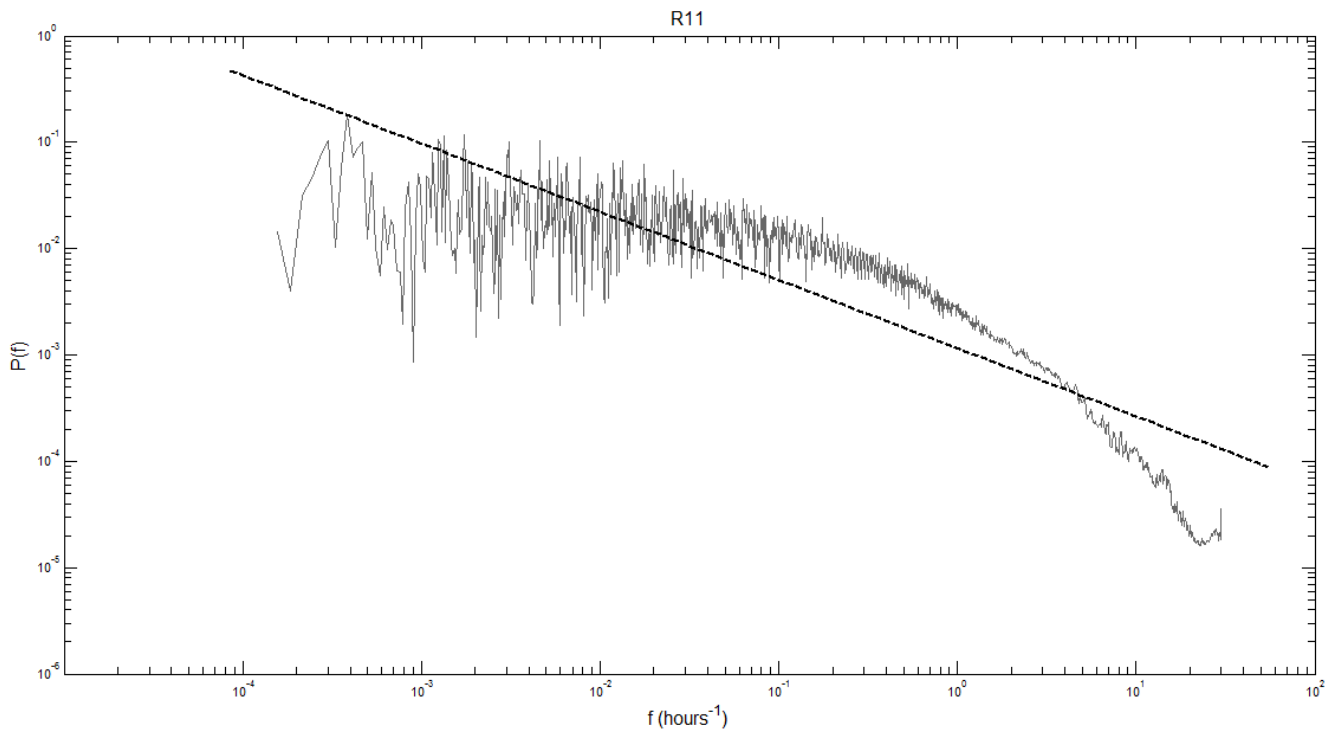


**Figure III.54.** Energy spectrum for 1-minute rainfall time-series from Warsaw, for rain gauge R11 with the overall slope

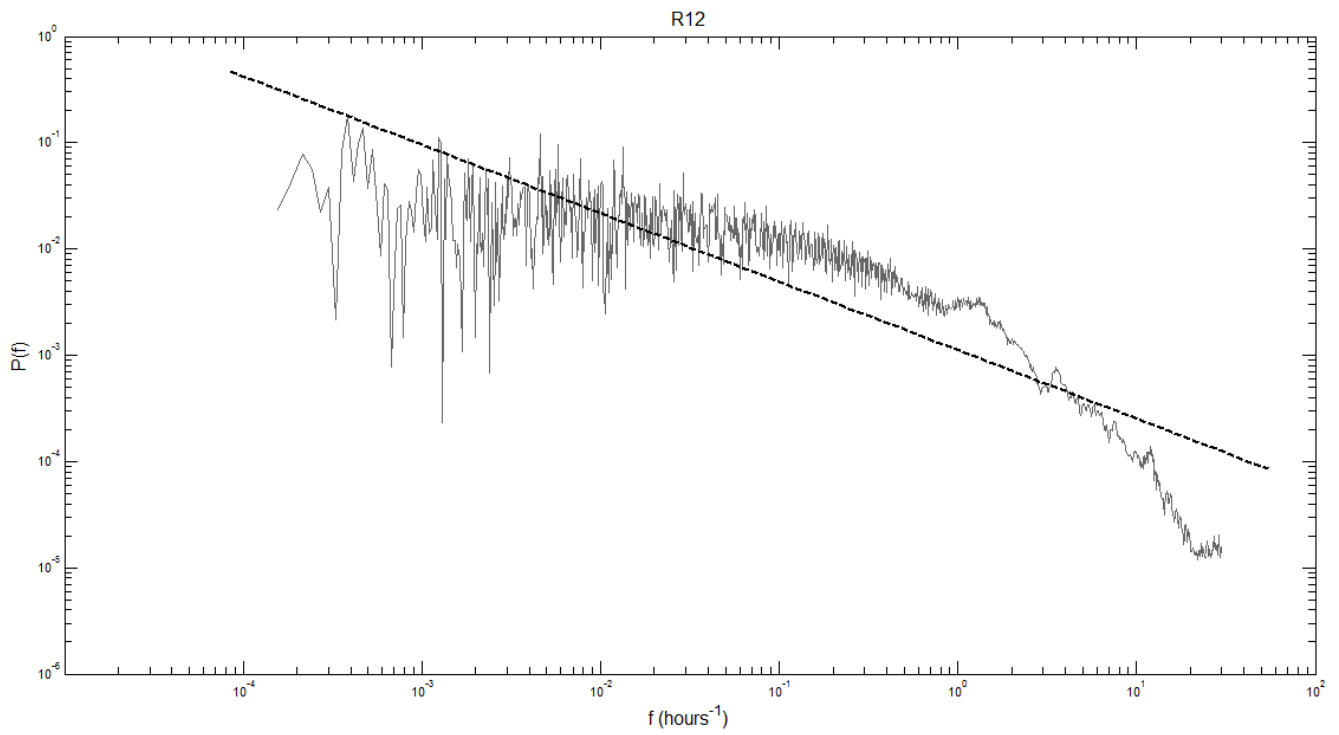


**Figure III.55.** Energy spectrum for 1-minute rainfall time-series from Warsaw, for rain gauge R12 with the overall slope

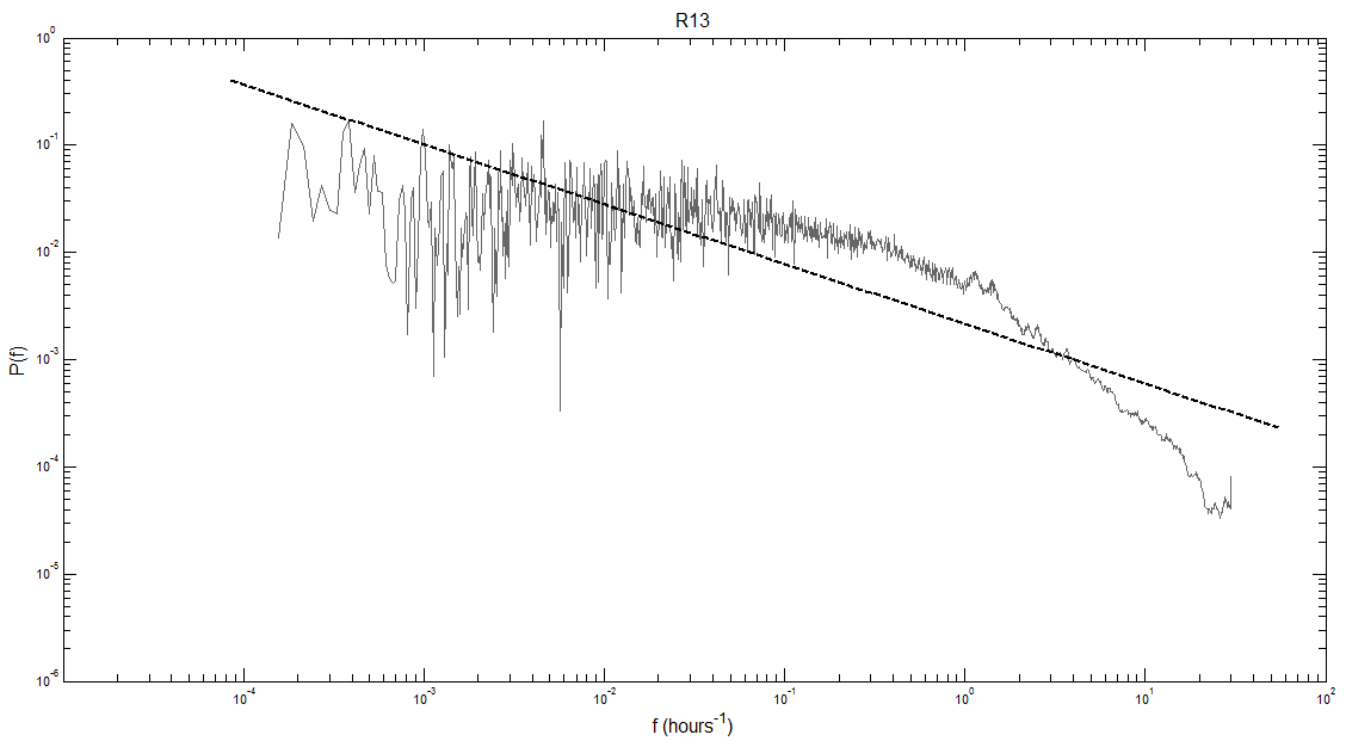


**Figure III.56.** Energy spectrum for 1-minute rainfall time-series from Warsaw, for rain gauge R13 with the overall slope

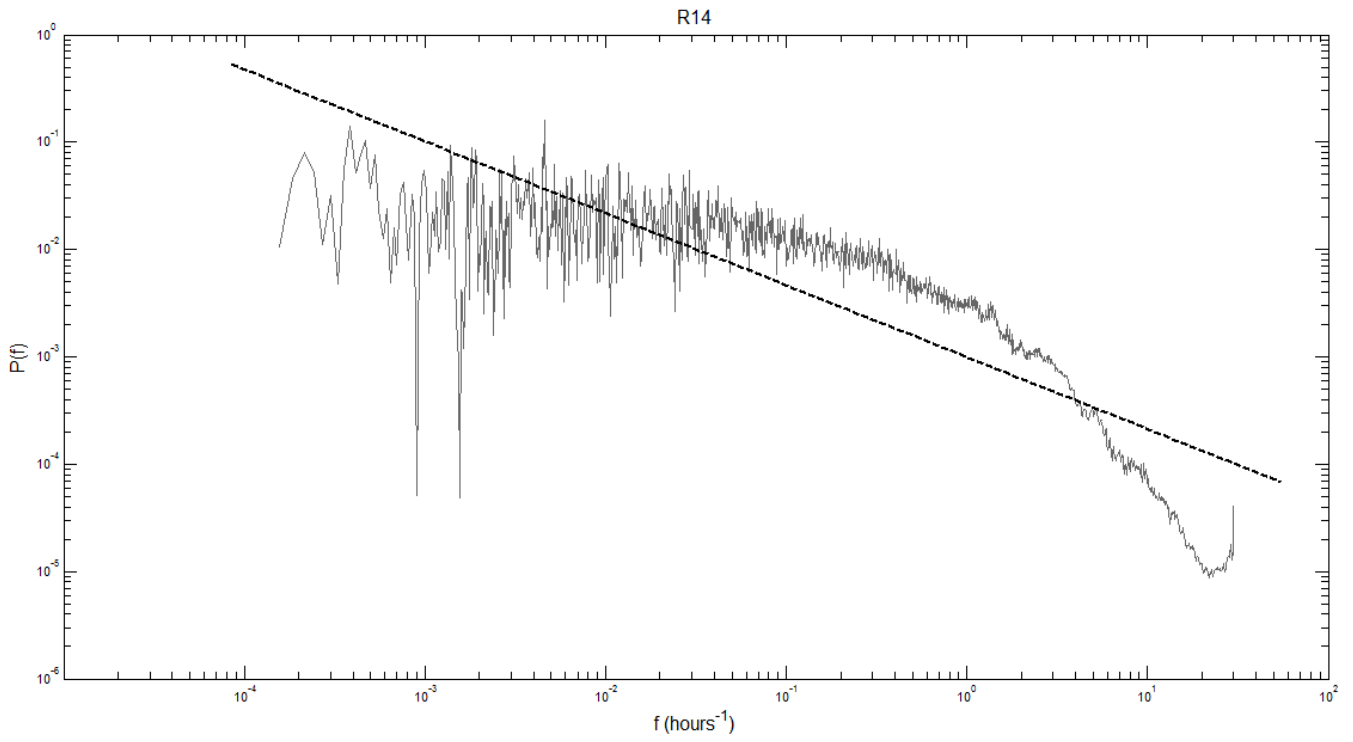


**Figure III.57.** Energy spectrum for 1-minute rainfall time-series from Warsaw, for rain gauge R14 with the overall slope

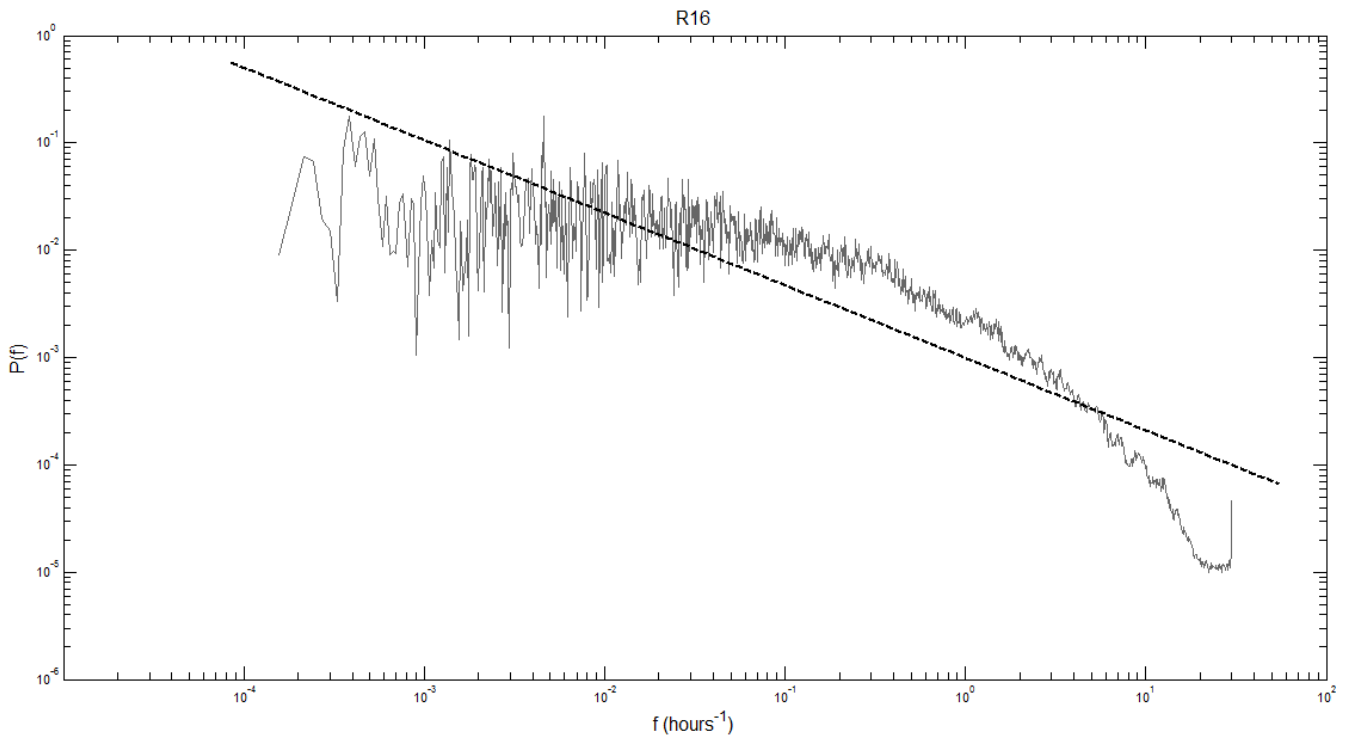


**Figure III.58.** Energy spectrum for 1-minute rainfall time-series from Warsaw, for rain gauge R16 with the overall slope

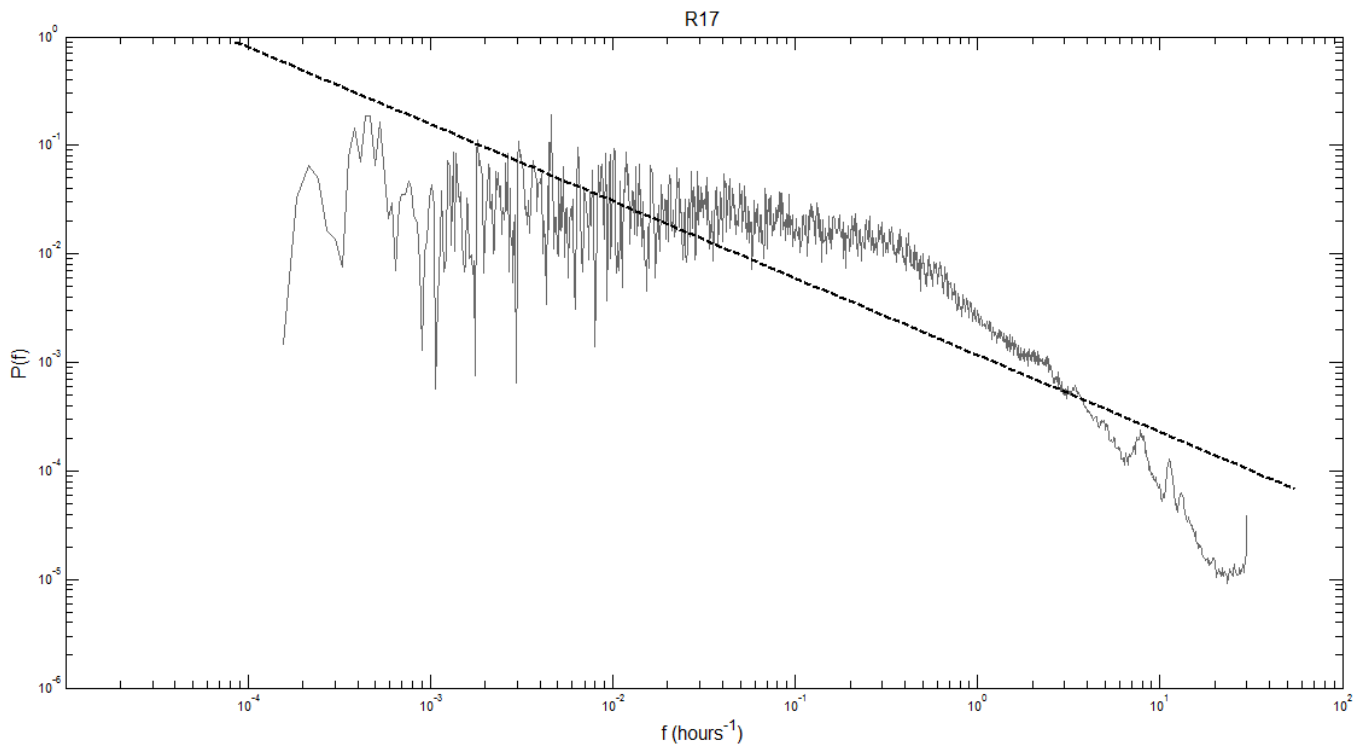


**Figure III.59.** Energy spectrum for 1-minute rainfall time-series from Warsaw, for rain gauge R17 with the overall slope

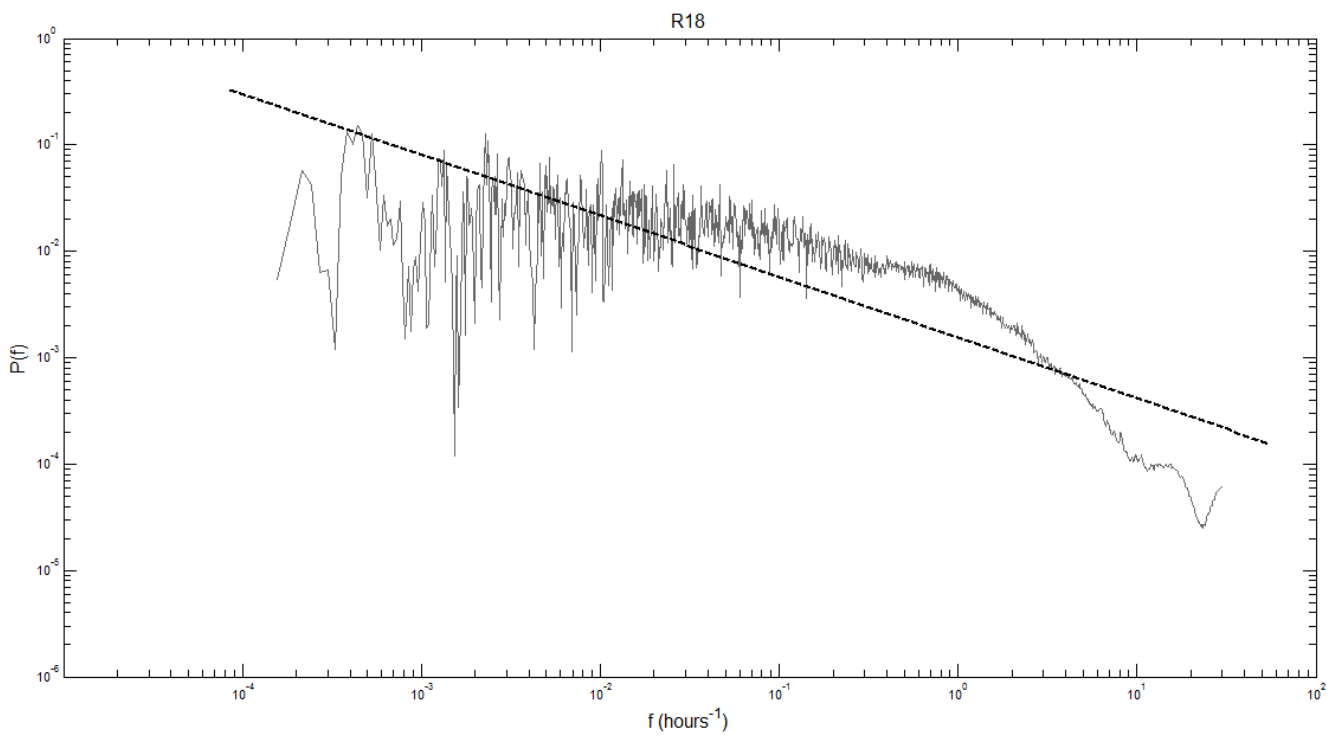


**Figure III.60.** Energy spectrum for 1-minute rainfall time-series from Warsaw, for rain gauge R18 with the overall slope

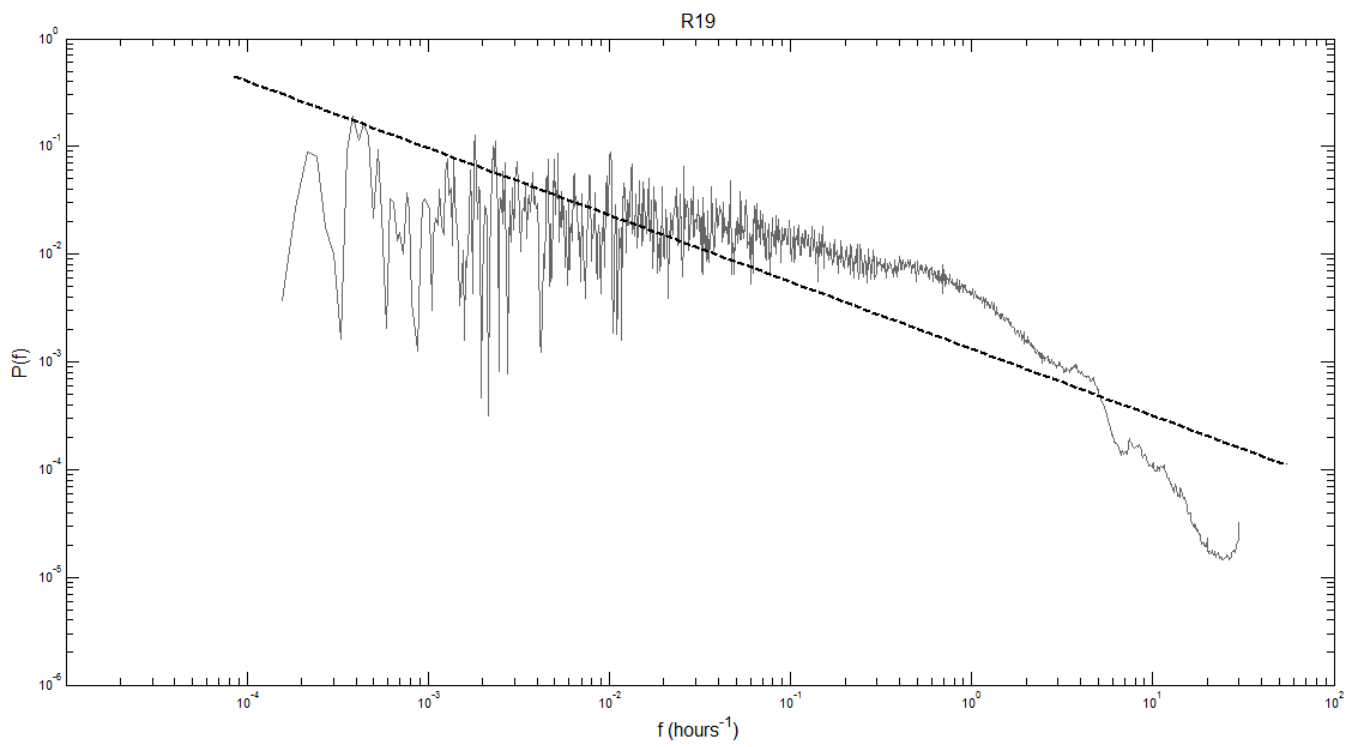


**Figure III.61.** Energy spectrum for 1-minute rainfall time-series from Warsaw, for rain gauge R19 with the overall slope

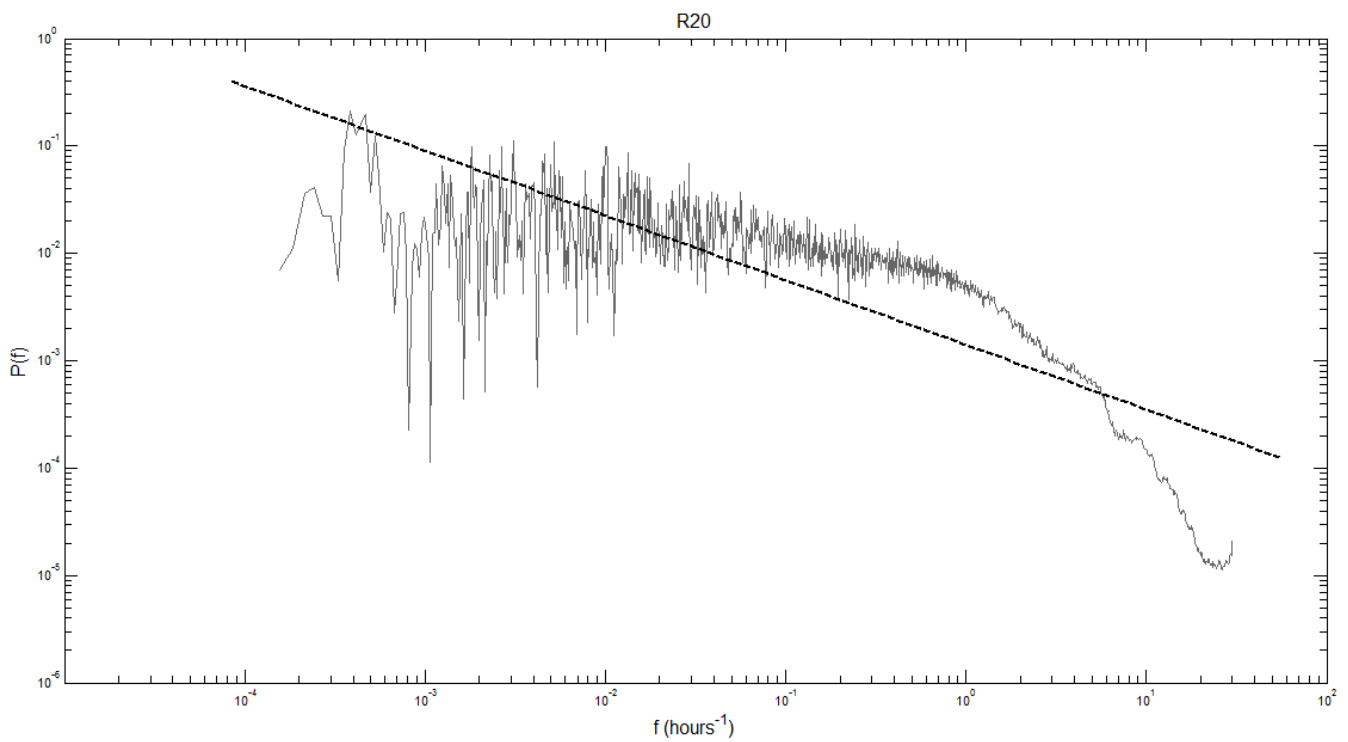


**Figure III.62.** Energy spectrum for 1-minute rainfall time-series from Warsaw, for rain gauge R20 with the overall slope

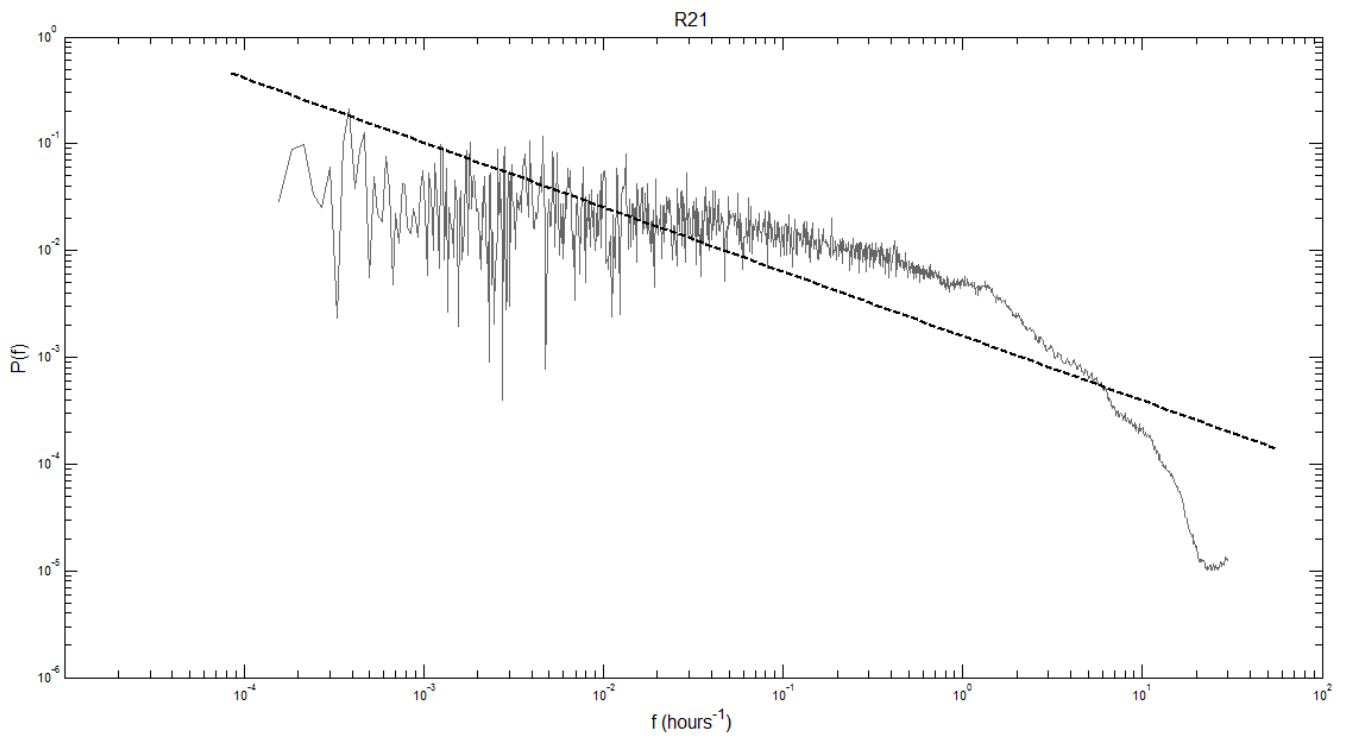


**Figure III.63.** Energy spectrum for 1-minute rainfall time-series from Warsaw, for rain gauge R21 with the overall slope

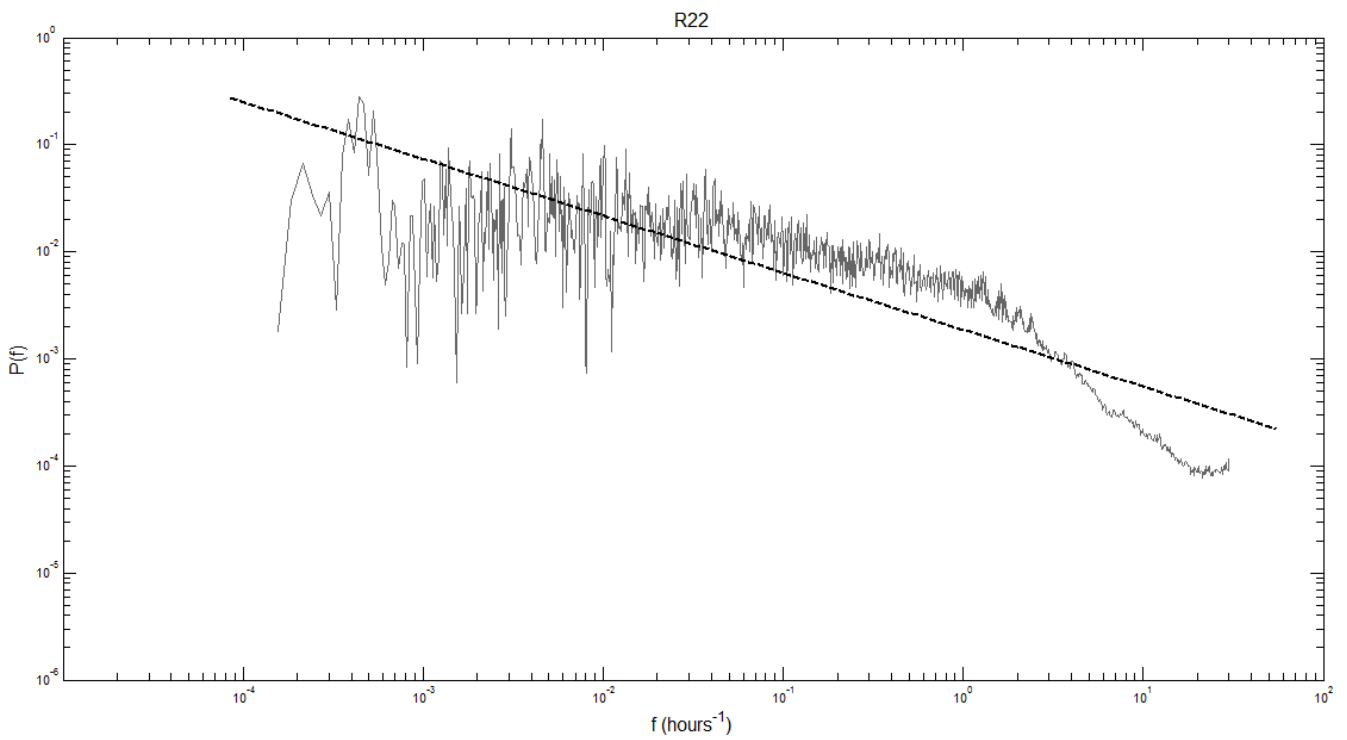


**Figure III.64.** Energy spectrum for 1-minute rainfall time-series from Warsaw, for rain gauge R22 with the overall slope

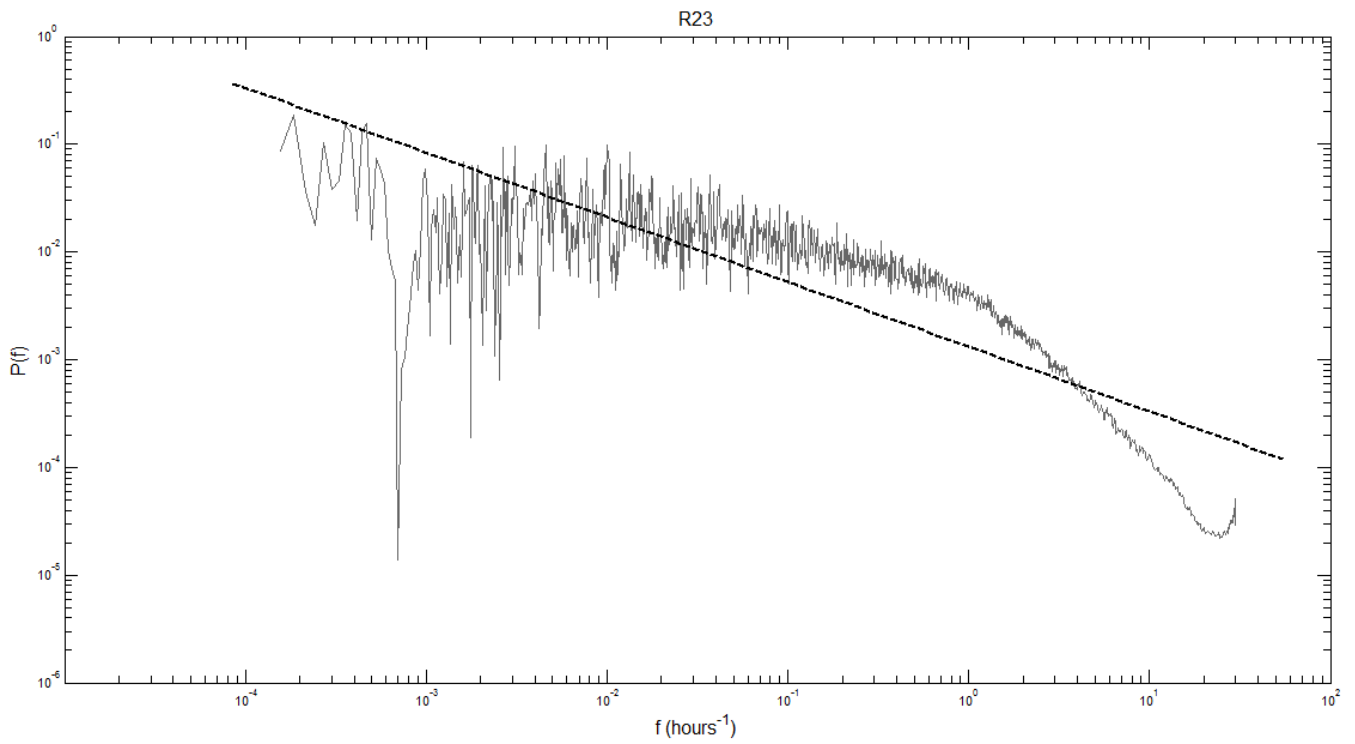


**Figure III.65.** Energy spectrum for 1-minute rainfall time-series from Warsaw, for rain gauge R23 with the overall slope

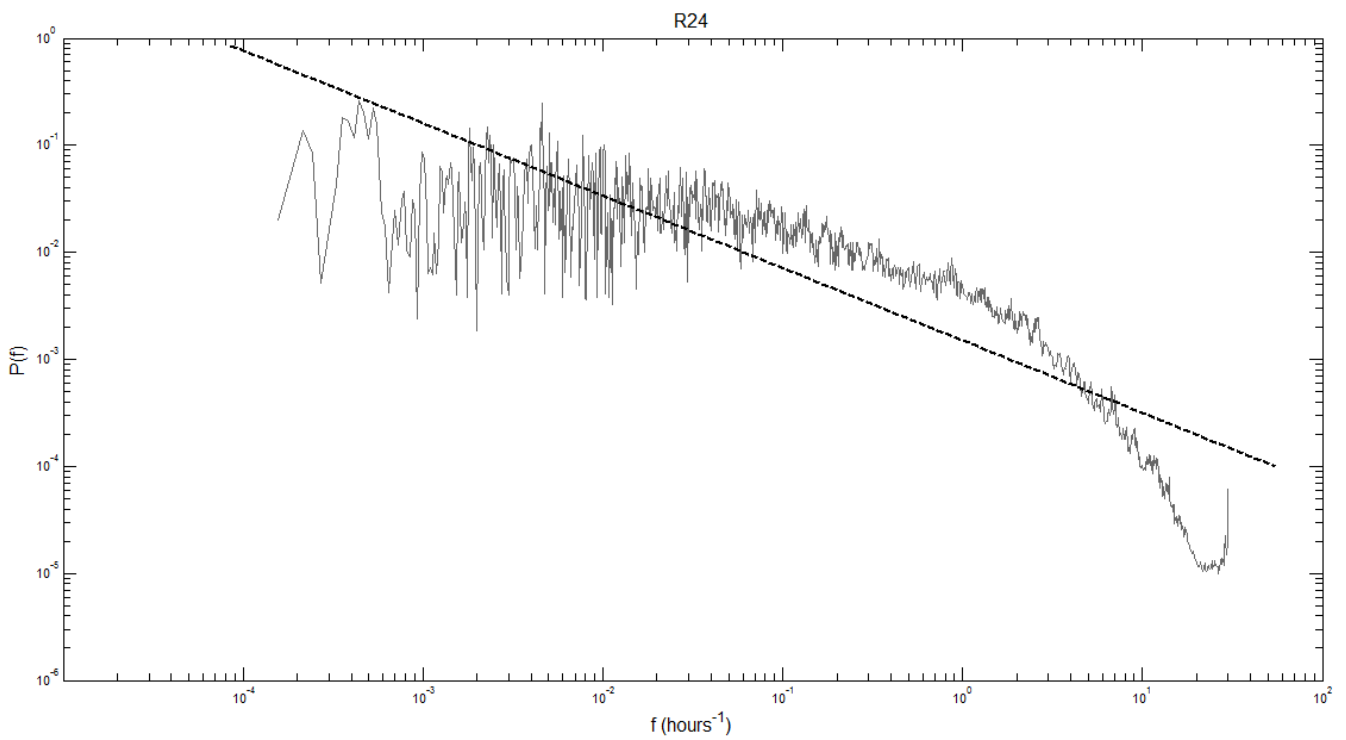


**Figure III.66.** Energy spectrum for 1-minute rainfall time-series from Warsaw, for rain gauge R24 with the overall slope

## APPENDIX IV.

### TRACE MOMENT METHOD PLOTS

#### Section A

Log-log plots of the relation between the average  $q^{\text{th}}$  order moments of the rainfall intensity  $\varepsilon_\lambda$  and the scale parameter  $\lambda$  obtained by the trace moment method for 1-minute rainfall from Warsaw, from 2008 to 2010. The analysis is performed for time scales from 1 minute up to 16384 minutes (11.4 days) for order moments  $q$  smaller than 1 (on the left) and greater than 1 (on the right side).

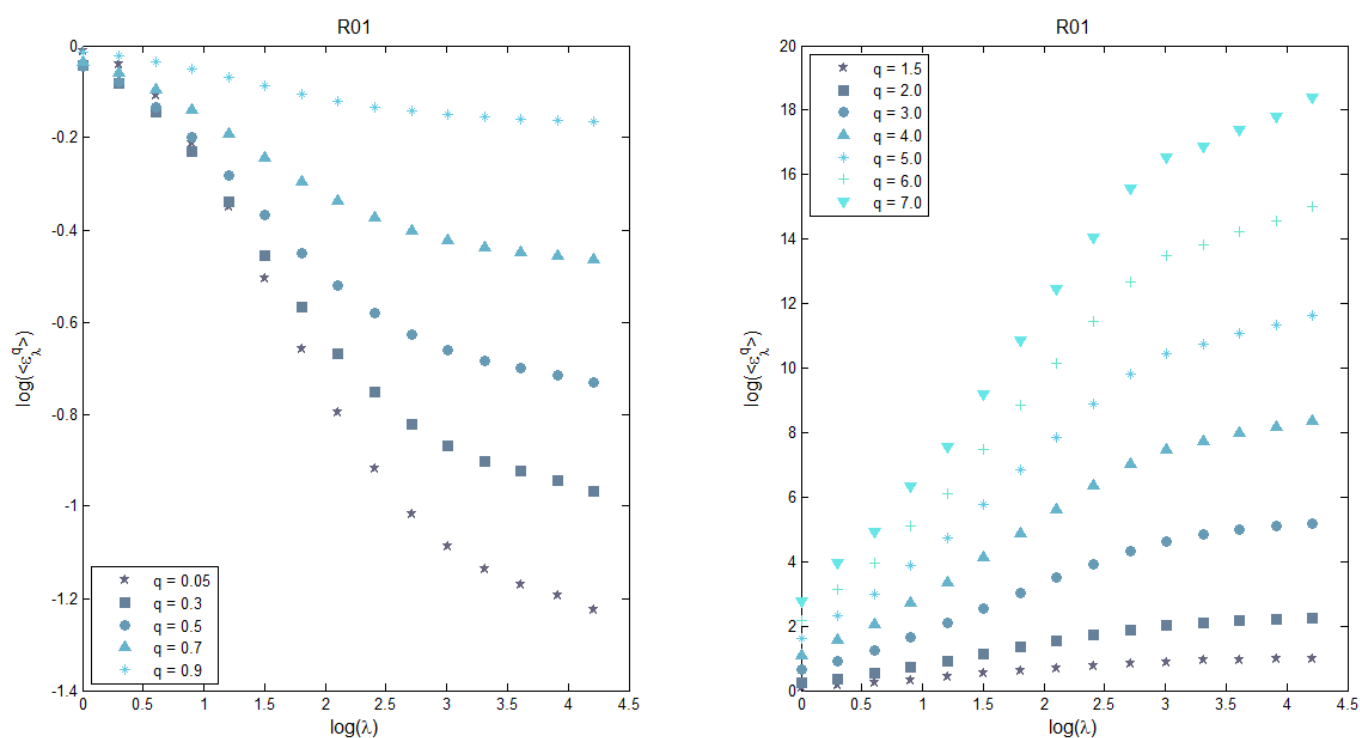


**Figure IV.1.** Log-log plot of the mean  $q$  moments of the rainfall intensity  $\varepsilon_\lambda$  against the scale coefficient  $\lambda$  for 1-minute precipitation data series from Warsaw rain gauge R01, for  $q < 1$  (on left) and for  $q > 1$  (on right). The time scales range from  $\lambda = 16384$  (1 minute) to  $\lambda = 1$  (11.4 days)

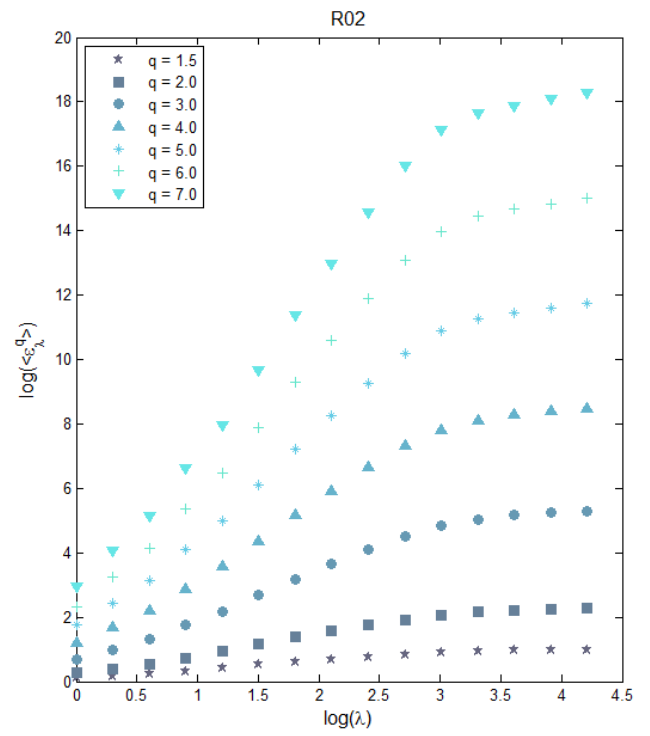
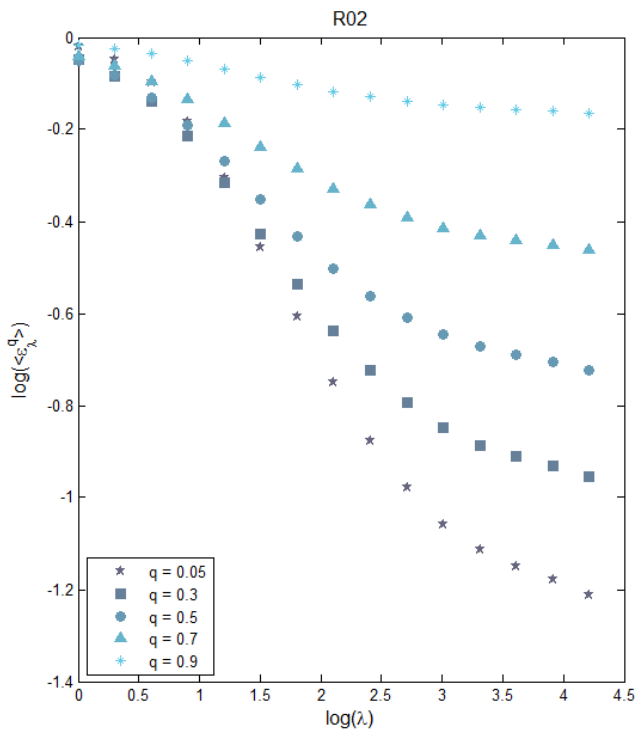


**Figure IV.2.** Log-log plot of the mean  $q$  moments of the rainfall intensity  $\varepsilon_\lambda$  against the scale coefficient  $\lambda$  for 1-minute precipitation data series from Warsaw rain gauge R02, for  $q < 1$  (on left) and for  $q > 1$  (on right). The time scales range from  $\lambda = 16384$  (1 minute) to  $\lambda = 1$  (11.4 days)

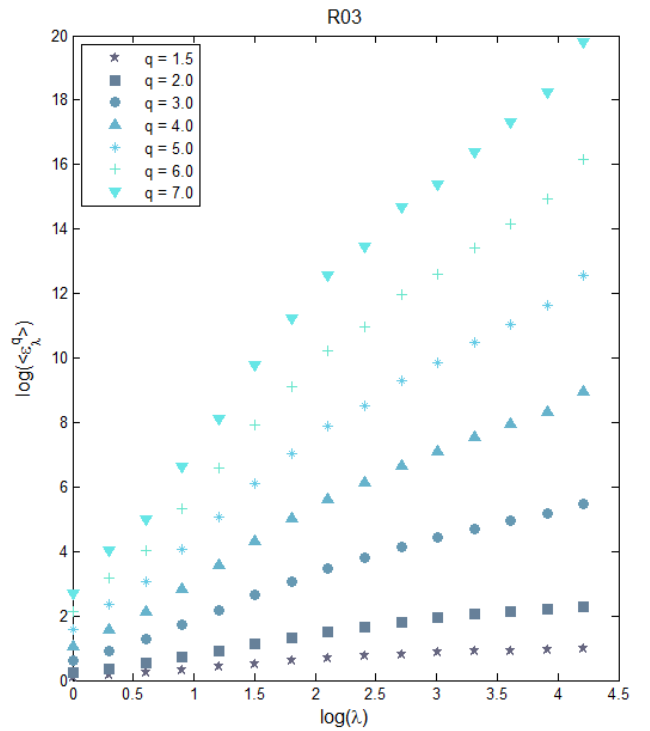
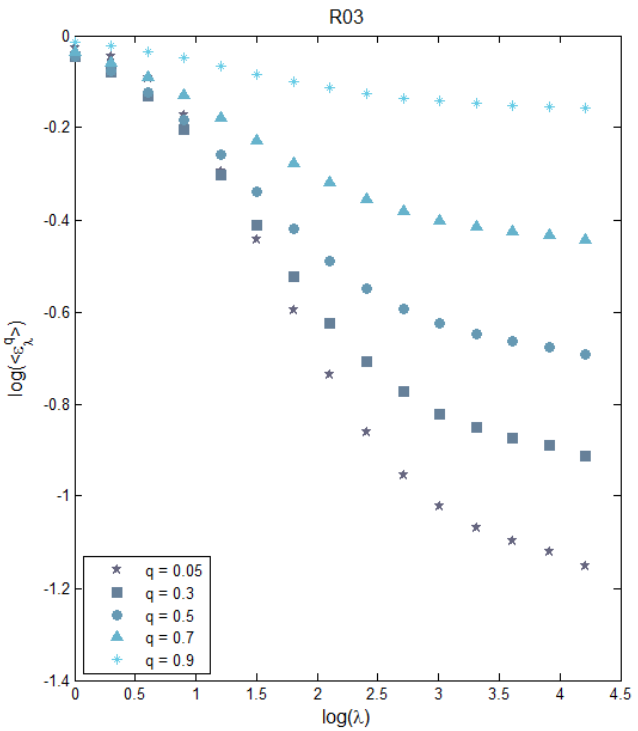


**Figure IV.3.** Log-log plot of the mean  $q$  moments of the rainfall intensity  $\varepsilon_\lambda$  against the scale coefficient  $\lambda$  for 1-minute precipitation data series from Warsaw rain gauge R03, for  $q < 1$  (on left) and for  $q > 1$  (on right). The time scales range from  $\lambda = 16384$  (1 minute) to  $\lambda = 1$  (11.4 days)

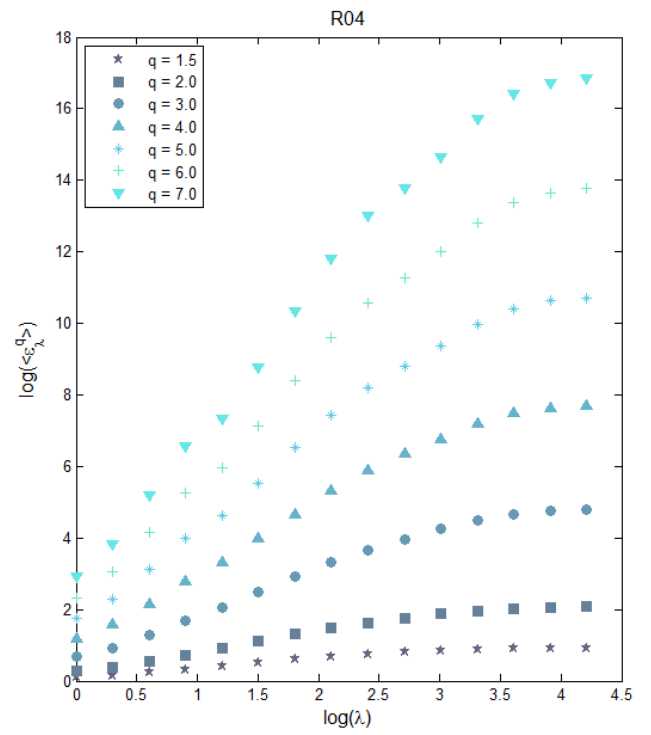
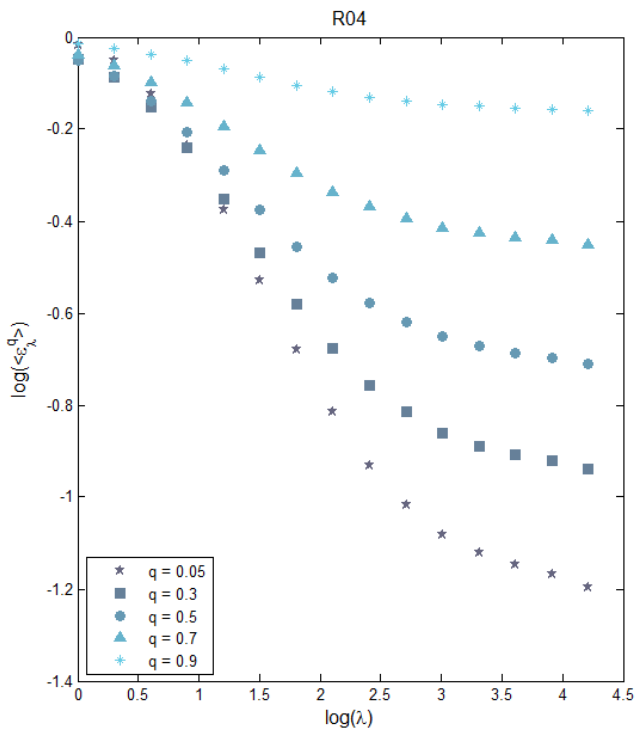


**Figure IV.4.** Log-log plot of the mean  $q$  moments of the rainfall intensity  $\varepsilon_\lambda$  against the scale coefficient  $\lambda$  for 1-minute precipitation data series from Warsaw rain gauge R04, for  $q < 1$  (on left) and for  $q > 1$  (on right). The time scales range from  $\lambda = 16384$  (1 minute) to  $\lambda = 1$  (11.4 days)

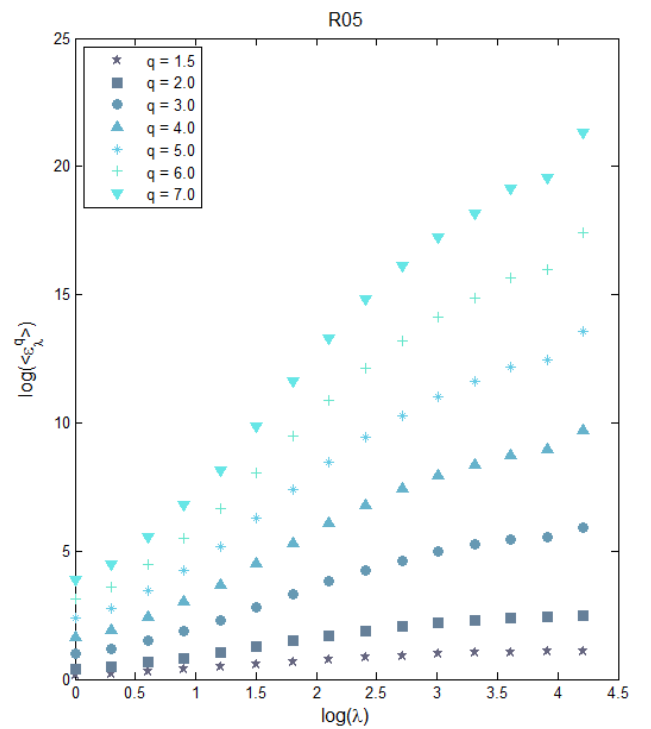
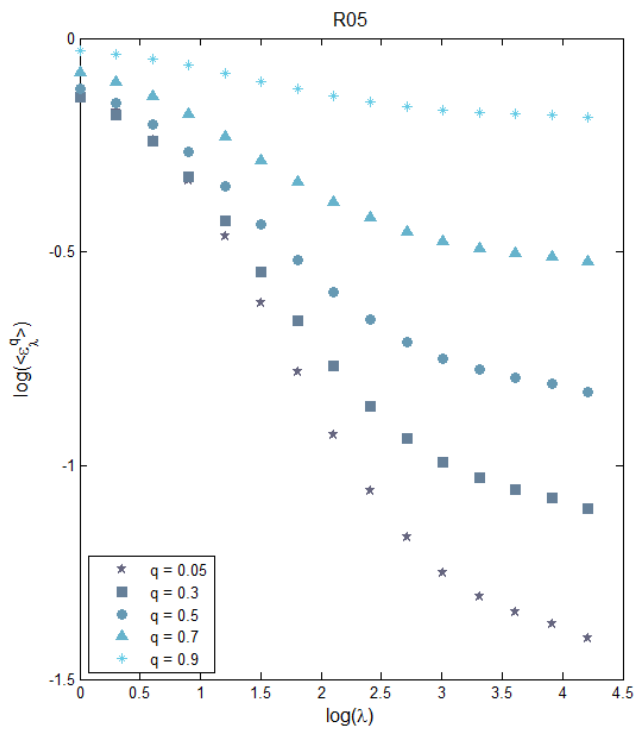


**Figure IV.5.** Log-log plot of the mean  $q$  moments of the rainfall intensity  $\varepsilon_\lambda$  against the scale coefficient  $\lambda$  for 1-minute precipitation data series from Warsaw rain gauge R05, for  $q < 1$  (on left) and for  $q > 1$  (on right). The time scales range from  $\lambda = 16384$  (1 minute) to  $\lambda = 1$  (11.4 days)

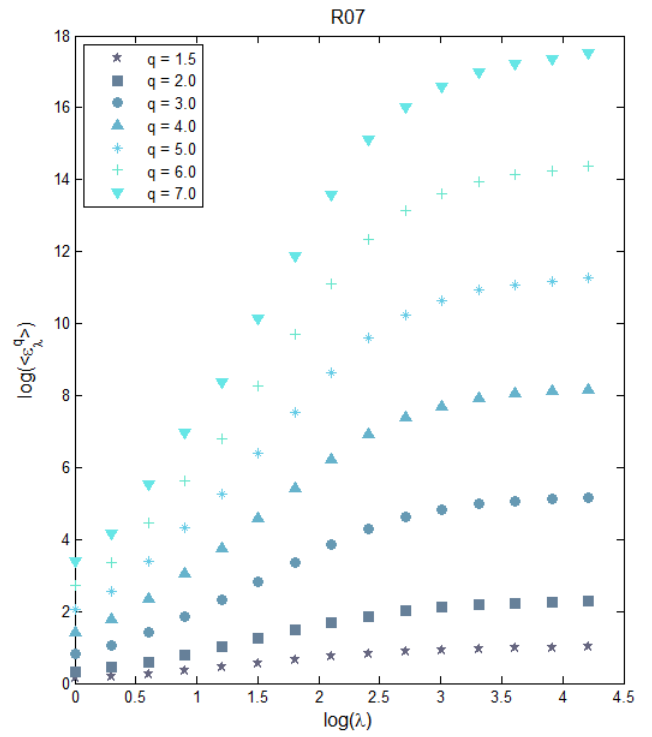
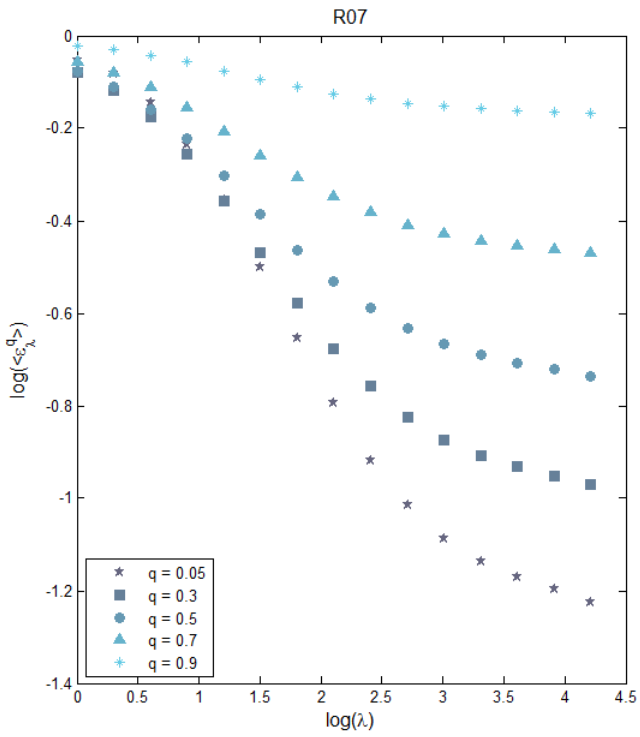


**Figure IV.6.** Log-log plot of the mean  $q$  moments of the rainfall intensity  $\varepsilon_\lambda$  against the scale coefficient  $\lambda$  for 1-minute precipitation data series from Warsaw rain gauge R07, for  $q < 1$  (on left) and for  $q > 1$  (on right). The time scales range from  $\lambda = 16384$  (1 minute) to  $\lambda = 1$  (11.4 days)

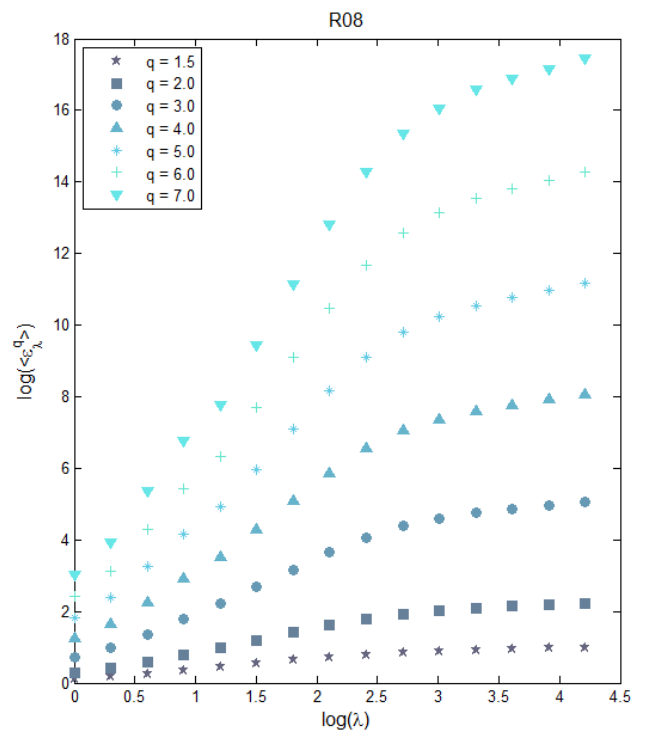
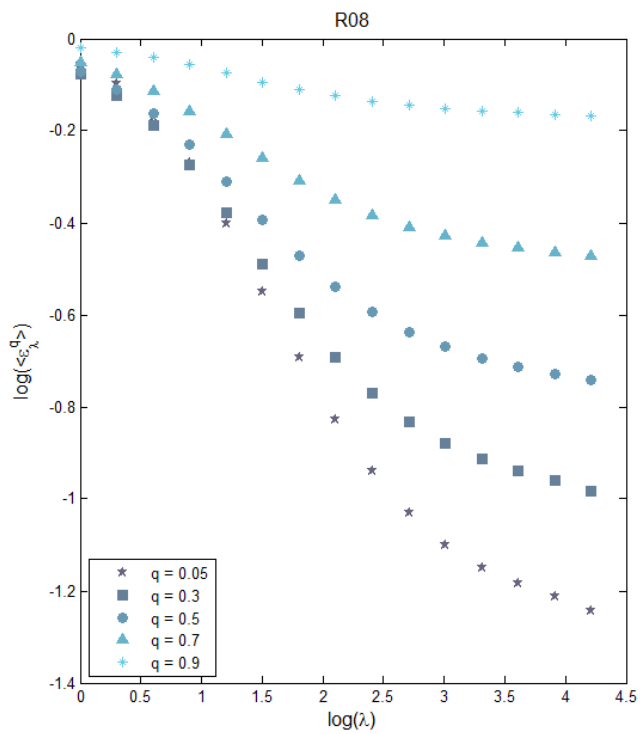


**Figure IV.7.** Log-log plot of the mean  $q$  moments of the rainfall intensity  $\varepsilon_\lambda$  against the scale coefficient  $\lambda$  for 1-minute precipitation data series from Warsaw rain gauge R08, for  $q < 1$  (on left) and for  $q > 1$  (on right). The time scales range from  $\lambda = 16384$  (1 minute) to  $\lambda = 1$  (11.4 days)

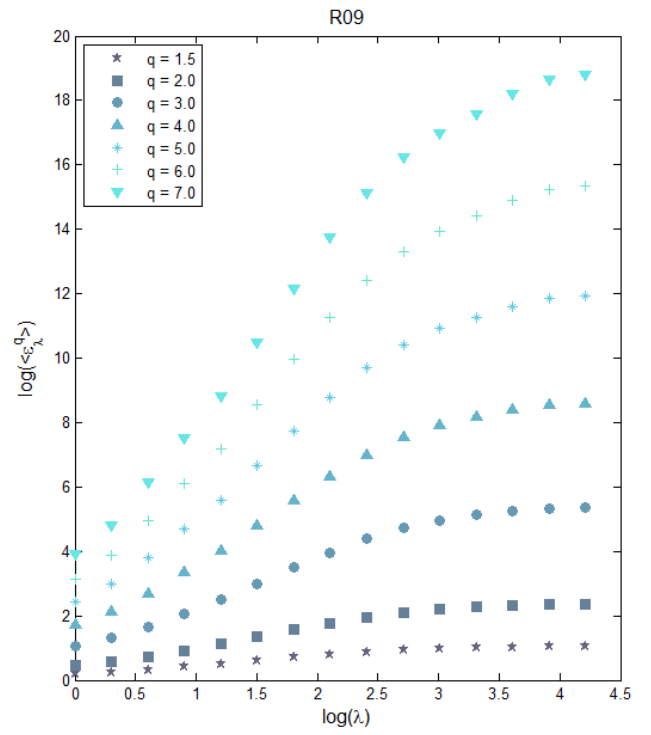
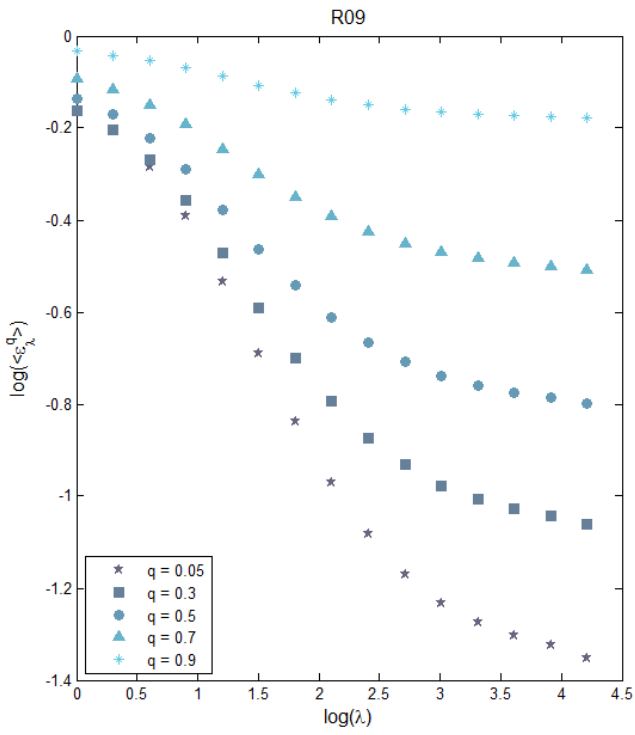


**Figure IV.8.** Log-log plot of the mean  $q$  moments of the rainfall intensity  $\varepsilon_\lambda$  against the scale coefficient  $\lambda$  for 1-minute precipitation data series from Warsaw rain gauge R09, for  $q < 1$  (on left) and for  $q > 1$  (on right). The time scales range from  $\lambda = 16384$  (1 minute) to  $\lambda = 1$  (11.4 days)

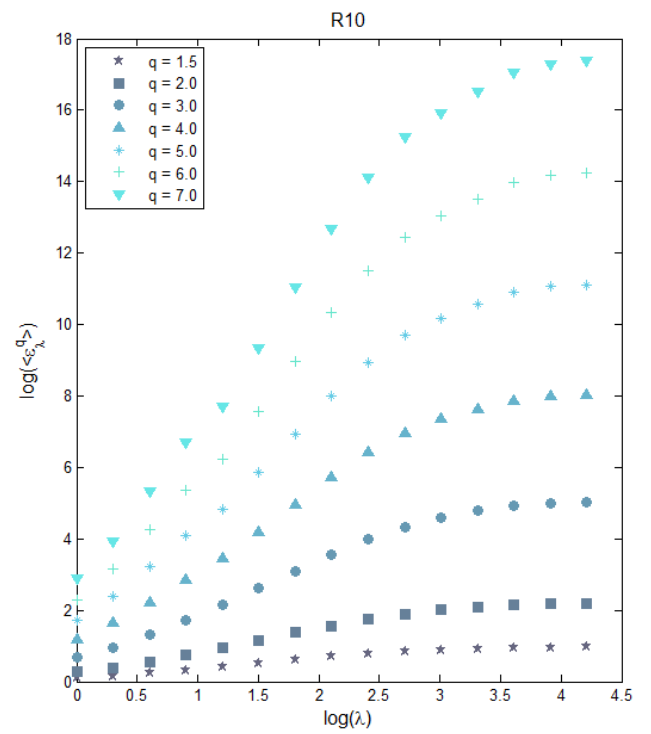
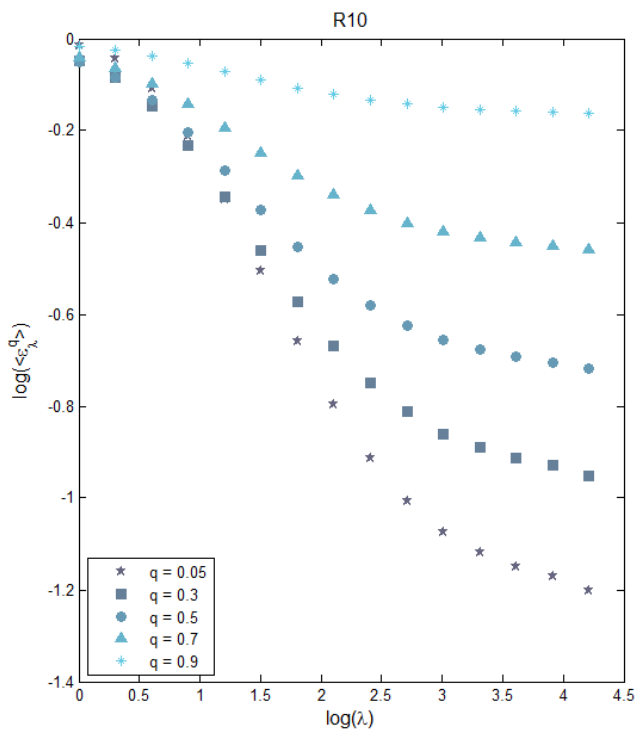


**Figure IV.9.** Log-log plot of the mean  $q$  moments of the rainfall intensity  $\varepsilon_\lambda$  against the scale coefficient  $\lambda$  for 1-minute precipitation data series from Warsaw rain gauge R10, for  $q < 1$  (on left) and for  $q > 1$  (on right). The time scales range from  $\lambda = 16384$  (1 minute) to  $\lambda = 1$  (11.4 days)

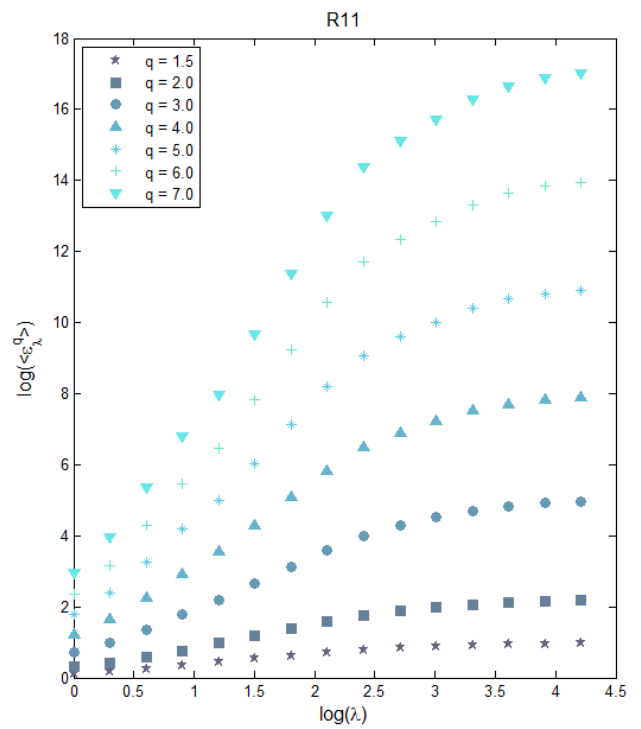
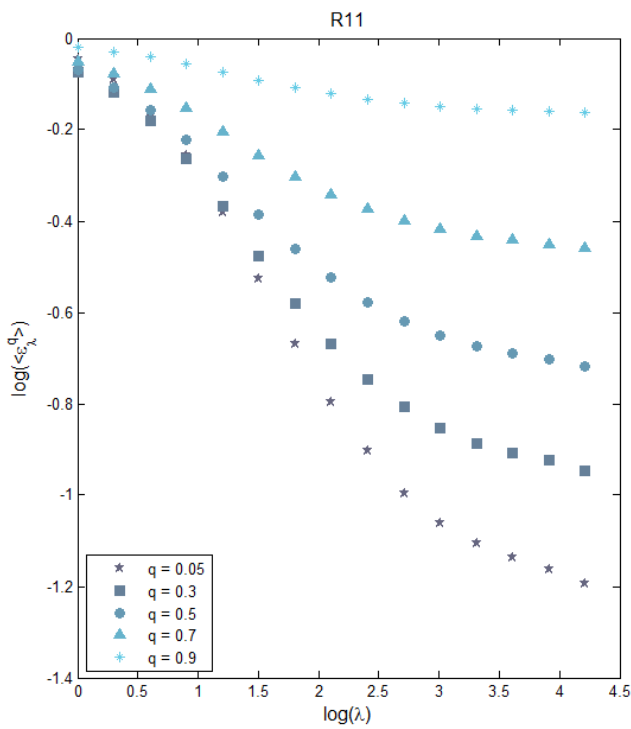


**Figure IV.10.** Log-log plot of the mean  $q$  moments of the rainfall intensity  $\varepsilon_\lambda$  against the scale coefficient  $\lambda$  for 1-minute precipitation data series from Warsaw rain gauge R11, for  $q < 1$  (on left) and for  $q > 1$  (on right). The time scales range from  $\lambda = 16384$  (1 minute) to  $\lambda = 1$  (11.4 days)

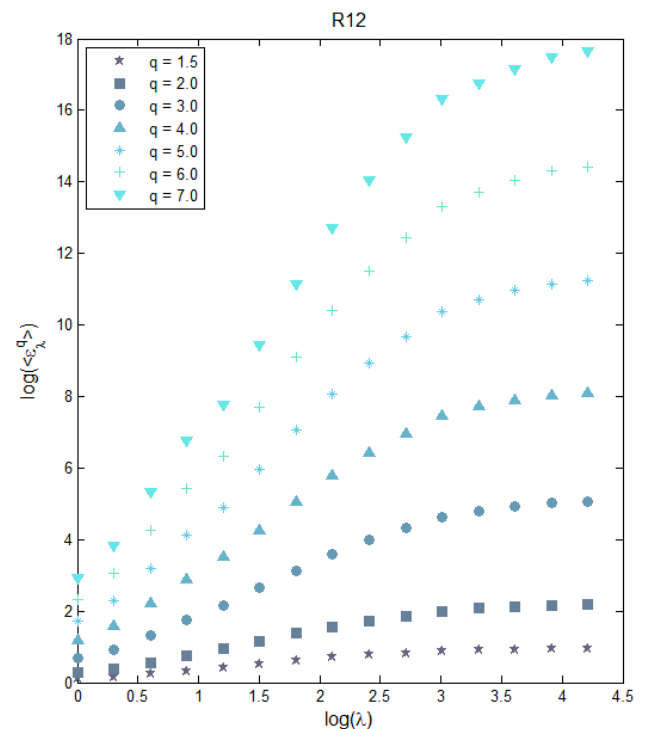
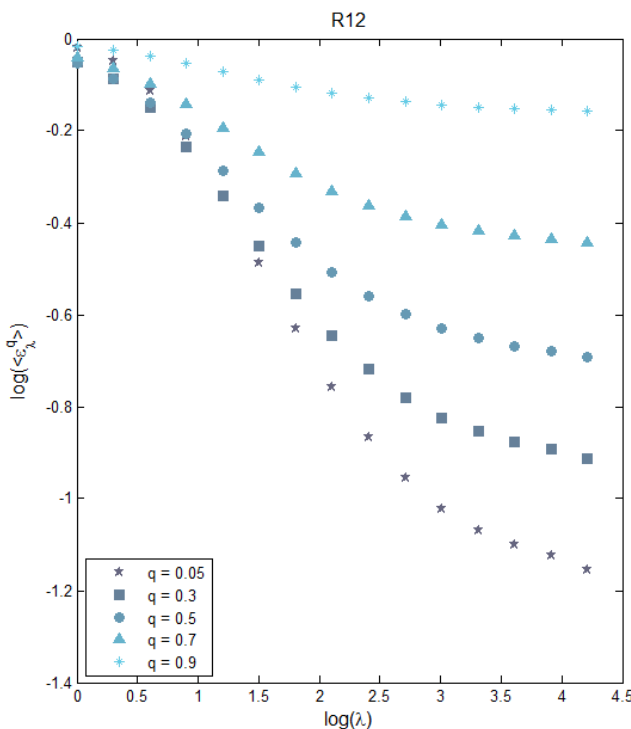


**Figure IV.11.** Log-log plot of the mean  $q$  moments of the rainfall intensity  $\varepsilon_\lambda$  against the scale coefficient  $\lambda$  for 1-minute precipitation data series from Warsaw rain gauge R12, for  $q < 1$  (on left) and for  $q > 1$  (on right). The time scales range from  $\lambda = 16384$  (1 minute) to  $\lambda = 1$  (11.4 days)

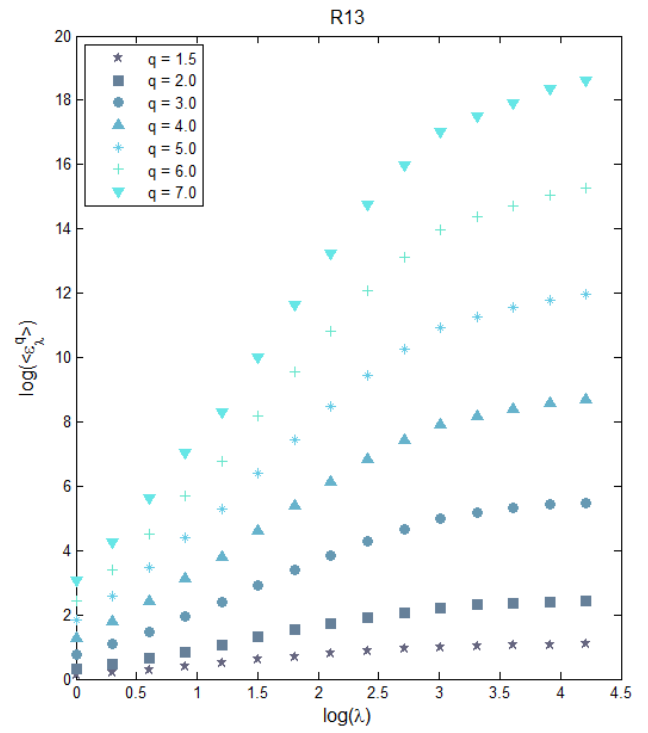
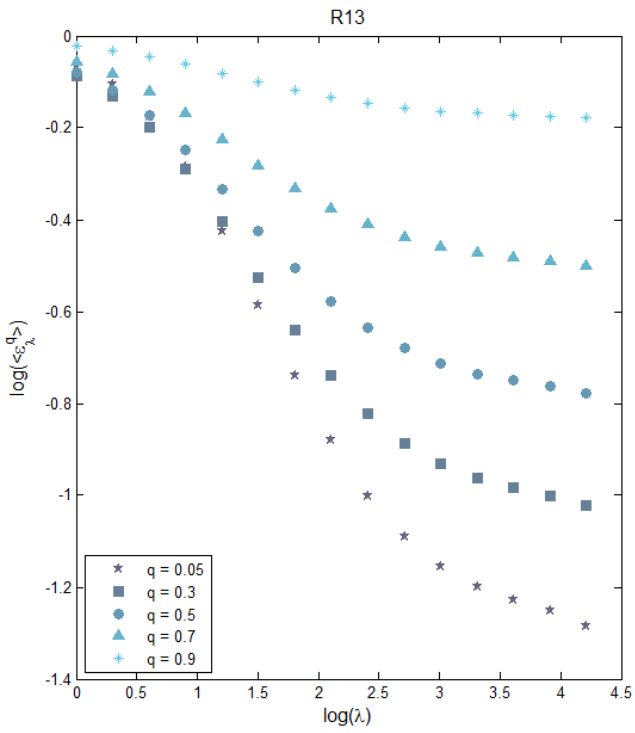


**Figure IV.12.** Log-log plot of the mean  $q$  moments of the rainfall intensity  $\varepsilon_\lambda$  against the scale coefficient  $\lambda$  for 1-minute precipitation data series from Warsaw rain gauge R13, for  $q < 1$  (on left) and for  $q > 1$  (on right). The time scales range from  $\lambda = 16384$  (1 minute) to  $\lambda = 1$  (11.4 days)

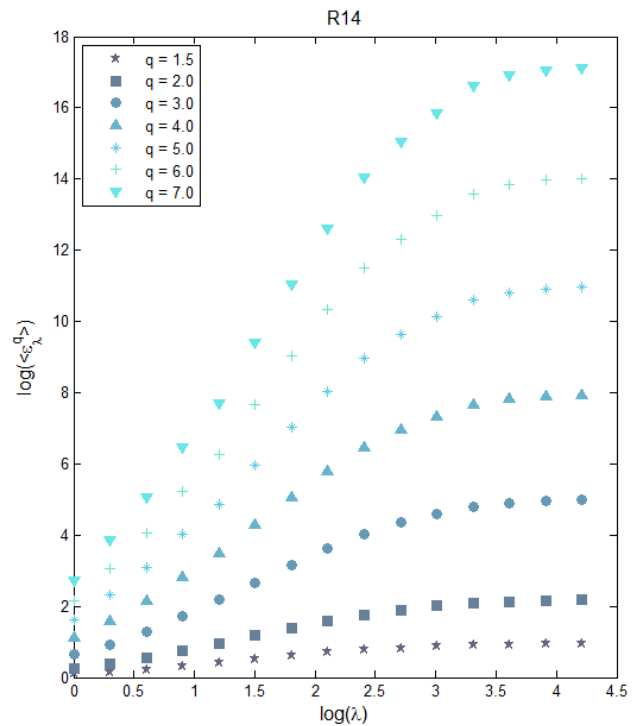
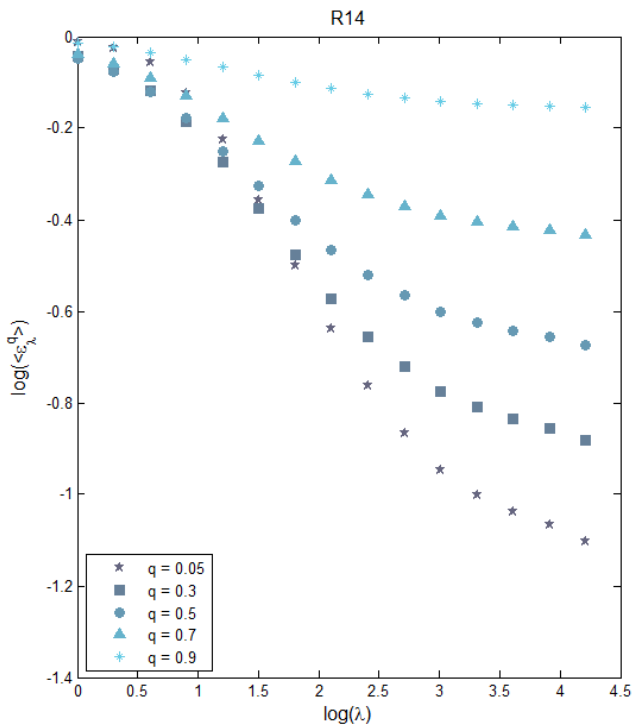


**Figure IV.13.** Log-log plot of the mean  $q$  moments of the rainfall intensity  $\varepsilon_\lambda$  against the scale coefficient  $\lambda$  for 1-minute precipitation data series from Warsaw rain gauge R14, for  $q < 1$  (on left) and for  $q > 1$  (on right). The time scales range from  $\lambda = 16384$  (1 minute) to  $\lambda = 1$  (11.4 days)

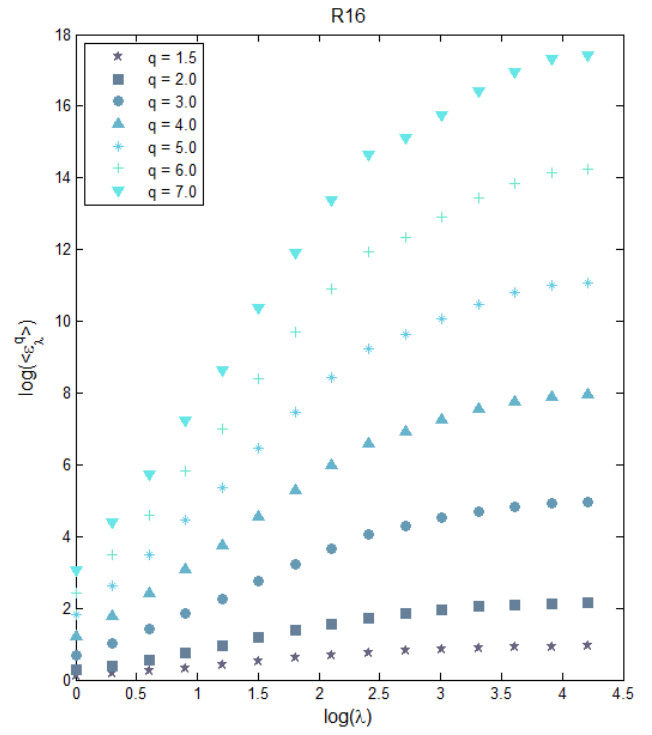
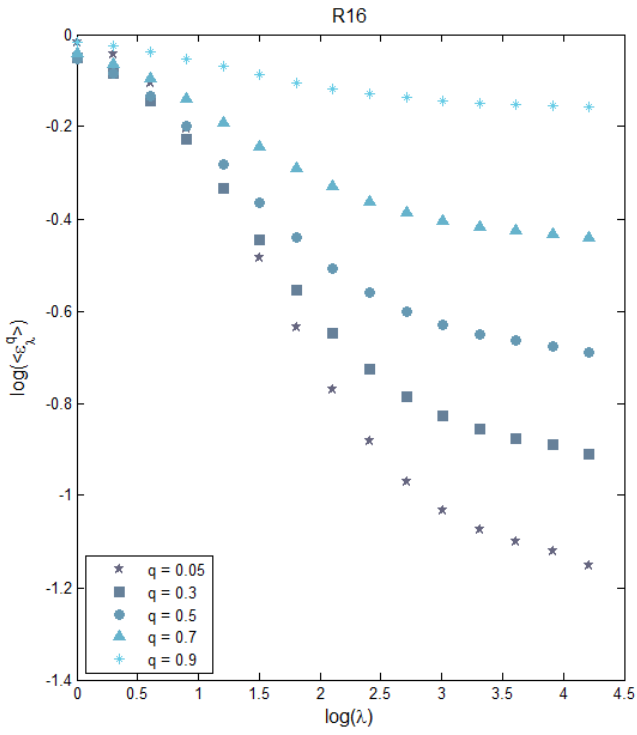


**Figure IV.14.** Log-log plot of the mean  $q$  moments of the rainfall intensity  $\varepsilon_\lambda$  against the scale coefficient  $\lambda$  for 1-minute precipitation data series from Warsaw rain gauge R16, for  $q < 1$  (on left) and for  $q > 1$  (on right). The time scales range from  $\lambda = 16384$  (1 minute) to  $\lambda = 1$  (11.4 days)

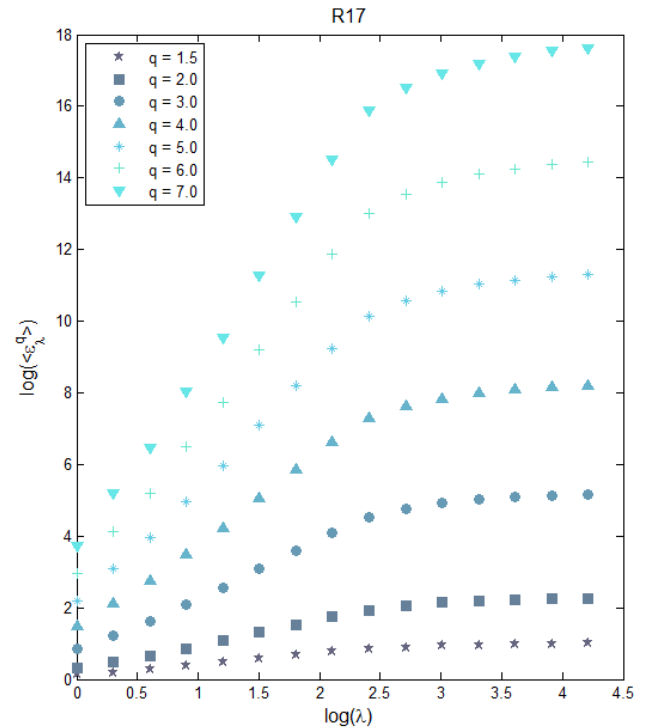
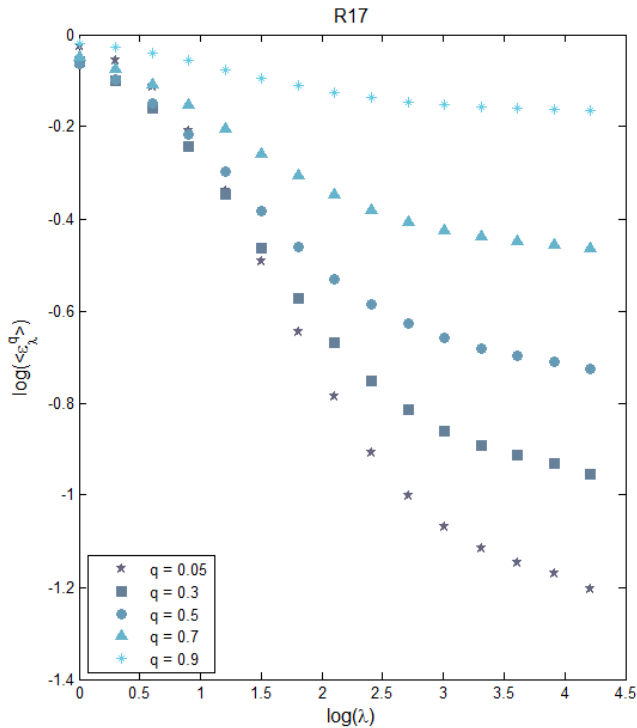


**Figure IV.15.** Log-log plot of the mean  $q$  moments of the rainfall intensity  $\varepsilon_\lambda$  against the scale coefficient  $\lambda$  for 1-minute precipitation data series from Warsaw rain gauge R17, for  $q < 1$  (on left) and for  $q > 1$  (on right). The time scales range from  $\lambda = 16384$  (1 minute) to  $\lambda = 1$  (11.4 days)

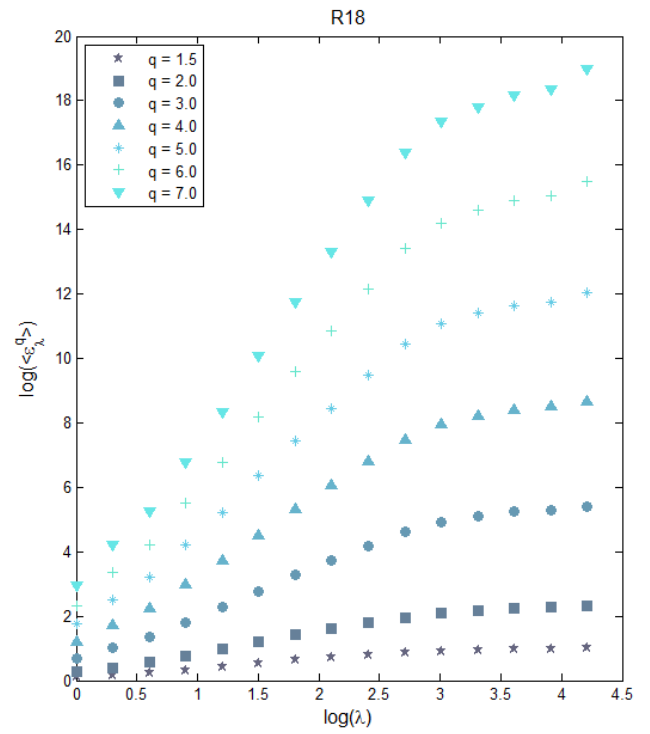
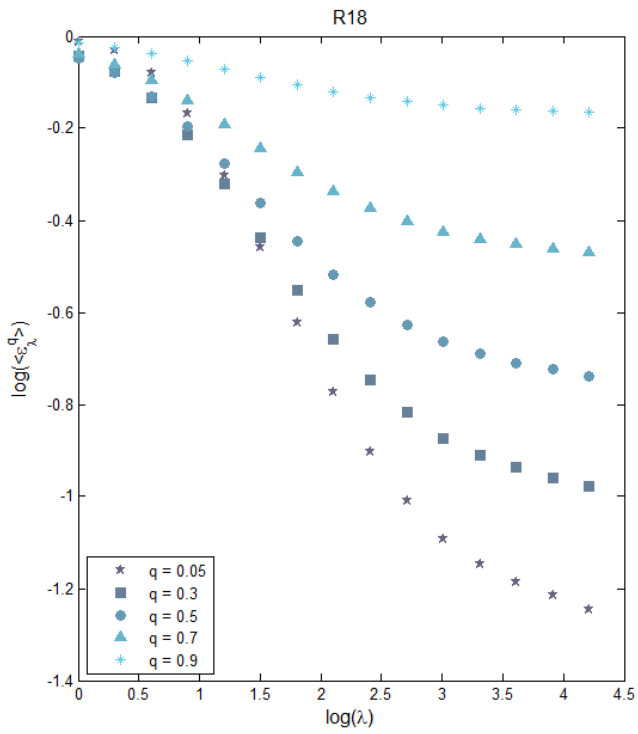


**Figure IV.16.** Log-log plot of the mean  $q$  moments of the rainfall intensity  $\varepsilon_\lambda$  against the scale coefficient  $\lambda$  for 1-minute precipitation data series from Warsaw rain gauge R18, for  $q < 1$  (on left) and for  $q > 1$  (on right). The time scales range from  $\lambda = 16384$  (1 minute) to  $\lambda = 1$  (11.4 days)

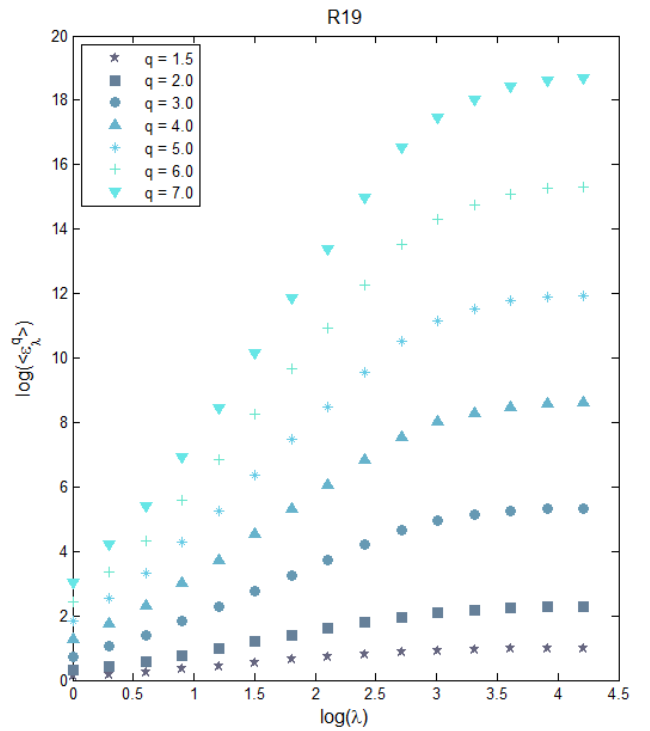
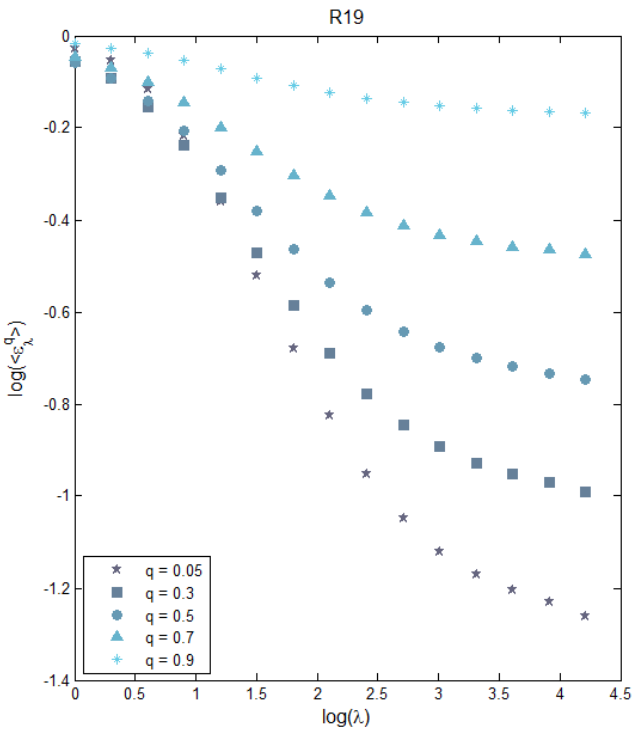


**Figure IV.17.** Log-log plot of the mean  $q$  moments of the rainfall intensity  $\varepsilon_\lambda$  against the scale coefficient  $\lambda$  for 1-minute precipitation data series from Warsaw rain gauge R19, for  $q < 1$  (on left) and for  $q > 1$  (on right). The time scales range from  $\lambda = 16384$  (1 minute) to  $\lambda = 1$  (11.4 days)

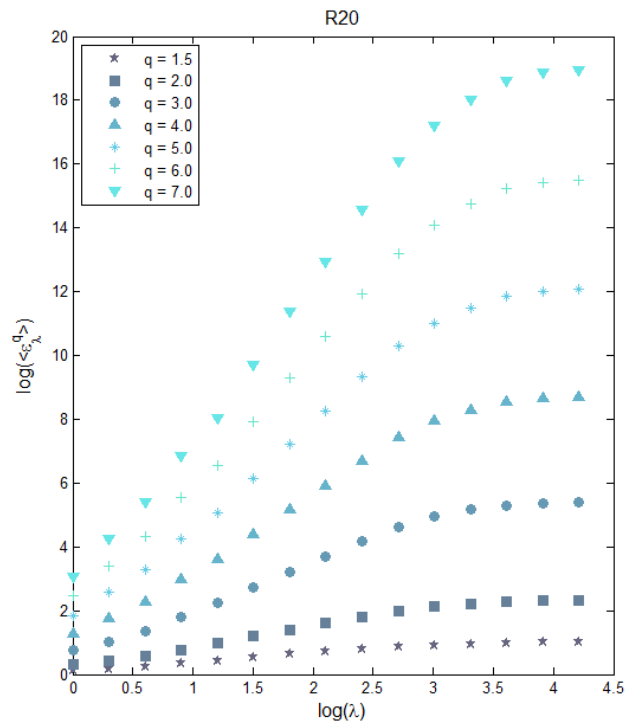
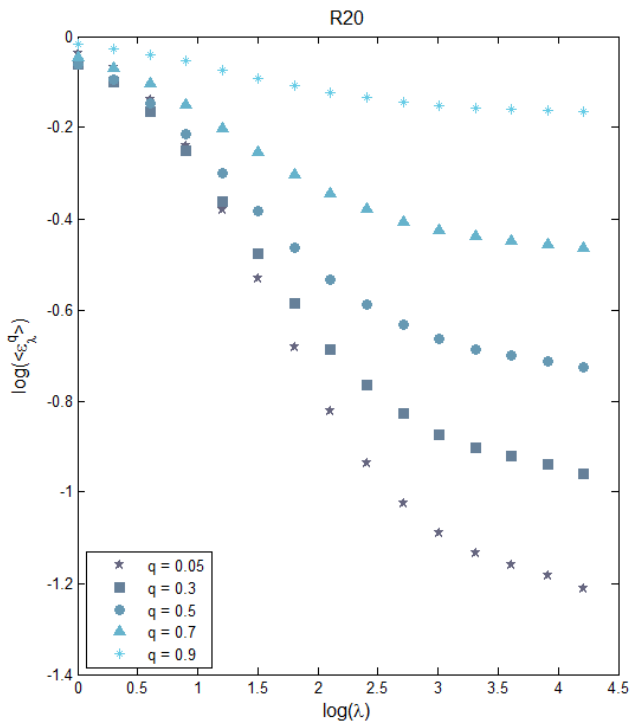


**Figure IV.18.** Log-log plot of the mean  $q$  moments of the rainfall intensity  $\varepsilon_\lambda$  against the scale coefficient  $\lambda$  for 1-minute precipitation data series from Warsaw rain gauge R20, for  $q < 1$  (on left) and for  $q > 1$  (on right). The time scales range from  $\lambda = 16384$  (1 minute) to  $\lambda = 1$  (11.4 days)

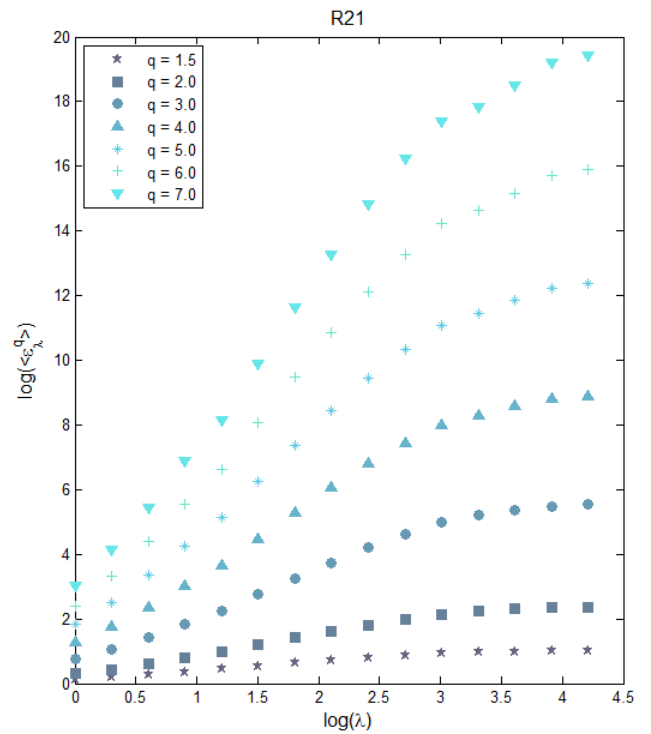
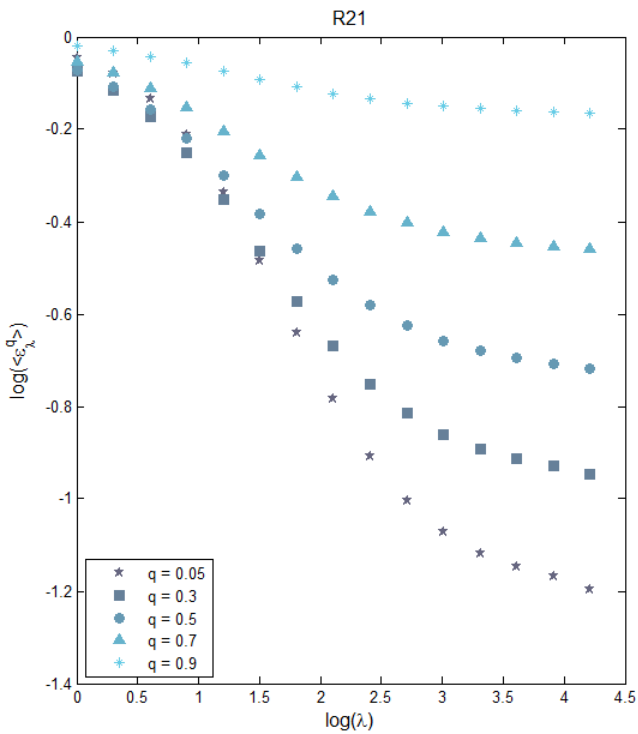


**Figure IV.19.** Log-log plot of the mean  $q$  moments of the rainfall intensity  $\varepsilon_\lambda$  against the scale coefficient  $\lambda$  for 1-minute precipitation data series from Warsaw rain gauge R21, for  $q < 1$  (on left) and for  $q > 1$  (on right). The time scales range from  $\lambda = 16384$  (1 minute) to  $\lambda = 1$  (11.4 days)

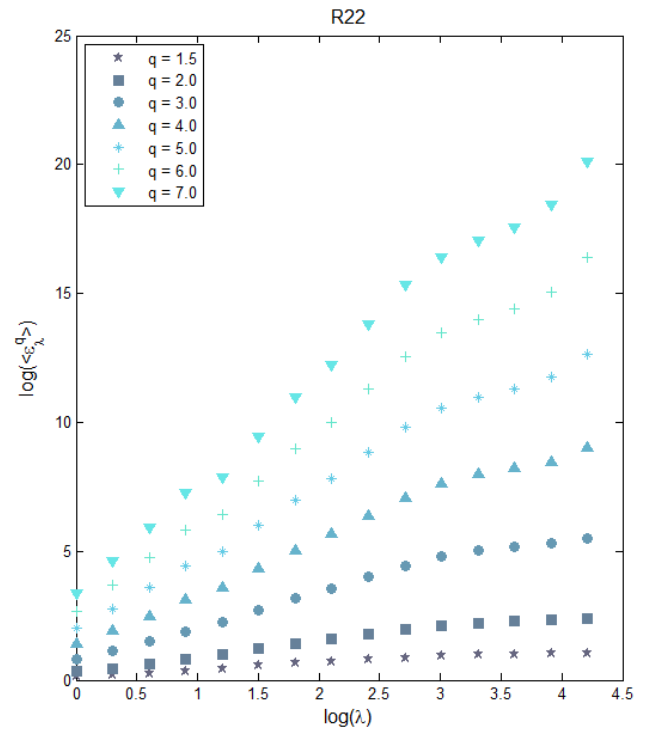
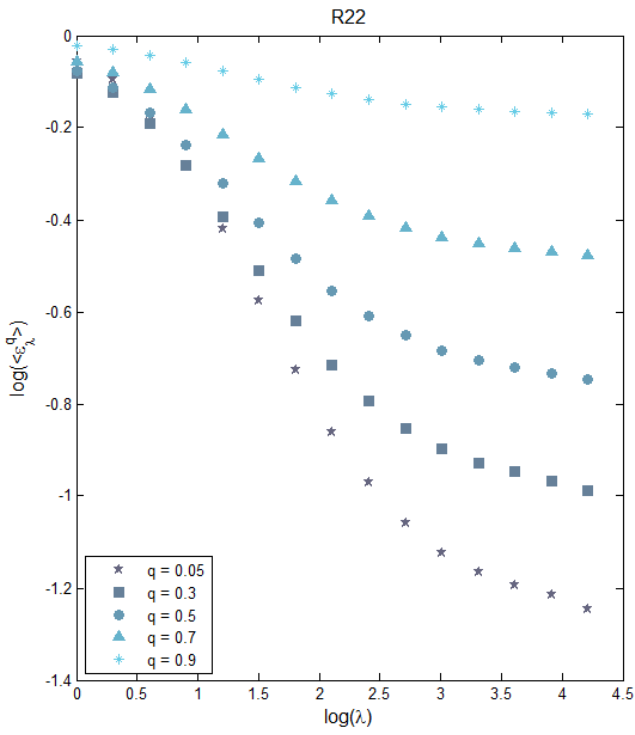


**Figure IV.20.** Log-log plot of the mean  $q$  moments of the rainfall intensity  $\varepsilon_\lambda$  against the scale coefficient  $\lambda$  for 1-minute precipitation data series from Warsaw rain gauge R22, for  $q < 1$  (on left) and for  $q > 1$  (on right). The time scales range from  $\lambda = 16384$  (1 minute) to  $\lambda = 1$  (11.4 days)

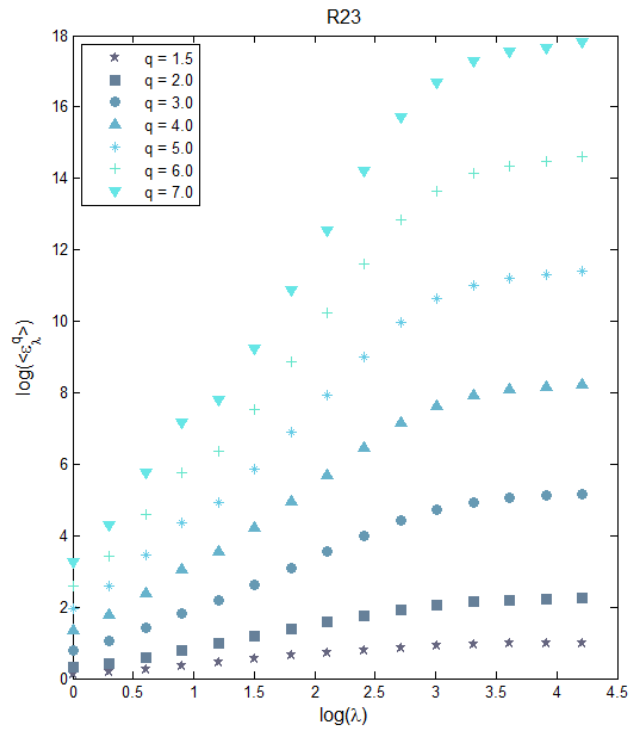
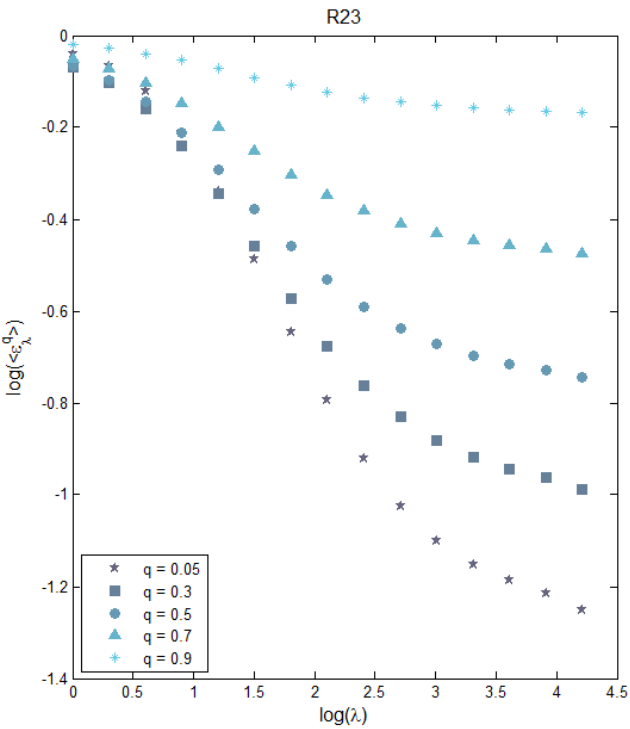


**Figure IV.21.** Log-log plot of the mean  $q$  moments of the rainfall intensity  $\varepsilon_\lambda$  against the scale coefficient  $\lambda$  for 1-minute precipitation data series from Warsaw rain gauge R23, for  $q < 1$  (on left) and for  $q > 1$  (on right). The time scales range from  $\lambda = 16384$  (1 minute) to  $\lambda = 1$  (11.4 days)

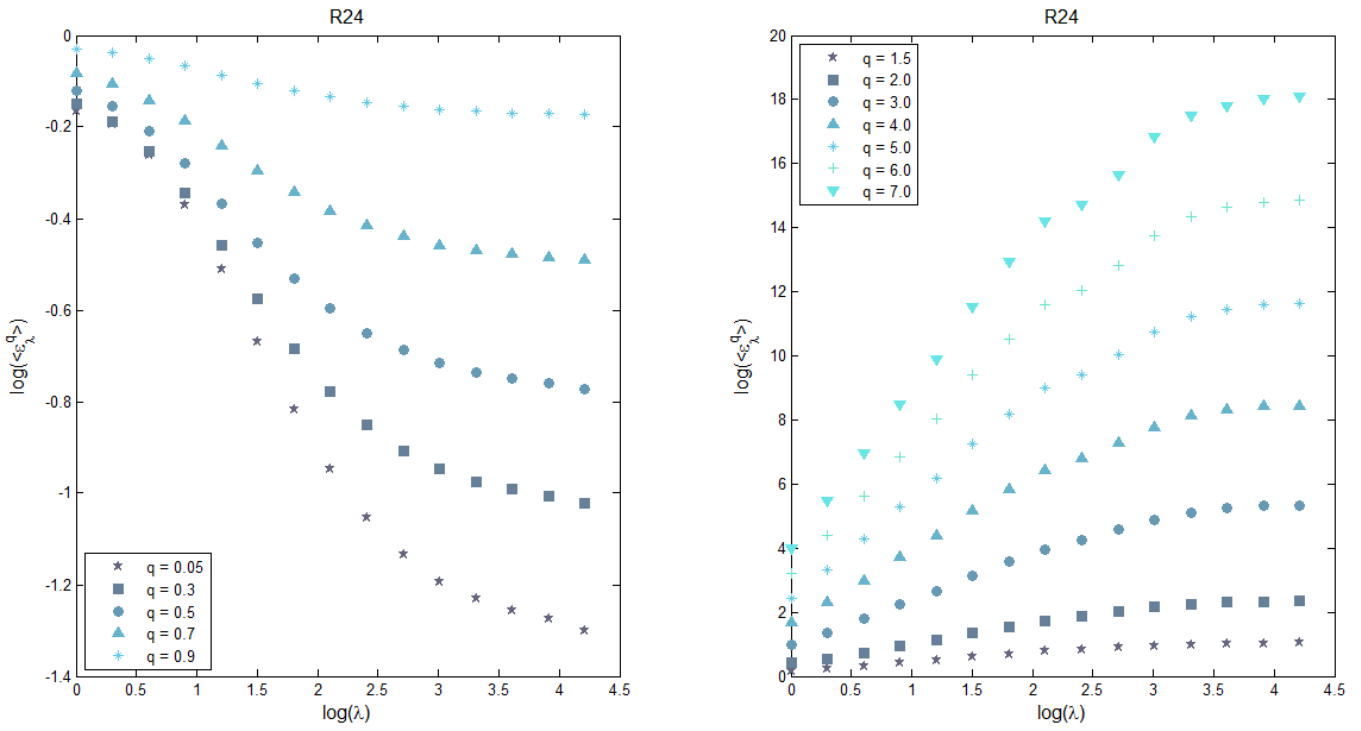


**Figure IV.22.** Log-log plot of the mean  $q$  moments of the rainfall intensity  $\varepsilon_\lambda$  against the scale coefficient  $\lambda$  for 1-minute precipitation data series from Warsaw rain gauge R24, for  $q < 1$  (on left) and for  $q > 1$  (on right). The time scales range from  $\lambda = 16384$  (1 minute) to  $\lambda = 1$  (11.4 days)

## Section B

Empirical moments scaling function plots obtained by the trace moment method for 1-minute rainfall from Warsaw, from 2008 to 2010, for time scales from 1 minute up to 16384 minutes (11.4 days).

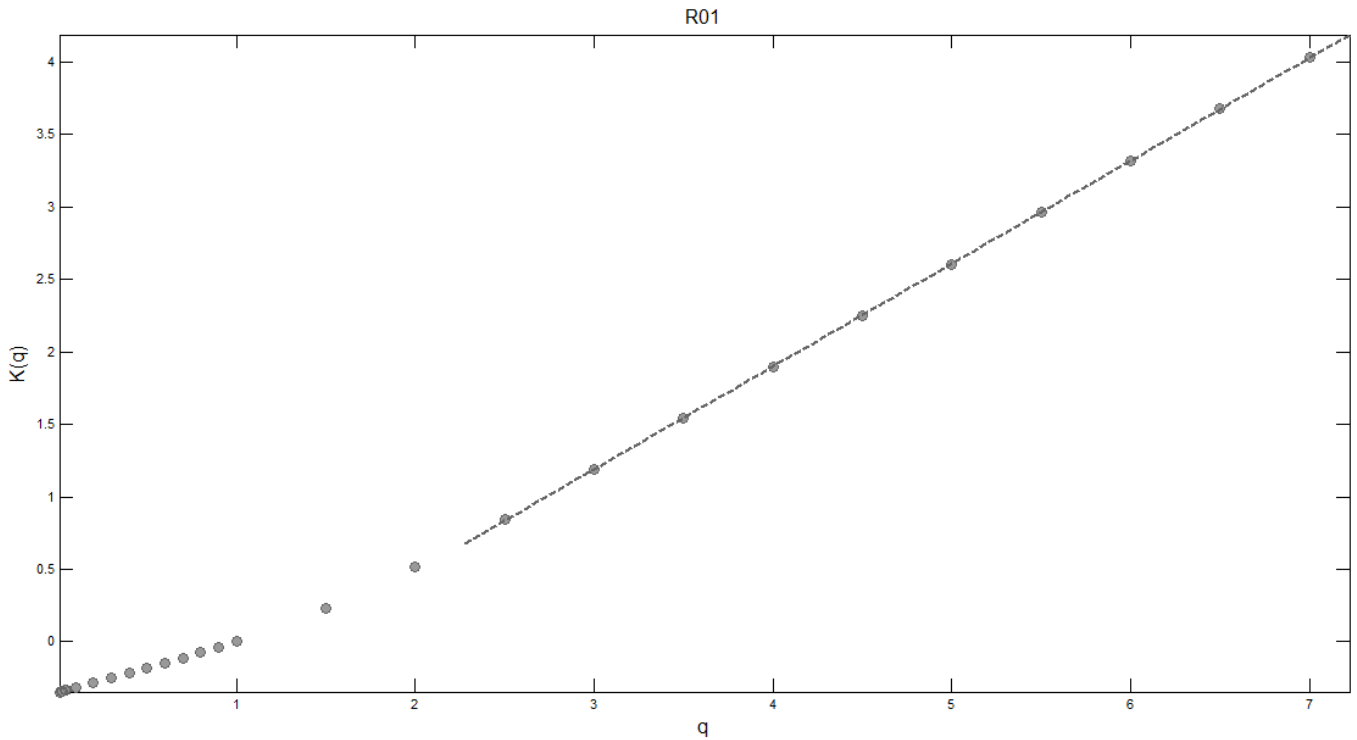


**Figure IV.23.** The empirical scaling moment function log-log plot obtained for 1-minute precipitation data series from Warsaw rain gauge R01 for time scales from  $\lambda = 16384$  (1 minute) to  $\lambda = 1$  (11.4 days)

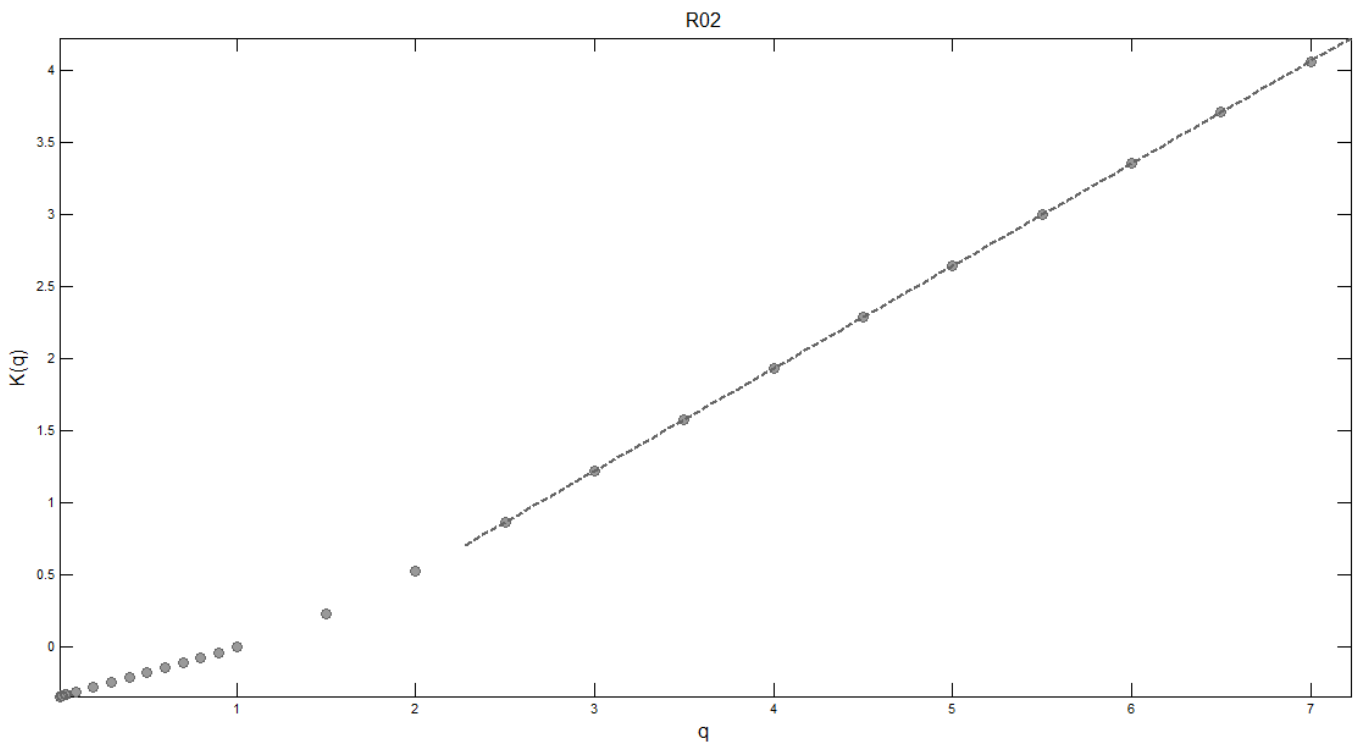


**Figure IV.24.** The empirical scaling moment function log-log plot obtained for 1-minute precipitation data series from Warsaw rain gauge R02 for time scales from  $\lambda = 16384$  (1 minute) to  $\lambda = 1$  (11.4 days)

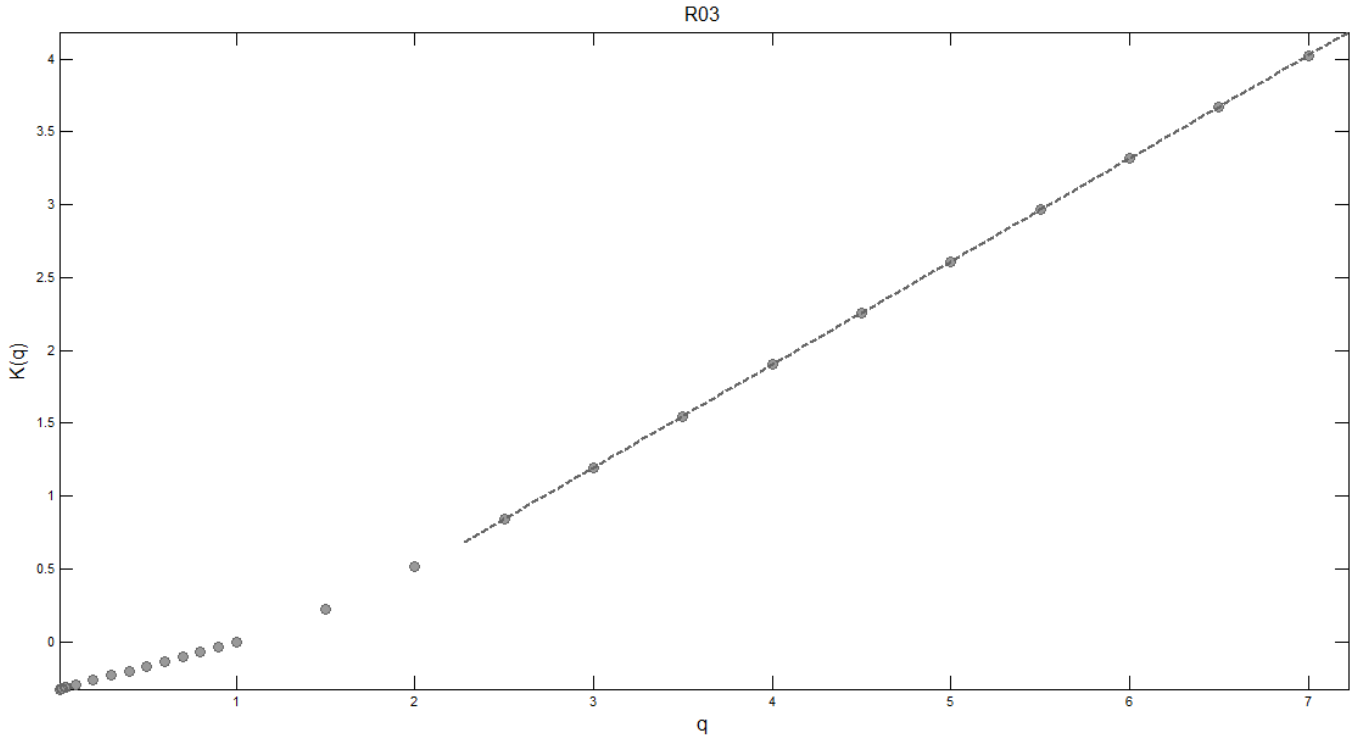


**Figure IV.25.** The empirical scaling moment function log-log plot obtained for 1-minute precipitation data series from Warsaw rain gauge R03 for time scales from  $\lambda = 16384$  (1 minute) to  $\lambda = 1$  (11.4 days)

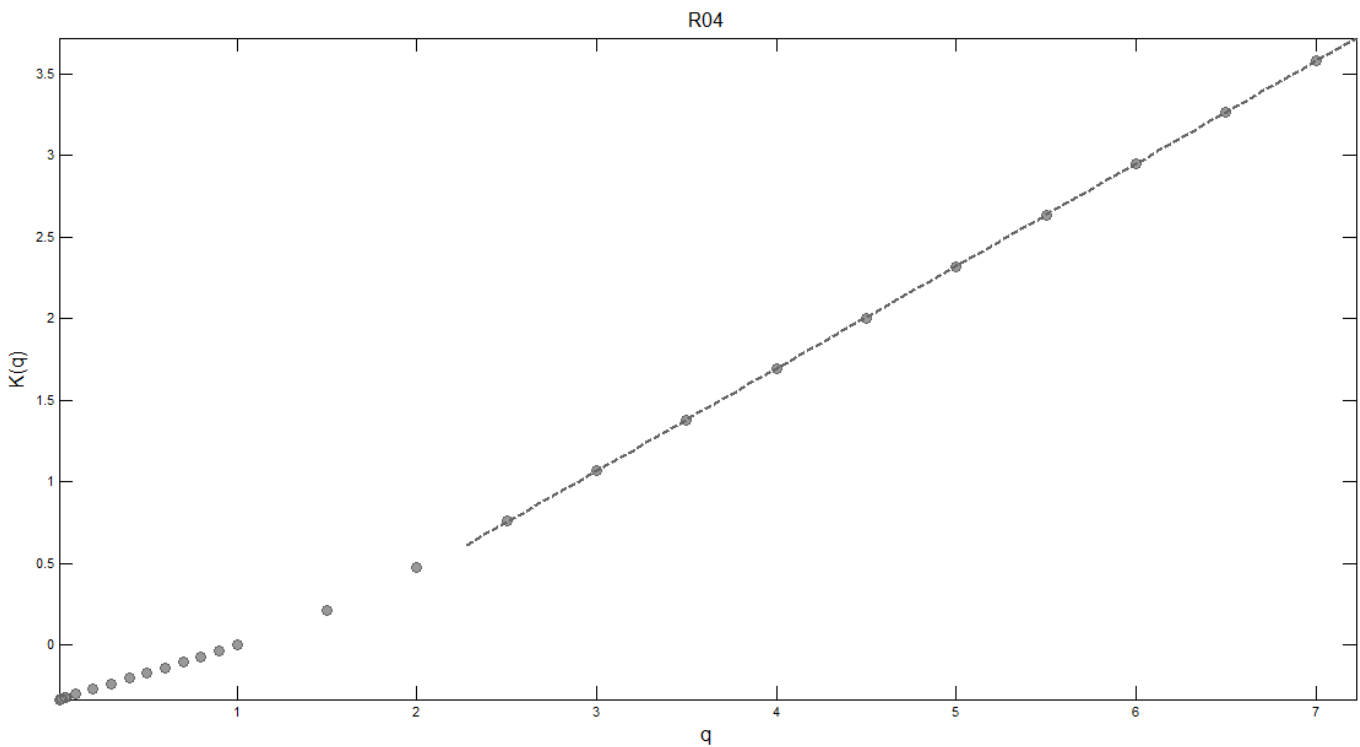


**Figure IV.26.** The empirical scaling moment function log-log plot obtained for 1-minute precipitation data series from Warsaw rain gauge R04 for time scales from  $\lambda = 16384$  (1 minute) to  $\lambda = 1$  (11.4 days)

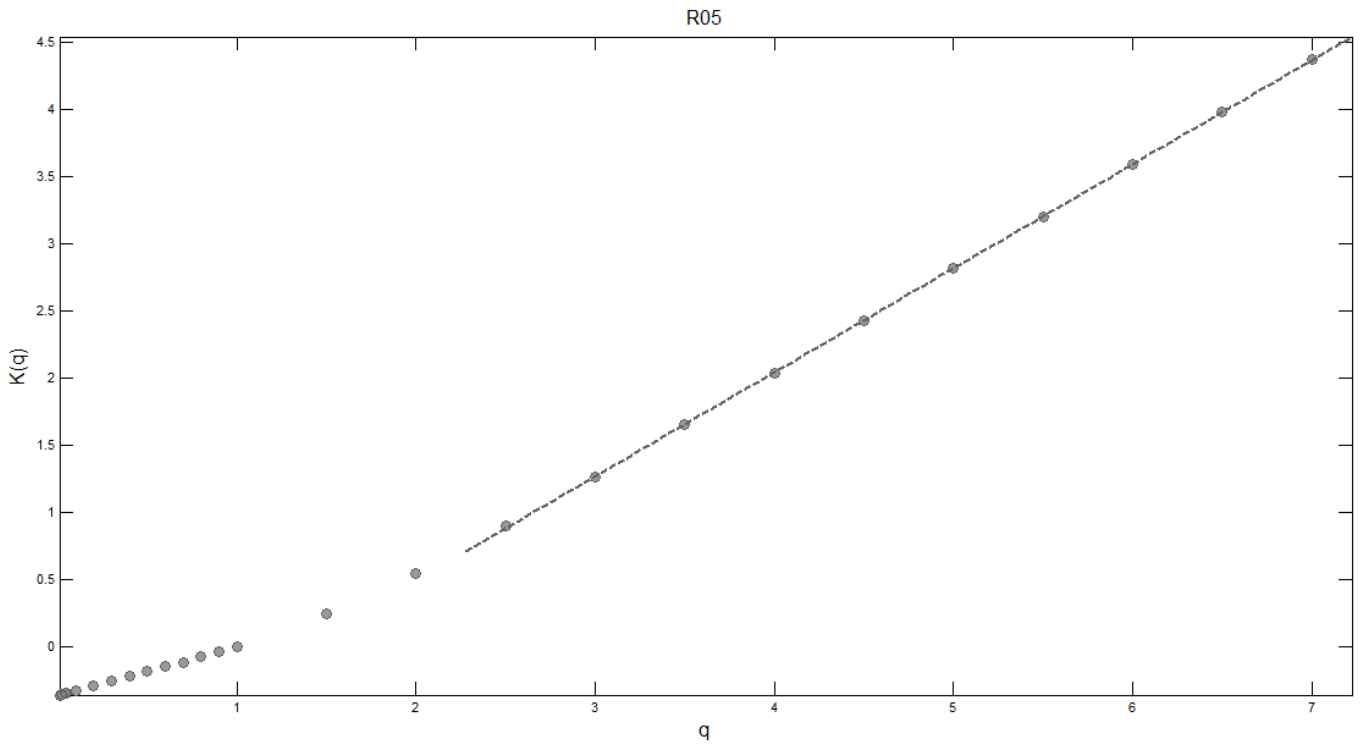


**Figure IV.27.** The empirical scaling moment function log-log plot obtained for 1-minute precipitation data series from Warsaw rain gauge R05 for time scales from  $\lambda = 16384$  (1 minute) to  $\lambda = 1$  (11.4 days)

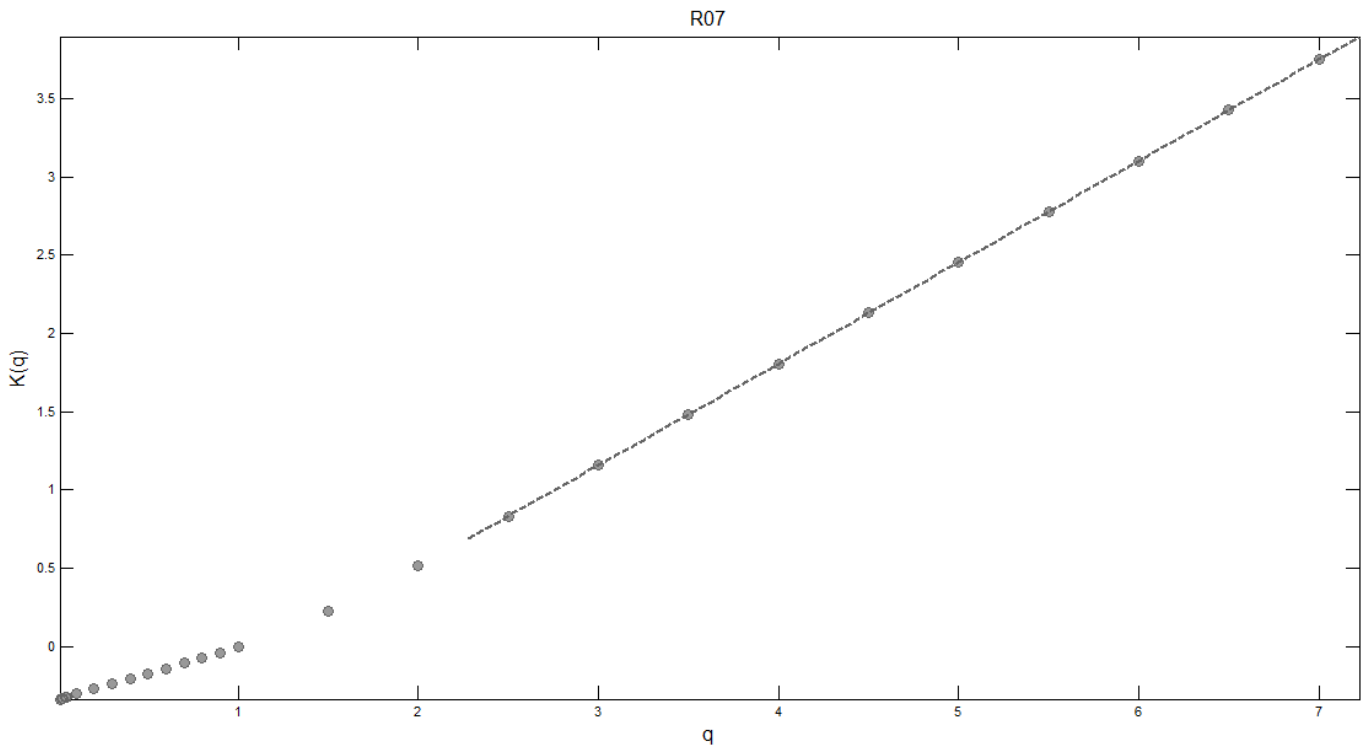


**Figure IV.28.** The empirical scaling moment function log-log plot obtained for 1-minute precipitation data series from Warsaw rain gauge R07 for time scales from  $\lambda = 16384$  (1 minute) to  $\lambda = 1$  (11.4 days)

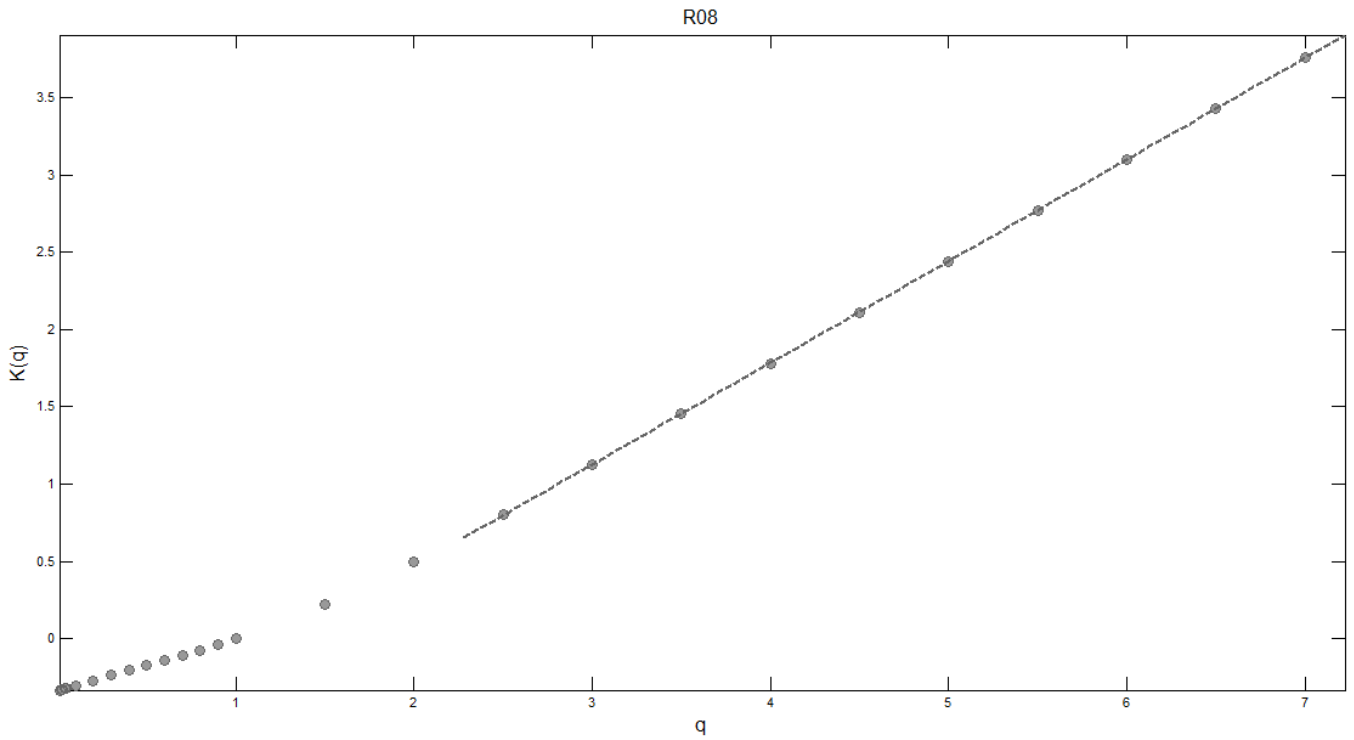


**Figure IV.29.** The empirical scaling moment function log-log plot obtained for 1-minute precipitation data series from Warsaw rain gauge R08 for time scales from  $\lambda = 16384$  (1 minute) to  $\lambda = 1$  (11.4 days)

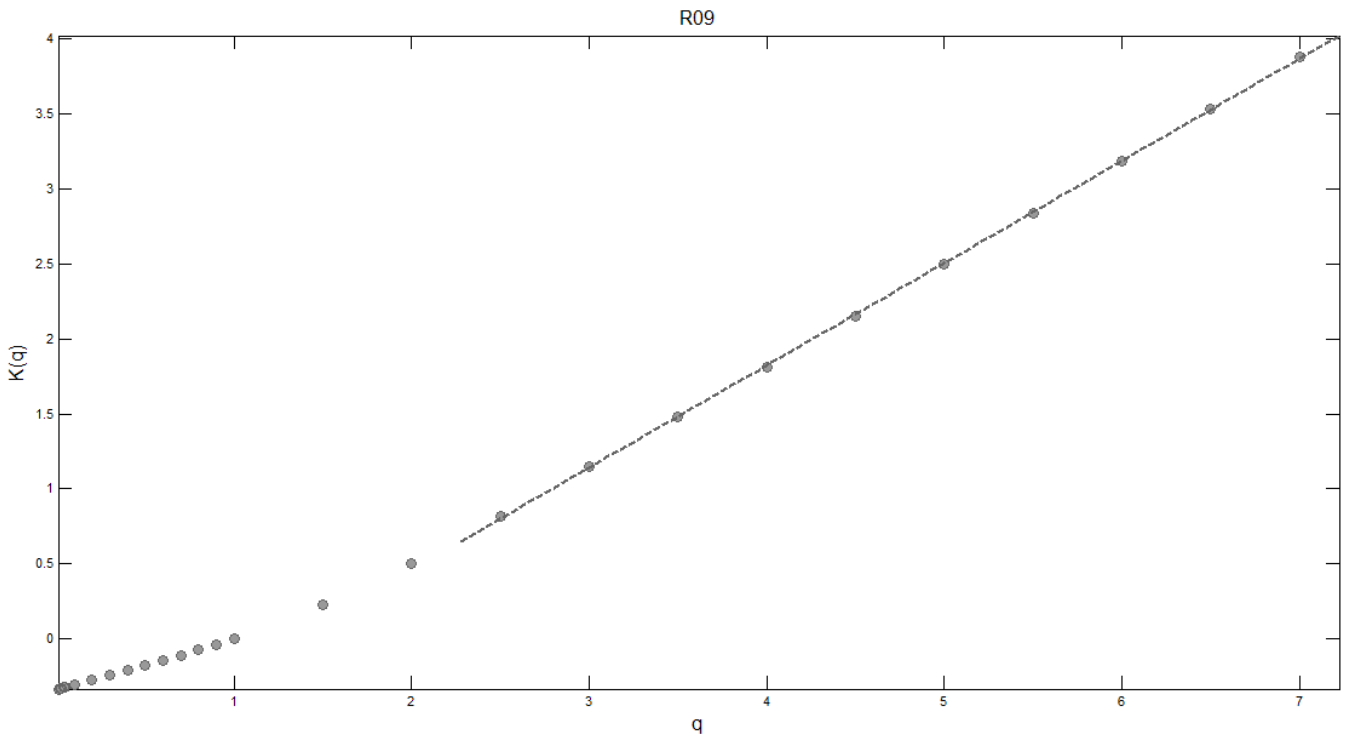


**Figure IV.30.** The empirical scaling moment function log-log plot obtained for 1-minute precipitation data series from Warsaw rain gauge R09 for time scales from  $\lambda = 16384$  (1 minute) to  $\lambda = 1$  (11.4 days)

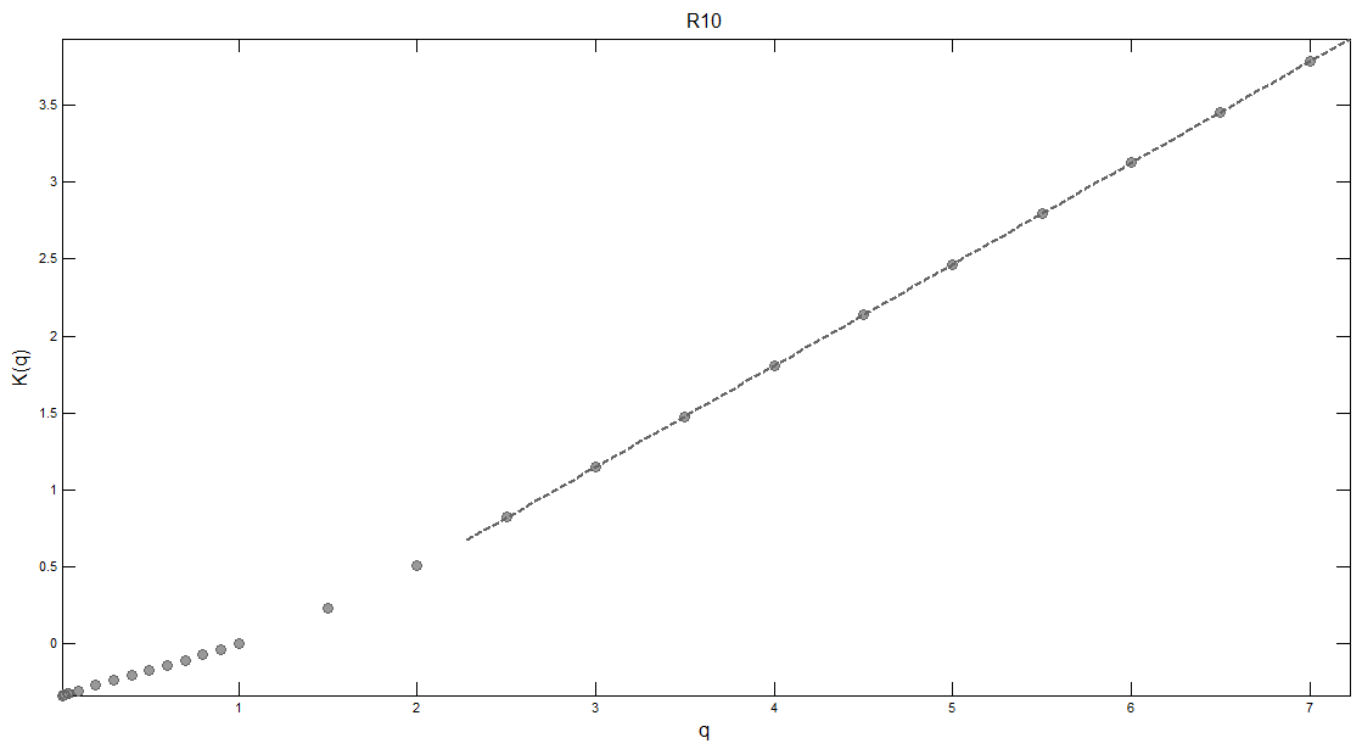


**Figure IV.31.** The empirical scaling moment function log-log plot obtained for 1-minute precipitation data series from Warsaw rain gauge R10 for time scales from  $\lambda = 16384$  (1 minute) to  $\lambda = 1$  (11.4 days)

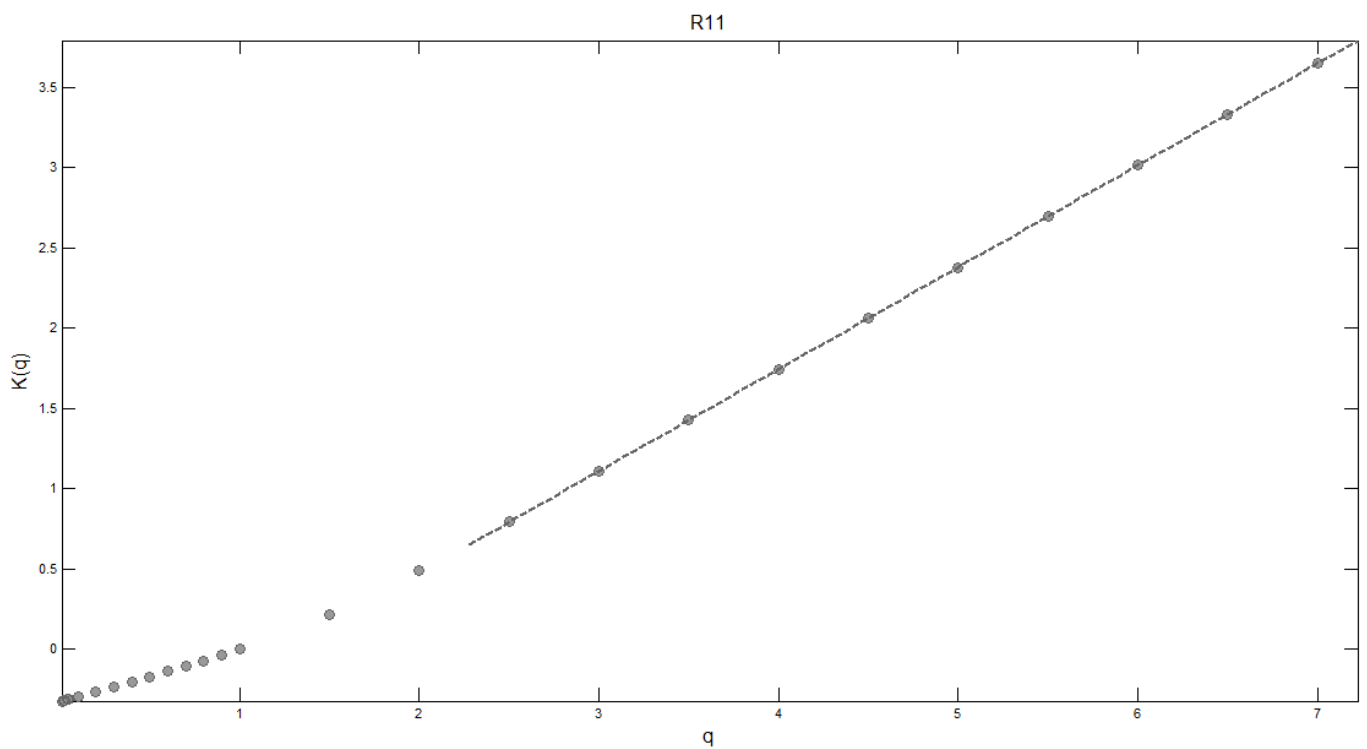


**Figure IV.32.** The empirical scaling moment function log-log plot obtained for 1-minute precipitation data series from Warsaw rain gauge R11 for time scales from  $\lambda = 16384$  (1 minute) to  $\lambda = 1$  (11.4 days)

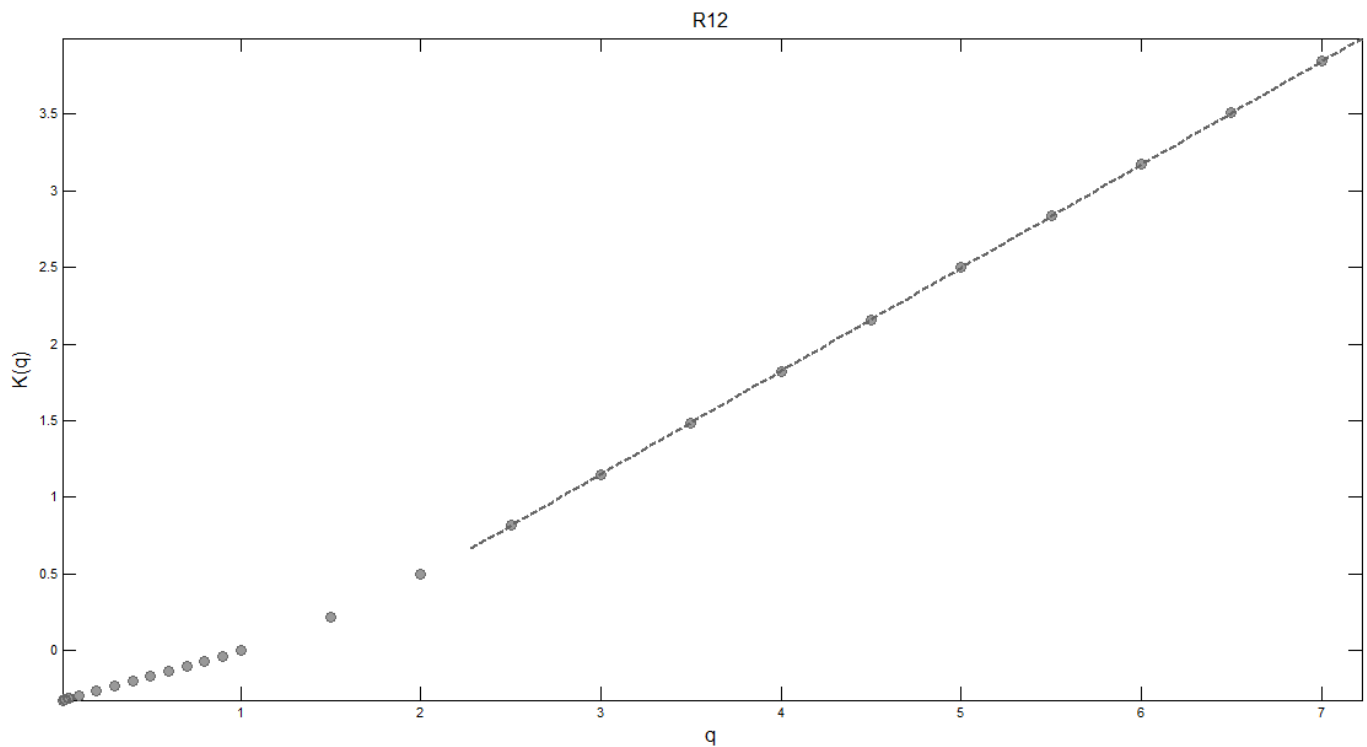


**Figure IV.33.** The empirical scaling moment function log-log plot obtained for 1-minute precipitation data series from Warsaw rain gauge R12 for time scales from  $\lambda = 16384$  (1 minute) to  $\lambda = 1$  (11.4 days)

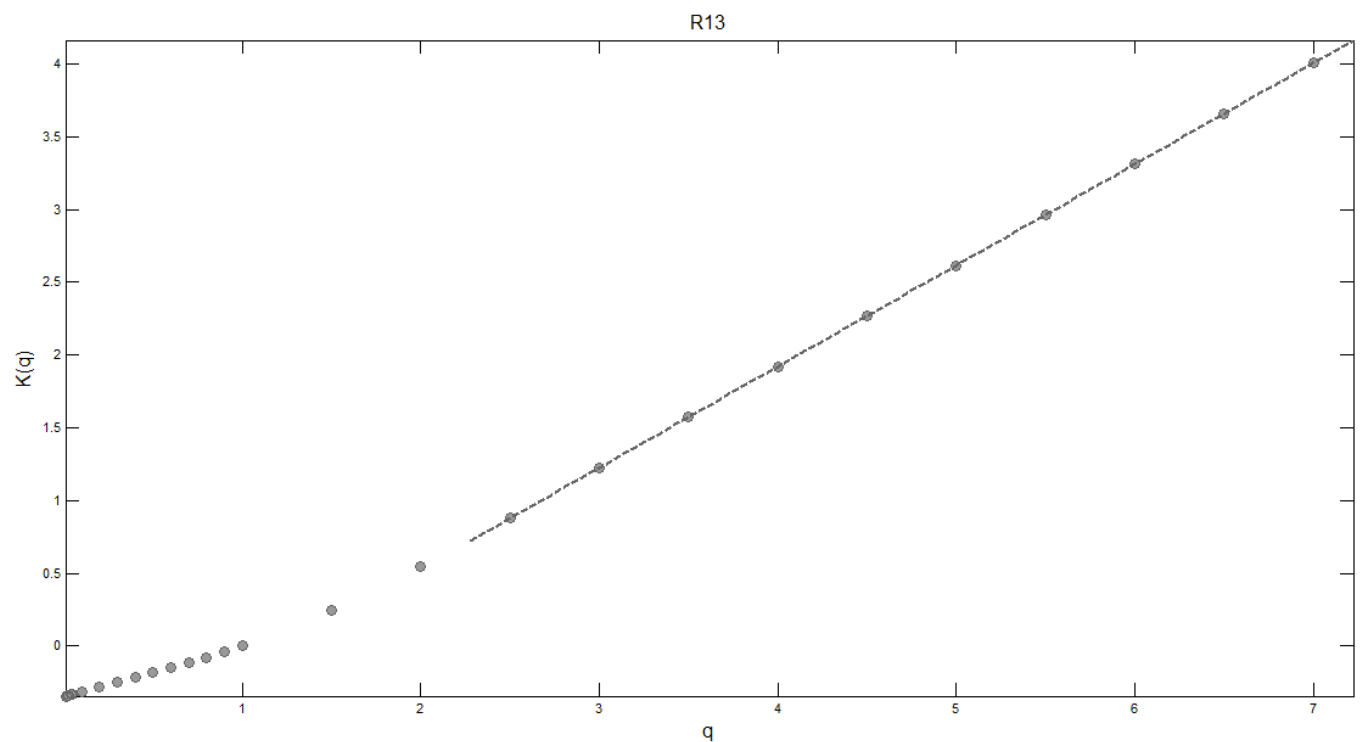


**Figure IV.34.** The empirical scaling moment function log-log plot obtained for 1-minute precipitation data series from Warsaw rain gauge R13 for time scales from  $\lambda = 16384$  (1 minute) to  $\lambda = 1$  (11.4 days)

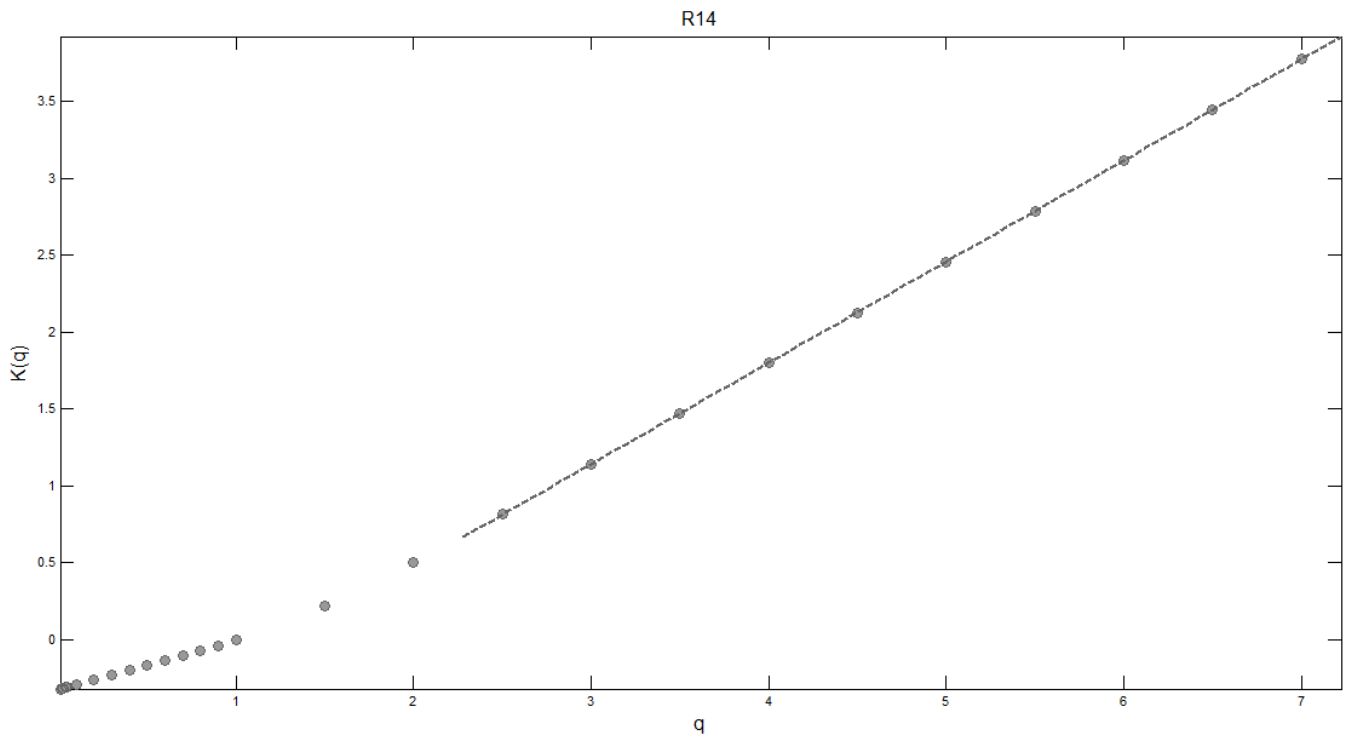


**Figure IV.35.** The empirical scaling moment function log-log plot obtained for 1-minute precipitation data series from Warsaw rain gauge R14 for time scales from  $\lambda = 16384$  (1 minute) to  $\lambda = 1$  (11.4 days)

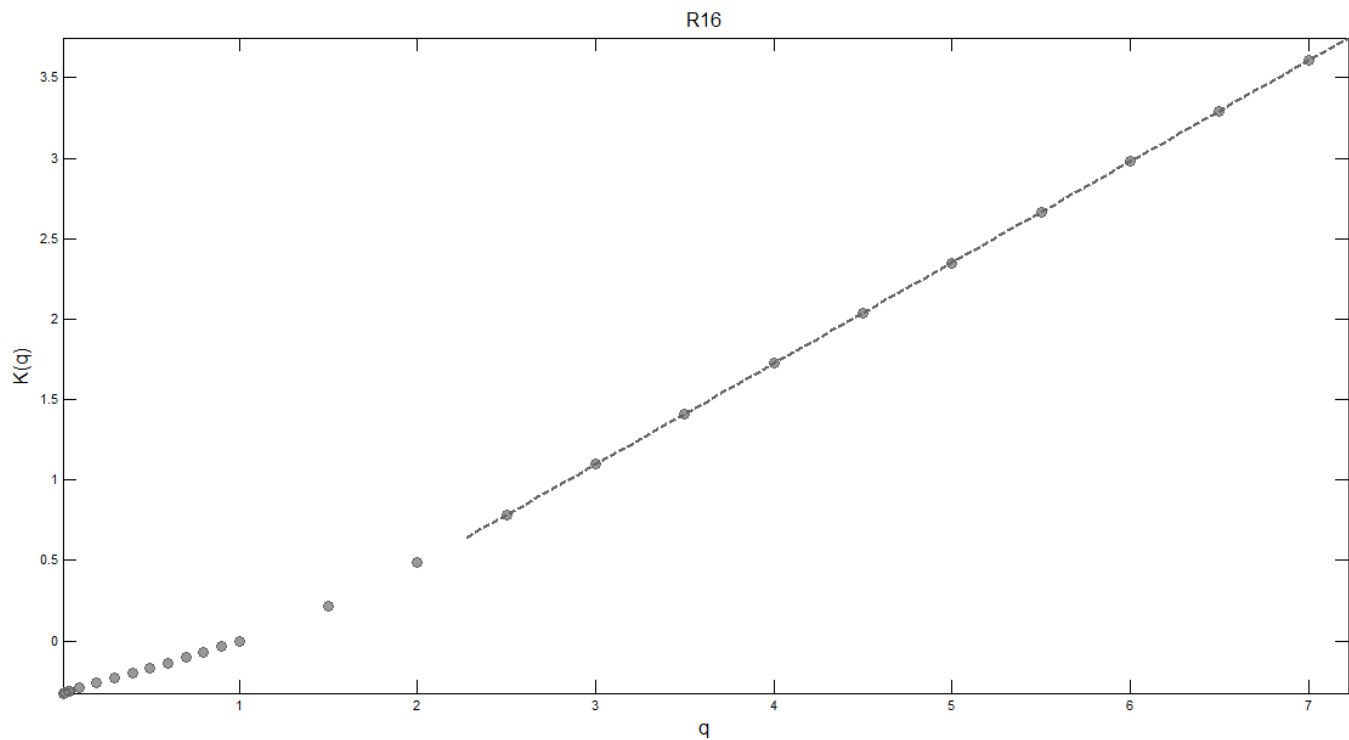


**Figure IV.36.** The empirical scaling moment function log-log plot obtained for 1-minute precipitation data series from Warsaw rain gauge R16 for time scales from  $\lambda = 16384$  (1 minute) to  $\lambda = 1$  (11.4 days)

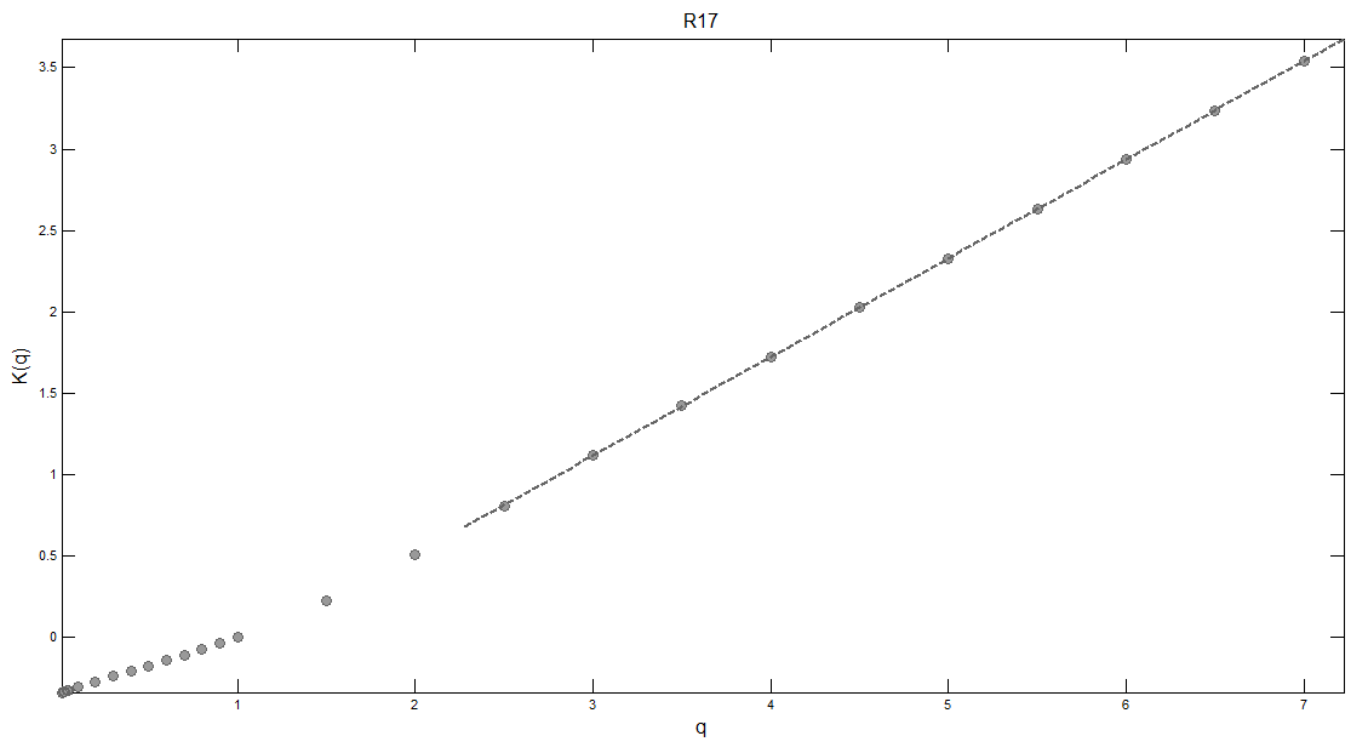


**Figure IV.37.** The empirical scaling moment function log-log plot obtained for 1-minute precipitation data series from Warsaw rain gauge R17 for time scales from  $\lambda = 16384$  (1 minute) to  $\lambda = 1$  (11.4 days)

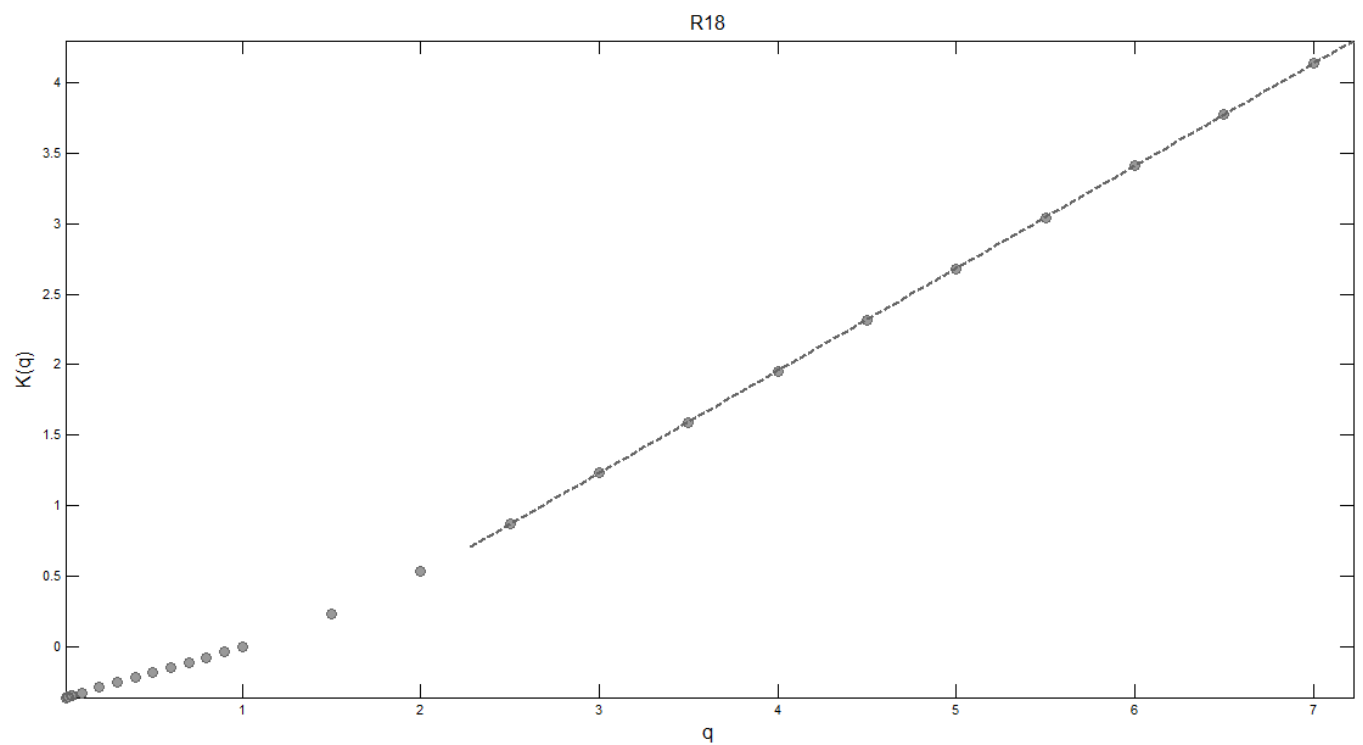


**Figure IV.38.** The empirical scaling moment function log-log plot obtained for 1-minute precipitation data series from Warsaw rain gauge R18 for time scales from  $\lambda = 16384$  (1 minute) to  $\lambda = 1$  (11.4 days)

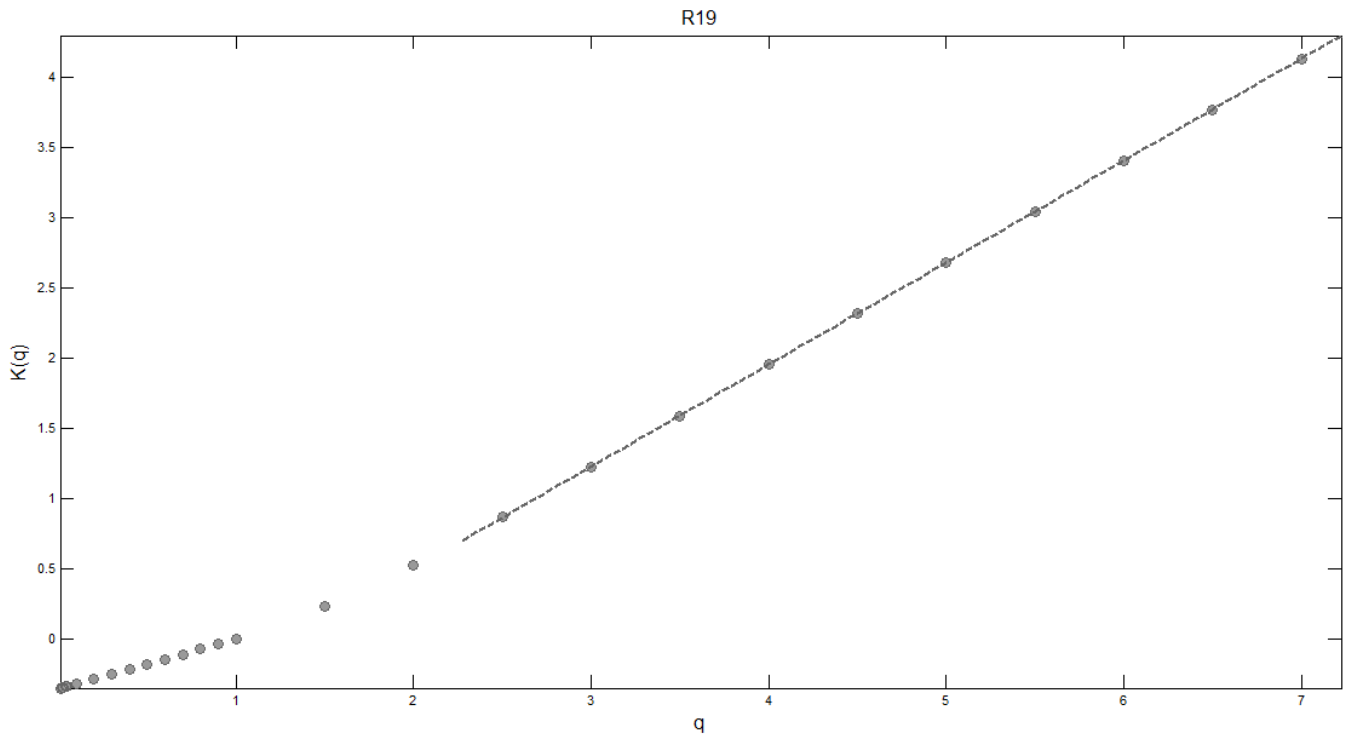


**Figure IV.39.** The empirical scaling moment function log-log plot obtained for 1-minute precipitation data series from Warsaw rain gauge R19 for time scales from  $\lambda = 16384$  (1 minute) to  $\lambda = 1$  (11.4 days)

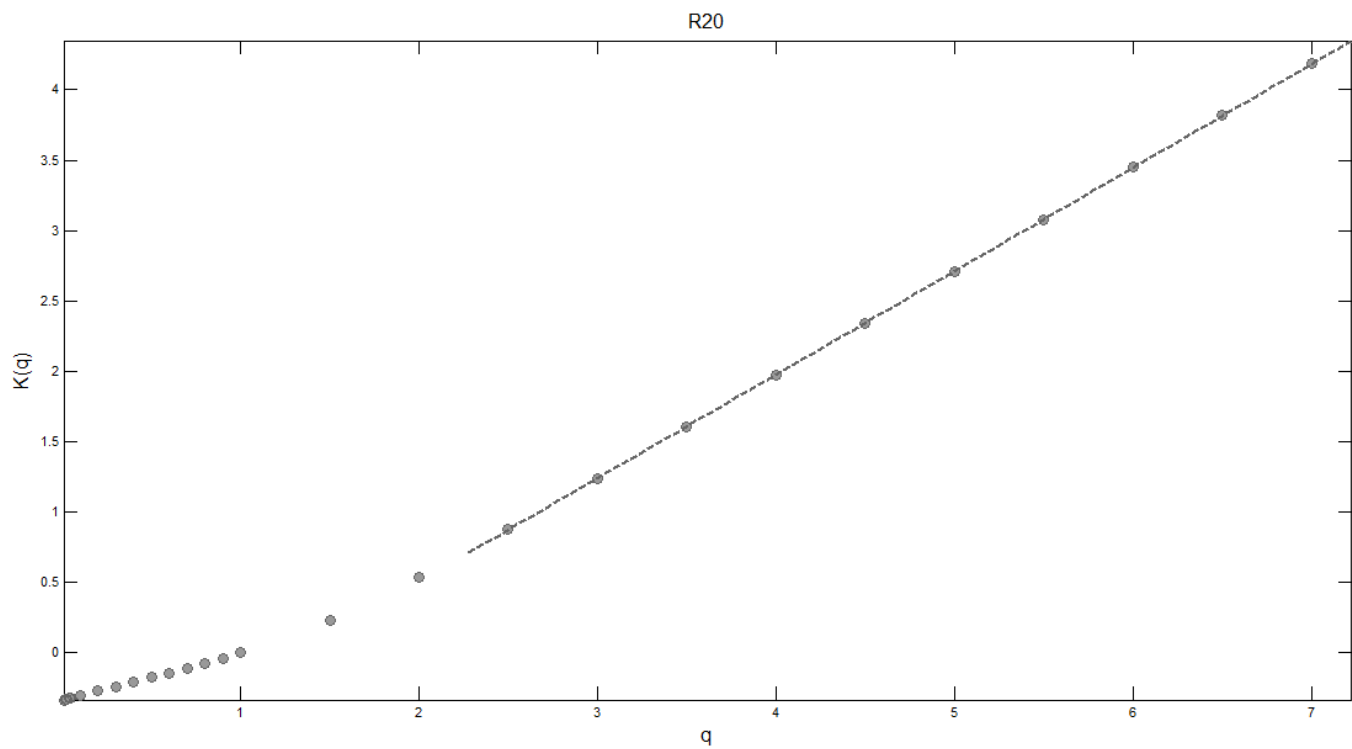


**Figure IV.40.** The empirical scaling moment function log-log plot obtained for 1-minute precipitation data series from Warsaw rain gauge R20 for time scales from  $\lambda = 16384$  (1 minute) to  $\lambda = 1$  (11.4 days)

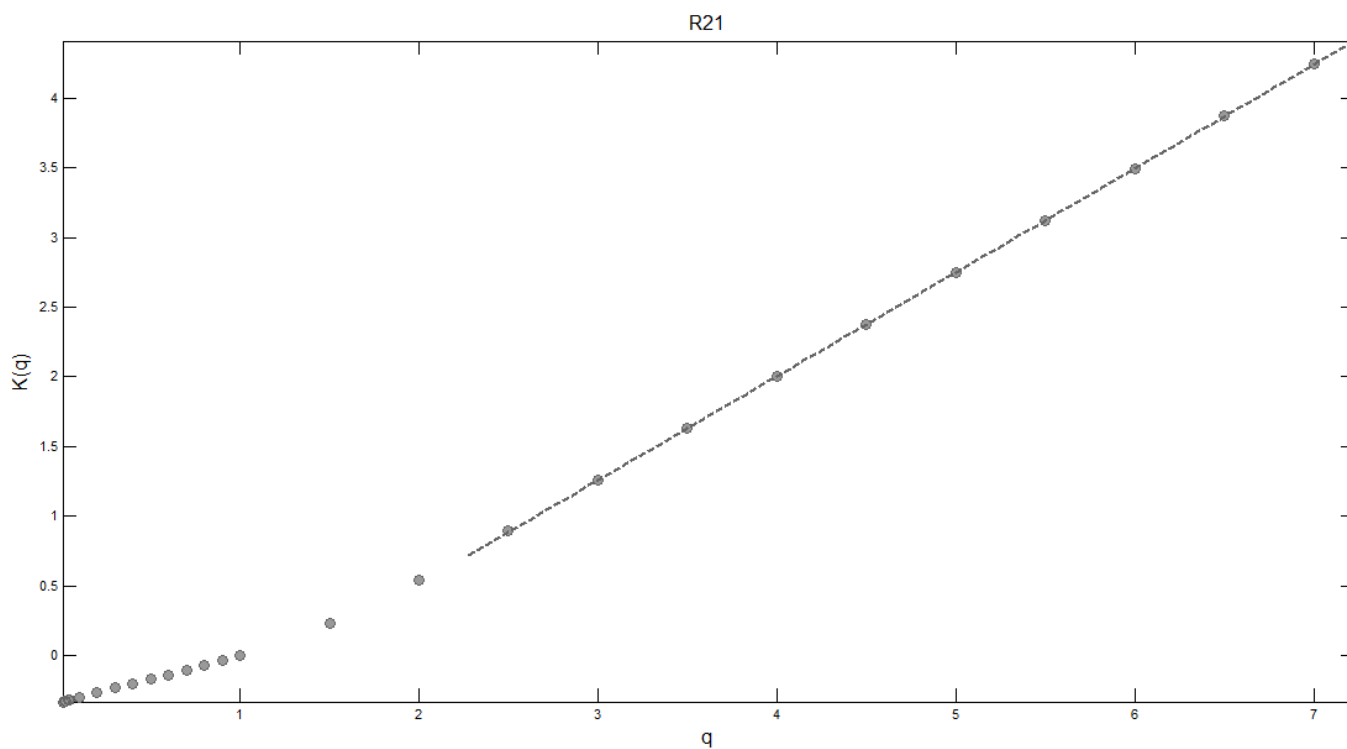


**Figure IV.41.** The empirical scaling moment function log-log plot obtained for 1-minute precipitation data series from Warsaw rain gauge R21 for time scales from  $\lambda = 16384$  (1 minute) to  $\lambda = 1$  (11.4 days)

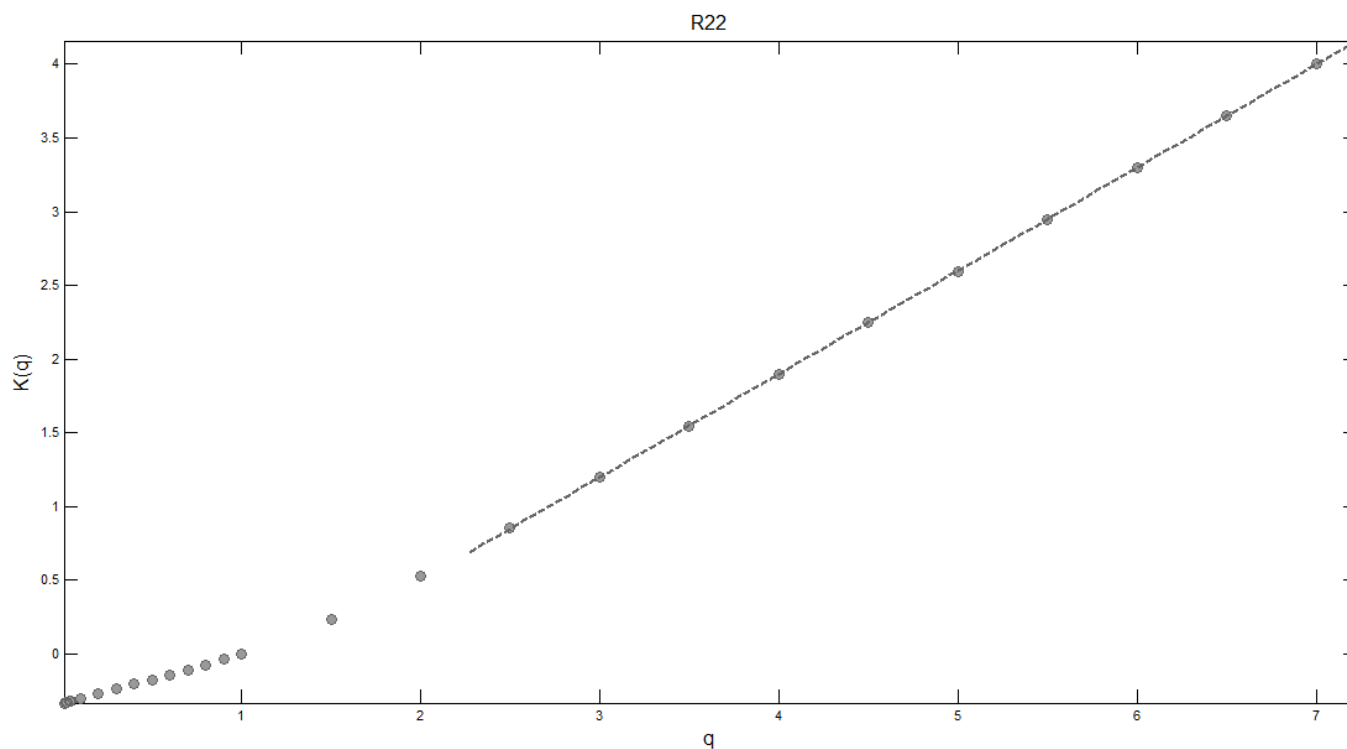


**Figure IV.42.** The empirical scaling moment function log-log plot obtained for 1-minute precipitation data series from Warsaw rain gauge R22 for time scales from  $\lambda = 16384$  (1 minute) to  $\lambda = 1$  (11.4 days)

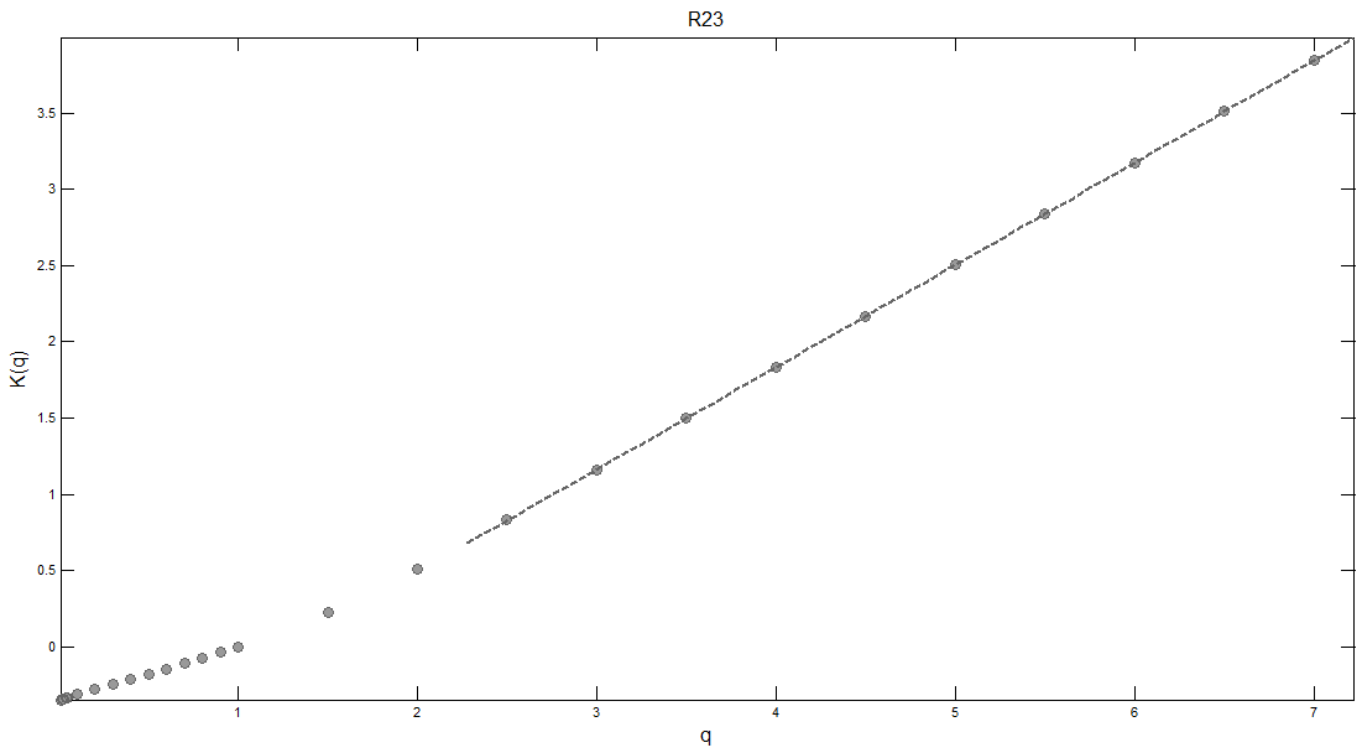


**Figure IV.43.** The empirical scaling moment function log-log plot obtained for 1-minute precipitation data series from Warsaw rain gauge R23 for time scales from  $\lambda = 16384$  (1 minute) to  $\lambda = 1$  (11.4 days)

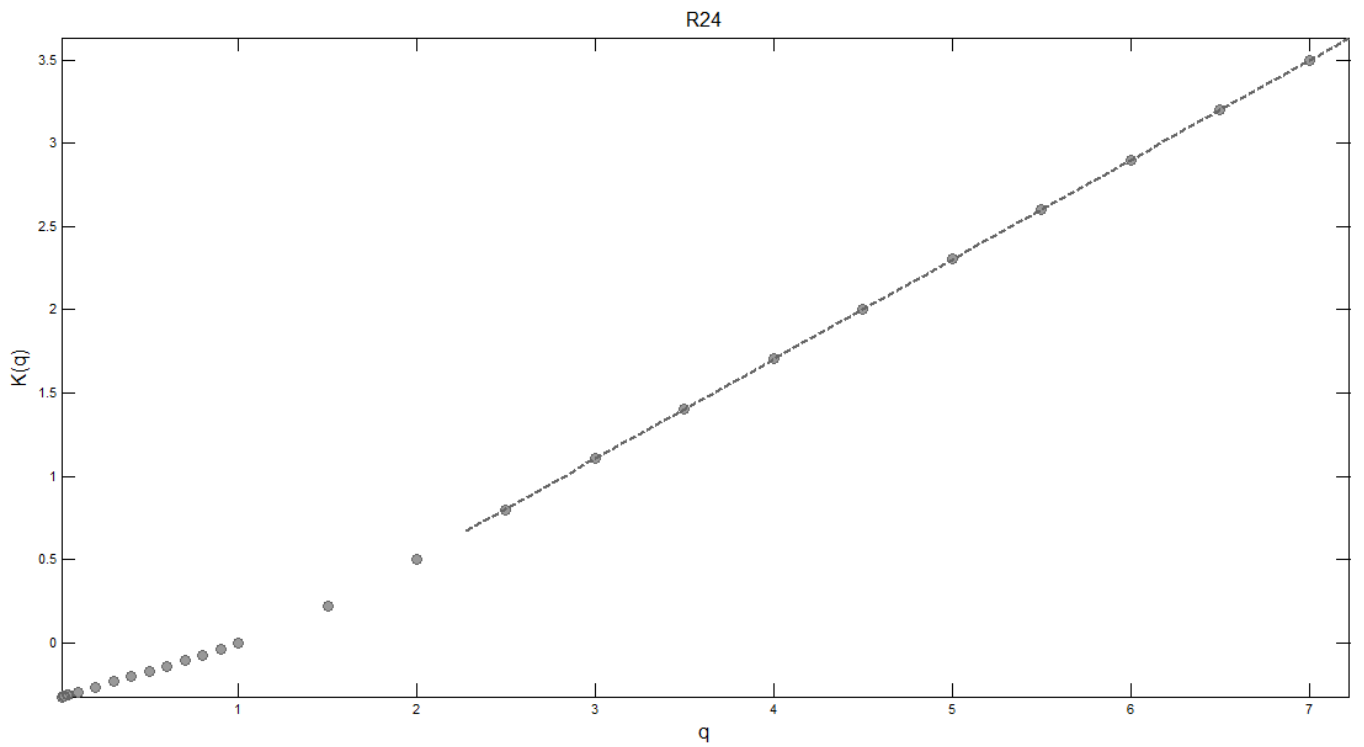


**Figure IV.44.** The empirical scaling moment function log-log plot obtained for 1-minute precipitation data series from Warsaw rain gauge R24 for time scales from  $\lambda = 16384$  (1 minute) to  $\lambda = 1$  (11.4 days)

## APPENDIX V.

### PROBABILITY DISTRIBUTION/MULTIPLE SCALING METHOD PLOTS

#### Section A

Log-log plots of the probability of exceeding rainfall-intensity levels for different values of singularity  $\gamma$  relation with scale parameter  $\lambda$ , obtained for the 1-minute precipitation intensity time-series from Warsaw, from 2008 to 2010.

The graphs refer only to sample singularity orders  $\gamma$  (to be read in the legend). The dotted line in the plots underlines the almost exact linear fitting for the specific case of  $\gamma = 0.4$ .

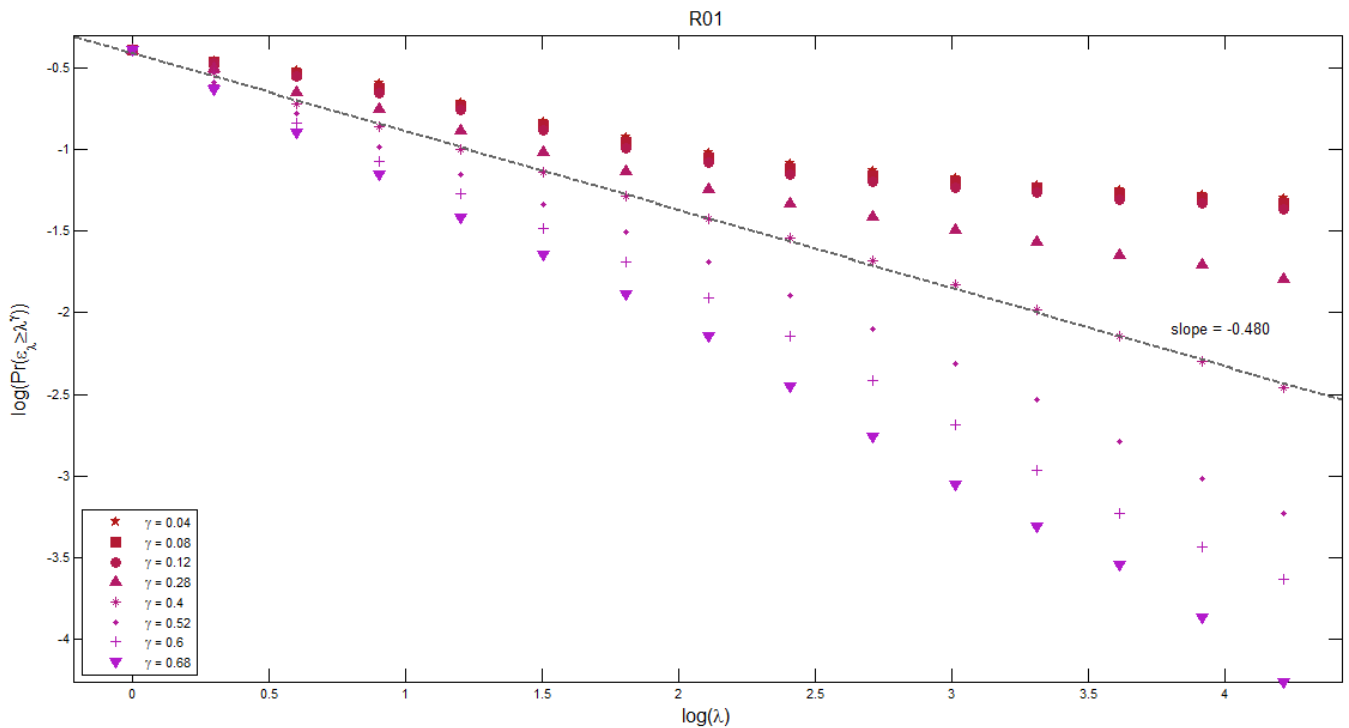


**Figure V.1.** Log-log plot of the probability of exceeding rainfall-intensity levels for sample values of singularity  $\gamma$  relation against scale parameter  $\lambda$ , obtained for 1-minute precipitation data series from Warsaw rain gauge R01. The time scales range from  $\lambda = 16384$  (1 minute) to  $\lambda = 1$  (11.4 days)

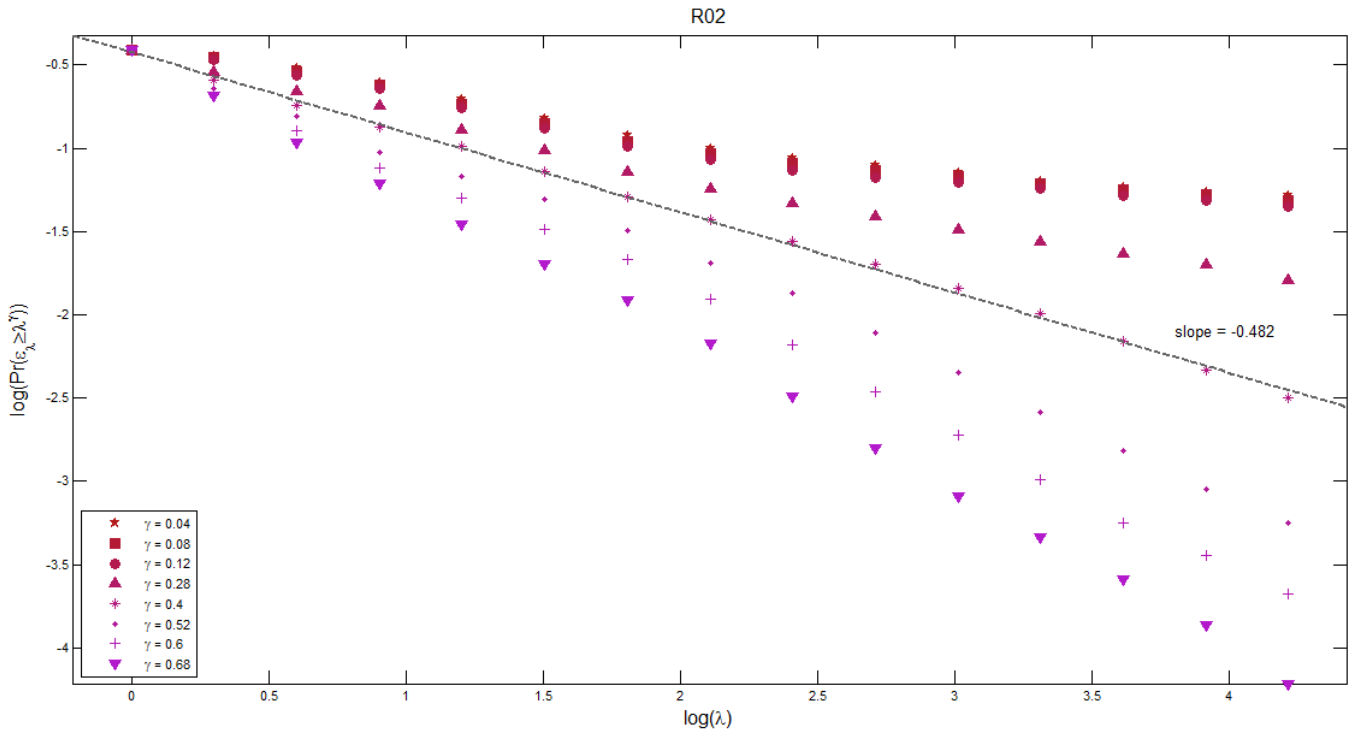


**Figure V.2.** Log-log plot of the probability of exceeding rainfall-intensity levels for sample values of singularity  $\gamma$  relation against scale parameter  $\lambda$ , obtained for 1-minute precipitation data series from Warsaw rain gauge R02. The time scales range from  $\lambda = 16384$  (1 minute) to  $\lambda = 1$  (11.4 days)

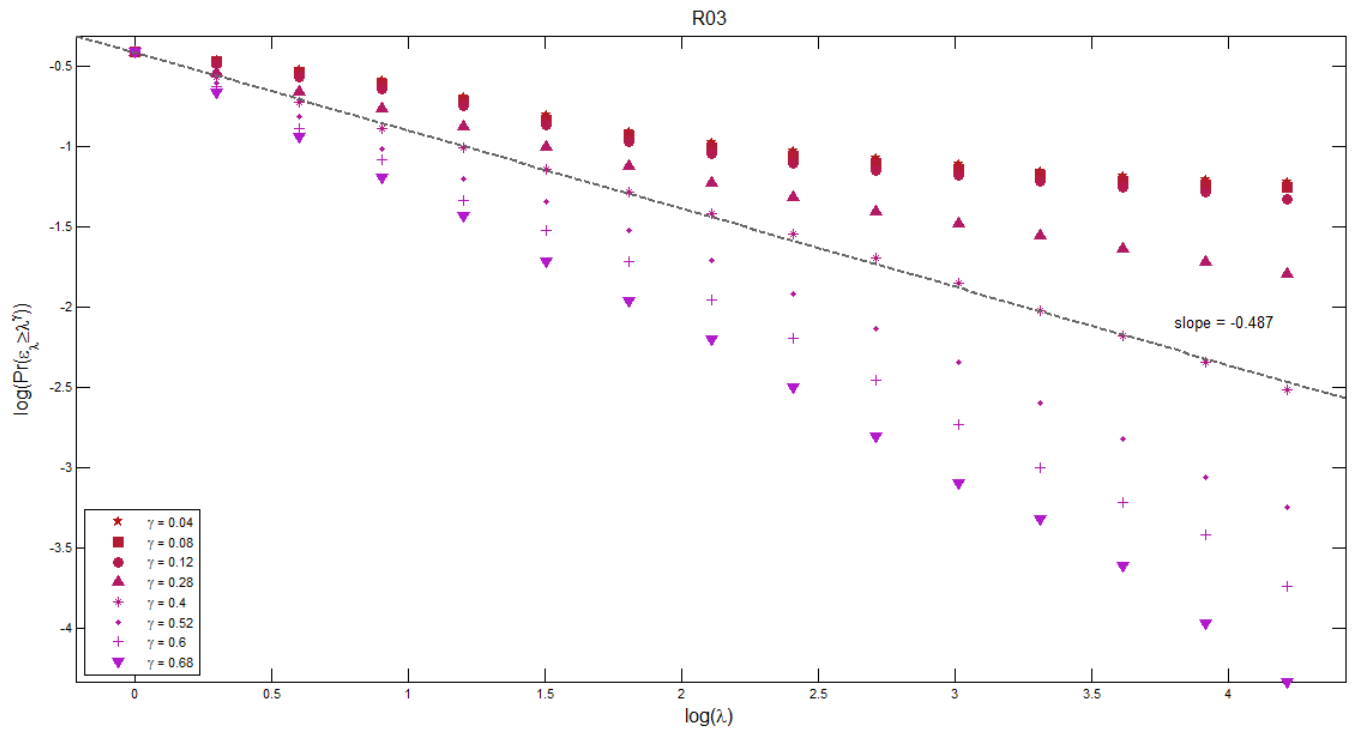


**Figure V.3.** Log-log plot of the probability of exceeding rainfall-intensity levels for sample values of singularity  $\gamma$  relation against scale parameter  $\lambda$ , obtained for 1-minute precipitation data series from Warsaw rain gauge R03. The time scales range from  $\lambda = 16384$  (1 minute) to  $\lambda = 1$  (11.4 days)

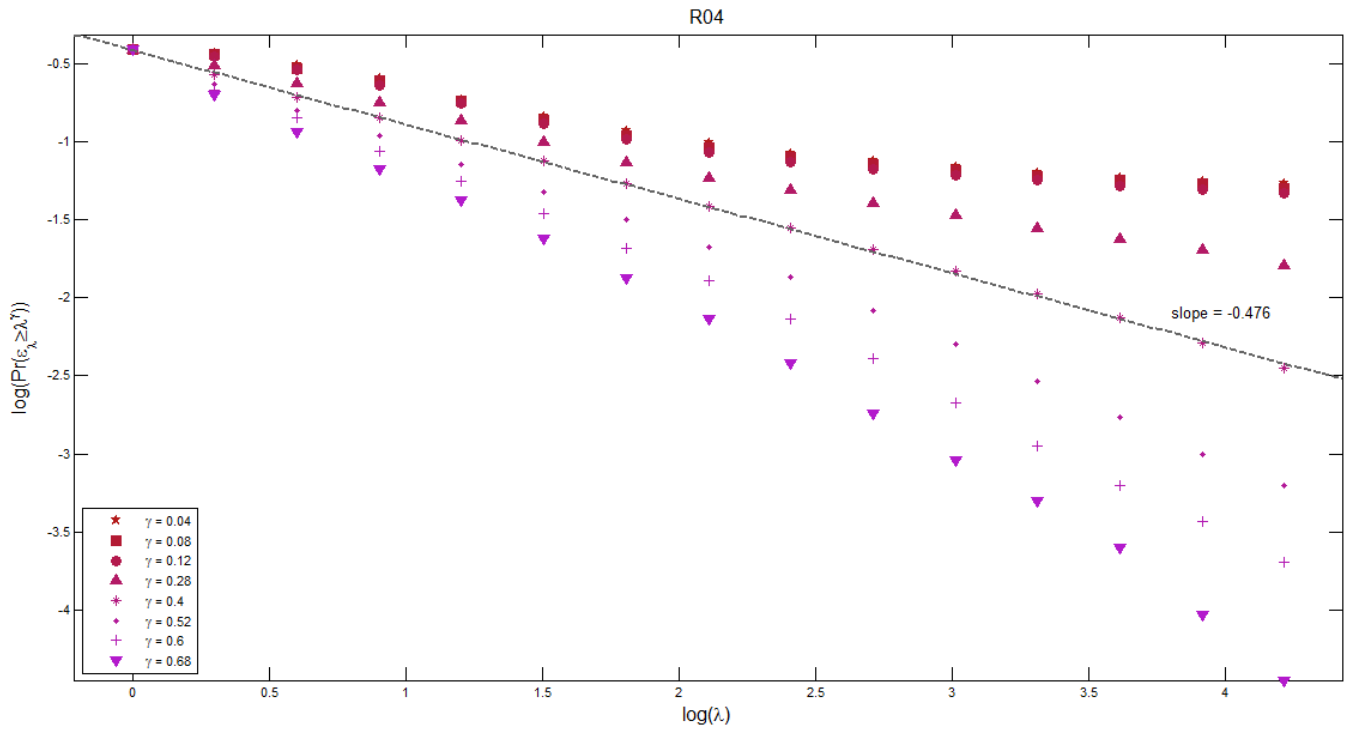


**Figure V.4.** Log-log plot of the probability of exceeding rainfall-intensity levels for sample values of singularity  $\gamma$  relation against scale parameter  $\lambda$ , obtained for 1-minute precipitation data series from Warsaw rain gauge R04. The time scales range from  $\lambda = 16384$  (1 minute) to  $\lambda = 1$  (11.4 days)

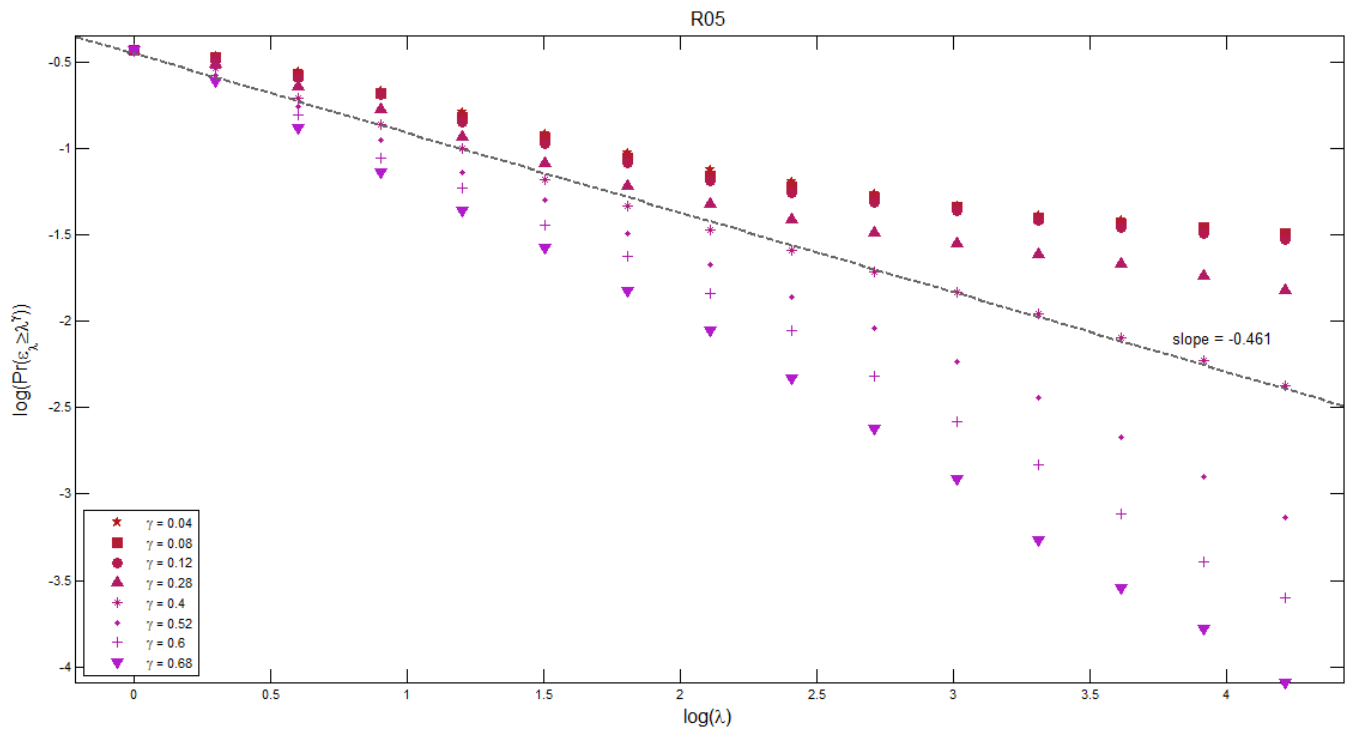


**Figure V.5.** Log-log plot of the probability of exceeding rainfall-intensity levels for sample values of singularity  $\gamma$  relation against scale parameter  $\lambda$ , obtained for 1-minute precipitation data series from Warsaw rain gauge R05. The time scales range from  $\lambda = 16384$  (1 minute) to  $\lambda = 1$  (11.4 days)

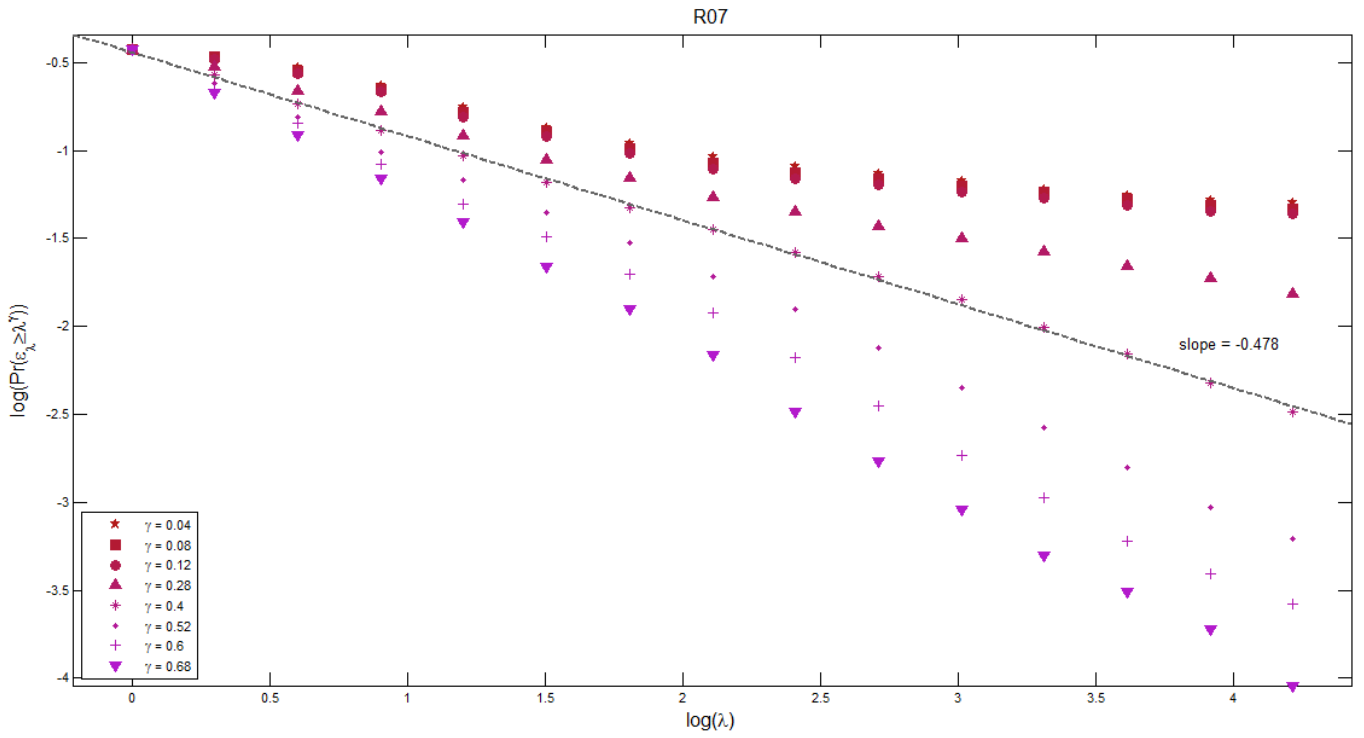


**Figure V.6.** Log-log plot of the probability of exceeding rainfall-intensity levels for sample values of singularity  $\gamma$  relation against scale parameter  $\lambda$ , obtained for 1-minute precipitation data series from Warsaw rain gauge R07. The time scales range from  $\lambda = 16384$  (1 minute) to  $\lambda = 1$  (11.4 days)

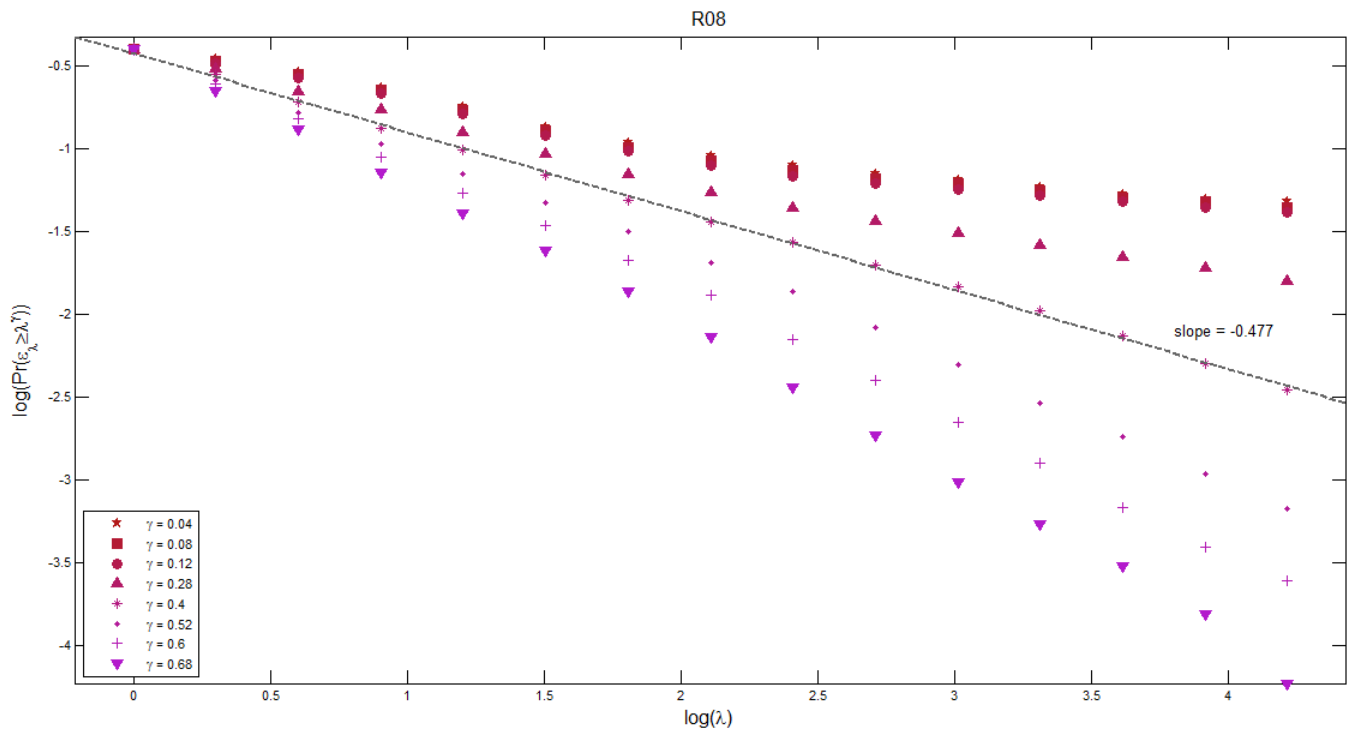


**Figure V.7.** Log-log plot of the probability of exceeding rainfall-intensity levels for sample values of singularity  $\gamma$  relation against scale parameter  $\lambda$ , obtained for 1-minute precipitation data series from Warsaw rain gauge R08. The time scales range from  $\lambda = 16384$  (1 minute) to  $\lambda = 1$  (11.4 days)

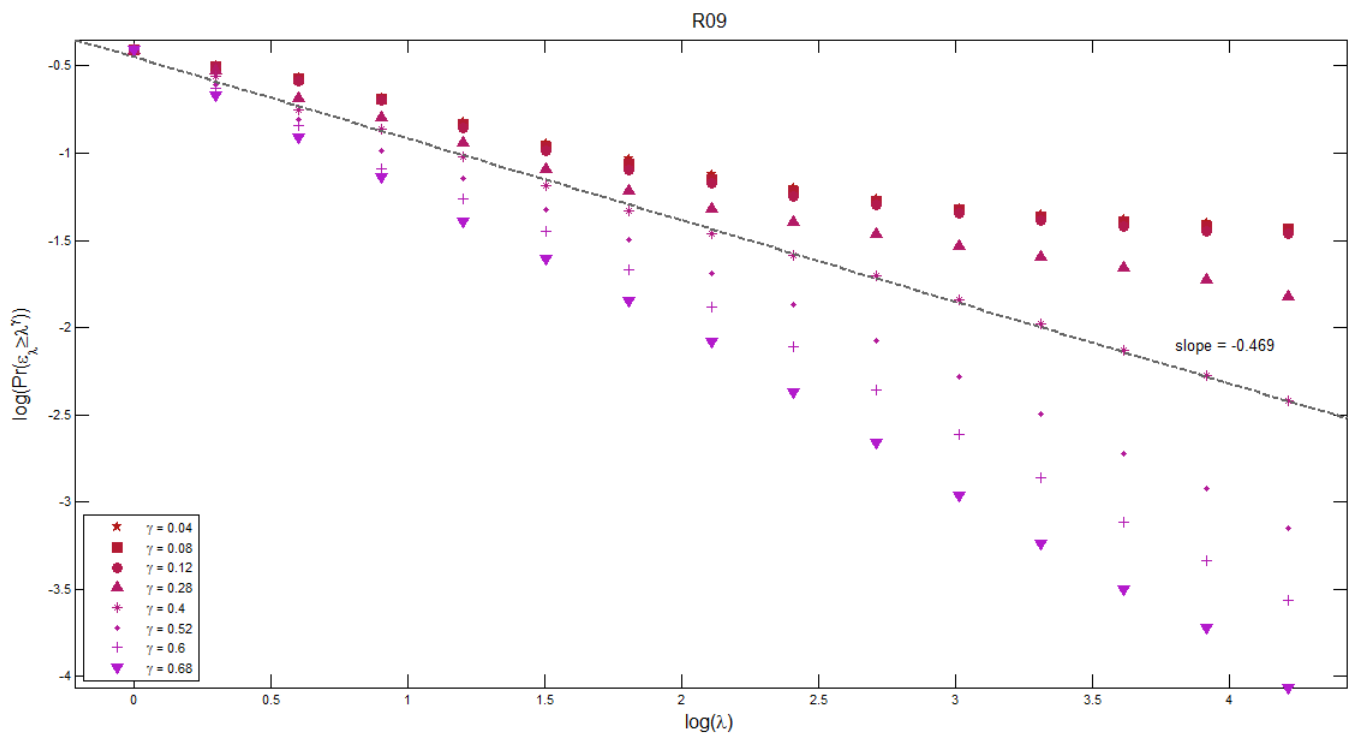


**Figure V.8.** Log-log plot of the probability of exceeding rainfall-intensity levels for sample values of singularity  $\gamma$  relation against scale parameter  $\lambda$ , obtained for 1-minute precipitation data series from Warsaw rain gauge R09. The time scales range from  $\lambda = 16384$  (1 minute) to  $\lambda = 1$  (11.4 days)

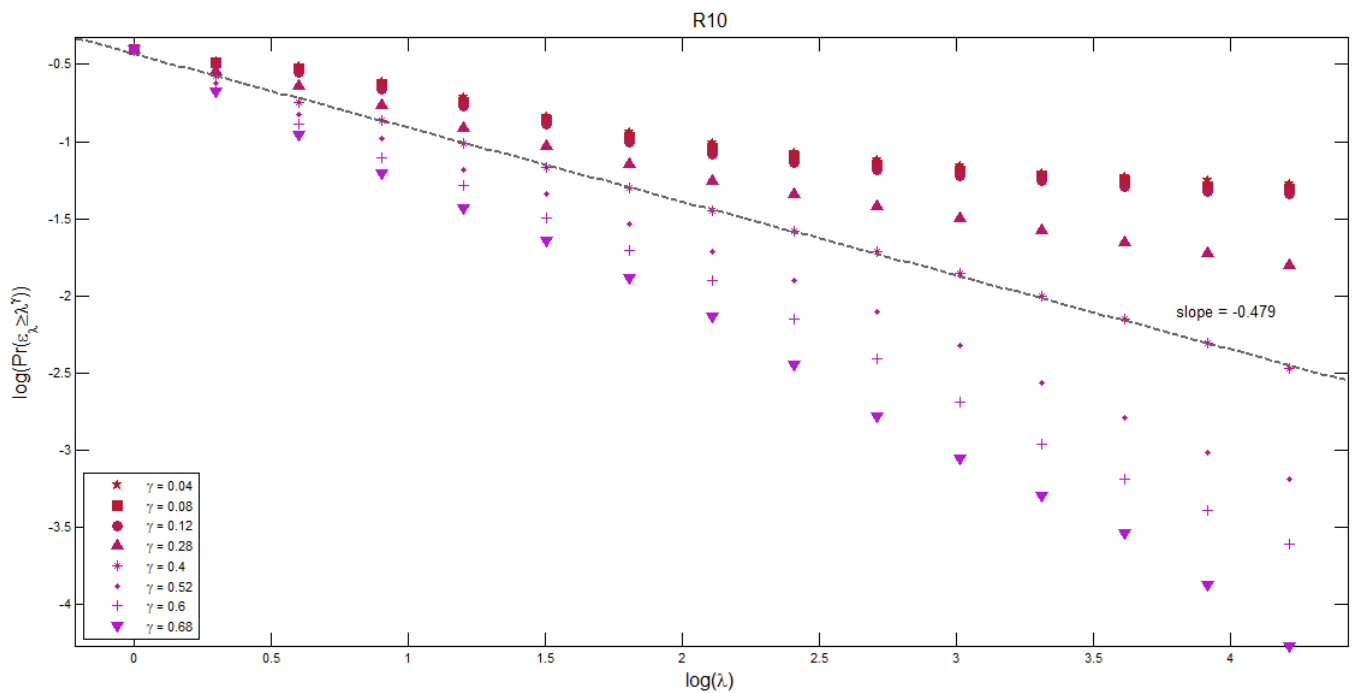


**Figure V.9.** Log-log plot of the probability of exceeding rainfall-intensity levels for sample values of singularity  $\gamma$  relation against scale parameter  $\lambda$ , obtained for 1-minute precipitation data series from Warsaw rain gauge R10. The time scales range from  $\lambda = 16384$  (1 minute) to  $\lambda = 1$  (11.4 days)

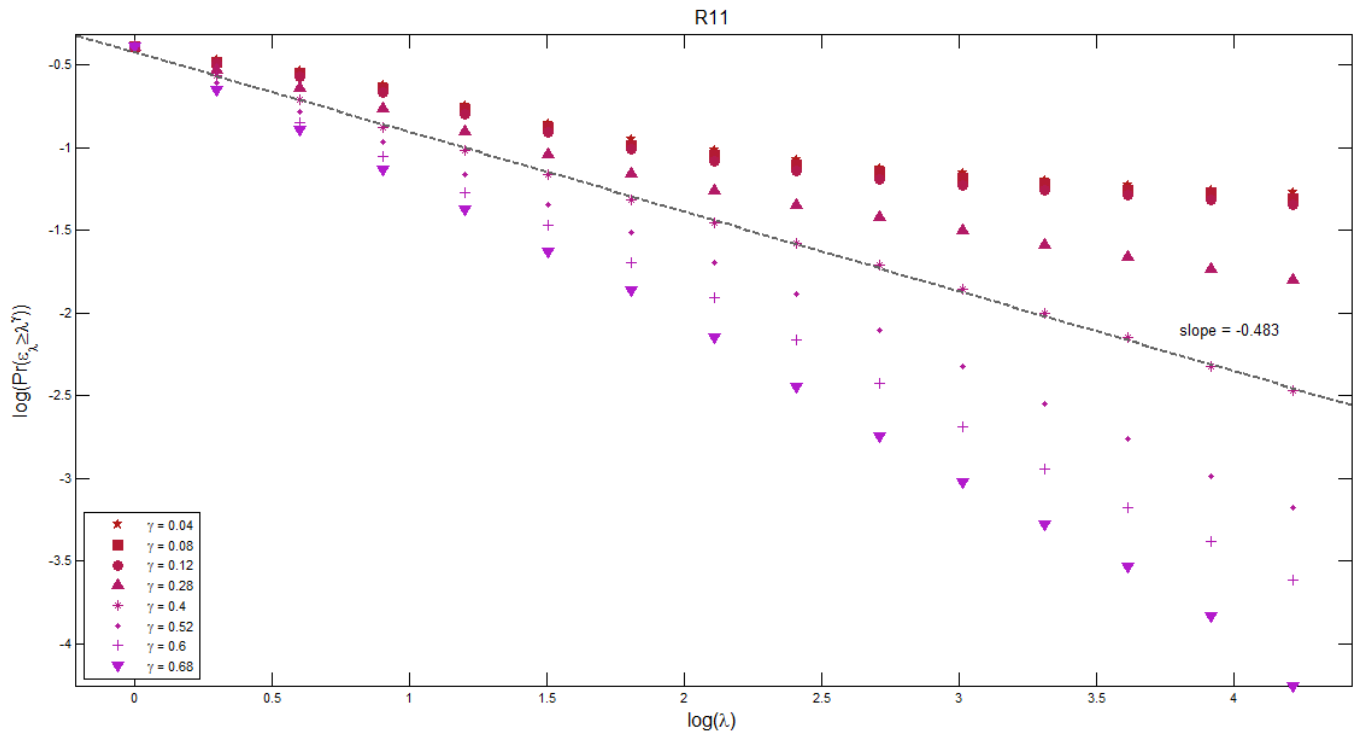


**Figure V.10.** Log-log plot of the probability of exceeding rainfall-intensity levels for sample values of singularity  $\gamma$  relation against scale parameter  $\lambda$ , obtained for 1-minute precipitation data series from Warsaw rain gauge R11. The time scales range from  $\lambda = 16384$  (1 minute) to  $\lambda = 1$  (11.4 days)

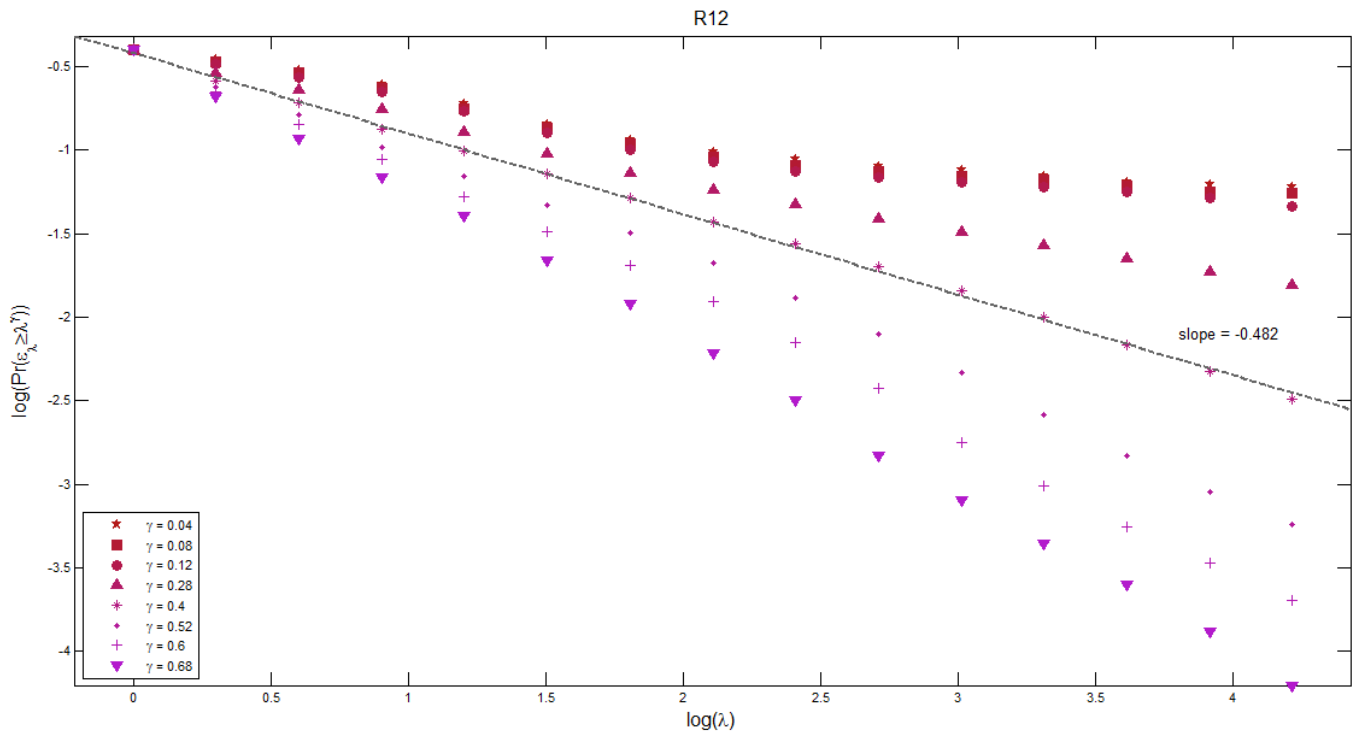


**Figure V.11.** Log-log plot of the probability of exceeding rainfall-intensity levels for sample values of singularity  $\gamma$  relation against scale parameter  $\lambda$ , obtained for 1-minute precipitation data series from Warsaw rain gauge R12. The time scales range from  $\lambda = 16384$  (1 minute) to  $\lambda = 1$  (11.4 days)

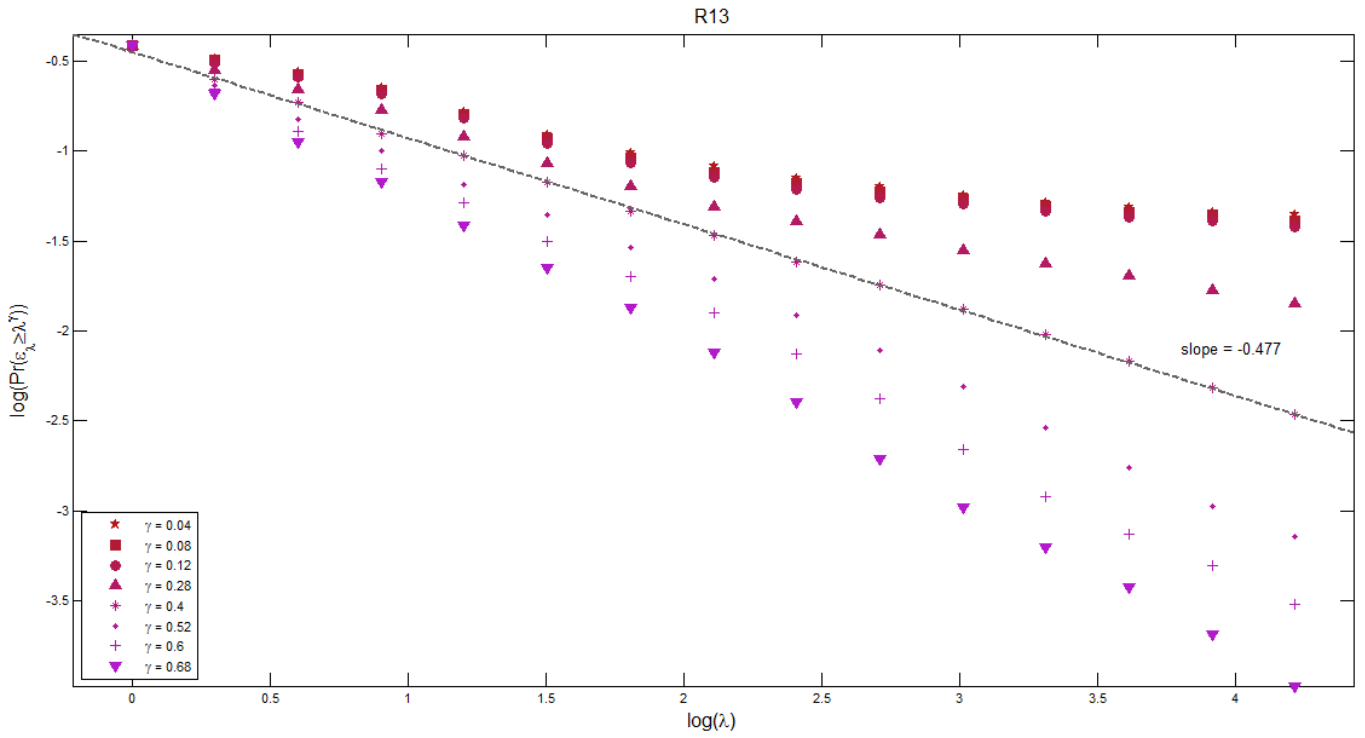


**Figure V.12.** Log-log plot of the probability of exceeding rainfall-intensity levels for sample values of singularity  $\gamma$  relation against scale parameter  $\lambda$ , obtained for 1-minute precipitation data series from Warsaw rain gauge R13. The time scales range from  $\lambda = 16384$  (1 minute) to  $\lambda = 1$  (11.4 days)

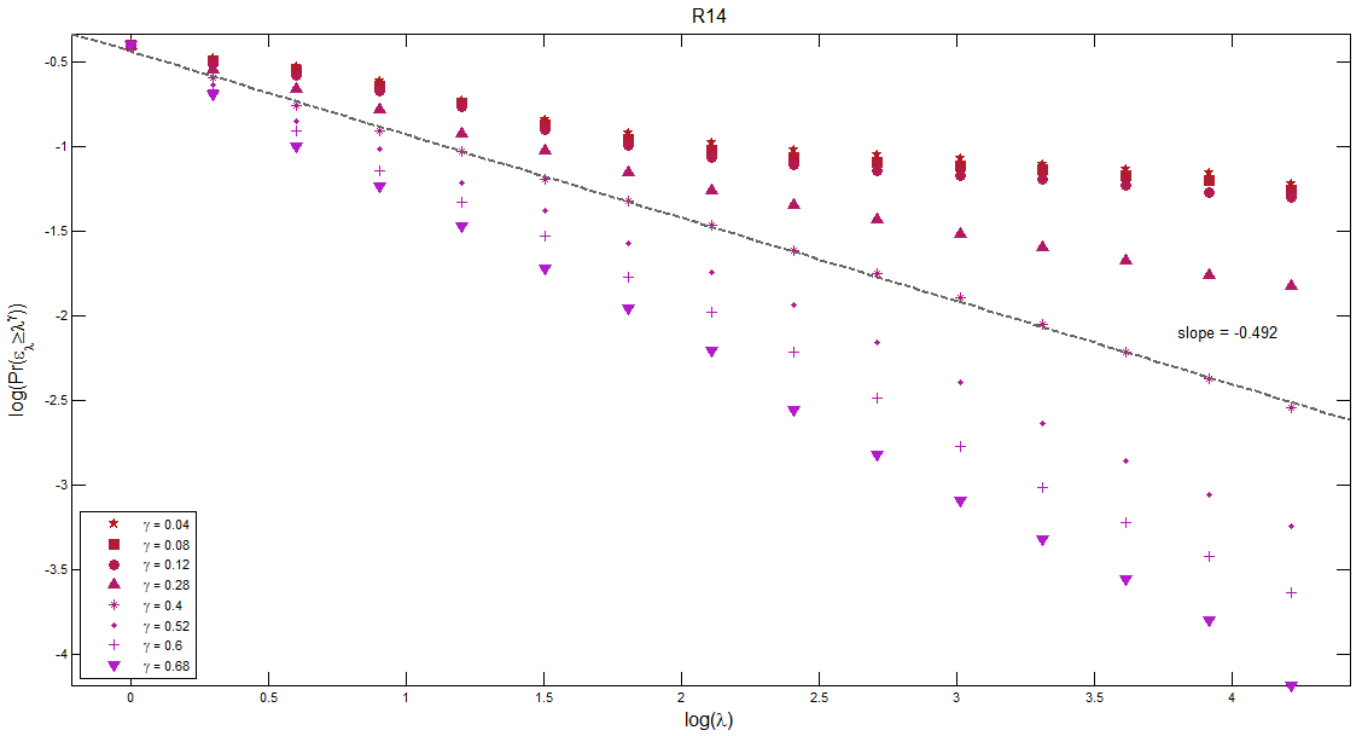


**Figure V.13.** Log-log plot of the probability of exceeding rainfall-intensity levels for sample values of singularity  $\gamma$  relation against scale parameter  $\lambda$ , obtained for 1-minute precipitation data series from Warsaw rain gauge R14. The time scales range from  $\lambda = 16384$  (1 minute) to  $\lambda = 1$  (11.4 days)

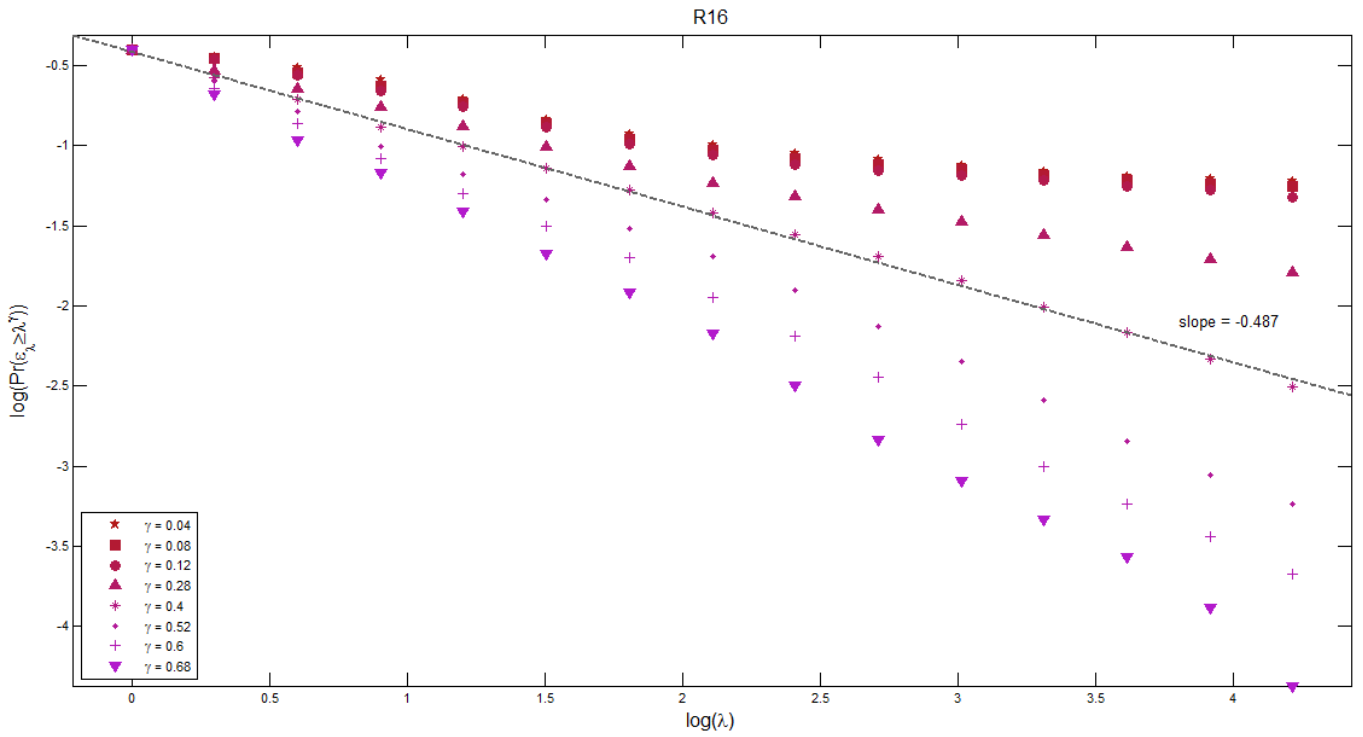


**Figure V.14.** Log-log plot of the probability of exceeding rainfall-intensity levels for sample values of singularity  $\gamma$  relation against scale parameter  $\lambda$ , obtained for 1-minute precipitation data series from Warsaw rain gauge R16. The time scales range from  $\lambda = 16384$  (1 minute) to  $\lambda = 1$  (11.4 days)

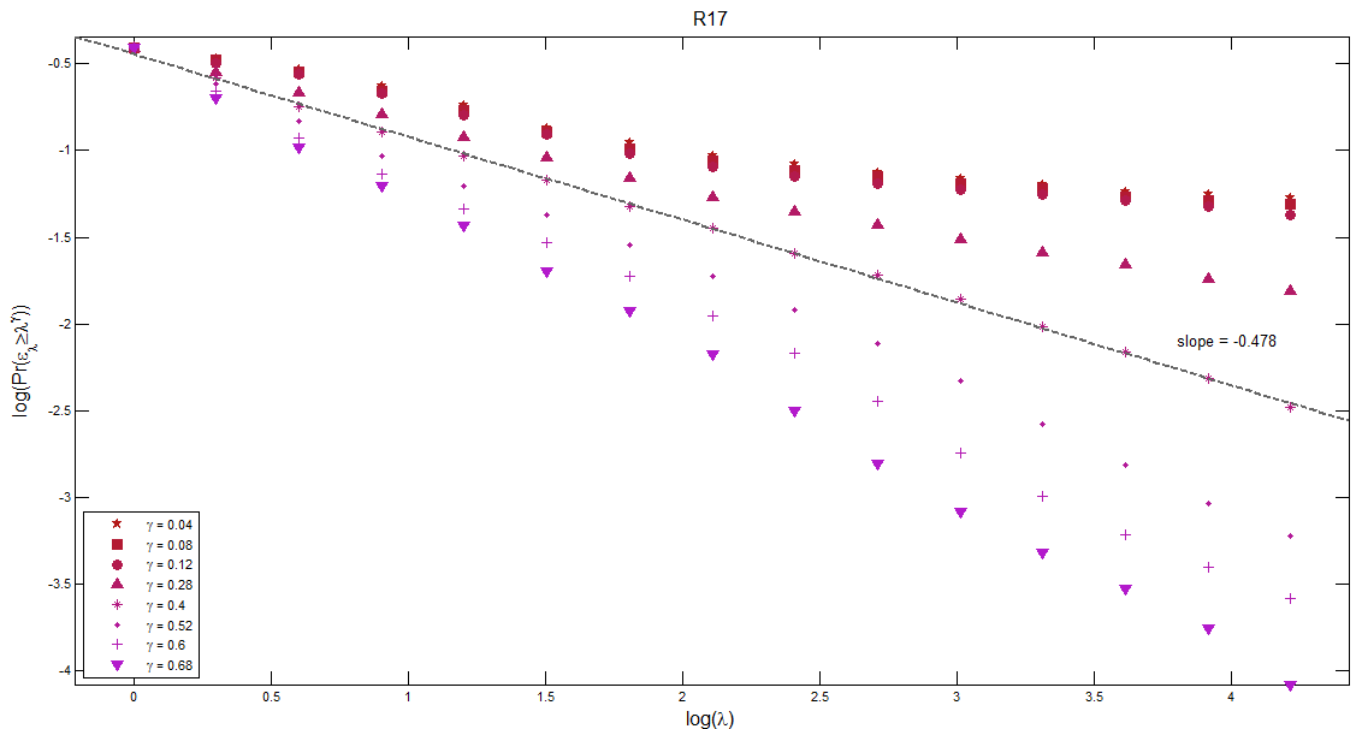


**Figure V.15.** Log-log plot of the probability of exceeding rainfall-intensity levels for sample values of singularity  $\gamma$  relation against scale parameter  $\lambda$ , obtained for 1-minute precipitation data series from Warsaw rain gauge R17. The time scales range from  $\lambda = 16384$  (1 minute) to  $\lambda = 1$  (11.4 days)

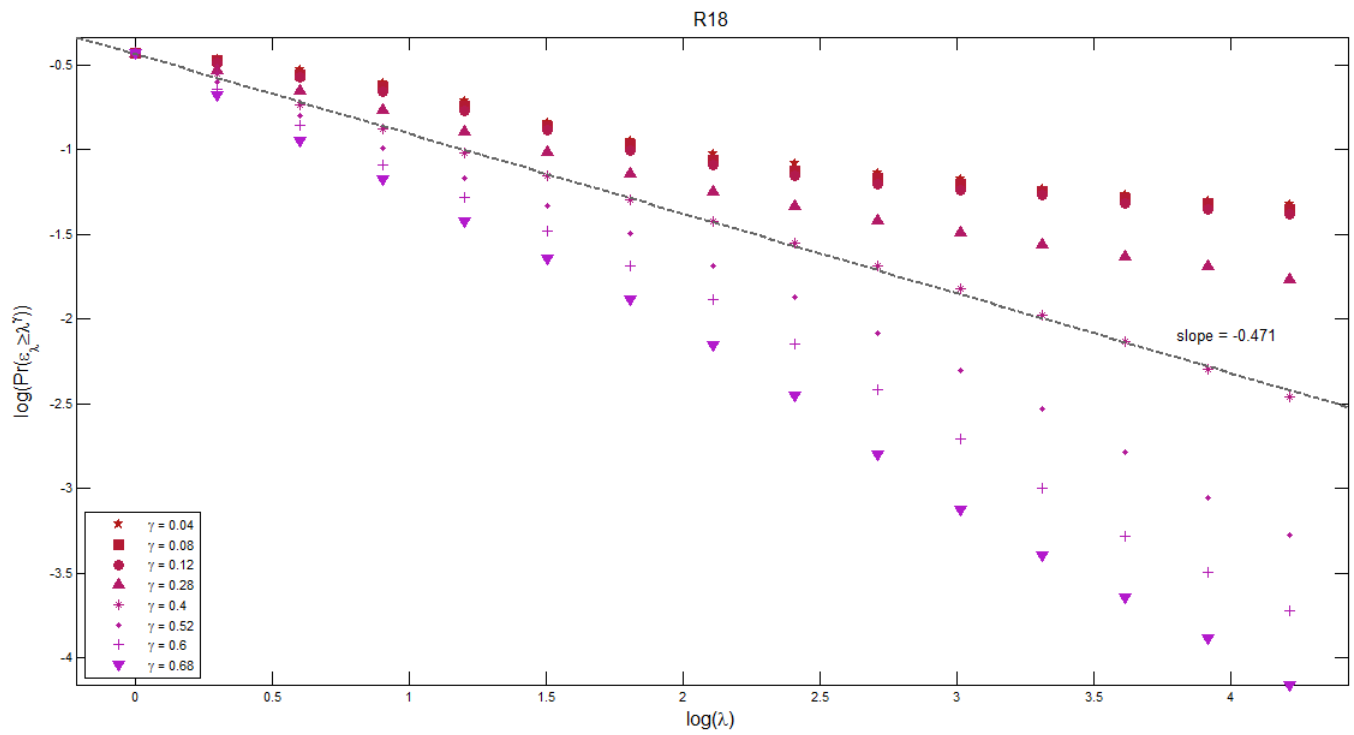


**Figure V.16.** Log-log plot of the probability of exceeding rainfall-intensity levels for sample values of singularity  $\gamma$  relation against scale parameter  $\lambda$ , obtained for 1-minute precipitation data series from Warsaw rain gauge R18. The time scales range from  $\lambda = 16384$  (1 minute) to  $\lambda = 1$  (11.4 days)

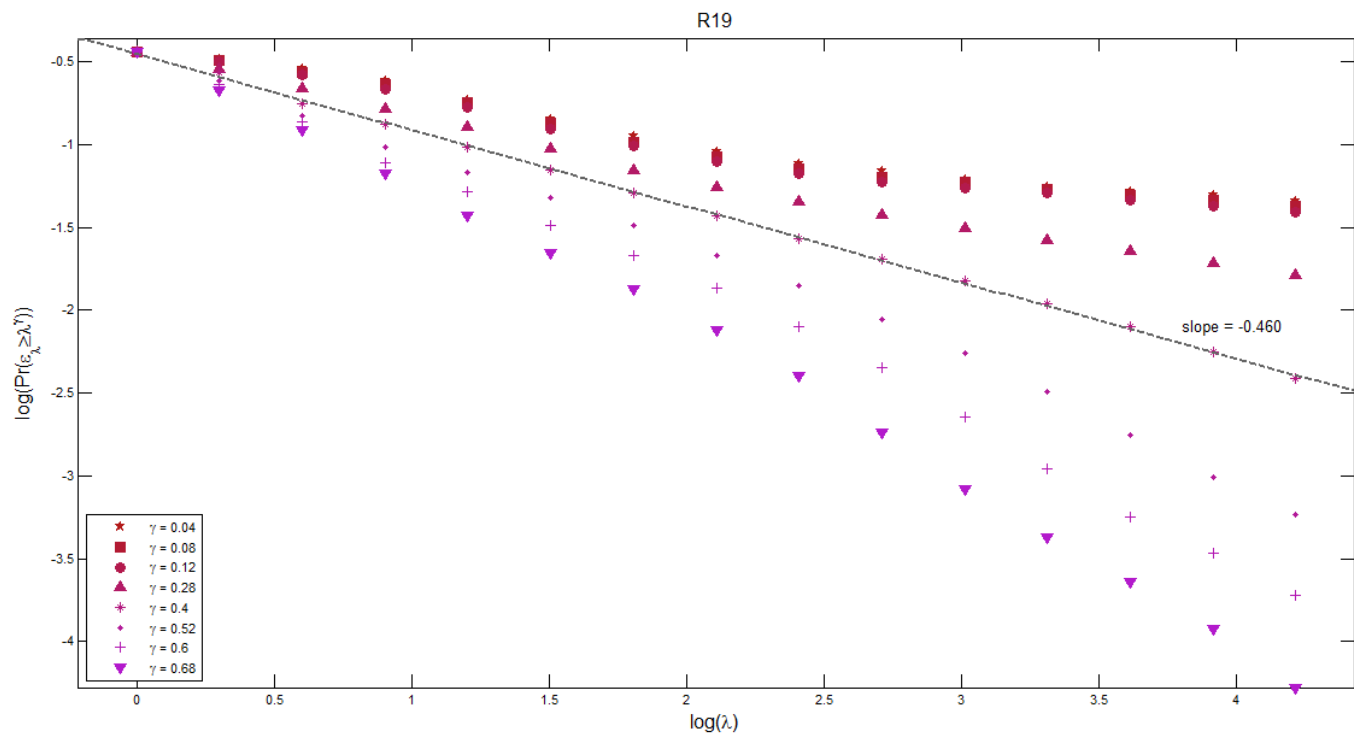


**Figure V.17.** Log-log plot of the probability of exceeding rainfall-intensity levels for sample values of singularity  $\gamma$  relation against scale parameter  $\lambda$ , obtained for 1-minute precipitation data series from Warsaw rain gauge R19. The time scales range from  $\lambda = 16384$  (1 minute) to  $\lambda = 1$  (11.4 days)

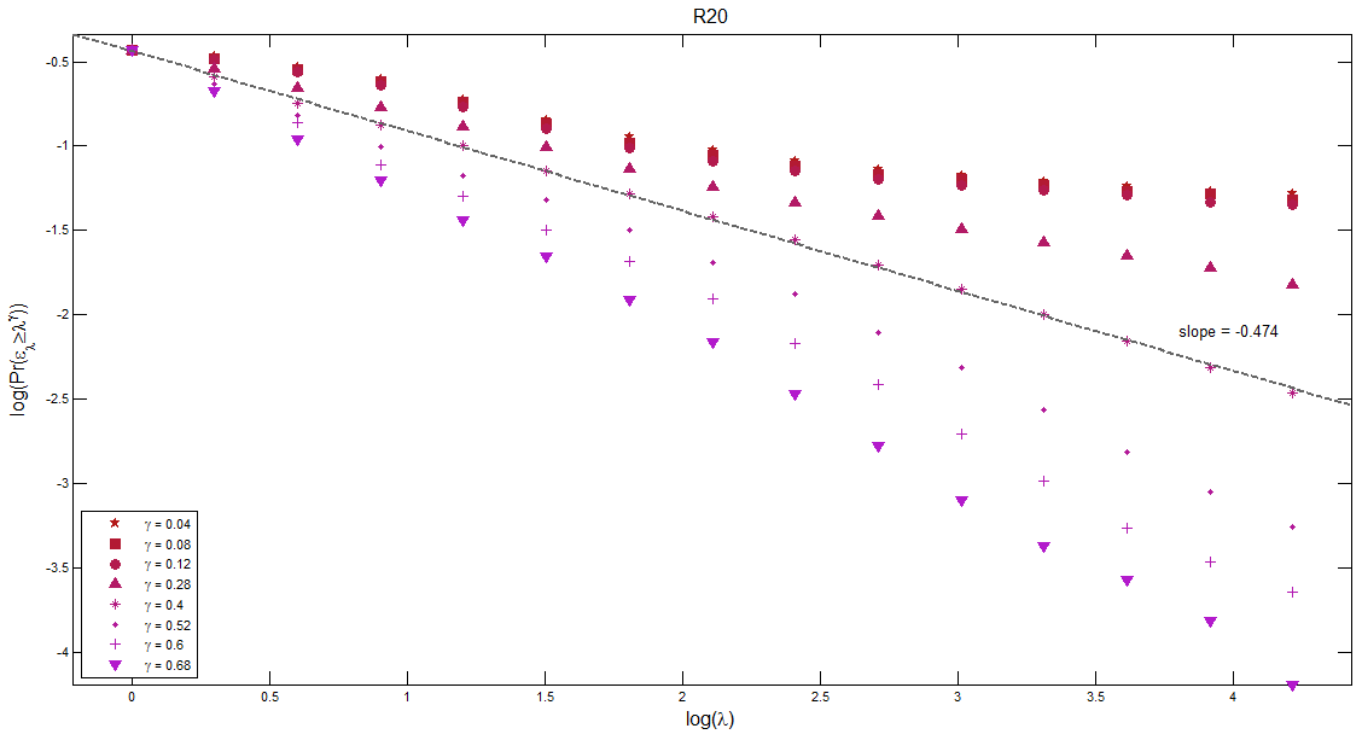


**Figure V.18.** Log-log plot of the probability of exceeding rainfall-intensity levels for sample values of singularity  $\gamma$  relation against scale parameter  $\lambda$ , obtained for 1-minute precipitation data series from Warsaw rain gauge R20. The time scales range from  $\lambda = 16384$  (1 minute) to  $\lambda = 1$  (11.4 days)

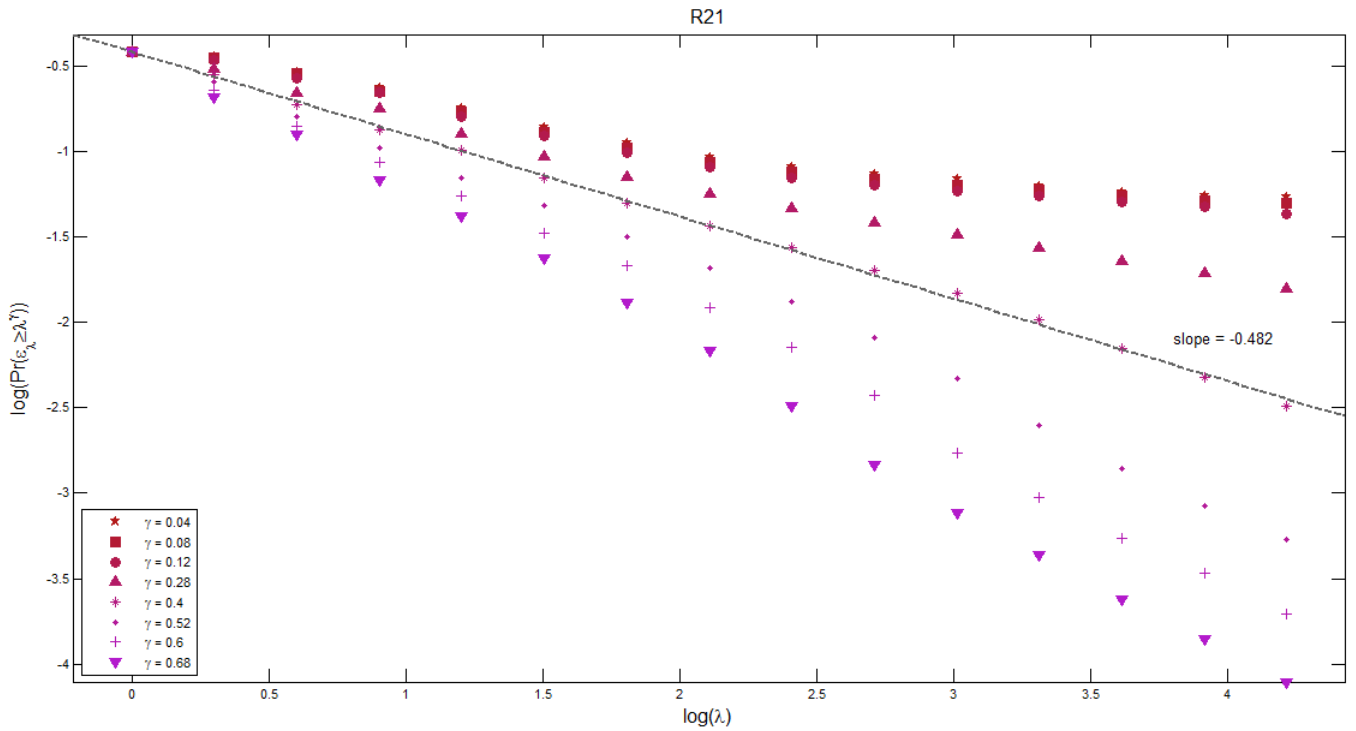


**Figure V.19.** Log-log plot of the probability of exceeding rainfall-intensity levels for sample values of singularity  $\gamma$  relation against scale parameter  $\lambda$ , obtained for 1-minute precipitation data series from Warsaw rain gauge R21. The time scales range from  $\lambda = 16384$  (1 minute) to  $\lambda = 1$  (11.4 days)

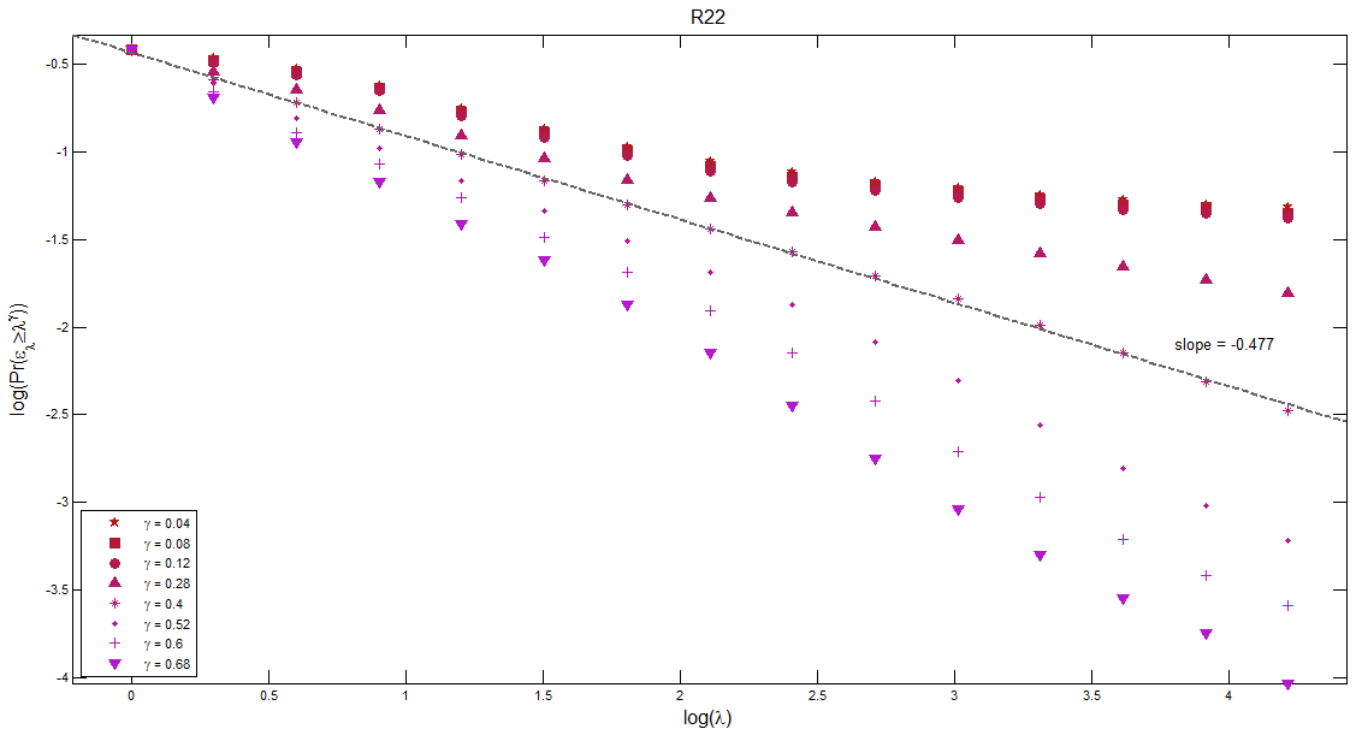


**Figure V.20.** Log-log plot of the probability of exceeding rainfall-intensity levels for sample values of singularity  $\gamma$  relation against scale parameter  $\lambda$ , obtained for 1-minute precipitation data series from Warsaw rain gauge R22. The time scales range from  $\lambda = 16384$  (1 minute) to  $\lambda = 1$  (11.4 days)

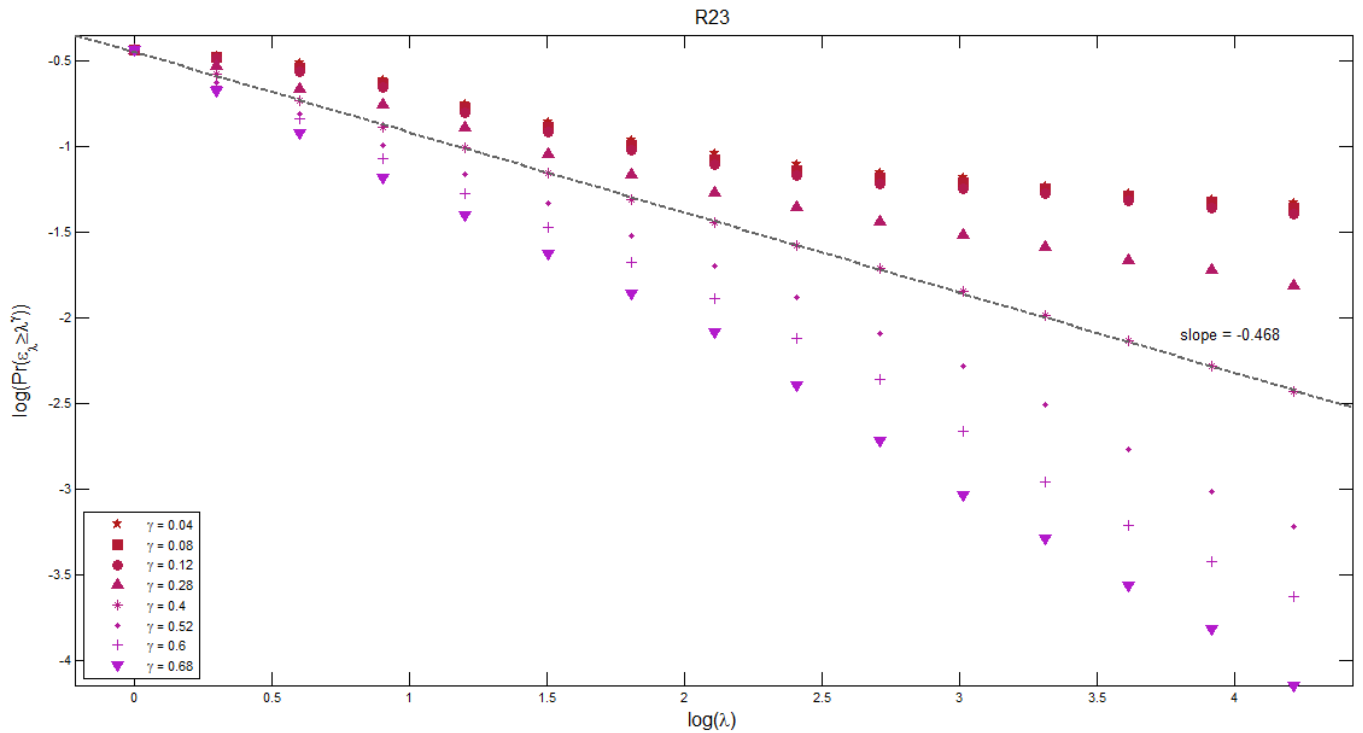


**Figure V.21.** Log-log plot of the probability of exceeding rainfall-intensity levels for sample values of singularity  $\gamma$  relation against scale parameter  $\lambda$ , obtained for 1-minute precipitation data series from Warsaw rain gauge R23. The time scales range from  $\lambda = 16384$  (1 minute) to  $\lambda = 1$  (11.4 days)

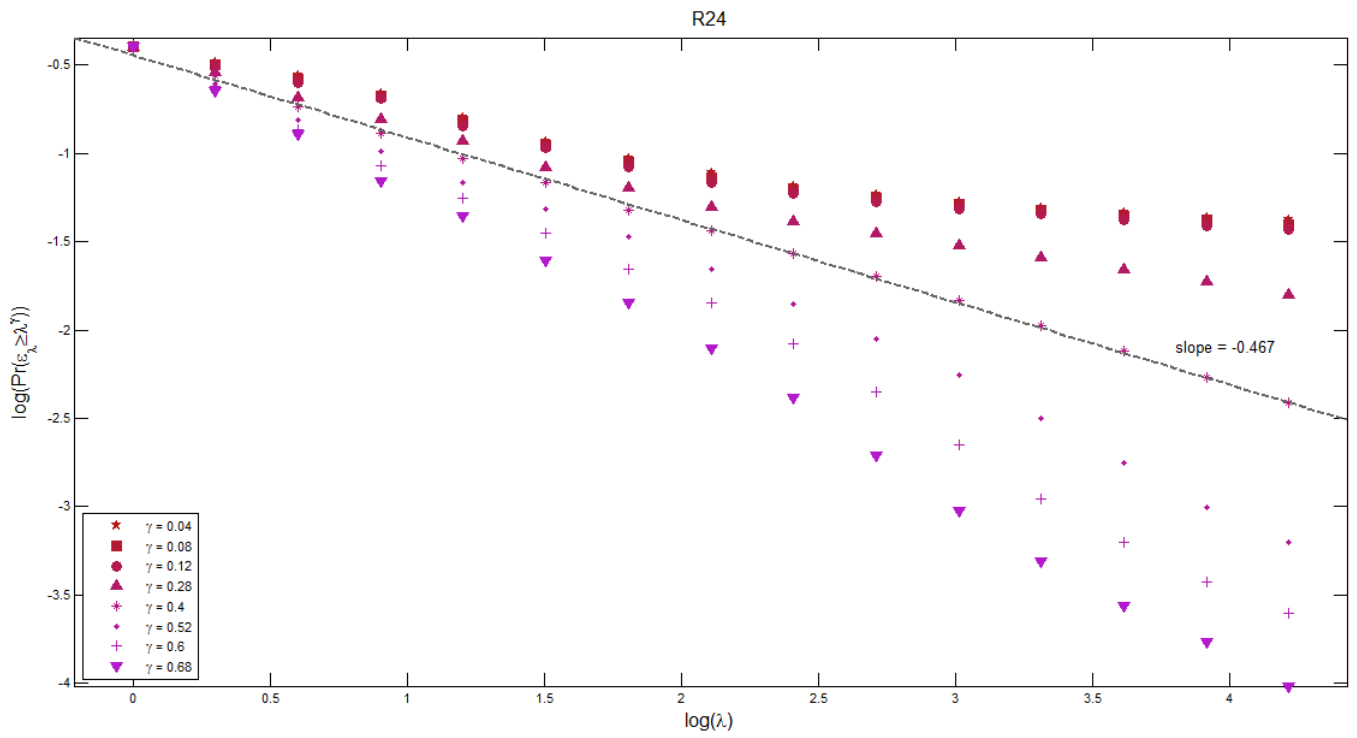


**Figure V.22.** Log-log plot of the probability of exceeding rainfall-intensity levels for sample values of singularity  $\gamma$  relation against scale parameter  $\lambda$ , obtained for 1-minute precipitation data series from Warsaw rain gauge R24. The time scales range from  $\lambda = 16384$  (1 minute) to  $\lambda = 1$  (11.4 days)

## Section B

Empirical codimension function plots obtained for the 1-minute rainfall intensity time-series from Warsaw, from 2008 to 2010, for time scales from  $\lambda = 16384$  (1 min.) up to  $\lambda = 1$  (16384 min. = 11.4 days). For singularity orders,  $\gamma > \gamma_D$ , the fitting lines (blue lines in figures) and their equations are visible on the graphs.

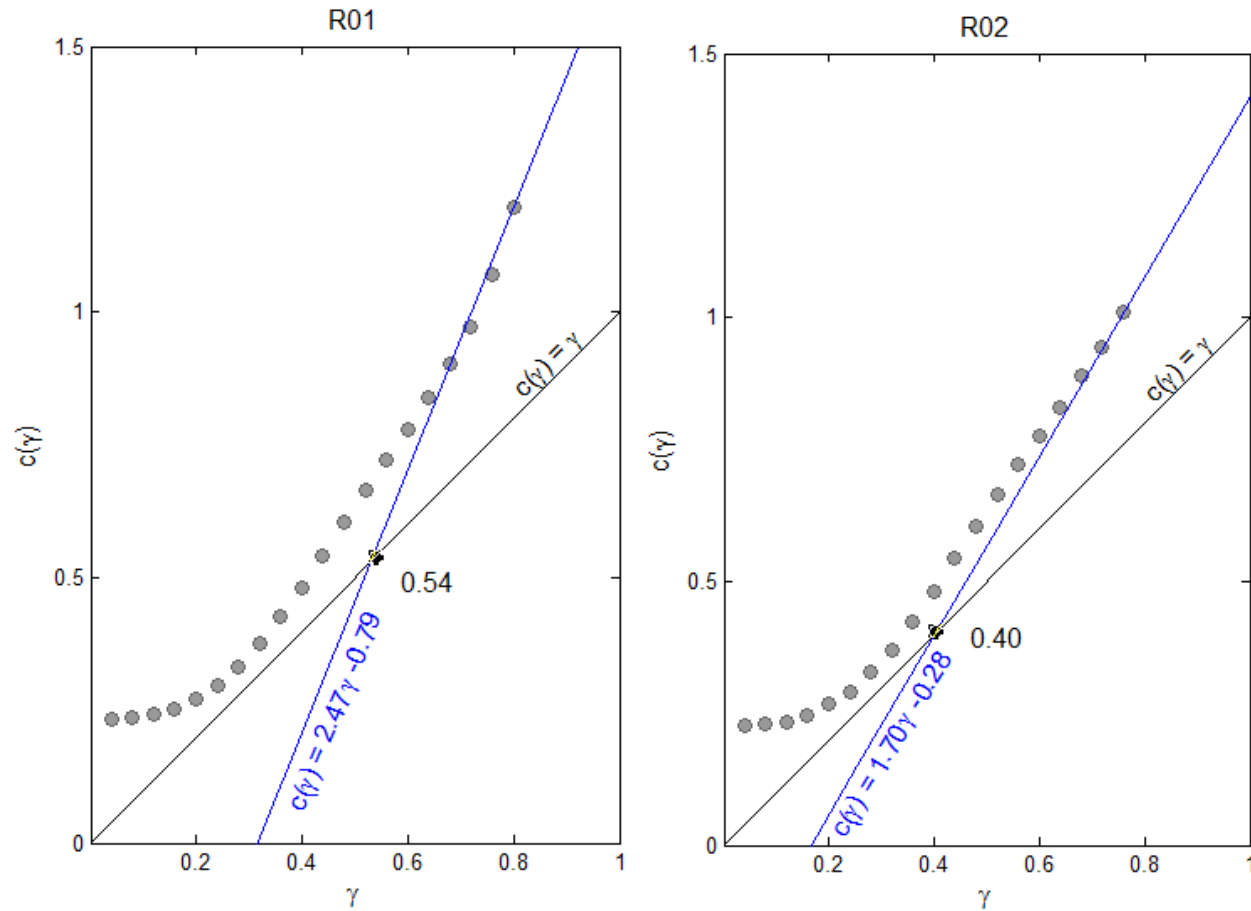


**Figure V.23.** Empirical codimension function (dotted line) obtained for 1-minute precipitation data series from Warsaw rain gauge R01 and R02, for time scales from 1 minute 11.4 days

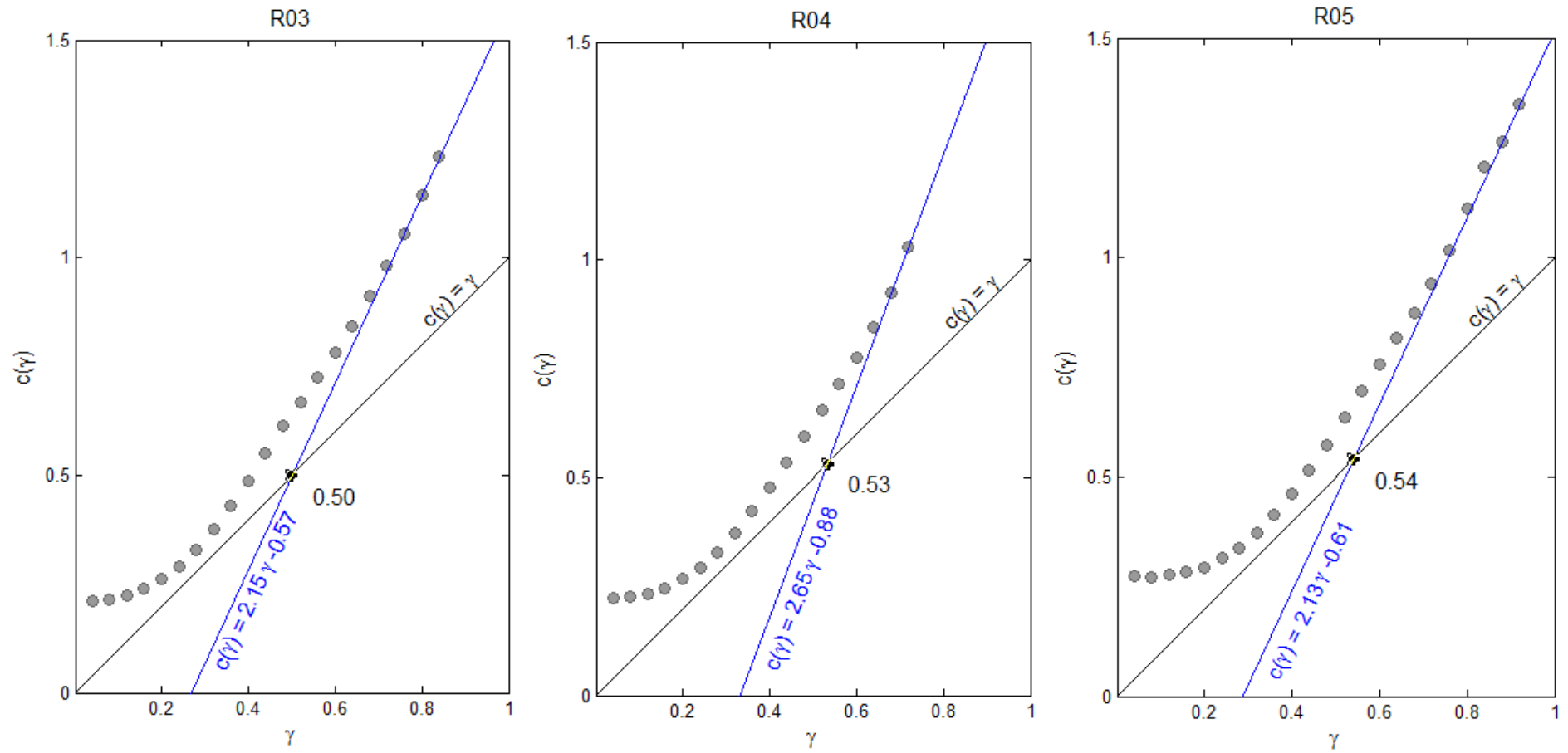


**Figure V.24.** Empirical codimension function (dotted line) obtained for 1-minute precipitation data series from Warsaw rain gauge R03, R04 and R05, for time scales from 1 minute 11.4 days

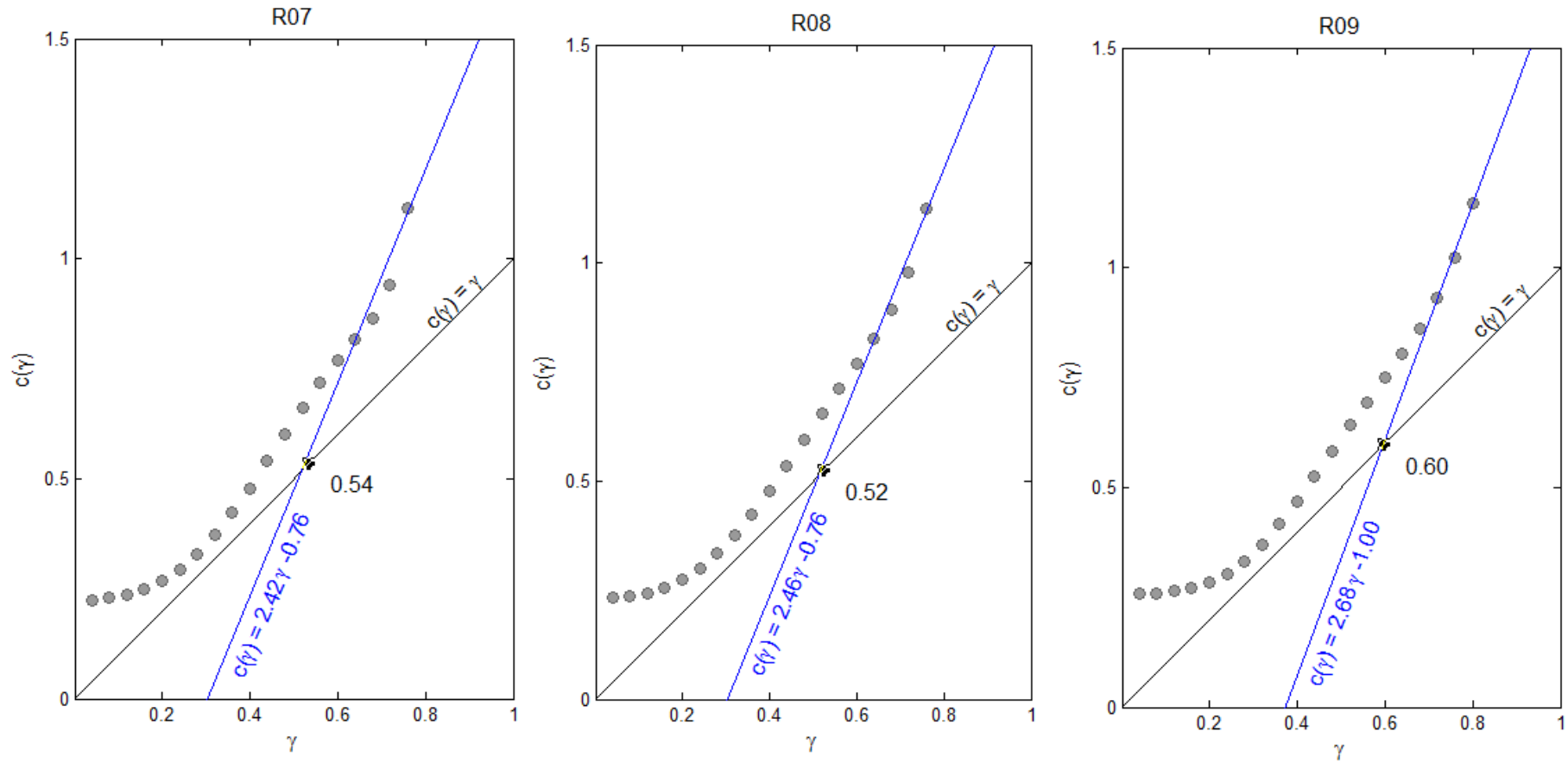


**Figure V.25.** Empirical codimension function (dotted line) obtained for 1-minute precipitation data series from Warsaw rain gauge R07, R08 and R09, for time scales from 1 minute 11.4 days

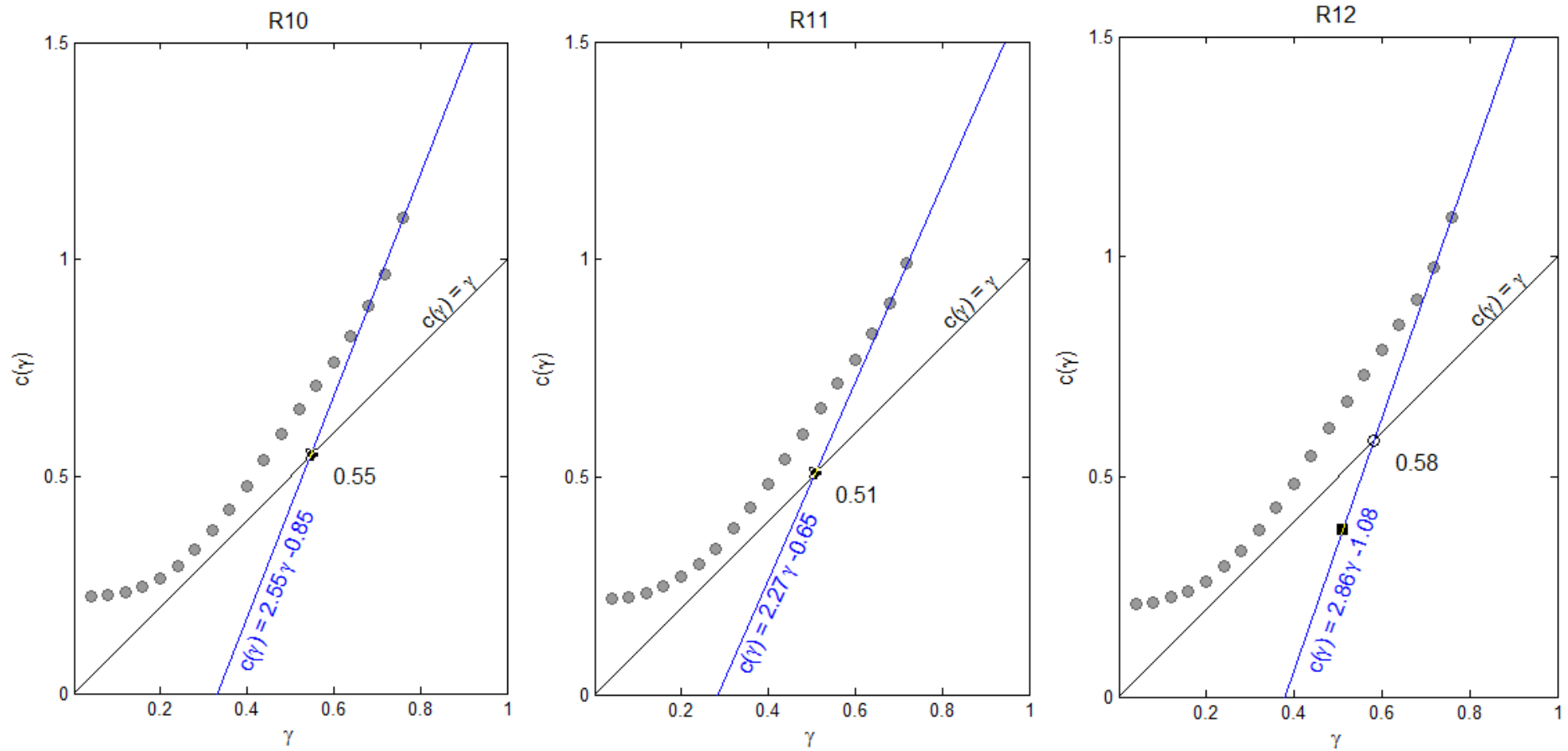


**Figure V.26.** Empirical codimension function (dotted line) obtained for 1-minute precipitation data series from Warsaw rain gauge R10, R11 and R12, for time scales from 1 minute 11.4 days

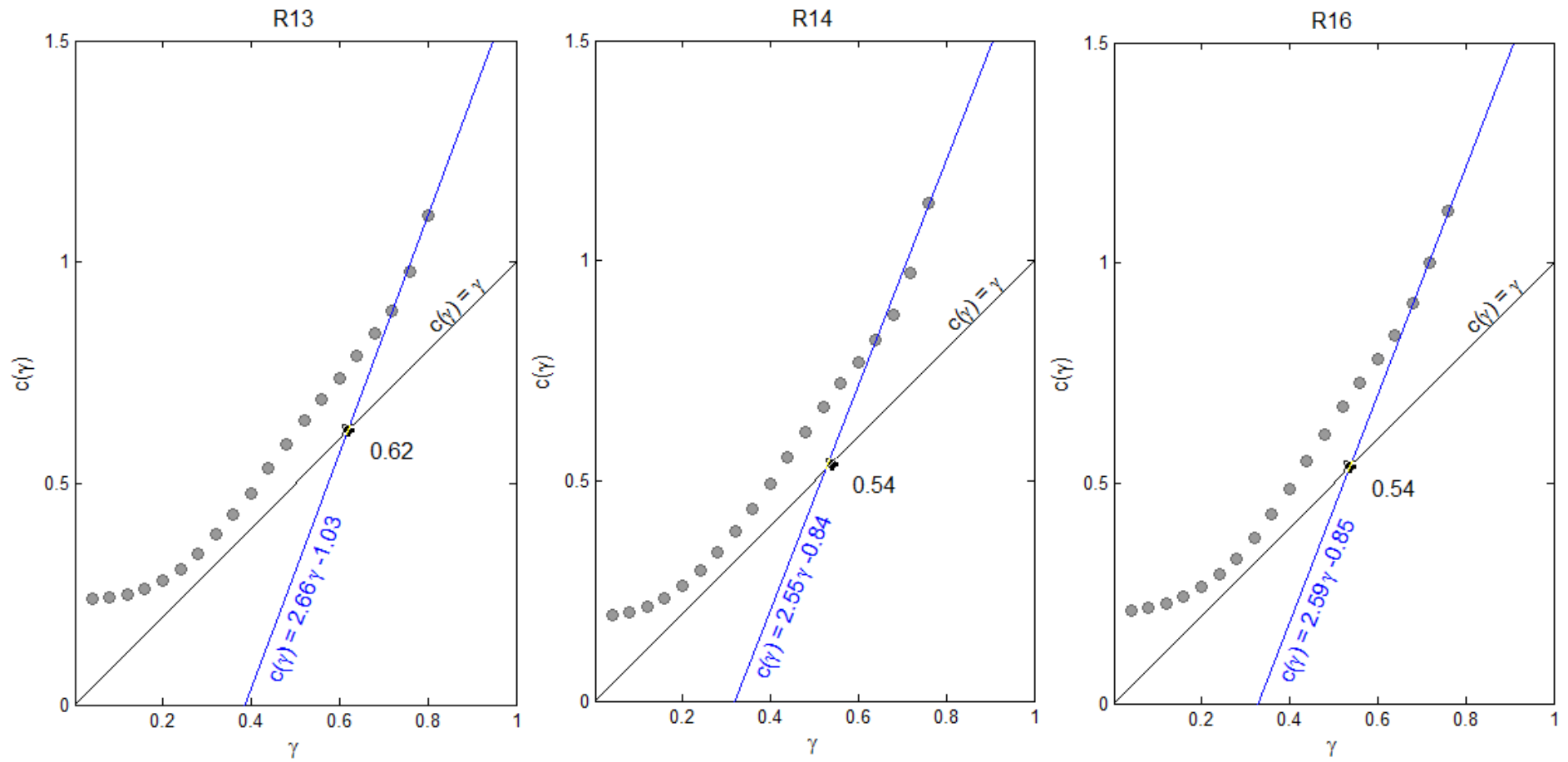


**Figure V.27.** Empirical codimension function (dotted line) obtained for 1-minute precipitation data series from Warsaw rain gauge R13, R14 and R16, for time scales from 1 minute 11.4 days

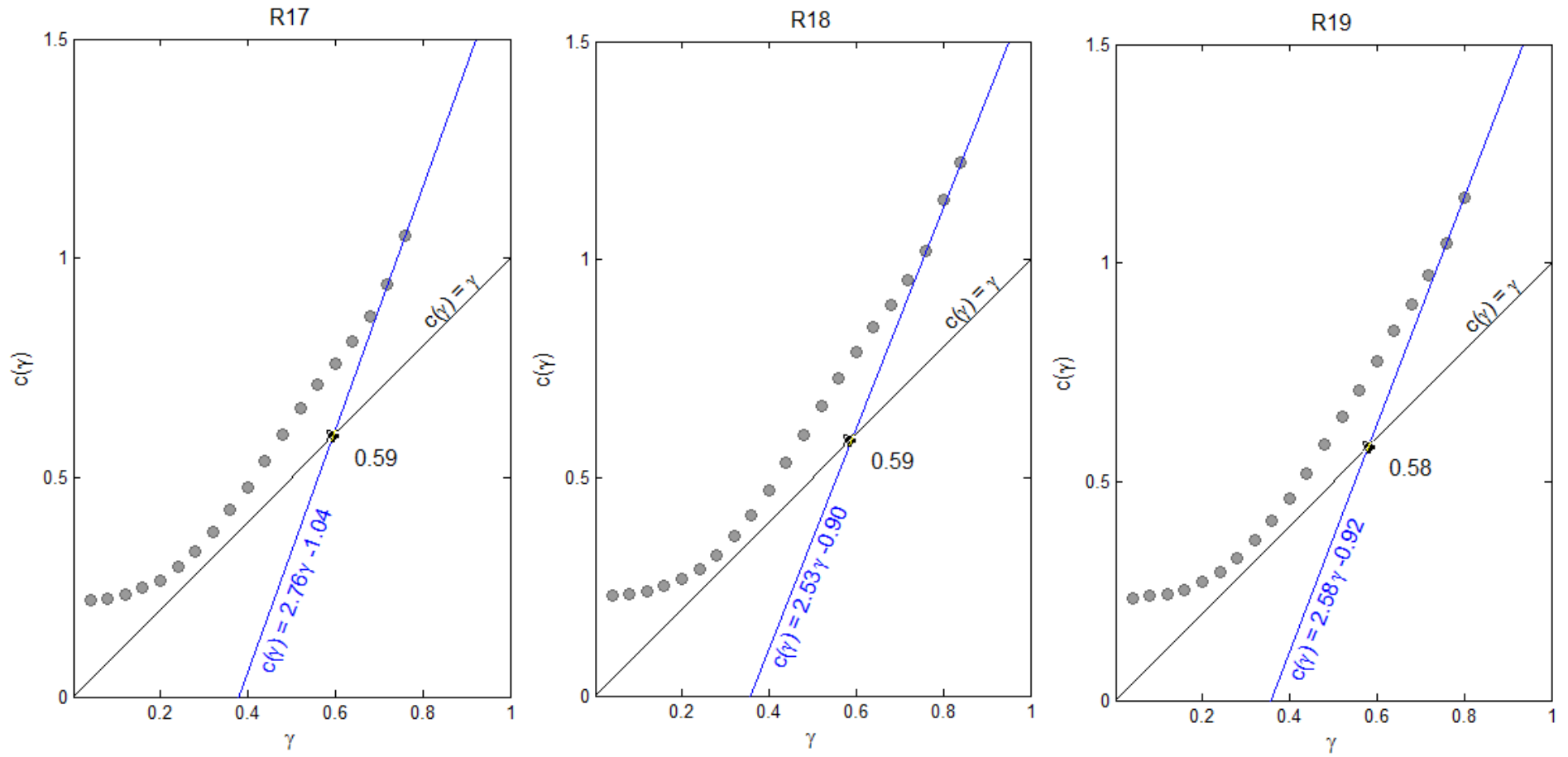


**Figure V.28.** Empirical codimension function (dotted line) obtained for 1-minute precipitation data series from Warsaw rain gauge R17, R18 and R19, for time scales from 1 minute 11.4 days

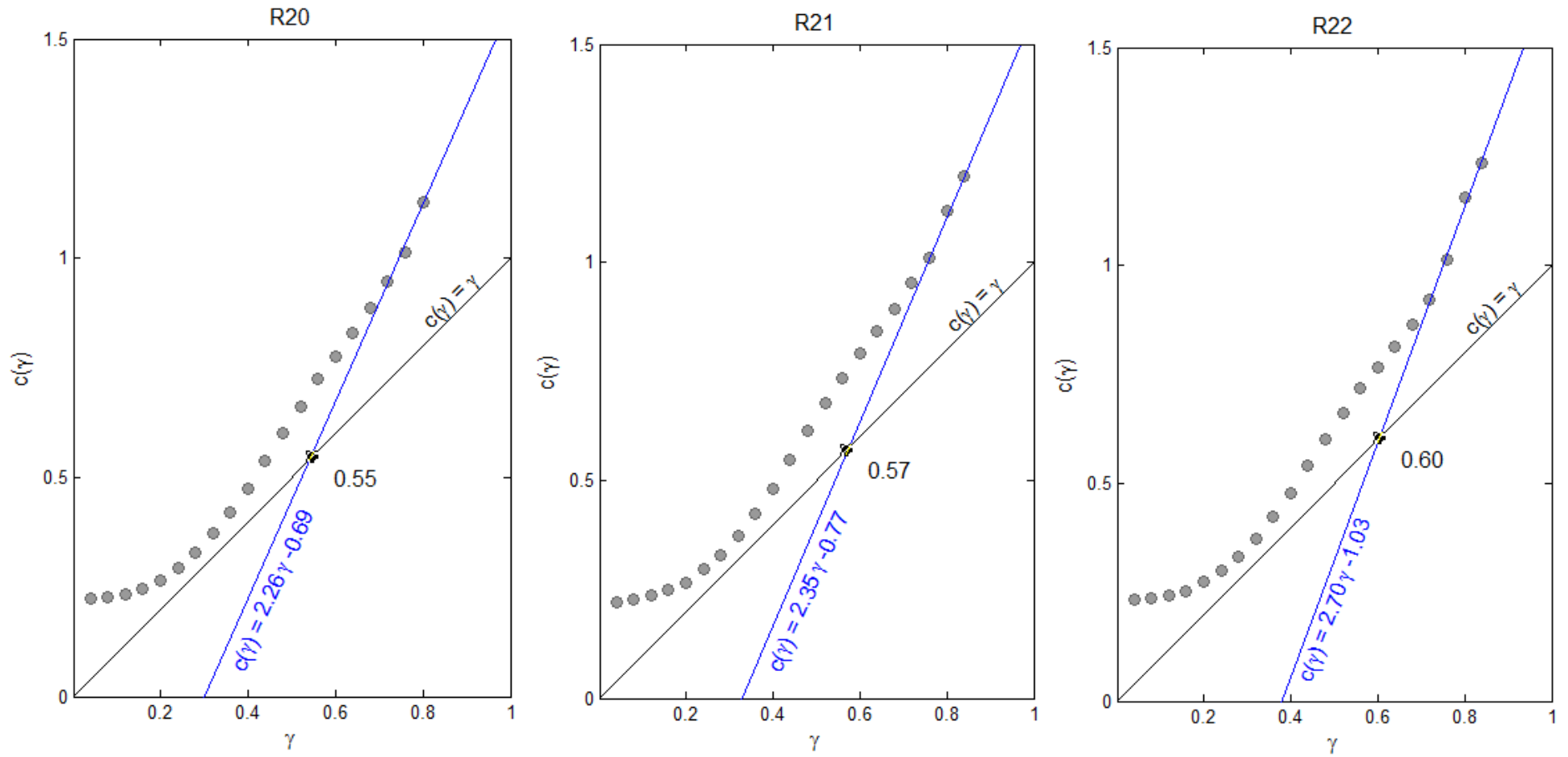


**Figure V.29.** Empirical codimension function (dotted line) obtained for 1-minute precipitation data series from Warsaw rain gauge R20, R21 and R22, for time scales from 1 minute 11.4 days

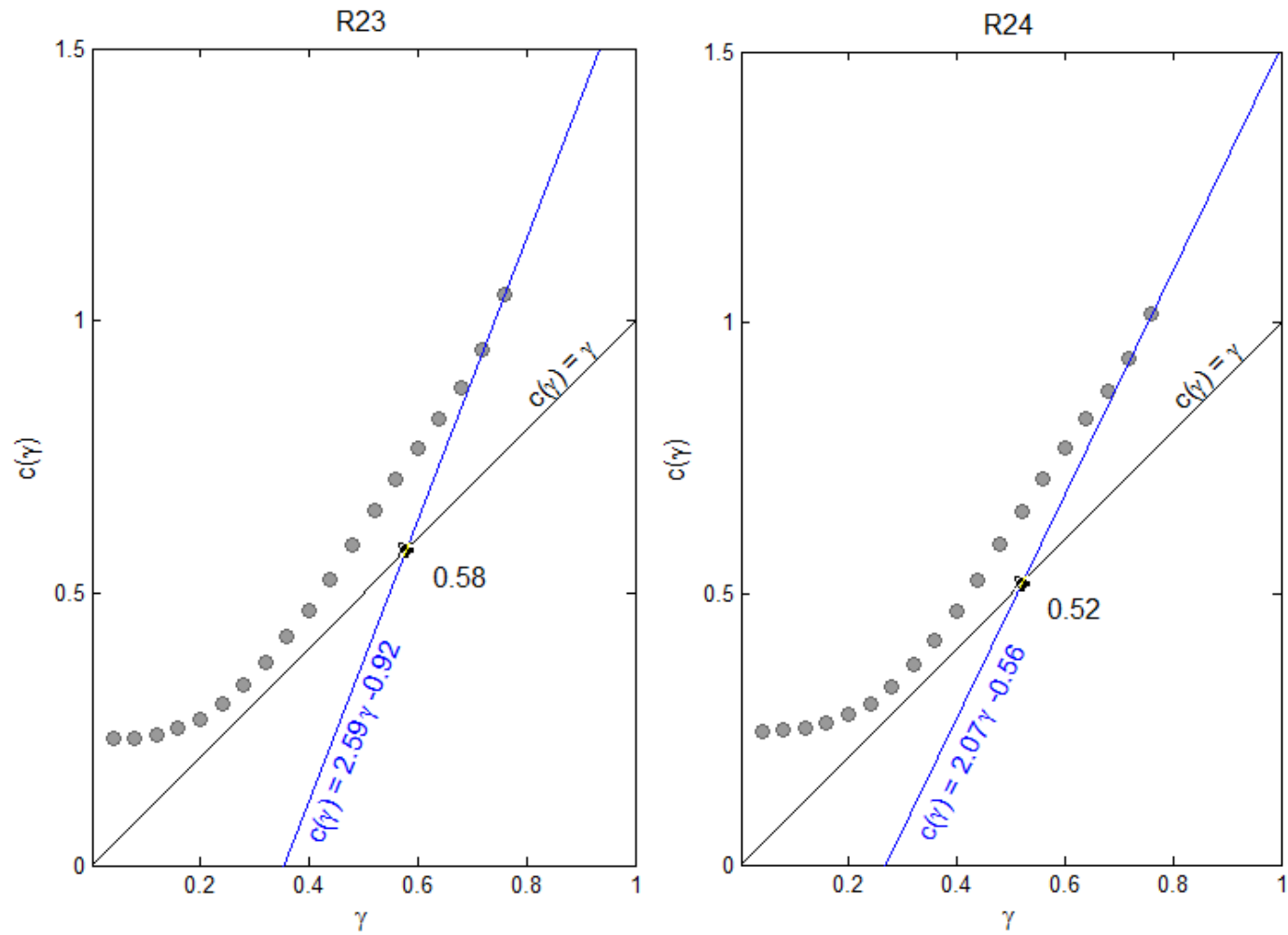


**Figure V.30.** Empirical codimension function (dotted line) obtained for 1-minute precipitation data series from Warsaw rain gauge R23 and R24, for time scales from 1 minute 11.4 days

## APPENDIX VI.

### DOUBLE TRACE MOMENT METHOD RESULTS

#### Section A

Plots of the relation between  $\log(|K(q,\eta)|)$  and  $\log(\eta)$  for selected moments order  $q$ , obtained for the 1-minute rainfall intensity time-series from Warsaw, from 2008 to 2010, for time scales from  $\lambda = 16384$  (1 min.) up to  $\lambda = 1$  (16384 min. = 11,4 days).

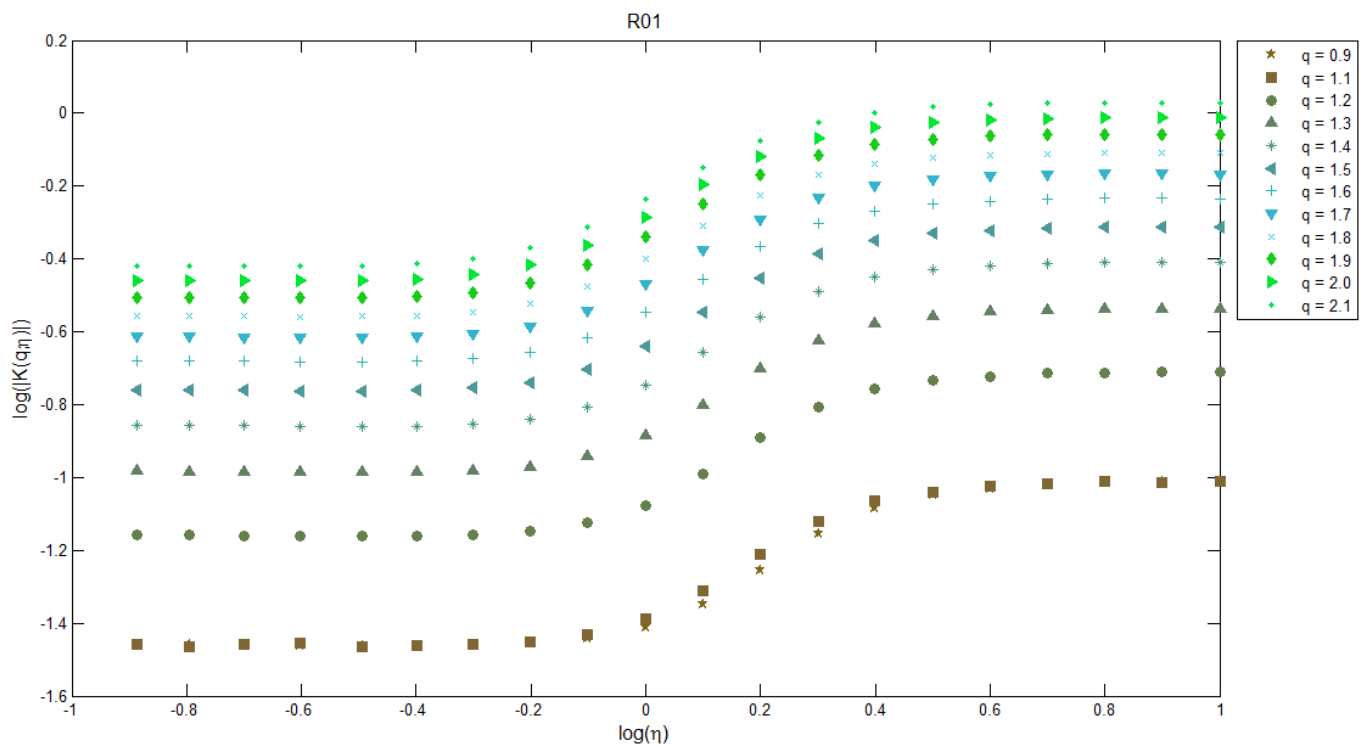


**Figure VI.1.** DTM plots of  $\log|K(q,\eta)|$  against  $\log(\eta)$  for selected order moments  $q$  obtained for 1-minute precipitation data series from Warsaw rain gauge R01

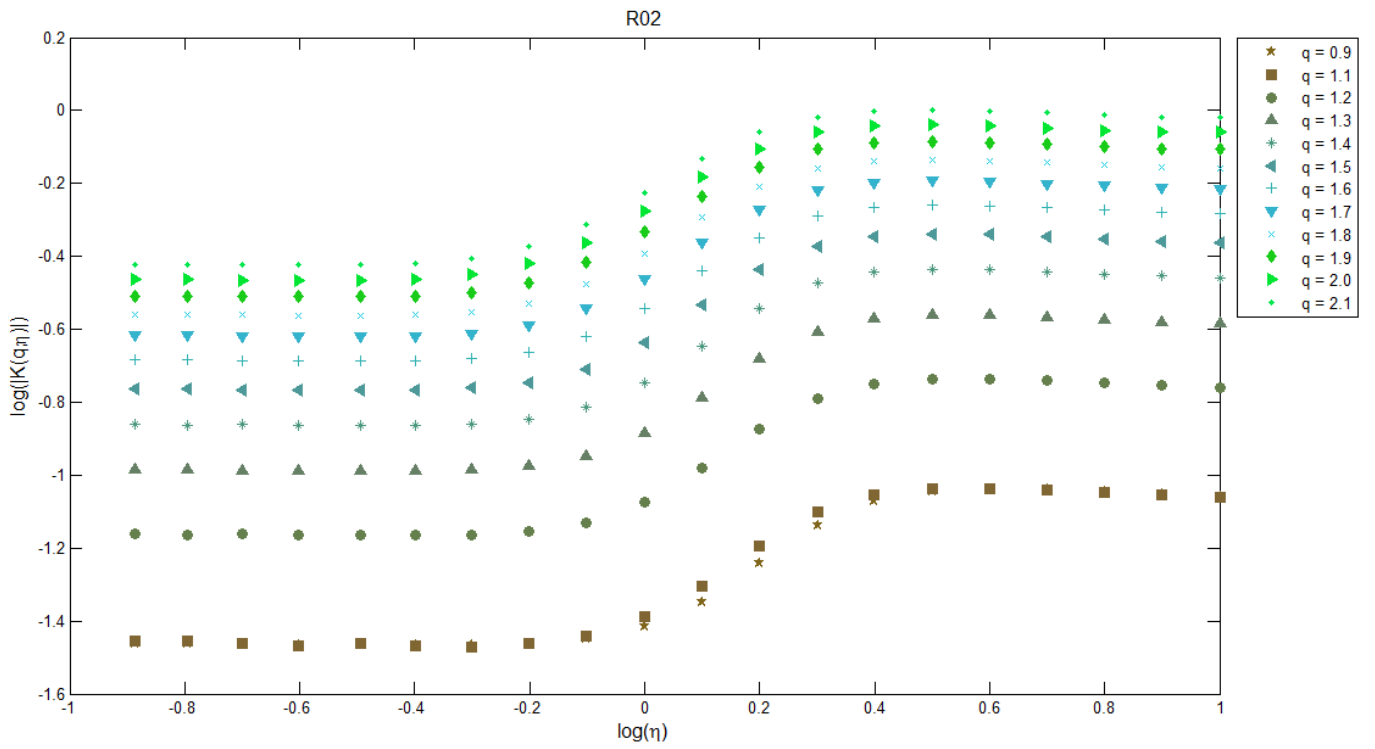


**Figure VI.2.** DTM plots of  $\log|K(q,\eta)|$  against  $\log(\eta)$  for selected order moments  $q$  obtained for 1-minute precipitation data series from Warsaw rain gauge R02

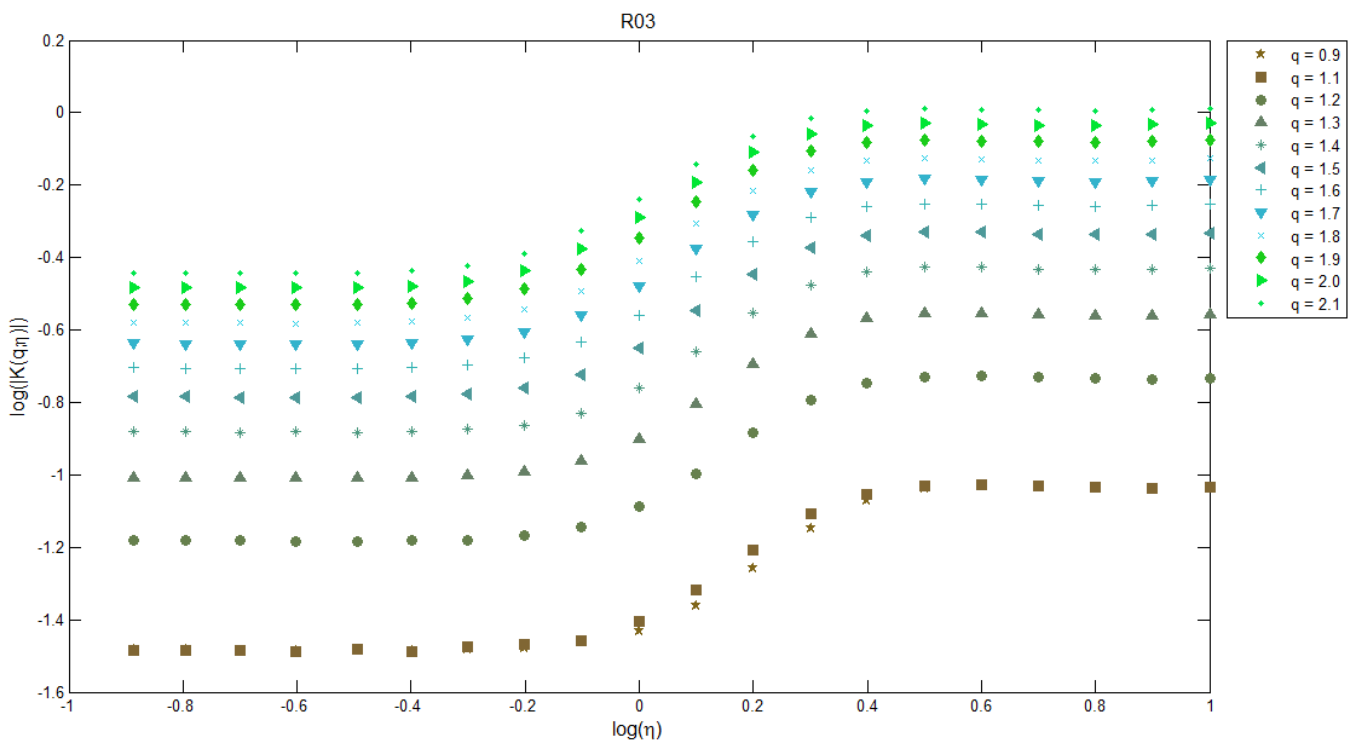


**Figure VI.3.** DTM plots of  $\log|K(q,\eta)|$  against  $\log(\eta)$  for selected order moments  $q$  obtained for 1-minute precipitation data series from Warsaw rain gauge R03

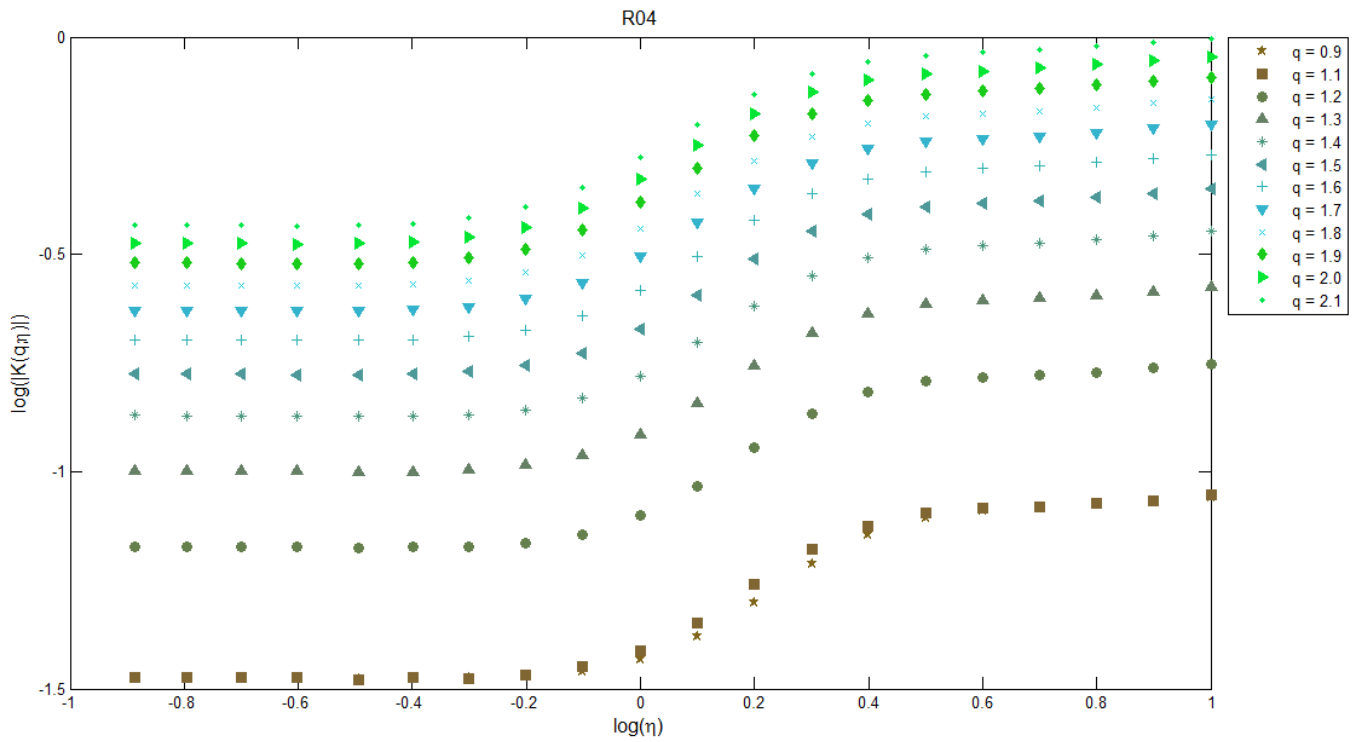


**Figure VI.4.** DTM plots of  $\log|K(q,\eta)|$  against  $\log(\eta)$  for selected order moments  $q$  obtained for 1-minute precipitation data series from Warsaw rain gauge R04

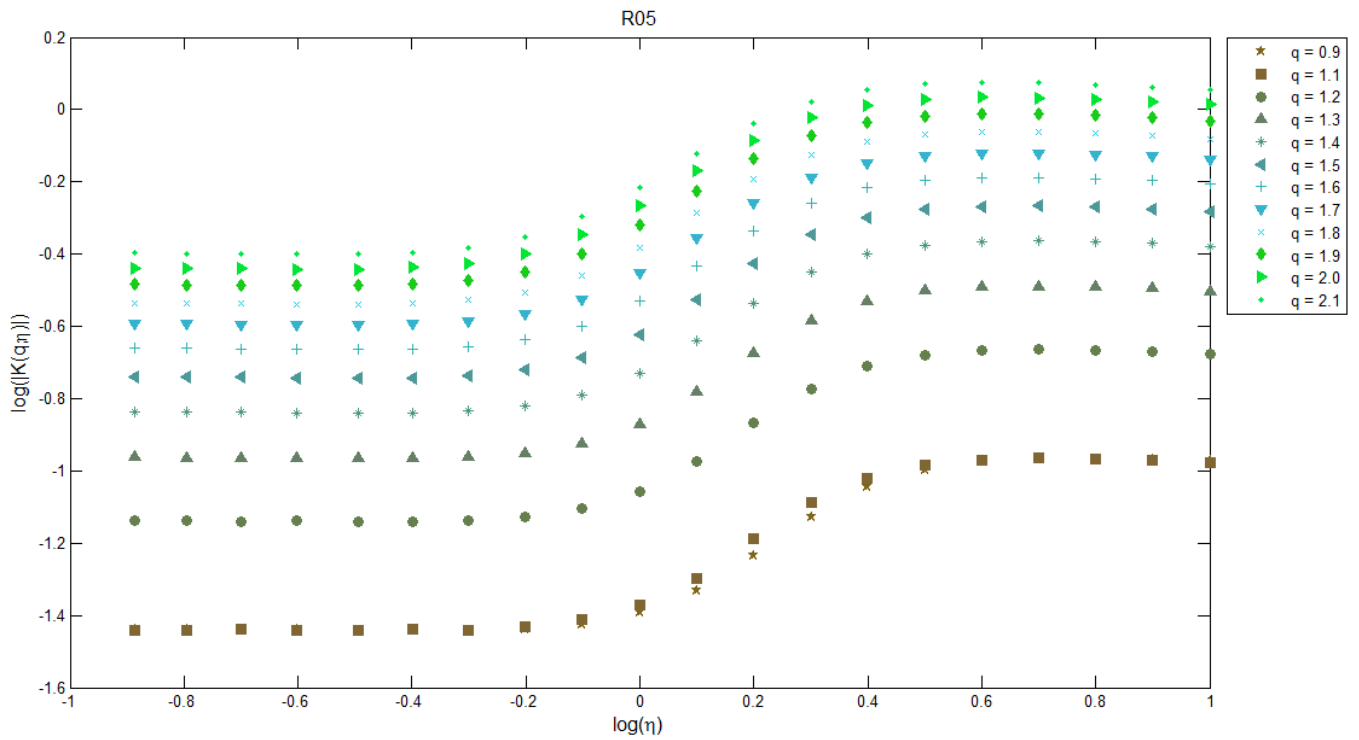


**Figure VI.5.** DTM plots of  $\log|K(q,\eta)|$  against  $\log(\eta)$  for selected order moments  $q$  obtained for 1-minute precipitation data series from Warsaw rain gauge R05

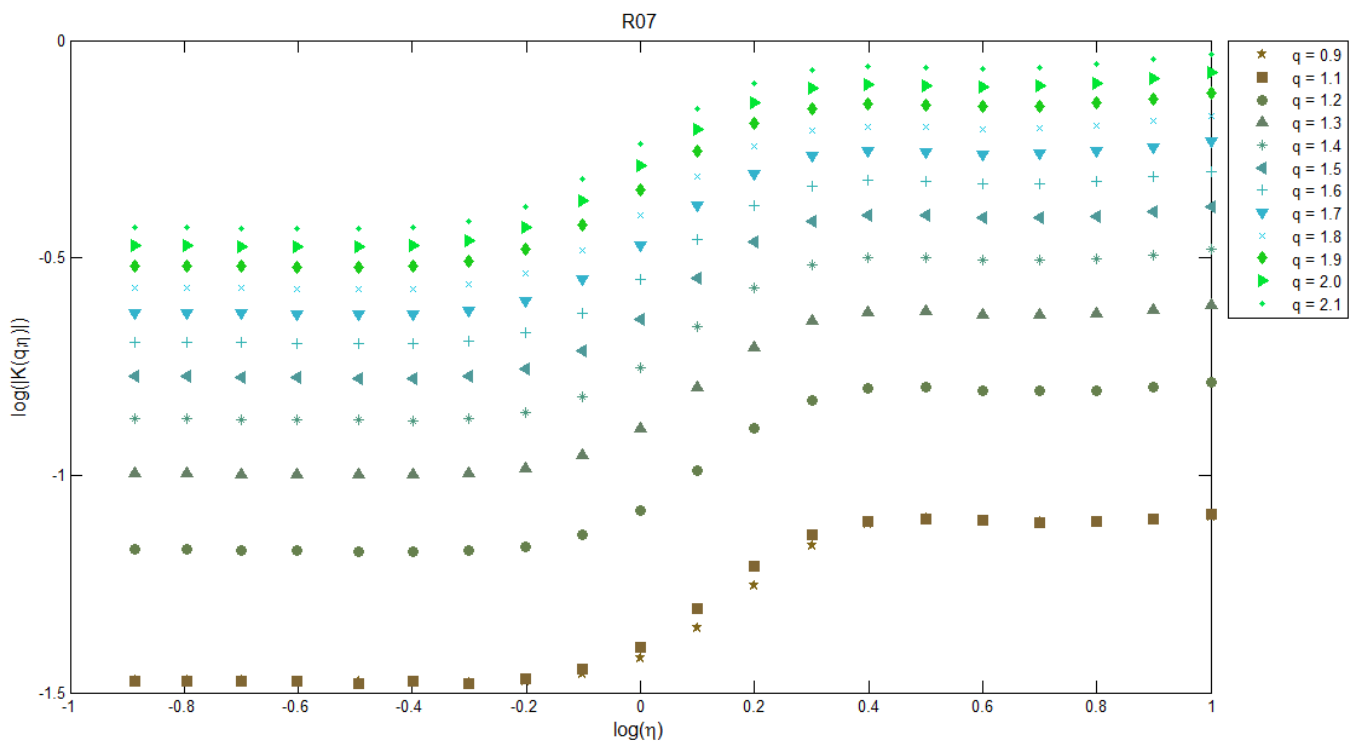


**Figure VI.6.** DTM plots of  $\log|K(q,\eta)|$  against  $\log(\eta)$  for selected order moments  $q$  obtained for 1-minute precipitation data series from Warsaw rain gauge R07

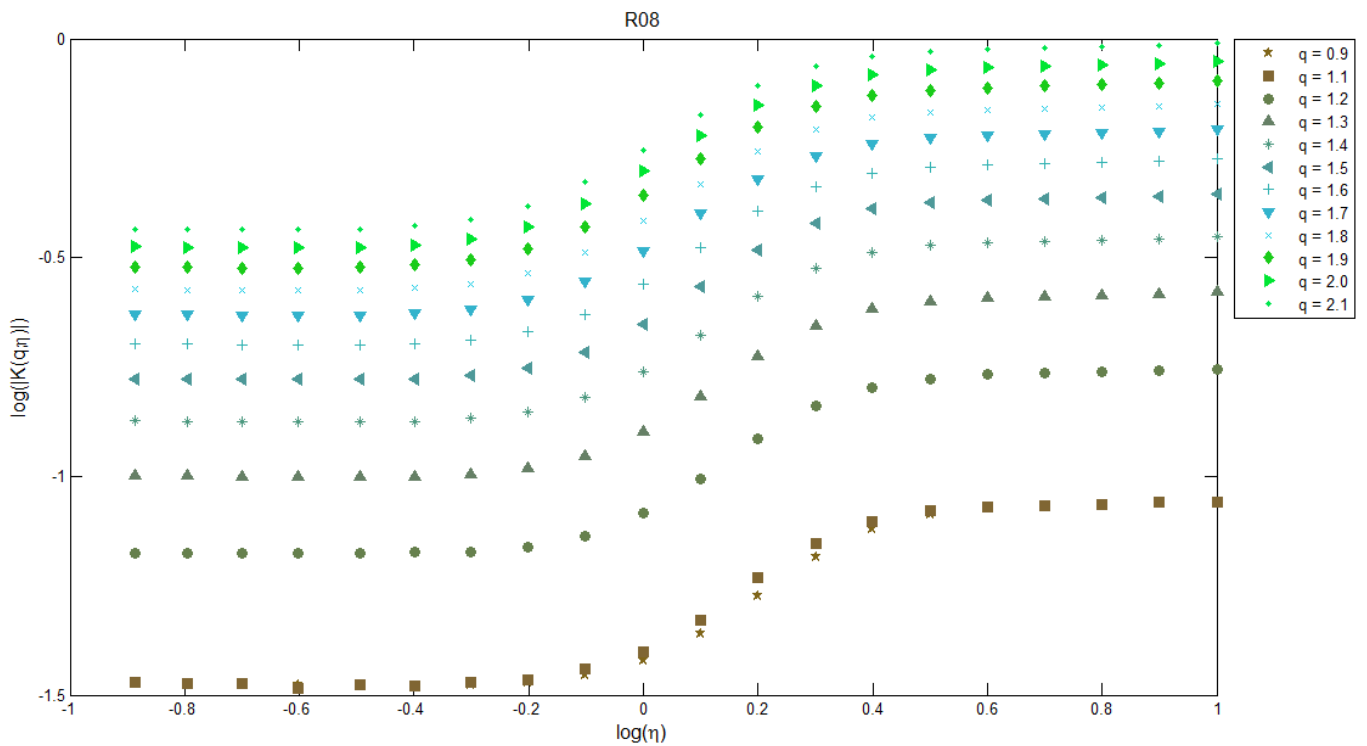


**Figure VI.7.** DTM plots of  $\log|K(q,\eta)|$  against  $\log(\eta)$  for selected order moments  $q$  obtained for 1-minute precipitation data series from Warsaw rain gauge R08

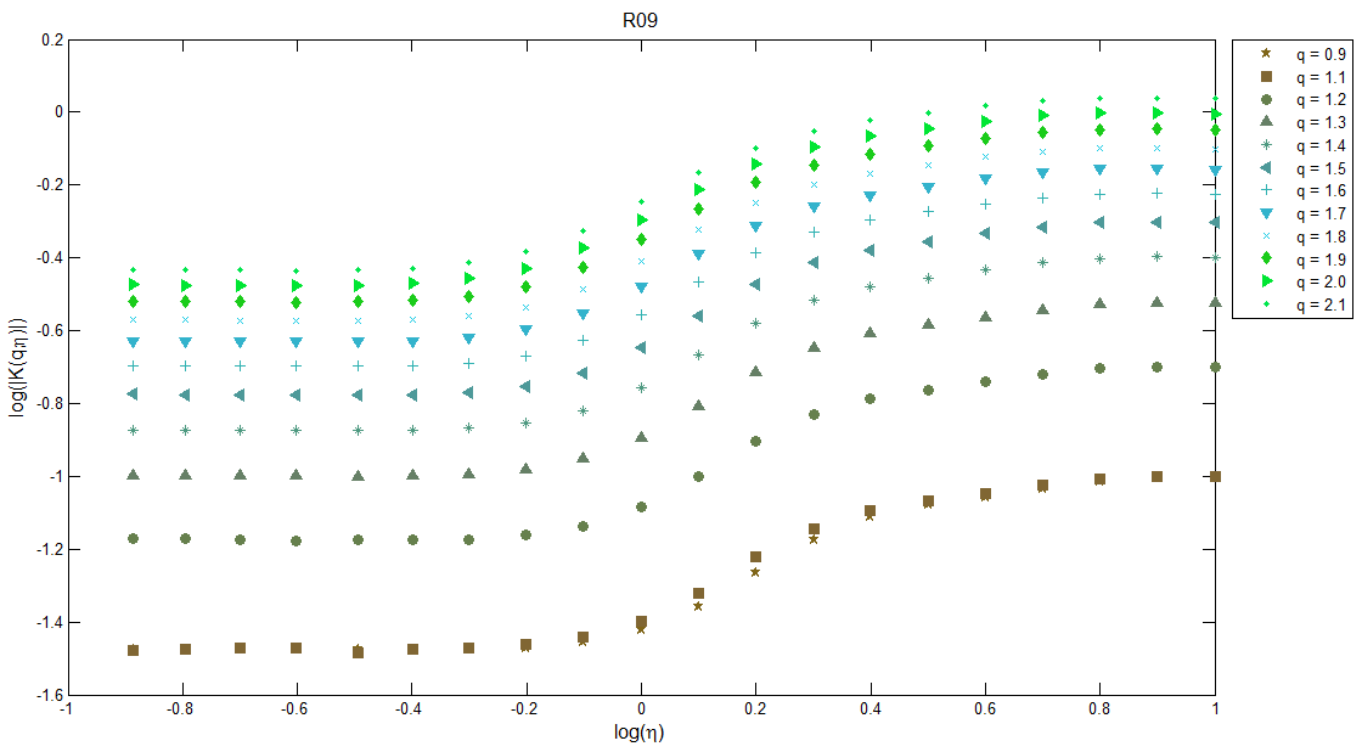


**Figure VI.8.** DTM plots of  $\log|K(q,\eta)|$  against  $\log(\eta)$  for selected order moments  $q$  obtained for 1-minute precipitation data series from Warsaw rain gauge R09

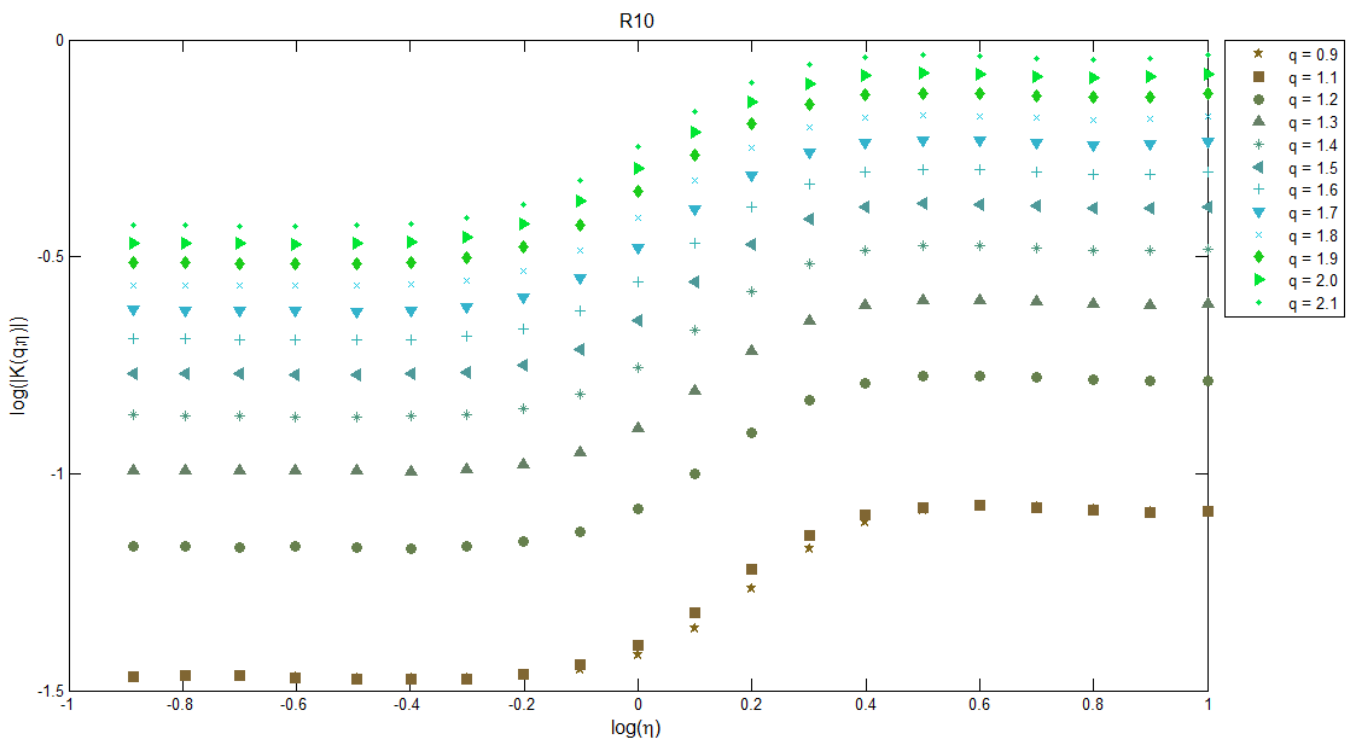


**Figure VI.9.** DTM plots of  $\log|K(q,\eta)|$  against  $\log(\eta)$  for selected order moments  $q$  obtained for 1-minute precipitation data series from Warsaw rain gauge R10

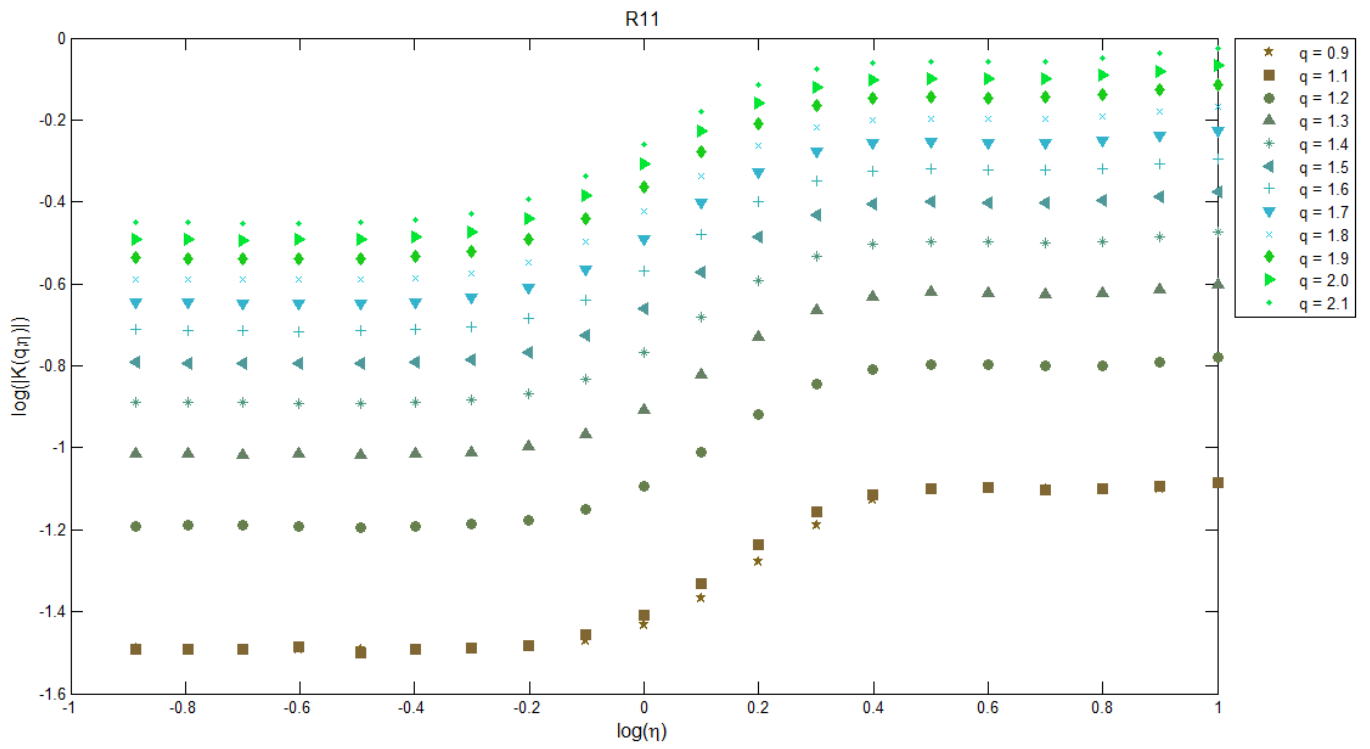


**Figure VI.10.** DTM plots of  $\log|K(q,\eta)|$  against  $\log(\eta)$  for selected order moments  $q$  obtained for 1-minute precipitation data series from Warsaw rain gauge R11

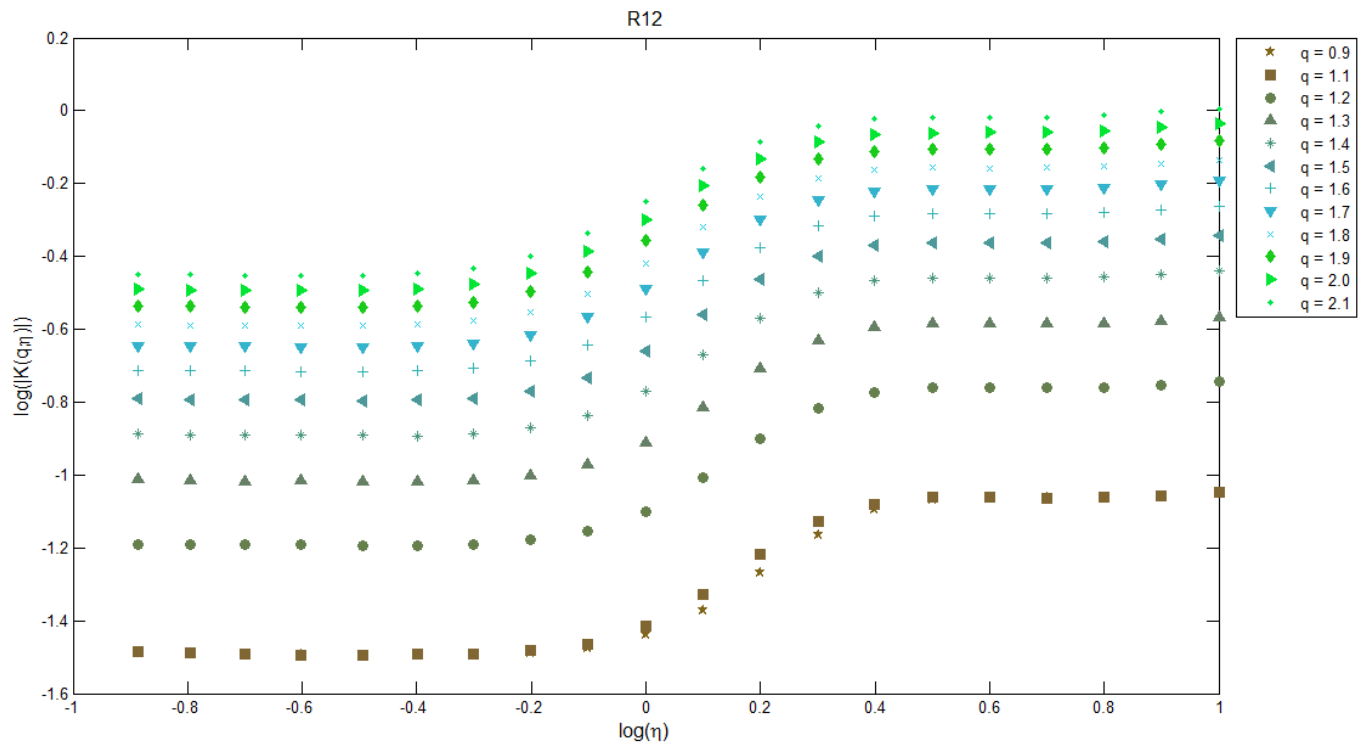


**Figure VI.11.** DTM plots of  $\log|K(q,\eta)|$  against  $\log(\eta)$  for selected order moments  $q$  obtained for 1-minute precipitation data series from Warsaw rain gauge R12

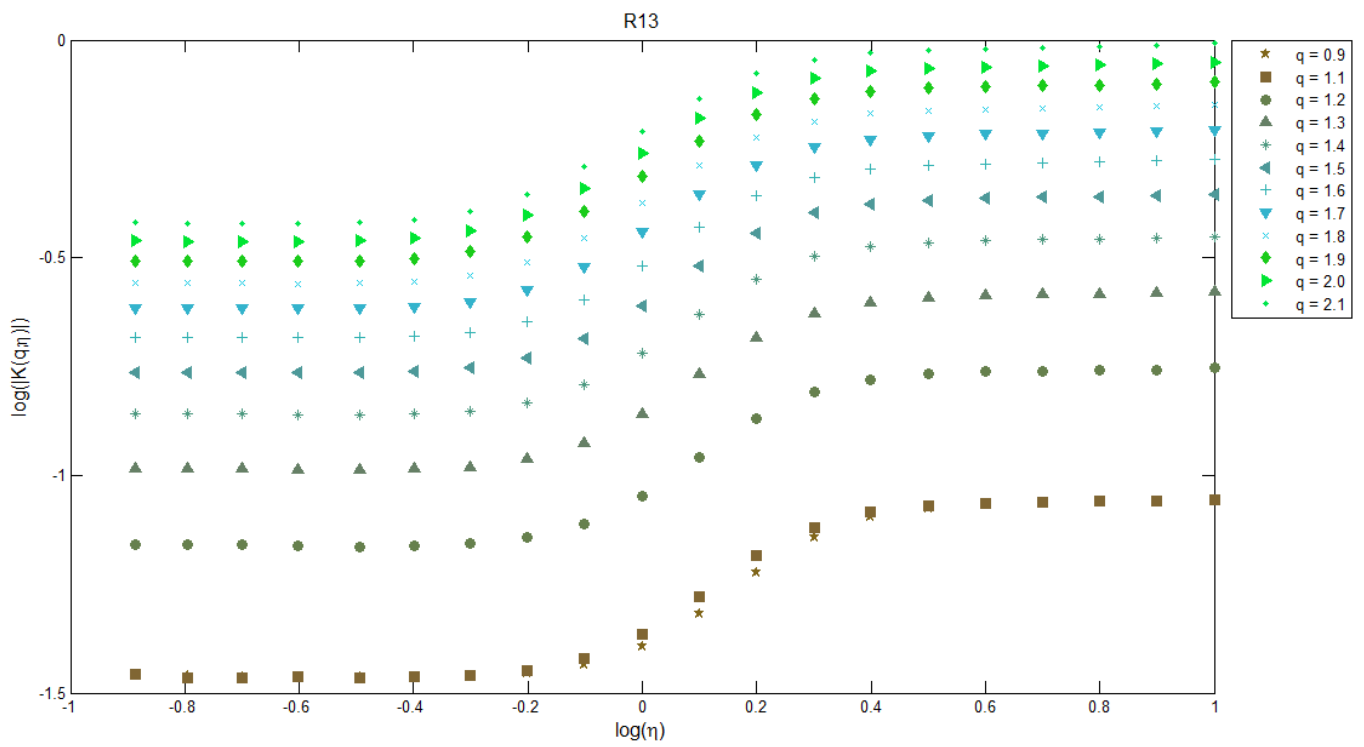


**Figure VI.12.** DTM plots of  $\log|K(q,\eta)|$  against  $\log(\eta)$  for selected order moments  $q$  obtained for 1-minute precipitation data series from Warsaw rain gauge R13

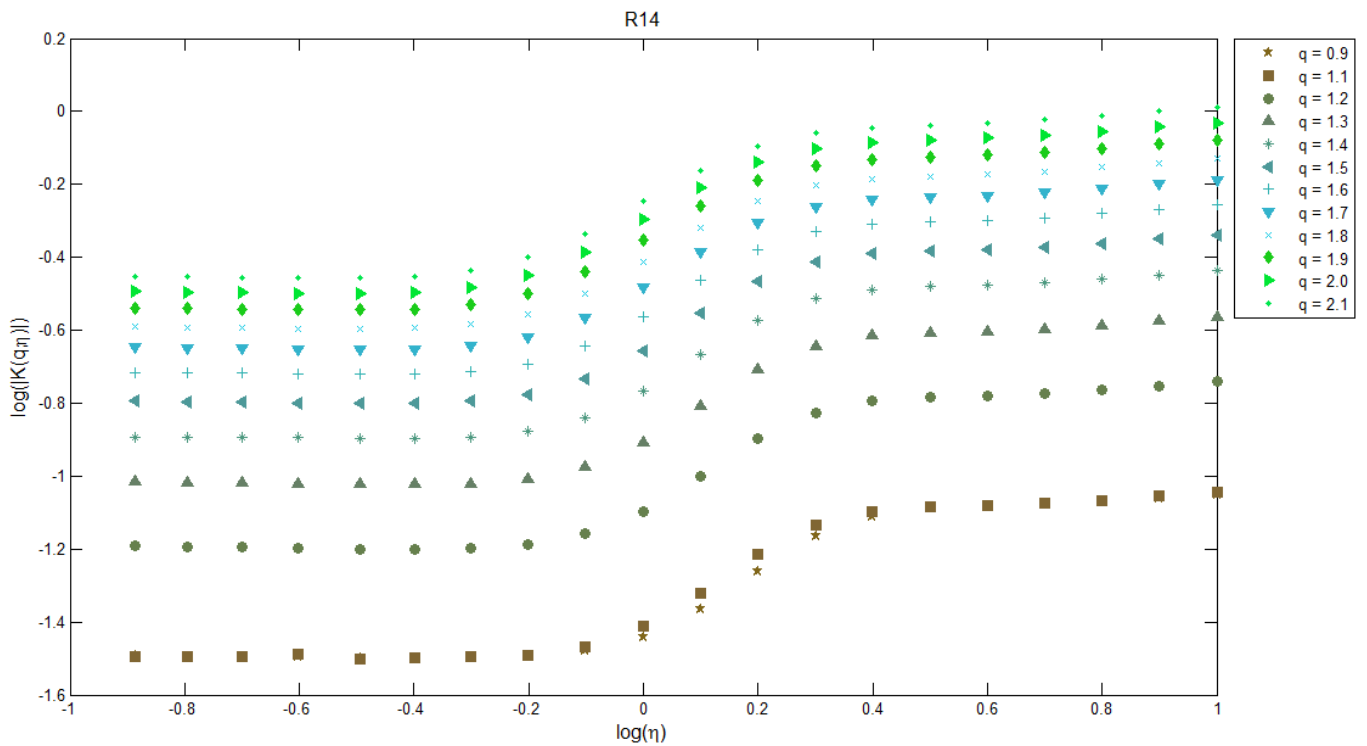


**Figure VI.13.** DTM plots of  $\log|K(q,\eta)|$  against  $\log(\eta)$  for selected order moments  $q$  obtained for 1-minute precipitation data series from Warsaw rain gauge R14

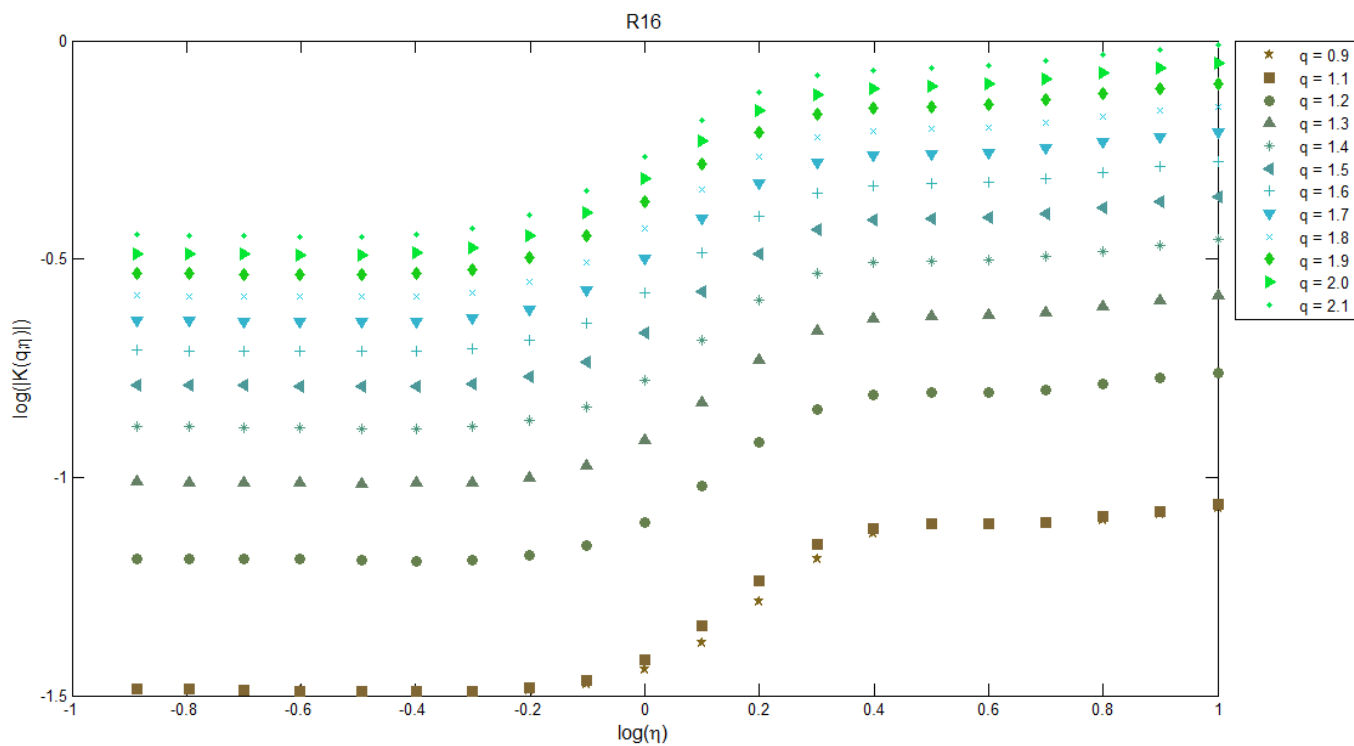


**Figure VI.14.** DTM plots of  $\log|K(q, \eta)|$  against  $\log(\eta)$  for selected order moments  $q$  obtained for 1-minute precipitation data series from Warsaw rain gauge R16

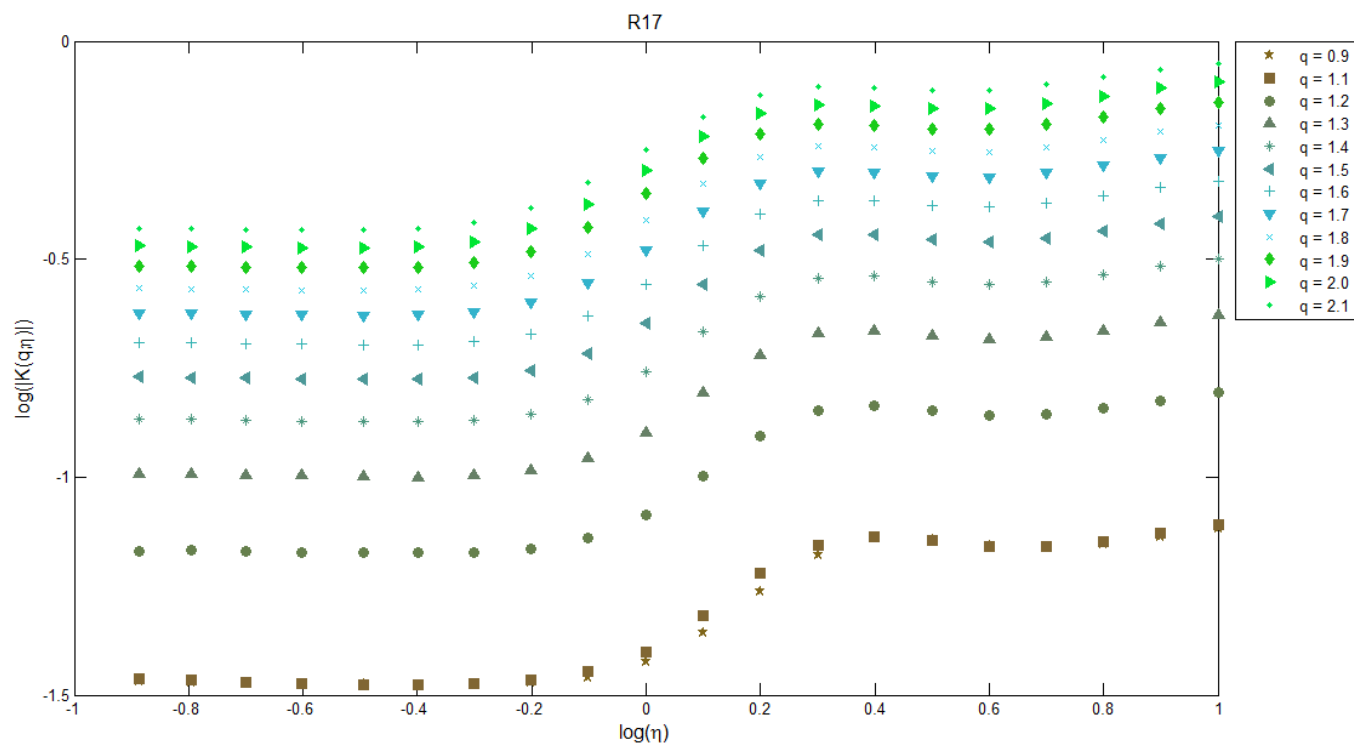


**Figure VI.15.** DTM plots of  $\log|K(q, \eta)|$  against  $\log(\eta)$  for selected order moments  $q$  obtained for 1-minute precipitation data series from Warsaw rain gauge R17

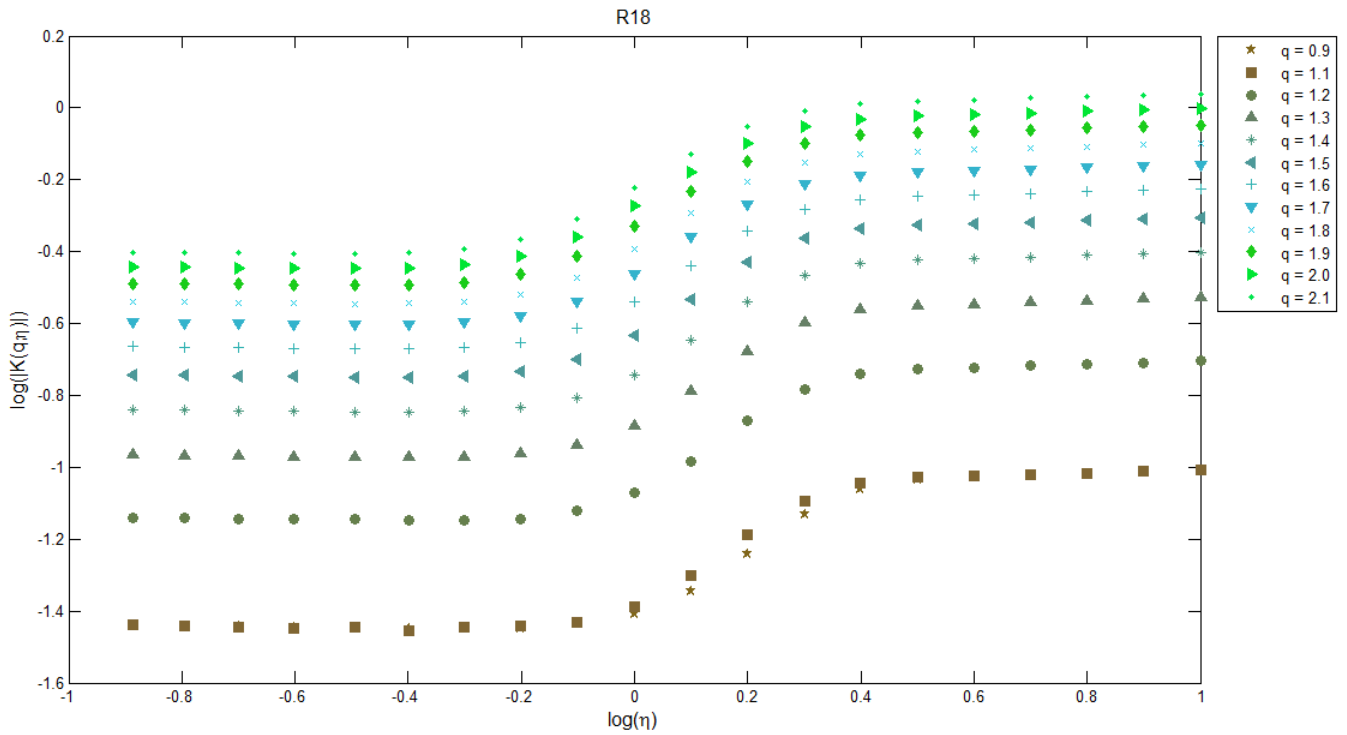


**Figure VI.16.** DTM plots of  $\log|K(q,\eta)|$  against  $\log(\eta)$  for selected order moments  $q$  obtained for 1-minute precipitation data series from Warsaw rain gauge R18

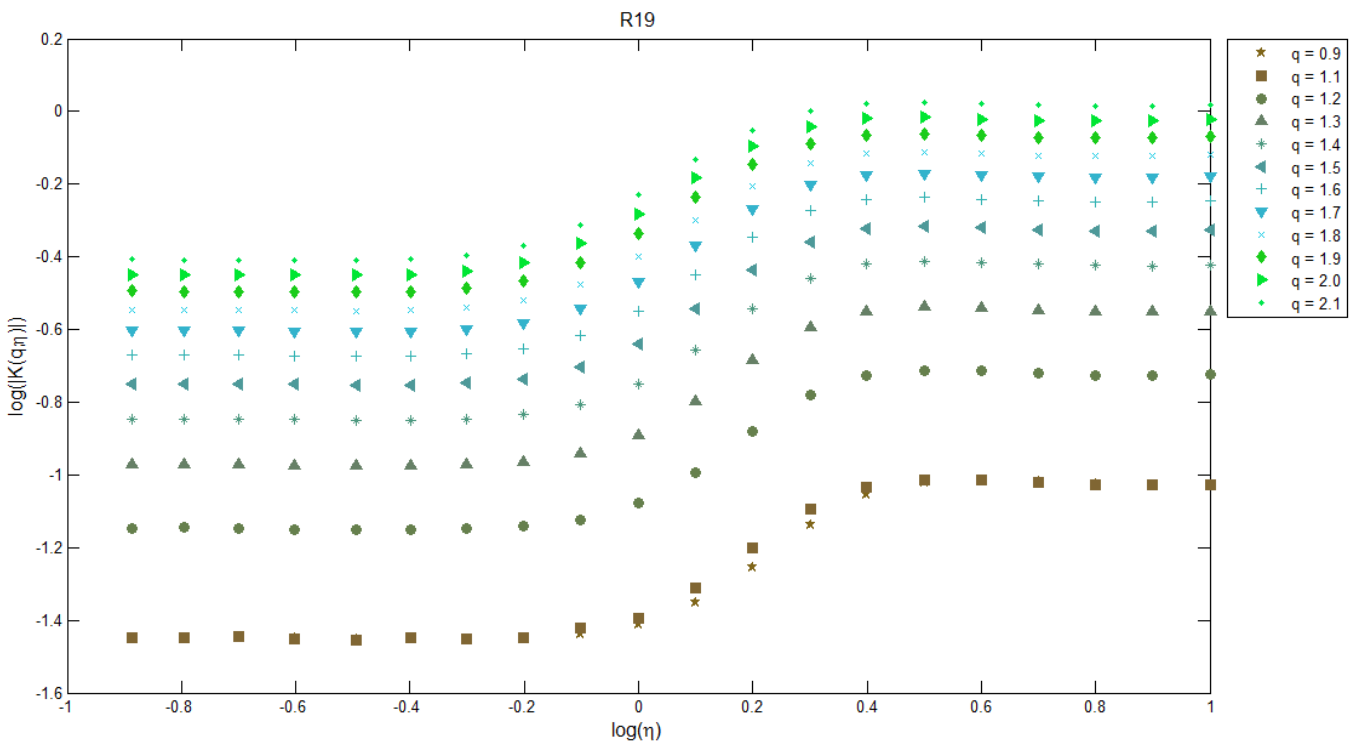


**Figure VI.17.** DTM plots of  $\log|K(q,\eta)|$  against  $\log(\eta)$  for selected order moments  $q$  obtained for 1-minute precipitation data series from Warsaw rain gauge R19

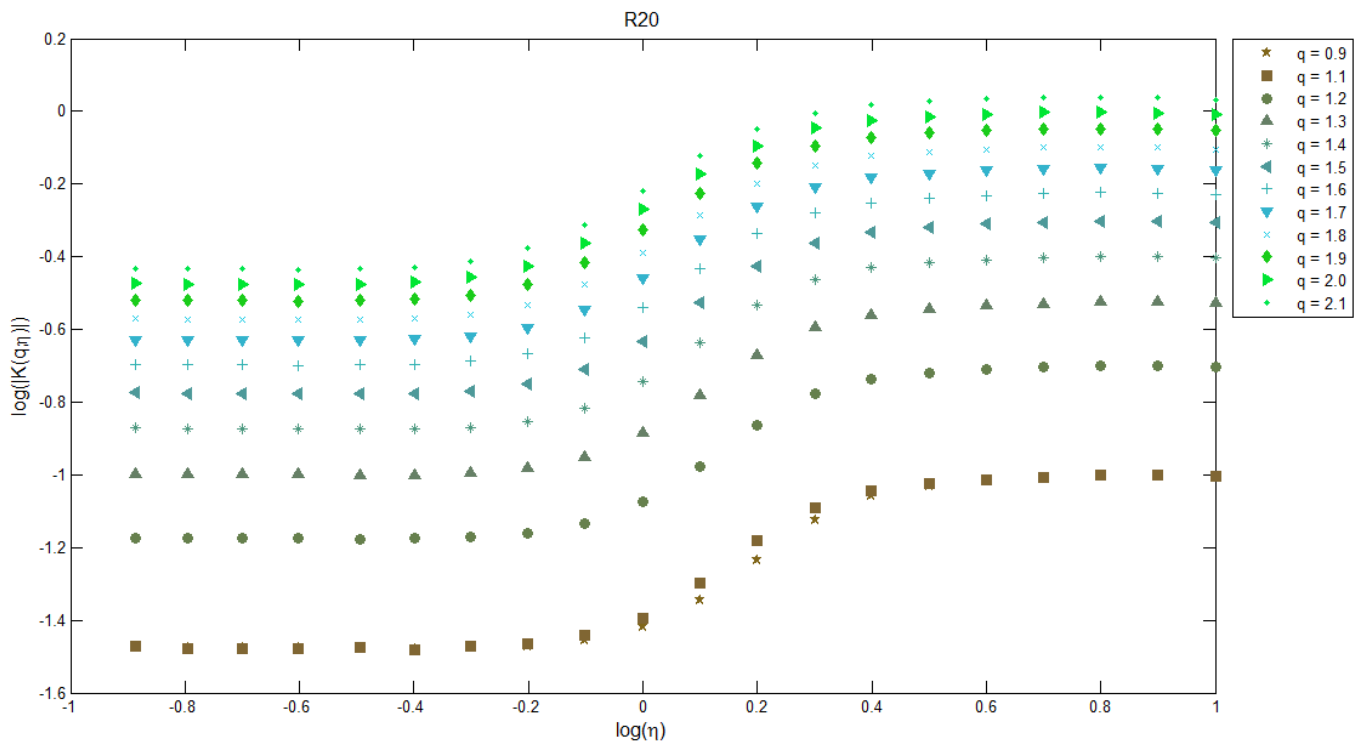


**Figure VI.18.** DTM plots of  $\log|K(q, \eta)|$  against  $\log(\eta)$  for selected order moments  $q$  obtained for 1-minute precipitation data series from Warsaw rain gauge R20

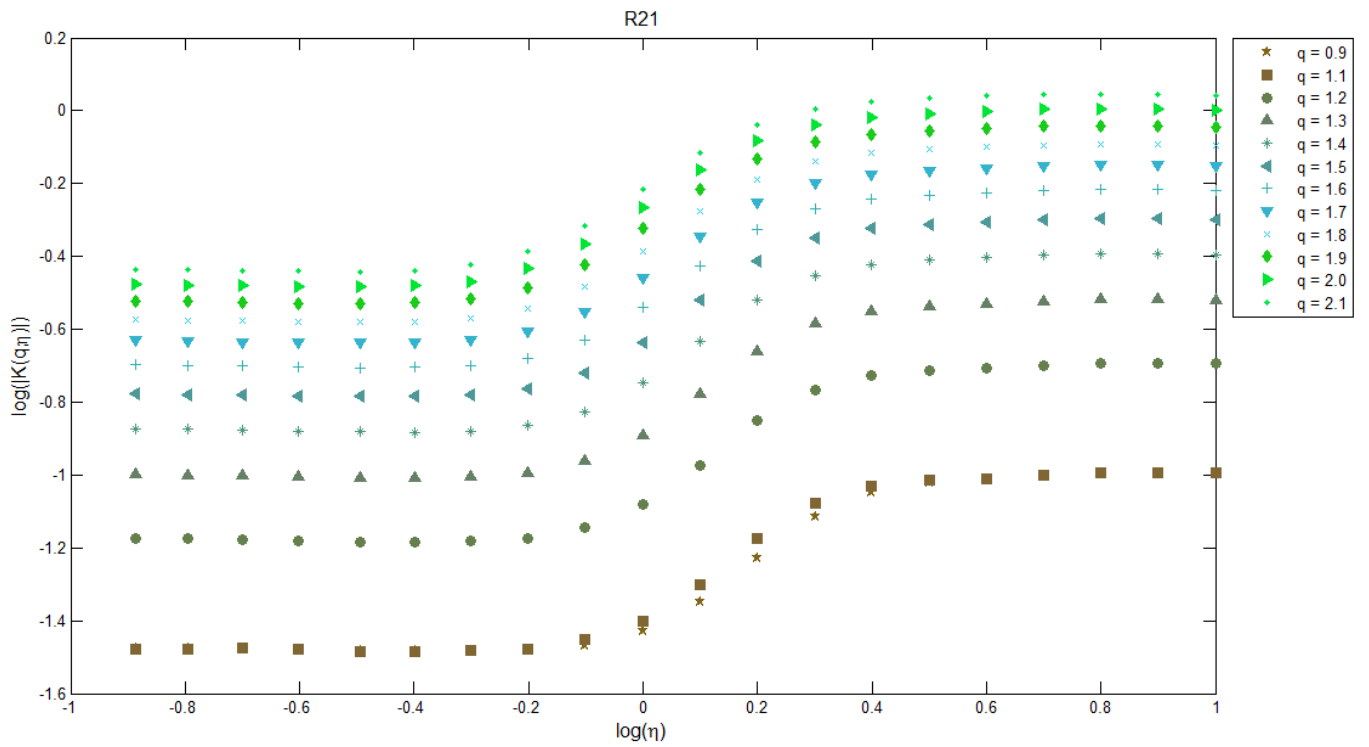


**Figure VI.19.** DTM plots of  $\log|K(q, \eta)|$  against  $\log(\eta)$  for selected order moments  $q$  obtained for 1-minute precipitation data series from Warsaw rain gauge R21

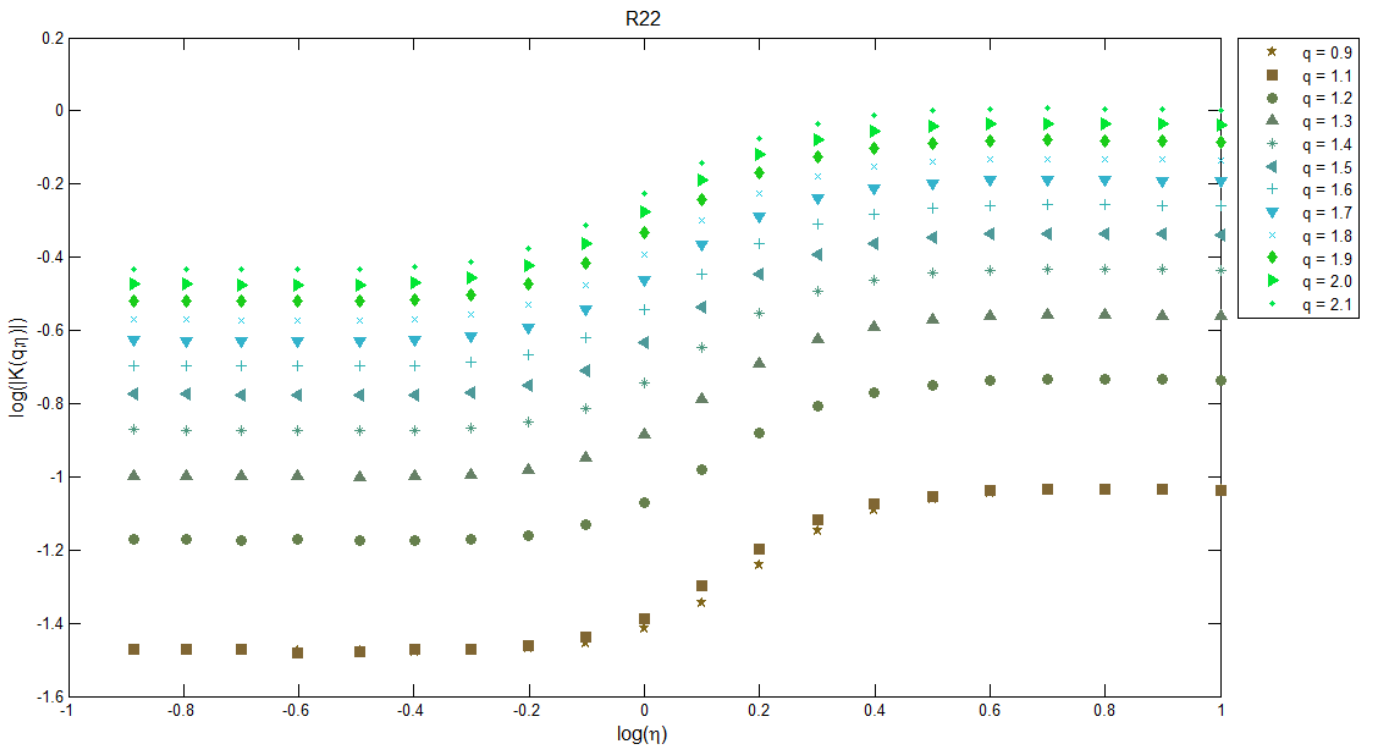


**Figure VI.20.** DTM plots of  $\log|K(q, \eta)|$  against  $\log(\eta)$  for selected order moments  $q$  obtained for 1-minute precipitation data series from Warsaw rain gauge R22

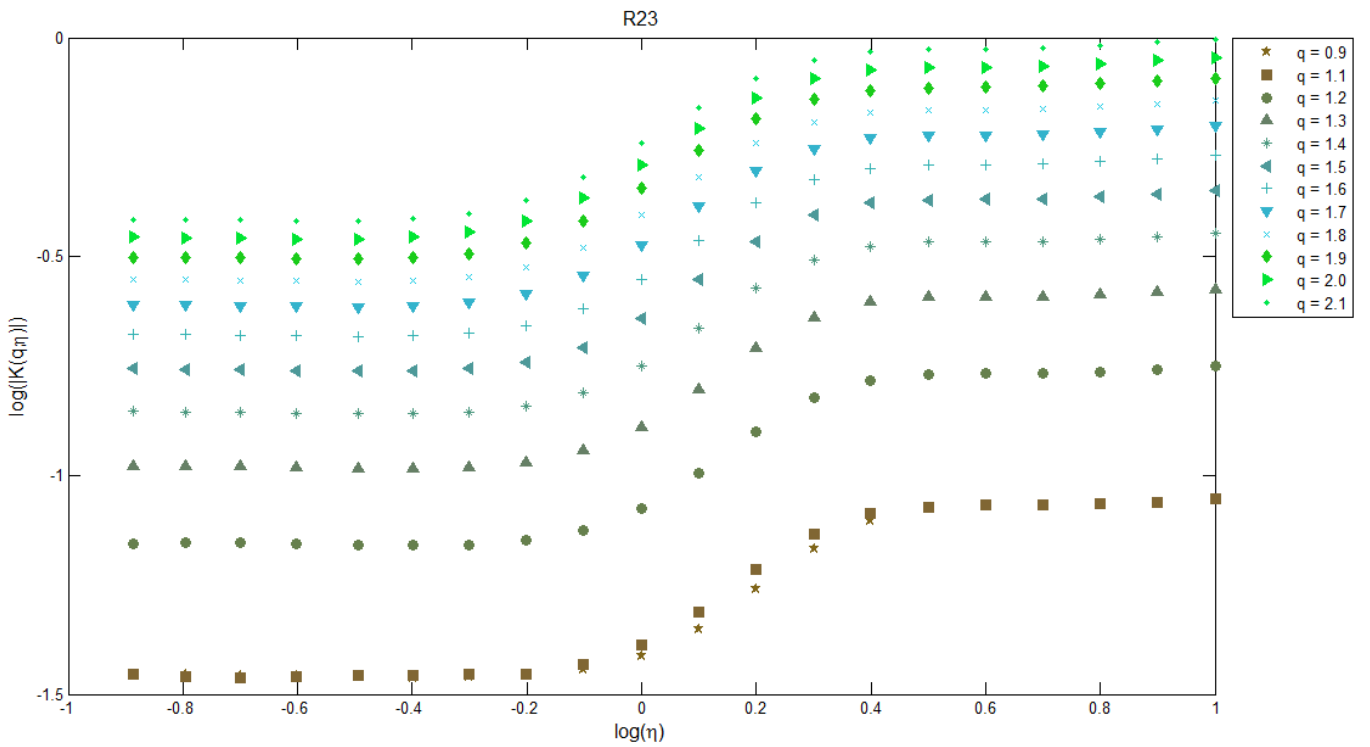


**Figure VI.21.** DTM plots of  $\log|K(q, \eta)|$  against  $\log(\eta)$  for selected order moments  $q$  obtained for 1-minute precipitation data series from Warsaw rain gauge R23

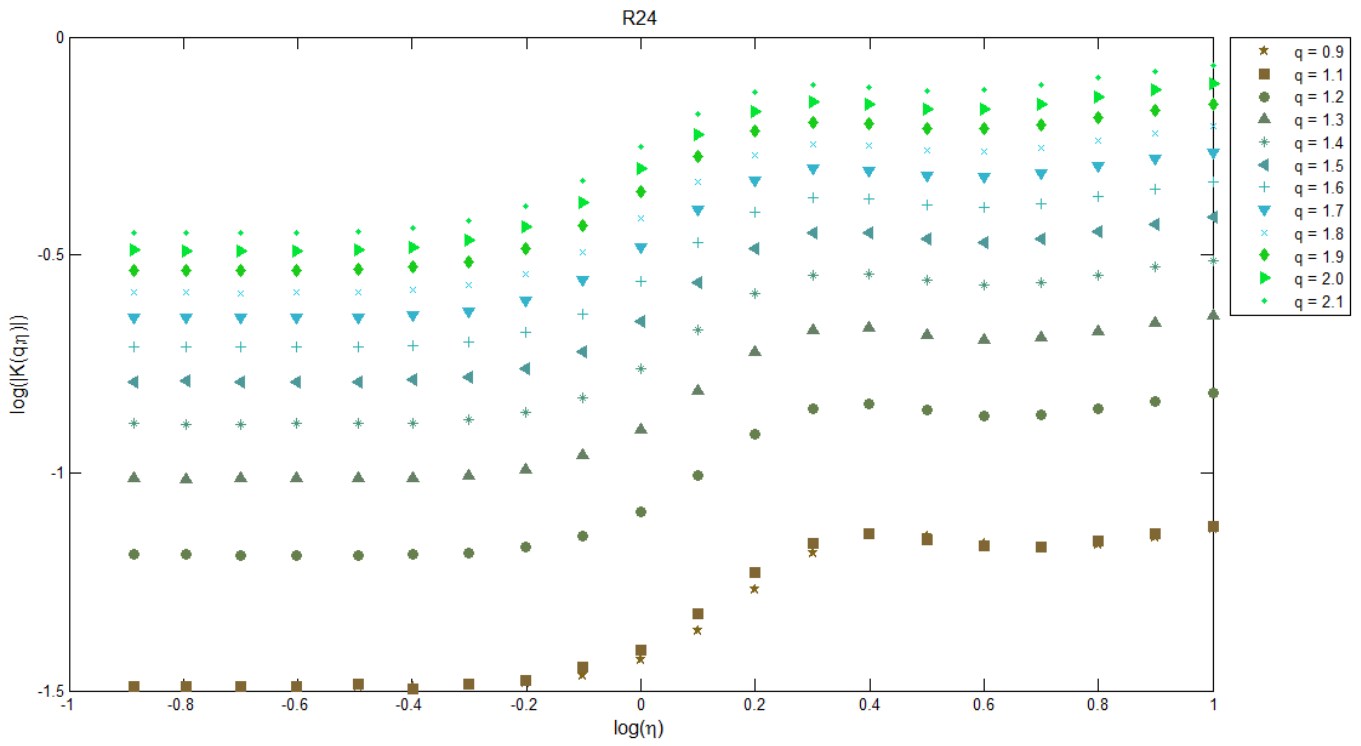


**Figure VI.22.** DTM plots of  $\log|K(q, \eta)|$  against  $\log(\eta)$  for selected order moments  $q$  obtained for 1-minute precipitation data series from Warsaw rain gauge R24

## Section B

Critical moments  $q_{min}$  and  $q_{max}$  estimated for plots breaks from the graphs presented in Section A, and below, the Lévy index  $\alpha$  and the mean values of the codimension  $C_1$  for selected moments order  $q$ .

**Table VI.1a.** Critical moments  $q_{min}$  and  $q_{max}$  estimated for selected values of order moment  $q$ , obtained for 1-minute precipitation data series from Warsaw rain gauges R01

R1						
Curve for $q$	Minimal critical moment $q_{min}$			Maximal critical moment $q_{max}$		
	$\log(\eta)$	$\eta$	$q_{min} = q\eta$	$\log(\eta)$	$\eta$	$q_{max} = q\eta$
0.90	0.1	1.26	1.13	0.5	3.16	2.85
1.10	0.0	1.00	1.10	0.4	2.51	2.76
1.20	0.0	1.00	1.20	0.4	2.51	3.01
1.30	0.0	1.00	1.30	0.3	2.00	2.59
1.40	-0.1	0.79	1.11	0.3	2.00	2.79
1.50	-0.1	0.79	1.19	0.3	2.00	2.99
1.60	-0.1	0.79	1.27	0.3	2.00	3.19
1.70	-0.1	0.79	1.35	0.3	2.00	3.39
1.80	-0.1	0.79	1.43	0.2	1.58	2.85
1.90	-0.2	0.63	1.20	0.2	1.58	3.01
2.00	-0.2	0.63	1.26	0.2	1.58	3.17
2.10	-0.2	0.63	1.33	0.2	1.58	3.33
Average			1.24	Average		3.00
Standard deviation			0.10	Standard deviation		0.24

**Table VI.1b.** Lévy indexes  $\alpha$  and the mean values of process codimension  $C_1$  calculations for 1-minute precipitation data series from Warsaw rain gauges R01

R1			
Curve for $q$	$K(q,1)$	$\alpha$	$C_1$
1.10	-1.387	0.834	0.394
1.20	-1.074	0.816	0.392
1.30	-0.885	0.792	0.392
1.40	-0.748	0.825	0.390
1.50	-0.639	0.820	0.392
1.60	-0.548	0.811	0.394
1.70	-0.469	0.799	0.397
1.80	-0.401	0.840	0.394
1.90	-0.339	0.761	0.405
2.00	-0.284	0.760	0.407
2.10	-0.234	0.757	0.409
Average		0.801	0.397
Standard deviation		0.030	0.007

**Table VI.2a.** Critical moments  $q_{min}$  and  $q_{max}$  estimated for selected values of order moment  $q$ , obtained for 1-minute precipitation data series from Warsaw rain gauges R02

R2						
Curve for $q$	Minimal critical moment $q_{min}$			Maximal critical moment $q_{max}$		
	$\log(\eta)$	$\eta$	$q_{min} = q\eta$	$\log(\eta)$	$\eta$	$q_{max} = q\eta$
0.90	0.0	1.00	0.90	0.5	3.16	2.85
1.10	-0.1	0.79	0.87	0.4	2.51	2.76
1.20	-0.1	0.79	0.95	0.4	2.51	3.01
1.30	-0.1	0.79	1.03	0.4	2.51	3.27
1.40	-0.2	0.63	0.88	0.4	2.51	3.52
1.50	-0.2	0.63	0.95	0.3	2.00	2.99
1.60	-0.2	0.63	1.01	0.3	2.00	3.19
1.70	-0.2	0.63	1.07	0.3	2.00	3.39
1.80	-0.2	0.63	1.14	0.3	2.00	3.59
1.90	-0.2	0.63	1.20	0.2	1.58	3.01
2.00	-0.3	0.50	1.00	0.2	1.58	3.17
2.10	-0.3	0.50	1.05	0.2	1.58	3.33
Average			1.01	Average		3.17
Standard deviation			0.10	Standard deviation		0.26

**Table VI.2b.** Lévy indexes  $\alpha$  and the mean values of process codimension  $C_1$  calculations for 1-minute precipitation data series from Warsaw rain gauges R02

R2			
Curve for $q$	$K(q,1)$	$\alpha$	$C_1$
1.10	-1.390	0.828	0.391
1.20	-1.076	0.821	0.390
1.30	-0.886	0.809	0.391
1.40	-0.747	0.748	0.397
1.50	-0.636	0.797	0.396
1.60	-0.543	0.796	0.399
1.70	-0.464	0.791	0.403
1.80	-0.394	0.784	0.407
1.90	-0.331	0.818	0.405
2.00	-0.275	0.724	0.420
2.10	-0.225	0.726	0.423
Average		0.785	0.402
Standard deviation		0.037	0.011

**Table VI.3a.** Critical moments  $q_{min}$  and  $q_{max}$  estimated for selected values of order moment  $q$ , obtained for 1-minute precipitation data series from Warsaw rain gauges R03

R3						
Curve for $q$	Minimal critical moment $q_{min}$			Maximal critical moment $q_{max}$		
	$\log(\eta)$	$\eta$	$q_{min} = q\eta$	$\log(\eta)$	$\eta$	$q_{max} = q\eta$
0.90	0.0	1.00	0.90	0.5	3.16	2.85
1.10	-0.1	0.79	0.87	0.4	2.51	2.76
1.20	-0.1	0.79	0.95	0.4	2.51	3.01
1.30	-0.1	0.79	1.03	0.4	2.51	3.27
1.40	-0.2	0.63	0.88	0.4	2.51	3.52
1.50	-0.2	0.63	0.95	0.3	2.00	2.99
1.60	-0.2	0.63	1.01	0.3	2.00	3.19
1.70	-0.2	0.63	1.07	0.3	2.00	3.39
1.80	-0.2	0.63	1.14	0.3	2.00	3.59
1.90	-0.2	0.63	1.20	0.3	2.00	3.79
2.00	-0.3	0.50	1.00	0.2	1.58	3.17
2.10	-0.3	0.50	1.05	0.2	1.58	3.33
Average			1.01	Average		3.24
Standard deviation			0.10	Standard deviation		0.31

**Table VI.3b.** Lévy indexes  $\alpha$  and the mean values of process codimension  $C_1$  calculations for 1-minute precipitation data series from Warsaw rain gauges R03

R3			
Curve for $q$	$K(q,1)$	$\alpha$	$C_1$
1.10	-1.405	0.856	0.378
1.20	-1.090	0.853	0.376
1.30	-0.900	0.844	0.377
1.40	-0.761	0.778	0.382
1.50	-0.651	0.819	0.381
1.60	-0.558	0.820	0.384
1.70	-0.478	0.818	0.387
1.80	-0.408	0.812	0.390
1.90	-0.345	0.805	0.394
2.00	-0.289	0.742	0.405
2.10	-0.238	0.745	0.407
Average		0.808	0.387
Standard deviation		0.039	0.011

**Table VI.4a.** Critical moments  $q_{min}$  and  $q_{max}$  estimated for selected values of order moment  $q$ , obtained for 1-minute precipitation data series from Warsaw rain gauges R04

R4						
Curve for $q$	Minimal critical moment $q_{min}$			Maximal critical moment $q_{max}$		
	$\log(\eta)$	$\eta$	$q_{min} = q\eta$	$\log(\eta)$	$\eta$	$q_{max} = q\eta$
0.90	0.0	1.00	0.90	0.5	3.16	2.85
1.10	-0.1	0.79	0.87	0.4	2.51	2.76
1.20	-0.1	0.79	0.95	0.4	2.51	3.01
1.30	-0.1	0.79	1.03	0.4	2.51	3.27
1.40	-0.1	0.79	1.11	0.4	2.51	3.52
1.50	-0.2	0.63	0.95	0.3	2.00	2.99
1.60	-0.2	0.63	1.01	0.3	2.00	3.19
1.70	-0.2	0.63	1.07	0.3	2.00	3.39
1.80	-0.2	0.63	1.14	0.3	2.00	3.59
1.90	-0.3	0.50	0.95	0.2	1.58	3.01
2.00	-0.3	0.50	1.00	0.2	1.58	3.17
2.10	-0.3	0.50	1.05	0.2	1.58	3.33
Average			1.00	Average		3.17
Standard deviation			0.08	Standard deviation		0.26

**Table VI.4b.** Lévy indexes  $\alpha$  and the mean values of process codimension  $C_1$  calculations for 1-minute precipitation data series from Warsaw rain gauges R04.

R4			
Curve for $q$	$K(q,1)$	$\alpha$	$C_1$
1.10	-1.412	0.689	0.375
1.20	-1.101	0.692	0.372
1.30	-0.915	0.690	0.372
1.40	-0.779	0.683	0.372
1.50	-0.672	0.652	0.375
1.60	-0.583	0.657	0.376
1.70	-0.507	0.658	0.377
1.80	-0.440	0.657	0.379
1.90	-0.380	0.579	0.390
2.00	-0.326	0.586	0.392
2.10	-0.277	0.591	0.393
Average		0.648	0.379
Standard deviation		0.043	0.008

**Table VI.5a.** Critical moments  $q_{min}$  and  $q_{max}$  estimated for selected values of order moment  $q$ , obtained for 1-minute precipitation data series from Warsaw rain gauges R05

R5						
Curve for $q$	Minimal critical moment $q_{min}$			Maximal critical moment $q_{max}$		
	$\log(\eta)$	$\eta$	$q_{min} = q\eta$	$\log(\eta)$	$\eta$	$q_{max} = q\eta$
0.90	-0.1	0.79	0.71	0.5	3.16	2.85
1.10	-0.1	0.79	0.87	0.4	2.51	2.76
1.20	-0.2	0.63	0.76	0.4	2.51	3.01
1.30	-0.2	0.63	0.82	0.4	2.51	3.27
1.40	-0.2	0.63	0.88	0.4	2.51	3.52
1.50	-0.2	0.63	0.95	0.4	2.51	3.77
1.60	-0.2	0.63	1.01	0.4	2.51	4.02
1.70	-0.2	0.63	1.07	0.3	2.00	3.39
1.80	-0.3	0.50	0.90	0.3	2.00	3.59
1.90	-0.3	0.50	0.95	0.3	2.00	3.79
2.00	-0.3	0.50	1.00	0.3	2.00	3.99
2.10	-0.3	0.50	1.05	0.3	2.00	4.19
Average			0.92	Average		3.51
Standard deviation			0.11	Standard deviation		0.47

**Table VI. 5b.** Lévy indexes  $\alpha$  and the mean values of process codimension  $C_l$  calculations for 1-minute precipitation data series from Warsaw rain gauges R05

R5			
Curve for $q$	$K(q,1)$	$\alpha$	$C_l$
1.10	-1.370	0.833	0.410
1.20	-1.057	0.754	0.410
1.30	-0.869	0.762	0.409
1.40	-0.731	0.766	0.410
1.50	-0.622	0.766	0.412
1.60	-0.530	0.764	0.414
1.70	-0.452	0.796	0.413
1.80	-0.382	0.713	0.426
1.90	-0.321	0.717	0.429
2.00	-0.265	0.719	0.431
2.10	-0.214	0.719	0.434
Average		0.755	0.418
Standard deviation		0.037	0.010

**Table VI.7a.** Critical moments  $q_{min}$  and  $q_{max}$  estimated for selected values of order moment  $q$ , obtained for 1-minute precipitation data series from Warsaw rain gauges R07

R7						
Curve for $q$	Minimal critical moment $q_{min}$			Maximal critical moment $q_{max}$		
	$\log(\eta)$	$\eta$	$q_{min} = q\eta$	$\log(\eta)$	$\eta$	$q_{max} = q\eta$
0.90	0.0	1.00	0.90	0.5	3.16	2.85
1.10	-0.1	0.79	0.87	0.4	2.51	2.76
1.20	-0.1	0.79	0.95	0.3	2.00	2.39
1.30	-0.1	0.79	1.03	0.3	2.00	2.59
1.40	-0.1	0.79	1.11	0.3	2.00	2.79
1.50	-0.2	0.63	0.95	0.3	2.00	2.99
1.60	-0.2	0.63	1.01	0.2	1.58	2.54
1.70	-0.2	0.63	1.07	0.2	1.58	2.69
1.80	-0.2	0.63	1.14	0.2	1.58	2.85
1.90	-0.2	0.63	1.20	0.2	1.58	3.01
2.00	-0.3	0.50	1.00	0.2	1.58	3.17
2.10	-0.3	0.50	1.05	0.1	1.26	2.64
Average			1.02	Average		2.77
Standard deviation			0.10	Standard deviation		0.22

**Table VI.7b.** Lévy indexes  $\alpha$  and the mean values of process codimension  $C_1$  calculations for 1-minute precipitation data series from Warsaw rain gauges R07

R7			
Curve for $q$	$K(q,1)$	$\alpha$	$C_1$
1.10	-1.396	0.740	0.388
1.20	-1.081	0.809	0.386
1.30	-0.891	0.804	0.387
1.40	-0.752	0.792	0.389
1.50	-0.642	0.725	0.396
1.60	-0.551	0.755	0.396
1.70	-0.472	0.756	0.399
1.80	-0.403	0.753	0.401
1.90	-0.342	0.747	0.404
2.00	-0.288	0.669	0.416
2.10	-0.238	0.658	0.420
Average		0.746	0.398
Standard deviation		0.049	0.011

**Table VI.8a.** Critical moments  $q_{min}$  and  $q_{max}$  estimated for selected values of order moment  $q$ , obtained for 1-minute precipitation data series from Warsaw rain gauges R08

R8						
Curve for $q$	Minimal critical moment $q_{min}$			Maximal critical moment $q_{max}$		
	$\log(\eta)$	$\eta$	$q_{min} = q\eta$	$\log(\eta)$	$\eta$	$q_{max} = q\eta$
0.90	0.0	1.00	0.90	0.5	3.16	2.85
1.10	-0.1	0.79	0.87	0.4	2.51	2.76
1.20	-0.1	0.79	0.95	0.4	2.51	3.01
1.30	-0.1	0.79	1.03	0.3	2.00	2.59
1.40	-0.1	0.79	1.11	0.3	2.00	2.79
1.50	-0.2	0.63	0.95	0.3	2.00	2.99
1.60	-0.2	0.63	1.01	0.3	2.00	3.19
1.70	-0.2	0.63	1.07	0.3	2.00	3.39
1.80	-0.2	0.63	1.14	0.3	2.00	3.59
1.90	-0.2	0.63	1.20	0.3	2.00	3.79
2.00	-0.3	0.50	1.00	0.2	1.58	3.17
2.10	-0.3	0.50	1.05	0.2	1.58	3.33
Average			1.02	Average		3.12
Standard deviation			0.10	Standard deviation		0.36

**Table VI.8b.** Lévy indexes  $\alpha$  and the mean values of process codimension  $C_1$  calculations for 1-minute precipitation data series from Warsaw rain gauges R08

R8			
Curve for $q$	$K(q,1)$	$\alpha$	$C_1$
1.10	-1.399	0.726	0.386
1.20	-1.086	0.723	0.385
1.30	-0.898	0.715	0.385
1.40	-0.761	0.766	0.383
1.50	-0.653	0.697	0.389
1.60	-0.562	0.698	0.391
1.70	-0.485	0.696	0.393
1.80	-0.417	0.691	0.396
1.90	-0.357	0.685	0.398
2.00	-0.303	0.636	0.407
2.10	-0.253	0.639	0.408
Average		0.697	0.393
Standard deviation		0.037	0.009

**Table VI.9a.** Critical moments  $q_{min}$  and  $q_{max}$  estimated for selected values of order moment  $q$ , obtained for 1-minute precipitation data series from Warsaw rain gauges R09

R9						
Curve for $q$	Minimal critical moment $q_{min}$			Maximal critical moment $q_{max}$		
	$\log(\eta)$	$\eta$	$q_{min} = q\eta$	$\log(\eta)$	$\eta$	$q_{max} = q\eta$
0.90	0.0	1.00	0.90	0.5	3.16	2.85
1.10	-0.1	0.79	0.87	0.4	2.51	2.76
1.20	-0.1	0.79	0.95	0.3	2.00	2.39
1.30	-0.1	0.79	1.03	0.3	2.00	2.59
1.40	-0.1	0.79	1.11	0.3	2.00	2.79
1.50	-0.2	0.63	0.95	0.3	2.00	2.99
1.60	-0.2	0.63	1.01	0.2	1.58	2.54
1.70	-0.2	0.63	1.07	0.2	1.58	2.69
1.80	-0.2	0.63	1.14	0.2	1.58	2.85
1.90	-0.2	0.63	1.20	0.2	1.58	3.01
2.00	-0.3	0.50	1.00	0.1	1.26	2.52
2.10	-0.3	0.50	1.05	0.1	1.26	2.64
Average			1.02	Average		2.72
Standard deviation			0.10	Standard deviation		0.19

**Table VI.9b.** Lévy indexes  $\alpha$  and the mean values of process codimension  $C_1$  calculations for 1-minute precipitation data series from Warsaw rain gauges R09

R9			
Curve for $q$	$K(q,1)$	$\alpha$	$C_1$
1.10	-1.397	0.745	0.387
1.20	-1.084	0.789	0.384
1.30	-0.895	0.792	0.384
1.40	-0.757	0.788	0.385
1.50	-0.648	0.719	0.391
1.60	-0.557	0.728	0.393
1.70	-0.479	0.734	0.394
1.80	-0.411	0.736	0.396
1.90	-0.350	0.735	0.398
2.00	-0.296	0.623	0.415
2.10	-0.247	0.633	0.416
Average		0.729	0.395
Standard deviation		0.057	0.011

**Table VI.10a.** Critical moments  $q_{min}$  and  $q_{max}$  estimated for selected values of order moment  $q$ , obtained for 1-minute precipitation data series from Warsaw rain gauges R10

R10						
Curve for $q$	Minimal critical moment $q_{min}$			Maximal critical moment $q_{max}$		
	$\log(\eta)$	$\eta$	$q_{min} = q\eta$	$\log(\eta)$	$\eta$	$q_{max} = q\eta$
0.90	0.0	1.00	0.90	0.5	3.16	2.85
1.10	-0.1	0.79	0.87	0.4	2.51	2.76
1.20	-0.1	0.79	0.95	0.4	2.51	3.01
1.30	-0.1	0.79	1.03	0.3	2.00	2.59
1.40	-0.1	0.79	1.11	0.3	2.00	2.79
1.50	-0.2	0.63	0.95	0.3	2.00	2.99
1.60	-0.2	0.63	1.01	0.3	2.00	3.19
1.70	-0.2	0.63	1.07	0.3	2.00	3.39
1.80	-0.2	0.63	1.14	0.3	2.00	3.59
1.90	-0.2	0.63	1.20	0.2	1.58	3.01
2.00	-0.3	0.50	1.00	0.2	1.58	3.17
2.10	-0.3	0.50	1.05	0.2	1.58	3.33
Average			1.02	Average		3.06
Standard deviation			0.10	Standard deviation		0.29

**Table VI.10b.** Lévy indexes  $\alpha$  and the mean values of process codimension  $C_1$  calculations for 1-minute precipitation data series from Warsaw rain gauges R10

R10			
Curve for $q$	$K(q,1)$	$\alpha$	$C_1$
1.10	-1.396	0.737	0.388
1.20	-1.082	0.732	0.387
1.30	-0.894	0.785	0.385
1.40	-0.757	0.781	0.386
1.50	-0.648	0.710	0.392
1.60	-0.557	0.709	0.395
1.70	-0.479	0.706	0.397
1.80	-0.411	0.700	0.400
1.90	-0.350	0.726	0.399
2.00	-0.296	0.647	0.412
2.10	-0.246	0.649	0.413
Average		0.717	0.396
Standard deviation		0.044	0.010

**Table VI.11a.** Critical moments  $q_{min}$  and  $q_{max}$  estimated for selected values of order moment  $q$ , obtained for 1-minute precipitation data series from Warsaw rain gauges R11

R11						
Curve for $q$	Minimal critical moment $q_{min}$			Maximal critical moment $q_{max}$		
	$\log(\eta)$	$\eta$	$q_{min} = q\eta$	$\log(\eta)$	$\eta$	$q_{max} = q\eta$
0.90	0.0	1.00	0.90	0.4	2.51	2.26
1.10	-0.1	0.79	0.87	0.4	2.51	2.76
1.20	-0.1	0.79	0.95	0.3	2.00	2.39
1.30	-0.1	0.79	1.03	0.3	2.00	2.59
1.40	-0.1	0.79	1.11	0.3	2.00	2.79
1.50	-0.1	0.79	1.19	0.3	2.00	2.99
1.60	-0.2	0.63	1.01	0.3	2.00	3.19
1.70	-0.2	0.63	1.07	0.3	2.00	3.39
1.80	-0.2	0.63	1.14	0.3	2.00	3.59
1.90	-0.2	0.63	1.20	0.2	1.58	3.01
2.00	-0.3	0.50	1.00	0.2	1.58	3.17
2.10	-0.3	0.50	1.05	0.2	1.58	3.33
Average			1.04	Average		2.96
Standard deviation			0.10	Standard deviation		0.41

**Table VI.11b.** Lévy indexes  $\alpha$  and the mean values of process codimension  $C_1$  calculations for 1-minute precipitation data series from Warsaw rain gauges R11

R11			
Curve for $q$	$K(q,1)$	$\alpha$	$C_1$
1.10	-1.396	0.737	0.388
1.20	-1.082	0.732	0.387
1.30	-0.894	0.785	0.385
1.40	-0.757	0.781	0.386
1.50	-0.648	0.773	0.387
1.60	-0.557	0.709	0.395
1.70	-0.479	0.706	0.397
1.80	-0.411	0.700	0.400
1.90	-0.350	0.726	0.399
2.00	-0.296	0.647	0.412
2.10	-0.246	0.649	0.413
Average		0.722	0.395
Standard deviation		0.047	0.010

**Table VI.12a.** Critical moments  $q_{min}$  and  $q_{max}$  estimated for selected values of order moment  $q$ , obtained for 1-minute precipitation data series from Warsaw rain gauges R12

R12						
Curve for $q$	Minimal critical moment $q_{min}$			Maximal critical moment $q_{max}$		
	$\log(\eta)$	$\eta$	$q_{min} = q\eta$	$\log(\eta)$	$\eta$	$q_{max} = q\eta$
0.90	0.0	1.00	0.90	0.4	2.51	2.26
1.10	-0.1	0.79	0.87	0.4	2.51	2.76
1.20	-0.1	0.79	0.95	0.3	2.00	2.39
1.30	-0.1	0.79	1.03	0.3	2.00	2.59
1.40	-0.1	0.79	1.11	0.3	2.00	2.79
1.50	-0.1	0.79	1.19	0.3	2.00	2.99
1.60	-0.2	0.63	1.01	0.3	2.00	3.19
1.70	-0.2	0.63	1.07	0.3	2.00	3.39
1.80	-0.2	0.63	1.14	0.3	2.00	3.59
1.90	-0.2	0.63	1.20	0.3	2.00	3.79
2.00	-0.2	0.63	1.26	0.2	1.58	3.17
2.10	-0.2	0.63	1.33	0.2	1.58	3.33
Average			1.09	Average		3.02
Standard deviation			0.14	Standard deviation		0.47

**Table VI.12b.** Lévy indexes  $\alpha$  and the mean values of process codimension  $C_1$  calculations for 1-minute precipitation data series from Warsaw rain gauges R12

R12			
Curve for $q$	$K(q,1)$	$\alpha$	$C_1$
1.10	-1.414	0.824	0.371
1.20	-1.099	0.876	0.368
1.30	-0.909	0.880	0.367
1.40	-0.770	0.876	0.368
1.50	-0.660	0.866	0.370
1.60	-0.568	0.792	0.378
1.70	-0.488	0.788	0.381
1.80	-0.418	0.781	0.384
1.90	-0.356	0.772	0.388
2.00	-0.301	0.809	0.385
2.10	-0.250	0.802	0.388
Average		0.824	0.377
Standard deviation		0.042	0.009

**Table VI.13a.** Critical moments  $q_{min}$  and  $q_{max}$  estimated for selected values of order moment  $q$ , obtained for 1-minute precipitation data series from Warsaw rain gauges R13

R13						
Curve for $q$	Minimal critical moment $q_{min}$			Maximal critical moment $q_{max}$		
	$\log(\eta)$	$\eta$	$q_{min} = q\eta$	$\log(\eta)$	$\eta$	$q_{max} = q\eta$
0.90	-0.1	0.79	0.71	0.5	3.16	2.85
1.10	-0.1	0.79	0.87	0.4	2.51	2.76
1.20	-0.2	0.63	0.76	0.3	2.00	2.39
1.30	-0.2	0.63	0.82	0.3	2.00	2.59
1.40	-0.2	0.63	0.88	0.3	2.00	2.79
1.50	-0.2	0.63	0.95	0.2	1.58	2.38
1.60	-0.2	0.63	1.01	0.2	1.58	2.54
1.70	-0.2	0.63	1.07	0.2	1.58	2.69
1.80	-0.2	0.63	1.14	0.2	1.58	2.85
1.90	-0.3	0.50	0.95	0.2	1.58	3.01
2.00	-0.3	0.50	1.00	0.2	1.58	3.17
2.10	-0.3	0.50	1.05	0.2	1.58	3.33
Average			0.94	Average		2.78
Standard deviation			0.13	Standard deviation		0.29

**Table VI.13b.** Lévy indexes  $\alpha$  and the mean values of process codimension  $C_1$  calculations for 1-minute precipitation data series from Warsaw rain gauges R13

R13			
Curve for $q$	$K(q,1)$	$\alpha$	$C_1$
1.10	-1.365	0.718	0.418
1.20	-1.049	0.709	0.419
1.30	-0.859	0.714	0.421
1.40	-0.720	0.714	0.424
1.50	-0.610	0.741	0.425
1.60	-0.519	0.743	0.427
1.70	-0.441	0.741	0.429
1.80	-0.373	0.736	0.432
1.90	-0.313	0.666	0.443
2.00	-0.259	0.665	0.445
2.10	-0.211	0.663	0.447
Average		0.710	0.430
Standard deviation		0.032	0.010

**Table VI.14a.** Critical moments  $q_{min}$  and  $q_{max}$  estimated for selected values of order moment  $q$ , obtained for 1-minute precipitation data series from Warsaw rain gauges R14

R14						
Curve for $q$	Minimal critical moment $q_{min}$			Maximal critical moment $q_{max}$		
	$\log(\eta)$	$\eta$	$q_{min} = q\eta$	$\log(\eta)$	$\eta$	$q_{max} = q\eta$
0.90	0.0	1.00	0.90	0.4	2.51	2.26
1.10	-0.1	0.79	0.87	0.3	2.00	2.19
1.20	-0.1	0.79	0.95	0.3	2.00	2.39
1.30	-0.1	0.79	1.03	0.3	2.00	2.59
1.40	-0.1	0.79	1.11	0.3	2.00	2.79
1.50	-0.1	0.79	1.19	0.2	1.58	2.38
1.60	-0.2	0.63	1.01	0.2	1.58	2.54
1.70	-0.2	0.63	1.07	0.2	1.58	2.69
1.80	-0.2	0.63	1.14	0.2	1.58	2.85
1.90	-0.2	0.63	1.20	0.1	1.26	2.39
2.00	-0.2	0.63	1.26	0.1	1.26	2.52
2.10	-0.3	0.50	1.05	0.1	1.26	2.64
Average			1.07	Average		2.52
Standard deviation			0.12	Standard deviation		0.21

**Table VI.14b.** Lévy indexes  $\alpha$  and the mean values of process codimension  $C_1$  calculations for 1-minute precipitation data series from Warsaw rain gauges R14

R14			
Curve for $q$	$K(q,1)$	$\alpha$	$C_1$
1.10	-1.413	0.859	0.371
1.20	-1.097	0.864	0.370
1.30	-0.906	0.859	0.371
1.40	-0.766	0.847	0.373
1.50	-0.655	0.903	0.371
1.60	-0.563	0.807	0.381
1.70	-0.483	0.808	0.383
1.80	-0.414	0.806	0.386
1.90	-0.352	0.806	0.387
2.00	-0.297	0.807	0.389
2.10	-0.247	0.705	0.404
Average		0.825	0.380
Standard deviation		0.051	0.011

**Table VI.16a.** Critical moments  $q_{min}$  and  $q_{max}$  estimated for selected values of order moment  $q$ , obtained for 1-minute precipitation data series from Warsaw rain gauges R16

R16						
Curve for $q$	Minimal critical moment $q_{min}$			Maximal critical moment $q_{max}$		
	$\log(\eta)$	$\eta$	$q_{min} = q\eta$	$\log(\eta)$	$\eta$	$q_{max} = q\eta$
0.90	0.0	1.00	0.90	0.5	3.16	2.85
1.10	-0.1	0.79	0.87	0.4	2.51	2.76
1.20	-0.1	0.79	0.95	0.3	2.00	2.39
1.30	-0.1	0.79	1.03	0.3	2.00	2.59
1.40	-0.1	0.79	1.11	0.3	2.00	2.79
1.50	-0.2	0.63	0.95	0.3	2.00	2.99
1.60	-0.2	0.63	1.01	0.2	1.58	2.54
1.70	-0.2	0.63	1.07	0.2	1.58	2.69
1.80	-0.2	0.63	1.14	0.2	1.58	2.85
1.90	-0.2	0.63	1.20	0.2	1.58	3.01
2.00	-0.3	0.50	1.00	0.2	1.58	3.17
2.10	-0.3	0.50	1.05	0.2	1.58	3.33
Average			1.02	Average		2.83
Standard deviation			0.10	Standard deviation		0.27

**Table VI.16b.** Lévy indexes  $\alpha$  and the mean values of process codimension  $C_1$  calculations for 1-minute precipitation data series from Warsaw rain gauges R16

R16			
Curve for $q$	$K(q,1)$	$\alpha$	$C_1$
1.10	-1.418	0.748	0.369
1.20	-1.105	0.803	0.366
1.30	-0.916	0.805	0.365
1.40	-0.778	0.799	0.366
1.50	-0.669	0.723	0.373
1.60	-0.577	0.736	0.374
1.70	-0.499	0.742	0.376
1.80	-0.430	0.743	0.378
1.90	-0.369	0.741	0.380
2.00	-0.315	0.658	0.393
2.10	-0.265	0.659	0.395
Average		0.742	0.376
Standard deviation		0.050	0.010

**Table VI.17a.** Critical moments  $q_{min}$  and  $q_{max}$  estimated for selected values of order moment  $q$ , obtained for 1-minute precipitation data series from Warsaw rain gauges R17

R17						
Curve for $q$	Minimal critical moment $q_{min}$			Maximal critical moment $q_{max}$		
	$\log(\eta)$	$\eta$	$q_{min} = q\eta$	$\log(\eta)$	$\eta$	$q_{max} = q\eta$
0.90	0.0	1.00	0.90	0.4	2.51	2.26
1.10	-0.1	0.79	0.87	0.3	2.00	2.19
1.20	-0.1	0.79	0.95	0.3	2.00	2.39
1.30	-0.1	0.79	1.03	0.3	2.00	2.59
1.40	-0.1	0.79	1.11	0.3	2.00	2.79
1.50	-0.2	0.63	0.95	0.2	1.58	2.38
1.60	-0.2	0.63	1.01	0.2	1.58	2.54
1.70	-0.2	0.63	1.07	0.2	1.58	2.69
1.80	-0.2	0.63	1.14	0.2	1.58	2.85
1.90	-0.2	0.63	1.20	0.2	1.58	3.01
2.00	-0.2	0.63	1.26	0.2	1.58	3.17
2.10	-0.3	0.50	1.05	0.2	1.58	3.33
Average			1.05	Average		2.68
Standard deviation			0.12	Standard deviation		0.36

**Table VI.17b.** Lévy indexes  $\alpha$  and the mean values of process codimension  $C_1$  calculations for 1-minute precipitation data series from Warsaw rain gauges R17

R17			
Curve for $q$	$K(q,1)$	$\alpha$	$C_1$
1.10	-1.399	0.760	0.385
1.20	-1.085	0.759	0.384
1.30	-0.896	0.749	0.385
1.40	-0.758	0.733	0.388
1.50	-0.648	0.708	0.392
1.60	-0.557	0.712	0.394
1.70	-0.479	0.710	0.397
1.80	-0.411	0.704	0.400
1.90	-0.350	0.695	0.403
2.00	-0.296	0.684	0.406
2.10	-0.248	0.620	0.416
Average		0.712	0.395
Standard deviation		0.040	0.010

**Table VI.18a.** Critical moments  $q_{min}$  and  $q_{max}$  estimated for selected values of order moment  $q$ , obtained for 1-minute precipitation data series from Warsaw rain gauges R18

R18						
Curve for $q$	Minimal critical moment $q_{min}$			Maximal critical moment $q_{max}$		
	$\log(\eta)$	$\eta$	$q_{min} = q\eta$	$\log(\eta)$	$\eta$	$q_{max} = q\eta$
0.90	0.0	1.00	0.90	0.5	3.16	2.85
1.10	0.0	1.00	1.10	0.4	2.51	2.76
1.20	-0.1	0.79	0.95	0.4	2.51	3.01
1.30	-0.1	0.79	1.03	0.4	2.51	3.27
1.40	-0.1	0.79	1.11	0.3	2.00	2.79
1.50	-0.1	0.79	1.19	0.3	2.00	2.99
1.60	-0.1	0.79	1.27	0.3	2.00	3.19
1.70	-0.2	0.63	1.07	0.3	2.00	3.39
1.80	-0.2	0.63	1.14	0.2	1.58	2.85
1.90	-0.2	0.63	1.20	0.2	1.58	3.01
2.00	-0.2	0.63	1.26	0.2	1.58	3.17
2.10	-0.3	0.50	1.05	0.2	1.58	3.33
Average			1.11	Average		3.05
Standard deviation			0.11	Standard deviation		0.22

**Table VI.18b.** Lévy indexes  $\alpha$  and the mean values of process codimension  $C_1$  calculations for 1-minute precipitation data series from Warsaw rain gauges R18

R18			
Curve for $q$	$K(q,1)$	$\alpha$	$C_1$
1.10	-1.386	0.891	0.394
1.20	-1.072	0.826	0.393
1.30	-0.883	0.816	0.393
1.40	-0.745	0.887	0.390
1.50	-0.634	0.879	0.391
1.60	-0.542	0.866	0.394
1.70	-0.462	0.789	0.404
1.80	-0.392	0.810	0.405
1.90	-0.330	0.811	0.408
2.00	-0.273	0.809	0.410
2.10	-0.222	0.713	0.427
Average		0.827	0.401
Standard deviation		0.052	0.011

**Table VI.19a.** Critical moments  $q_{min}$  and  $q_{max}$  estimated for selected values of order moment  $q$ , obtained for 1-minute precipitation data series from Warsaw rain gauges R19

R19						
Curve for $q$	Minimal critical moment $q_{min}$			Maximal critical moment $q_{max}$		
	$\log(\eta)$	$\eta$	$q_{min} = q\eta$	$\log(\eta)$	$\eta$	$q_{max} = q\eta$
0.90	0.0	1.00	0.90	0.5	3.16	2.85
1.10	0.0	1.00	1.10	0.4	2.51	2.76
1.20	-0.1	0.79	0.95	0.3	2.00	2.39
1.30	-0.1	0.79	1.03	0.3	2.00	2.59
1.40	-0.1	0.79	1.11	0.3	2.00	2.79
1.50	-0.1	0.79	1.19	0.3	2.00	2.99
1.60	-0.1	0.79	1.27	0.3	2.00	3.19
1.70	-0.1	0.79	1.35	0.3	2.00	3.39
1.80	-0.2	0.63	1.14	0.2	1.58	2.85
1.90	-0.2	0.63	1.20	0.2	1.58	3.01
2.00	-0.2	0.63	1.26	0.2	1.58	3.17
2.10	-0.2	0.63	1.33	0.2	1.58	3.33
Average			1.15	Average		2.94
Standard deviation			0.14	Standard deviation		0.30

**Table VI.19b.** Lévy indexes  $\alpha$  and the mean values of process codimension  $C_1$  calculations for 1-minute precipitation data series from Warsaw rain gauges R19

R19			
Curve for $q$	$K(q,1)$	$\alpha$	$C_1$
1.10	-1.389	0.927	0.391
1.20	-1.077	0.880	0.387
1.30	-0.888	0.896	0.384
1.40	-0.751	0.901	0.383
1.50	-0.641	0.899	0.383
1.60	-0.549	0.892	0.385
1.70	-0.470	0.879	0.388
1.80	-0.400	0.810	0.398
1.90	-0.338	0.815	0.400
2.00	-0.281	0.817	0.402
2.10	-0.230	0.815	0.405
Average		0.867	0.391
Standard deviation		0.043	0.008

**Table VI.20a.** Critical moments  $q_{min}$  and  $q_{max}$  estimated for selected values of order moment  $q$ , obtained for 1-minute precipitation data series from Warsaw rain gauges R20

R20						
Curve for $q$	Minimal critical moment $q_{min}$			Maximal critical moment $q_{max}$		
	$\log(\eta)$	$\eta$	$q_{min} = q\eta$	$\log(\eta)$	$\eta$	$q_{max} = q\eta$
0.90	-0.1	0.79	0.71	0.4	2.51	2.26
1.10	-0.1	0.79	0.87	0.4	2.51	2.76
1.20	-0.1	0.79	0.95	0.3	2.00	2.39
1.30	-0.1	0.79	1.03	0.3	2.00	2.59
1.40	-0.1	0.79	1.11	0.3	2.00	2.79
1.50	-0.1	0.79	1.19	0.3	2.00	2.99
1.60	-0.2	0.63	1.01	0.2	1.58	2.54
1.70	-0.2	0.63	1.07	0.2	1.58	2.69
1.80	-0.2	0.63	1.14	0.2	1.58	2.85
1.90	-0.2	0.63	1.20	0.2	1.58	3.01
2.00	-0.2	0.63	1.26	0.2	1.58	3.17
2.10	-0.3	0.50	1.05	0.1	1.26	2.64
Average			1.05	Average		2.73
Standard deviation			0.15	Standard deviation		0.26

**Table VI.20b.** Lévy indexes  $\alpha$  and the mean values of process codimension  $C_1$  calculations for 1-minute precipitation data series from Warsaw rain gauges R20

R20			
Curve for $q$	$K(q,1)$	$\alpha$	$C_1$
1.10	-1.391	0.862	0.390
1.20	-1.076	0.924	0.387
1.30	-0.885	0.926	0.386
1.40	-0.745	0.919	0.387
1.50	-0.633	0.906	0.390
1.60	-0.540	0.850	0.398
1.70	-0.459	0.857	0.400
1.80	-0.389	0.858	0.403
1.90	-0.326	0.856	0.405
2.00	-0.270	0.851	0.408
2.10	-0.219	0.736	0.427
Average		0.868	0.398
Standard deviation		0.054	0.012

**Table VI.21a.** Critical moments  $q_{min}$  and  $q_{max}$  estimated for selected values of order moment  $q$ , obtained for 1-minute precipitation data series from Warsaw rain gauges R21

R21						
Curve for $q$	Minimal critical moment $q_{min}$			Maximal critical moment $q_{max}$		
	$\log(\eta)$	$\eta$	$q_{min} = q\eta$	$\log(\eta)$	$\eta$	$q_{max} = q\eta$
0.90	0.0	1.00	0.90	0.4	2.51	2.26
1.10	-0.1	0.79	0.87	0.3	2.00	2.19
1.20	-0.1	0.79	0.95	0.3	2.00	2.39
1.30	-0.1	0.79	1.03	0.3	2.00	2.59
1.40	-0.1	0.79	1.11	0.3	2.00	2.79
1.50	-0.2	0.63	0.95	0.2	1.58	2.38
1.60	-0.2	0.63	1.01	0.2	1.58	2.54
1.70	-0.2	0.63	1.07	0.2	1.58	2.69
1.80	-0.2	0.63	1.14	0.2	1.58	2.85
1.90	-0.2	0.63	1.20	0.2	1.58	3.01
2.00	-0.2	0.63	1.26	0.2	1.58	3.17
2.10	-0.3	0.50	1.05	0.1	1.26	2.64
Average			1.05	Average		2.63
Standard deviation			0.12	Standard deviation		0.30

**Table VI.21b.** Lévy indexes  $\alpha$  and the mean values of process codimension  $C_1$  calculations for 1-minute precipitation data series from Warsaw rain gauges R21

R21			
Curve for $q$	$K(q,1)$	$\alpha$	$C_1$
1.10	-1.399	0.978	0.381
1.20	-1.082	0.988	0.379
1.30	-0.890	0.987	0.379
1.40	-0.748	0.976	0.381
1.50	-0.635	0.901	0.389
1.60	-0.540	0.912	0.391
1.70	-0.459	0.917	0.394
1.80	-0.387	0.917	0.397
1.90	-0.323	0.912	0.401
2.00	-0.266	0.905	0.404
2.10	-0.215	0.789	0.423
Average		0.926	0.393
Standard deviation		0.058	0.013

**Table VI.22a.** Critical moments  $q_{min}$  and  $q_{max}$  estimated for selected values of order moment  $q$ , obtained for 1-minute precipitation data series from Warsaw rain gauges R22

R22						
Curve for $q$	Minimal critical moment $q_{min}$			Maximal critical moment $q_{max}$		
	$\log(\eta)$	$\eta$	$q_{min} = q\eta$	$\log(\eta)$	$\eta$	$q_{max} = q\eta$
0.90	0.0	1.00	0.90	0.4	2.51	2.26
1.10	-0.1	0.79	0.87	0.4	2.51	2.76
1.20	-0.1	0.79	0.95	0.3	2.00	2.39
1.30	-0.1	0.79	1.03	0.3	2.00	2.59
1.40	-0.2	0.63	0.88	0.3	2.00	2.79
1.50	-0.2	0.63	0.95	0.2	1.58	2.38
1.60	-0.2	0.63	1.01	0.2	1.58	2.54
1.70	-0.2	0.63	1.07	0.2	1.58	2.69
1.80	-0.2	0.63	1.14	0.2	1.58	2.85
1.90	-0.2	0.63	1.20	0.2	1.58	3.01
2.00	-0.3	0.50	1.00	0.2	1.58	3.17
2.10	-0.3	0.50	1.05	0.1	1.26	2.64
Average			1.01	Average		2.67
Standard deviation			0.10	Standard deviation		0.27

**Table VI.22b.** Lévy indexes  $\alpha$  and the mean values of process codimension  $C_1$  calculations for 1-minute precipitation data series from Warsaw rain gauges R22

R22			
Curve for $q$	$K(q,1)$	$\alpha$	$C_1$
1.10	-1.389	0.784	0.394
1.20	-1.074	0.844	0.391
1.30	-0.883	0.841	0.392
1.40	-0.744	0.763	0.398
1.50	-0.634	0.778	0.400
1.60	-0.542	0.786	0.402
1.70	-0.463	0.789	0.404
1.80	-0.393	0.788	0.406
1.90	-0.332	0.784	0.409
2.00	-0.277	0.704	0.422
2.10	-0.227	0.687	0.426
Average		0.777	0.404
Standard deviation		0.048	0.011

**Table VI.23a.** Critical moments  $q_{min}$  and  $q_{max}$  estimated for selected values of order moment  $q$ , obtained for 1-minute precipitation data series from Warsaw rain gauges R23

R23						
Curve for $q$	Minimal critical moment $q_{min}$			Maximal critical moment $q_{max}$		
	$\log(\eta)$	$\eta$	$q_{min} = q\eta$	$\log(\eta)$	$\eta$	$q_{max} = q\eta$
0.90	-0.1	0.79	0.71	0.4	2.51	2.26
1.10	-0.1	0.79	0.87	0.3	2.00	2.19
1.20	-0.1	0.79	0.95	0.3	2.00	2.39
1.30	-0.1	0.79	1.03	0.3	2.00	2.59
1.40	-0.1	0.79	1.11	0.3	2.00	2.79
1.50	-0.2	0.63	0.95	0.3	2.00	2.99
1.60	-0.2	0.63	1.01	0.2	1.58	2.54
1.70	-0.2	0.63	1.07	0.2	1.58	2.69
1.80	-0.2	0.63	1.14	0.2	1.58	2.85
1.90	-0.2	0.63	1.20	0.2	1.58	3.01
2.00	-0.2	0.63	1.26	0.2	1.58	3.17
2.10	-0.2	0.63	1.33	0.1	1.26	2.64
Average			1.05	Average		2.68
Standard deviation			0.17	Standard deviation		0.30

**Table VI.23b.** Lévy indexes  $\alpha$  and the mean values of process codimension  $C_1$  calculations for 1-minute precipitation data series from Warsaw rain gauges R23

R23			
Curve for $q$	$K(q,1)$	$\alpha$	$C_1$
1.10	-1.390	0.770	0.393
1.20	-1.077	0.784	0.391
1.30	-0.888	0.789	0.390
1.40	-0.751	0.786	0.390
1.50	-0.642	0.711	0.397
1.60	-0.552	0.717	0.399
1.70	-0.474	0.724	0.400
1.80	-0.405	0.727	0.402
1.90	-0.345	0.727	0.404
2.00	-0.290	0.724	0.406
2.10	-0.241	0.717	0.409
Average		0.743	0.398
Standard deviation		0.032	0.007

**Table VI.24a.** Critical moments  $q_{min}$  and  $q_{max}$  estimated for selected values of order moment  $q$ , obtained for 1-minute precipitation data series from Warsaw rain gauges R24

R24						
Curve for $q$	Minimal critical moment $q_{min}$			Maximal critical moment $q_{max}$		
	$\log(\eta)$	$\eta$	$q_{min} = q\eta$	$\log(\eta)$	$\eta$	$q_{max} = q\eta$
0.90	0.00	1.00	0.90	0.4	2.51	2.26
1.10	-0.10	0.79	0.87	0.3	2.00	2.19
1.20	-0.10	0.79	0.95	0.3	2.00	2.39
1.30	-0.10	0.79	1.03	0.3	2.00	2.59
1.40	-0.10	0.79	1.11	0.3	2.00	2.79
1.50	-0.20	0.63	0.95	0.3	2.00	2.99
1.60	-0.20	0.63	1.01	0.3	2.00	3.19
1.70	-0.20	0.63	1.07	0.2	1.58	2.69
1.80	-0.20	0.63	1.14	0.2	1.58	2.85
1.90	-0.20	0.63	1.20	0.2	1.58	3.01
2.00	-0.20	0.63	1.26	0.2	1.58	3.17
2.10	-0.20	0.63	1.33	0.2	1.58	3.33
Average			1.07	Average		2.79
Standard deviation			0.14	Standard deviation		0.37

**Table VI.24b.** Lévy indexes  $\alpha$  and the mean values of process codimension  $C_1$  calculations for 1-minute precipitation data series from Warsaw rain gauges R24

R24			
Curve for $q$	$K(q,1)$	$\alpha$	$C_1$
1.10	-1.390	0.770	0.393
1.20	-1.077	0.784	0.391
1.30	-0.888	0.789	0.390
1.40	-0.751	0.786	0.390
1.50	-0.642	0.711	0.397
1.60	-0.552	0.711	0.399
1.70	-0.474	0.724	0.400
1.80	-0.405	0.727	0.402
1.90	-0.345	0.727	0.404
2.00	-0.290	0.724	0.406
2.10	-0.241	0.719	0.409
Average		0.743	0.398
Standard deviation		0.032	0.007